Universitat de Girona

CHELATION-ASSISTED METAL-CATALYZED FUNCTIONALIZATION OF STRONG CSP2-H/HETEROATOM BONDS: TRAPPING INTERMEDIATE SPECIES AND UNVEILING MECHANISTIC DETAILS

Lorena Capdevila Güell

DOCTORAL THESIS

CHELATION-ASSISTED METAL-CATALYZED FUNCTIONALIZATION OF STRONG C$_{sp2}$-H / HETEROATOM BONDS: TRAPPING INTERMEDIATE SPECIES AND UNVEILING MECHANISTIC DETAILS
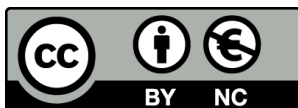
LORENA CAPDEVILA i GÜELL

2022

Doctoral programme in Chemistry

Supervised by Dr. Xavi Ribas Salamaña
Tutor: Dr. Xavi Ribas Salamaña

Presented in partial fulfilment of the requirements for a doctoral degree from the Universitat de Girona.

Dr. Xavi Ribas Salamaña from Universitat de Girona.

DECLARE:

That the thesis entitled "Chelation-assisted metal-catalyzed functionalization of strong C_{sp2}-H/Heteroatom bonds: trapping intermediate species and unveiling mechanistic details", presented by Lorena Capdevila i Güell to obtain a doctoral degree, has been completed under my supervision and meets the requirements to opt for an International Doctorate.

For all intents and purposes, I hereby sign this document.

Dr Xavi Ribas Salamaña

Girona, 15th December 2021

Als meus pares, l'Èric, la Sílvia i la Sira
als avis
i en Carlos

LIST OF PUBLICATIONS

This thesis is based on a compendium of the following publications:

Chapter III

''Cobalt-catalyzed cross-coupling reactions" **Lorena Capdevila**, Xavi Ribas. In: *Chemistry of organocobalt compounds*; Ilan Marek and Corinne Gosmini (eds); Wiley & Sons **2022**, DOI:10.1002/9780470682531.PAT0995.

Chapter IV

''C_{sp2}–H amination reactions mediated by metastable Oh masked aryl–Co^{III}-nitrene species'', **Lorena Capdevila**, Marc Montilla, Oriol Planas, Artur Brotons, Pedro Salvador, Vlad Martin-Diaconescu, Teodor Parella, Josep M. Luis, Xavi Ribas.
Submitted

Chapter V

''Chemodivergent Nickel(0)-Catalyzed Arene C−F Activation with Alkynes: Unprecedented C−F/C−H Double Insertion'', **Lorena Capdevila**, Tjark H. Meyer, Steven Roldán-Gómez, Josep M. Luis, Lutz Ackermann and Xavi Ribas. *ACS Catal.* **2019**, 9,11074-11081. (Impact factor: 13.084, position 12/159 in chemistry, 1st quartile)

Chapter VI

''Nickel-catalyzed C_{sp2}-OMe functionalization for chemoselective aromatic homologation en route to nanographenes'' **Lorena Capdevila**, Judith Sala, Lutz Ackermann, Xavi Ribas.
Manuscript accepted for publication in Chem. Eur. J. (doi.org/10.1002/chem.202200625)

Chapter VII

''Silver(I)-Catalyzed C−X, C−C, C−N, and C−O Cross-Couplings Using Aminoquinoline Directing Group via Elusive Aryl-Ag(III) Species'', **Lorena Capdevila**, Erik Andris, Anamarija Briš, Màrius Tarrés, Steven Roldán-Gómez, Jana Roithová and Xavi Ribas. ACS Catal. **2018**, 8, 10430-10436. (Impact factor: 13.084, position 11/148 in chemistry, 1st quartile)

Publications not included in this thesis:

'High-Valent Cu, Ag, and Au Coordination Compounds" Xavi Ribas, Lorena Capdevila, Pau Font. In: *Comprehensive Coordination Chemistry III*; Constable, E. C., Parkin, G., Que Jr, L. (eds); Volume 6, Elsevier, **2021** (pp 474–516)

''C−F Activation for C(sp2)−C(sp3) Cross-Coupling by a Secondary Phosphine Oxide (SPO)-Nickel Complex'' Valentin Müller, Debasish Ghorai, Lorena Capdevila, Antonis M. Messinis, Xavi Ribas and Lutz Ackermann. *Org. Lett.* **2020**, 22, 17, 7034–7040.

LIST OF ABBREVIATIONS

Å	Ångström
μ_{eff}	Effective magnetic moment
σ_p	Hammet *para*-substituted constant
AcO	Acetate
AcOEt	Ethyl acetat
AcOH	Acetic acid
AQ	Aminoquinoline
Ar	Aryl
atm	Atmosphere
BDE	Bond dissociation energy
Bipy	2,2'-bipyridine
Bu	Butyl
Cat	Catalyst
cod	1,5-Cyclooctadiene
CMD	Concerted Metalation-Deprotonation
Conv.	Conversion
COSY	Correlation Spectroscopy
Cp^*	1,2,3,4,5-pentamethylcyclopentadiene
Cy	Cyclohexyl
DCE	Dichloroethane
DDQ	2,3-dichloro-5,6-ddicyano-1,4-benzoquinone
deg	Degrees
DFT	Density Functional Theory
DG	Directing Group
DME	Dimethoxyethane
DMPU	N,N'-dimethylpropyleneurea
DMSO	Dimethylsulfoxide
DPA	Diphenylacetylene
EDG	Electron-Donating Group
EPR	Electron Paramagnetic Resonance spectroscopy
Equiv.	Equivalent
ESI-MS	Electrospray Ionization Mass spectrometry
Et	Ethyl
EWG	Electron-Withdrawing Group
EXAFS	Extended X-ray Absorption Fine Structure
FT-IR	Fourier Transform Infrared spectroscopy
h	Hour
HFIP	1,1,1,3,3,3-hexafluoroisopropanol
HMBC	Heteronuclear multiple-bond correlation spectroscopy
HOMO	Highest occupied molecular orbital
HRMS	High-resolution mass spectrometry
HSQC	Heteronuclear single-quantum correlation spectroscopy
ICP-MS	Inductively coupled plasma mass spectrometry

IR	Infrared spectroscopy
IRPD	Infrared photodissociation spectroscopy
KIE	Kinetic Isotope Effect
L	Ligand
LA	Lewis Acid
LUMO	Lowest unoccupied molecular orbital
M	Metal
m/z	Mass to charge ratio
Me	Methyl
MeCN	Acetonitrile
Min	Minute
MO	Molecular orbital
MS	Mass spectromety
n.d.	Not-detected
NMR	Nuclear Magnetic Resonance
NOESY	Nuclear Overhauser effect spectroscopy
Nuc	Nucleophile
Oh	Octahedral
OTf	Trifluoromethanesulfonate anion
OX	Oxidant
Ph	Phenyl
PivOH	Pivalic acid
Pr	Propyl
Py	Pyridine
Pym	Pyrimidine
Q	Qunioline
QTOF	Quadrupole Time-of-flight
Rds	Rate determining step
Rf	Retardation factor
RT	Room temperatura
SN	Nucleophilic substitution
S$_E$Ar	Electrophilic aromatic substitution
T	Temperature
t	Time
TBAI	Tetrabutylammonium iodide
TEMPO	(2,2,6,6-Tetramethyl-piperidin-1-yl)oxyl
TFA	Trifluoroacetic acid
TFE	2,2,2-Trifluoroethanol
tr	Traces
TS	Transition State
Ts	Tosyl (toluene sulfonyl)
wt	Weight
XAS	X-ray Absorption Spectroscopy
XANES	X-ray Absorption Near Edge Structure
XRD	X-ray Diffraction

ACKNOWLEDGEMENTS

GRAPHICAL ABSTRACT

C–C and C–Heteroatom bond formation reactions

◐—X + Y ⟶ (Co) ⟶ ◐—Y

◐ = aryl, alkenyl, alkyl, alkynyl

X = halide, OTf

---

aryl–Co(III) — *C–H amination* N_3—R → *aryl-N coupling*

via

Co(III) nitrene (Fischer type) → *"masked Co(III) nitrene"*

C–F functionalization R≡R (Ni) → and/or

via

9-membered nickelacyclic species

Chapter VI. Nickel-catalyzed C$_{sp2}$–OMe functionalization for chemoselective aromatic homologation en route to nanographenes (p. 135)

Chapter VII. Silver(I)-catalyzed C-X, C-C, C-N, and C-O cross-coupling using aminoquinoline directing group via elusive aryl-Ag(III) species (p. 145)

TABLE OF CONTENTS

Supplementary Data Information

The material listed below can be found in the attached CD:

- Pdf file of the PhD dissertation

- Pdf file of the Digital Annex containing complete spectroscopic and spectrometric characterization corresponding to Chapters IV, V, VI and VII.

- CIF files for each crystal structure presented in this thesis and they are organized as indicated in the following table:

Chapter	File name
IV	**1-OBzOMe**
IV	**1-OBzOCF$_3$**
IV	**3'-N$_3$(N$_3$)**
IV	**5a-OAc**
IV	**6b-OAc**
IV	**7-OAc**
V	**INT4-E-H**
VI	**4**

LIST OF FIGURES

LIST OF SCHEMES

4

LIST OF TABLES

SUMMARY

The development of novel methodologies for the construction of complex architectures is one of the main objectives in synthetic organic chemistry. In this context, the use of first-row transition metals is a step forward for the construction of variety of organic compounds in a catalytic manner. Although huge advances have been made on cross-coupling reactions using prefunctionalized electrophiles, there is continuous research on using non-prefunctionalized substrates for the direct C–H functionalization. Moreover, the use of more challenging substrates bearing C-F or C-OR groups has also attracted attention. Understanding the fundamental steps that govern such transformations are crucial to facilitate the development of novel and/or improved methodologies. This doctoral dissertation is focused on the use of model substrates to guide the reactivity of first row (Co, Ni) and also second row (Ag) transition metals towards the selective C–Y (Y = H, F, OMe, Halide) functionalization in C–C and C–Heteroatom bond-forming reactions. The coordinative properties of the model substrates will allow the stabilization of organometallic species, thus special attention will be paid to the underlying mechanisms in order to elucidate the crucial steps of these transformations.

In the first part, an update review on the progress achieved in cobalt cross coupling catalysis is presented, highlighting the potential use of cobalt in these transformations as valuable and more sustainable approach for the construction of a broad variety of organic compounds.

Then, this thesis builds upon the mechanistic understanding of the C–H amination transformations using a high-valent cobalt system. The reactivity of well-defined aryl–Co(III) organometallic complex towards inorganic and organic azides is studied. Special focus is devoted to the interaction of the cobalt center with the aliphatic azide and the subsequent aryl–N bond formation step, in order to shed light into the operating mechanism. As a consequence of the stability offered by the model macrocyclic platform, Co(III) complexes featuring the new aryl-N are stabilized. Moreover, complementary DFT studies are crucial to elucidate the elusive intermediate species involved in this transformation, where the key role of the carboxylic acids in stabilizing the aryl-Co^{III}=NR nitrene will be discussed.

Non-cyclic model platforms bearing directing groups are also used to study the Ni-catalyzed C-X functionalization, specifically, for the synthesis of isoquinolones and aromatic homologation products using alkynes. The ability of the 8-aminoquinoline as a bidentate directing group (DG) to assist the challenging selective C–F and C-OMe functionalization under nickel catalysis is demonstrated. The coordination properties provided by the 8-aminoquinoline DG allows the detection and isolation of key double alkyne inserted intermediate species en route to the aromatic homologation products. Moreover, the latter are proved as valid precursor towards the synthesis of nanographene-like compounds, which stands as a novel use of these compounds.

On the last part of this thesis, the 8-aminoquinoline assisted aryl-halide functionalization under silver catalysis is tested using different nucleophiles to afford the formation of C–C and C–Heteroatom cross coupling products. DFT and IRPD-MS studies are useful to elucidate the operating mechanism in rare silver-catalyzed cross-coupling reactions, where the two-electron redox Ag(I)/Ag(III) reactivity is operating.

RESUM

El desenvolupament de noves metodologies per la construcció de compostos elaborats és un dels principals objectius de la química orgànica sintètica. En aquest context, l'ús de metalls de la primera sèrie de transició ha esdevingut un pas endavant per la preparació de diferents compostos orgànics de manera catalítica. Malgrat els importants avenços que s'han realitzat en reaccions d'acoblament creuat utilitzant electròfils prefuncionalitzats, l'ús de substrats no funcionalitzats per la funcionalització directa d'enllaços C-H és encara motiu d'investigació contínua. A més, l'ús de substrats més desafiants que presenten grups C–F o C–OR ha esdevingut també d'elevat interès. Per tal de desenvolupar noves i/o millorades metodologies per dur a terme aquestes reaccions és crucial entendre les etapes fonamentals que governen aquests processos. Aquesta tesi doctoral es focalitza en l'ús de substrats model per tal de guiar la reactivitat de metalls de la primera (Co, Ni) i també de la segona (Ag) sèrie de transició en la funcionalització selectiva d'enllaços C–Y (Y = H, F, OMe, Halur) per la formació d'enllaços C–C i C–Heteroàtom. Les propietats coordinatives que presenten els substrats models permetrà l'estabilització d'espècies organometàl·liques, de manera que aquesta tesi també es focalitzarà en esbrinar el mecanisme de les reaccions per tal d'elucidar les etapes principals d'aquestes transformacions.

En la primera part es presenta una actualització del progrés fet en el camp de reaccions d'acoblament creuat catalitzades per cobalt, destacant el potencial d'aquest metall com una alternativa més sostenible per la preparació d'una gran varietat de compostos orgànics.

Posteriorment, aquesta tesi es focalitza en esbrinar el mecanisme que opera en els processos d'aminació a través de l'activació d'enllaços C–H utilitzant espècies de cobalt en alt estat d'oxidació. Per a fer-ho, s'estudia la reactivitat d'espècies organometàl·liques aril–Co(III) ben definides amb azides inorgàniques i orgàniques. Es dedica especial atenció en entendre la interacció del centre metàl·lic de cobalt amb les azides alifàtiques i la posterior formació de l'enllaç C–N per tal d'entendre'n el mecanisme de reacció. Degut a l'estabilitat proporcionada pel model macrocíclic, s'han estabilitzat i aïllat diferents complexos de Co(III) que contenen el nou enllaç aril-N. S'han realitzat estudis complementaris de DFT, que han estat crucials per elucidar intermedis difícils de detectar implicats en aquest procés, on es discutirà també el paper clau dels àcids carboxílics en l'estabilització de les espècies aril–Co(III)=nitrè.

Per altra banda, s'utilitzen plataformes model no cícliques que contenen grups directors per a estudiar la funcionalització d'enllaços C-X catalitzades per níquel, específicament, per a la síntesi d'isoquinolnones i productes d'homologació aromàtica utilitzant alquins. Es demostra l'habilitat de la 8-aminoquinolina com a grup director bidentat (DG) per assistir la desafiant funcionalització d'enllaços C-F i C-OMe. Les propietats de coordinació de la 8-aminoquinolina permeten la detecció i estabilització d'espècies intermèdies que contenen dos alquins insertats, claus per la síntesi de productes d'homologació aromàtics. Es mostra que aquests compostos poden ser usats per a la preparació de materials similars als nanografens, demostrant així una nova aplicació dels productes sintetitzats.

La última part d'aquesta tesi, es centra en la funcionalització d'enllaços aril–X catalitzada per plata utilitzant diferents nucleòfils que permeten la formació de nous enllaços C–C i C–Heteròatom mitjançant reaccions d'acoblament creuat. S'utilitzen estudis de DFT i IRDP-MS per esbrinar el mecanisme que opera en aquestes reaccions catalitzades per plata, on s'evidencia la implicació de cicles redox Ag(I)/Ag(III) en aquesta reactivitat.

RESUMEN

El desarrollo de nuevas metodologías para la construcción de compuestos elaborados es uno de los principales objetivos de la química orgánica sintética. En este contexto, el uso de metales de la primera serie de transición ha supuesto un paso adelante para la preparación de diferentes compuestos orgánicos de manera catalítica. A pesar de los importantes avances que se han realizado en reacciones de acoplamiento cruzado utilizando electrófilos prefuncionalizados, el uso de substratos no funcionalizados para la funcionalización directa de enlaces C-H es aún motivo de investigación continua. Además, el uso de sustratos más desafiantes que presentan grupos C–F o C–OR es también de especial interés. Para desarrollar nuevas y/o mejoradas metodologías es crucial entender los pasos fundamentales que gobiernan estos procesos. Esta tesis doctoral se focaliza en el uso de substratos modelo para guiar la reactividad de los metales de la primera (Co, Ni) y también de la segunda (Ag) serie de transición en la funcionalización selectiva de enlaces C–Y (Y = H, F, OMe, Haluro) para la formación de enlaces C–C y C–Heteroátomo. Las propiedades coordinativas que presentan los sustratos modelos permitirán la estabilización de especies organometálicas, de manera que esta tesis también se centrará en averiguar el mecanismo de las reacciones para elucidar las etapas principales de estas transformaciones.

En la primera parte se presenta una actualización del progreso realizado en el campo de las reacciones de acoplamiento cruzado catalizadas por cobalto, destacando el potencial de este metal como una alternativa más sostenible para la preparación de una gran variedad de compuestos orgánicos.

Posteriormente, esta tesis se focaliza en averiguar el mecanismo que opera en los procesos de aminación a través de la activación de enlaces C–H utilizando especies de cobalto en alto estado de oxidación. Se lleva a cabo el estudio de la reactividad de especies organometálicas de arilo-Co(III) bien definidas con azidas inorgánicas y orgánicas. Se dedica especial atención en entender la interacción del centro metálico de cobalto con las azidas alifáticas y la posterior formación del enlace C–N, para entender el mecanismo de la reacción. Gracias a la estabilidad que ofrece el modelo macrocíclico, se estabilizan y aíslan distintos complejos de Co(III) que contienen el nuevo enlace aril-N. Se han realizado estudios complementarios de DFT, que han sido cruciales para elucidar intermedios difíciles de detectar implicados en este proceso, donde se discutirá también el papel clave de los ácidos carboxílicos en la estabilización de las especies arilo-Co(III)=nitreno.

Por otra parte, se utilizan plataformas modelo no cíclicas que contienen grupos directores para estudiar la funcionalización de enlaces C-X catalizadas por níquel, específicamente para la síntesis de isoquinolonas y productos de homologación aromática usando alquinos. Se demuestra la habilidad de la 8-aminoquinolina como grupo director bidentado (DG) para asistir la desafiante funcionalización de enlaces C-F y C-OMe. Las propiedades de coordinación de la 8-aminoquinolina permiten la detección y estabilización de especies intermedias que contienen dos alquinos insertados, claves para la síntesis de productos de homologación aromáticos. Se muestra que estos compuestos pueden ser usados para la preparación de materiales similares a los nanografenos, demostrando así un nuevo uso de los productos sintetizados.

La última parte de esta tesis se centra en la funcionalización de enlaces aril–X catalizada por plata usando diferentes nucleófilos que permiten la formación de nuevos enlaces C–C y C–Heteroátomo a través de reacciones de acoplamiento cruzado. Los estudios DFT e IRDP-MS son claves para averiguar el mecanismo que opera en estas reacciones, donde se evidencia la implicación de ciclos redox Ag(I)(Ag(III) en esta reactividad.

CHAPTER I

General Introduction

The development of novel methods to construct complex molecules is the main objective of synthetic chemists. Transition metal catalysis was a stimulating thrust to academia as well as chemical industry to construct a wide variety of organic compounds. After the huge improvement on cross-coupling reactions discovered in the late seventies, there is ongoing research on using less-activated $C(sp^2)$-electrophiles, such as fluoride, amides and esters. Furthermore, the use of non-prefunctionalized substrates for the direct coupling via C–H activation was also achieved as an alternative strategy with economic and environmental benefits. The importance of finding protocols for the direct functionalization of C–H and C–O bonds is due to the fact that they are fundamental structural units in raw organic compounds. On the other hand, different efforts have been put in the functionalization of C–F bonds due to the presence of them in different pharmaceutical compounds. Indeed, the inertness of this bond has a positive effect in a pharmaceutical point of view, this also means that the degradation of these compounds in the wastewater it's a challenging task. Although, late and novel metals played an important role in these transformations, the use of transition metals to activate C–H, C–F and C–O bond skyrocketed in the last decades opening the door to new synthetic approaches. Furthermore, the corresponding aryl–Y building block (Y = H, F, O) are largely available, and in some cases less expensive than the corresponding iodide, bromide and chloride congeners wide used in cross-coupling reactions. Although there represents an improvement on the C–C and C–heteroatom bond forming reactions, the mechanism behind these transformations are poorly understood. For this reason, there is a huge demand on understanding the operando mechanisms in order to develop new strategies to construct complex molecules in a more efficient manner.
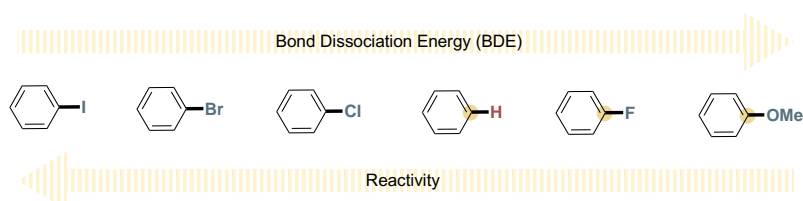
Scheme I.1. Bond dissociation energy and reactivity of aryl–Halide, aryl–H, aryl–OMe and Aryl–F.

In the following sections, the construction of $C(sp^2)$–$C(sp^2)$ bonds using aryl–F and aryl–OR as substrates via nickel catalytic systems will be discussed with some highlighted examples. Furthermore, the direct functionalization of C–H bonds will be also debated focusing on the importance of the directing group assisted C–H functionalization, highlighting the use of 8-aminoquinoline directing group to construct C–C and C–N bonds. The last section will be focused on how the chelating model and the macrocyclic model systems can help to stabilize intermediates shedding light to both the cross-coupling and C–H functionalization mechanism using nickel and cobalt transition metals.

I.1 CROSS-COUPLING REACTIONS

Cross-coupling reactions lies among the most important reactions in chemistry. In a general term, cross coupling transformation are based on the coupling between organo(pseudo)halide electrophile and a nucleophile to forge a new C–C and C–Heteroatom bond mediated by a metal catalyst. They were discovery almost 50 years ago and are nowadays widely used in academia as well as in industry to prepare a variety of organic compounds. Despite the huge progress made in this area, the research in this topic remains active aiming at improving the scope and the efficiency of the processes. In this context, the construction of C–C bond formation has been widely explored using activated organometallic nucleophiles such has organoboron, organotin and organomagnesium (Grignard) reagents, among others. Regarding the mechanism, it is well-accepted that the low-valent metal-catalyzed cross-coupling reactions proceeds

through two electron redox pathway and the typical mechanism proposed is the depicted in Scheme I.2. Oxidative addition of the M^{n+} to the aryl-halide is initially proposed, followed by a transmetallation step with the nucleophile. The M^{n+2} organometallic species formed reductive eliminates to form the R^1–R^2 coupling product and restart the catalytic cycle.
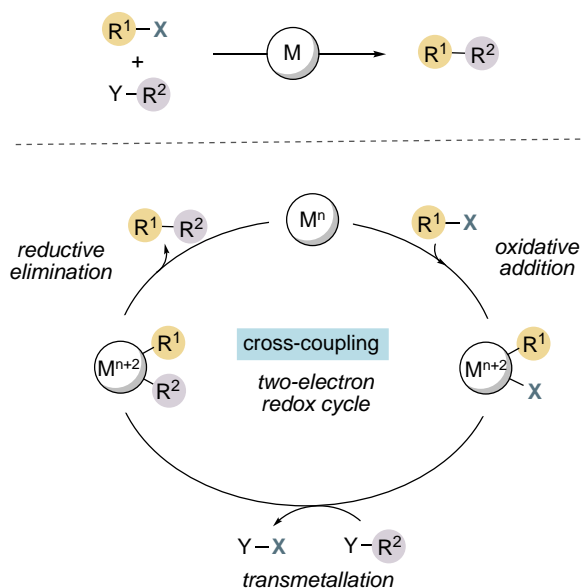
Scheme I.2. Typical scheme for cross-coupling reaction. Mechanism proposed based on two-electron redox cycle.

Numerous reviews on cross-coupling have been already published and will not be covered in this introduction.[1, 2 3-9]

I.1.1 C–F functionalization

Fluorinated organic compounds are essential scaffolds in different fields such as pharmaceutical and agrochemicals, since the electronic properties of C–F bonds change the chemical, physical and biological properties of a given molecules, which render long-life metabolism-resistant compounds.[10-15] As mentioned above, aryl fluorides are widely available representing an attractive choice of electrophiles. However, the inertness of C–F bonds compared to other C–Halides makes more difficult their functionalization with high selectivity, and normally highly reactive catalysts are needed. Among the different C–F containing substrates, we have focused our attention to the functionalization of aryl–F bonds. In the past decades, different strategies have been reported on the formation of aryl–C bonds via aryl–F activation using a set of metals. In this context, nickel has played a significant role on the aryl–F functionalization reactions showing their ability to activate strong C–F bonds. Initial reports were focused on C–F activation using stoichiometric amounts of Ni(0) catalyst. Fahey and Mahan pioneered the observation of the formation of the pentafluorophenyl fluoronickel(II) complexes using hexafluorobenzene and stoichiometric amounts of Ni(cod)(PEt$_3$)$_2$, albeit in very low yields (7%).[16] After 20 years, Perutz and coworkers isolate the *trans*-Ni(PEt$_3$)$_2$(C$_6$F$_5$)F complex by reaction of hexafluorobenzene with Ni(PEt$_3$)$_4$.[17] Although the reaction proceed slowly, the compound was achieved in 48% yield and the structure was further confirmed by X-ray analysis. The same authors also explored the C–F activation using the octafluoronaphtalene yielding at room temperature the [Ni(η_2-1,2-C$_{10}$F$_8$)(PEt$_3$)$_2$] complex. The X-ray crystallographic data shows an η_2-C$_{10}$F$_8$ coordination to the nickel center with almost trigonal planar geometry. The organometallic nickel(0) complex evolve at higher temperature to the corresponding aryl–Ni(II)–F complex via concerted oxidative addition[18, 19].

a) Aryl-Ni(II) complex formed via aryl–F bond cleavage
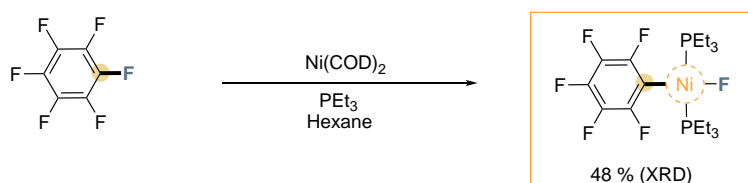
b) η2-coordination of the polifluoroaromatic at nickel center and the corresponding aryl–Ni(II) complex

color code: Ni(0) and Ni(II)
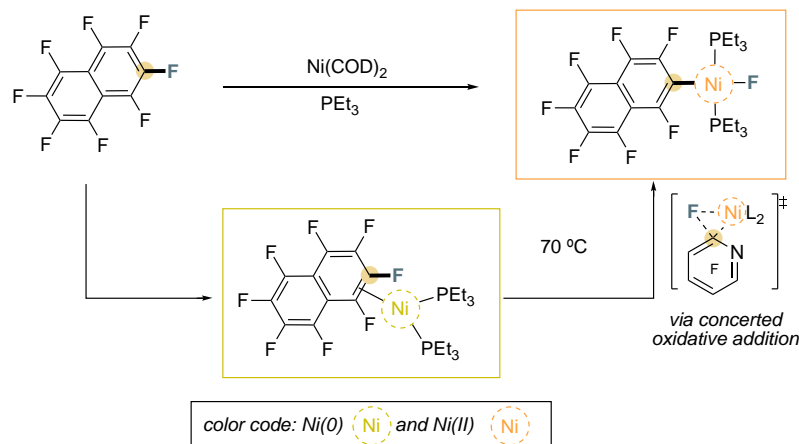
Scheme I.3. Aryl–F activation using stoichiometric amounts of Ni(cod)$_2$ forming the corresponding aryl–Ni(II)–F complex.

After the first reports on stoichiometric aryl–F activation demonstrating the ability of nickel to activate strong bonds, different efforts has been put in the use of fluoroarenes as building blocks for the C–C bond formation reactions.[20-25] Nickel-catalyzed aryl–F functionalization with the concomitant C–C bond formation reaction has been achieved using activated nucleophiles such as Grignard reagents,[26-32] zincates[33] and boronic acids.[34-37] In this context, selected examples will be showed to highlight the potential of nickel to catalyze the aryl–F functionalization transformations.

This area is dominated by the use of Grignard reagents as a coupling partner. Hermann and coworkers pioneered this field reporting the arylation of aryl–F bonds catalyzed by NHC/nickel complex using aryl Grignard reagents (scheme I.4).[38] The authors suggested that the C–F cleavage proceeds via oxidative addition of aryl fluorides to the nickel(0) complex based on the product selectivity and the Hammett correlation observed. In 2005, the arylation of aryl fluorides electrophiles mediated by nickel(0) using air-stable phosphine oxide ligand at ambient temperatures was disclosed by Ackermann and coworkers (see scheme I.4).[39]
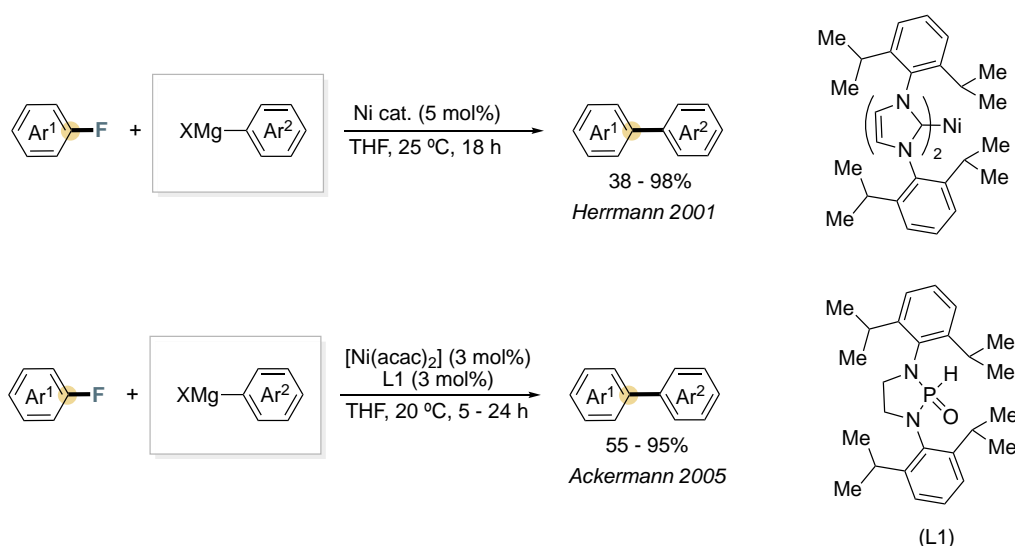
Scheme I.4. Arylation of aryl–F bonds using Grignard reagents promoted by a Ni(0) catalyst.

Cornella and coworkers showed that the coupling of secondary alkyl nucleophiles with unactivated aryl fluorides in a selective manner can be accomplished at room temperature (scheme I.5).[40] The high selectivity observed was attributed to the Thorpe-Ingold effect in the ligand backbone avoiding further isomerization.
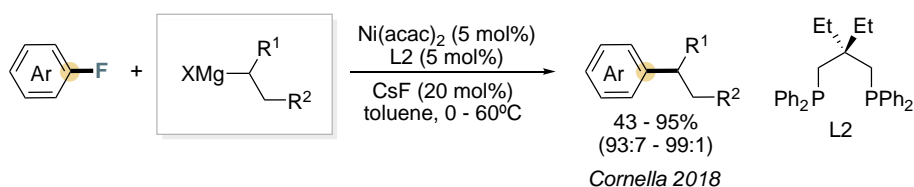
Scheme I.5. Alkylation of aryl–F bonds using alkyl Grignard reagents catalyzed by Ni(0) catalyst.

The arylation of aryl–F bonds was also achieved using boronic acids as coupling partner. Radius pioneered this field by reporting the arylation of perfluorinated arenes catalyzed by nickel complex (scheme I.6).[41] They observed the selective activation of the $C(sp^2)$–F over the $C(sp^3)$–F yielding the corresponding biaryl product. Subjecting the perfluorotoluene together with stoichiometric amounts of nickel catalyst led to the formation of the corresponding aryl–Ni(II)–F complex in 75% yield. In 2011, Love expanded the scope of Suzuki-type transformation using Ni(cod)$_2$ and PPh$_3$ (Scheme I.6). The installation of an imine as directing group assisted the $C(sp^2)$–F cleavage achieving good to excellent yields and high selectivity affording a broad range on fluorinated biaryl products.[42]
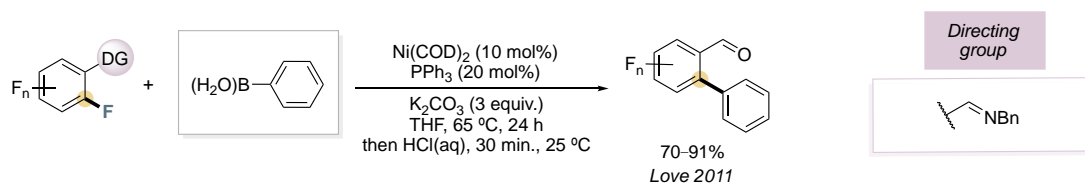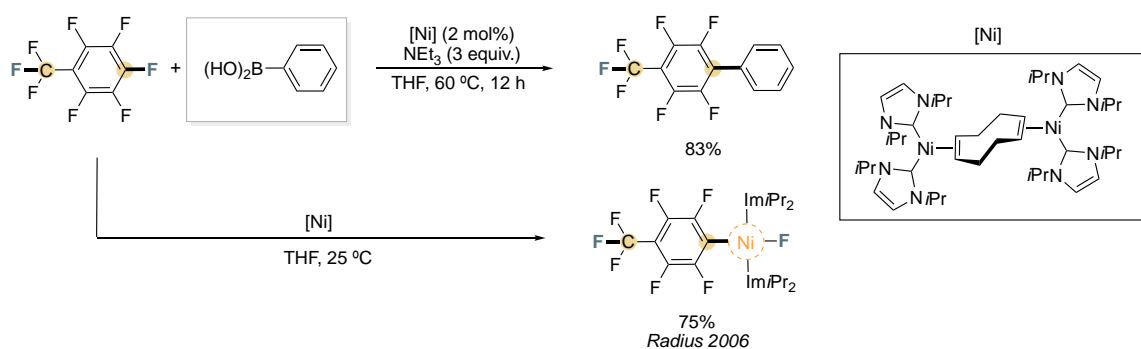
Scheme I.6. Nickel-catalyzed aryl–C bond formation via aryl–F activation of polyfluorinated substrates with boronic acids.

As shown before, the aryl–F functionalization and the concomitant biaryl formation has been successfully applied using polyfluorinated substrates as electrophiles. Chatani also contributed to this field by developing two different protocols for the nickel-catalyzed Suzuki-Miyaura cross-coupling of aryl fluorides as depicted in scheme I.7.[35] Electron-deficient aryl fluorides were used in the arylation coupling using a Ni/Zr bimetallic catalyst. The authors observed that the addition of the cocatalyst ZrF_4 accelerate the reaction while expanding the substrate scope. The second approach is based on the incorporation of a directing group on the aryl fluoride substrate, facilitating the activation of the aryl–F activation bond, which yielded the biaryl products in good to excellent yields without the need of a cocatalyst.
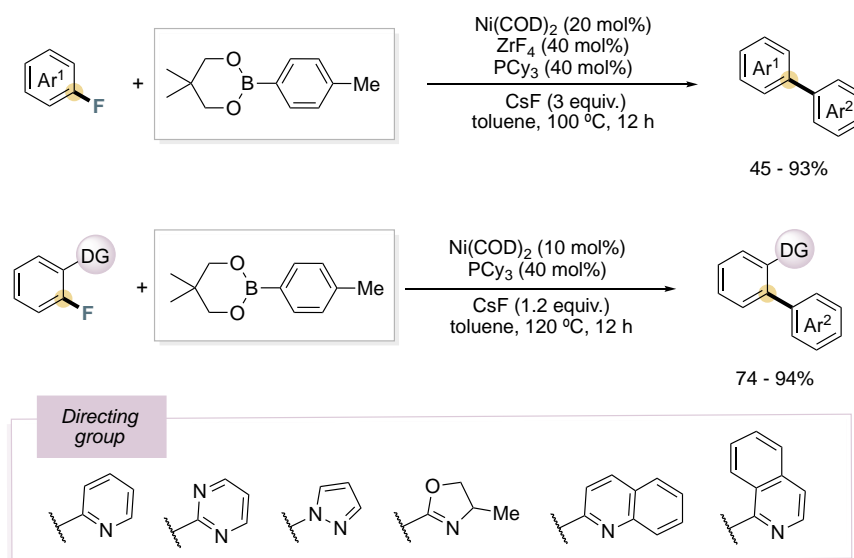
Scheme I.7. Directing - and nondirecting group assisted Suzuki–Miyaura reaction via C–F cleavage.

19

I.1.2. C–OR functionalization

The use of phenol derivatives as electrophiles in cross-coupling reactions has probed a challenging but viable alternative approach to construct C–C bonds. The availability of phenol derivatives compared to the aryl halides together with the absence of the halogenated waste make them very interesting candidates as aromatic building blocks that can be obtained from raw materials as lignin.[43-50] In recent years, notable progress has been made in the development of metal-catalyzed aryl–OR bond functionalization reactions.[51-59] Within the different phenol derivatives, aryl sulfonates has been extensively studied representing one the most employed C–OR electrophile due to the low activation barrier for the aryl–OR cleavage. Aryl ester and aryl carbamate derivatives have been also used in cross-coupling reaction, thus overcoming the limitation of the more common aryl sulfonates. In this line, a step-forward was made using aryl ethers as electrophiles providing a greener alternative methodology from sustainable raw materials as wood (lignin). This field is also governed by the use of activated nucleophiles and some highlighted examples using the most appealing aryl ethers will be disclosed.

The first aryl–OMe functionalization reaction dates to 1979 when Wenkert reported the coupling product by reacting methoxyarene with Grignard reagents in the presence of a nickel catalyst.[60] However, this field remains dormant until 2004 when Dankwardt disclosed the Ni-catalyzed Kumada-Corriu type of transformation using methoxy arenes (see scheme I.8).[61] The nickel(II)-based catalytic system reported using PCy_3 or $PhOCy_2$ as auxiliary ligand permits the synthesis of a wide range of biaryl coupling products in good to excellent yield. This work inspired the community and different examples were reported on nickel-catalyzed cross-coupling transformations using methoxy arenes as electrophiles.[62-64] Albeit there are some examples for alkylation and alkynylation of aryl ethers this topic remains underdeveloped.[65-68] The use of aryl ethers was also extended to other activated nucleophiles. In this context, Chatani and coworkers developed a methodology for the Suzuki-Miyaura-like biaryl formation using aryl boronic ethers catalyzed by $Ni(cod)_2$.[69] In 2012, Uchiyama reported the nickel-catalyzed Negishi-type cross-coupling reactions using aryl ethers and dianion-type zincate ($PhZnMe_3Li_2$) as coupling partner (scheme I.8).[70]
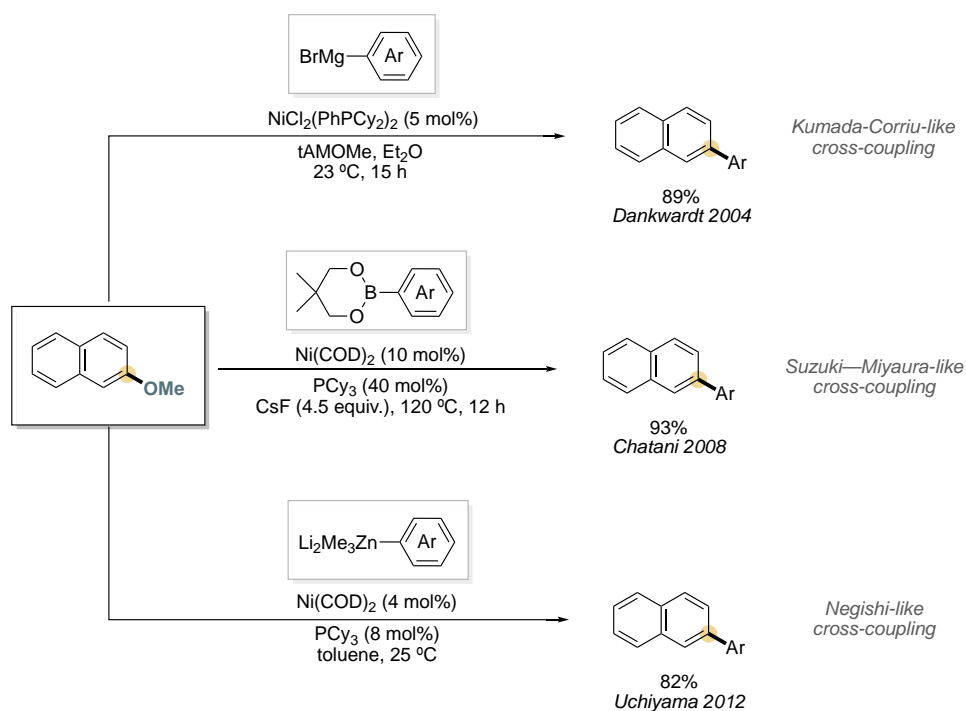
Scheme I.8. Nickel-catalyzed cross-coupling reactions using methoxyarenes as electrophiles.

More recently, in 2021 Chatani developed nickel(0)-catalyzed C–OPh/N–H annulation of amides with alkynes as depicted in scheme I.9.[71] They reported the use of non-activated nucleophiles (alkynes) for the formation of 1(2H)-isoquinolines. The C–OPh bond was successfully activated by the Ni(cod)$_2$ catalyst, assisted by a monodentate directing group. The authors suggested that the reaction started with the deprotonation of the amide to form the lithium amidate intermediate. Then, the nickel(0) is coordinated to the amidate and the C–OPh was activated via oxidative addition to form an aryl–Ni(II) complex and the concomitant formation of LiOPh. Finally, the alkyne is inserted and the complex reductive eliminate to render the coupling product. Electron-withdrawing groups on the phenolate (i.e. *p*-CF$_3$) quenched the reaction. The authors proposed that the C–O cleavage is not the rate-limiting step of the reaction.
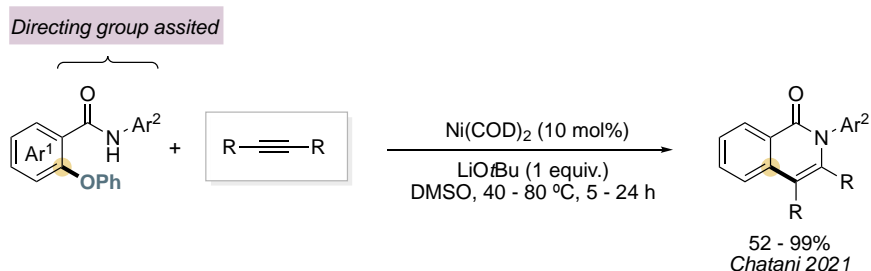
Scheme I.9. Directing group assisted Ni-catalyzed annulation of aromatic amides with alkynes.

I.2. DIRECTING GROUP APPROACH FOR THE SELECTIVE C–H FUNCTIONALIZATION

The transition metal-based direct activation of carbon–hydrogen (C–H) and the concomitant formation of C–C and C-N bonds has witnessed impressive advances during the last decades. The use of non- functionalized feedstock makes this strategy an environmentally benign alternative to cross-coupling reactions. Nonetheless, the unreactive nature, high stability of C–H bonds and lack of selectivity among multiple C–H bonds present, makes its functionalization a challenging task. TM-catalyzed direct functionalization of C–H bonds is widely-accepted as one the most innovative fields and today represents a real and feasible approach in synthetic chemistry.[72-77]

I.2.1 Mechanistic considerations

In an inner-sphere pathway, the activation of C–H bonds by a transition metal undergoes via the formation of an organometallic species featuring a C–Metal bond, which can occur via several mechanistic pathways[78] which are detailed below.

These pathways can be divided by two-, one-electron or electron-neutral processes. Two-electron oxidative addition (OA) pathways can occur using a transition metal in low-oxidation state (electron-rich metal center), where the C–H bond is cleaved in a concerted manner oxidizing the metal center in two units (scheme I.10a). This results in the formation of an organometallic species which has a hydride and an alkyl/aryl moiety. On the other hand, single electron transfer (SET) processes consist on an homolytic cleavage of the C–H bond affording a M–Hydride complex and a carbon-centered radical. Subsequently, the aryl–M–hydride species is formed via recombination of the radical and the metal center (Scheme I.10b). On the other hand, other possibilities exist including the electron-neutral processes such as σ-bond metathesis, concerted metalation-deprotonation (CMD) and electrophilic aromatic substitution (S$_E$Ar). σ-bond metathesis occurs with metals in a high oxidation state (electron poor metal center), where the C–H cleavage and the formation of C–M bond take place in a concerted

manner via a four-membered metallacycle transition state (scheme I.10c). Concerted metalation-deprotonation pathway is favored using directing group strategy, with metal center located closely to the C–H bond (scheme I.10d). A coordinated internal base, normally carboxylates, promotes the deprotonation of the C–H bonds in a concerted manner while the C–M bond is formed concomitantly. On the other hand, the electrophilic aromatic substitution occurs when metal center acts as a Lewis acid (scheme I.10e). The electronic interaction between the metal and the substrate via interaction with the π-aromatic system. The formation of a C–M organometallic Wheland-type complex and the concomitant proton release is accelerated by the presence of the base.

a. *oxidative addition*
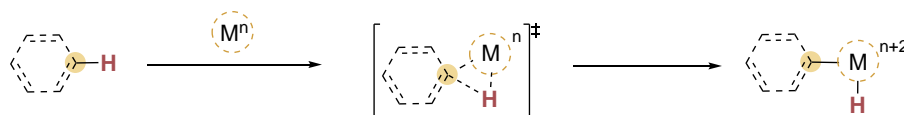
b. Single electron transfer (SET)
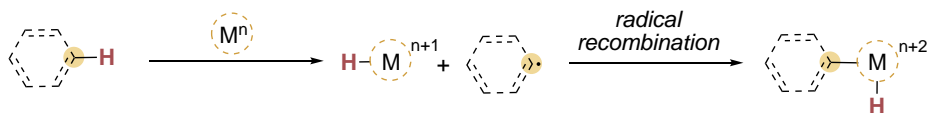
c. σ-bond metathesis

d. concerted metalation-deprotonation (CMD)
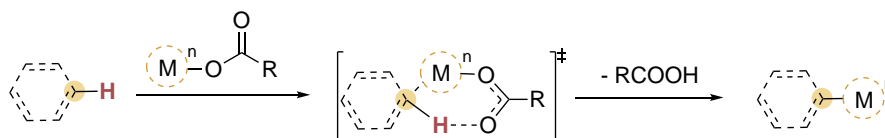
e. Electrophilic aromatic substitution (S$_E$Ar)

Scheme I.10. Different mechanisms for inner-sphere metal-catalyzed C–H activation.

To improve the activity and the efficiency of these transformations, a deep understanding of the catalytic mode of action in the C–H activation reactions is needed, and different strategies have been explored to trap the organometallic intermediate species involved.

I.2.2 Directing group approach

The direct C–H activation processes has been popular as an alternative strategy for the straightforward synthesis of organic compounds. However, achieving positional selectivity is a challenging task due to the presence of multiple unsubstituted bonds in a given compound. The regiocontrol have been successfully addressed by using several strategies such as the use of elaborated ligands on the metal catalyst or the use of directing groups (DGs). The transient directing group strategy is based on the in situ coordination and removal of the directing group.[79-82] In contrast, the second strategy is based on the installation of the directing group on the substrates, which is able to

effectively bind to the metal center and directs the metal into close proximity to the C–H bond to force the activation of the specific bond in a regioselective manner; however, the DG is left installed in the final product. It is worth to note that the improvement of regioselectivity come with the catalyst's efficiency due to the coordination of the metal to the DG.
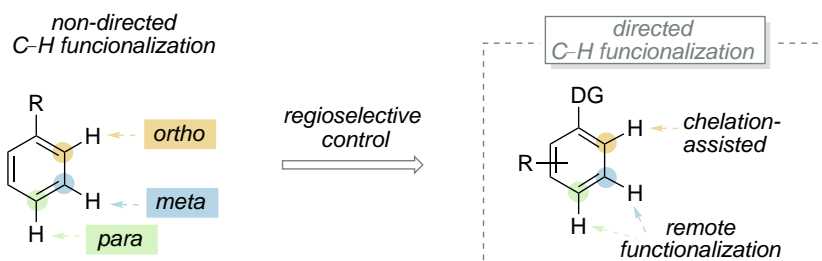
Scheme I.11. Directed C–H functionalization in a selective manner using a directing group scaffold.

Over the last few years, direct TM-catalyzed C–H functionalization using the directing group strategy has attracted lots of attention and reports have grown exponentially.[83-85] The site-selective activation of C–H bonds was achieved by modifying the directing group allowing the suitable orientation of the template towards a specific bond. In this context, chelation-assisted transformation has become a powerful tool for the *ortho*-selective C–H functionalization. Several mono- and bidentate directing groups have been extensively studied facilitating the *ortho*-selective functionalization. The differences of these directing groups rely on the coordination environment of the metal by one or two binding sites capable of facilitating the interaction between the metal and the C–H bond.
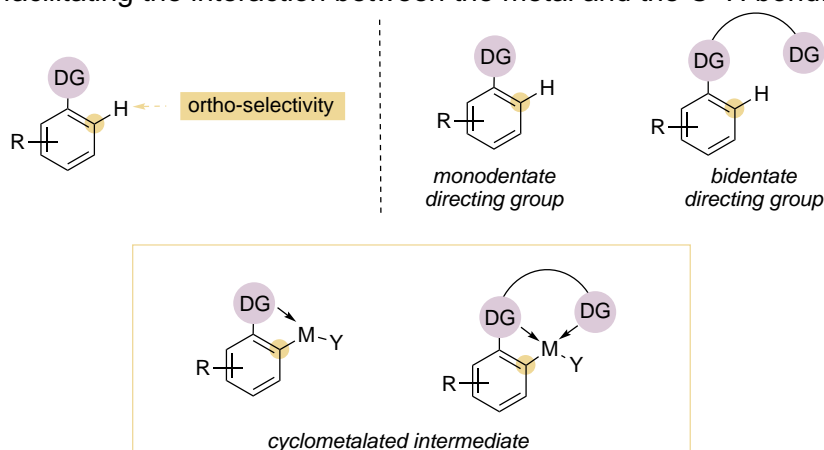
Scheme I.12. Selective functionalization assisted by Mono- and bidentate directing group.

In this context, directing group moiety has to present different properties, such as it should be stable under reaction conditions and should coordinate reversibly to the metal center, among others. In this line, a wide variety of monodentate directing groups have been evaluated for the *ortho* C–H functionalization transformation. Daugulis in 2005 pioneered the field of bidentate directing group by reporting the palladium-catalyzed arylation of $C(sp^3)$–H and $C(sp^2)$–H bonds of aliphatic and aromatic amides using 8-aminoquinoline and picolinamide as directing groups[86] which was a breakthrough in the field of chelation-assisted C–H functionalization using bidentate directing groups. After that, numerous examples have been reported showcasing that bidentate chelating systems such as N,N-dentate, N,O-dentate or N,S-dentate directing group are promising tools at achieving non-activated C–H bonds functionalization reactions.[87] In fact, the use of bidentate directing group promotes transformations that have not been achieved using monodentate systems. N,N-bidentate directing groups are the more well-established ones, including quinoline-, pyridine-, oxazole-, triazole-, pyrazole- based and a $HN(sp^2)$

unit. The secondary amine moiety acts as an anionic coordinating site to complete the N,N-bidentate directing group. Although a huge progress has been made, the development of different types of directing groups still important by exploring new C–H functionalization transformations that cannot be performed using the common directing groups.
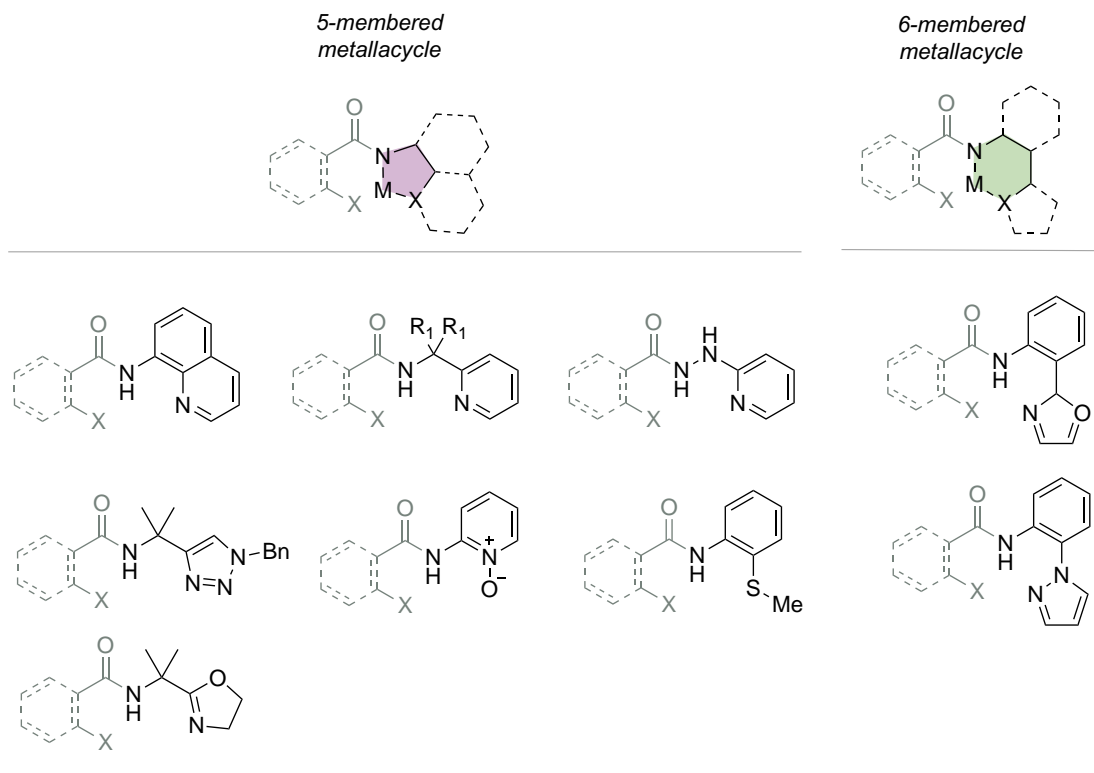
Scheme I.13. Selected examples of bidentate directing group.

Despite the recent flourishing of the first-row transition metal catalyzed C–H functionalization reactions, the underlying operating mechanism is still unclear. In this context, several efforts have been made towards the isolation and characterization of such intermediates to elucidate the mechanism. As it is mentioned above, the use of directing group aid to arrange the correct geometry of the metal to deliver the catalyst close to a specific C–H bond, yielding the formation of thermodynamically stable five- or six membered metallacycle intermediate, which is the key step in these transformations. The cyclometallated intermediate formed can be stabilized by the coordination sites of the directing group. Indeed, some examples of aryl-M bond (M = Ni and Co) have been reported using this strategy. Nevertheless, there is still lack of knowledge on their behavior in front of different coupling partners due to their instability. The isolation and characterization of the aryl-M organometallic complexes will be further discussed and how they react with different coupling partners in section I.3.

I.2.2.1   C–C bond formation

C–C bond formation reaction protocols stand as a fundamental research topic of great interest, and a huge improvement has been made during the last decades. As in mentioned above, the use of directing group enhance the reactivity and selectivity in C–H functionalization enabling hitherto unknown or difficult synthetic reactions. The discoveries of the directing group-assisted approach have sparked the field, and a wide methodologies has been reported using also first-row transition metals.[88-93] The use of C–H bond as a functional group offers a straightforward and efficient route for the

construction of C–C bonds. In contrast to cross-coupling reactions, in C–H functionalization reactions a higher variety of coupling partners can be used and different mechanisms can take place. Furthermore, these transformations require different additives (oxidants, carboxylates, auxiliary ligands, Lewis acids, base), which complicates the investigations of the mechanistic details. The synthesis of heterocycles compounds via C–H functionalization transformations has been explored using different coupling partners such as alkynes, alkenes, allenes, nitrils among others. In this context, cobalt- and nickel-catalyzed C(sp^2)–H/alkyne bond coupling have been reported using different directing groups.[87] This section will be focused on the Co- and Ni-catalyzed aryl–H/alkyne coupling assisted by 8-aminoquinoline directing group and the different mechanism scenarios for this transformation will be disclosed.

Since Daugulis[86] reported the use of 8-aminoquinoline as directing group to assist the C–H functionalization with Pd in 2005, the bidentate DG strategy has exponentially grown with first-row transition metals, offering new routes with high efficiency for the C–H functionalization in several coupling reactions. In this context, Daugulis reported the Cobalt-catalyzed alkyne annulation reactions assisted by a 8-aminoquinoline directing group. The use of a cooxidant such as Mn(OAc)$_2$ was crucial to achieve the cyclic coupling partner.[94] The same authors also expanded the Cobalt-catalyzed annulation reactions using phosphinic amides.[95] Ribas also contributed to this field by reporting the synthesis of sultam motif via Cobalt-catalyzed annulation of aryl sulfonamides with alkynes.[96] Sundaraju[97] and Yang[98] independently also provide a methodology for the C–H/N–H annulation of sulfonamides with alkynes mediated by cobalt system. The formation of 5-membered ring cyclic product was also achieved in Cobalt-catalyzed annulation of aromatic amides with terminal alkynes by Zhang and coworkers.[99] Finally, the Balaraman disclosed a methodology for aryl–H /alkyne coupling product in a linear manner using ethynyltriisopropylsilane coupling partner.[100]
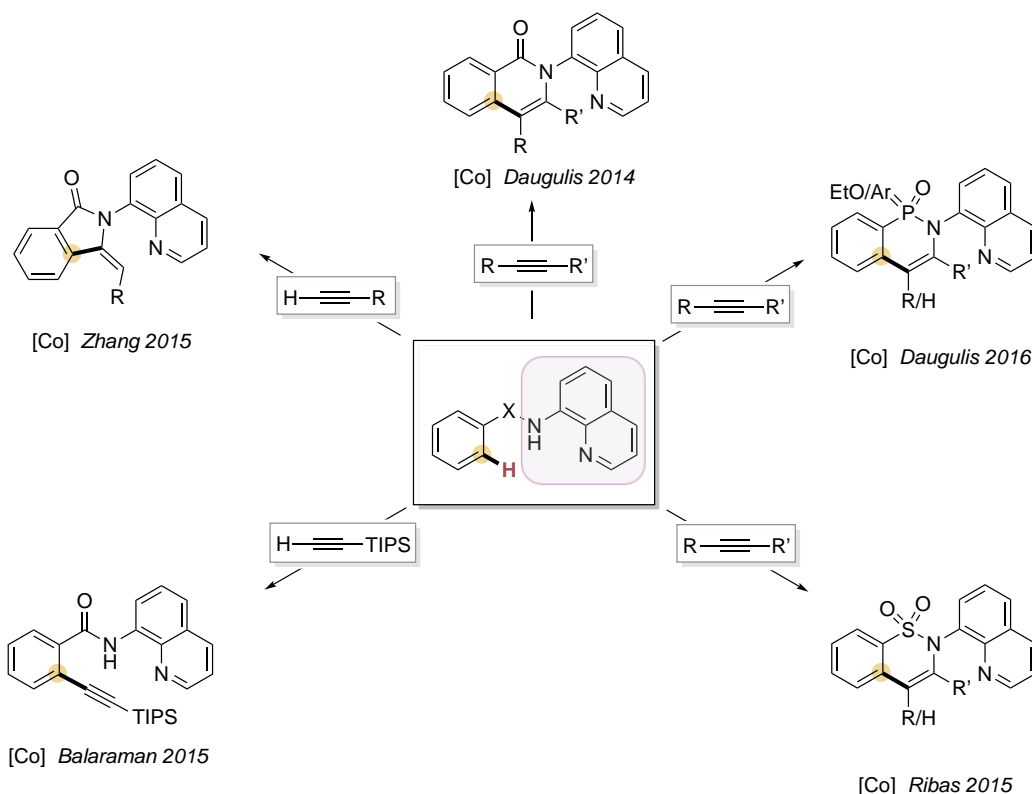
Scheme I.14. Co-catalyzed C-H functionalization using alkynes as coupling partner.

Two different mechanisms have been proposed for cobalt-catalyzed C–H functionalization with alkynes depending on the alkyne used (terminal or internal). The formation of isoquinolones is based on Co(I)/Co(III) catalytic system started by the coordination of Co(II) to the benzamide substrate. Then, the oxidation of the Co(II) to Co(III) and the C–H activation assisted by the base take place to render the aryl–Co(III) intermediate **A**. After that, a 7-membered cobaltacycle **B** is proposed via migratory insertion into the C–Co(III) bond, which reductive eliminate to end up with the desired isoquinolone product. The Co(I) formed is reoxidized and the catalytic cycle restarts.
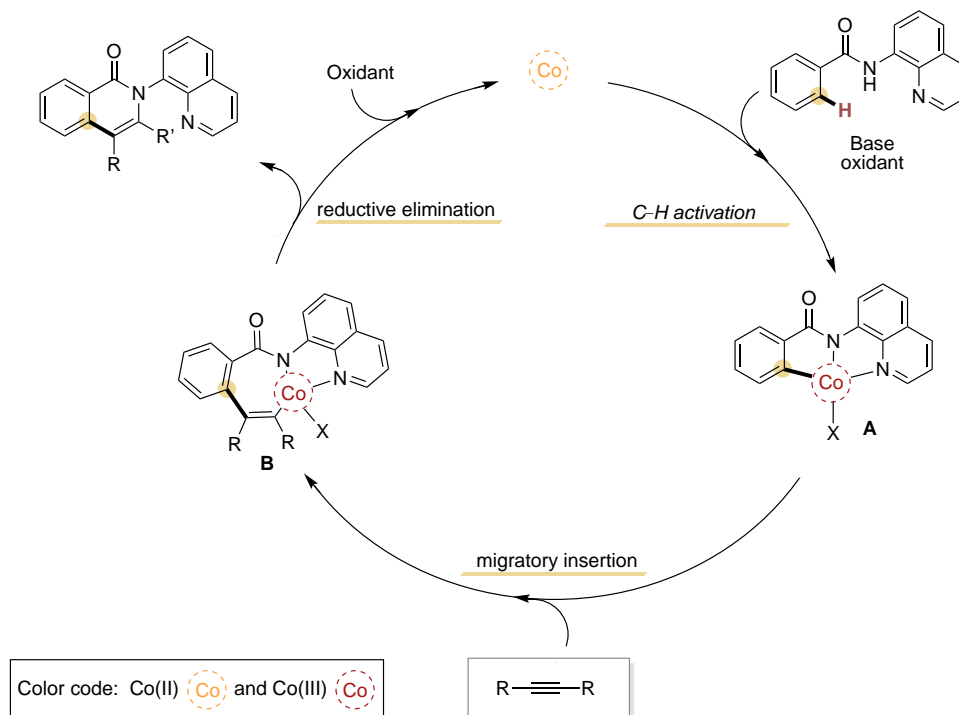
Scheme I.15. General mechanism proposed for cobalt-catalyzed C–H annulation reaction using alkynes.

As it is mentioned above, the formation of isoindolinones (5-membered ring) was reported by Zhang[99] and coworkers using terminal alkynes. The authors proposed the following mechanism depicted in scheme I.16. Firstly, the oxidation of the Co(II) to Co(III) take place, which activates the aryl–H bond giving the aryl–Co(III) intermediate **A**. The authors proposed the formation of the alkyne radical which attack the intermediate **A** to form the aryl–Co(IV)–alkynyl species **B.** Then, the alkynylated product is form via reductive elimination step and the Co(II) species can chelate to the benzamide substrate restarting the cycle. The 5-membered isoindolin-1-one product was formed by the cyclization of the alkynylated one. The same mechanism was proposed by Balaraman[100] for the linear coupling product. Ribas and coworkers contributed in the mechanism understanding using terminal alkynes and a macrocyclic model substrate.[101] The well-defined aryl–Co(III) complexes were reacted with terminal alkynes and the authors postulated an acetylide pathway via aryl–Co(III)–alkynyl intermediate which will be further discussed in the following section.
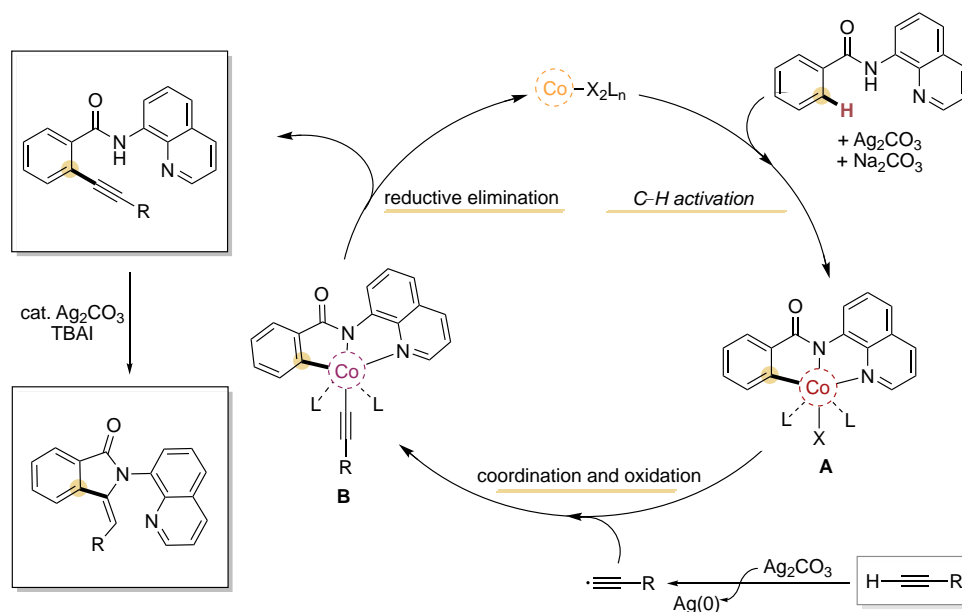
Scheme I.16. Mechanism proposed for the cobalt-catalysed C–H functionalization using terminal alkynes.

The use of alkynes as coupling partner for the annulation reactions using 8-aminoquinoline directing group have been also explored using nickel catalysts. In this context, Zhang reported a methodology for the formation of 5-membered lactam compounds catalyzed by Ni(II) catalyst (scheme I.17).[102] Similar mechanism was proposed starting with the formation of aryl–Ni(II) intermediate via C–H activation assisted by the 8-aminoquinoline directing group. Then, the oxidation of Ni(II) to Ni(III) and ligand exchange take place forming a aryl–Ni(III)–alkynyl intermediate, which reductive eliminates to render the alkynylated product. The cyclization to formation of 5-membered lactams derivatives from the lineal alkynylated compounds was promoted by the silver salt in combination with TBAI. Chatani and Huang independently observed a different behavior by reporting the homologation of aromatic amides with internal alkynes mediated by nickel catalyst depicted in scheme I.17.[103, 104] Both authors proposed that the use of a rigid directing group such as 8-aminoquinoline was essential to afford the double C–H bond activation and the concomitant alkyne insertion reaction.
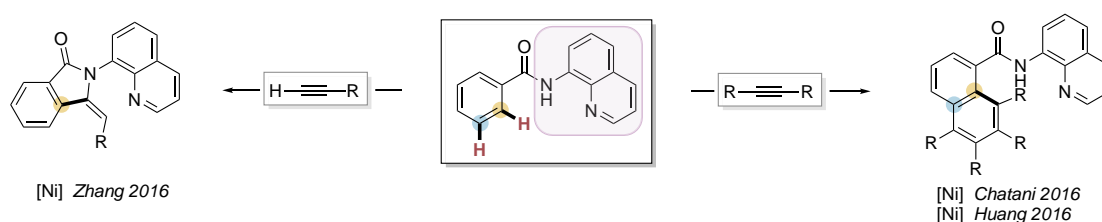
Scheme I.17. Nickel-catalyzed C – H functionalization using alkynes as coupling partner.

Regarding the mechanism, Huang and coworkers disclosed a plausible reaction mechanism for this nickel(0)-catalyzed dehydrogenative homologation of amides (see scheme I.18). The catalytic cycle starts with the oxidative addition of the ortho C-H bond to nickel(0) affording species **A**. A set of H/D exchange experiments were performed suggesting that the nickel hydride **A** intermediate species has been formed in an irreversible manner. The authors proposed two different pathways for the formation of the intermediate aryl–Ni(II) species **D**. The first one, the C-H bond cleavage forms a H2 bonded nickelacycle **B,** which reacts with a second substrate leading the formation of the complex **D** and the corresponding alkene as a byproduct. The second mechanism proposed is based on the alkyne insertion before the C–H cleavage. It is worth to note,

that they observe the formation of stilbene as a side-product of the reaction. After that, a fast alkyne insertion to **D** forms species **E**, which is followed by ligand exchange upon coordination of a second molecule of substrate, leading the formation of intermediate **F**. The second C–H activation at *meta* position affords species **G**, which the authors suggest that this step corresponds to the slowest one. Finally, a second alkyne is inserted into C–Ni(II) bond followed by C–C reductive elimination rendering the final product. The mechanism proposed is similar to the one reported by Chatani and coworkers suggesting a Ni(0)/Ni(II) as main catalytic cycle.
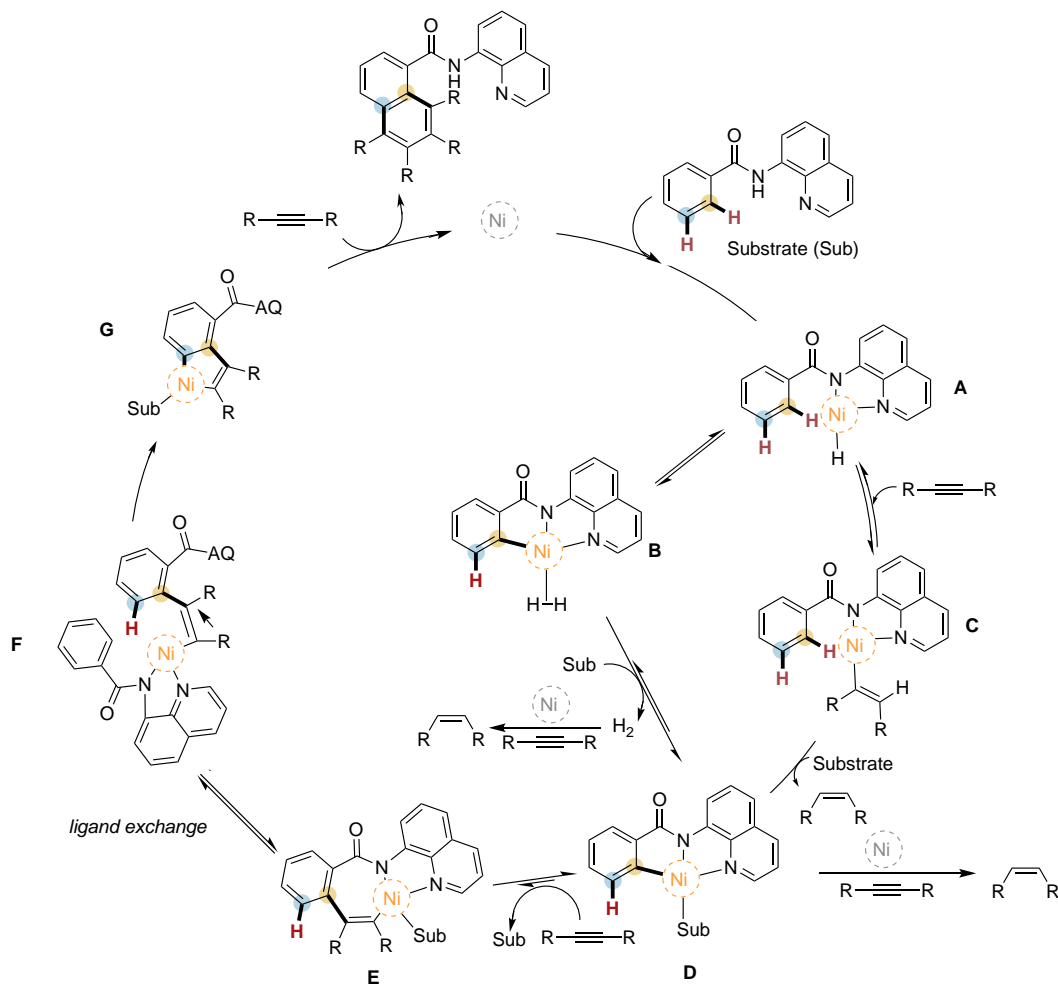
Scheme I.18. Mechanism proposed by Huang and coworkers for double alkyne insertion reaction.

I.2.2.2 C–H amination reaction

In contrast to C–C bond formation reactions, the incorporation of a heteroatom moiety into a given molecule remains challenging. In this context, the introduction of nitrogen functionality has motivated synthetic chemists to develop practical amination reaction due to their widespread occurrence in pharmaceuticals and natural products.[105] A huge effort has been put forward to develop new methodologies for the construction of C–N bonds based on *C–N cross-coupling*[6, 106] and *C–H amination* reactions.[107-111] After the tremendous progress in Buchwald-Hartwig Pd-catalyzed aryl halide aminations reactions, the exploration of novel and more sustainable catalytic system for C–N cross coupling transformation is still highly desired. In the other hand, direct C–H amination reactions offers a great opportunity to access nitrogen-functionalized molecules avoiding the use of pre-functionalized substrates.

Different aminating reagents have been tested as nitrogen sources, i.e. amines, amides and derivatives. The use of derivatized amines can avoid the requirement of external oxidant which usually is needed, due to the presence of a polarized N–X bond which can be oxidatively cleaved by the metal catalyst. In this context, organic azides present very particular properties converting them as promising aminating reagents. Their easy preparation, high reactivity and the formation of N_2 gas as by-product upgrade these reagents as promising candidates as nitrogen source.
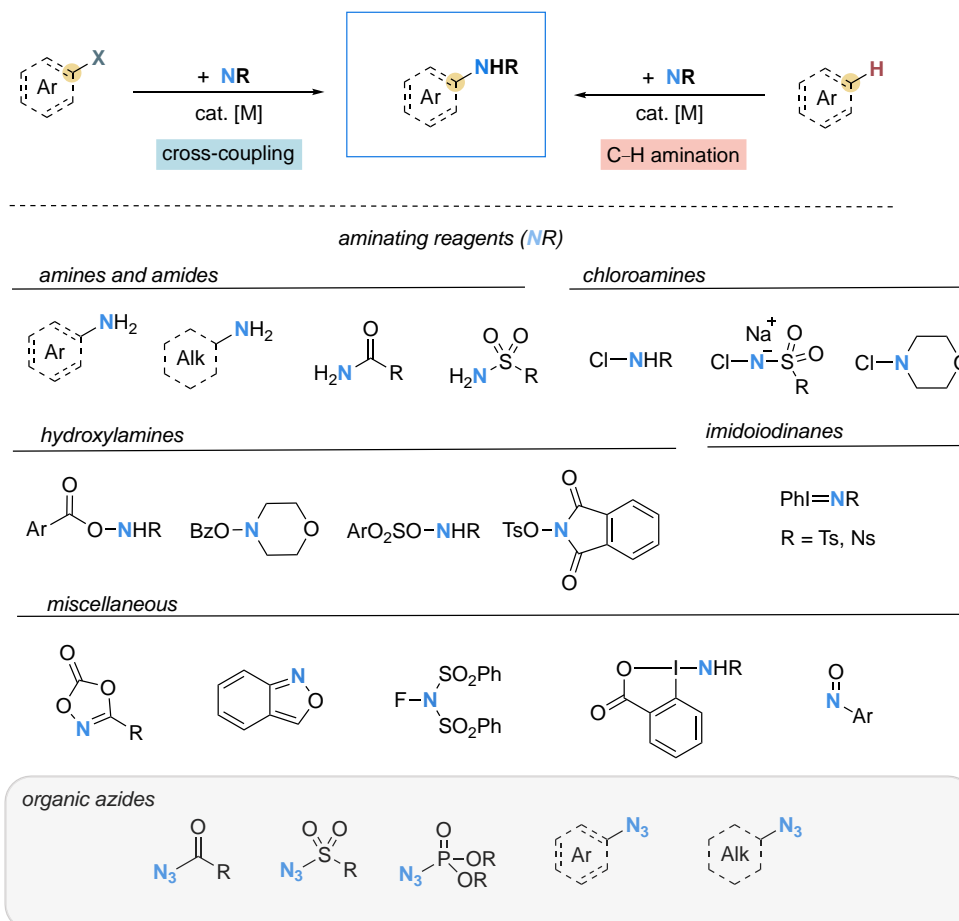
Scheme I.19. Different aminating reagents.

New horizons in the field of C–H amination were opened by the use of organic azides and have been recognized as a convenient nitrogen source in C–N couplings.[112] Two different mechanisms can be considered to proceed (scheme I.20): a) C–H insertion catalysis (outer-sphere mechanism) initially a metal nitrenoid species is formed, which subsequently interacts with the substrate in a stepwise or concerted way to furnish the desired C–N bond product. It is proposed that the substrate do not bind to the inner-sphere of the metal complex and the selectivity is highly dependent on the stereoelectronic nature of the Metal–N bond such as the putative metal-nitrenoid species. The second action of mode is based on, firstly, the generation of organometallic species yielding a metal–C bond as a result of C–H bond activation. In contrast to the outer-sphere mechanism, the C–H cleavage is postulated to operate inside the coordination sphere of the metal, where the C–H activation step is promoted by the close interaction of the metal center and the substrate. In this context, the chelation-assisted strategy can help the C–H activation system and may help the efficiency of both C–H activation and C–N formation steps. However, the use of azides has not been widely exploited in direct C–H amination transformations, although there are some examples of C–H insertion reactions.
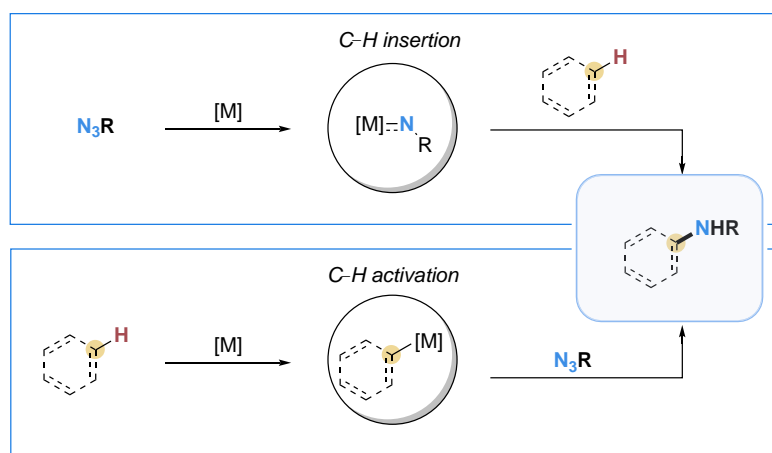
Scheme I.20. Two different pathways for the C–N coupling using azides as aminating reagent.

Cobalt-catalyzed C–H insertion reaction via outer-sphere mode has been well explored,[113-117] whereas the viability of Cobalt in C–H amination reactions via inner-sphere pathway has not been scrutinized. Chang and Musaev reported a compressive study of group 9 metals in C–H amination of benzamides using Cp*M(III) catalyst. They observed high efficiency using Cp*Rh(III) (54% yield) compared to the analogous Co (10% yield) and Ir (7% yield) catalyst. The authors suggested that the low reactivity of the Cp*Co(III) catalyst compared to the analogous Rh catalyst can be attributed to both kinetically and thermodynamically less favored C–H bond cleavage.[110] After that, Kanai and coworkers pioneered this field by reporting the Cp*Co(CO)I₂ catalyst which is able to achieve the amidation of N-pyrimidylindole using sulfonyl azides in excellent yields (scheme I.21).[118] The same research group expand this cobalt system further by reporting the amination reaction using phosphoryl azides.[119] Punniyamurthy take advantage of this Cp* Cobalt system reporting the C2-amidation of indoles employing acyl azides in good yields (see scheme I.21).[120] The use of high valent Co(III) was also applied for the intermolecular version of C–H amination reaction reported by Chang and coworkers using a Cp*Co(III)(L) with phenyl azidoformates via outer-sphere mechanism.[117]
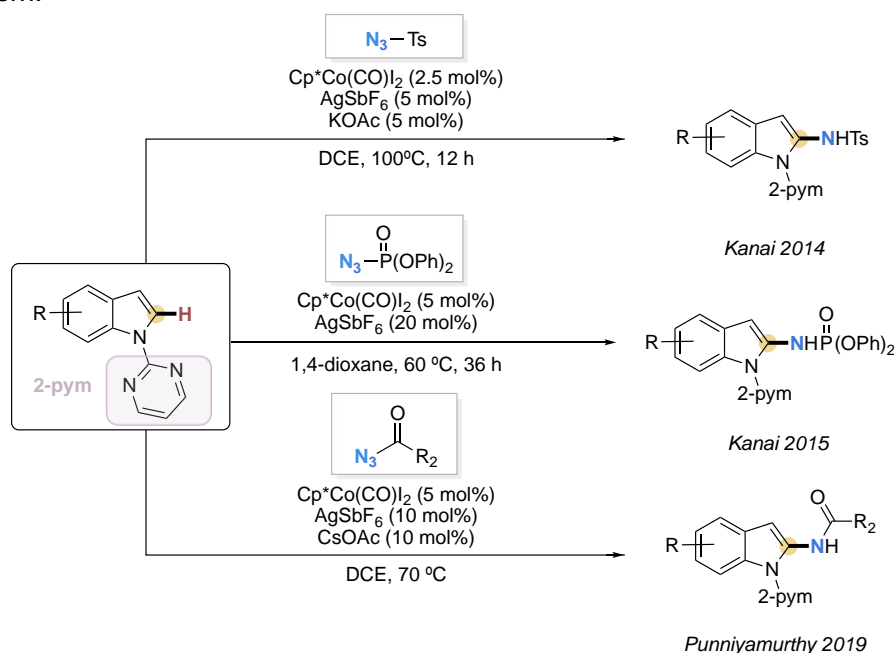
Scheme I.21. C–H amidation reactions using organic azides and the Co(III) catalyst Cp*Co(CO)I₂ catalyst.

The detailed mechanistic details of C–N coupling in an inner-sphere system using azides as nitrogen-source is poorly understood. Kanai and coworkers proposed that the catalytic cycle (scheme I.22) starts with the halogen abstraction from Cp*Co(CO)I$_2$ with Ag(I) salt and the dissociation of CO forming the active species Cp*Co(OAc)$_2$. Then, coordination of the Cp*Co(OAc)$_2$ to the pyrimidyl moiety of the substrate forming the intermediate **A.** Then, the C–H is cleavage via S$_E$Ar or a concerted metalation-deprotonation mechanism to render the aryl–Co(III) intermediate **B.** Finally, the coordination of the azide to the Co center followed by migratory insertion affords the Co(III) –amido complex **C** together with the release of N$_2$. The final product was formed after protonation of **C** with AcOH regenerating the Co active species. Despite these examples, the precise molecular mechanism by which the organic azides react with aryl–M organometallic species remains still unclear; different pathways such as concerted or stepwise pathway and a putative M(V) nitrenoid species have been proposed.
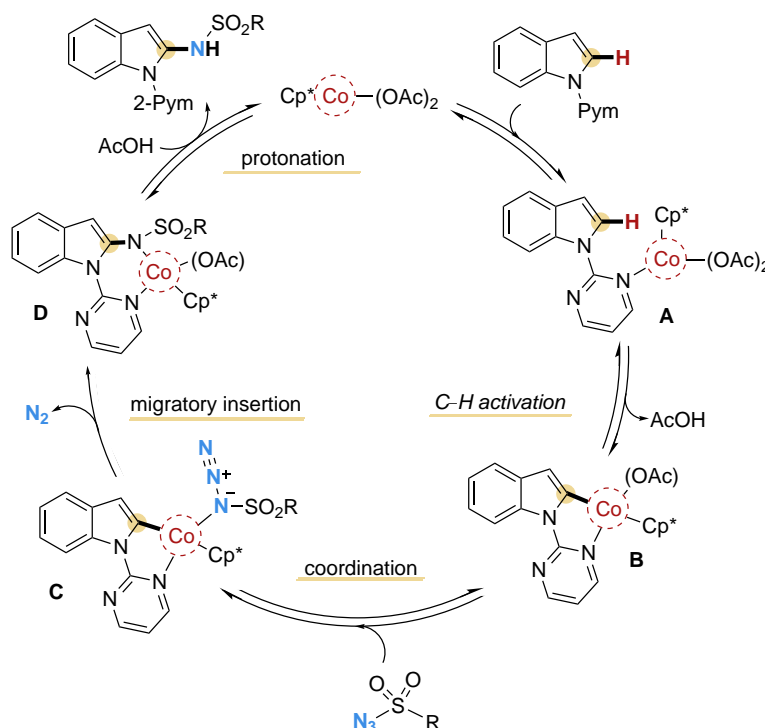
Scheme I.22. Proposed mechanism for C–H amination using azides reported by Kanai and coworkers.

On the other hand, the use of Ni to catalyzed direct C–H amination reactions using azides as nitrogen source is still underexplored. Recently, Xu and coworkers disclosed the nickel-catalyzed direct amidation of arenes using TsN$_3$ (scheme I.23).[121] After exploring different mono- and bidentate directing groups, 8-aminoquinoline (8-AQ) directing group was the optimal for C–H amidation reaction. Chang and coworkers reported the directing group assisted nickel-catalyzed intermolecular C(sp^3)–amidation of carboxamides (Scheme I.23).[122] They use also TsN$_3$ as an aminating reagent affording the intermolecular amidation avoiding the formation of the corresponding intramolecular product. Mechanistic experiments were carried out using the organometallic aryl-Ni(II) complex, which undergoes the C–N coupling in the presence of the TsN$_3$. DFT calculations suggested a Ni(II)/(Ni(III) catalytic cycle presumably via Ni(III)-nitrenoid intermediate species.
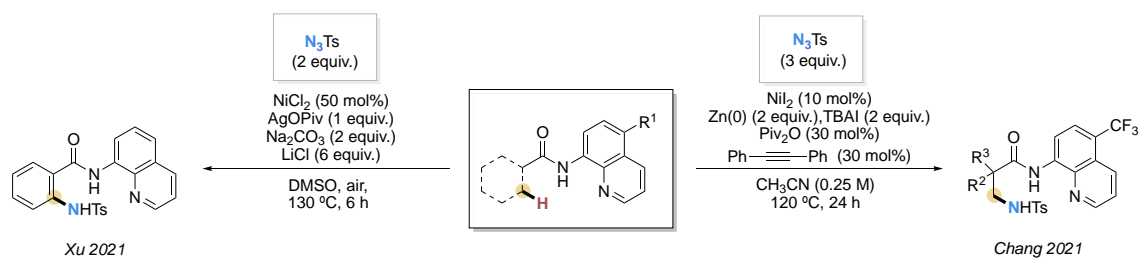
Scheme I.23. Nickel-catalyzed intermolecular C(sp^2)–H and C(sp^3)–H amination using a chelation assisted strategy.

I.3 STRATEGIES FOR FAVOURING THE ARYL–M BOND FORMATION

Nickel- and cobalt-catalyzed cross-coupling reaction are well explored and most of the reported examples are based on low-valent metal catalysts. Several oxidation states of the active catalyst are postulated due to the use of reducing agents in the reaction which compromises the assignment. As it is mentioned above, the isolation and characterization of intermediates is of vital importance for unveiling the mechanistic details. In this context, the formation of C–Metal bond is involved in several reactions in the initial steps of the reaction pathway. In C–H and C–X functionalization reactions the activation of these bonds renders the formation of a new C–Metal bond. Indeed, several cyclometallated complexes have been prepared via C–X and C–H metalation reaction in stoichiometric manner decades ago.

Different strategies have been explored for the formation of this C–Metal bond to understand the mechanism involved in these transformations. Non-cyclic substrate bearing a directing group are well explored achieving the functionalization of these bonds in a selective manner. Furthermore, this strategy has been useful to trap some cyclometallated intermediates due to the coordination of the directing group to the metal center. However, in most of the cases an external ligand is needed to fulfil the coordination sphere and stabilize the organometallic intermediate species. Although some examples are reported (see below), the low stability of these organometallic complex hamper their characterization. On the other hand, the use of macrocyclic model system has been shown a good strategy to trap reaction intermediates. The model macrocyclic substrates present the ideal environment to stabilize high valent metal centers allowing its isolation and characterization. However, the mechanism involved in the C–M cleavage and the subsequent construction of C–C and C-heteroatom bond remains unexplored due to the high reactivity of these intermediates in front the coupling partner, as well as the low stability often associated with these compounds.
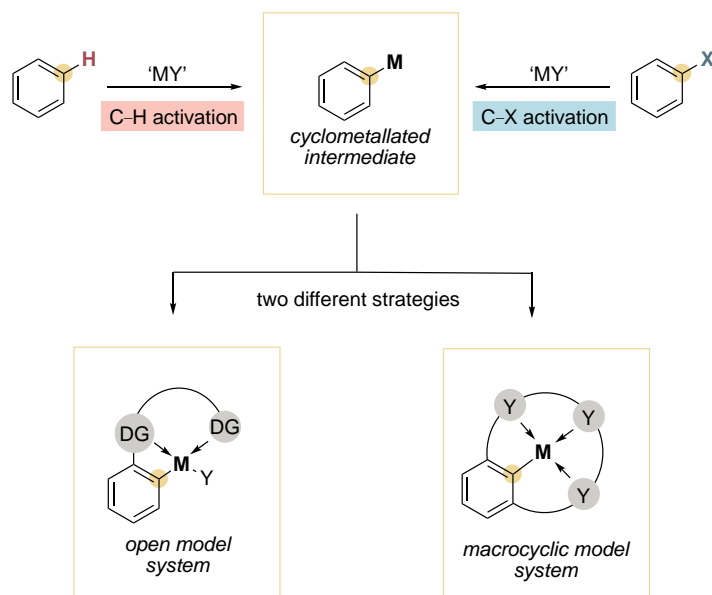
Scheme I.24. Different strategies to study the C–M bond formation reaction via C–H and C–X coupling.

Early examples demonstrated the ability of first-row transition metals to cleave C–X and C–H bonds. Some examples of stoichiometric metalation showed the formation of cyclometallated complexes, stable enough for their characterization.

In this line, Granell and Muller reported the formation of five-member nickelacycle complexes via C–X bond cleavage.[123] The ability of Nickel(0) to activate this bonds was confirmed by reporting a set of aryl-Ni(II) complexes using halo-ortho-substituted imines or N,N-dimethylbenzylamines. The cyclometallated cobalt complexes via C–X activation were also achieved using stoichiometric amounts of cobalt. Li and coworkers reported the feasibility of the aryl chloride oxidative addition at Co(I) metal center.[124] They achieved the isolation and characterization of a key aryl–Co(III)–Me complexes by reacting the chloro-substrate bearing a imine as directing group with Co(I) catalyst. Furthermore, the authors observed that the organometallic complex underwent reductive elimination leading the formation of methyl-arene product (depicted in scheme I.25).
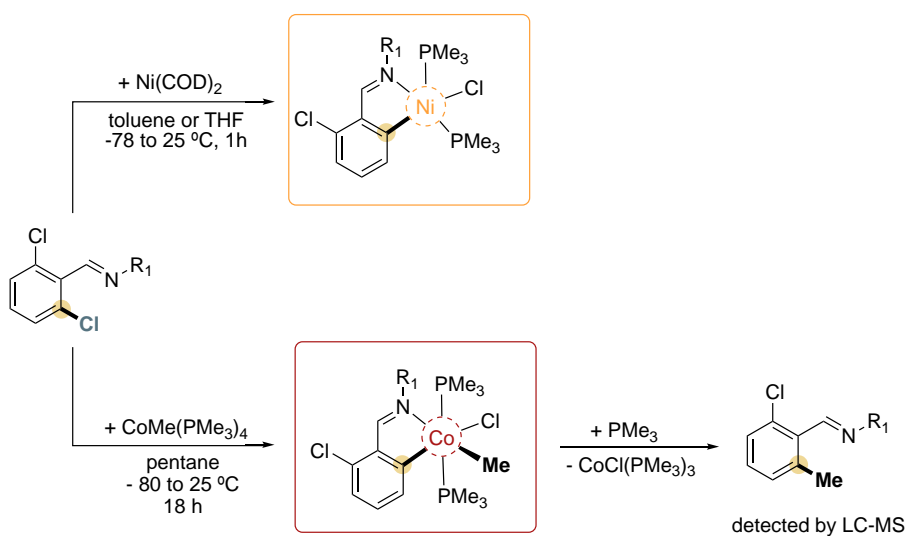
Scheme I.25. Aryl–Co(III) organometallic complex formed via C–Cl cleavage.

Despite these examples demonstrate the ability of metal to activate the C–X bonds, those complexes are not active in catalysis due to their high stability. To get insight into the mechanism involved in these transformations, mechanistic studies as kinetic isotope effects (KIE), radical trap or competition experiments have been performed. However, the involved mechanism remains elusive due to the instability of the corresponding organometallic complexes in catalysis.

I.3.1 Directing group approach in open model systems

In the context of open model substrates, 8-aminoquinoline stands as one of the most effective bidentate directing groups. The first example was reported by Daugulis[94] and coworkers and opened the door to new methodologies based on C–H functionalization using a variety of transition metal with novel selectivities. Indeed, 8-aminoquinoline DG enables the correct environment thanks to the rigid bidentate N,N coordination, which could stabilize organometallic intermediate species involved in the catalysis allowing their detection and, in some cases, their isolation. In this section, relevant cyclometallated intermediate species in C–H functionalization transformations assisted by 8-aminoquinoline DG mediated by nickel and cobalt will be disclosed.

In the context of Ni catalysis, cyclometallated aminoquinoline aryl–Ni(II) intermediates have been proposed for the 8-aminoquinoline directed C–H functionalization reactions. The C–H activation at Ni(II) to form a nickelacycle has been suggested in several catalytic reactions based on kinetic isotope effect (KIE) and experimental H/D exchange, as well as by computational studies. In this line, Sanford group reported the synthesis and the characterization of aryl–Ni(II) complex by reacting $Ni(PEt_3)_4$ with cyclic imide 2-(quinoline-8-yl)isoindoline-1,3-dione (scheme I.26).[125] The addition of picoline as auxiliary ligand gives the enough stabilization to characterize the aryl–Ni(II) complex. The X-ray crystal structure shows a sort of distorted square planar nickel center. The addition of stoichiometric amounts of AgOTf affords the corresponding aryl–Ni(III) organometallic complex. A slightly distorted square pyramidal geometry was revealed by XRD. Sanford explored the C–I bond formation reaction by addition of I_2 using both isolated complexes. Only the aryl–Ni(II) complex underwent aryl–I bond formation using 1 equivalent of I_2 in only 30 minutes. Indeed, the use of this complex as catalyst for the $C(sp^2)$–H iodination afforded 48% of the desired product (56% yield using $Ni(OTf)_2$ catalyst) demonstrating that the complex is catalytically competent. In contrast, the aryl–Ni(III) complex results to be completely inert towards $C(sp^2)$–I bond formations reaction, under stoichiometric as well as catalytic conditions. Different pathways have been proposed for the aryl–Ni bond functionalization such as the direct electrophilic functionalization of aryl–Ni(II) without changing the oxidation state or the involvement of aryl–Ni(III) or aryl–Ni(IV) intermediates which underwent reductive elimination leading the product formation.
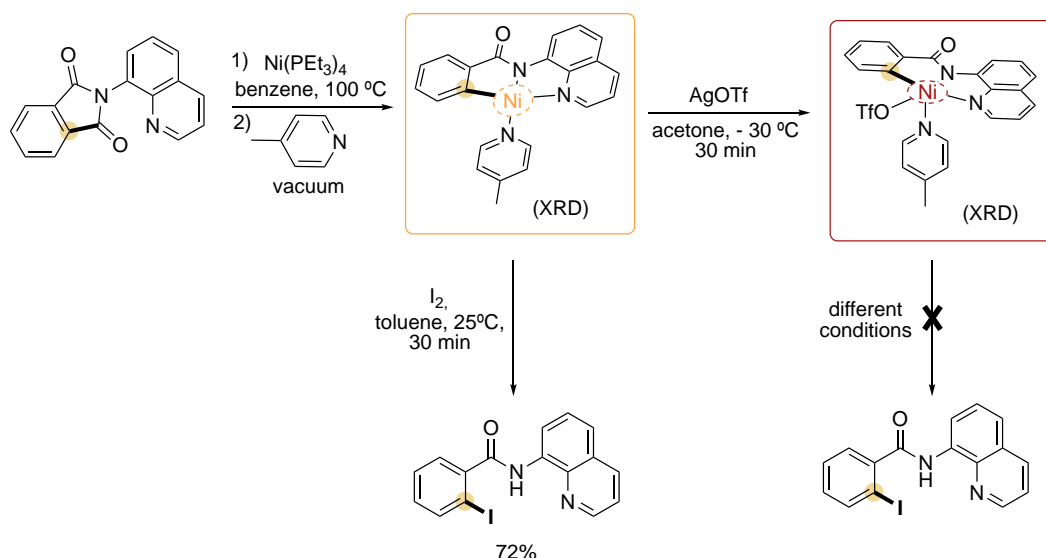
Scheme I.26. Synthesis of aryl–Ni(II) and aryl–Ni(III) organometallic complex bearing a aminoquinoline DG.

The use of external ligands are needed to fulfill the coordination sphere and stabilize the organometallic intermediate species. In some cases, it has been shown that the same 8-aminoquinoline based substrate can also act as external ligand filling the coordination sphere of the metal center. Huang and coworkers developed the dehydrogenative homologation of aromatic amides mediated by nickel(0) catalyst, where a Ni(0)/Ni(II) catalytic cycle was proposed.[104] The authors performed NMR studies and they postulated the detection of the aryl–Ni(II) intermediate, where the nickel(II) center is stabilized by a second 8-aminoquinoline substrate. However, upon isolation, the oxidized aryl–Ni(III) organometallic complex was obtained (scheme I.27). A similar aryl–Ni(III) complex was isolated and characterized by Ackermann in nickel-electrocatalyzed C–H alkoxylation which was competent intermediate in alkoxylation reactions.[126]
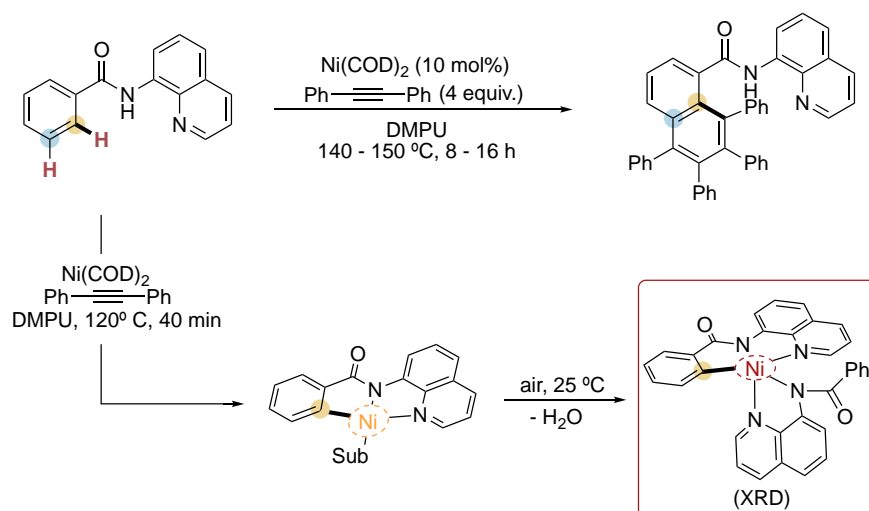
Scheme I.27. Isolation of aryl-Ni(III) organometallic complex via C–H activation.

Within Cobalt-catalyzed C–H functionalization, the C–H cleavage at Co(III) leading a cobalacycle has been proposed in different catalytic systems. The cyclometallated aminoquinoline aryl–Co(III) intermediate have been postulated and in some cases isolated thanks to the right stability offered by the 8-aminoquinoline DG (see scheme I.28). In this context, Daugulis reported cobalt-catalyzed 8-aminoquinoline assisted

alkenylation of C(sp^2)–H bond.[94] By reacting the 8-aminoquinolie scaffold with Co(OAc)$_2$ and NaOPiv as a base with saturated O$_2$ atmosphere in TFE at 60 ºC, the corresponding metalated species is obtained. Thanks to the coordinative properties of the 8-aminoquinoline moiety, they were able to isolate and characterize the aryl–Co(III) intermediate by NMR spectroscopy. It was not until 2016, when Maiti reported the isolation and the first crystallographic evidence of aryl-Co(III) intermediate via C–H activation.[127] The isolated aryl-Co(III) organometallic complex in both stoichiometric and catalytic modes led the corresponding C–C annulated product verifying the involvement of the isolated cobalacycle in the C–H annulation reaction promoted by a dual cobalt catalysis and photocatalysis. Further mechanistic experiments such as radical quenching and kinetic isotope experiments were performed, which suggested a single electron transfer (SET) process. In this line, Niu and Song also took advantage of the 8-aminoquinoline directing group by reporting the synthesis of triarylamines catalyzed by Co(OAc)$_2$·4H$_2$O.[128] They were able to isolate and crystallize the C–H cobalacycle intermediate species. The aryl-Co(III) complex underwent reductive elimination under thermal conditions to end up with the corresponding triarylamine product, thus pointing out the involvement of aryl–Co(III) organometallic intermediate in this C–H amination system. The organometallic aryl–Co(III) intermediate species was also isolated by Ribas and coworkers using the 5-nitro-8-aminoquinoline directing group strategy. The reaction of Co(OAc)$_2$ and NaOPiv·H$_2$O with saturated O$_2$ solution of TFE affords the aryl–Co(III) cobalacycle intermediate. The use of bipy as a co-ligand allows the stabilization of this Oh intermediate allowing its characterization by X-ray diffraction.[101]

Daugulis, 2014
(NMR Characterization)

Maiti, 2016
(XRD)

Niu and Song, 2016
(XRD)

Ribas, 2016
(XRD)
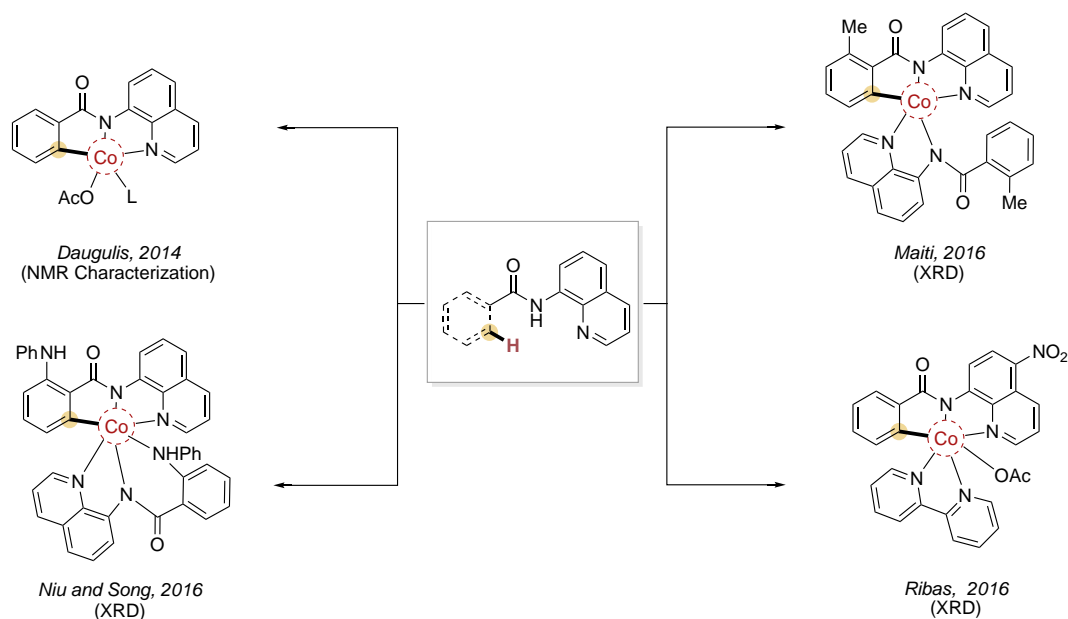
Scheme I.28. Aryl–Co(III) organometallic intermediates isolated using open model 8-aminoquinoline directing group.

I.3.1.1   *Aryl-Co(III) reactivity in front of unsaturated coupling partners*

The C–H activation and the concomitant C–M bond formation is the first step proposed in most of the direct assisted metal-catalyzed C–H functionalization reactions. The isolation of the metallacycle species allows to gain insight into this step, however the low stability of these organometallic complexes often makes challenging to understand how the coupling partner react with the aryl–M complexes to end up with the desired final product.

For this reason, the design of scaffolds to stabilize these intermediates are needed to gain deeper insight into the reactivity of well-defined aryl–M. In this context, Pérez-Temprano reported the isolation of aryl–Co(III)Cp* organometallic complex bearing a pyridine as directing group substantiating the stabilizing effect of Cp* ligand. They explored the aryl–Co(III) cleavage by using different electrophiles as coupling partners to explore the migratory insertion step. The use of diphenylacetyelene and phenylacetylene affords the formation of the corresponding 1,2-inserted complexes (scheme I.29). In contrast, styrene afforded the [1,1]-inserted organometallic complex. In all the cases, the vacant coordination site was filled with an acetonitrile molecule, which fulfills the coordination of the organometallic complex. On the other hand, the use of vinyl acetate also gives the corresponding [1,2]-inserted product with an acetate coordinated to the metal center, instead of the acetonitrile. This study demonstrates the different reactivity on the migratory insertion reaction depending on the unsaturated coupling used obtaining 6- or 7-membered cobaltacycle complexes.[129, 130] The same reactivity was studied using N-pyrimidinylindole and diphenylacetylene achieving the same [1,2]-inserted complex, which was used as catalyst achieving excellent yields of annulated product.[131]
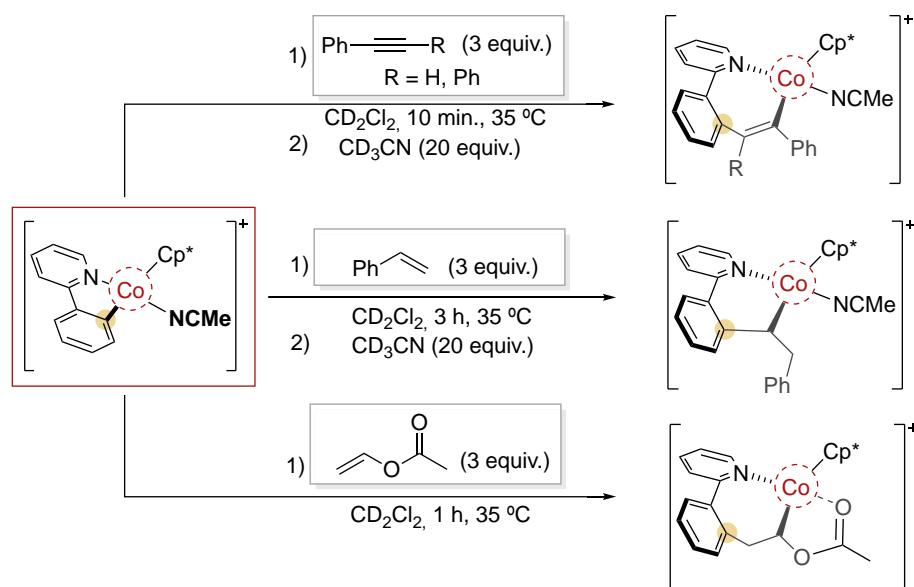
Scheme I.29. Reactivity of aryl-Co(III) with different saturated electrophiles.

I.3.2 Macrocyclic models

A deep understanding of the operating coupling mechanism through aryl–M intermediate species is crucial to develop new methodologies with higher efficiency and selectivity. To overcome the general instability of the intermediate species in open model systems, macrocyclic model systems have been successfully used to stabilize aryl–M species, allowing the detailed study of their reactivity. Macrocyclic model substrates have become useful as an alternative strategy to unravel the mechanism involved in such reaction. The model substrates are able to stabilize metals in a high oxidation state due to the coordinative sphere presented maintaining the reactivity. This synergistic property makes them a good candidate for the isolation and characterization of reaction intermediates which in open model substrates are so instable to trap. This way, the reactivity of a given organometallic complex can be explored in front of different coupling partners. This approach has been applied in several reactions such as cross-coupling reactions as well as in direct C–H functionalization processes. Different tridentate ligands have been explored to stabilize metals in a high oxidation state.[132-138] In this context,

triazamacrocylcic type ligands has been shown excellent model substrates allowing the stabilization of high valent metal complexes.

I.3.2.1 Well-defined Aryl–Ni organometallic complexes

In this context, macrocyclic model aryl halide substrates have been used to explore the nickel-mediated aryl–X and aryl–H activation bond, and several Ni complexes with different oxidation states have been isolated. Different model ligands have been used to stabilize these complexes as shown below, highlighting the importance of the ligand design to adopt the correct geometry such as square-planar or octahedral geometry.

I.3.2.1.1 Stabilization of Aryl–Ni complexes

Most of the nickel-catalyzed organic transformation are based on Ni(0)/Ni(II) catalytic systems via the formation of $C(sp^2)$–Ni(II) complex. Wang and coworkers reported the use of macrocyclic azacalix[m]arene[n]pyridine ligands, which can react with a Ni(II) source to form a aryl–Ni(II) complex through a direct electrophilic metalation (scheme I.30).[139] The macrocyclic model substrate is able to stabilize the aryl–Ni(II) organometallic complex exhibiting a square-planar coordination geometry for the nickel center. Furthermore, the authors also studied its reactivity in front of a range of nucleophiles, which will be discussed in the following section.
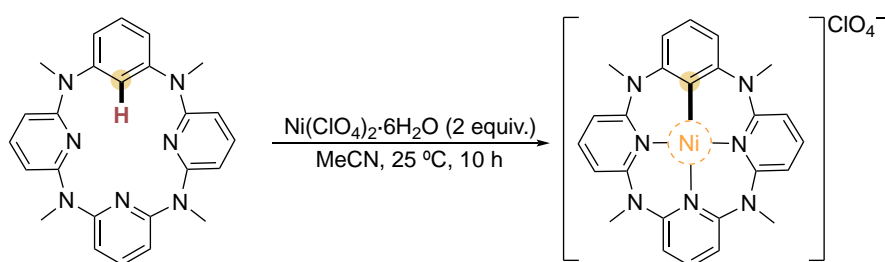
Scheme I.30. Synthesis of Aryl–Ni(II) organometallic complex via $C(sp^2)$–H cleavage by Wang.

Ribas and coworkers also contributed in this field by reporting the synthesis of a square-planar aryl–Ni(II) complex via oxidative addition to Ni(cod)$_2$.[140] The oxidative addition product was also achieved under mild conditions in THF in an inert atmosphere. Furthermore, they reported the synthesis of the same aryl–Ni(II) organometallic complex via C–H nickelation as depicted in scheme I.31.[141] Since nickel does not change its oxidation state, the authors proposed a concerted-metalation-deprotonation (CMD) mechanism for the C–H bond cleavage. In this case, the complex was formed only with substrate bearing secondary amines, confirming that the nature of the RN$_{amino}$ group on the triazamacrocylic model affect drastically the reactivity of the substrates. The square-planar aryl–Ni(II) complex reacts with Umemoto or Togni reagent to afford the trifluoromethylation of the triazamacrocyclic substrate.
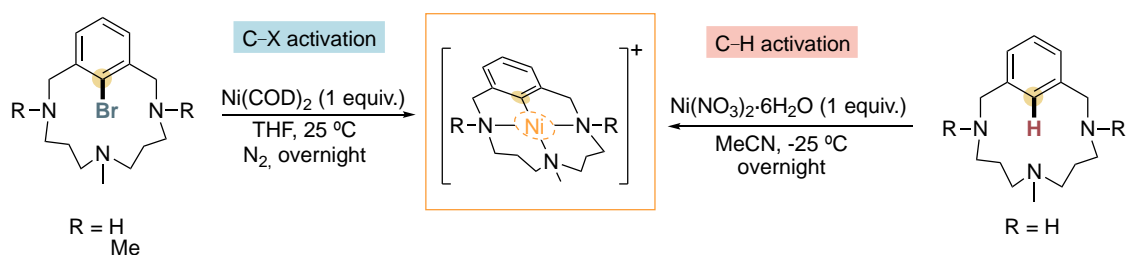
Scheme I.31. Aryl–Ni(II) organometallic complex synthetized via C–X or C–H activation using a triazamacrocyclic model substrate by Ribas.

High-valent nickel species were also proposed as intermediates in nickel-catalyzed organic transformation. Octahedral aryl–Ni(III) organometallic species was also isolated using a macrocyclic model substrates. Mirica and coworkers reported the synthesis of aryl–Ni(II) and aryl–Ni(III) complexes using a triazamacrocylic ligand as depicted in scheme I.32.[142] Firstly, a trigonal bipyramidal aryl–Ni(II) organometallic complex was synthetized via oxidative addition to a aryl–Br bond (scheme I.32a). Moreover, the aryl–Ni(II) complex can be oxidized to a Ni(III) complex with several oxidants, such as $FcPF_6$ in CH_3CN. The XRD structure reveals a distorted octahedral geometry around the Ni(III) complex, where a CH_3CN moiety fulfills the 6 coordination sites. On the other hand, when the complex aryl–Ni(II) is subjected to $TlSbF_6$ to remove the bromide, a diamagnetic Ni(II) organometallic species is formed, where the two axial N_{amine} weakly coordinate the metal center, adopting a pseudo square-planar geometry. The complex is easily oxidized using $FcPF_6$ forming a stable aryl–Ni(III) species. The same group, synthesized a derivate ligand by changing the *tert*-butyl (*t*Bu) groups by a neopentyl group (Np) (scheme I.32b).[143] In the presence of $NiBr_2(DME)$, both complexes afforded the corresponding Ni(II) complex. The XRD structure showed a metal–arene interaction, however with no $C(sp^2)$–H activation. Interestingly, the neopentyl derivative ligand showed a stronger interaction between the $C(sp^2)$–H and the nickel metal center (agostic interaction) than *tert*-butyl, suggesting that the use of less sterically hindered group (Np) can promote the $C(sp^2)$–H activation, again pointing out the effect of the N_{amino} groups in the model ligand. Indeed, adding 3 equivalents of $AgBF_4$ afforded the aryl–Ni(III) organometallic complex via $C(sp^2)$–H activation. A set of experiments were done, confirming that the $C(sp^2)$–H cleavage is at Ni(III). The aryl–Ni(III) complex can reductive eliminate easily to form C–C and C–Heteroatom bond where will be discussed in the following section.

a. Synthesis of aryl–Ni(III) complex using aryl–Br model substrate
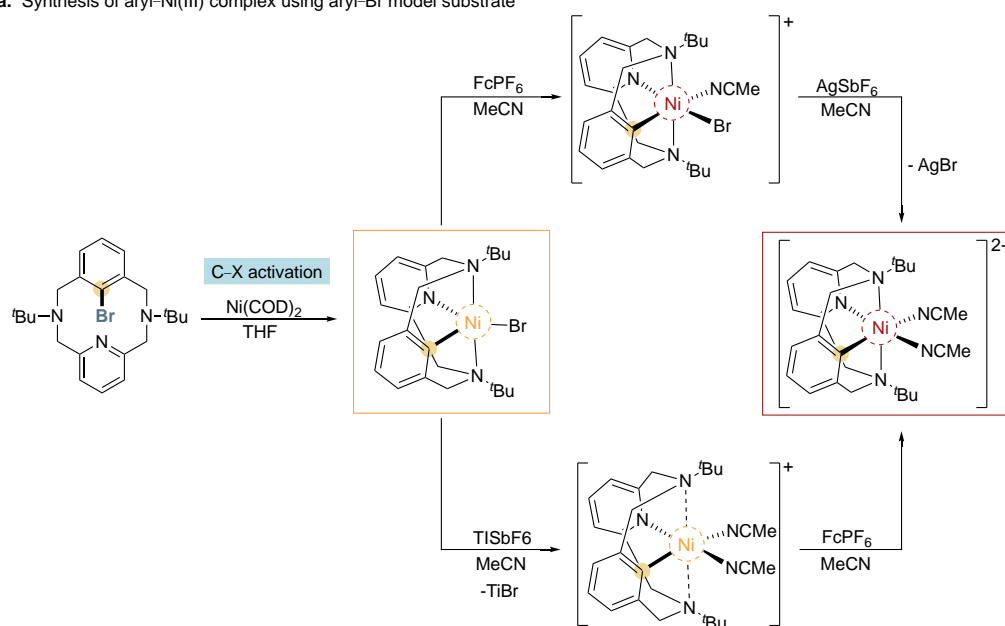
b. Synthesis of aryl–Ni(III) complex using aryl–H model substrate
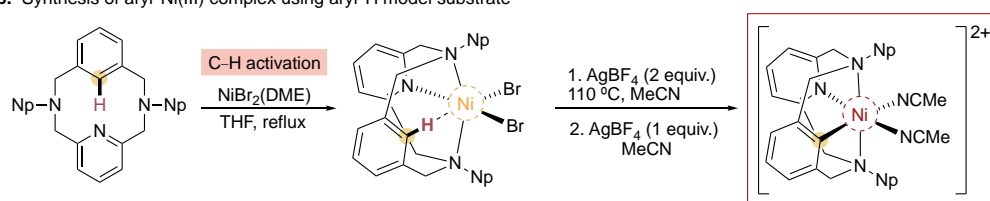
Scheme I.32. Synthesis of aryl–Ni(III) organometallic complex using triazamacrocyclic model substrates via C–X and C–H activation.

I.3.2.1.2 Reactivity of macrocyclic Aryl–Ni organometallic complexes

As mentioned above, to understand the mechanism of how the coupling partner interacts with the metal center to achieve the desired functionalization, a delicate balance between stability of aryl-M intermediate species and reactivity with the corresponding coupling partners is needed. In this line, Wang and coworkers subjected their macrocyclic azacalix[1]arene[3]pyridine-based aryl–Ni(II) complex with several nucleophiles such as organolithium reagents achieving the corresponding arylated and alkylated product (see scheme I.33).[139] Moreover, they achieved also the C–Heteroatom bond formation such as C–N, C–O as well as C–Br when the aryl–Ni complex reacts with sodium azide, phenol, hydroxyl and potassium bromide.
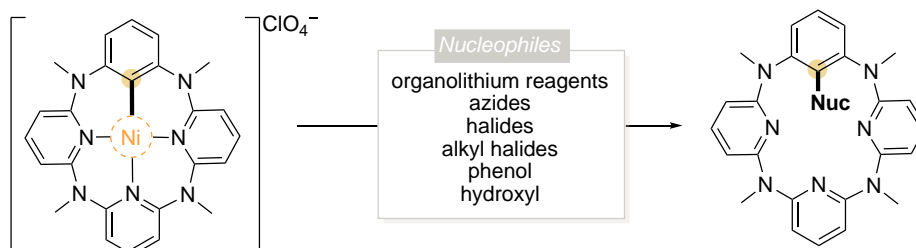
Scheme I.33. Reactivity of the azacalix[1]arene[3]pyridine-based aryl–Ni(II) complex with different nucleophiles forming C–C and C–Heteroatom bonds reported by Wang and coworkers.

Ribas and coworkers also explored the reactivity of a well-defined triazamacrocyclic square-planar aryl–Ni(II) complex.[140] In contrast to Wang's system, the aryl–Ni(II) complex did not react with nucleophiles as boronic acid, phenols or sodium azide. The lack reactivity observed with different nucleophiles clearly indicated a higher stability of the Ni(II) organometallic complex, based on its shorter C–Ni(II) bond. However, when they used electrophilic CF_3^+ sources such as Umemoto or Togni reagents the trifluoromethylation of the macrocyclic architecture was observed under mild conditions (see scheme I.34). Experimental and theoretical studies together suggested a single electron transfer (SET) mechanism, firstly forming a transient aryl–Ni(III)/CF$_3$· adduct which rapidly leads to a transient aryl–Ni(IV)–CF$_3$ complex. The trifluoromethylated product was finally formed via reductive elimination of the Ni(IV) complex.
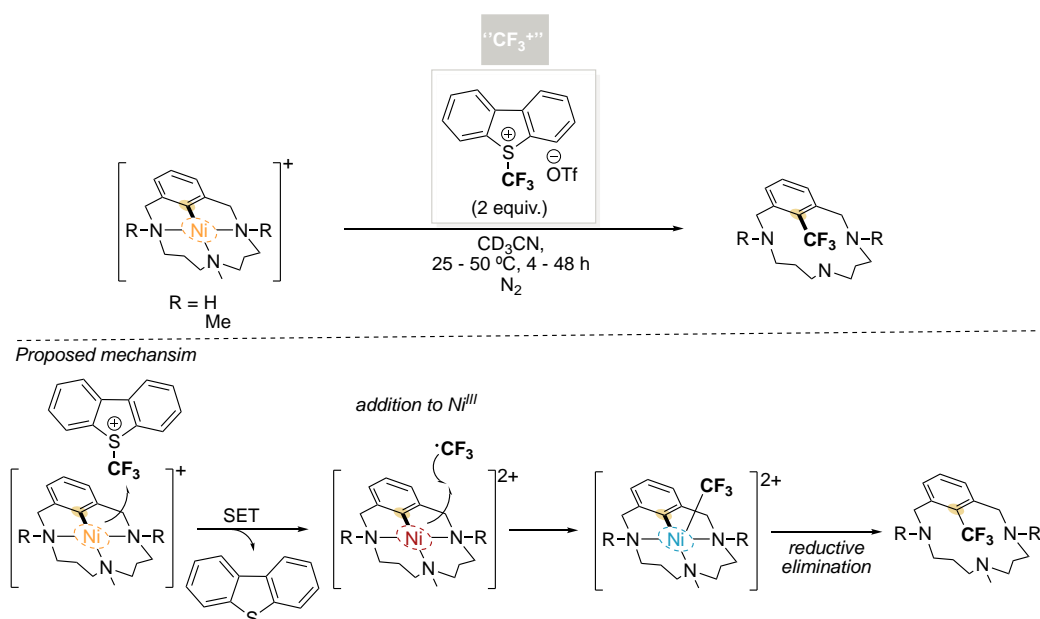
Scheme I.34. Proposed mechanism for the trifluoromethylation of the aryl–Ni(II) model substrate involving aryl-Ni(III)/CF$_3$· and aryl-Ni(IV)–CF$_3$ intermediates.

The reactivity of a well-defined octahedral aryl–Ni(III) organometallic complex bearing a N_3C-type ligand was also studied to form a new C–C bond and C–O bond. Mirica and coworkers explored the alkoxylation, cyanation and cyanoalkylation of the aryl–Ni(III) complex. The reactivity of the aryl–Ni(III) complex in front of –OMe and –OH sources afforded the corresponding methoxylation and hydroxylation product (scheme I.35).[142] Subjecting the aryl–Ni(III) bearing two acetonitrile in the labile positions with and excess of NaOMe in CH_3CN/CH_3OH leads the formation of the Oh aryl–Ni(III)–$(OMe)_2$. The XRD crystal structure reveled a distorted octahedral geometry of the Ni(III) center bearing two –OMe moieties. This complex evolves slowly at room temperature to the formation of the corresponding methoxylation product and the protonation ligand in a 1:1 ratio. The authors observed a quantitative formation of the aryl–OMe product adding an excess of NaOMe together with $PhI(PyOMe)_2OTf$ as oxidant. These results suggested the involvement of high valent Ni species in Ni-catalyzed C–O bond formation reactions.
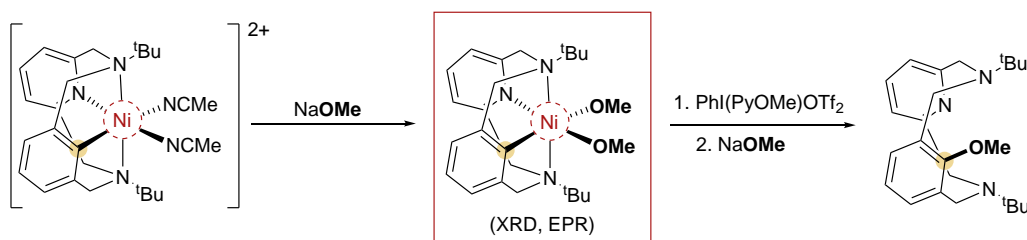
Scheme I.35. Methoxylation and hydroxylation of well-defined aryl-Ni(III) organometallic complex.

Mirica group also investigate the mechanism involved in the aryl cyanation mediated by nickel (see scheme I.36a).[144] They reported the synthesis of Oh aryl–Ni(II)–$(CN^tBu)_2$ complex by reacting the aryl–Ni(II) with CN^tBu and $TlPF_6$ in THF. The single crystal X-ray structure shows a distorted octahedral Ni(II) complex bearing two –CN^tBu units. This complex did not evolve toward the cyanation product at room temperature. However, the oxidation of this complex using $NOPF_6$ led to the formation of aryl–CN coupling product quantitatively in only 5 minutes, suggesting that the cyanation reaction occur at Ni(III). To confirm this hypothesis, the authors reacted the starting aryl–Ni(III)–$(CH_3CN)_2$ complex with 2 equivalents of CN^tBu, observing the formation of the aryl-CN product. Based on their results, an oxidatively-induced aromatic cyanation by a Ni(III) center was proposed. The modification of the side arms of the macrocyclic model system with less sterically hindered (^tBu to Np moiety) was also reported by the same group. Oxidatively induced aryl–H bond activation at Ni(III) center was observed using the less sterically model system. The corresponding well-defined aryl–Ni(III) organometallic center reacts rapidly with different nitriles giving the corresponding cyanoalkylation product at room temperature (scheme I.36b).[143]

a) Cyanation mediated by Ni(III)
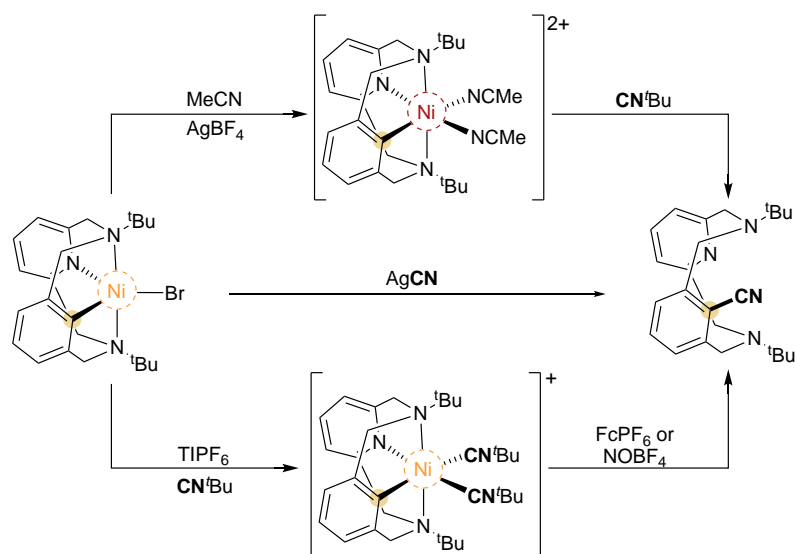
b) Cyanoalkylation mediated by Ni(III)
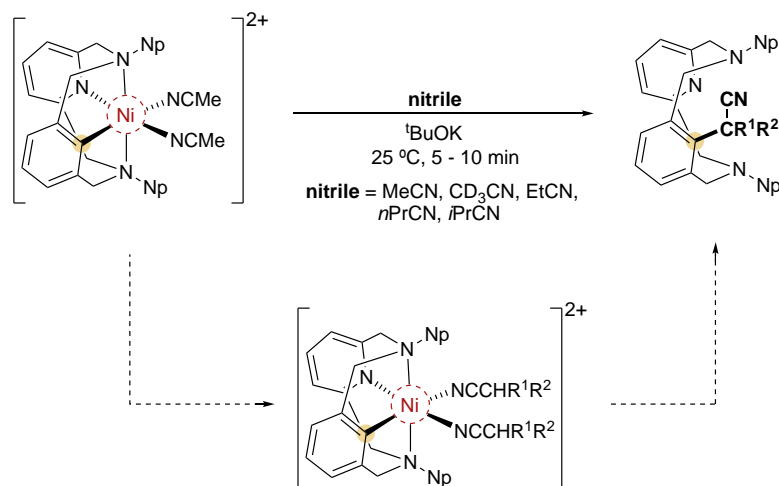
Scheme I.36. a) Aromatic cyanation by well-defined aryl–Ni(III) complex. b) Aromatic cyanoalkylation mediated by Ni(III) organometallic complex.

I.3.2.2 Well-defined Aryl–Co organometallic complexes

I.3.2.2.1 Stabilization of Aryl–Co(III) complexes

The use of N_3C macrocyclic ligand as a model platform architecture has been used to explore the C–H activation to form aryl–Co(III) and their reactivity. Ribas pioneered this field by reacting the macrocyclic ligand with $CoBr_2$ salt and AgOAc afforded the Co(II) organometallic complexes under mild conditions.[101] Its crystal structure showed that the ligand coordinates to the cobalt center by the pyridine moiety and only one pending N_{amine} with two acetates in a bidentate fashion to fill the 6 coordination sites. The incipient interaction of the Co(II) center with the aryl C–H bond suggested the possibility to cleavage this bond. Indeed, by heating at 100 ºC the corresponding aryl–Co(III) organometallic species was formed via C–H activation. A set of aryl–Co(III) organometallic species were synthetized with different benzoate as counter anions as depicted in scheme I.37.[145]
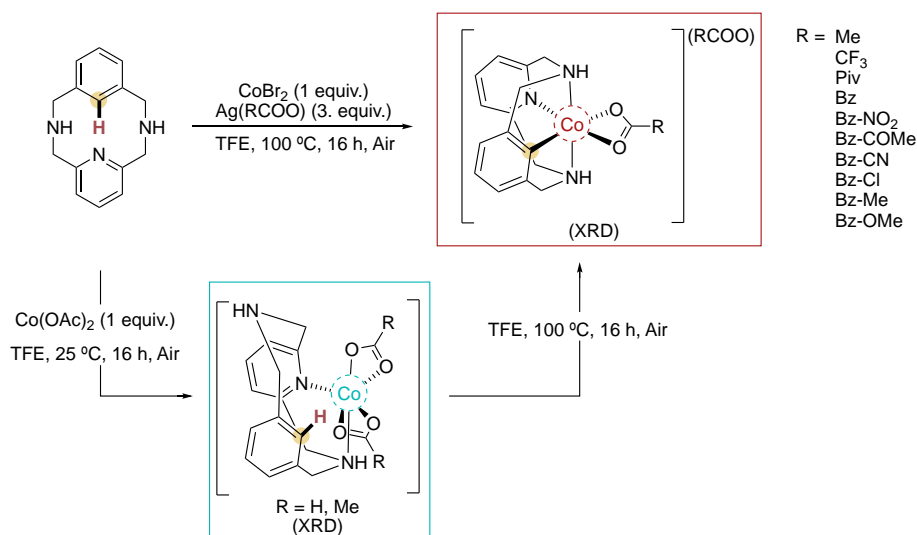
Scheme I.37. Synthesis of Co(II) intermediate species and the corresponding aryl–Co(III) complexes reported by Ribas and coworkers.

I.3.2.2.2 Reactivity of Oh Aryl–Co(III) complexes

Ribas group explored the reactivity of the well-defined Oh aryl–Co(III) complexes with different reagents. When aryl–Co(III) organometallic complex was reacted with terminal alkynes, 5- or 6-memebered products annulation coupling products were obtained, depending on the alkyne used (see scheme I.38). 1-ethylnyl-4-nitrobenzene led to the dihydroisoindoline product (5-membered ring) in a regioselective manner via intramolecular cyclization.[101] Different reactivity was observed using phenylacetylene, obtaining regioselectively the dihydroisoquinoline (6-membered ring) product. DFT calculations suggested an acetylide pathway, which explained the formation of 5-membered cyclic product, thus ruling out the commonly proposed migratory insertion mechanism (scheme I.38).
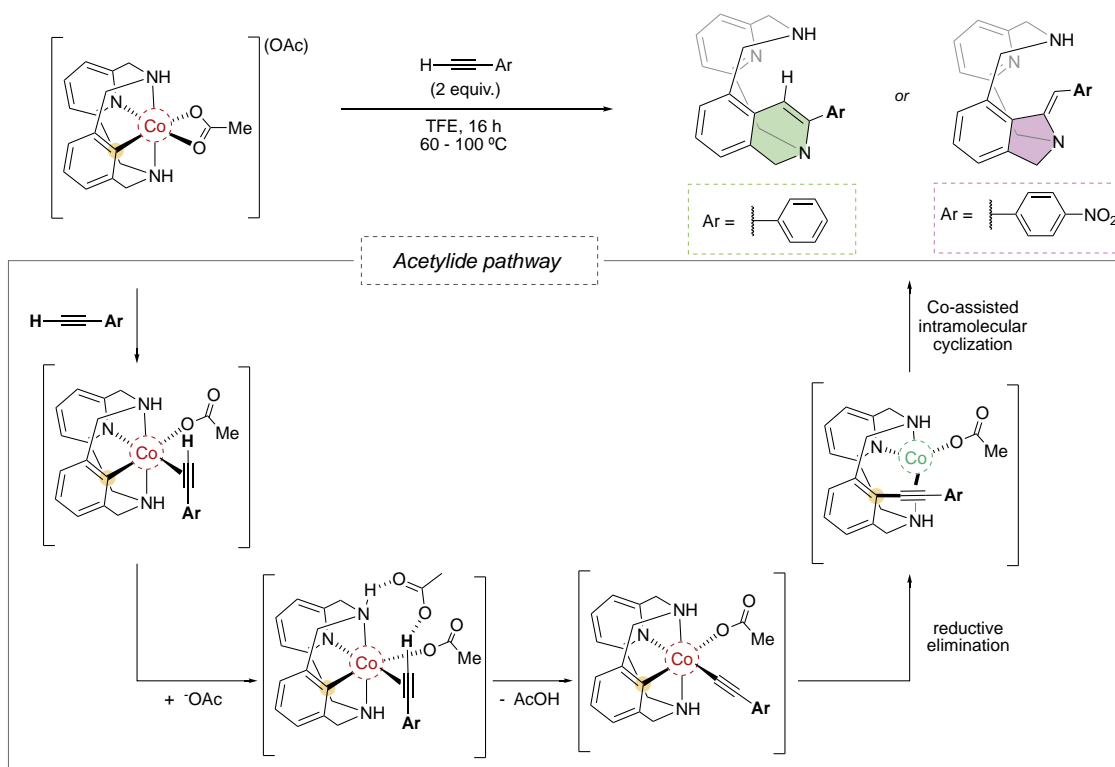
Scheme I.38. Reactivity of a well-defined aryl–Co(III) organometallic complex with terminal alkynes via acetylide pathway.

With this observed reactivity using terminal cs, the same group explored the C–C bond formation using diazo esters.[146] The use of ethyl diazoacetate (EDA) with the aryl–Co(III) complex led to the formation of 1,4-dihydroisoquinolin-3(2H)-one annulation product depicted in scheme I.39. The addition of a Lewis acid enhanced the reactivity significantly. Furthermore, the high stability of the model system allowed the isolation and characterization an aryl–Co(III)–alkyl enolate intermediate, which was also defined as a "masked carbene" species. The evolution of the aryl–Co(III) alkyl enolate complex to the desired product confirmed that is an actual intermediate species of the reactivity observed. DFT calculations pointed out that this occurs via intramolecular S_N2-like pathway. The role of Li^+ as Lewis acid was proposed as a promoter of the "masked carbene" activation leading the C–O bond cleavage and the concomitant C–C bond formation.
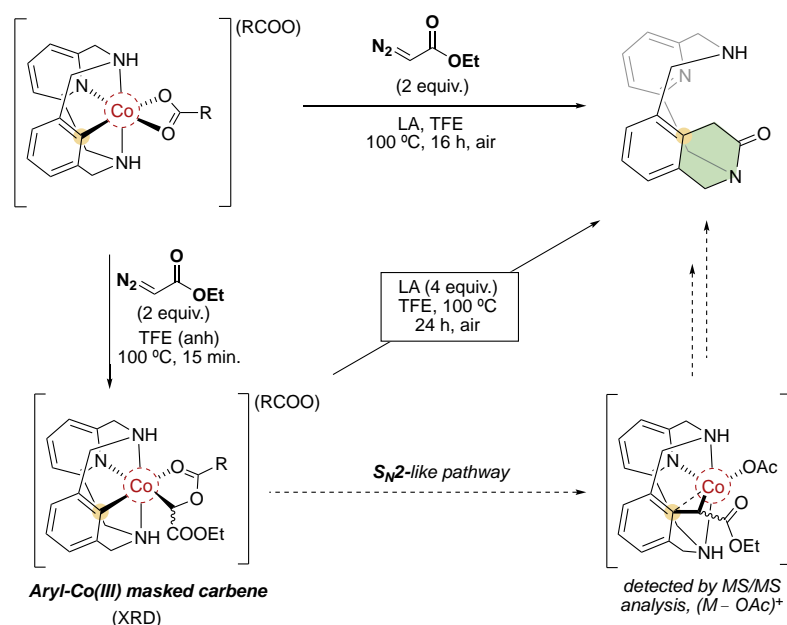
Scheme I.39. Reactivity of well-defined aryl–Co(III) complexes with EDA forming a aryl–Co(III) masked carbene intermediate and the corresponding annulated product.

I.3.2.3 Aryl-M (Cu and Ag) organometallic complexes

In the above section, the beneficial use model macrocyclic substrates to understand the operating mechanism in different reactions using Cobalt (group 9) and Nickel (group 10) metals has been shown. Copper is a well-studied metal which is able to catalyze different reaction such as the well-studied C-heteroatom Ullmann-type transformation. In this context, the use of trizamacrocyclic model platforms permitted the isolation and characterization of a range of well-defined aryl–Cu(III) organometallic complexes via C–H activation.[141, 147-150] For instance, the most relevant two-electron redox processes in Ullmann-type coupling, i.e. Cu(I)/Cu(III) oxidative addition and reductive elimination, were demonstrated for the first time using a triazamacrozyclic model scaffold reported by Ribas and Stahl (Scheme I.40).[151] Subjecting the well-defined aryl–Cu(III) to different nucleophiles such as halides, phenols, amides, carboxylic acids and thiols afforded the desired aryl-heteroatom coupling product.[152-156] Furthermore, the catalytic version was also explored in which the aryl–Cu(III)–X intermediate species was also characterized.
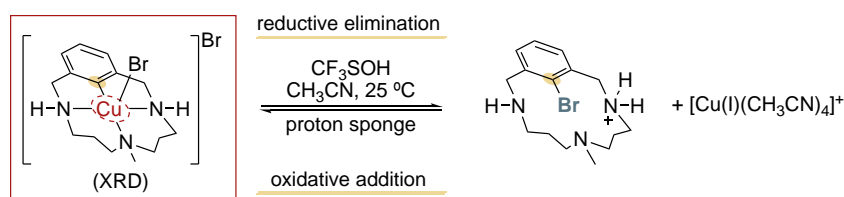
Scheme I.40. Reversible oxidative addition of aryl halides to Cu(I) using a triazamacrocyclic model substrate.

In contrast to copper, silver-catalyzed cross-coupling reactions are underdeveloped. Despite silver salts are frequently used as cocatalyst or as additives in cross-coupling reactions, the use of silver salts as a main catalyst in these transformation remains unusual. However, some examples have been reported based on Sonogashira-type coupling[157] and Ullmann-type C–N and C–O coupling[158], albeit without a clear operative mechanism. Some examples of high-valent Ag(III) complexes have been reported, highlighting the Ag(III)-N-confused porphyrins (NCPs).[150] These scaffolds offer the correct square planar geometry allowing the stabilization of the d[8]-electronic

configuration Ag(III) species. Also the use of triazamacrocyclic ligands to stabilize aryl-Ag(III) organometallic species was reported by Ribas.[159] The well-defined aryl–Ag(III) complex was synthesized by reaction the aryl-halide model system with $AgClO_4$ through an oxidative addition step, a two-electron process not known for silver at that time. Furthermore, a C–C and C–Heteroatom bond formation was achieved by subjecting the aryl–Ag(III) complex with a range of nucleophiles. The authors also designed a catalytic version using aryl-halide scaffold and Ag(I) catalyst achieving both C–O and C–C coupling demonstrating the viability of using silver in two-electron redox processes. This breakthrough opened the door the develop novel methodologies based on Ag-catalyzed cross-coupling transformations.
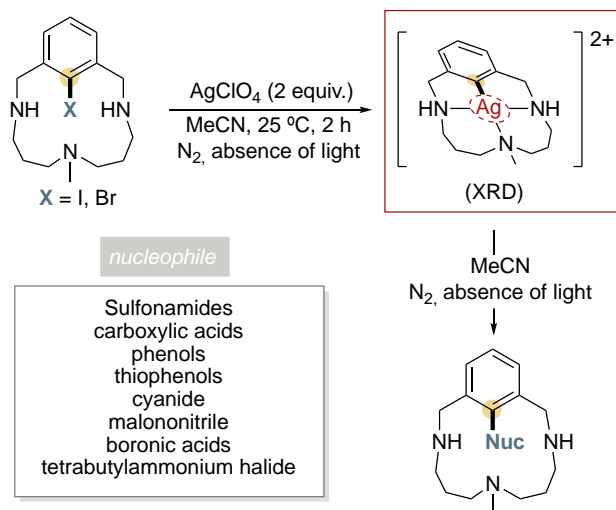
Scheme I.41. Synthesis of a well-defined aryl–Ag(III) complex and its reactivity in front of different nucleophiles.

I.4 REFERENCES

[1]   Magano, J.; Dunetz, J. R. *Chem. Rev.* **2011,** *111*, 2177-2250.

[2]   Campeau, L.-C.; Hazari, N. *Organometallics* **2019,** *38*, 3-35.

[3]   Knappke, C. E. I.; Jacobi von Wangelin, A. *Chem. Soc. Rev.* **2011,** *40*, 4948-4962.

[4]   Han, F.-S. *Chem. Soc. Rev.* **2013,** *42*, 5270-5298.

[5]   Su, B.; Cao, Z.-C.; Shi, Z.-J. *Acc. Chem. Res.* **2015,** *48*, 886-896.

[6]   Ruiz-Castillo, P.; Buchwald, S. L. *Chem. Rev.* **2016,** *116*, 12564-12649.

[7]   Choi, J.; Fu, G. C. *Science* **2017,** *356*, eaaf7230.

[8]   Buskes, M. J.; Blanco, M.-J. *Molecules* **2020,** *25*, 3493.

[9]   Jana, R.; Pathak, T. P.; Sigman, M. S. *Chem. Rev.* **2011,** *111*, 1417-1492.

[10] Jeschke, P. *ChemBioChem* **2004,** *5*, 570-589.

[11] Böhm, H.-J.; Banner, D.; Bendels, S.; Kansy, M.; Kuhn, B.; Müller, K.; Obst-Sander, U.; Stahl, M. *ChemBioChem* **2004,** *5*, 637-643.

[12] Müller, K.; Faeh, C.; Diederich, F. *Science* **2007,** *317*, 1881-1886.

[13] Pike, S. D.; Crimmin, M. R.; Chaplin, A. B. *Chem. Commun.* **2017,** *53*, 3615-3633.

[14] Purser, S.; Moore, P. R.; Swallow, S.; Gouverneur, V. *Chem. Soc. Rev.* **2008,** *37*, 320-330.

[15] Wang, J.; Sánchez-Roselló, M.; Aceña, J. L.; del Pozo, C.; Sorochinsky, A. E.; Fustero, S.; Soloshonok, V. A.; Liu, H. *Chem. Rev.* **2014,** *114*, 2432-2506.

[16] Fahey, D. R.; Mahan, J. E. *J. Am. Chem. Soc.* **1977,** *99*, 2501-2508.

[17] Cronin, L.; Higgitt, C. L.; Karch, R.; Perutz, R. N. *Organometallics* **1997,** *16*, 4920-4928.

[18] Braun, T.; Perutz, R. N. *Chem. Commun.* **2002**, 2749-2757.

[19] Braun, T.; Cronin, L.; Higgitt, C.; McGrady, J.; Perutz, R.; Reinhold, M. *New J. Chem.* **2001,** *25*, 19-21.

[20] Zhao, B.; Rogge, T.; Ackermann, L.; Shi, Z. *Chem. Soc. Rev.* **2021,** *50*, 8903-8953.

[21] Fu, L.; Chen, Q.; Nishihara, Y. *Chem. Rec.* **2021,** *n/a*.

[22] Amii, H.; Uneyama, K. *Chem. Rev.* **2009,** *109*, 2119-2183.

[23] Sun, A. D.; Love, J. A. *Dalton Trans.* **2010,** *39*, 10362-10374.

[24] O'Hagan, D. *Chem. Soc. Rev.* **2008,** *37*, 308-319.

[25] Ahrens, T.; Kohlmann, J.; Ahrens, M.; Braun, T. *Chem. Rev.* **2015,** *115*, 931-972.

[26] Kiso, Y.; Tamao, K.; Kumada, M. *J. Organomet. Chem.* **1973,** *50*, C12-C14.

[27] Yoshikai, N.; Mashima, H.; Nakamura, E. *J. Am. Chem. Soc.* **2005,** *127*, 17978-17979.

[28] Yoshikai, N.; Matsuda, H.; Nakamura, E. *J. Am. Chem. Soc.* **2009,** *131*, 9590-9599.

[29] Wang, J.-R.; Manabe, K. *Org. Lett.* **2009,** *11*, 741-744.

[30] Nakamura, Y.; Yoshikai, N.; Ilies, L.; Nakamura, E. *Org. Lett.* **2012,** *14*, 3316-3319.

[31] Ackermann, L.; Wechsler, C.; Kapdi, A.; Althammer, A. *Synlett* **2010,** *2010*, 294-298.

[32] Guo, W.-J.; Wang, Z.-X. *J. Org. Chem.* **2013,** *78*, 1054-1061.

[33] Yu, D.-G.; Wang, C.-s.; Yao, C.; Shen, Q.; Lu, L. *Org. Lett.* **2014,** *16 21*, 5544-7.

[34] Zhou, J.; Berthel, J. H. J.; Kuntze-Fechner, M. W.; Friedrich, A.; Marder, T. B.; Radius, U. *J. Org. Chem.* **2016,** *81*, 5789-5794.

[35] Tobisu, M.; Xu, T.; Shimasaki, T.; Chatani, N. *J. Am. Chem. Soc.* **2011,** *133*, 19505-19511.

[36] Ho, Y. A.; Leiendecker, M.; Liu, X.; Wang, C.; Alandini, N.; Rueping, M. *Org. Lett.* **2018,** *20*, 5644-5647.

[37] Yu, D.; Shen, Q.; Lu, L. *J. Org. Chem.* **2012,** *77*, 1798-1804.

[38] Böhm, V. P. W.; Gstöttmayr, C. W. K.; Weskamp, T.; Herrmann, W. A. *Angew. Chem. Int. Ed.* **2001,** *40*, 3387-3389.

[39] Ackermann, L.; Born, R.; Spatz, J. H.; Meyer, D. *Angew. Chem. Int. Ed.* **2005,** *44*, 7216-7219.

[40] O'Neill, M. J.; Riesebeck, T.; Cornella, J. *Angew. Chem. Int. Ed.* **2018,** *57*, 9103-9107.

[41] Schaub, T.; Backes, M.; Radius, U. *J. Am. Chem. Soc.* **2006,** *128*, 15964-15965.

[42] Sun, A. D.; Love, J. A. *Org. Lett.* **2011,** *13*, 2750-2753.

[43] Schutyser, W.; Renders, T.; Van den Bosch, S.; Koelewijn, S. F.; Beckham, G. T.; Sels, B. F. *Chem. Soc. Rev.* **2018,** *47*, 852-908.

[44] Sun, Z.; Fridrich, B.; de Santi, A.; Elangovan, S.; Barta, K. *Chem. Rev.* **2018,** *118*, 614-678.

[45] Li, C.; Zhao, X.; Wang, A.; Huber, G. W.; Zhang, T. *Chem. Rev.* **2015,** *115*, 11559-11624.

[46] Ragauskas, A. J.; Beckham, G. T.; Biddy, M. J.; Chandra, R.; Chen, F.; Davis, M. F.; Davison, B. H.; Dixon, R. A.; Gilna, P.; Keller, M.; Langan, P.; Naskar, A. K.; Saddler, J. N.; Tschaplinski, T. J.; Tuskan, G. A.; Wyman, C. E. *Science* **2014,** *344*, 1246843.

[47] Mosier, N.; Wyman, C.; Dale, B.; Elander, R.; Lee, Y. Y.; Holtzapple, M.; Ladisch, M. *Bioresour. Technol.* **2005,** *96*, 673-686.

[48] Tuck, C. O.; Pérez, E.; Horváth, I. T.; Sheldon, R. A.; Poliakoff, M. *Science* **2012,** *337*, 695-699.

[49] Subbotina, E.; Rukkijakan, T.; Marquez-Medina, M. D.; Yu, X.; Johnsson, M.; Samec, J. S. M. *Nat. Chem.* **2021**.

[50] Luo, H.; Weeda, E. P.; Alherech, M.; Anson, C. W.; Karlen, S. D.; Cui, Y.; Foster, C. E.; Stahl, S. S. *J. Am. Chem. Soc.* **2021,** *143*, 15462-15470.

[51] Mesganaw, T.; Garg, N. K. *Org. Process Res. Dev.* **2013,** *17*, 29-39.

[52] Yamaguchi, J.; Muto, K.; Itami, K. *Eur. J. Org. Chem.* **2013,** *2013*, 19-30.

[53] Correa, A.; Cornella, J.; Martin, R. *Angew. Chem. Int. Ed.* **2013,** *52*, 1878-1880.

[54] Rosen, B. M.; Quasdorf, K. W.; Wilson, D. A.; Zhang, N.; Resmerita, A.-M.; Garg, N. K.; Percec, V. *Chem. Rev.* **2011,** *111*, 1346-1416.

[55] Li, B.-J.; Yu, D.-G.; Sun, C.-L.; Shi, Z.-J. *Chem. Eur. J.* **2011,** *17*, 1728-1759.

[56] Yu, D.-G.; Li, B.-J.; Shi, Z.-J. *Acc. Chem. Res.* **2010,** *43*, 1486-1495.

[57] Tobisu, M.; Chatani, N., Metal-Catalyzed Aromatic C-O Bond Activation/Transformation. In *Organometallics for Green Catalysis*, Dixneuf, P. H.; Soulé, J.-F., Eds. Springer International Publishing: Cham, 2019; pp 103-140.

[58] Tobisu, M.; Chatani, N. *Acc. Chem. Res.* **2015,** *48*, 1717-1726.

[59] Zeng, H.; Qiu, Z.; Domínguez-Huerta, A.; Hearne, Z.; Chen, Z.; Li, C.-J. *ACS Catal.* **2017,** *7*, 510-519.

[60] Wenkert, E.; Michelotti, E. L.; Swindell, C. S. *J. Am. Chem. Soc.* **1979,** *101*, 2246-2247.

[61] Dankwardt, J. W. *Angew. Chem. Int. Ed.* **2004,** *43*, 2428-2432.

[62] Xie, L.-G.; Wang, Z.-X. *Chem. Eur. J.* **2011,** *17*, 4972-4975.

[63] Iglesias, M. J.; Prieto, A.; Nicasio, M. C. *Org. Lett.* **2012,** *14*, 4318-4321.

[64] Zhang, J.; Xu, J.; Xu, Y.; Sun, H.; Shen, Q.; Zhang, Y. *Organometallics* **2015,** *34*, 5792-5800.

[65] Liu, X.; Hsiao, C.-C.; Kalvet, I.; Leiendecker, M.; Guo, L.; Schoenebeck, F.; Rueping, M. *Angew. Chem. Int. Ed.* **2016,** *55*, 6093-6098.

[66] Guan, B.-T.; Xiang, S.-K.; Wang, B.-Q.; Sun, Z.-P.; Wang, Y.; Zhao, K.-Q.; Shi, Z.-J. *J. Am. Chem. Soc.* **2008,** *130*, 3268-3269.

[67] Liu, X.; Jia, J.; Rueping, M. *ACS Catal.* **2017,** *7*, 4491-4496.

[68] Tobisu, M.; Takahira, T.; Ohtsuki, A.; Chatani, N. *Org. Lett.* **2015,** *17*, 680-683.

[69] Tobisu, M.; Shimasaki, T.; Chatani, N. *Angew. Chem. Int. Ed.* **2008,** *47*, 4866-4869.

[70] Wang, C.; Ozaki, T.; Takita, R.; Uchiyama, M. *Chem. Eur. J.* **2012,** *18*, 3482-3485.

[71] Iyori, Y.; Ueno, R.; Morishige, A.; Chatani, N. *Chem. Sci.* **2021,** *12*, 1772-1777.

[72] Bergman, R. G. *Nature* **2007,** *446*, 391-393.

[73] Ackermann, L.; Vicente, R.; Kapdi, A. R. *Angew. Chem. Int. Ed.* **2009,** *48*, 9792-9826.

[74] McMurray, L.; O'Hara, F.; Gaunt, M. J. *Chem. Soc. Rev.* **2011,** *40*, 1885-1898.

[75] Yamaguchi, J.; Yamaguchi, A. D.; Itami, K. *Angew. Chem. Int. Ed.* **2012,** *51*, 8960-9009.

[76] Wencel-Delord, J.; Glorius, F. *Nat. Chem.* **2013,** *5*, 369-375.

[77] Guillemard, L.; Kaplaneris, N.; Ackermann, L.; Johansson, M. J. *Nat. Rev. Chem.* **2021,** *5*, 522-545.

[78] Gallego, D.; Baquero, E. A. *Open Chem.* **2018,** *16*, 1001-1058.

[79] Gandeepan, P.; Ackermann, L. *Chem* **2018,** *4*, 199-222.

[80] Lapuh, M. I.; Mazeh, S.; Besset, T. *ACS Catal.* **2020,** *10*, 12898-12919.

[81] Bhattacharya, T.; Pimparkar, S.; Maiti, D. *RSC Adv.* **2018,** *8*, 19456-19464.

[82] Kim, D.-S.; Park, W.-J.; Jun, C.-H. *Chem. Rev.* **2017,** *117*, 8977-9015.

[83] Sambiagio, C.; Schönbauer, D.; Blieck, R.; Dao-Huy, T.; Pototschnig, G.; Schaaf, P.; Wiesinger, T.; Zia, M. F.; Wencel-Delord, J.; Besset, T.; Maes, B. U. W.; Schnürch, M. *Chem. Soc. Rev.* **2018,** *47*, 6603-6743.

[84] Kuhl, N.; Hopkinson, M. N.; Wencel-Delord, J.; Glorius, F. *Angew. Chem. Int. Ed.* **2012,** *51*, 10236-10254.

[85] Kalepu, J.; Pilarski, L. T. *Molecules* **2019,** *24*, 830.

[86] Zaitsev, V. G.; Shabashov, D.; Daugulis, O. *J. Am. Chem. Soc.* **2005,** *127*, 13154-13155.

[87] Rej, S.; Ano, Y.; Chatani, N. *Chem. Rev.* **2020,** *120*, 1788-1887.

[88] Castro, L. C. M.; Chatani, N. *Chem. Lett.* **2015,** *44*, 410-421.

[89] Rej, S.; Das, A.; Chatani, N. *Coord. Chem. Rev.* **2021,** *431*, 213683.

[90] Rouquet, G.; Chatani, N. *Angew. Chem. Int. Ed.* **2013,** *52*, 11726-11743.

[91] Lukasevics, L.; Cizikovs, A.; Grigorjeva, L. *Chem. Commun.* **2021**.

[92] Khake, S. M.; Chatani, N. *Trends. Chem.* **2019,** *1*, 524-539.

[93] Harry, N. A.; Saranya, S.; Ujwaldev, S. M.; Anilkumar, G. *Catal. Sci. Technol.* **2019,** *9*, 1726-1743.

[94] Grigorjeva, L.; Daugulis, O. *Angew. Chem. Int. Ed.* **2014,** *53*, 10209-10212.

[95] Nguyen, T. T.; Grigorjeva, L.; Daugulis, O. *ACS Catal.* **2016,** *6*, 551-554.

[96] Planas, O.; Whiteoak, C. J.; Company, A.; Ribas, X. *Adv. Synth. Catal.* **2015,** *357*, 4003-4012.

[97] Kalsi, D.; Sundararaju, B. *Org. Lett.* **2015,** *17*, 6118-6121.

[98] Ran, Y.; Yang, Y.; Zhang, L. *Tetrahedron Lett.* **2016,** *57*, 3322-3325.

[99] Zhang, J.; Chen, H.; Lin, C.; Liu, Z.; Wang, C.; Zhang, Y. *J. Am. Chem. Soc.* **2015,** *137*, 12990-12996.

[100] Landge, V. G.; Jaiswal, G.; Balaraman, E. *Org. Lett.* **2016,** *18*, 812-815.

[101] Planas, O.; Whiteoak, C. J.; Martin-Diaconescu, V.; Gamba, I.; Luis, J. M.; Parella, T.; Company, A.; Ribas, X. *J. Am. Chem. Soc.* **2016,** *138*, 14388-14397.

[102] Lin, C.; Zhang, J.; Chen, Z.; Liu, Y.; Liu, Z.; Zhang, Y. *Adv. Synth. Catal.* **2016,** *358*, 1778-1793.

[103] Misal Castro, L. C.; Obata, A.; Aihara, Y.; Chatani, N. *Chem. Eur. J.* **2016,** *22*, 1362-1367.

[104] He, Z.; Huang, Y. *ACS Catal.* **2016,** *6*, 7814-7823.

[105] Hili, R.; Yudin, A. K. *Nat. Chem. Biol.* **2006,** *2*, 284-287.

[106] Bariwal, J.; Van der Eycken, E. *Chem. Soc. Rev.* **2013,** *42*, 9283-9303.

[107] Davies, H. M. L.; Long, M. S. *Angew. Chem. Int. Ed.* **2005,** *44*, 3518-3520.

[108] Park, Y.; Kim, Y.; Chang, S. *Chem. Rev.* **2017,** *117*, 9247-9301.

[109] Shin, K.; Kim, H.; Chang, S. *Acc. Chem. Res.* **2015,** *48*, 1040-1052.

[110] Figg, T. M.; Park, S.; Park, J.; Chang, S.; Musaev, D. G. *Organometallics* **2014,** *33*, 4076-4085.

[111] Powers, I. G.; Andjaba, J. M.; Zeller, M.; Uyeda, C. *Organometallics* **2020,** *39*, 3794-3801.

[112] Liu, Z.-K.; Zhao, Q.-Q.; Gao, Y.; Hou, Y.-X.; Hu, X.-Q. *Adv. Synth. Catal.* **2021,** *363*, 411-424.

[113] Hojilla Atienza, C. C.; Bowman, A. C.; Lobkovsky, E.; Chirik, P. J. *J. Am. Chem. Soc.* **2010,** *132*, 16343-16345.

[114] Kuijpers, P. F.; van der Vlugt, J. I.; Schneider, S.; de Bruin, B. *Chem. Eur. J.* **2017,** *23*, 13819-13829.

[115] Baek, Y.; Hennessy, E. T.; Betley, T. A. *J. Am. Chem. Soc.* **2019,** *141*, 16944-16953.

[116] Baek, Y.; Das, A.; Zheng, S.-L.; Reibenspies, J. H.; Powers, D. C.; Betley, T. A. *J. Am. Chem. Soc.* **2020,** *142*, 11232-11243.

[117] Lee, J.; Lee, J.; Jung, H.; Kim, D.; Park, J.; Chang, S. *Journal of the American Chemical Society* **2020,** *142*, 12324-12332.

[118] Sun, B.; Yoshino, T.; Matsunaga, S.; Kanai, M. *Adv. Synth. Catal.* **2014,** *356*, 1491-1495.

[119] Sun, B.; Yoshino, T.; Matsunaga, S.; Kanai, M. *Chem. Commun.* **2015,** *51*, 4659-4661.

[120] Shah, T. A.; De, P. B.; Pradhan, S.; Banerjee, S.; Punniyamurthy, T. *J. Org. Chem.* **2019,** *84*, 16278-16285.

[121] Xu, P.; Ding, P.-F.; Zhang, M.-Q.; Xia, Y.-S.; Xie, T. *Tetrahedron Lett.* **2021,** *66*, 152825.

[122] Kim, Y. B.; Won, J.; Lee, J.; Kim, J.; Zhou, B.; Park, J.-W.; Baik, M.-H.; Chang, S. *ACS Catal.* **2021,** *11*, 3067-3072.

[123] Ceder, R. M.; Granell, J.; Muller, G.; Font-Bardia, M.; Solans, X. *Organometallics* **1995,** *14*, 5544-5551.

[124] Chen, Y.; Sun, H.; Flörke, U.; Li, X. *Organometallics* **2008,** *27*, 270-275.

[125] Roy, P.; Bour, J. R.; Kampf, J. W.; Sanford, M. S. *J. Am. Chem. Soc.* **2019,** *141*, 17382-17387.

[126] Zhang, S.-K.; Struwe, J.; Hu, L.; Ackermann, L. *Angew. Chem. Int. Ed.* **2020,** *59*, 3178-3183.

[127] Maity, S.; Kancherla, R.; Dhawa, U.; Hoque, E.; Pimparkar, S.; Maiti, D. *ACS Catal.* **2016,** *6*, 5493-5499.

[128] Du, C.; Li, P.-X.; Zhu, X.; Han, J.-N.; Niu, J.-L.; Song, M.-P. *ACS Catal.* **2017,** *7*, 2810-2814.

[129] Sanjosé-Orduna, J.; Gallego, D.; Garcia-Roca, A.; Martin, E.; Benet-Buchholz, J.; Pérez-Temprano, M. H. *Angew. Chem. Int. Ed.* **2017,** *56*, 12137-12141.

[130] Sanjosé-Orduna, J.; Benet-Buchholz, J.; Pérez-Temprano, M. H. *Inorg. Chem.* **2019,** *58*, 10569-10577.

[131] Sanjosé-Orduna, J.; Sarria Toro, J. M.; Pérez-Temprano, M. H. *Angew. Chem. Int. Ed.* **2018,** *57*, 11369-11373.

[132] Grove, D. M.; Van Koten, G.; Zoet, R.; Murrall, N. W.; Welch, A. J. *J. Am. Chem. Soc.* **1983,** *105*, 1379-1380.

[133] van de Kuil, L. A.; Veldhuizen, Y. S. J.; Grove, D. M.; Zwikker, J. W.; Jenneskens, L. W.; Drenth, W.; Smeets, W. J. J.; Spek, A. L.; van Koten, G. *J. Organomet. Chem.* **1995,** *488*, 191-197.

[134] Grove, D. M.; Van Koten, G.; Mul, P.; Zoet, R.; Van der Linden, J. G. M.; Legters, J.; Schmitz, J. E. J.; Murrall, N. W.; Welch, A. J. *Inorg. Chem.* **1988,** *27*, 2466-2473.

[135] Spasyuk, D. M.; Zargarian, D.; van der Est, A. *Organometallics* **2009,** *28*, 6531-6540.

[136] Watson, M. B.; Rath, N. P.; Mirica, L. M. *J. Am. Chem. Soc.* **2017,** *139*, 35-38.

[137] Nebra, N. *Molecules* **2020,** *25*, 1141.

[138] Jongbloed, L.; García-López, D.; Heck, R.; Siegler, M.; Carbó, J.; van der Vlugt, J. I. *Inorg. Chem.* **2016,** *55*.

[139] Yang, C.; Wu, W.-D.; Zhao, L.; Wang, M.-X. *Organometallics* **2015,** *34*, 5167-5174.

[140] Rovira, M.; Roldán-Gómez, S.; Martin-Diaconescu, V.; Whiteoak, C. J.; Company, A.; Luis, J. M.; Ribas, X. *Chem. Eur. J.* **2017,** *23*, 11662-11668.

[141] Ribas, X.; Calle, C.; Poater, A.; Casitas, A.; Gómez, L.; Xifra, R.; Parella, T.; Benet-Buchholz, J.; Schweiger, A.; Mitrikas, G.; Solà, M.; Llobet, A.; Stack, T. D. P. *J. Am. Chem. Soc.* **2010,** *132*, 12299-12306.

[142] Zhou, W.; Schultz, J. W.; Rath, N. P.; Mirica, L. M. *J. Am. Chem. Soc.* **2015,** *137*, 7604-7607.

[143] Zhou, W.; Zheng, S.; Schultz, J. W.; Rath, N. P.; Mirica, L. M. *J. Am. Chem. Soc.* **2016,** *138*, 5777-5780.

[144] Zhou, W.; Rath, N. P.; Mirica, L. M. *Dalton Trans.* **2016,** *45*, 8693-8695.

[145] Planas, O.; Roldán-Gómez, S.; Martin-Diaconescu, V.; Luis, J. M.; Company, A.; Ribas, X. *Chem. Sci.* **2018,** *9*, 5736-5746.

[146] Planas, O.; Roldán-Gómez, S.; Martin-Diaconescu, V.; Parella, T.; Luis, J. M.; Company, A.; Ribas, X. *J. Am. Chem. Soc.* **2017,** *139*, 14649-14655.

[147] Ribas, X.; Jackson, D. A.; Donnadieu, B.; Mahía, J.; Parella, T.; Xifra, R.; Hedman, B.; Hodgson, K. O.; Llobet, A.; Stack, T. D. P. *Angew. Chem. Int. Ed.* **2002,** *41*, 2991-2994.

[148] Xifra, R.; Ribas, X.; Llobet, A.; Poater, A.; Duran, M.; Solà, M.; Stack, T. D. P.; Benet-Buchholz, J.; Donnadieu, B.; Mahía, J.; Parella, T. *Chem. Eur. J.* **2005,** *11*, 5146-5156.

[149] King, A. E.; Huffman, L. M.; Casitas, A.; Costas, M.; Ribas, X.; Stahl, S. S. *J. Am. Chem. Soc.* **2010,** *132*, 12068-12073.

[150] Ribas, X.; Capdevila, L.; Font, P. In *High-Valent Cu, Ag, and Au Coordination Compounds*, 2021.

[151] Casitas, A.; King, A. E.; Parella, T.; Costas, M.; Stahl, S. S.; Ribas, X. *Chem. Sci.* **2010,** *1*, 326-330.

[152] Huffman, L. M.; Casitas, A.; Font, M.; Canta, M.; Costas, M.; Ribas, X.; Stahl, S. S. *Chem. Eur. J.* **2011,** *17*, 10643-10650.

[153] Casitas, A.; Canta, M.; Solà, M.; Costas, M.; Ribas, X. *J. Am. Chem. Soc.* **2011,** *133*, 19386-19392.

[154] Font, M.; Parella, T.; Costas, M.; Ribas, X. *Organometallics* **2012,** *31*, 7976-7982.

[155] Casitas, A.; Ribas, X. *Chem. Sci.* **2013,** *4*, 2301-2318.

[156]   Rovira, M.; Font, M.; Acuña-Parés, F.; Parella, T.; Luis, J. M.; Lloret-Fillol, J.; Ribas, X. *Chem. Eur. J.* **2014,** *20*, 10005-10010.

[157]   Li, P. *Cheminform* **2006,** *37*.

[158]   Das, R.; Mandal, M.; Chakraborty, D. *Asian J. Org. Chem.* **2013,** *2*, 579-585.

[159]   Font, M.; Acuña-Parés, F.; Parella, T.; Serra, J.; Luis, J. M.; Lloret-Fillol, J.; Costas, M.; Ribas, X. *Nat. Commun.* **2014,** *5*, 4373.

CHAPTER II

General Objectives

Getting deeper insight into the mechanism involved in C–C and C–Heteroatom bond formation reactions via cross-coupling or C-H activation is crucial to improve and expand protocols to streamline the synthesis of essential compounds. For this reason, the isolation and characterization of the intermediates involved is vital and different strategies have been reported. The stabilization of the metal can be accomplished by providing the correct coordination environment to the metal depending of its nature and oxidation state. In this context, this thesis we will focused on the use of 12-membered macrocyclic substrate as a model substrate to get insight into C–N bond formation reactions mediated by high valent cobalt system. Furthermore, we will attempt the use of 8-aminoquinoline moiety as directing group scaffold as an non-cyclic model system. Thanks to the bidentate coordination environment of the 8-aminoquinoline, we will attempt both the catalytic *ortho*-directed functionalization of C-halide, C-H, C-F, C-OMe bonds in a selective manner as well as the isolation of the key intermediates to shed light into the mechanism involved in the transformations.
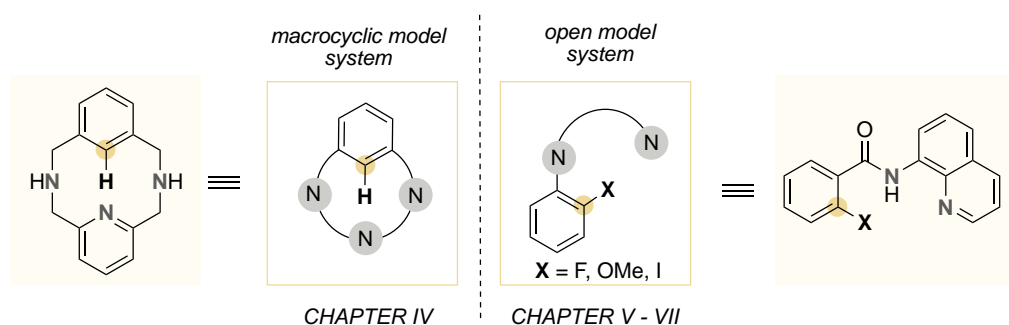
Scheme II.1. Macrocyclic and open model system used.

First, we will review the most relevant Co-catalyzed C-C and C-heteroatom cross-coupling reactions from the literature in Chapter III.

The development of new protocols for the formation of C–N bonds have blossomed over the last decades due to the presence of these functionalities in different important compounds. Few examples have been reported for the direct C–N bond amination reactions using high valent cobalt systems. Despite these reported examples, the mechanism involved is still unclear and few proofs of the key intermediates involved exist. Previously in the group, a set of aryl-Co(III) organometallic complexes bearing a 12-membered macrocyclic model substrate were demonstrated as competent catalysts for the alkyne annulation reactions, as well as for the C–H functionalization using diazo esters as coupling partner. Thus, in Chapter IV, we will study the reactivity of aryl-Co(III) complexes with inorganic and organic azides to provide new insight in cobalt-catalyzed C–H amination reactions with azides. We target the investigation of putative cobalt-nitrene intermediate species to form C–N bonds.
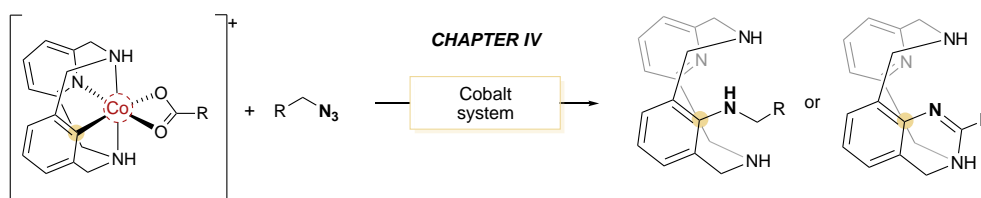
Scheme II.2. Study of C–N bond formation using aryl-Co(III) macrocyclic model substrate.

In Chapter V and VI, we turned our attention towards the activation of strong bonds using a chelation-assisted approach. Different examples have been reported using nickel catalyst although activated nucleophiles were needed. Here we take advantage of the use of 8-aminoquinoline *ortho*-directing group to promote the functionalization of strong aryl–F and aryl–OMe bonds using alkynes as a coupling partner. The corresponding aryl–X substrate was reacted with Ni(cod)$_2$ in the presence of alkynes to attempt the formation of annulated products. The mechanism behind the formation of the products is targeted by trapping intermediates of the reaction.

Finally, in Chapter VII we will attempt the two-electron redox silver(I)-catalyzed cross-coupling transformations using a non-cyclic substrate bearing the 8-aminoquinoline directing group. We will study different nucleophiles to construct C–C and C–Heteroatom bonds.
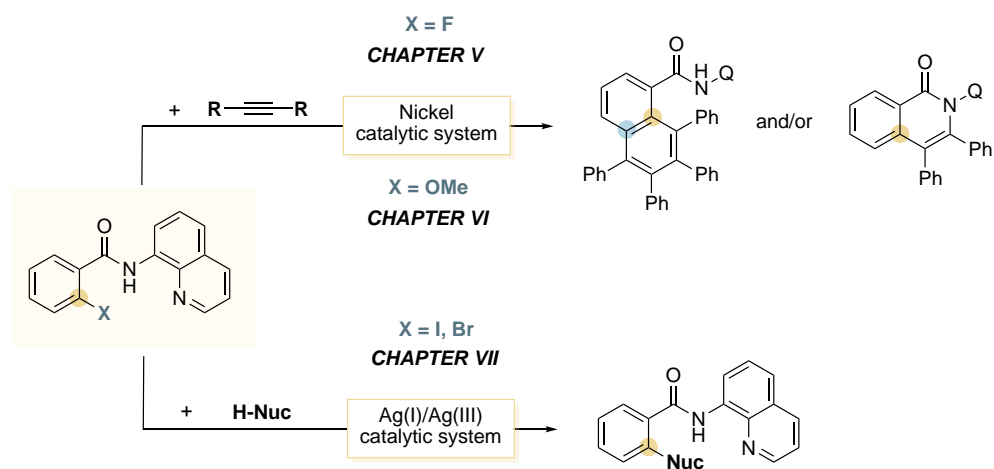
Scheme II.3. Chelation-assisted cross-coupling reactions mediated by nickel and silver systems.

CHAPTER III

Cobalt-catalyzed cross-coupling reactions
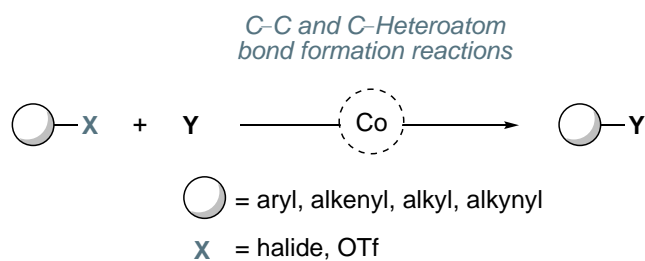
C–C and C–Heteroatom bond formation reactions

◯ = aryl, alkenyl, alkyl, alkynyl

X = halide, OTf

This Chapter corresponds to the following publication:

Cobalt-catalyzed cross-coupling reactions

LORENA CAPDEVILA and XAVI RIBAS

QBIS-CAT Research Group, Departament de Química, Institut de Química Computacional i Catàlisi (IQCC), Universitat de Girona, Campus Montilivi, Girona, E17003, Catalonia, Spain
e-mails: lorena.capdevila@udg.edu; xavi.ribas@udg.edu

I. INTRODUCTION

The construction of C−C and C−heteroatom bonds via cross-coupling reaction using prefunctionalized substrates is among the most important protocols in organic synthesis. The use of more abundant, cheaper, and less-toxic metals for cross-coupling reactions has gained interest in order to overcome the use of scarce palladium-based catalysts. In the past years, different research groups have demonstrated the potential of first row-transition metal catalysts for cross-coupling reactions becoming a hot topic in organic synthesis.

Early in 1939, Gilman and Lichtenwalter reported the first Co-mediated homocoupling transformation by reacting phenylmagnesium iodide (PhMgI) with substoichiometric amounts of $CoBr_2$, leading to the quantitative formation of biphenyl product[1]. Soon after, Kharasch and Fields disclosed in 1941 the cobalt-catalyzed homocoupling reaction of aryl Grignard reagents using organic halides (Scheme 1)[2].

Since these pioneering works, many different cobalt-catalyzed cross-coupling reactions have been discovered using prefunctionalized substrates, the C−C bond-forming catalysis being the most abundant transformation. Also, C−heteroatom bond-forming reactions analogous to Pd-catalyzed C−N Buchwald−Hartwig couplings and Cu-catalyzed C−N, C−O, and C−S Ullmann-type couplings have been reported. Cobalt-catalyzed cross-coupling reaction is dominated by the use of R-halides as electrophiles and organomagnesium nucleophile acting as transmetalating agents, albeit their role as *in situ* reducing agents will also be discussed along the chapter. Moreover, organozinc and organoboron reagents have also been also used as transmetalating agents, and even coupling between two R-halide compounds has been described. This chapter is an updated revision of the important advances in the field of Co-catalyzed cross-coupling protocols[3−6]. Co-catalyzed C−H functionalization methodologies are also experiencing exponential growth, but those are reviewed elsewhere and will not be included in this chapter[7−11].

II. C−C COUPLING REACTIONS USING ORGANOMAGNESIUM REAGENTS

A. Aryl or Alkenyl Halides, C(sp^2)−X

Many decades after the early reports on cobalt-catalyzed homocoupling reactions using aryl halides, Cahiez and Avedissian reported in 1998 the stereo- and chemo-selective reaction between organomagnesium reagents with alkenyl iodide, bromide, and chloride derivatives using catalytic amounts of $Co(acac)_2$ in THF, where N-methyl pyrrolidine (NMP) addition is key to the success of the transformation[12]. The catalytic system afforded good to excellent yields when primary and secondary alkylmagnesium reagents were used, while less efficiency was observed for tertiary ones (Scheme 2). Based on this reaction, Hoffmann and Hölzer reported in 2003 that a single-electron transfer (SET) mechanism was behind this reaction due to the formation of a racemized coupling product when enantiomerically enriched secondary Grignard reagent reacted with vinyl bromide using $Co(acac)_2$ as a catalyst[13].

On the other hand, Knochel and coworkers reported in 2003 the functionalization of heterocyclic aryl chlorides with aryl Grignard reagents (ArMgX) catalyzed by $CoCl_2$ at low temperatures (Scheme 3a)[14]. Remarkably, it was shown that metallic cobalt powder can also catalyze the formation of the coupling product. Later in 2006, the same group broadened the scope of the reaction using aryl chlorides, bromides, fluorides, and tosylates with a variety of organomagnesium and organocopper compounds as transmetalating agents[15]. The functionalization of heterocyclic aryl chlorides was also studied by Oshima and coworkers in 2004, who described the trimethylsilylmethylation and benzylation of 2-chloropyridine derivatives using $Co(acac)_2$ as a catalyst (10 mol%) in dioxane at room temperature (Scheme 3b)[16]. Okamoto and coworkers reported the synthesis of γ-substituted
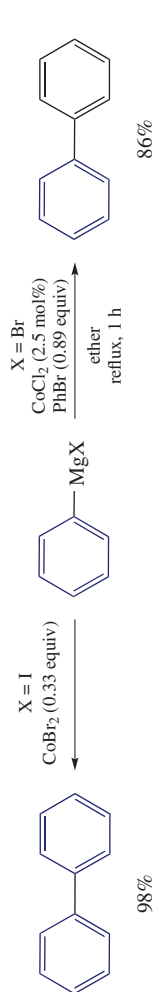
SCHEME 1. Early examples of Co-mediated and Co-catalyzed $C(sp^2)-C(sp^2)$ cross-coupling reactions.
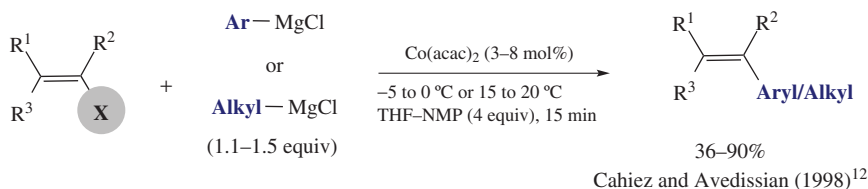
SCHEME 2. Cobalt-catalyzed $C(sp^2)-C(sp^2)$ and $C(sp^2)-C(sp^3)$ cross-couplings of alkenyl halides using NMP as key additive.

(*E*)-allylsilanes by reacting (*E*)-1,2-dihalogenoethylene with trimethylsilylmethylmagnesium chloride ($TMSCH_2MgCl$)[17]. The reaction proceeded using 1 mol% of $Co(acac)_2$ or $Co(acac)_3$ in THF−NMP giving exclusively the (*E*)-allylsilane products, whereas (*Z*)-1,2-dihalogenoethylene did not react.

Hayashi group described in 2007 the alkynylation of alkenyl triflates using alkynyl Grignard reagents and $Co(acac)_3$ as a catalyst (Scheme 4a)[18]. The preferential functionalization of alkenyl triflates over bromides or iodides was noticeable from competition experiments. One year later, the same authors expanded the methodology reporting the Co-catalyzed $C(sp^2)-C(sp^2)$ bond-formation reaction using alkenyl and aryl Grignard reagents under analogous experimental conditions, albeit with the addition of catalytic amounts of PPh_3 (Scheme 4b,c)[19]. The authors rationalized that the catalytic improvement observed was related to the stabilization of the cobalt catalyst by the phosphine ligand. In all cases they proposed the reduction of the Co^{III} to Co^0 by the organomagnesium reagent.

The formation of unsymmetrically biaryls has attracted attention in the field of Co cross-coupling reactions. In this context, Nakamura reported in 2009 the hetero-biaryl coupling using $CoF_2 \cdot 4H_2O$ in combination with *N*-heterocyclic carbene (NHC) ligands in catalytic amounts (Scheme 5a)[20]. The biaryl cross-coupling was achieved with high selectivity over homocoupling, and the methodology was applicable to electron-rich chloroanisoles, fluorine-substituted aryls, and heteroaromatic aryls, and also different ArMgX Grignard reagents (and even 2-thienyl-MgBr) were tolerated. The use of NHC ligands in cobalt catalysis for the C−C coupling has been studied by different groups[21, 22]. Chen and coworkers reported the synthesis of well-defined Co^{III}−NHC complex **1** and its application as catalyst for the cross-coupling of aryl halides with aryl−Grignard reagents (Scheme 5b)[23]. The authors proposed *in situ* reduction of Co^{III} to Co^I, which then undergoes an aryl halide oxidative addition to form aryl−Co^{III} intermediate species. Finally, the biaryl coupling product was formed via reductive elimination.

In this context, Yu and coworkers reported a procedure for the homocoupling of aryl or alkenyl bromides using metallic Mg^0, oxygen as a mild oxidant, and $CoCl_2$ as catalyst[24]. Duan and coworkers also contributed in this area reporting the biaryl couplings of aryl halides and aryl Grignard reagents using $CoCl_2/Ti(OEt)_4$ catalyst and PBu_3 as a ligand (Scheme 6)[25]. Ester, phenyl ketone, amide, sulfonate, and sulfonamide functional groups in the electrophilic partner were tolerated, affording good to excellent yields. Recently, the functionalization of Aryl−F bonds forming C−C bonds via cobalt catalysis was also investigated by Duan and coworkers (Scheme 6). They used a ligand-free methodology consisting of $CoCl_2$ as catalyst, 1,3-dimethyl-3,4,5,6-tetrahydro-2(1*H*)-pyrimidinone (DMPU) in catalytic amounts, and $Ti(OEt)_4$ to afford the biaryl coupling product using unactivated aryl fluorides in good yield[26]. Ester, ketone, amide, imine, sulfonamide, and carboxylic acid functionalities on the aryl−F substrates were tolerated. The role of titanium species for the selective C−F activation was deemed crucial.

(a) Knochel and coworkers (2003)[14]

40–91%

Ar (2.19 equiv) MgX

CoCl$_2$ (5 mol%)

ether
−40 to 25 °C
1–96 h

(b) Oshima and coworkers (2004)[16]

42–84%

R $\diagup$ MgX

R = Ph, Si(CH$_3$)$_3$
(3 equiv)

Co(acac)$_2$ (10 mol%)

dioxane
25 °C, 30 min

Heterocyclic chlorides

=

Y = C, N
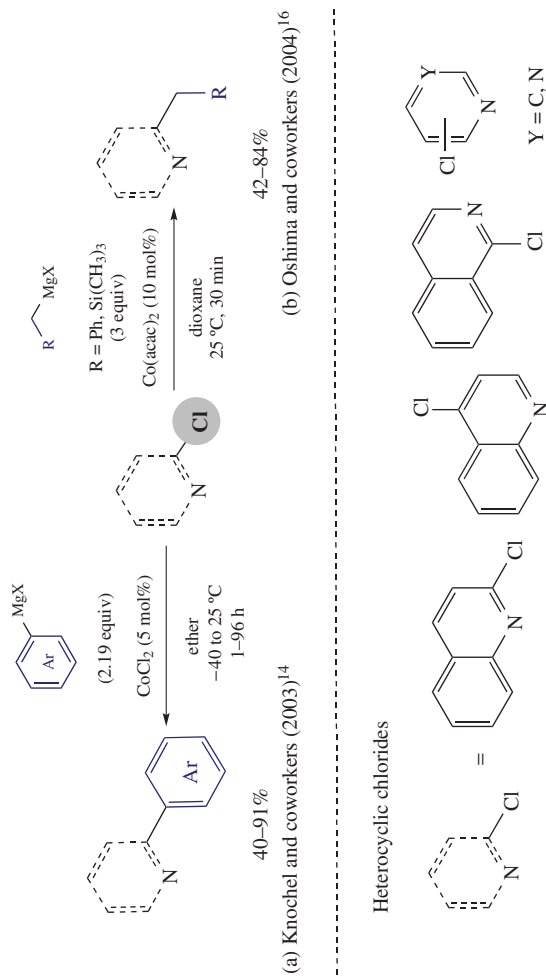
SCHEME 3. Cobalt-catalyzed cross-coupling reactions of chloropyridine derivatives using (a) aryl Grignard reagents and (b) benzyl and trimethylsilylmethyl Grignard reagents.
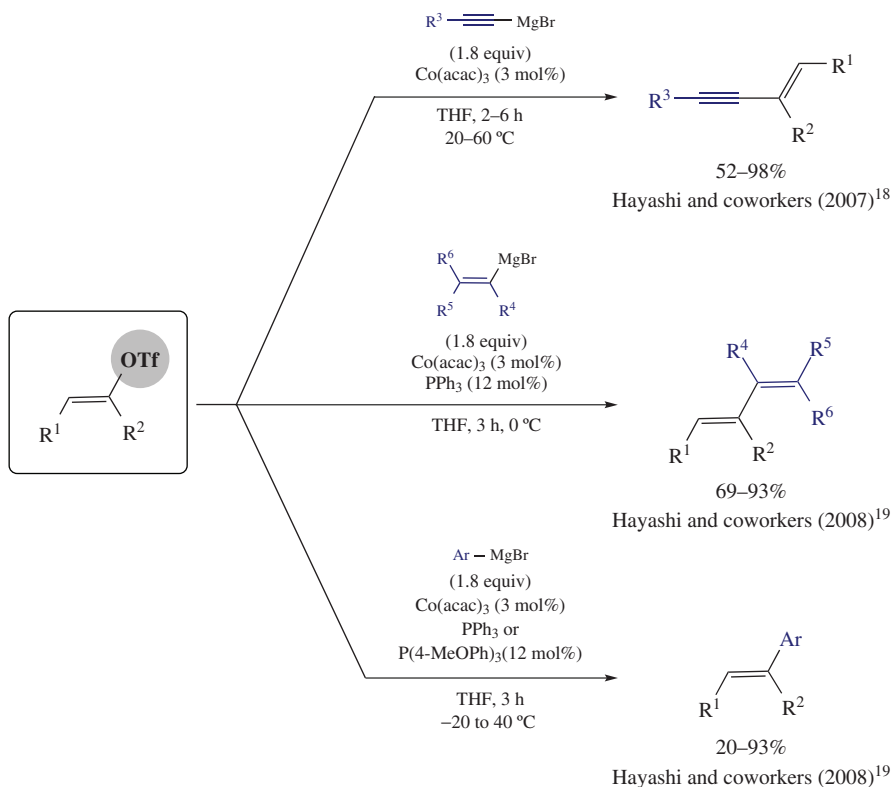
SCHEME 4. Cobalt-catalyzed coupling of alkenyl triflates with aryl, alkenyl, and alkynyl Grignard reagents.

In 2013, Jacobi von Wangelin and coworkers reported a protocol for the aryl–aryl coupling using substituted chlorostyrenes and ArMgBr using 1 mol% of Co(acac)$_3$ (Scheme 7)[27]. Best results were observed using chlorostyrenes, confirming the role of the olefin as activating group (or even directing group if in *ortho*). Mechanistic experiments were carried out, indicating the formation of active Co^I species by reduction of Co(acac)$_3$ with ArMgBr.

B. Alkyl Halides, C(sp³)–X

Alkyl halides have also been used as electrophiles in Co-catalyzed cross-couplings. The oxidative addition of alkyl halides is much slower compared to aryl and vinyl halides, and β-hydride elimination side reactions make their functionalization more challenging. Both alkenyl and aryl Grignard reagents were successfully coupled, forming a C(sp³)–C(sp²) bond via cobalt catalysis. More recently, the use of allylic and aliphatic Grignard reagents as coupling partners was also achieved, leading to the construction of C(sp³)–C(sp³) bonds. Furthermore, the use of alkynyl halides to form C(sp³)–C(sp) has also been investigated via cobalt cross-coupling reactions.
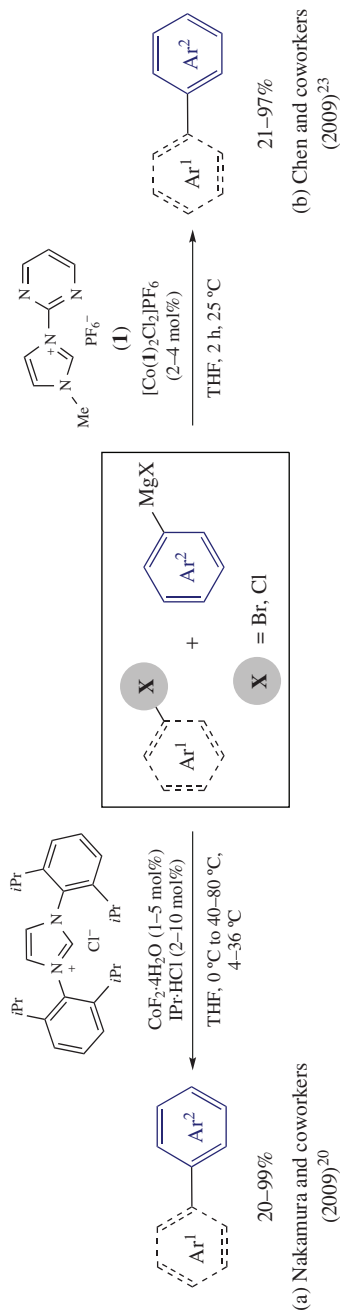
SCHEME 5. Cobalt-catalyzed biaryl formation using NHC-type ligands.
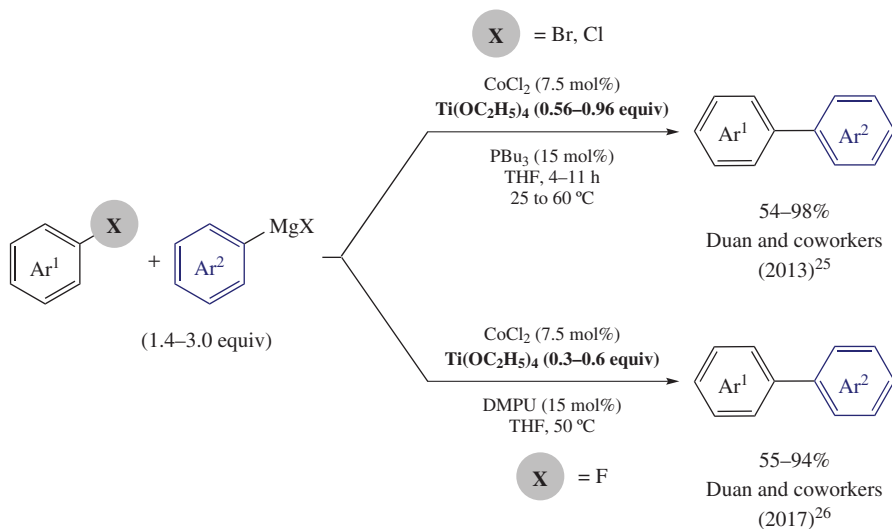
SCHEME 6. Biaryl couplings using aryl halides and aryl Grignard reagents under the $CoCl_2/Ti(OEt)_4$ catalytic system.
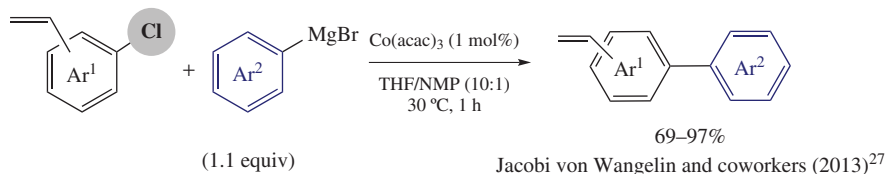
SCHEME 7. Cobalt-catalyzed $C(sp^2)-C(sp^2)$ coupling using chlorostyrenes and ArMgBr.

1. $C(sp^3)-C(sp^2)$

Oshima, Yorimitsu, and coworkers reported in 2006 the coupling of alkyl halides with an excess of aryl Grignard reagents in the presence of a diphosphine ligand, that is, 1,3-bis(diphenylphosphino)propane (dppp), and catalytic amounts of $CoCl_2$[28]. The authors concluded that the reaction proceeded through a SET mechanism, and they expanded this methodology to secondary alkyl halides using diamine ligands (Scheme 8a)[29]. The authors attributed the higher efficiency to the conformations, bite angles, and/or steric hindrance of the diamine ligand, allowing the use of only 1.2 equiv of the arylmagnesium halide. The same authors also demonstrated the ability of cobalt to catalyze the phenylation of 2-alkenyl methyl ethers[30] and the alkenylation of primary and secondary alkyl halides using 1-(trimethylsilyl)ethenylmagnesium bromide[31]. Cahiez and coworkers also contributed to this field, reporting in 2009 the arylation of primary and secondary alkyl bromides using $Co(acac)_3$, N,N,N',N'-tetramethylethylenediamine (TMEDA) as a ligand, and slight excess of the ArMgCl (Scheme 8b)[32]. Acetate, ester, amide, and ketone functional groups were well tolerated. Inspired by these works, in 2011, Wu and coworkers reported the synthesis of
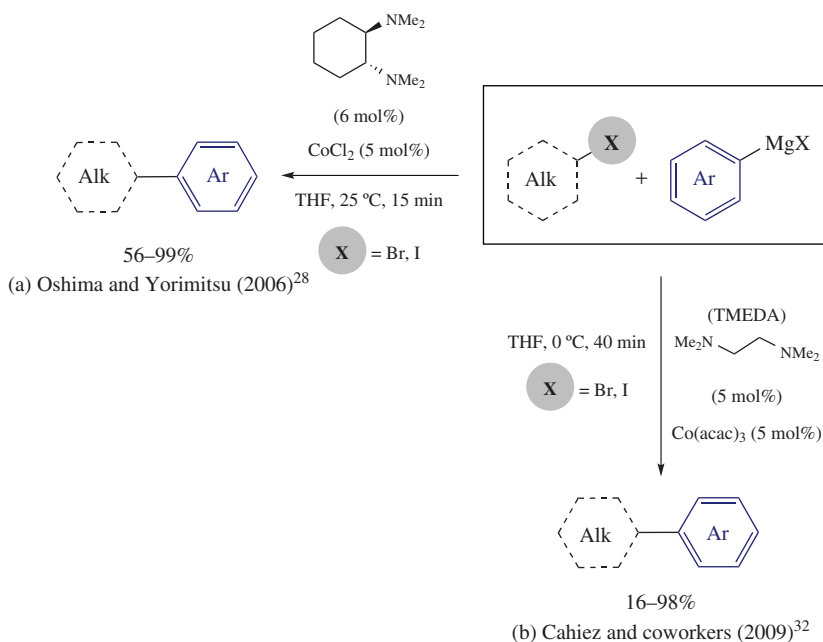
SCHEME 8. Cobalt-catalyzed C(sp^2)−C(sp^3) bond formation using Grignard reagents and diamine ligands.

enantiopure pyrrolidine derivatives by coupling (S)-2-(iodomethyl)pyrrolidine with PhMgBr, using CoCl$_2$(PPh$_3$)$_2$, and TMEDA as catalysts[33].

Later, Časar and coworkers disclosed a new methodology based on cobalt-catalyzed cross-coupling between allylic bromides and PhMgBr using sarcosine and CoBr$_2$ as catalysts (Scheme 9)[34]. The allylic substitution proceeded with high α-regioselectivity. This protocol allowed the authors to use benzylmagnesium bromide as well as alkenyl bromides as coupling partners and targeted the synthesis of (E)-methyl-4-(2,4,5-trifluorophenyl)but-2-enoate, which is an intermediate for the synthesis of sitagliptin phosphate.

Saturated N-heterocyclic compounds are widespread scaffolds with remarkable biologic activities. New routes to access substituted saturated N-heterocyclic compounds have been recently provided by Cossy and coworkers through cobalt-catalyzed arylation of iodinated N-heterocycles with Grignard reagents (Scheme 10)[35–37]. They developed a methodology for the functionalization of 3-iodopyrrolidines, 4-iodopiperidines, and 3-iodo-azetidines with a wide range of organomagnesium reagents, including aryl, alkenyl, and allyl Grignard reagents. CoCl$_2$ was used as catalyst, and (R,R)-tetramethylcyclohexane-1,2-diamine was the best ligand. The same authors implemented this methodology for the synthesis of C-furanosides *en route* to the total synthesis of (−)-isoaltholactone[38]. Later, Linclau and coworkers also showed the potential of cobalt by reporting the synthesis of (±)-paroxetine via cobalt catalysis using ArMgBr[39].

Knochel and coworkers demonstrated the ability of cobalt to catalyze cross-coupling reactions in a diastereoselective manner (Scheme 11). In 2014, they reported the coupling of TBS-protected (TBS, *tert*-butyldimethylsilyl) cyclic iodohydrins and ArMgX
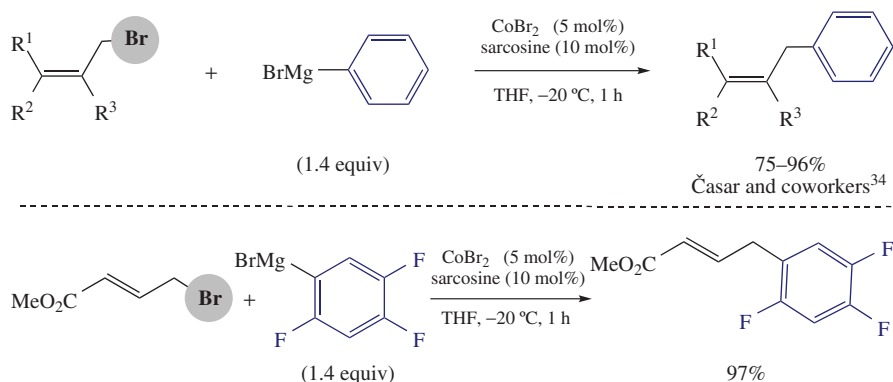
SCHEME 9. Cobalt-catalyzed cross-coupling of allylic bromides and Grignard reagents using sarcosine as ligand.
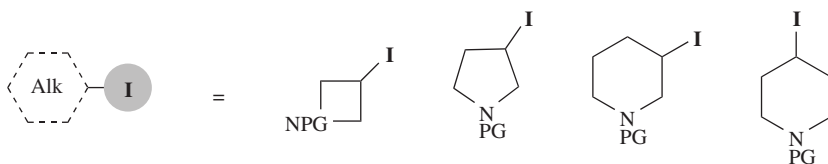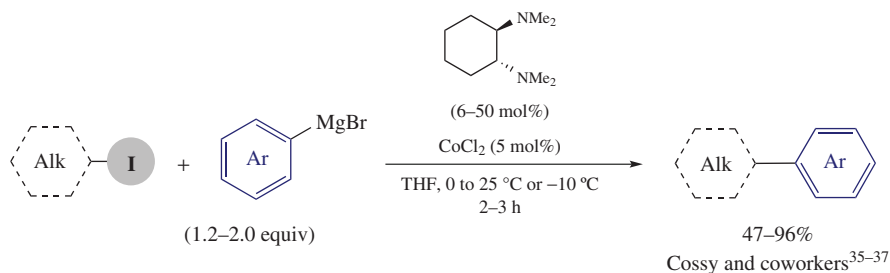
SCHEME 10. Arylation of iodinated azetidines, pyrrolidines, and piperidines by cobalt catalysis.

using $CoCl_2 \cdot 2LiCl$ catalyst and TMEDA ligand in THF[40]. The reaction tolerated both electron-donating and -withdrawing groups in the Grignard reagent, affording *trans*-α-arylated cyclic alcohols with high diastereoselectivity. Furthermore, diastereoselectivity was maintained using less-reactive bromohydrins, although with moderate yields. Later in 2016, the authors applied this methodology for the diastereoselective arylation of 1,2-substituted heterocyclic alkyl iodides with $ArMgX$[41].

The enantioselective Co-catalyzed Kumada cross-coupling using aryl Grignard reagents was pioneered by Zhong and coworkers using chiral bisoxazoline ligands and CoI_2 catalyst in THF at very low temperature (−80 °C)[42]. The catalytic system showed excellent reactivity and enantioselectivity using a wide range of racemic α-bromo esters (Scheme 12). The potential
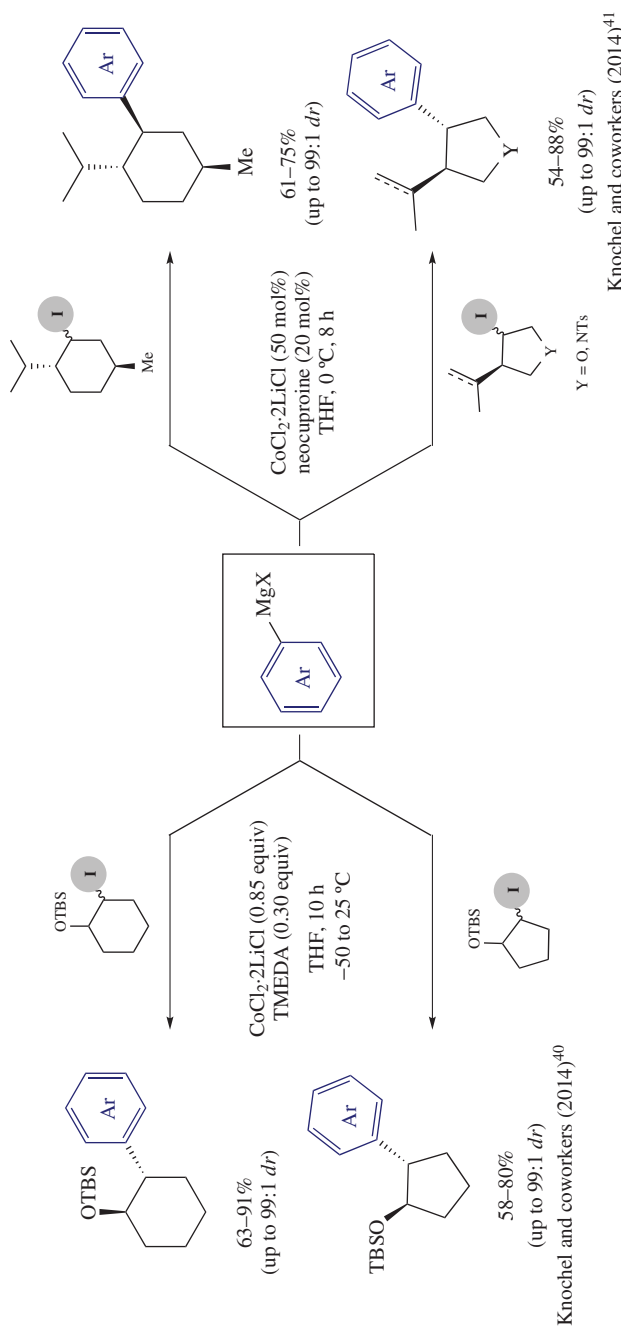
SCHEME 11. Stereoselective cobalt-catalyzed arylation reactions of alkyl iodides.

12
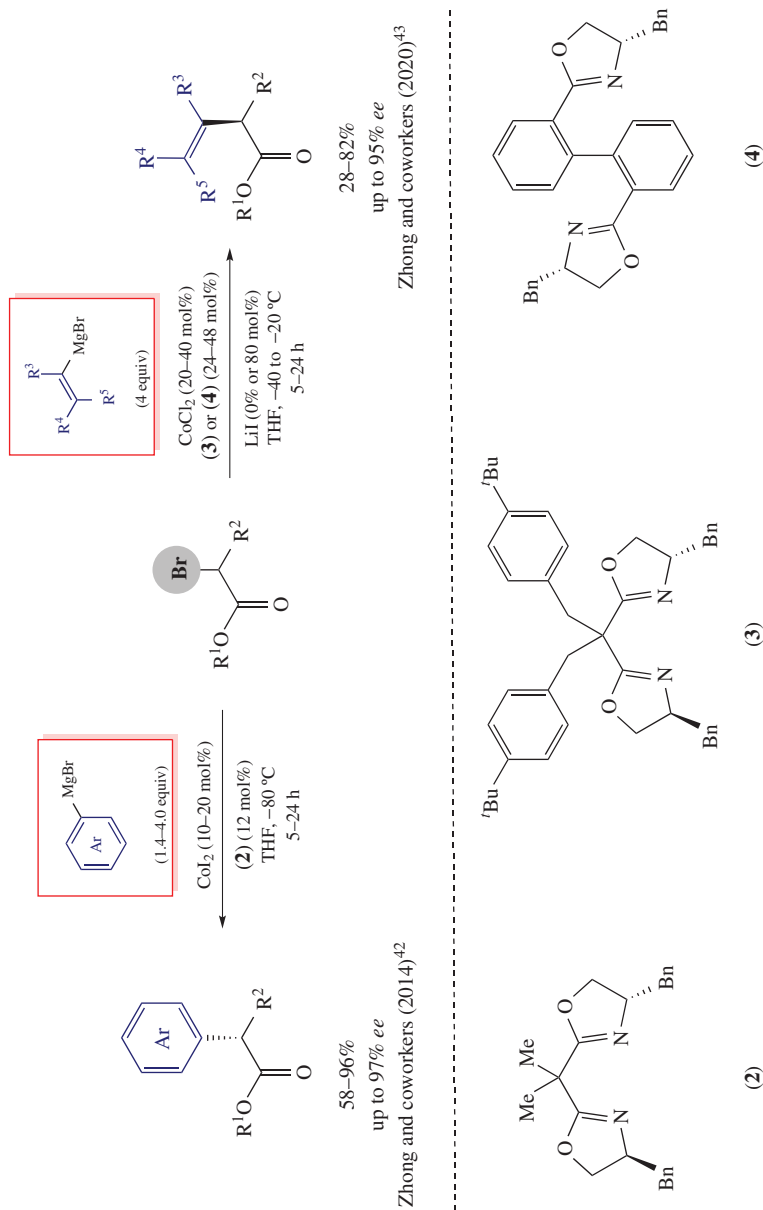
SCHEME 12. Cobalt-catalyzed asymmetric cross-coupling reactions of α-bromo esters and Grignard reagents using bisoxazoline-based dinucleating ligands.

utility of their methodology was shown in the straighforward synthesis of (*S*)-fenoprofen and (*S*)-*ar*-turmerone. Very recently, Zhong and coworkers developed an analogous methodology for the enantioselective alkenylation of racemic α-bromo esters with ligands **2−4** (Scheme 12)[43]. Different substituents at the α-carbon of the bromo ester were tolerated such as primary alkyl groups, allyl, ester, silyloxy, and benzene.

Cossy, Guérinot, and coworkers reported in 2017 the cobalt-catalyzed cross-coupling reactions using α-bromo amides and Grignard reagents, affording a variety of α-aryl and β,γ-unsaturated amides (Scheme 13)[45]. The authors suggested that after reduction of $CoCl_2$ to Co^0 or Co^I by the Grignard reagent, a concerted oxidative addition took place, affording the coupling product through a subsequent reductive elimination step. As a follow-up of their previous work, they recently developed the diastereoselective α-arylation of β-lactams using $CoCl_2$ and TMEDA (Scheme 13)[44].

The formation of $C(sp^3)−C(sp^2)$ via cobalt-catalyzed Heck-type reaction using alkyl halides was also explored by several groups. The major drawback is the facile β-hydride elimination of alkyl–metal intermediate species; thus, enhancing the stability of the alkyl–cobalt species proved to be a good strategy. The cobalt-catalyzed Heck-type reaction was pioneered by Branchaud and Detlefsen in 1991 by reporting cobaloxime-catalyzed radical alkyl–styryl cross-couplings using bromoalkyls and styrene.[46] The Heck-type alkylation of styrenes was further studied in 2002 by Oshima and coworkers[47]. In order to obtain the styrrylation of alkyl halides, they used catalytic amounts of $CoCl_2$, dpph (1,6-bis(diphenylphosphino)hexane) biphosphine ligand, and 2.5 equiv of Me_3SiCH_2MgCl (needed as a reducing agent). A radical-based SET mechanism was proposed[48]. Intermolecular coupling with styrene using primary, secondary, and tertiary alkyl halides, as well as the intramolecular Heck-type version, were reported (Scheme 14a). In this context, Carreira and coworkers developed the coupling of alkyl iodides with olefins in an intramolecular fashion using well-defined alkyl- or stannyl-cobaloximes under light irradiation (Scheme 14b)[49].

2. C(sp³)−C(sp³)

The coupling between alkyl halides and allyl Grignard reagents via cobalt catalysis was pioneered by Oshima and coworkers in 2002[50]. Allylated products were observed using a variety of alkyl halides with $(CH_2=CHCH_2)MgCl$, using $CoCl_2(dppp)$ as catalyst. The coupling of primary and secondary alkyl bromides and iodides was also achieved in good to excellent yields. The catalytic system reported was also used for the benzylation of alkyl halides[51]. Later in 2006, the authors also succeeded in the functionalization of allylic ethers with $TMSCH_2MgCl$ via C−OR activation by Co catalyst[30]. The allylation of cinnamyl methyl ether was also performed in moderate yields. Later, Cahiez and coworkers reported the coupling of alkyl halides with alkyl Grignard reagents using $CoCl_2 \cdot 2LiI$ as catalyst and TMEDA as ligand (Scheme 15a)[52]. High product yields were obtained, particularly with alkyl iodides, but cyclic and acyclic alkyl bromides were also tolerated. Kambe and coworkers in 2013 extended the substrate scope further, using tertiary alkyl Grignard reagents as coupling partners and isoprene as a key additive for stabilizing the Co center along the catalytic cycle[53]. The same authors extended the cobalt-catalyzed alkyl–alkyl cross-coupling with alkyl–F using the $CoCl_2/LiI/1,3$-pentadiene catalytic system (Scheme 15b)[54]. Alkyl fluorides bearing thiophene, terminal, and internal alkyne groups also afforded the expected coupling products. The protocol proved to be selective for the functionalization of $C(sp^3)−F$ even in the presence of Ar−Br or $C(sp^3)−Cl$ bonds. The authors suggested that the catalytic cycle was initiated by the reduction of Co^{II} to Co^I. Later in 2018, Koszinowski and Kregenschmidt published a mechanistic proposal based on thorough ESI-MS studies[55].
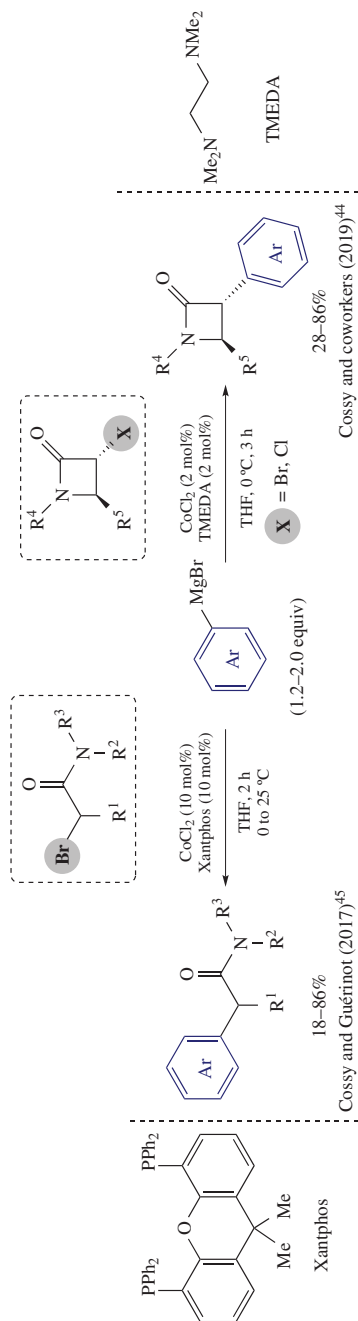
SCHEME 13. Cobalt-catalyzed cross-coupling of α-bromo amides and α-halogeno β-lactams.

SCHEME 14. Intermolecular (a) and intramolecular (b) cobalt-catalyzed Heck-type reactions.
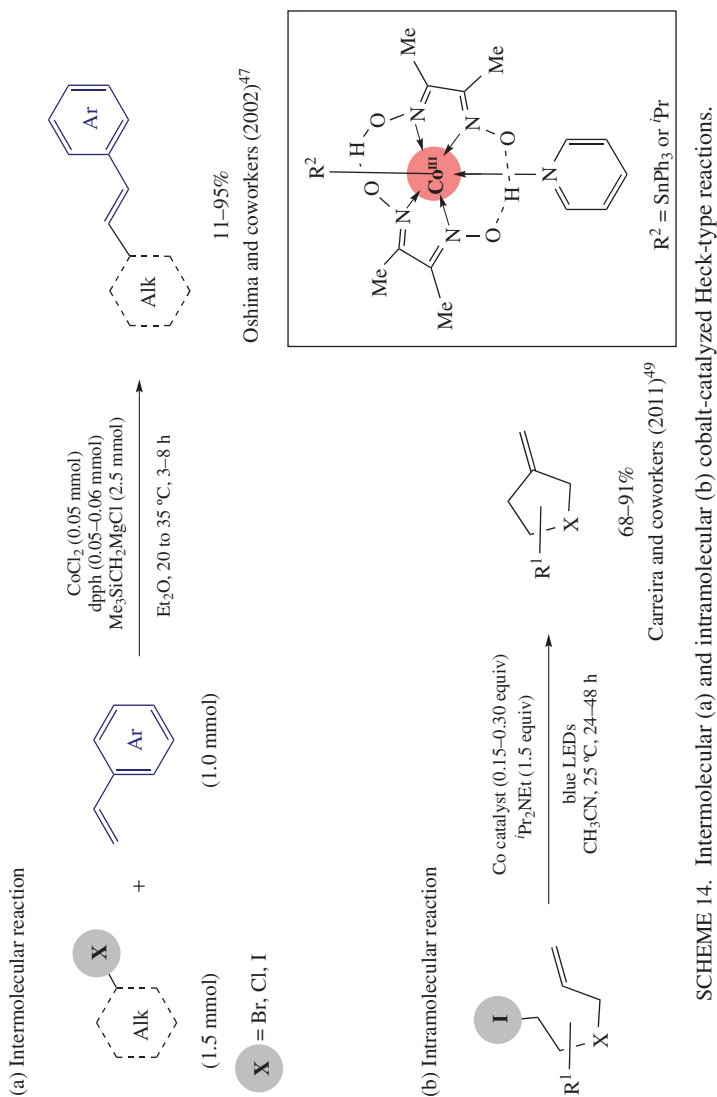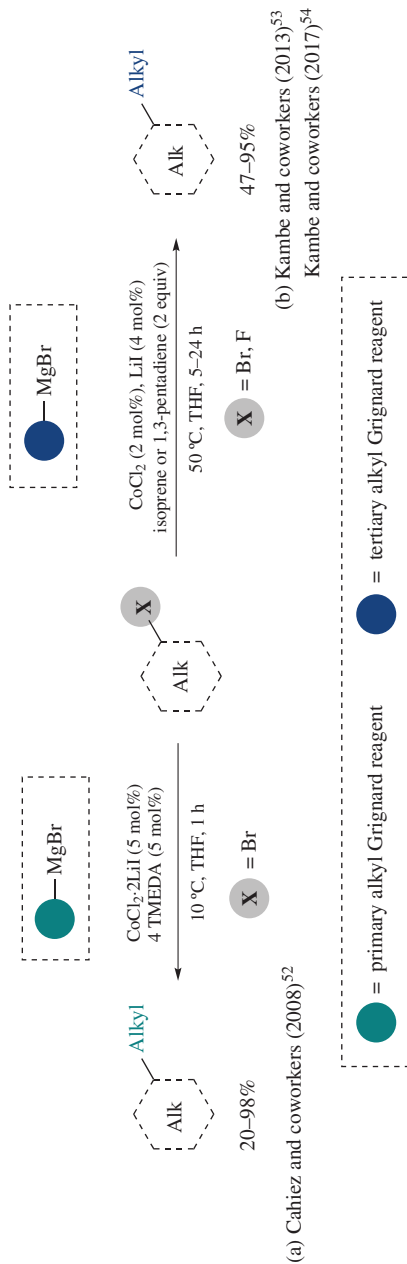
SCHEME 15. Cobalt-catalyzed $C(sp^3)$–$C(sp^3)$ cross-coupling of alkyl halides and alkyl Grignard reagents.
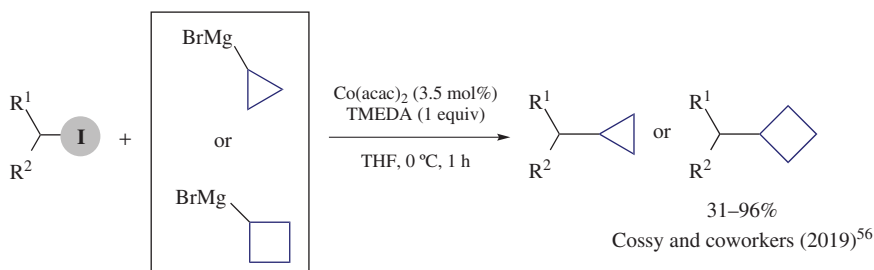
SCHEME 16. Cobalt-catalyzed coupling between alkyl iodides and cyclopropyl and cyclobutyl Grignard reagents.

Very recently, Cossy and coworkers developed a new methodology on cobalt-catalyzed cross-coupling reactions using cyclopropyl or cyclobutyl Grignard reagents as a coupling partner[56]. The reaction proceeded with primary and secondary alkyl iodides (Scheme 16).

3. $C(sp^3)-C(sp)$

Co-catalyzed alkynylation of alkyl halides using alkynyl Grignard reagents as nucleophiles is still rare, and only few examples have been reported. In 2006, Okamoto and coworkers reported the $Co(acac)_3$-catalyzed benzyl–alkynyl coupling using benzylic halides and $Me_3SiC{\equiv}CMgBr$ or n-$BuC{\equiv}CMgBr$ (Scheme 17a)[57]. Electron-donating substituents on the benzylic halide substrate improved reaction yields of the trimethylsilyl alkynylated product. The same year, Oshima, Yorimitsu, and coworkers independently disclosed the
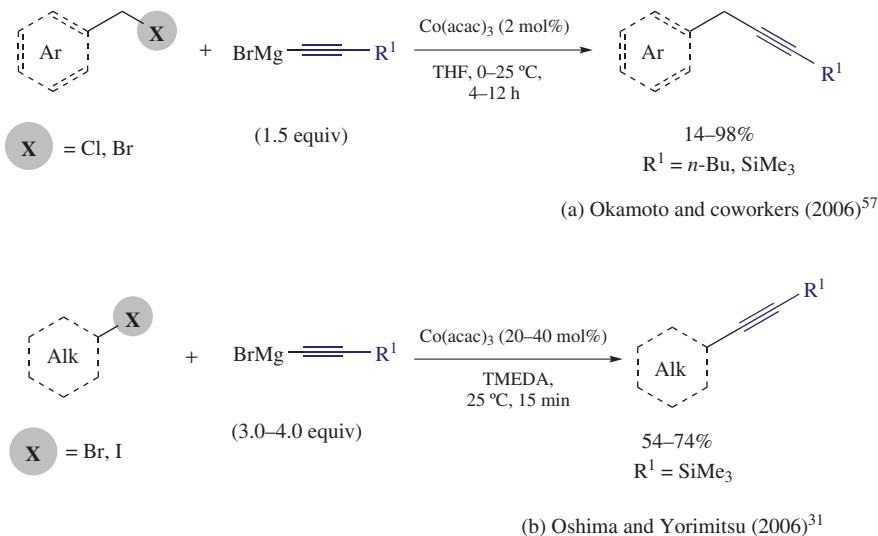
SCHEME 17. Cobalt-catalyzed $C(sp^3)-C(sp)$ bond formation of aryl or alkyl halides with alkynyl Grignard reagents.

alkynylation reactions using primary and secondary halides and $Me_3SiC\equiv CMgBr$ using the $Co(acac)_3$/TMEDA catalytic system, affording the coupling products at room temperature (Scheme 17b)[31].

Knochel and coworkers also contributed in this area by developing a methodology for the diastereoselective cobalt-catalyzed $C(sp^3)-C(sp)$ cross-coupling reaction using $CoCl_2\cdot 2LiCl_2$/neocuproine with cycloalkyl iodides and alkynyl derivatives (Scheme 18)[41]. Furthermore, alkynyl Grignard reagents bearing a silyl group was also well tolerated, leading moderate to good yields and excellent diastereoselectivity.

C. Alkynyl Halides, C(sp)−X

The cobalt-catalyzed construction of C−C bonds using alkynyl halides and Grignard reagents is less studied and was pioneered by Kharasch and coworkers in 1945. They reported the alkynylation of Grignard reagents catalyzed by $CoCl_2$ where 2-bromo-1-phenylacetylene reacted with methylmagnesium bromide to give 1-phenyl-1-propyne in 62% yield[58]. In 1954, Weedon and coworkers reported a similar protocol with alkynyl halides, to provide the coupling products with alkyl and aryl Grignard reagents (Scheme 19)[59].

III. C−C COUPLING REACTIONS USING ORGANOZINC REAGENTS

A. Aryl or Alkenyl Halides, C(sp²)−X

The replacement of Grignard reagents by organozinc compounds as coupling counterparts has been successfully achieved for Co-catalyzed C−C bond formation. In 1998, Knochel, Cahiez, and coworkers applied this methodology for the formation of $C(sp^2)-C(sp^3)$ using alkenyl iodides (depicted in Scheme 20)[60]. The reaction proceeded using $Co(acac)_n$ ($n = 2$ or 3) in THF:NMP at 55 °C, affording the corresponding alkene in moderate to good yields with high E/Z stereoselectivity.

Later, Gosmini and Begouin developed a new methodology for the synthesis of aryldiazines by coupling of 2-chloropyrimidines or 2-chloropyrazines with aryl−ZnX (generated *in situ* by $CoBr_2$-catalyst and metallic Zn)[61]. The reaction proceeded either by one-pot or sequential addition of the heteroaryl halide, depending on the nature of the aryl halide (Scheme 21). The presence of allylchloride in the catalytic system was helpful in avoiding the reduction of arylzinc compounds to form Ar−H side products. The authors extended this methodology for the functionalization of triazines[62] or the preparation of N-heterocycles via direct C−SMe functionalization[63].

In order to further expand the potential of cobalt catalysis, in 2016, Knochel and coworkers provided a new route toward the arylation of aryl and heteroaryl zinc reagents[64, 65]. The catalytic system consisting of $CoCl_2\cdot 2LiCl$ together with substoichiometric amounts of HCO_2Na efficiently coupled 2-chlorinated aromatic ketones and arylzinc reagents. The reaction tolerated a variety of aryl- and heteroaryl-zinc compounds bearing different substituents, including 2,3- and 2,5-disubstituted N-heterocyclic chlorides. The authors also applied this system to halogenated quinolones, pyrimidines, and triazines, affording the coupling product in good to excellent yields. The same year, the authors developed a new protocol using various benzyl zinc chlorides for the functionalization of aryl- and hetero-aryl halides[66]. The synthesis of novel polyfunctionalized naphthyridines via cobalt cross-coupling reactions was also reported by Knochel and coworkers[67]. The addition of HCO_2Na was also beneficial for the functionalization of N-heterocycles with arylzinc reagents using $CoCl_2$ as catalyst. The use of air- and moisture-stable organozinc pivalates[68] allowed the development of a robust and broadly applicable cobalt-catalyzed cross-coupling methodology using a variety of substituted aryl-
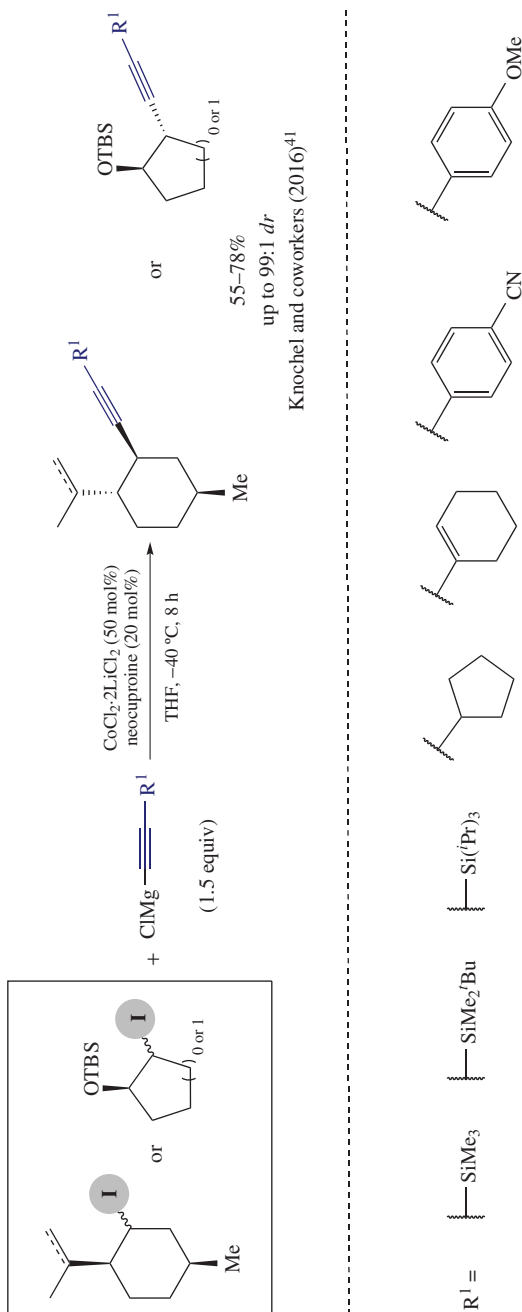
SCHEME 18. Cobalt-catalyzed cross-coupling of cycloalkyl iodides with alkynyl Grignard reagents.

$$R^1 \mathrel{\text{\textemdash}}\!\equiv\!\mathrel{\text{\textemdash}} Br \quad + \quad R^2 \mathrel{\text{\textemdash}} MgBr \xrightarrow[\text{ether, 25 °C, 12 h}]{CoCl_2 \ (10 \ mol\%)} R^1 \mathrel{\text{\textemdash}}\!\equiv\!\mathrel{\text{\textemdash}} R^2$$

Weedon and coworkers (1954)[59]

Ph—C≡C—Me

40%

Ph—C≡C—Ph

39%

Bu—C≡C—C≡C—Bu

28%
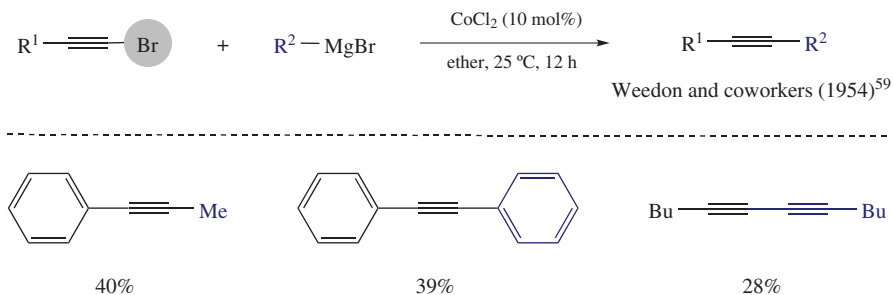
SCHEME 19. Cobalt-catalyzed C(sp)−C bond-formation reactions with alkynyl halides and aryl or alkyl Grignard nucleophiles.

$$\text{Alkyl}^1 \diagup\!\!\diagdown\!\! I \quad + \quad \text{Alkyl}^2 \mathrel{\text{\textemdash}} ZnI \xrightarrow[\text{THF:NMP, 55 °C, 8 h}]{Co(acac)_2 \ (10\text{–}30 \ mol\%)} \text{Alkyl}^1 \diagup\!\!\diagdown \text{Alkyl}^2$$

(3 equiv)

50–81%
>99% E
Knochel and Cahiez (1998)[60]

Oct—ZnI

Bu ⟍⟍⟋ I

Co(acac)₂ (26 mol%)
THF:NMP (5:2), 55 °C, 8 h

Bu ⟍⟍⟋ Oct

81%; >99% E

Bu ⟍⟍⟍ Oct

71%; >99% Z
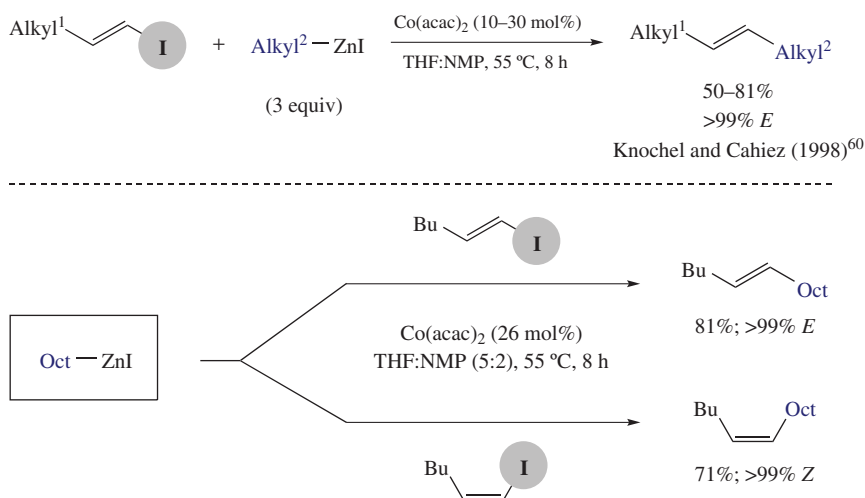
SCHEME 20. Cobalt-catalyzed C(sp²)−C(sp³) bond formation of alkenyl iodides and alkyl zinc reagents.

and hetero-aryl halides (Scheme 22)[69]. The protocol tolerated different aryl- and hetero-aryl halides such as mono- and di-substituted aryl halides, chlorobenzophenone derivatives, halo-quinolines, and 2-chloropyridazine. The use of alkenyl halides was also investigated, affording the coupling product in a stereoselective manner. The construction of C(sp²)−C(sp²) bond using aryl−ZnX or alkenyl−ZnX via cobalt catalysis was further expanded by Knochel and coworker using alkenyl acetates as electrophiles[70]. The coupling products were obtained in good yields using CoBr₂ and bpy as catalysts, in THF at room temperature. A variety of functional groups are well tolerated, and high E/Z stereoselectivity was observed. The method allowed the unprecedented synthesis of estrone derivatives, demonstrating the versatility of this methodology.

Recently in 2020, Knochel and coworkers expanded the functionalization of heteroaryl and aryl halides using primary and secondary alkylzinc reagents (Scheme 23)[71]. N-Heterocyclic halides were coupled with alkylzinc compounds bearing different functional groups such
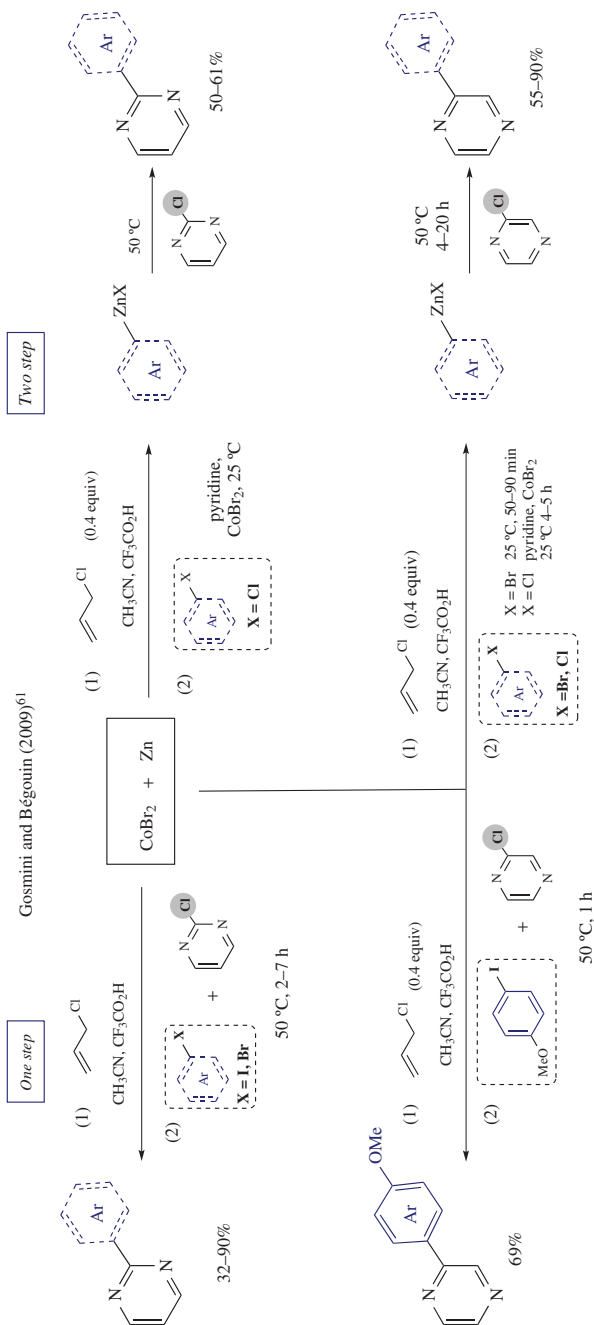
SCHEME 21. Cobalt-catalyzed C(sp^2)–C(sp^2) bond-formation reaction of hetero-aryl halides and *in situ* formed organozinc reagents.
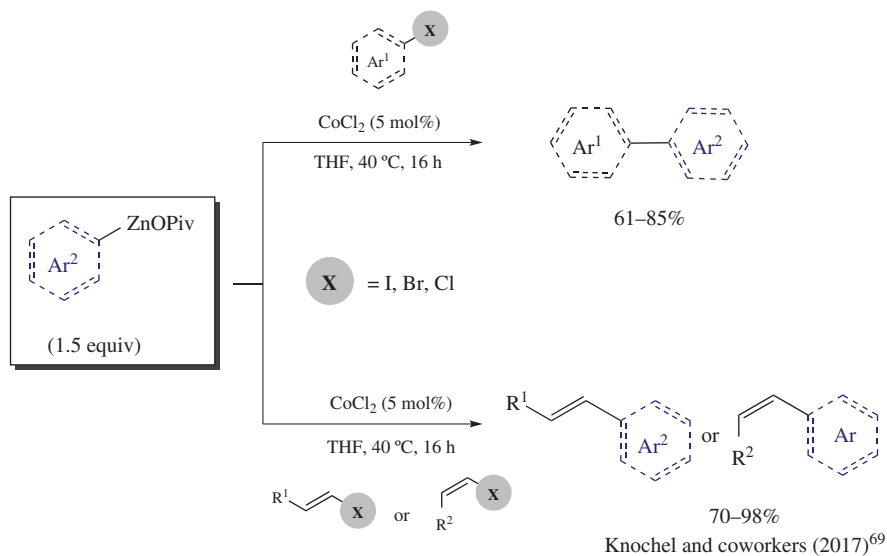
SCHEME 22. Cobalt-catalyzed cross-coupling reactions using arylzinc pivalates.
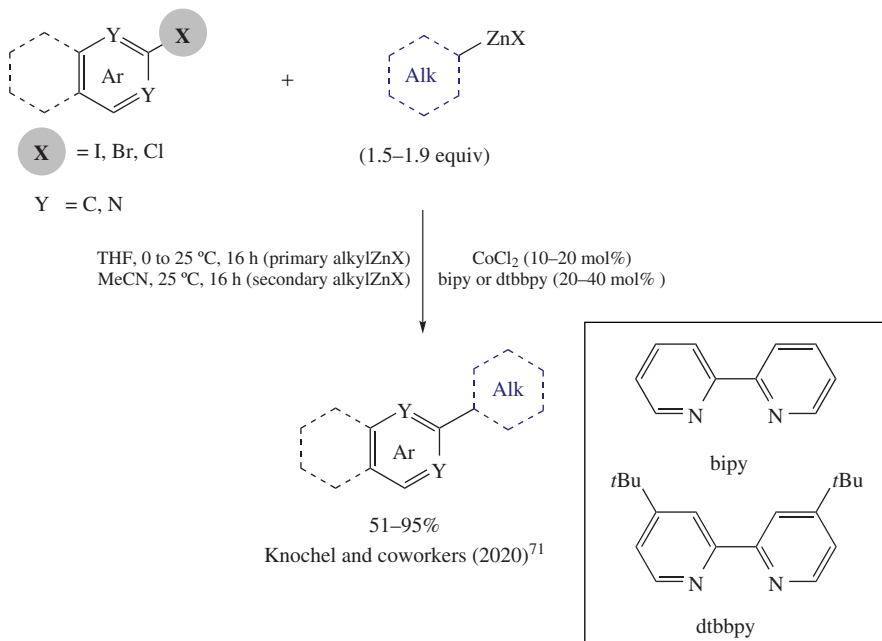
SCHEME 23. Cobalt-catalyzed cross-coupling of heteroaryl halides with alkylzinc reagents.

as nitrile, masked amines, and acetates. Quinoline, isoquinoline, quinazoline, and pyrimidine halide derivatives were also successfully used as electrophile partners as well as electron-deficient aryl halides. They also applied this methodology to the coupling between 2-bromopyrimidine with alkylzinc reagents prepared from steroid and sesquiterpene derivatives, showing good yields and high diastereoselectivity.

The alkynylation of aryl halides using alkynylzinc via cobalt catalysis was also reported by Knochel and coworkers[72]. In 2017, they developed a catalytic system using $CoCl_2 \cdot 2LiCl$ and TMEDA, enabling the construction of $C(sp^2)-C(sp)$. 2-Chlorobenzophenone was subjected to several alkynyl zinc pivalates, yielding the coupling products in good to excellent yields (Scheme 24). Different substituted aryl- and hetero-aryl halides bearing electron-donating and electron-poor functional groups were tolerated.

B. Alkyl Halides, $C(sp^3)-X$

Cobalt-catalyzed $C(sp^3)-C(sp^3)$ cross-coupling reaction using organozinc compounds was pioneered by Knochel and Reddy in 1996 using alkyl halides[73]. Thereafter, different alkyl halides have been used as electrophiles in Negishi-type cross-coupling based on cobalt catalysis (Scheme 25). In 2007, Knochel and Dunet developed the arylation of allyl chlorides in good yields and high stereoselectivity[74]. They further extended this reactivity to primary and secondary alkyl iodides and several polyfunctional diaryl- and dihetero-aryl zinc compounds, using $CoCl_2 \cdot 2LiCl$ as catalyst[75]. Inoue and Araki reported the coupling between ethyl bromodifluoroacetate and arylzinc reagents, leading to the formation of ethyl aryldifluoroacetates in moderate to good yields[76]. Bian and coworkers also contributed to this field by reporting the cobalt-catalyzed enantioselective Negishi cross-coupling reactions using α-halo esters with arylzinc halides, affording α-arylalkanoic esters in excellent yields[77]. The authors suggested that the catalytic system involves a radical pathway due to the formation of ring-opened product when they use α-bromo cyclopropyl ester derivatives. Recently, Knochel and coworkers developed the highly trans-diastereoselective formation of α-arylated butyrolactones and α-arylated-protected β-hydroxy esters[78]. They also applied this methodology to the synthesis of a bioactive artificial rotenoid derivative (munduserol).

Also in 2020, the α-arylation of substituted α-bromo α-fluoro β-lactams with diaryl reagents was disclosed by Cossy and coworkers, using the $CoCl_2$/TMEDA catalytic system[79]. Several substituted α-bromo α-fluoro β-lactams, as well as a wide range of arylzinc reagents, are well tolerated. Different carbonyl compounds such as α-bromo lactams and lactones, α-bromo amides, and esters are well tolerated as electrophiles. Furthermore, the methodology could also be applied to N- and O-containing heterocycle substrates.

Few examples of Co-catalyzed alkylation of alkyl halides via Negishi cross-coupling reactions are reported. Knochel and coworkers used dialkylzinc reagents and primary and secondary alkyl iodides with $CoCl_2$/neocuproine as catalytic system, enabling the corresponding $C(sp^3)-C(sp^3)$ couplings (Scheme 26)[80].

On the other hand, the alkynylation of alkyl halides was also achieved by Knochel and coworkers, reporting the coupling between 1,2-, 1,3-, and 1,4-substituted five- and six-membered cyclic (hetero)alkyl halides with several alkynylzinc pivalates in excellent yields and high diastereoselectivity (Scheme 27)[81]. In this method they observed better results using $CoCl_2$ and trans-N,N,N',N'-tetramethylcyclohexane-1,2-diamine as ligand in THF at 0 °C, and this methodology was applied for the alkynylation of steroid derivatives with excellent diastereoselectivity.

24
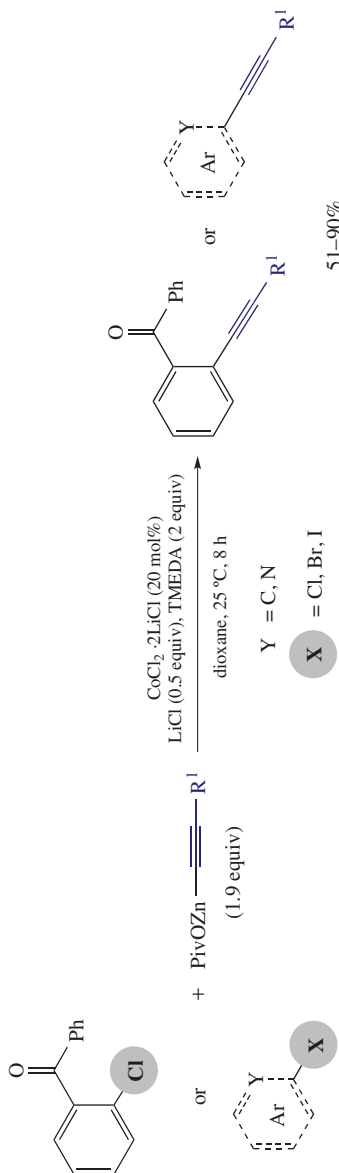
SCHEME 24. Cobalt-catalyzed C(sp^2)−C(sp) using alkynylzinc pivalates.
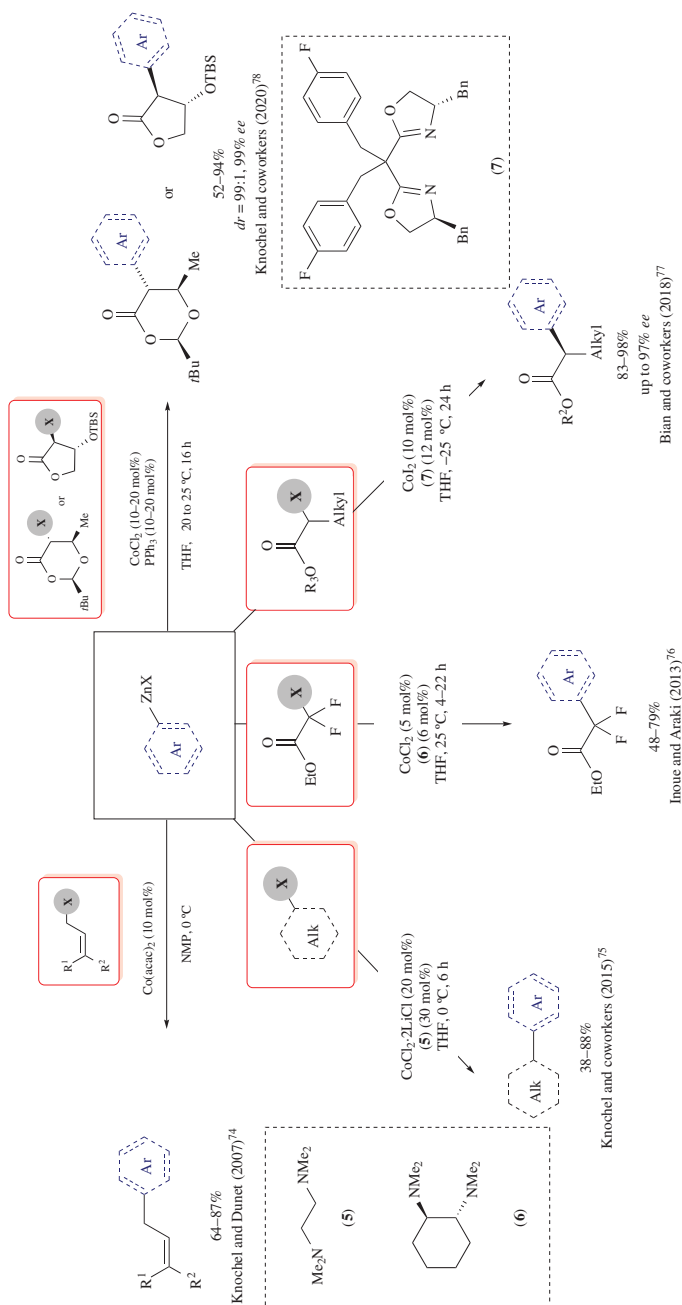
SCHEME 25. Cobalt-catalyzed C(sp^3)–C(sp^2) bond formation of different alkyl halides with arylzinc halides.
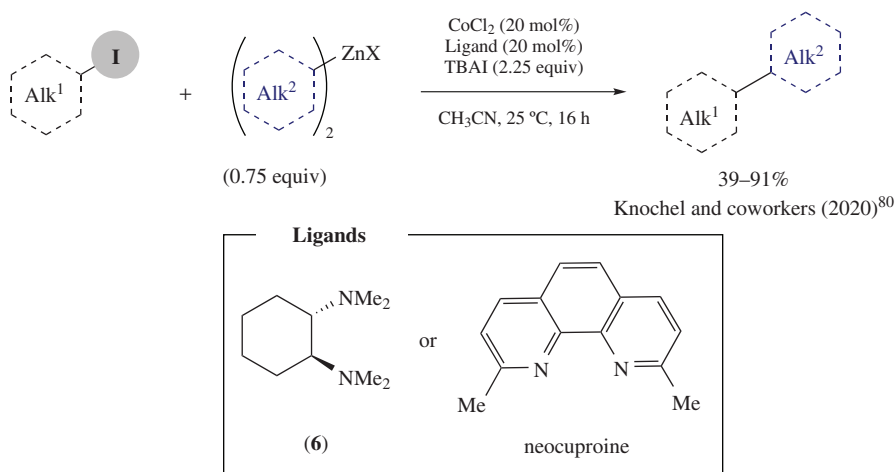
SCHEME 26. Cobalt-catalyzed C(sp^3)−C(sp^3) cross-coupling reactions of iodoalkyls and alkylzinc halides.
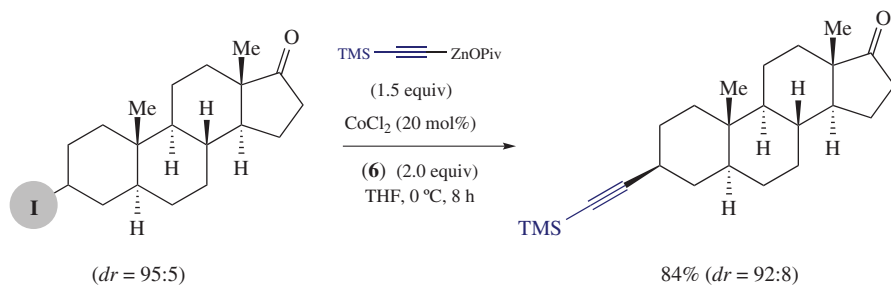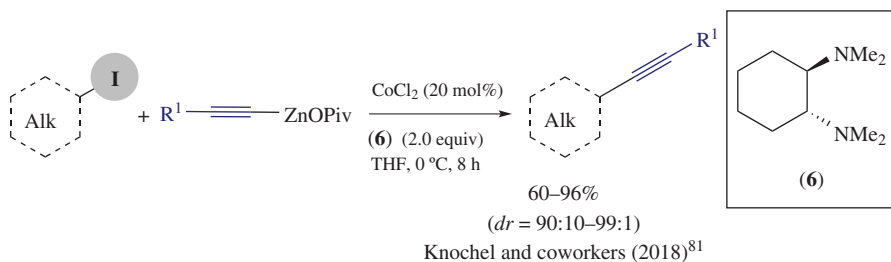
SCHEME 27. Cobalt-catalyzed alkynylation of alkyl iodides with alkylzinc pivalates.

C. Alkynyl Halides, C(sp)−X

The use of alkynyl bromides as electrophiles in cobalt-catalyzed cross-coupling reaction was first disclosed by Gosmini and coworkers[82]. A wide range of aryl- and alkyl-bromoalkynes were coupled with arylzinc reagents using $CoBr_2$ in the presence of 1,10-phenanthroline or dppe (1,2-bis(diphenylphosphino)ethane) as ligands (Scheme 28). On the other hand, Knochel and coworkers also contributed with examples of cobalt-catalyzed cross-coupling reactions using alkynyl bromides and alkylzinc reagents[71].

IV. C−C COUPLING REACTIONS USING ORGANOBORON REAGENTS

The use of organoboron reagents as nucleophiles in transition metal-catalyzed cross-coupling reactions has become a widely employed methodology for the formation of biaryl compounds. The easy preparation and safe handling, combined with their relative stability, makes them suitable nucleophiles in cross-coupling transformation, the well-known Pd-catalyzed Suzuki−Miyaura reaction being one of the most powerful methods for aryl−aryl coupling. Its widespread use had stimulated a great interest in developing new methodologies using first-row transition metals, and cobalt is not an exception. It was not until 2016, when Chirik and coworkers pioneered this field by reporting the cobalt-catalyzed Suzuki−Miyaura $C(sp^2)−C(sp^2)$ cross-coupling using aryl triflate and 2-benzofuranylBPin (Scheme 29)[83]. The use of a tridentate pincer ligand allowed to isolate a key Co^I intermediate species in this reaction. They proposed the catalytic system based on the transmetalation of an aryl from the organoboron reagent to a $Co^I−OR$ to render the $Co^I−aryl$ complex, followed by the interaction of the electrophile to end up with the aryl−aryl product and the regeneration of the $Co^I−OR$ species (Scheme 29a). The authors reported a variety of Co^I-phenoxide, -alkoxide, and -carboxylate complexes featuring a tetrahedral geometry. The resulting transmetalation product with 2-benzofuranylBPin switched to a planar geometry, which was attributed to the flexibility of the ^{iPr}PNP ligand. Mechanistic studies suggested the initial coordination of the heteroatom lone pair from 2-benzofuranylBPin to the cobalt center, bringing the boron atom in proximity to the alkoxide moiety, thus initiating the transmetalation process (Scheme 29b). The catalytic version of the reaction was achieved using ArOTf, 2-benzofuranylBPin, and NaOCH(Ph)Me as base with catalytic amounts of $(^{iPr}PNP)CoCl$, forming 2-phenylbenzofuran derivatives products in good yields (Scheme 29c).

The use of tridentate pincer cobalt complex was also studied by Bhat and Kumar, and PNCOP, PNCNP, and PNNNP tridentate ligands were used to stabilize the corresponding Co^{II} complexes, which were further used as catalysts for the Suzuki−Miyaura coupling between phenyl boronic acid ($PhB(OH)_2$) and bromobenzenes (Scheme 30)[84]. Among the three catalysts, $Co^{II}PNNNP$ catalyst showed the best results, and a Co^0/Co^{II} catalytic cycle was proposed.

Bedford and coworkers introduced in 2017 the use of NHC-based ligands to broaden the scope of Co-catalyzed C−B coupling reactions (Scheme 31a)[85]. A wide range of substituted aryl chlorides and bromides (with either electron-withdrawing or -donating groups) were successfully coupled to arylBPin esters, previously activated with alkyllithium. Thereafter, Duong and coworkers reported the arylation of *N*-heterocyclic halide compounds with arylboronic esters (PhB(neo)) using the $CoCl_2$/terpyridine catalytic system (Scheme 31b)[86]. Substituted 2-chloropyridines featuring electron-withdrawing and -donating groups as well as other *N*-heteroaryl chlorides were tolerated. On the contrary, aryl chlorides were poorly reactive. The authors proposed a Co^I/Co^{III} catalytic cycle, where the reduction of Co^{II} to Co^I was attained by reaction with phenylborate. Two years later, the same authors reported an analogous methodology to synthesize biaryl coupling products using activated lithium arylborates and ArOTf (Scheme 31c)[87]. Also in 2019, Shen, Wei, and coworkers reported the
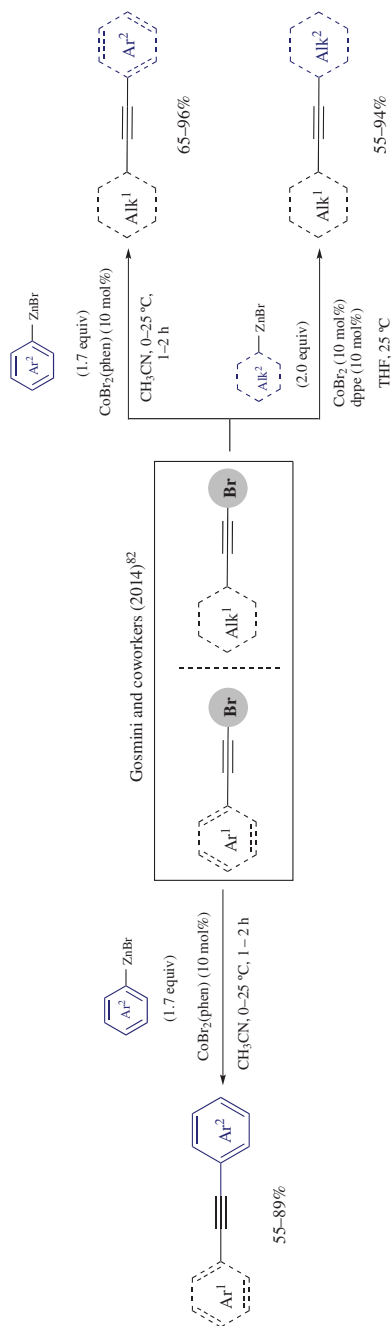
SCHEME 28. Cobalt-catalyzed cross-coupling of aryl and alkyl zinc reagents with haloalkynes.

(b) Transmetalation step

Transmetalation step

(c) Cobalt-catalyzed Suzuki–Miyaura type reaction

Ar^2 =

NaOCH(Ph)Me (1 equiv)
$(^{tBu}PNP)CoCl$ (5 mol%)

THF, 60 °C, 24 h

BPin — Ar^2
(1 equiv)

OTf

Ar^1

Ar^1 — Ar^2

30–95%
Chirik and coworkers (2016)[83]
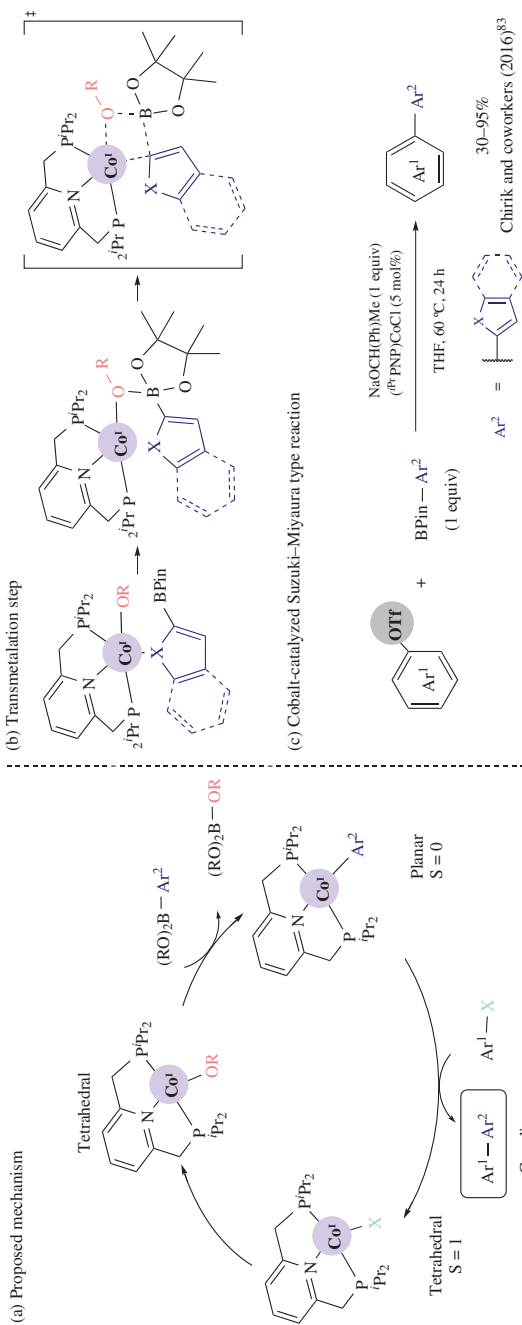
SCHEME 29. Cobalt-catalyzed Suzuki-type cross-coupling.

(a) Proposed mechanism

$(RO)_2B$ — Ar^2

$(RO)_2B$ — OR

Planar
S = 0

Tetrahedral

OR

Ar^1 — X

Ar^1 — Ar^2
Coupling
Product

Tetrahedral
S = 1
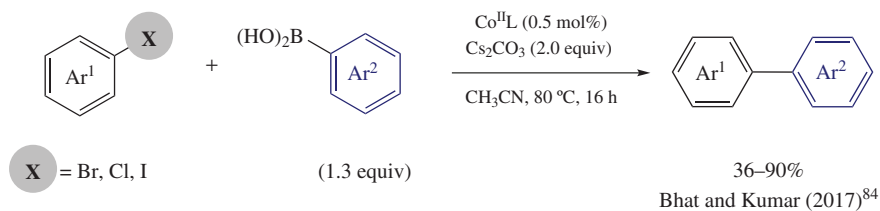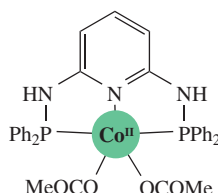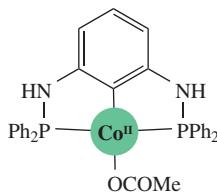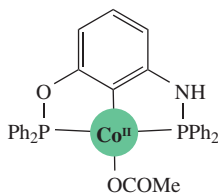
SCHEME 30. Cobalt-catalyzed cross-couplings of aryl halide and arylboronic acid.

coupling of (hetero)aryl halides with lithium arylboronates in the presence of $ZnBr_2$ to *in situ* form lithium arylzincates as the actual nucleophiles[88].

Chirik and coworkers disclosed very recently the elusive coupling between aryl boronic ester and alkyl bromides, using the Co^{II} complex (DMCyDA)$CoBr_2$ (DMCyDA = *trans-N,N′-*dimethylcyclohexane-1,2-diamine) as a successful catalyst to effect the desired $C(sp^3)-C(sp^2)$ coupling product in a broad scope, while minimizing β-hydride elimination side reactions (Scheme 32)[89]. The authors proposed an electrophile-derived radical-based mechanism and also proved the enhanced reactivity of activated aryl borates.

In this line, Shen and coworkers disclosed a cobalt-catalyzed asymmetric cross-coupling reaction of α-bromo-α-fluorotoluene derivatives with lithium aryl boronates using the $CoBr_2$/bisoxazoline as catalytic system in order to synthesize α-fluorinated diarylmethane derivatives (Scheme 33)[90].

V. C−C COUPLING REACTION WITH NONCONVENTIONAL NUCLEOPHILES

Although the vast majority of Co-catalyzed C−C bond-forming methodologies are based on the use of organomagnesium, organozinc, and organoboron nucleophiles, other methodologies have reported the direct use of allyl acetates or carbonates, alkenyl acetates, and benzonitriles as the nucleophile counterparts. The mechanisms behind these cross-couplings reactions differ from the standard ones as described below.

Gosmini and coworkers developed in 2003 the arylation of allyl acetates or carbonates via $CoBr_2$ catalysis under electrochemical processes (Scheme 34)[91]. Aryl bromides with electron-withdrawing or -donating groups were well tolerated, as well as aryl chlorides, albeit using higher loading of catalyst (up to 40 mol%). On the contrary, Ar−I were too reactive, and Ar−Ar side products appeared.

Later in 2005, the same authors reported the cobalt-catalyzed cross-coupling reaction of alkenyl acetates and ArX, using manganese as reducing agent (Scheme 35)[92]. The aryl-alkenylated products were obtained via a proposed concerted six-centered transition

Ligands

SIPr·HCl

TPy

IAd·HBF$_4$

CoCl$_2$ (10 mol%)
SIPr·HCl (10 mol%)

THF, 60 °C, 48 h

33–93%

(a) Bedford and coworkers (2017)[85]

CoCl$_2$ (5 mol%)
TPy (5 mol%)

KOMe (1.5 equiv)
DMF, 80 °C, 16 h

11–95%

(b) Duong and coworkers (2017)[86]

CoCl$_2$ (10 mol%)
IAd·HBF$_4$ (10 mol%)

^{n}BuLi (1.5 equiv)
THF, 70 °C, 16 h

30–94%

(c) Duong and coworkers (2019)[87]

Li$^+$(THF)$_2$

B(neo)

(1.5 equiv)

B(pin)

(2.0 equiv)

X = Cl, Br

X = Cl, Br

X = OTf
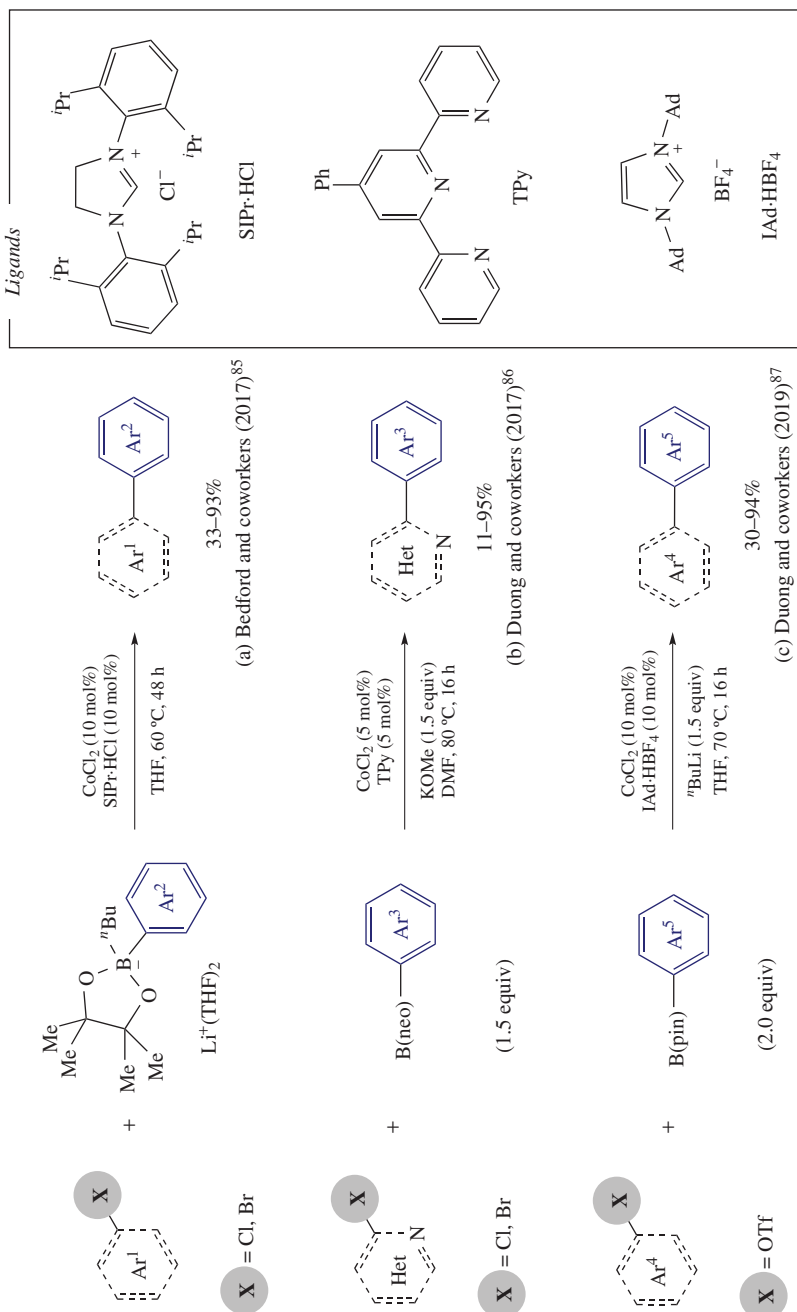
SCHEME 31. Cobalt-catalyzed construction of C(sp^2)–C(sp^2) using boronic esters.
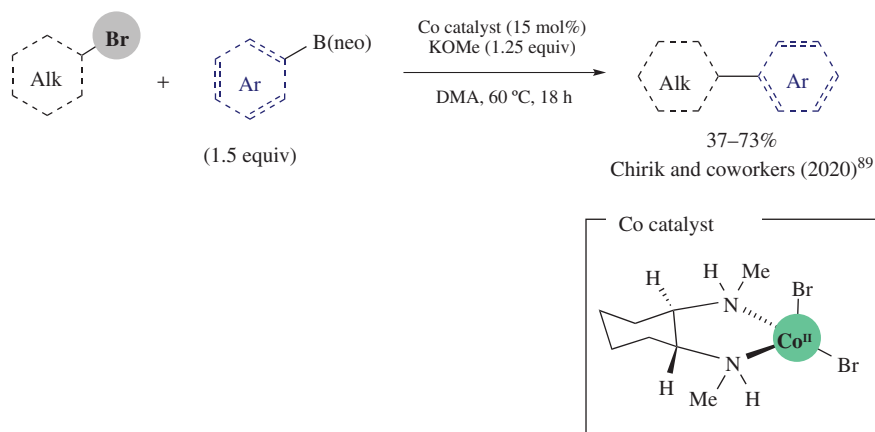
SCHEME 32. Cobalt-catalyzed C(sp^3)−C(sp^2) bond-forming reaction using alkyl halides and aryl-boronic reagents.
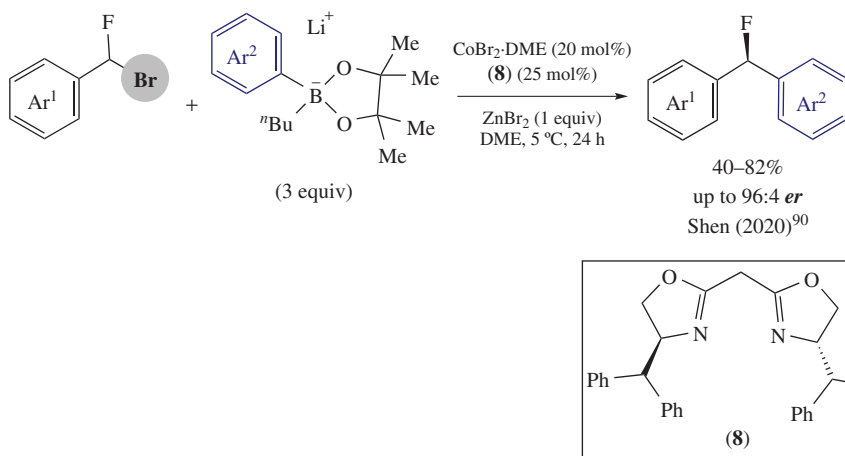
SCHEME 33. Cobalt-catalyzed asymmetric cross-coupling reaction using a bisoxazoline-based ligand.

state in which the Ar group is well positioned to be transferred to the alkenyl moiety. Later, Gosmini and coworker applied similar methodology for the construction of unsymmetrical biaryl compounds from different aryl halides using CoBr$_2$/PPh$_3$ as catalyst and Mn as reducing agent[93]. The authors proposed a catalytic system based on Co^I/Co^{III} catalytic cycle with the key role of Mn^0 to provide the key-reduced Co^I species.

The C(sp^3)−C(sp^3) allylation of alkyl halides with allylic acetates or carbonates was reported by Gosmini and coworkers using CoBr$_2$ catalyst with stoichiometric amount of metallic Mn as the reducing agent (Scheme 36)[94]. Alkyl halides bearing nitriles, esters, carbamates, and
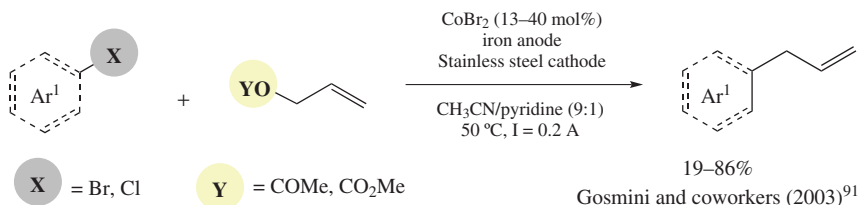
SCHEME 34. Cobalt-catalyzed $C(sp^2)-C(sp^2)$ cross-coupling using aryl halides and allyl acetates under electrochemical conditions.
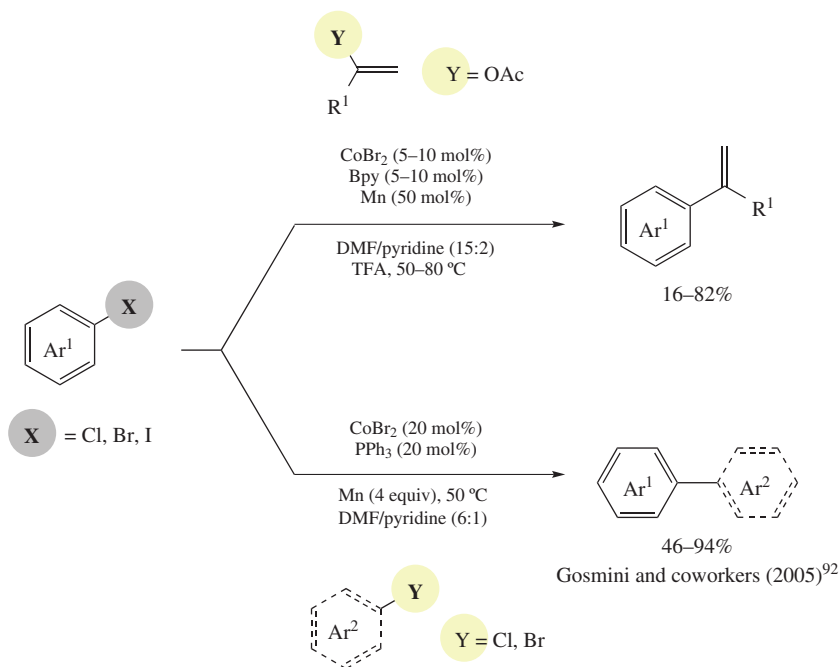
SCHEME 35. Cobalt-catalyzed $C(sp^2)-C(sp^2)$ cross-coupling using metallic Mn as reducing agent.

chlorine moieties as well as long-chain alkyl halides were tolerated. Cyclic and acyclic secondary alkyl halides reacted with allylic acetates forming the desired products in high yields. The authors proposed that radical species were involved and that the role of the added trifluoroacetic acid (TFA) was crucial for the generation of the catalytically active Co species.

Recently, Gosmini and coworkers disclosed a new methodology for the formation of biaryl compounds using benzonitrile derivatives and aryl halides (see Scheme 37)[95]. The direct activation of $C(sp^2)-CN$ was achieved using acetals, benzyl-, silyl-protected phenol-, and alcohol-substituted benzonitriles. The use of $AlMe_3$ Lewis acid as additive afforded improved yields and reduced homocoupling products from aryl halide electrophiles.
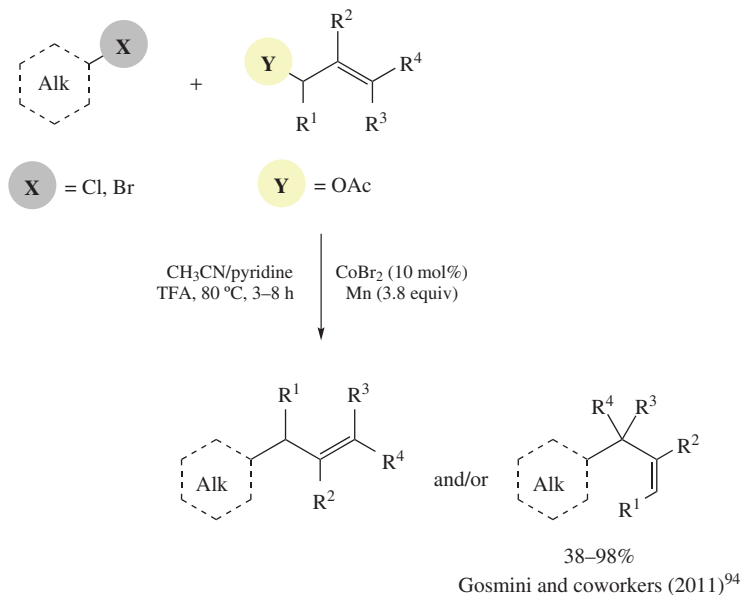
SCHEME 36. Cobalt-catalyzed allylation of alkyl halides using metallic Mn as reducing agent.
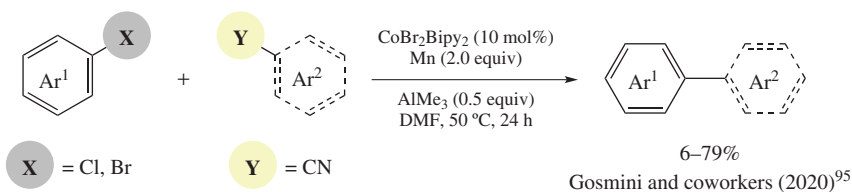
SCHEME 37. Cobalt-catalyzed biaryl formation via $C(sp^2)-CN$ functionalization.

VI. MECHANISTIC ASPECTS IN C–C BOND-FORMING REACTION

In Co-catalyzed cross-coupling reaction, most strategies are based on using low-valent cobalt species as active catalysts, although *in situ* generation by the presence of a reducing agent complicates the assignment of the oxidation state of the active catalyst. In this context, several oxidative states of the active cobalt species have been proposed for the catalytic cycle.

Jacobi von Wangelin and coworkers reported in 2013 the cobalt-catalyzed biaryl coupling reactions with aryl chlorides and ArMgBr using cobalt-based precatalysts in three oxidation states: cobalt(III) Co(acac)$_3$, cobalt(I) CoCl(PPh$_3$)$_3$, and cobalt(−1) [(Co(anthracene)$_2$]$^-$ [K(dme)$_2$]$^+$ [27]. The authors found very similar outcomes for the biaryl coupling products irrespective of the precatalyst used, and this was interpreted as a clear indication that catalysts of identical oxidation states were operative in all three cases. The redox adjustment of the

precatalysts converged into the formation of catalytically active Co^I species by reduction with ArMgBr or by oxidation with ArCl substrate.

On the other hand, Li and coworkers reported the isolation and characterization of key aryl–Co^{III} complexes by reacting imine-containing aryl chlorides with Co^I reagents ($[CoCl(PMe_3)_3]$ or $CoBr(PMe_3)_3]$), demonstrating the feasibility of the aryl chloride oxidative addition at Co^I (Scheme 38)[97]. Furthermore, the use of $[CoMe(PMe_3)_4]$ afforded the corresponding aryl–Co^{III}–Me complex that underwent reductive elimination to obtain the methyl–arene coupling product.

Pérez-Temprano and coworkers also reported the synthesis of metalacyclic aryl–Co^{III} complexes by reacting aryl iodide-bearing mono-coordinating directing groups with Cp*Co^I via an oxidative addition (Scheme 38)[96]. Moreover, they succeeded in designing the catalytic version of this process coupled to the corresponding annulation reaction with internal acetylenes.

On the other hand, in 2012 Budzelaar and coworkers disclosed the reactivity of well-defined *NNN*-pincer-based cobalt(0) complexes ($[LCo^0(N_2)]$) with aryl halides, which underwent a radical-based formation of a mixture of LCo^IAr and LCo^IX complexes.[98] Reaction of $[LCo^0(N_2)]$ with alkyl halide also drove to the formation of LCo^Ialkyl species through a radical mechanism.

With respect to transmetalation, Chirik and coworkers explored this specific step by reacting tridentate pincer Co^I complexes with organoboron reagents in cobalt-catalyzed Suzuki–Miyaura reaction, isolating a set of key Co^I–aryl intermediate species[83].

Regarding the intrinsic reactivity of organometallic Co^{III} species, Ozerov and coworkers contributed in studying the $C(sp^2)$–$C(sp^2)$ reductive elimination step from well-defined penta-coordinated aryl–Co^{III} complexes bearing POCOP pincer ligand (Scheme 39)[99]. The authors did not observe the desired C–S coupling despite bearing a thiophenolate ligand. In contrast, (POCOP)Co^{III}(Ph)(SPh) complex underwent intramolecular C–C coupling with the phenyl ligand affording the biaryl coupling product. Very recently, the same authors reported the observation of concerted C–S reductive elimination, avoiding the intramolecular $C(sp^2)$–$C(sp^2)$ reductive elimination by switching to a PNP ligand[100].

Ribas and coworkers also contributed in this area by investigating the C–C bond-formation reaction and exploring the reactivity of the well-defined macrocyclic aryl–Co^{III} organometallic complex with alkynes and diazo compounds as carbon counterpart (Scheme 40). The use of tetradentate macrocyclic ligand allowed the stabilization and crystallization of aryl–Co^{III} complexes through C–H activation[101]. The reaction between the aryl–Co^{III} complex and 1-ethynyl-4-nitrobenzene afforded the expected $C(sp^2)$–$C(sp)$ coupling products, which suffered an ulterior intramolecular cyclization to form the dihydroisoindoline product (five-membered ring) in a regioselective manner. In sharp contrast, reaction with phenylacetylene resulted in the regioselective formation of dihydroisoquinoline coupling product (six-membered ring). DFT calculations provide insight into the mechanistic proposal of a so-called acetylide pathway instead of the commonly accepted migratory insertion of the triple bond into the aryl–Co^{III} bond, so that a rational explanation was given for the formation of the unexpected five-membered ring product. The same group also explored the reactivity of the same aryl–Co^{III} complexes with diazo esters[102]. The 1,4-dihydroisoquinolin-3(2*H*)-one annulation product using ethyl diazoacetate (EDA) and the aryl–Co^{III} organometallic complex was observed in excellent yields when a Lewis acid was added in the reaction. Moreover, the authors isolated and structurally characterized an aryl–Co^{III}–alkyl enolate stopping the reaction at short reaction times, unraveling a carboxylate-assisted formation of aryl–Co^{III}-masked carbenes. They observed that the aryl–Co^{III}–alkyl enolate evolves to the annulation product via an intramolecular S_N2-like pathway for the C–O bond cleavage and C–C bond-formation reaction[103].

Concerning the mechanistic insights into alkyl–alkyl couplings, Bernskoetter and Xu studied in detail the ethane $C(sp^3)$–$C(sp^3)$ coupling via reductive elimination from

SCHEME 38. Aryl–Co^{III} complex formation via C–Cl and C–I bond activation using (a) the directing group strategy or (b) the stabilizing effect of Cp* ligand.
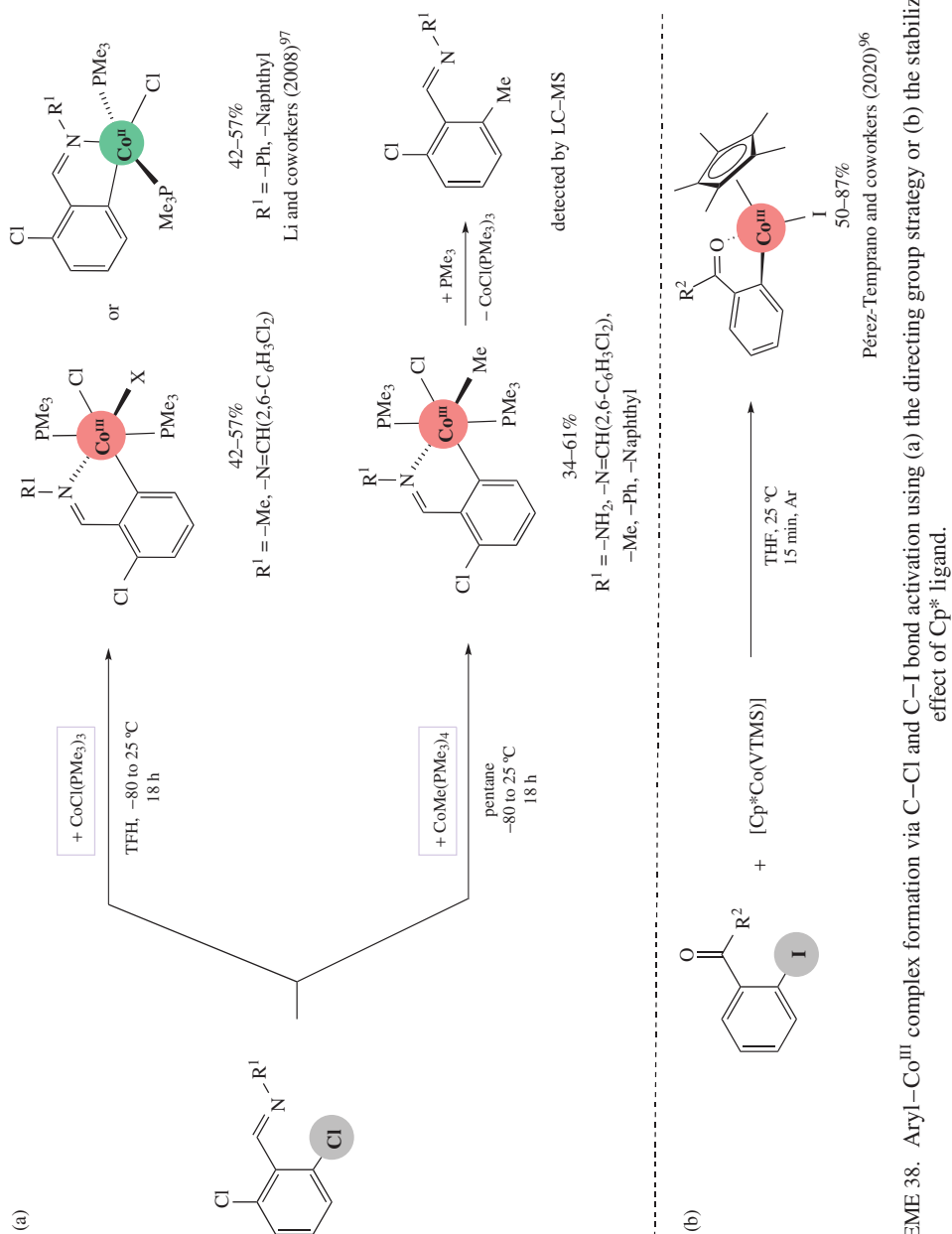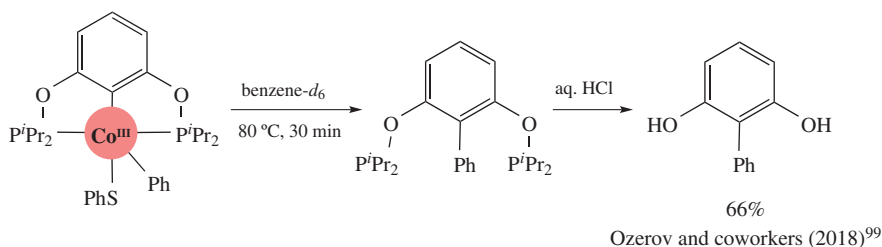
SCHEME 39. Aryl–Aryl reductive coupling at Co^{III} center using a pincer-based complex. Reproduced with permission from Ref. 99. © John Wiley & Sons, 2018.

cis,mer-$(PMe_3)_3Co^{III}(CH_3)_2I$ complex[104]. The authors proposed a reversible PMe_3 dissociation prior to ethane formation via a five-coordinated intermediate, as the intermediate species undergo a concerted reductive elimination (Scheme 41). Later, Ahmad, Roy, and coworkers supported with a thorough DFT study the concerted $C(sp^3)-C(sp^3)$ bond-formation pathway[105].

In relation to $C(sp^2)-C(sp^3)$ couplings, Soper and coworkers explored the reactivity of square planar Co^{III} complexes bearing two redox-active amidophenolate ligands[106]. Their reaction with ethyl bromide afforded the corresponding square-pyramidal ethylcobalt(III) complexes via ligand-mediated oxidative additions; thus, no change in metal oxidation state occurred. The alkylcobalt(III) complex was subjected to Negishi-like cross-coupling reactions using phenylzinc halide, affording the desired ligand-assisted $C(sp^2)-C(sp^3)$ reductive elimination coupling product, although in low yield (15%) (Scheme 42).

VII. C−HETEROATOM CROSS-COUPLING REACTIONS

A. C−N Coupling Reactions

Among all the important cross-coupling transformations, the formation of C−N bonds is of special interest due to their widespread occurrence in pharmaceuticals and natural products. Transition metal-catalyzed C−N cross-coupling reactions have emerged as a valuable tool for these transformations. Despite the progress made in Buchwald−Hartwig Pd-catalyzed aryl aminations, the use of other more abundant and sustainable metals to catalyze the C−N coupling is highly desired. In this context, cobalt-catalyzed C−N cross-coupling methodologies, although still limited, have received attention in the past decade.

Teo and Chua pioneered this field in 2009 with the arylation of N-based nucleophiles mediated by cobalt[107]. The authors described the first N-arylation process using substituted aryl iodides and bromides with several amines and heterocyclic compounds, utilizing catalytic amounts of $CoCl_2 \cdot 6H_2O$ and N,N'-dimethylethylenediamine (DMEDA) in water (Scheme 43a). The same group extended this methodology using substituted benzyl amides as nitrogen nucleophiles with good to excellent yields[109]. Tentatively, a Co^{II}/Co^{IV} catalytic cycle was proposed. However, Chang, Li, and coworker in 2018 performed a thorough DFT study on Teo's system and concluded that a radical-based mechanism was operating, specifically with a SET step for the aryl−halide activation with the bis(diamine)Co^I complex (Scheme 43b)[108]. Other mechanistic pictures such as oxidative addition/reductive elimination, iodine atom transfer, and σ-bond metathesis were discarded based on their computational studies.

Toma, Yamaguchi, and coworker reported the formation of tertiary amines by reacting 2-chloropyridine derivatives and a variety of secondary amines using $CoCl_2$ and the diphosphine dppp ligand[110]. The authors explored further this reactivity by reporting the synthesis of
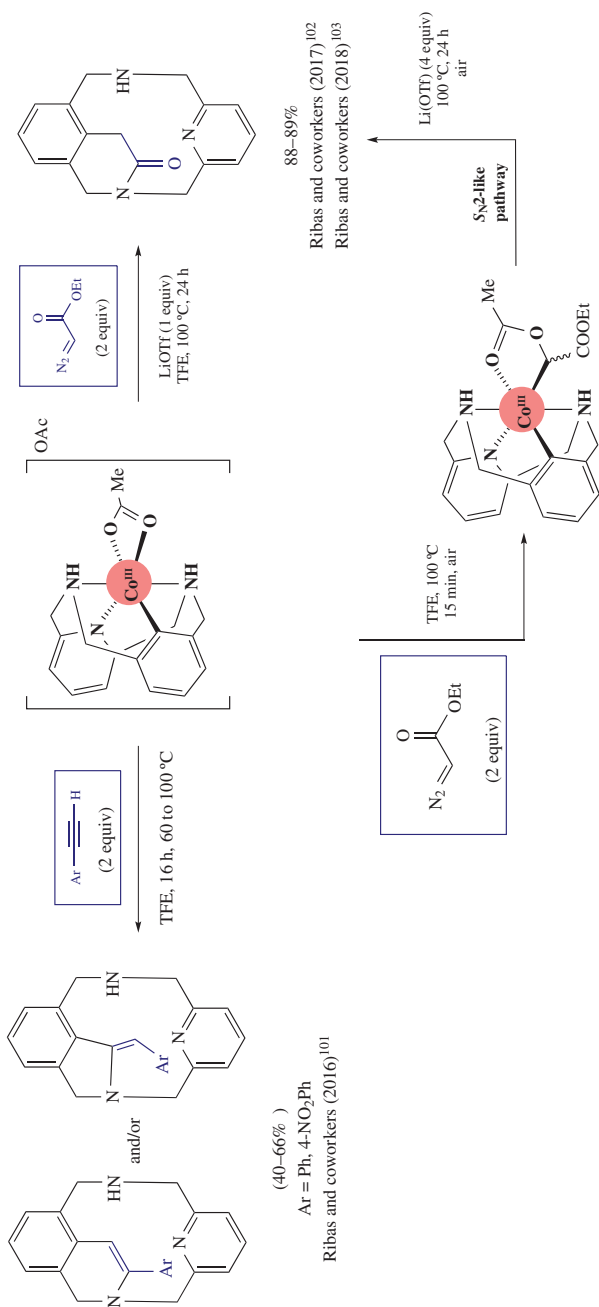
SCHEME 40. Reaction of alkynes and diazo esters with well-defined aryl−Co[III] species forming the expected C−C bonds together with subsequent intramolecular reorganization.
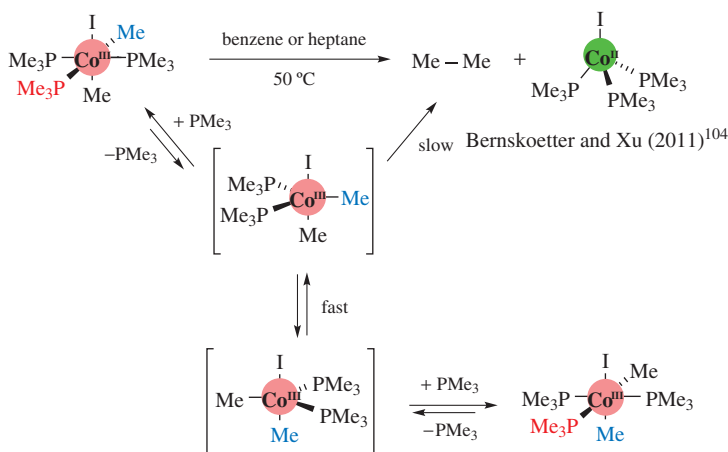
SCHEME 41. Study C(sp³)−C(sp³) reductive coupling at a Co^III complex.

nitro-substituted tertiary amines involving *ortho-* and *para-*chloronitrobenzene derivatives and secondary amines (Scheme 44a), since *meta-*chloronitrobenzene moieties were unreactive[112].

On the other hand, Punniyamurthy and coworkers reported the intramolecular cyclization of 2-bromoarylbenzamidines to form benzimidazoles using Co^II(acac)₂ as a catalyst in the presence of 1,10-phenanthroline and K₂CO₃ (Scheme 44b)[111].

In 2014, Fout and coworkers pioneered the use of (PPh₃)₃Co^ICl as a catalyst in the amination of aryl iodides using lithium hexamethyldisilazide (LiHMDS) (Scheme 45a)[113]. They proposed that (PPh₃)₂Co^I(N(SiMe₃)₂) complex was *in situ* generated and underwent oxidative addition with aryl iodide to form (PPh₃)₂Co^III(N(SiMe₃)₂)(I). Then, the reaction with a second equivalent of LiHMDS afforded (PPh₃)₂Co(N(SiMe₃)₂)₂ that subsequently underwent reductive elimination to form the C−N coupling product (Ar−N(SiMe₃)₂). The use of Co^II salts with metallic zinc as reducing agent also afforded the desired C−N coupling, thus giving support to a Co^I/Co^III catalytic cycle (Scheme 45b). Moreover, the use of (PPh₃)₂Co^I(N(SiMe₃)₂) as a catalyst with a variety of lithiated amines allowed the synthesis of the corresponding C−N coupling products.

Alternatively, in 2013, Gosmini and coworkers disclosed the electrophilic amination of arylzincs with *N-*chloroamines catalyzed by CoBr₂ in the presence of Zn dust (Scheme 46a)[114]. Based on their previous works, they proposed a Co^I/Co^III mechanism where CoBr₂ is reduced by metallic Zn to afford the active Co^I species, undergoing subsequent oxidative addition with the electrophilic *N-*chloroamine to yield a Co^III complex. Then, the latter is transmetalated with arylzinc reagent to finally furnish the desired amination product by reductive elimination. In the same line, Knochel and coworkers reported in 2018 an alternative electrophilic amination methodology using alkyl-, aryl-, and heteroaryl-zinc reagents with *O-*benzoylhydroxylamines as electrophilic nitrogen source via CoCl₂ catalysis[117, 118]. The authors applied this protocol to late-stage amination of hydroxylamine benzoates[119]. In 2019, the same authors described electrophilic amination methodology combining aryl- and alkyl-zinc pivalates with different anthranils via cobalt catalysis under mild conditions (Scheme 46b)[115, 116].

Very few examples of heterogeneous Co-catalyzed cross-couplings have been reported. Thus, a highlighted example is the one reported by Chatterjee, Ranu, and coworker in 2015, where a Co/Al₂O₃-supported heterogeneous catalyst was used to achieve the C−N cross-coupling of activated chloroarenes and chloroheteroarenes with secondary amines
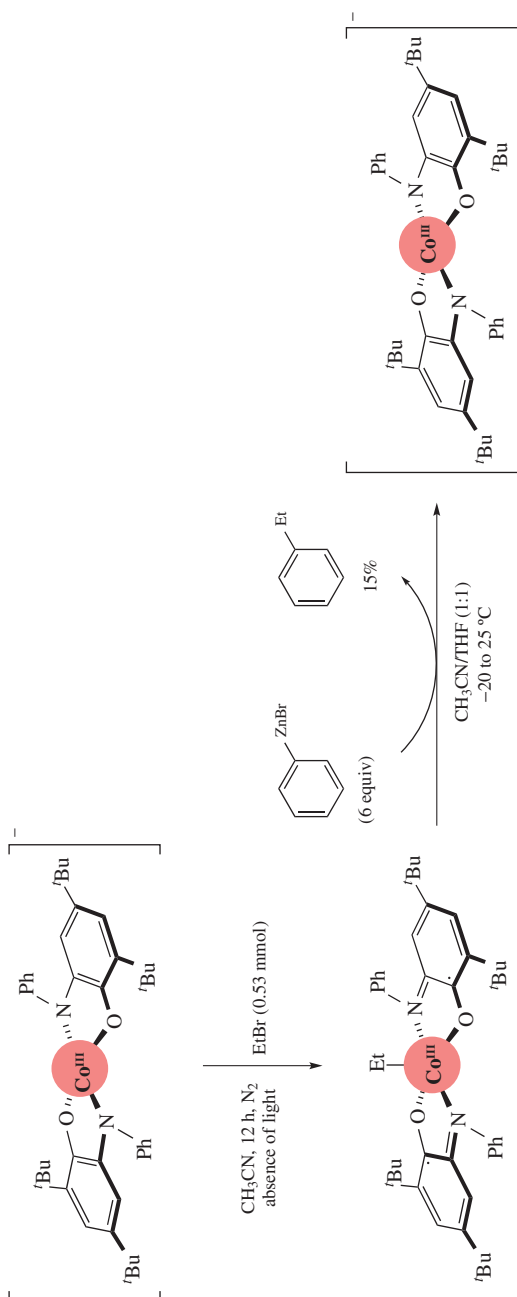
SCHEME 42. Study the redox-active ligand-mediated oxidative addition and reductive elimination at a Co[III] center.
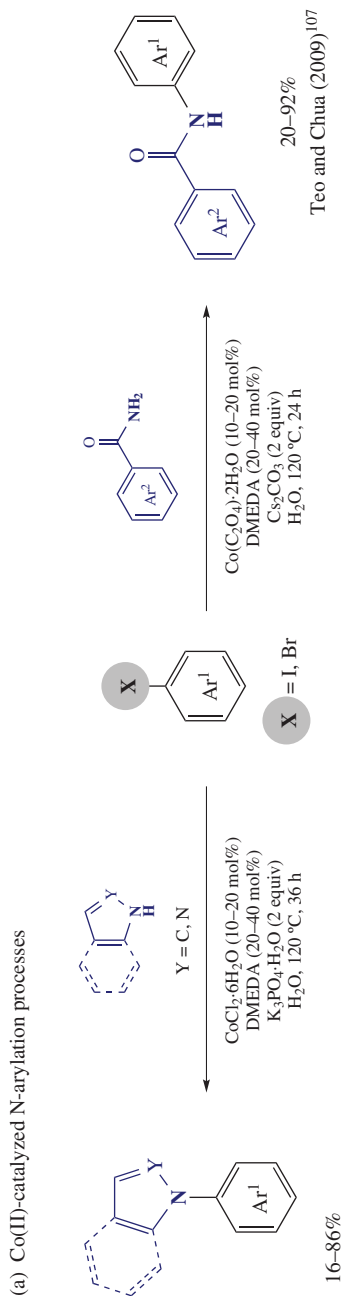
SCHEME 43. (a) Cobalt-catalyzed C–N coupling using heterocyclic amines and amides. (b) Computational study based on Teo's protocol reported by Chang and Li.

42

(b) Proposed mechanism by Chang and Li[108] for N-arylation of nitrogen nucleophiles mediated by Co^II
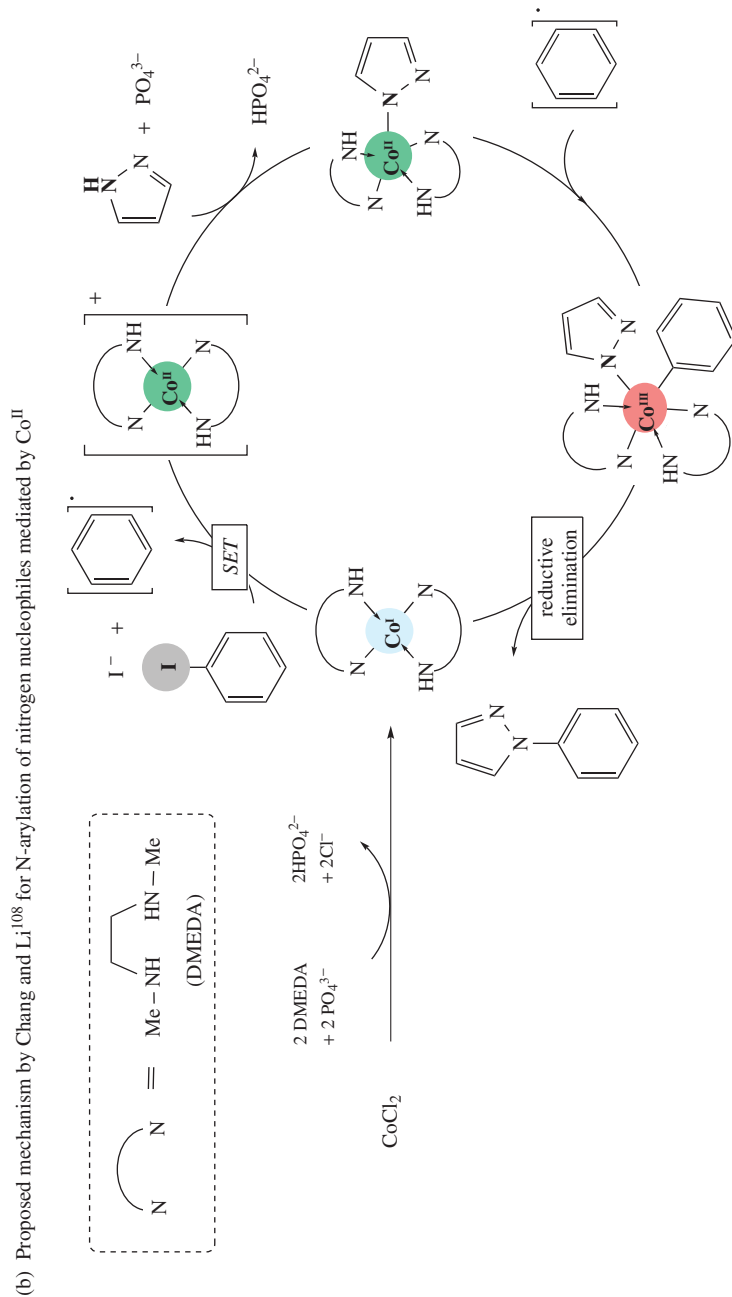
SCHEME 43. (*continued*)

(a) C–N coupling using N-aromatic chlorides or chloronitrobenzenes with secondary amines

CoCl$_2$ (20 mol%)
(**9**) (0–20 mol%)

KHCO$_3$ (1 equiv)
p-xylene, 140 °C, 2–4 h

36–93%

Toma and Yamaguchi (2010)[112]

CoCl$_2$ (10–30 mol%)
(**9**) (0–10 mol%)

K$_2$CO$_3$ (1 equiv), *p*-xylene
135 to 140 °C, 3–20 h

Y = C, N

30–91%

Toma and Yamaguchi (2009)[110]
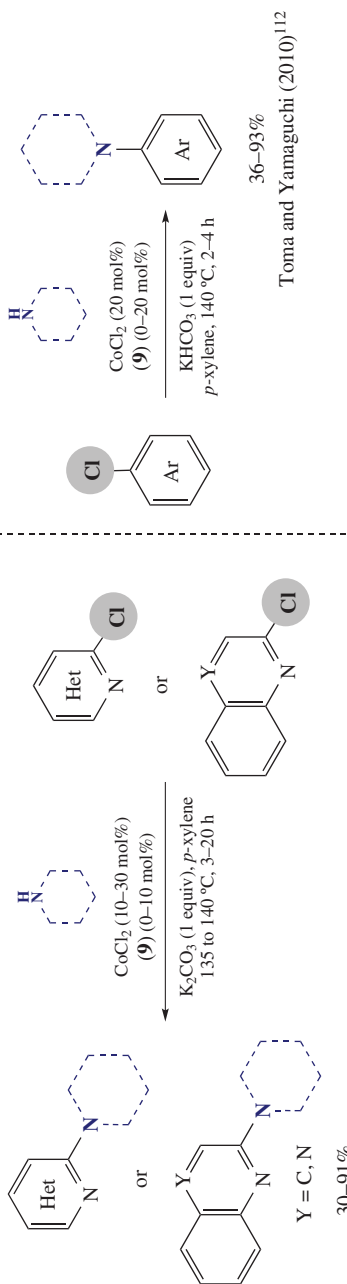
(b) Intramolecular C–N cross-coupling reactions to form benzimidazoles

Co(acac)$_2$ · 2H$_2$O (10 mol%)
(**10**) (20 mol%)

K$_2$CO$_3$ (2 equiv)
toluene, 110 °C, 11–18 h

84–97%

Punniyamurthy and coworkers (2010)[111]

(**9**)

Ph$_2$P   PPh$_2$

(**10**)
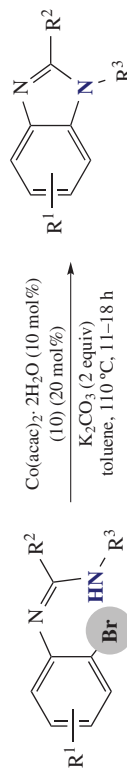
SCHEME 44. Cobalt-catalyzed C–N cross-coupling reactions using (a) 2-chloropyridine derivatives as substrates and a diphosphine ligand and (b) using 2-bromoarylbenzamidines substrates and 1,10-phenanthroline.

(a) Co-catalyzed C–N cross-coupling reactions
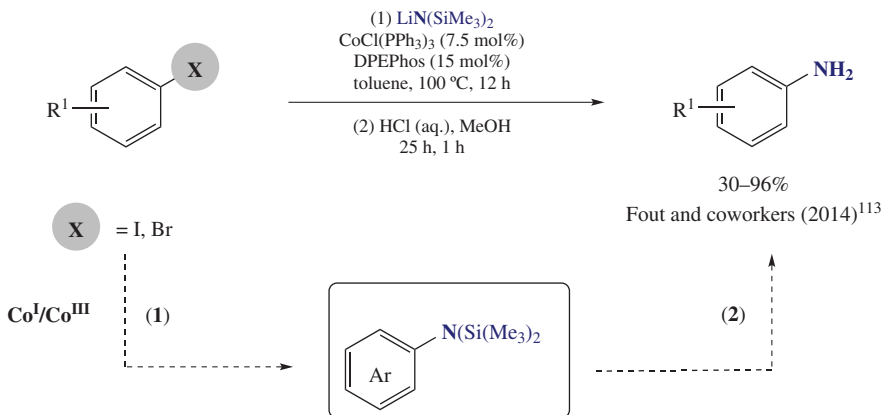
(b) Proposed catalytic cycle
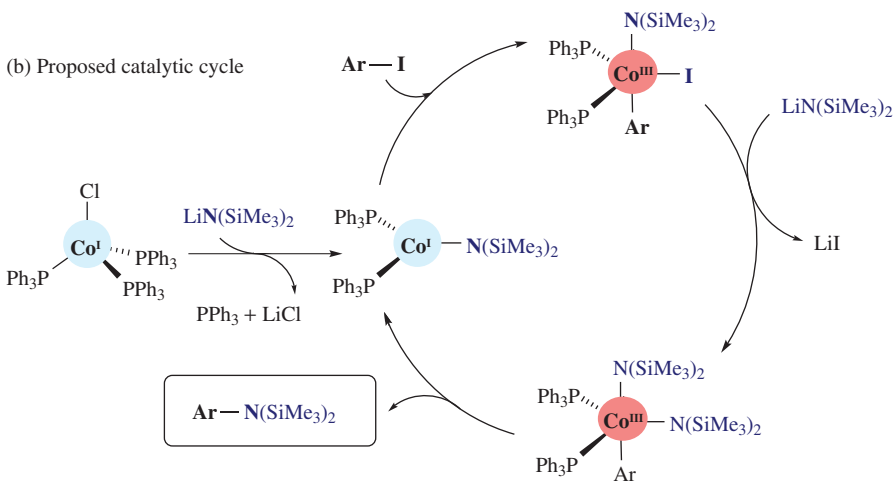
SCHEME 45. (a) Cobalt-catalyzed amination of aryl halides via the formation of Ar−N(SiMe$_3$)$_2$. (b) Proposed Co^I/Co^{III} catalytic cycle.

(a) Cobalt-catalyzed amination of arylzincs with chloroamines

$$39\text{–}88\%$$

Gosmini and coworkers (2013)[114]
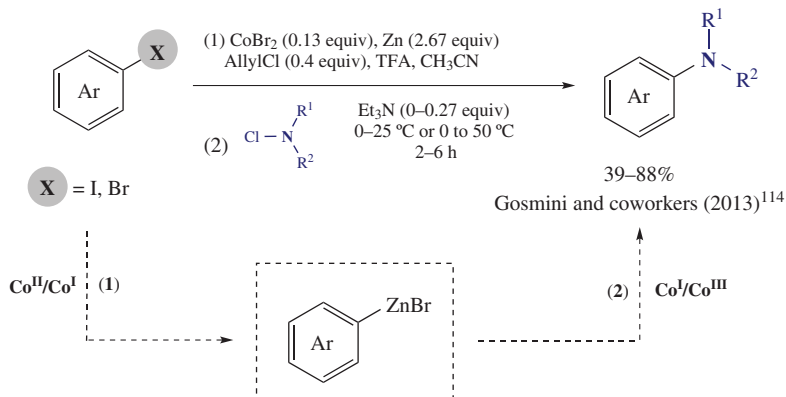
(b) Cobalt-catalyzed amination of aryl- and alkylzincs with anthranils

Knochel and coworkers (2019)[115]
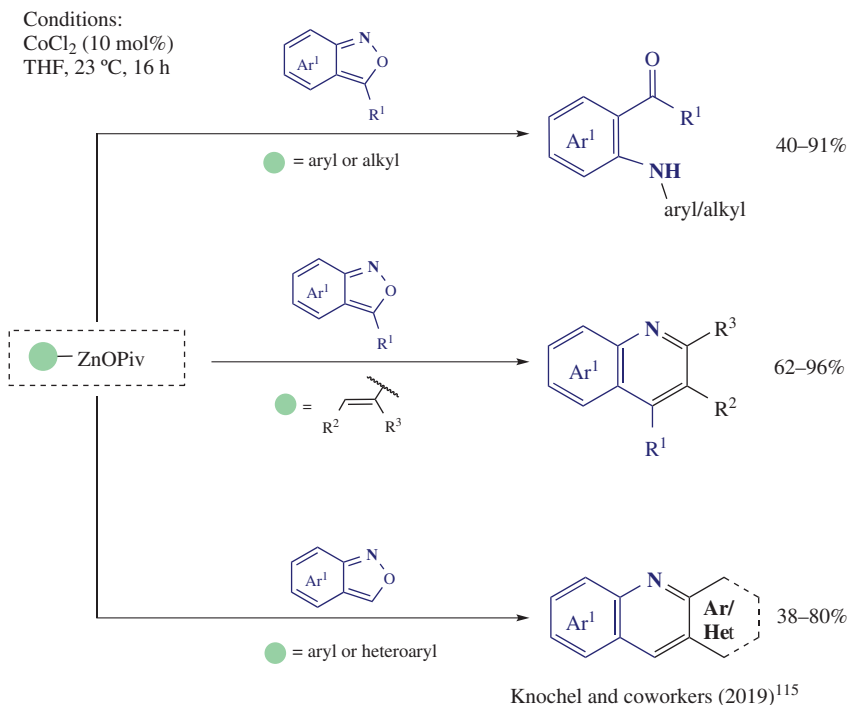
SCHEME 46. Cobalt-catalyzed C(sp^2)−N coupling using organozinc compounds and (a) chloroamines or (b) anthranils.
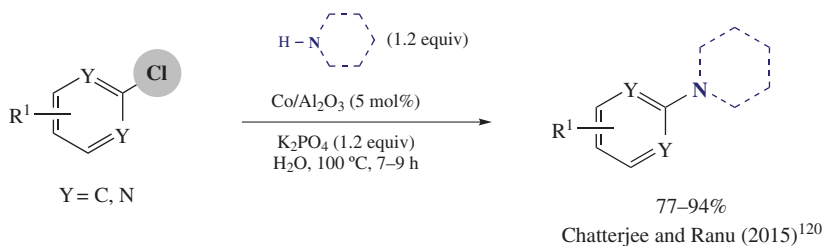
SCHEME 47. Heterogeneous cobalt-catalyzed $C(sp^2)-N$ coupling using a Co/Al_2O_3 catalyst.

and *N*-heterocycles (Scheme 47)[120]. The advantages of this methodology are the high yields obtained, recyclability of the heterogeneous catalyst, operation in water solvent, and ligand-free conditions.

B. C−O Coupling Reactions

Already in 2010, Punniyamurthy and coworkers showed the ability of $Co(acac)_2$ to catalyze an intramolecular C−O cross-coupling reaction, reporting the synthesis of benzoxazoles (Scheme 48a)[111]. Later in 2015, Ranu and coworkers reported for the first time the intermolecular $C(sp^2)-O$ cross-coupling via a dual Co^{II}/Cu^{I} catalysis[122]. They reported the synthesis of (hetero)aryl–vinyl ethers by reacting a variety of vinyl and styrenyl halides with different aryl and heteroaryl phenols as depicted in Scheme 48b. Several functional groups attached to the phenol moiety underwent efficient coupling, and sterically congested styrenyl bromides were well tolerated. Mechanistic investigations suggested the initial reduction of Co^{II} to Co^{I} and subsequent oxidative addition with vinyl halide to render the Co^{III} complex. In parallel, the *in situ* formed aryloxy–Cu^{I} species undergo transmetalation to form the vinyl–Co^{III}–OAr species, which after reductive elimination form the corresponding (hetero)aryl–vinyl ethers. Inspired by Ranu's work, Anilkumar and coworkers in 2019 reported a new methodology for cobalt-catalyzed C−O cross-coupling reaction between aryl halides and phenols using Co as the sole catalyst (Scheme 48c)[121].

C. C−S Coupling Reactions

Molecules containing C−S bonds are common in pharmaceuticals and natural products, representing an important class of organic compounds. Several Co-catalyzed methodologies to construct C−S bonds have been reported, with a first report from Cheng and coworkers in 2006 on the Co-catalyzed synthesis of thioethers via C−S cross-coupling[123]. The authors used a diphosphine dppe-based Co^{II} complex and metallic Zn as reducing agent (Scheme 49a); thus, a Co^{I}/Co^{III} was again proposed. This protocol tolerated the use of several aryl halides with aryl and alkyl thiols under mild conditions. In 2011, Tsai and coworkers provided a route to synthetize a wide range of thioethers via Co catalysis using water-soluble cationic 2,2′-bipyridyl ligand and $CoCl_2 \cdot 6H_2O$ as catalytic mixture for the cross-coupling of aryl halides with aromatic and aliphatic thiols in aqueous media (Scheme 49b)[124].

On the other hand, a wide range of benzo[*b*]thio-fused imidazo[1,2-*a*]pyridines were obtained in good yields via Co-catalyzed cross-coupling of 2-(2-bromophenyl)imidazo [1,2-*a*]pyridine and thiocyanate, as reported by Jiang, Xu, and coworkers[125]. The authors used $Co^{II}(C_2O_4)$ as a catalyst in the presence of 1,10-phenanthroline as the ligand and NaSCN as the sulfur source (Scheme 49c).

(a) Cobalt-catalyzed intramolecular C–O cross-coupling reaction

$$Co(acac)_2 \cdot 2H_2O \ (10 \ mol\%)$$
$$\xrightarrow{\text{1,10-phenanthroline (20 mol\%)}}$$
$$K_2CO_3 \ (2 \ equiv), \ DMSO, \ 110 \ °C$$

33–97%

Punmiyamurthy and coworkers (2010)[111]

(b) Cobalt-catalyzed intermolecular C–O cross-coupling reaction

Ar — OH

$$Co(acac)_2 \ (10 \ mol\%)$$
$$CuI \ (10 \ mol\%)$$
$$\xrightarrow{\hspace{2cm}}$$
$$Cs_2CO_3 \ (2 \ equiv), \ NMP$$
$$100–110 \ °C, \ 8–12 \ h$$

73–91%

Ranu and coworkers (2015)[122]

(c) Cobalt-catalyzed intermolecular C–O bond formation reaction

Ar — OH

$$Co(OAc)_2 \cdot 4H_2O \ (15 \ mol\%)$$
$$L\text{-valine} \ (30 \ mol\%)$$
$$\xrightarrow{\hspace{2cm}}$$
$$Cs_2CO_3 \ (2 \ equiv), \ CH_3CN$$
$$110–135 \ °C, \ N_2, \ 24–48 \ h$$

17–95%

Anilkumar and coworkers (2019)[121]

SCHEME 48. Intra- and inter-molecular cobalt-catalyzed C(sp²)–O cross-coupling reactions. (a) Reproduced with permission from Ref. 111. © John Wiley & Sons, 2019. (b) Reproduced with permission from Ref. 111. © John Wiley & Sons, 2010. (c) Reproduced with permission from Ref. 121. © John Wiley & Sons, 2019.

(a) Cheng and coworkers (2006)[123]

CoI$_2$(dppe) (1–2 mol%)
Zn (1.5 equiv)
pyridine, CH$_3$CN or toluene
80 °C, 10 h

X = I, Br   R^1 = Aryl, alkyl

29–99%

Ph$_2$P   PPh$_2$

dppe

X—Ar   +   HS—R^1

CoCl$_2$·6H$_2$O (**10**) (3 mol%)
Zn (1.5 equiv), KOH (1.0 equiv)
H$_2$O, 100–140 °C, air, 24–72 h

X = I, Br, Cl   R^1 = Aryl, alkyl

26–99%   (b) Tsai and coworkers (2011)[124]

S—R^1
Ar

[NMe$_3$ +   +   NMe$_3$] 2Br$^-$

(**10**)

NaSCN

CoC$_2$O$_4$ (20 mol%)
(**11**) (10 mol%)
Cs$_2$CO$_3$ (1.5 equiv), NCS (1.5 equiv)
CH$_3$CN, 130 °C, 5 h

66–84%   (c) Jiang and Xu (2018)[125]

(**11**)

R^3

R^2 Br   R^3

SCHEME 49. Cobalt-catalyzed C—S bond-formation cross-coupling.

SCHEME 50. Cobalt-catalyzed $C(sp^2)-S$ bond formation using arylzinc pivalates and diaryl disulfides.

The synthesis of biaryl thioethers from organozinc pivalates and diaryl disulfides using $CoCl_2$ as catalyst was reported by Knochel and coworkers[126]. This protocol allowed the use of electron-rich and -poor organozinc pivalates, affording biaryl thioethers in good to excellent yields, and the methodology tolerated sensitive functional groups such as amides, nitriles, and esters (Scheme 50).

D. C−P Coupling Reactions

Among the C-heteroatom bonds, only a few C−P cross-coupling methodologies have been reported. Ranu and coworkers described a phosphorylation protocol based on a cobalt–copper catalytic system, which allowed the synthesis of P-vinylation of (E)-naphthyl vinyl bromide with diethyl phosphite in good yields (Scheme 51)[127]. The methodology was extended to
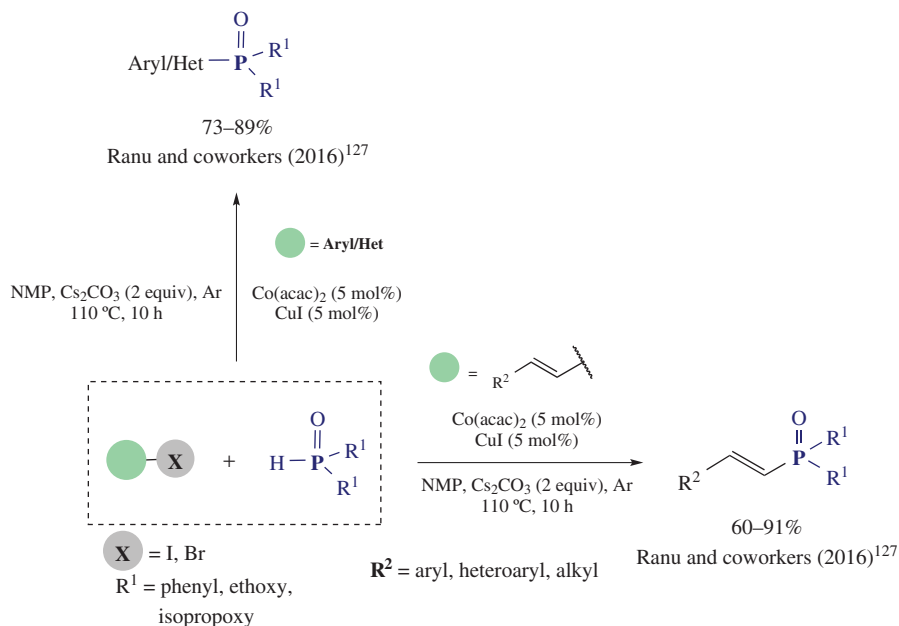
SCHEME 51. Cobalt-catalyzed $C(sp^2)-P$ cross-coupling with the assistance of CuI in catalytic amounts.

P-arylation with the use of a wide range of H-phosphinates and diphenyl phosphine oxide. The observations that radical scavengers as (2,2,6,6-tetramethylpiperidin-1-yl)oxyl (TEMPO) did not affect the reaction outcome, together with high stereoselectivity in the P-vinylated products, discarded a radical-based mechanism. The authors suggested that the transformation is not radical based and undergoes through a cooperative Co−Cu catalysis. The mechanistic proposal involved the reduction of Co^{II} to Co^{I} promoted by acetylacetonate moiety, followed by oxidative addition of C−halide bond at Co^{I} to render the Co^{III} intermediate species. In a parallel cycle, the formation of phosphonate−Cu^{I} complex allowed transmetalation from Cu^{I} to Co^{III} center, which underwent reductive elimination to form the final product.

VIII. CONCLUSIONS

In summary, cobalt catalysis has a broad potential in cross-coupling transformations, and C−C cross-couplings in almost all types of C-hybridizations have been reported. Grignard reagents are extensively used, aiming at delivering the nucleophile counterpart and also as reducing agent, in order to generate the active Co^{I} species *in situ*. Indeed, it is widely accepted that in general the operating catalytic mechanism involves two two-electron redox processes in a Co^{I}/Co^{III} system, although some mechanistic proposals involving SET steps and $Co^{I}/Co^{II}/Co^{III}$ catalytic cycles have also been proposed. Moreover, recently, Co catalysis has proven effective for C−heteroatom cross-coupling reaction in a parallel reactivity as Pd-catalyzed C−N Buchwald−Hartwig couplings or Cu-catalyzed C−N, C−O, C−S, and C−P Ullmann-type couplings. Furthermore, cobalt(I)-catalyzed C−Boron couplings are also appearing through the borylation aryl and alkyl halides, thus broadening the range of organoboron starting nucleophiles for metal-catalyzed Suzuki−Miyaura couplings. In this respect, a bright future is expected for expanding the Co-catalyzed methodologies for C−heteroatom cross-couplings. Not covered in this chapter, cobalt-catalyzed C−H functionalizations have rapidly grown in the past decade[7, 9, 11, 128] and ensure a bright future for cobalt catalysis in the following years.

IX. ACKNOWLEDGMENTS

X. REFERENCES

1. H. Gilman and M. Lichtenwalter, *J. Am. Chem. Soc.*, **61**, 957 (1939).
2. M. S. Kharasch and E. K. Fields, *J. Am. Chem. Soc.*, **63**, 2316 (1941).
3. C. Gosmini, J.-M. Bégouin and A. Moncomble, *Chem. Commun.*, 3221 (2008).
4. G. Cahiez and A. Moyeux, *Chem. Rev.*, **110**, 1435 (2010).
5. C. Dorval and C. Gosmini, in *Cobalt Catalysis in Organic Synthesis* (Eds. M. Hapke and G. Hilt), Wiley, 2020, p. 163.
6. A. Rérat and C. Gosmini, *Phys. Sci. Rev.*, **20160021**, 3 (2018).
7. O. Planas, P. G. Chirila, C. J. Whiteoak and X. Ribas, in *Advances in Organometallic Chemistry* (Ed. P. J. Pérez), Vol. 69, Academic Press, 2018, p. 209.
8. K. Gao and N. Yoshikai, *Acc. Chem. Res.*, **47**, 1208 (2014).
9. M. Moselage, J. Li and L. Ackermann, *ACS Catal.*, **6**, 498 (2016).
10. D. Wei, X. Zhu, J.-L. Niu and M.-P. Song, *ChemCatChem*, **8**, 1242 (2016).
11. O. Planas, C. J. Whiteoak and X. Ribas, in *Non-Noble Metal Catalysis* (Eds. R. J. M. K. Gebbink and M. E. Moret), Wiley, 2019, p. 297.

12. G. Cahiez and H. Avedissian, *Tetrahedron Lett.*, **39**, 6159 (1998).
13. B. Hölzer and R. W. Hoffmann, *Chem. Commun.*, **732** (2003).
14. T. J. Korn, G. Cahiez and P. Knochel, *Synlett*, **2003**, 1892 (2003).
15. T. J. Korn, M. A. Schade, M. N. Cheemala, S. Wirth, S. A. Guevara, G. Cahiez and P. Knochel, *Synthesis*, **2006**, 3547 (2006).
16. H. Ohmiya, H. Yorimitsu and K. Oshima, *Chem. Lett.*, **33**, 1240 (2004).
17. T. Kamachi, A. Kuno, C. Matsuno and S. Okamoto, *Tetrahedron Lett.*, **45**, 4677 (2004).
18. E. Shirakawa, T. Sato, Y. Imazaki, T. Kimura and T. Hayashi, *Chem. Commun.*, 4513 (2007).
19. E. Shirakawa, Y. Imazaki and T. Hayashi, *Chem. Lett.*, **37**, 654 (2008).
20. T. Hatakeyama, S. Hashimoto, K. Ishizuka and M. Nakamura, *J. Am. Chem. Soc.*, **131**, 11949 (2009).
21. Z. Mo, Y. Li, H. K. Lee and L. Deng, *Organometallics*, **30**, 4687 (2011).
22. K. Matsubara, T. Sueyasu, M. Esaki, A. Kumamoto, S. Nagao, H. Yamamoto, Y. Koga, S. Kawata and T. Matsumoto, *Eur. J. Inorg. Chem.*, **2012**, 3079 (2012).
23. Z. Xi, B. Liu, C. Lu and W. Chen, *Dalton Trans.*, 7008 (2009).
24. S.-Y. Chen, J. Zhang, Y.-H. Li, J. Wen, S.-Q. Bian and X.-Q. Yu, *Tetrahedron Lett.*, **50**, 6795 (2009).
25. J. Zeng, K. M. Liu and X. F. Duan, *Org. Lett.*, **15**, 5342 (2013).
26. J. Wei, K.-M. Liu and X.-F. Duan, *J. Org. Chem.*, **82**, 1291 (2017).
27. S. Gülak, O. Stepanek, J. Malberg, B. R. Rad, M. Kotora, R. Wolf and A. Jacobi von Wangelin, *Chem. Sci.*, **4**, 776 (2013).
28. H. Ohmiya, K. Wakabayashi, H. Yorimitsu and K. Oshima, *Tetrahedron*, **62**, 2207 (2006).
29. H. Ohmiya, H. Yorimitsu and K. Oshima, *J. Am. Chem. Soc.*, **128**, 1886 (2006).
30. H. Yasui, K. Mizutani, H. Yorimitsu and K. Oshima, *Tetrahedron*, **62**, 1410 (2006).
31. H. Ohmiya, H. Yorimitsu and K. Oshima, *Org. Lett.*, **8**, 3093 (2006).
32. G. Cahiez, C. Chaboche, C. Duplais and A. Moyeux, *Org. Lett.*, **11**, 277 (2009).
33. S.-F. Hsu, C.-W. Ko and Y.-T. Wu, *Adv. Synth. Catal.*, **353**, 1756 (2011).
34. R. Frlan, M. Sova, S. Gobec, G. Stavber and Z. Časar, *J. Org. Chem.*, **80**, 7803 (2015).
35. B. Barré, L. Gonnard, A. Guérinot and J. Cossy, *Molecules*, **23**, 1449 (2018).
36. B. Barré, L. Gonnard, R. Campagne, S. Reymond, J. Marin, P. Ciapetti, M. Brellier, A. Guérinot and J. Cossy, *Org. Lett.*, **16**, 6160 (2014).
37. L. Gonnard, A. Guérinot and J. Cossy, *Chem.-Eur. J.*, **21**, 12797 (2015).
38. L. Nicolas, E. Izquierdo, P. Angibaud, I. Stansfield, L. Meerpoel, S. Reymond and J. Cossy, *J. Org. Chem.*, **78**, 11807 (2013).
39. C. F. Despiau, A. P. Dominey, D. C. Harrowven and B. Linclau, *Eur. J. Org. Chem.*, **2014**, 4335 (2014).
40. J. M. Hammann, A. K. Steib and P. Knochel, *Org. Lett.*, **16**, 6500 (2014).
41. J. M. Hammann, D. Haas, C.-P. Tüllmann, K. Karaghiosoff and P. Knochel, *Org. Lett.*, **18**, 4778 (2016).
42. J. Mao, F. Liu, M. Wang, L. Wu, B. Zheng, S. Liu, J. Zhong, Q. Bian and P. J. Walsh, *J. Am. Chem. Soc.*, **136**, 17662 (2014).
43. Y. Zhou, L. Wang, G. Yuan, S. Liu, X. Sun, C. Yuan, Y. Yang, Q. Bian, M. Wang and J. Zhong, *Org. Lett.*, **22**, 4532 (2020).
44. V. Koch, M. M. Lorion, E. Barde, S. Bräse and J. Cossy, *Org. Lett.*, **21**, 6241 (2019).
45. E. Barde, A. Guérinot and J. Cossy, *Org. Lett.*, **19**, 6068 (2017).
46. B. P. Branchaud and W. D. Detlefsen, *Tetrahedron Lett.*, **32**, 6273 (1991).
47. Y. Ikeda, T. Nakamura, H. Yorimitsu and K. Oshima, *J. Am. Chem. Soc.*, **124**, 6514 (2002).
48. W. Affo, H. Ohmiya, T. Fujioka, Y. Ikeda, T. Nakamura, H. Yorimitsu, K. Oshima, Y. Imamura, T. Mizuta and K. Miyoshi, *J. Am. Chem. Soc.*, **128**, 8068 (2006).
49. M. E. Weiss, L. M. Kreis, A. Lauber and E. M. Carreira, *Angew. Chem., Int. Ed.*, **50**, 11125 (2011).
50. T. Tsuji, H. Yorimitsu and K. Oshima, *Angew. Chem., Int. Ed.*, **41**, 4137 (2002).
51. H. Ohmiya, T. Tsuji, H. Yorimitsu and K. Oshima, *Chem.-Eur. J.*, **10**, 5640 (2004).

52. G. Cahiez, C. Chaboche, C. Duplais, A. Giulliani and A. Moyeux, *Adv. Synth. Catal.*, **350**, 1484 (2008).
53. T. Iwasaki, H. Takagawa, S. P. Singh, H. Kuniyasu and N. Kambe, *J. Am. Chem. Soc.*, **135**, 9604 (2013).
54. T. Iwasaki, K. Yamashita, H. Kuniyasu and N. Kambe, *Org. Lett.*, **19**, 3691 (2017).
55. F. Kreyenschmidt and K. Koszinowski, *Chem.-Eur. J.*, **24**, 1168 (2018).
56. C. Andersen, V. Ferey, M. Daumas, P. Bernardelli, A. Guérinot and J. Cossy, *Org. Lett.*, **21**, 2285 (2019).
57. A. Kuno, N. Saino, T. Kamachi and S. Okamoto, *Tetrahedron Lett.*, **47**, 2591 (2006).
58. M. S. Kharasch, F. L. Lambert and W. H. Urry, *J. Org. Chem.*, **10**, 298 (1945).
59. H. K. Black, D. H. S. Horn and B. C. L. Weedon, *J. Chem. Soc.*, **1704** (1954).
60. H. Avedissian, L. Bérillon, G. Cahiez and P. Knochel, *Tetrahedron Lett.*, **39**, 6163 (1998).
61. J.-M. Bégouin and C. Gosmini, *J. Org. Chem.*, **74**, 3221 (2009).
62. J. M. Bégouin, S. Claudel and C. Gosmini, *Synlett*, **2009**, 3192 (2009).
63. J.-M. Begouin, M. Rivard and C. Gosmini, *Chem. Commun.*, **46**, 5972 (2010).
64. D. Haas, J. M. Hammann, R. Greiner and P. Knochel, *Angew. Chem., Int. Ed.*, **55**, 3809 (2016).
65. D. Haas, J. M. Hammann, R. Greiner and P. Knochel, *ACS Catal.*, **6**, 1540 (2016).
66. A. D. Benischke, I. Knoll, A. Rérat, C. Gosmini and P. Knochel, *Chem. Commun.*, **52**, 3171 (2016).
67. R. Greiner, D. S. Ziegler, D. Cibu, A. C. Jakowetz, F. Auras, T. Bein and P. Knochel, *Org. Lett.*, **19**, 6384 (2017).
68. Y.-H. Chen, M. Ellwart, V. Malakhov and P. Knochel, *Synthesis*, **49**, 3215 (2017).
69. J. M. Hammann, F. H. Lutter, D. Haas and P. Knochel, *Angew. Chem., Int. Ed.*, **56**, 1082 (2017).
70. J. Li and P. Knochel, *Angew. Chem., Int. Ed.*, **57**, 11436 (2018).
71. F. H. Lutter, L. Grokenberger, P. Spieß, J. M. Hammann, K. Karaghiosoff and P. Knochel, *Angew. Chem., Int. Ed.*, **59**, 5546 (2020).
72. J. M. Hammann, L. Thomas, Y.-H. Chen, D. Haas and P. Knochel, *Org. Lett.*, **19**, 3847 (2017).
73. C. K. Reddy and P. Knochel, *Angew. Chem., Int. Ed. Engl.*, **35**, 1700 (1996).
74. G. Dunet and P. Knochel, *Synlett*, **2007**, 1383 (2007).
75. J. M. Hammann, D. Haas and P. Knochel, *Angew. Chem., Int. Ed.*, **54**, 4478 (2015).
76. K. Araki and M. Inoue, *Tetrahedron*, **69**, 3913 (2013).
77. F. Liu, J. Zhong, Y. Zhou, Z. Gao, P. J. Walsh, X. Wang, S. Ma, S. Hou, S. Liu, M. Wang, M. Wang and Q. Bian, *Chem.-Eur. J.*, **24**, 2059 (2018).
78. M. S. Hofmayer, A. Sunagatullina, D. Brösamlen, P. Mauker and P. Knochel, *Org. Lett.*, **22**, 1286 (2020).
79. M. M. Lorion, V. Koch, M. Nieger, H.-Y. Chen, A. Lei, S. Bräse and J. Cossy, *Chem.-Eur. J.*, **26**, 13163 (2020).
80. F. H. Lutter, L. Grokenberger, M. Benz and P. Knochel, *Org. Lett.*, **22**, 3028 (2020).
81. L. Thomas, F. H. Lutter, M. S. Hofmayer, K. Karaghiosoff and P. Knochel, *Org. Lett.*, **20**, 2441 (2018).
82. M. Corpet, X.-Z. Bai and C. Gosmini, *Adv. Synth. Catal.*, **356**, 2937 (2014).
83. J. M. Neely, M. J. Bezdek and P. J. Chirik, *ACS Cent. Sci.*, **2**, 935 (2016).
84. L. M. Kumar and B. R. Bhat, *J. Organomet. Chem.*, **827**, 41 (2017).
85. S. Asghar, S. B. Tailor, D. Elorriaga and R. B. Bedford, *Angew. Chem., Int. Ed.*, **56**, 16367 (2017).
86. H. A. Duong, W. Wu and Y.-Y. Teo, *Organometallics*, **36**, 4363 (2017).
87. H. A. Duong, Z.-H. Yeow, Y.-L. Tiong, N. H. B. Mohamad Kamal and W. Wu, *J. Org. Chem.*, **84**, 12686 (2019).
88. S. Liu, W. Huang, D. Wang, P. Wei and Q. Shen, *Org. Chem. Front.*, **6**, 2630 (2019).
89. J. R. Ludwig, E. M. Simmons, S. R. Wisniewski and P. J. Chirik, *Org. Lett.*, DOI: https://doi.org/10.1021/acs.orglett.0c02934 (2020).
90. W. Huang, X. Wan and Q. Shen, *Org. Lett.*, **22**, 4327 (2020).
91. P. Gomes, C. Gosmini and J. Périchon, *J. Org. Chem.*, **68**, 1142 (2003).

92. M. Amatore, C. Gosmini and J. Périchon, *Eur. J. Org. Chem.*, **2005**, 989 (2005).
93. M. Amatore and C. Gosmini, *Angew. Chem., Int. Ed.*, **47**, 2089 (2008).
94. X. Qian, A. Auffrant, A. Felouat and C. Gosmini, *Angew. Chem., Int. Ed.*, **50**, 10402 (2011).
95. C. Dorval, M. Tricoire, J.-M. Begouin, V. Gandon and C. Gosmini, *ACS Catal.*, **10**, 12819 (2020).
96. S. Martínez de Salinas, J. Sanjosé-Orduna, C. Odena, S. Barranco, J. Benet-Buchholz and M. H. Pérez-Temprano, *Angew. Chem., Int. Ed.*, **59**, 6239 (2020).
97. Y. Chen, H. Sun, U. Flörke and X. Li, *Organometallics*, **27**, 270 (2008).
98. D. Zhu, I. Korobkov and P. H. M. Budzelaar, *Organometallics*, **31**, 3958 (2012).
99. B. J. Foley, C. M. Palit, S. D. Timpa and O. V. Ozerov, *Organometallics*, **37**, 3803 (2018).
100. B. J. Foley, C. M. Palit, N. Bhuvanesh, J. Zhou and O. V. Ozerov, *Chem. Sci.*, **11**, 6075 (2020).
101. O. Planas, C. J. Whiteoak, V. Martin-Diaconescu, I. Gamba, J. M. Luis, T. Parella, A. Company and X. Ribas, *J. Am. Chem. Soc.*, **138**, 14388 (2016).
102. O. Planas, S. Roldán-Gómez, V. Martin-Diaconescu, T. Parella, J. M. Luis, A. Company and X. Ribas, *J. Am. Chem. Soc.*, **139**, 14649 (2017).
103. O. Planas, S. Roldán-Gómez, V. Martin-Diaconescu, J. M. Luis, A. Company and X. Ribas, *Chem. Sci.*, **9**, 5736 (2018).
104. H. Xu and W. H. Bernskoetter, *J. Am. Chem. Soc.*, **133**, 14956 (2011).
105. K. Ahmad, B. A. Khan, S. K. Roy, A. Zainul, R. Mahmood, J. Khan and H. Ashraf, *Comput. Theor. Chem.*, **1130**, 140 (2018).
106. A. L. Smith, K. I. Hardcastle and J. D. Soper, *J. Am. Chem. Soc.*, **132**, 14358 (2010).
107. Y.-C. Teo and G.-L. Chua, *Chem.-Eur. J.*, **15**, 3072 (2009).
108. K. Ahmad, C.-R. Chang and J. Li, *J. Organomet. Chem.*, **868**, 144 (2018).
109. B. Y.-H. Tan and Y.-C. Teo, *Org. Biomol. Chem.*, **12**, 7478 (2014).
110. G. Toma, K.-i. Fujita and R. Yamaguchi, *Eur. J. Org. Chem.*, **2009**, 4586 (2009).
111. P. Saha, M. A. Ali, P. Ghosh and T. Punniyamurthy, *Org. Biomol. Chem.*, **8**, 5692 (2010).
112. G. Toma and R. Yamaguchi, *Eur. J. Org. Chem.*, **2010**, 6404 (2010).
113. M. R. Brennan, D. Kim and A. R. Fout, *Chem. Sci.*, **5**, 4831 (2014).
114. X. Qian, Z. Yu, A. Auffrant and C. Gosmini, *Chem.-Eur. J.*, **19**, 6225 (2013).
115. J. Li, E. Tan, N. Keller, Y.-H. Chen, P. M. Zehetmaier, A. C. Jakowetz, T. Bein and P. Knochel, *J. Am. Chem. Soc.*, **141**, 98 (2019).
116. F. H. Lutter, S. Graßl, L. Grokenberger, M. S. Hofmayer, Y.-H. Chen and P. Knochel, *ChemCatChem*, **11**, 5188 (2019).
117. Y.-H. Chen, S. Graßl and P. Knochel, *Angew. Chem., Int. Ed.*, **57**, 1108 (2018).
118. S. Graßl and P. Knochel, *Org. Lett.*, **22**, 1947 (2020).
119. S. Graßl, Y.-H. Chen, C. Hamze, C. P. Tüllmann and P. Knochel, *Org. Lett.*, **21**, 494 (2019).
120. N. Mukherjee, T. Chatterjee and B. C. Ranu, *Eur. J. Org. Chem.*, **2015**, 4018 (2015).
121. S. M. Ujwaldev, S. Saranya, N. A. Harry and G. Anilkumar, *Monatsh. Chem.*, **150**, 339 (2019).
122. D. Kundu, M. Tripathy, P. Maity and B. C. Ranu, *Chem.-Eur. J.*, **21**, 8727 (2015).
123. Y.-C. Wong, T. T. Jayanth and C.-H. Cheng, *Org. Lett.*, **8**, 5613 (2006).
124. M.-T. Lan, W.-Y. Wu, S.-H. Huang, K.-L. Luo and F.-Y. Tsai, *RSC Adv.*, **1**, 1751 (2011).
125. T. Wang, J. Chen, J. Wang, S. Xu, A. Lin, H. Yao, S. Jiang and J. Xu, *Org. Biomol. Chem.*, **16**, 3721 (2018).
126. Z.-B. Dong, M. Balkenhohl, E. Tan and P. Knochel, *Org. Lett.*, **20**, 7581 (2018).
127. T. Ghosh, P. Maity, D. Kundu and B. C. Ranu, *New J. Chem.*, **40**, 9556 (2016).
128. P. G. Chirila and C. J. Whiteoak, *Dalton Trans.*, **46**, 9721 (2017).

CHAPTER IV

C$_{sp2}$–H amination reactions mediated by metastable Oh masked aryl–Co^{III}-nitrene species

This Chapter corresponds to the following publication:

Lorena Capdevila, Marc Montilla, Oriol Planas, Artur Brotons, Pedro Salvador, Vlad Martin-Diaconescu, Teodor Parella, Josep M. Luis, Xavi Ribas (submitted),

Journal Name

ARTICLE

C_{sp2}-H amination reactions mediated by metastable Oh masked aryl-Co^{III}-nitrene species

Lorena Capdevila,[a] Marc Montilla,[a] Oriol Planas,[a] Artur Brotons,[a] Pedro Salvador,[a] Vlad Martin Diaconescu,[b] Teodor Parella,[c] Josep M. Luis,[a]* Xavi Ribas[a]*

Cobalt-catalyzed C-H amination via M-nitrenoid species is spiking the interest of the community. Understanding this process at a molecular level is a challenging task and here we report a well-defined macrocyclic system featuring an Oh aryl-Co^{III} species that reacts with aliphatic azides to effect the intramolecular C(sp2)-N bond formation. Strikingly, a putative aryl-Co=NR nitrenoid intermediate species is formed and rapidly trapped by a carboxylate ligand to form a carboxylate masked-nitrene, which functions as a shortcut to stabilize and guide the reaction to a productive intramolecular C(sp2)-N bond formation. On one hand, several intermediate species featuring the C(sp2)-N bond formed have been isolated and structurally characterized and the essential role of the carboxylate ligand has been proved. Complementarily, a thorough DFT study of the C(sp2)-N bond formation mechanism explains at molecular level the key role of carboxylate-masked nitrene species, which is essential to tame the metastability of the putative aryl-Co^{III}=NR nitrene species to effectively yield the C(sp2)-N products. The solid molecular mechanistic scheme unraveled for the C(sp2)-N bond forming reaction is fully supported by both experimental and computation complementary studies.

Introduction

The introduction of nitrogen functionalities into organic frameworks has attracted considerable interest in the development of new methodologies, given their ubiquitous occurrence in pharmaceuticals and natural products.[1] A powerful strategy to achieve the construction of C-N bonds is based on the direct functionalization of C-H bonds, which has been of widely studied during the last decades.[2-8] This field has been mainly dominated by the use of noble metal catalysis, yet the development of more sustainable methodologies using M-nitrenoid species with first-row transition metals has recently become a hot topic.[9]

M-nitrenoid species are rare and unstable species for late transition metals. For Group 8 M-nitrenoids, a prominent example of is the relatively stable octahedral iron(IV) terminal imido complex [Fe^{IV}(N4Py)(NTs)]$^{2+}$ reported by Que and co-workers,[10] with S = 1 and a half-life of 3 h at room temperature. The reactivity of this compound was studied independently by

de Visser and Latour revealing that is active in N transfer with thioanisole[11] and in styrene aziridination.[12] For transition metals in Group 9 and beyond, the common instability of Oh M-nitrenoid species may be overcome by changing the spin state or the geometry of the complex. In particular, the isolation of Group 9 Co-nitrene species has been achieved by lowering the symmetry and coordination number of the complex,[13] highlighting four-coordinated complexes featuring tetrahedral geometry.[14, 15] Among all aminating reagents used to forge C-N bonds with cobalt catalysis, organic azides constitute an attractive N-source due to its 2e- oxidant character with concomitant extrusion of inert N$_2$.[9, 16] The latter, together with the low-symmetry requirement, force the design of low oxidation state Co^I species that form isolable Co^{III}-imido multiple-bonded species upon reaction with N$_3$-R.[14, 15] Although this chemistry is dominated by the use of low valent cobalt systems, few examples are reported on direct C(sp2)-N bond formation through C-H activation involving putative high-valent Co platforms.[17, 18] Indeed, highly unstable octahedral high valent M^V=NR species with Group 9 metals are proposed as key intermediate species in C(sp2)-N bond forming processes. Remarkably, their relevance has been clearly pointed out in formally Oh M^V Group 9 complexes bearing a Cp* ligand.[9, 19] Reaction of cyclometallated Cp*Rh^{III} and Cp*Ir^{III} complexes with N$_3$-R render the proposed Cp*M^V=NR intermediate species,[20, 21] which are essential for the inner-sphere C(sp2)-N bond forming step with the cyclometallated ligand (Figure 1a). Regarding the analogous cobalt chemistry bearing a Cp* ligand, Matsunaga and Kanai demonstrated the ability of Cp*Co^{III} catalysts to perform the C(sp2)-H amidation of indoles using sulfonyl azides and phosphoryl azides.[22, 23] The C(sp2)-H amidation of indoles using

acyl azides has also been reported using Cp*Co^{III} by Punniyamurthy and coworkers (Figure 1b),[24] and using phenyl azidoformates by Chang and coworkers.[25] Also, isoquinolone synthesis via Cp*Co^V cobaltacycles using N-chloroamides was reported by Zhu and coworkers.[26] Although these incipient reports, the high valent approach in Co-catalyzed C(sp2)-H amination is still in its infancy.

The examination of structure and electronic properties of key intermediate species is capital for unveiling the mechanistic intricacies of inner-sphere N-atom transfer chemistry. To this end, our group has been interested in the elucidation of transient intermediates involved in several C(sp2)-H functionalization reactions. In 2016, we reported a set of aryl-Co^{III} complexes synthetized through C(sp2)-H activation which were catalytically competent in alkyne and diazoacetate annulation reactions.[27-31] Thanks to the stability offered by the 12-membered macrocyclic model substrate employed, we were able to isolate an unprecedented C-metalated *cis*-aryl-Co^{III}-alkyl enolate complex, i.e. a masked-carbene species, which was demonstrated to be an on-cycle intermediate in the catalytic formation of the final C(sp2)-C products.[27, 28] Due to the extra stabilization offered by these model platforms, we hypothesized that they could offer a suitable electronic and geometric environment for studying the reactivity of Oh aryl-Co^{III} organometallic complexes towards organic azides.
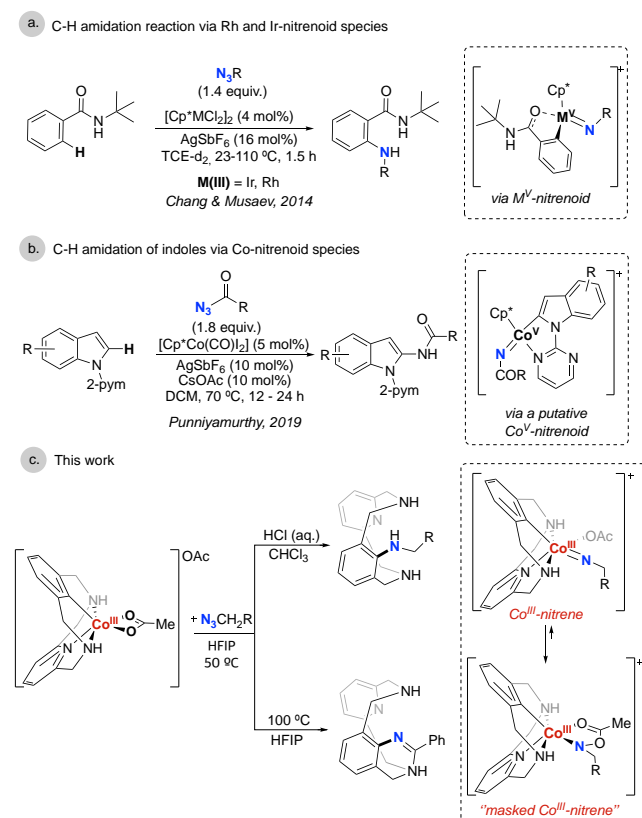
Fig. 1 Cp*-M-nitrenoid species proposed for the C–H amination reactions (M = Ir, Rh, Co).

Herein we report the N-atom transfer reactivity of inorganic and organic azides with well-defined aryl-Co^{III} complexes (Figure 1c), focusing on the step-by-step reactivity of intermediate species to unravel key mechanistic details of the C(sp2)-N bond formation. First, we explored the reactivity of aryl-Co^{III} complex with NaN$_3$, affording a very stable aryl-Co^{III}-N$_3$ complex. Then, we screened various organic azides, and were the aliphatic azides, the one that efficiently effected the C(sp2)-N bond products. With a combination of experimental and density functional theory (DFT) studies, the full reconstruction of the N-atom transfer process is revealed. Several intermediate species featuring the C(sp2)-N bond formed have been isolated and structurally characterized. The essential role of carboxylate-masked nitrenoid species to tame the metastability of the putative Co-nitrenoid is confirmed both experimentally and theoretically, affording a solid mechanistic picture of the C(sp2)-N bond forming process. The Co-nitrenoid is clearly described as an Oh aryl-Co^{III}-nitrene based on molecular orbital and electron density analyses, in contrast to the previously reported Oh Cp*Co^V=NR imido species (Figure 1a and 1b).[22, 23]

Results and Discussion

The reactivity of the well-defined aryl-Co^{III} complex (**1-OAc**) with nitrene precursors started by examining its reaction with an excess of inorganic sodium azide (NaN$_3$). The expected substitution of acetate by azide ligands in a monomeric complex was obtained in solution (characterized by NMR an HRMS). Quite surprisingly, the [aryl-Co^{III}-(N$_3$)$_2$] complex co-crystallized with the [Co^{II}(N$_3$)$_2$] unit, forming a stable trimeric Co$^{III}_2$Co^{II} complex [(L$_H$Co^{III})$_2$Co^{II}(N$_3$)$_2$(μ-N$_3$)$_4$] (**3'-N$_3$(N$_3$)**), which was characterized by X-Ray diffraction (Scheme 1). To our knowledge, this is the first example of an organometallic aryl-Co^{III}-azide complex. This result prompted us to explore the light-induced activation of the azide ligand to target inner-sphere N-transfer reactions. Unfortunately, neither extended light irradiation (254 or 420 nm) nor heating triggered the activation of the azide by N$_2$ release, resulting in a very stable compound.
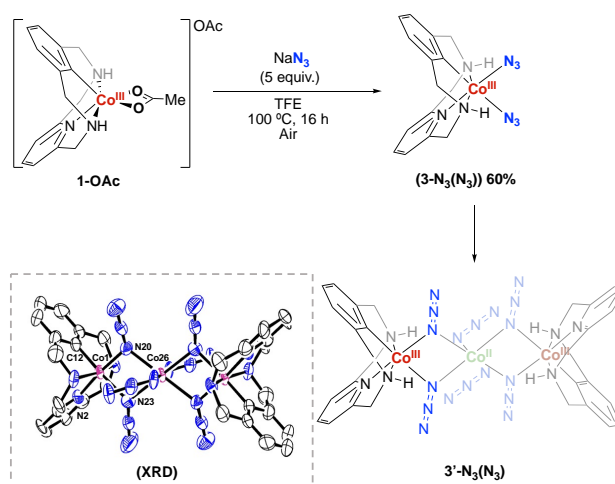
Scheme. 1 Formation of **3'-N$_3$(N$_3$)** organometallic complex by reacting the aryl Co^{III} (**1-OAc**) with NaN$_3$. Selected bond distances [Å] and angles [deg]: C(12)–Co(1) 1.853(11), Co(1)–N2 1.856(12), Co(1)–N(20) 1.955(12), Co(1)–N(23) 2.062, N(20)–Co(26) 2.175(9), N(23)–Co(26) 2.136(12), C(12)–Co(1)–N(20) 94.1(5), Co(1)–N(20)–Co(26) 101.5(4), Co(1)–N(23)–Co(26) 99.4(4), N(2)–Co(1)–N(23) 93.1(4).

Seeking the effective N-atom transfer, we resorted to organic azides, starting with *p*-NO$_2$-phenyl azide. Unfortunately, the use of aryl azides led to decomposition and formation of unidentified products.

Gratifyingly, positive results were obtained with aliphatic azides. We started with the addition of benzyl azide (**a**) to **1-OAc** complex using fluorinated alcohols as solvent (TFE or HFIP) at 50 °C, affording the aryl-amine coupling complex **4a-OAc** in 46% yield (Scheme 2). This complex was structurally characterized by 2D NMR studies, where a diagnostic HMBC peak between the benzylic –CH$_2$ of the formal azide and the quaternary carbon of the aryl moiety was observed, proving the formation of a new C(sp2)-NH bond. The coordinatively saturated complex **4a-OAc** slowly evolved at room temperature to a more stable dinuclear species, **5a-OAc**, in quantitative yield, (see ^{1}H-NMR time-evolution in Figure S1). Crystals of **5a-OAc** were obtained from slow evaporation from a CH$_2$Cl$_2$ solution (DCM/pentane) at -4 °C, allowing for an unambiguous characterization of this dimeric species. Compound **5a-OAc** features the new C(sp2)-NH bond and each Co^{III} center presents a distorted octahedral geometry, with coordination to N$_{py}$, NH$_L$, NH$_{azide}$ as well as one OAc and two μ-hydroxo bridging ligands.

Encouraged by these results, we explored the reactivity of **1-OAc** with (2-azidoethyl)benzene (**b**) and (2-azidopropyl)benzene (**c**) (Scheme 2). Using an excess of the azide **b** and **c** (6 equiv.) the corresponding inserted complex (**4b-OAc** and **4c-OAc**) was obtained in 26% and 25% yield, respectively. Both complexes led to the quantitative formation of the corresponding dimer **5b-OAc** and **5c-OAc**, analogously to complex **5a-OAc** (vide supra).
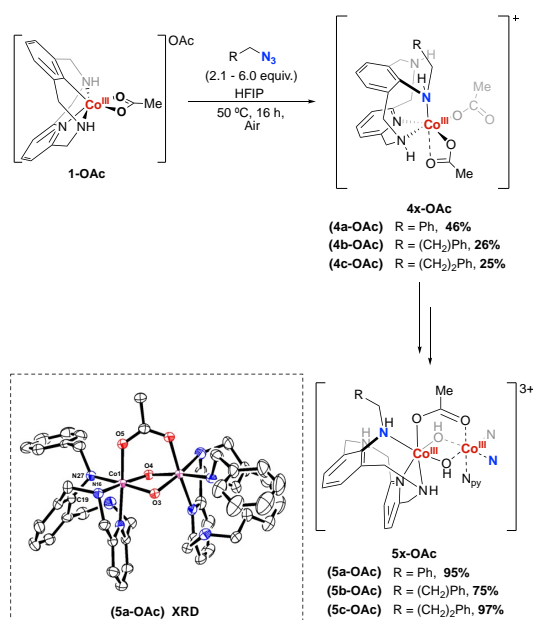
Scheme. 2 Reactivity of the aryl-Co^{III} (**1-OAc**) with organic azides to afford complexes **4x-OAc** and **5x-OAc** (yields of **5x-OAc** are based on **4x-OAc**). Selected bond distances for [Å] and angles [deg]: C(19)–N(27) 1.441(16), N(27)–Co(1) 2.009(11), C(19)–N(27)–Co(1) 110.3(9), Co(1)–O(5) 1.924(9), Co(1)–N(16) 1.955(12), Co(1)–O(3) 1.932(9), Co(1)–O(4) 1.930 (9).

The better yields observed for **4a-OAc** after treatment of **1-OAc** with benzyl azide prompted us to scrutinize the demetallation step. Based on previous reports,[19] the protodemetallation step to render the aminated product was predicted to be kinetically and thermodynamically disfavored.

Thus, in order to favor this step, we designed alternative strategies based on the use of strong acids and thermolysis (Scheme 3). Firstly, HCl (2M) was added to a solution of **4a-OAc** in CHCl$_3$, and after 16 h the crude mixture was basified and extracted affording the aminated product **P1** in 44% isolated yield. The analogous reaction using **4b-OAc** and **4c-OAc** afforded the corresponding aminated product **P2** and **P3** in 40% and 42% respectively. On the other hand, heating **4a-OAc** to 100 °C in HFIP furnished the cyclized product **P4** in 27% yield. The analogous cyclic products using **4b-OAc** and **4c-OAc** were not formed under the same conditions, which highlights the importance of the benzylic position for the formation of cyclized product (see mechanistic proposal for **P4** formation in Scheme S9).
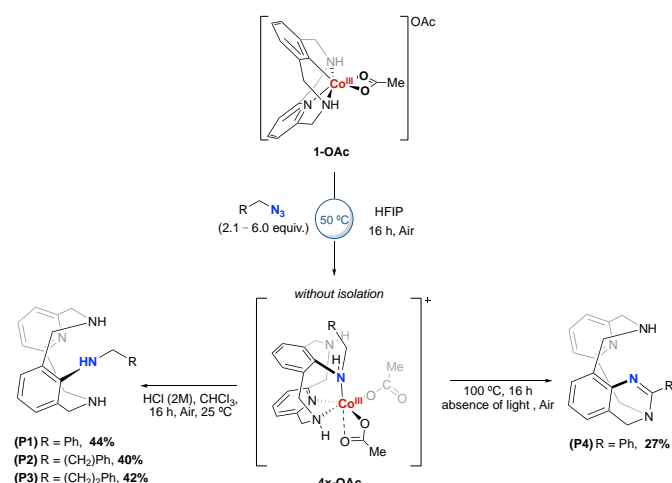
Scheme. 3 Thermal decomposition and acidic work-up affording the corresponding aminated product **P1**, **P2**, **P3** and **P4** (isolated yields shown).

The absence of an analogous cyclic product from **4b-OAc** and **4c-OAc** led us to investigate in depth the reactivity of these azides under different thermal conditions (Scheme 4). When **1-OAc** was mixed with an excess of azide **b** at 100 °C in TFE a new paramagnetic species appeared and resulted to be stable under inert atmosphere. XRD analysis showed a Co^{II} complex with distorted octahedral geometry bearing the phenylethan-1-amine moiety inserted (**6b-OAc**), which under acid conditions forms the product **P2** in 41% yield respect to **6b-OAc** complex.

A) Reactivity of **1-OAc** with organic azide (**b**)

B) Crystal structure of **6b-OAc**

6b-OAc (XRD)
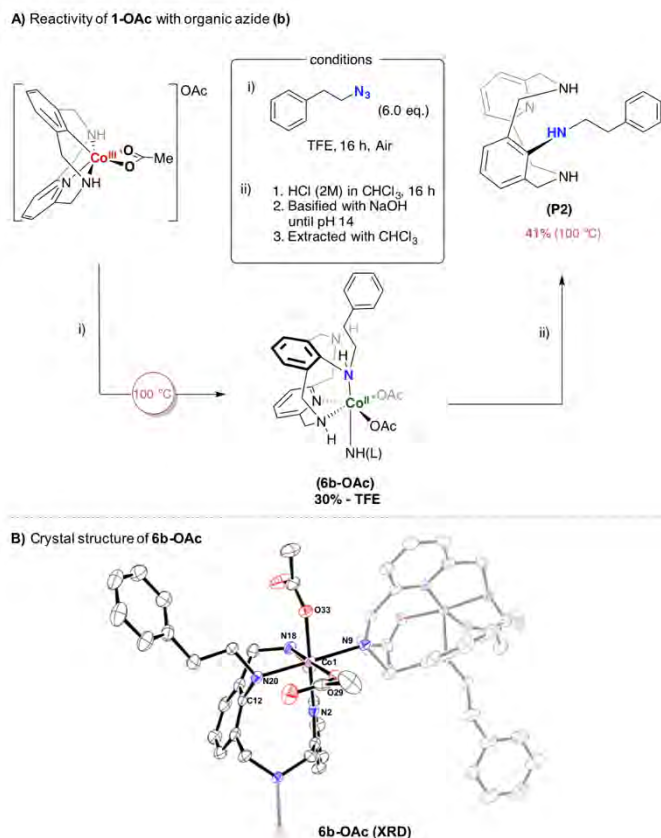
Scheme. 4 A) Reactivity of aryl-Co^{III} (**1-OAc**) with organic azide (**b**) at 100 °C. Yields of **P2** are based on **6b-OAc**. B) Crystal structure of **6b-OAc** complex. Selected bond distances for [Å] and angles [deg]: C(12)–N(20) 1.439(5), N(20)–Co(1) 2.176(4), C(12)–N(20)–Co(1) 109.7(2), Co(1)–N(18) 2.127(4), Co(1)–N(9) 2.259(4), Co(1)–N(2) 2.255(4), Co(1)–O(33) 2.075(3), Co(1)–O(29) 2.056(3).

Moreover, X-ray Absorption spectroscopy was conducted for **6b-OAc**, clearly confirming the Co^{II} oxidation state for the metal center (Table S2, Figure S20, Panels S1-S3) by comparison to Co^{III} species **1-OAc** and the newly synthesized aryl-Co^{III}-benzylamine complex (**7-OAc**, see Figures S28, S85-S92). The Co-ligand bond distances in the crystal structure of **6b-OAc** (>2.1 Å) suggest a high spin Co^{II} – d^7 electronic configuration, which was supported by the μ_{eff} calculated using Evans method in CD$_2$Cl$_2$. The obtained value of μ_{eff} = 4.22 MB is in agreement with the presence of 3 unpaired electrons. We hypothesized that the Co^{II} complex **6b-OAc** stemmed from reductive elimination of an in situ aryl-Co^{IV}-imido, although more investigations are needed to shed some light into the detailed mechanism of formation of **6b-OAc**.

The nature of the carboxylate ligand was also investigated, and we prepared the analogous **1-(OOCR)** complex bearing a substituted benzoate instead of the initial acetate (see Figures S21-S22 for the XRD of **1-(OBz-CF₃)** and **1-(OBz-OMe)**). The use of EWG and EDG substituents did not affect the formation of the inserted **4a-OBz-X** complex (Scheme S11). Subjecting the mixture to acidic conditions led the formation of **P1** product in similar yields. Moreover, the direct formation of **P4** product was achieved by reacting several **1-(OBz-X)** with benzyl azide (**a**)

under thermal conditions. **1-OBz-OMe** and **1-OBz-Cl** complexes showed slightly better than for **1-OAc** (27%), affording 42% and 49% yields, respectively (Scheme S12).

Mechanistic investigations

In order to gain more mechanistic insights of the C(sp2)-N bond formation, additional tests were performed. By adding TEMPO radical at 50 °C, MS peaks matching with a Co^{II} complex bearing the formed C(sp2)-N bond were detected, whereas at 100 °C the yield of **P4** dropped from a 27% to a 7%. These results are not conclusive for either a radical or non-radical pathway, since C(sp2)-N coupling is occurring, although in lower yields. Therefore, based on all experimental evidences, a thorough computational DFT study was mandatory to unravel the precise mechanism for the intriguing C(sp2)-N bond forming step using benzyl azide and **1-OAc** (Figure 2). The calculations were performed at the revTPSS-D3BJ/Def2TZVP//BP86-D3BJ/Def2SVP level of theory (see SI for full computational details and benchmark study). The rate-determining step of the reaction corresponds to the N$_2$ extrusion **TS1** to yield the short-lived species **2**. Wavefunction analysis of **2** afforded without doubt that **2** is best described as an aryl-Co^{III}=N-R (R = -CH$_2$Ph) nitrene species (Fischer-type) with a σ and a π bonds between the Co and the N atoms (bond order of 1.51 and bond length of 1.71 Å). Effective oxidation state (EOS) analysis in **2** dissects the N-Co π bond into two contributions with occupations 0.34 and 0.62 from N and Co, respectively (see Figure S27), clearly indicating that **2** is an aryl Co^{III}-nitrene with significant back-donation from Co to N. Qualitative analysis of the relative contributions of N and Co to the π and π* canonic molecular orbitals also characterize **2** as a aryl Co^{III}-nitrene (Figure S32 and Table S11), ruling out an aryl-Co^V-imido species (Schrock-type).[32]

The EOS analysis of the S=1 spin state of **2** indicates that the triplet **2** can also be described as a Co^{III}-nitrene with a Co-N bond length of 1.73 Å. As it can be seen by the occupation and shape of the effective fragment orbitals (EFOs) depicted in the Figure S35, in the singlet-triplet transition the S=0 beta electron of the lone-pair of the N is transferred to a p-type EFO of the N, resulting in a triplet state with two alpha p-type nonbonding electrons on the N. In addition, the remaining two beta electrons form two Co-N one-electron π bonds polarized toward the Co (see Figure S36). This analysis agrees with the fact that the major contribution of the spin density (i.e., electron density of alpha electrons minus the electron density of the beta electrons, which indicates the localization of the unpaired electrons) of the S=1 state of **2** is localized in the N (see Figure S33 and Table S13), and that the singlet → triplet spin-crossing does not cause significant change in the Co-N bond distance or in the formal oxidation state of the Co.
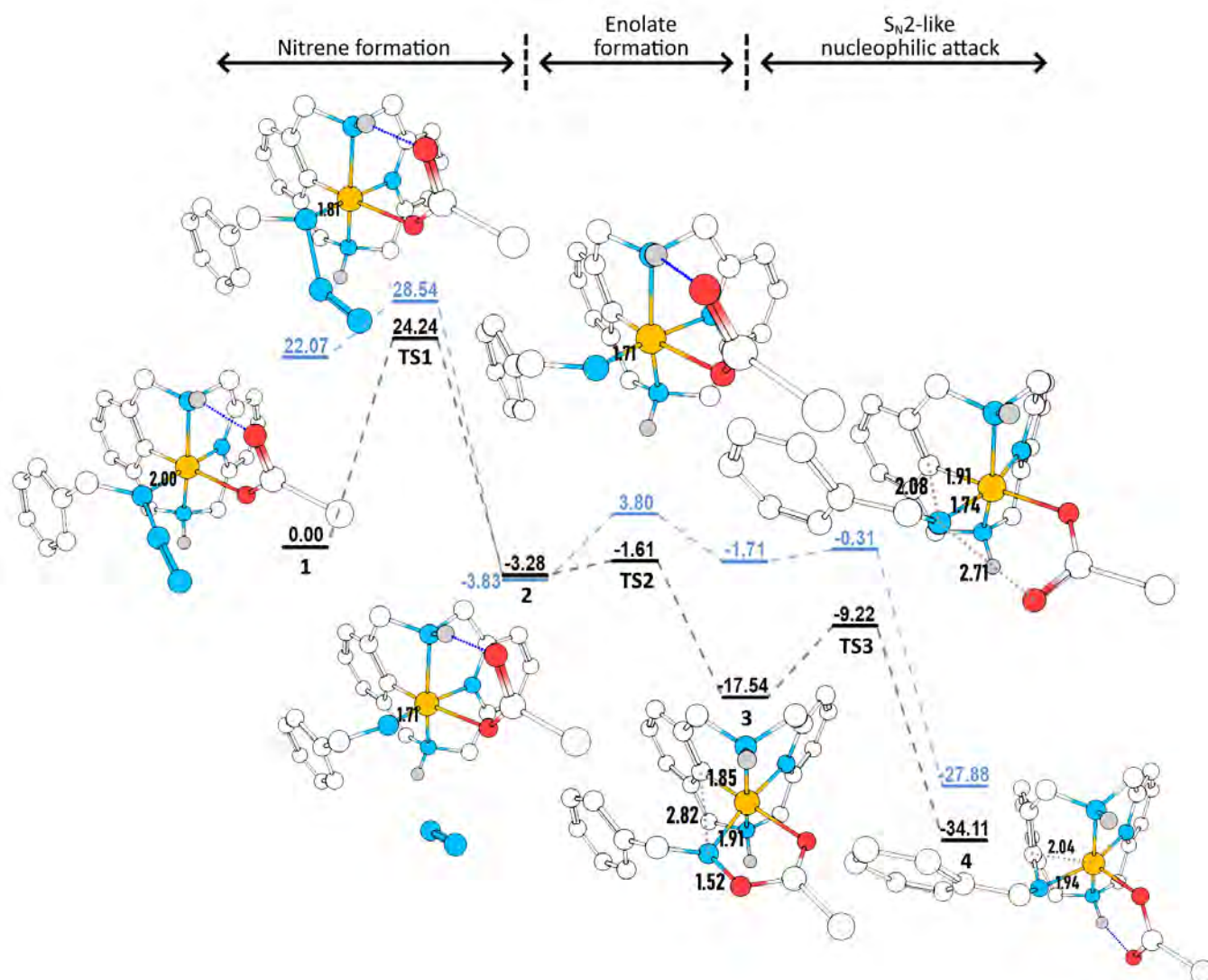
Fig. 2 RevTPSS-D3BJ/Def2TZVP//BP86-D3BJ/Def2SVP free energy profile for the studied reaction mechanism. Gibbs free energies (G, in kcal·mol^{-1}) are relative to 1. The pathway in black corresponds to the singlet species (S=0), while the blue pathway corresponds to the triplet species (S=1). Geometries for all S=0 intermediates and transition states are shown (nitrogen atoms are represented in blue, oxygens in red, cobalt in orange, carbon in white, and hydrogens in grey. Note that hydrogens bonded to carbon have been hidden for clarity). Relevant distances have also been included (in Å).

This intermediate species rapidly evolves overcoming a very low barrier (< 2 kcal/mol, **TS2**) to a 14 kcal/mol more stable **3** species by formation of a five-member acetoxy(benzyl)amide ring via carboxylate attack to the N atom, formally defined as a masked aryl-Co-nitrene. Wavefunction analysis describes **3** as a masked Co^{III} nitrene with a single σ bond between the Co and the N. The lack of Co=N π bond is also evidenced by the increased bond distance of 1.91 Å (1.71 Å for **2**) and a decreased bond order of 0.78.

The masked aryl-Co^{III}-nitrene is not sufficiently stabilized to be experimentally trapped, since it allows the formal nucleophilic attack of the aryl moiety to the N atom of the masked nitrene to finally achieve the C(sp2)-N coupling through a barrier lower than 9 kcal/mol, **TS3**. The partial atomic charge of the N atom in **3** (-0.51) vs **2** (-0.74) explains the enhanced electrophilic character of the former, induced by the formation of the

acetoxy(benzyl)amide. Moreover, EOS analysis also reveals a larger occupation of the aryl sigma contribution in **3** compared to **2**, which favours the S$_N$2 attack, and is an indication of the enhanced nucleophilic character of the aryl in **3** (see Figure S31). The reaction profile has also been evaluated for S=2 and S=1 spin states. The energies of the S=2 state of all intermediates and transition states involved in the reaction mechanism are far higher than the singlet, and therefore the quintuplet states play no role in the studied reaction mechanism (see Table S12). The triplet states does not play a key role either. S=1 state of the initial complex interacting with the benzyl azide is 22.07 kcal/mol above the singlet (Figure 2). The Gibbs energy of S=1 states for **TS1, TS2, 3**, **TS3** and **4** are also clearly higher than their S=0 counterparts. The only exception is Co-nitrene intermediate **2**, for which the triplet state is only 0.55 kcal/mol more stable than the singlet. However, due to the important

electron reorganization that takes places on the N in the singlet-triplet transition, the probability of a spin-crossing between the singlet and the triplet Gibbs energy surfaces is strongly reduced. Thus, all the computational evidences indicate that the reaction profile undergoes via singlet species. We have performed several DFT relaxed PES scans to explore the stability of aryl-Co^{III}-nitrene complex **2** upon distortion or disconnection of one of the coordinating N.[15] However, all the calculations confirm that the tight coordination environment imposed by the macrocyclic ligand in the aryl-Co^{III}-nitrene complex **2** is mandatory for its stabilization.

The role of carboxylate anions was experimentally confirmed by using the acetate-free organometallic [aryl-Co^{III}-(CH$_3$CN)$_2$]$^{2+}$ complex (**1-CH$_3$CN**) (Scheme S18). Applying reaction conditions at 50 ºC and 100ºC using benzyl azide (**a**) neither the aryl-amine coupling complex (analogous to **4a-OAc**) (50 ºC) nor final organic product **P4** (100 ºC) were detected. Furthermore, the presence of benzylaldehyde as side product suggested the degradation of benzyl azide, pointing out the importance of the formation of the masked-aryl-Co-nitrene species **3** towards the C(sp2)-N coupling.

Previously, some of us studied the mechanism of C(sp2)-H functionalization with diazo esters catalyzed with a aryl-Co^{III}-carboxylate compound,[28] in which the key role of a carboxylate-masked aryl-Co^{III}-carbene was proved. Analogously, the formation of the aryl-Co-nitrene, the facile evolution of the nitrene through a low-lying transition state to form a five-member acetoxy(benzyl)amide ring, as well as the final S$_N$2-type nucleophilic attack of the aryl-Co to the masked nitrene are reminiscent to the mechanism of the cobalt-catalyzed C(sp2)-H functionalization with diazo esters. The key difference between both mechanisms is the stability of the masked carbene and the masked nitrene. Whereas the masked-carbene could be isolated and fully experimentally characterized because the final nucleophilic attack is the rate determining step of the reaction, the analogous masked nitrene could not be isolated due to the barrier to form the coupling product being much smaller than the barrier for the formation of the aryl-Co^{III}-nitrene.

The proposed general mechanism is shown in Scheme 5. This study demonstrates the stabilizing masking effect of the carboxylate group to the Co-nitrene moiety, to tame the extraordinary reactivity and elusiveness of Co-nitrene species.
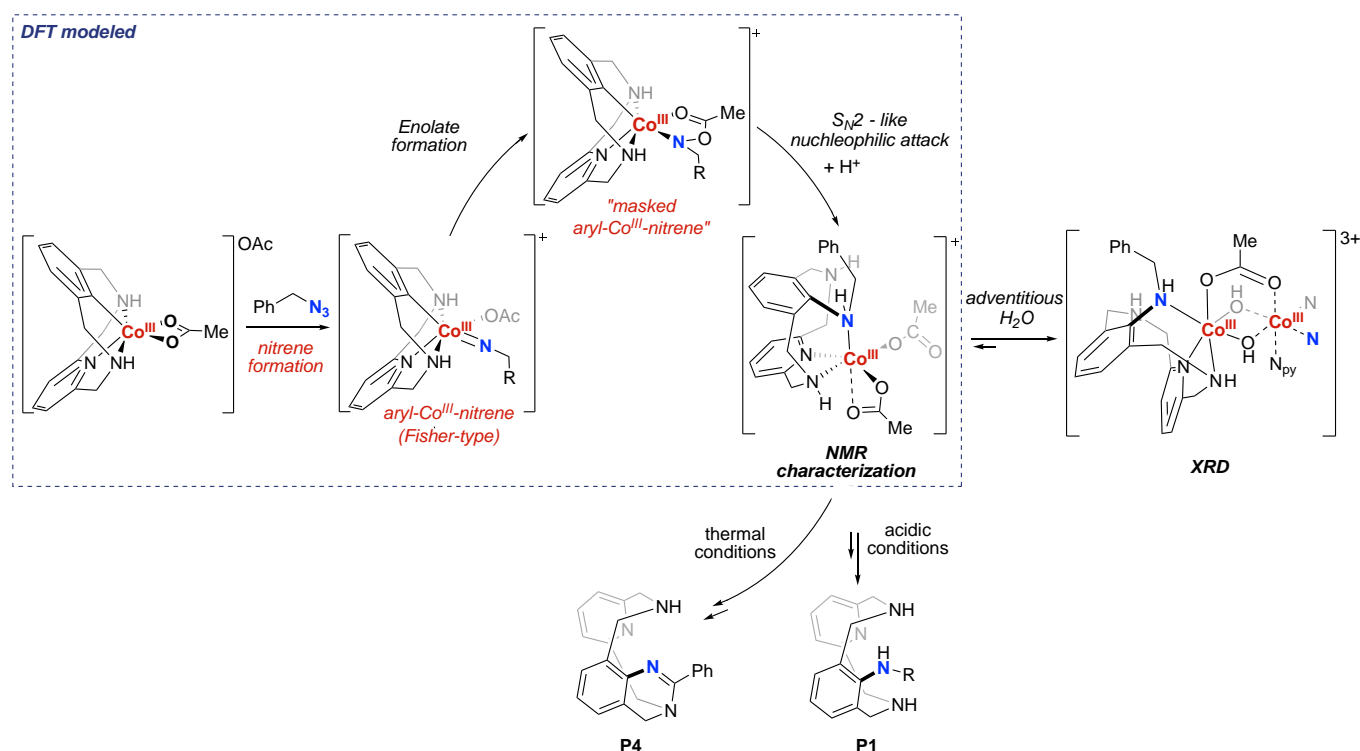
Scheme 5 Proposed mechanism for the reaction of **1-OAc** with benzylazide (**a**)

Intermolecular nitrene-transfer attempts

Additionally, nitrene transfer was attempted by adding xanthene (2 equiv.) to the mixture of **1-OAc** and benzyl azide (**a**), but no intermolecular C(sp2)-N coupling product with xanthene was detected, and intramolecular **4a-OAc** (20 %) was formed.

Comparing the reactivity of organometallic Co^{III} and Rh^{III} complexes

In order to gain more insight into the mechanism, we explored the reactivity of benzyl azide using an analogous aryl-Rh^{III} complex. **L-H** ligand was mixed with benzyl azide (**a**) and stoichiometric amounts of Rh(OAc)$_3$ in TFE at 100 °C. In contrast to the aryl-Co^{III} complex, we detected the formation of hydrazine and **P4** cyclic product was not formed. The sharply

different reactivity observed led us to explore the comparison of reactivities between Co^{III} (1_{Me}-OAc) and Rh^{III} (2_{Me}-OAc) complexes using the N-methylated ligand **L-Me**, where we isolated the aryl-Rh^{III}-imine species $8x_{Me}$-OAc which did not provide the C(sp2)-N bond-formed complexes (Scheme S19). The contrasting reactivity of Co versus Rh analogues highlights the uniqueness of Co reactivity, its versatility to stabilize metastable species via carboxylate masking and the value of studying in depth the role of first row metals in C-N formation.

Conclusions

In summary, we have studied the reactivity of well-defined Oh aryl-Co^{III} species (**1-OAc**) with different azides, with successful intramolecular C(sp2)-N bond formation with aliphatic azides. In brief, when benzyl azide is used we are able to trap the just-formed C(sp2)-N bond species, consisting in a Co^{III} complex (**4a-OAc**) that tends to dimerize to form complex **5a-OAc**. Analogous reactivity is found for (2-azidoethyl)benzene (**b**) and (2-azidopropyl)benzene (**c**). However, only **4a-OAc** evolves to an intramolecular cyclization to obtain the organic product **P4**, whereas **1-OAc** reacts with **b** under thermal treatment to afford a well-defined Co^{II} complex featuring the already formed C(sp2)-N bond (**6b-OAc**). The thorough DFT study performed demonstrates the stabilizing masking effect of the carboxylate group to the nitrenoid moiety, to tame the extraordinary reactivity and elusiveness of an aryl-Co^{III}=N-R nitrene species (**2**). First, the Gibbs energy barrier of the rate-determining step of the reaction, which corresponds to the N_2 extrusion, is in agreement with the mild experimental conditions applied (50ºC). More importantly, detailed wavefunction analysis of the masked aryl-Co^{III}-nitrene species **3** clearly shows an increase of electrophilicity on the N and an increase of nucleophilicity on the C(sp2)-aryl compared to **2**, thus promoting the facile S_N2-like attack to effect the C(sp2)-N coupling. This is in line with the fact that the S_N2-like barrier is far lower than the barrier for the formation of the aryl-Co^{III}-nitrene and with the fact that these masked species could not be trapped as in the case of the masked carbene.[28] The key role of carboxylate anions in the formation of masked aryl-Co^{III}-nitrene species, fully supported by both experimental and computation studies, culminated in a solid mechanistic picture of the C(sp2)-N bond forming amination process, which is thought to be valuable for the future development of catalytic C(sp2)-N methodologies via Co=NR species. Interestingly, this in-situ masking strategy is a straightforward alternative to the use of stabilized nitrene sources such as dioxazolones (CO_2-evolving reagent), which focus the scope in amidation reactions.[33-35]

Experimental section

See Supporting information for materials, instrumentation, spectroscopic characterization of all compounds and computational details.

Formation of 4x-OAc and 5x-OAc complexes. 1-OAc (0.048 mmol) and organic azides (**a-c**) with 1 mL of HFIP were mixed in a 2 mL vial and sealed. The mixture was heated at 50 ºC overnight. Then the crude mixture was concentrated under vacuum line until the initial volume was reduced to two-thirds observing the formation of **4x-OAc** intermediate complex by ^{1}H-NMR ($CDCl_3$) and HRMS. The corresponding dimeric species **5x-OAc** were slowly formed by recrystallization with $CHCl_3$ layered with pentane under air.

Synthesis of P1-P3 products. Once the **4x-OAc** were formed, each crude mixture was dissolved in $CHCl_3$ and HCl (3 mmol, 2M) was added and stirred overnight. The crude was basified until pH 14 and extracted with $CHCl_3$. The products were purified by column chromatography using neutral alumina ($CHCl_3$, then $CHCl_3$/MeOH 8:2) giving the corresponding C(sp2)-N coupling products (**P1-P3**).

Synthesis of P4 product. 1-OAc (0.048 mmol) and benzyl azide (**a**) (2.1 equiv.) were mixed in HFIP (1 mL) in a 2 mL vial and sealed. The crude was heated at 100 ºC overnight in the absence of light. The solvent was then removed, and the cyclic product was purified by column chromatography using neutral alumina ($CHCl_3$, then $CHCl_3$/MeOH. 8:2).

Formation of 6b-OAc. 1-OAc (0.048 mmol) and (2-azidoethyl)benzene (**b**) (6.0 equiv.) were mixed in TFE (1 mL) in a 2 mL vial and sealed. The crude was heated at 100 ºC and after 16 h the solvent was removed. Pentane diffusion in a concentrated solution of CH_2Cl_2 anhydrous under inert atmosphere yields the **6b-OAc** complex.

Theoretical calculations. All DFT calculations have been carried out using Gaussian16 program. Geometry optimizations have been performed without any symmetry restrictions, considering the effect of the HFIP solvent via the Self-Consistent Reaction Field method using SMD solvation model,[36] and taking into account dispersion effects with Grimme and coworkers DFT-D3BJ correction,[37, 38] at the BP86-D3BJ(SMD)/Def2SVP level of theory.[39-42] The HFIP solvent is not implemented in GAUSSIAN16, so we performed those calculations using the *Solvent=Generic,Read* options for the *SCRF* keyword (see Sup. Inf. for further details)**.** All geometry optimized structures were characterized by analytical frequency calculations, which also afforded enthalpy and entropy corrections at 298.15K. All points in the reaction pathway have been connected via IRC calculations. Single point calculations on the equilibrium geometries, including the solvent and dispersion effects (E_{sp}), have been carried out at the RevTPSS-D3BJ(SMD)/Def2TZVP level of theory.[43] Then, the total Gibbs Energy values (G) are given by:

$$G = E_{sp} + G_{corr.} + G^{°/*} \tag{1}$$

where the Gibbs Energy correction ($G_{corr.}$) has been obtained from the thermodynamical analysis at the optimization level of theory, but corrected using the GoodVibes code[44] so that

ARTICLE   Journal Name

frequencies below 100 are not treated with the Harmonic Approximation, but rather with the Quasi-Harmonic Approximation as described by Grimme.[45] Finally, the additional correction term $G^{\circ/*}$ accounts for the transition from the standard state concentration (gas phase, pressure of 1 atm) to the concentrations used experimentally.

Conflicts of interest

There are no conflicts to declare.

Acknowledgements

Notes and references

1. R. Hili and A. K. Yudin, *Nat. Chem. Biol.*, 2006, **2**, 284-287.
2. H. M. L. Davies and M. S. Long, *Angew. Chem. Int. Ed.*, 2005, **44**, 3518-3520.
3. A. H. Jason, *Curr. Org. Chem.*, 2005, **9**, 657-669.
4. H. M. L. Davies and J. R. Manning, *Nature*, 2008, **451**, 417-424.
5. F. Collet, R. H. Dodd and P. Dauban, *Chem. Commun.*, 2009, DOI: 10.1039/B905820F, 5061-5074.
6. D. N. Zalatan and J. D. Bois, in *C-H Activation*, eds. J.-Q. Yu and Z. Shi, Springer Berlin Heidelberg, Berlin, Heidelberg, 2010, DOI: 10.1007/128_2009_19, pp. 347-378.
7. P. Müller and C. Fruit, *Chem. Rev.*, 2003, **103**, 2905-2920.
8. M.-L. Louillat and F. W. Patureau, *Chem. Soc. Rev.*, 2014, **43**, 901-910.
9. K. Shin, H. Kim and S. Chang, *Acc. Chem. Res.*, 2015, **48**, 1040-1052.
10. E. J. Klinker, T. A. Jackson, M. P. Jensen, A. Stubna, G. Juhász, E. L. Bominaar, E. Münck and L. Que Jr., *Angew. Chem. Int. Ed.*, 2006, **45**, 7394-7397.
11. S. Kumar, A. S. Faponle, P. Barman, A. K. Vardhaman, C. V. Sastri, D. Kumar and S. P. de Visser, *J. Am. Chem. Soc.*, 2014, **136**, 17102-17115.
12. G. Coin, R. Patra, S. Rana, J. P. Biswas, P. Dubourdeaux, M. Clémancey, S. P. de Visser, D. Maiti, P. Maldivi and J.-M. Latour, *ACS Catal.*, 2020, **10**, 10010-10020.
13. L. Zhang, Y. Liu and L. Deng, *J. Am. Chem. Soc.*, 2014, **136**, 15525-15528.
14. Y. Baek, A. Das, S.-L. Zheng, J. H. Reibenspies, D. C. Powers and T. A. Betley, *J. Am. Chem. Soc.*, 2020, **142**, 11232-11243.
15. W. Mao, D. Fehn, F. W. Heinemann, A. Scheurer, D. Munz and K. Meyer, *Angew. Chem. Int. Ed.*, 2021, **60**, 16480-16486.
16. G. Dequirez, V. Pons and P. Dauban, *Angew. Chem. Int. Ed.*, 2012, **51**, 7384-7395.
17. C. Du, P.-X. Li, X. Zhu, J.-N. Han, J.-L. Niu and M.-P. Song, *ACS Catal.*, 2017, **7**, 2810-2814.
18. Q. Jia, L. Kong and X. Li, *Org. Chem. Front.*, 2019, **6**, 741-745.
19. T. M. Figg, S. Park, J. Park, S. Chang and D. G. Musaev, *Organometallics*, 2014, **33**, 4076-4085.
20. S. H. Park, J. Kwak, K. Shin, J. Ryu, Y. Park and S. Chang, *J. Am. Chem. Soc.*, 2014, **136**, 2492-2502.
21. Y.-K. Sau, X.-Y. Yi, K.-W. Chan, C.-S. Lai, I. D. Williams and W.-H. Leung, *J. Organomet. Chem.*, 2010, **695**, 1399-1404.
22. B. Sun, T. Yoshino, S. Matsunaga and M. Kanai, *Adv. Synth. Catal.*, 2014, **356**, 1491-1495.
23. B. Sun, T. Yoshino, S. Matsunaga and M. Kanai, *Chem. Commun.*, 2015, **51**, 4659-4661.
24. T. A. Shah, P. B. De, S. Pradhan, S. Banerjee and T. Punniyamurthy, *J. Org. Chem.*, 2019, **84**, 16278-16285.
25. J. Lee, J. Lee, H. Jung, D. Kim, J. Park and S. Chang, *J. Am. Chem. Soc.*, 2020, **142**, 12324-12332.
26. X. Yu, K. Chen, S. Guo, P. Shi, C. Song and J. Zhu, *Org. Lett.*, 2017, **19**, 5348-5351.
27. O. Planas, S. Roldán-Gómez, V. Martin-Diaconescu, J. M. Luis, A. Company and X. Ribas, *Chem. Sci.*, 2018, **9**, 5736-5746.
28. O. Planas, S. Roldán-Gómez, V. Martin-Diaconescu, T. Parella, J. M. Luis, A. Company and X. Ribas, *J. Am. Chem. Soc.*, 2017, **139**, 14649-14655.
29. O. Planas, C. J. Whiteoak, V. Martin-Diaconescu, I. Gamba, J. M. Luis, T. Parella, A. Company and X. Ribas, *J. Am. Chem. Soc.*, 2016, **138**, 14388-14397.
30. O. Planas, C. J. Whiteoak and X. Ribas, in *Non-Noble Metal Catalysis*, eds. R. J. M. K. Gebbink and M. E. Moret, Wiley, 2019, DOI: https://doi.org/10.1002/9783527699087.ch12, pp. 297-328.
31. O. Planas, P. G. Chirila, C. J. Whiteoak and X. Ribas, in *Advances in Organometallic Chemistry*, ed. P. J. Pérez, Academic Press, 2018, vol. 69, pp. 209-282.
32. P. F. Kuijpers, J. I. van der Vlugt, S. Schneider and B. de Bruin, *Chem. Eur. J.*, 2017, **23**, 13819-13829.
33. S. Y. Hong, Y. Hwang, M. Lee and S. Chang, *Acc. Chem. Res.*, 2021, **54**, 2683-2700.
34. S. Lee and T. Rovis, *ACS Catal.*, 2021, **11**, 8585-8590.
35. S. Sunny and R. Karvembu, *Adv. Synth. Catal.*, 2021, **18**, 4309-4331.
36. A. V. Marenich, C. J. Cramer and D. G. Truhlar, *J. Phys. Chem. B*, 2009, **113**, 6378-6396.
37. S. Grimme, S. Ehrlich and L. Goerigk, *J. Comput. Chem.*, 2011, **32**, 1456-1465.
38. S. Grimme, J. Antony, S. Ehrlich and H. Krieg, *J. Chem. Phys.*, 2010, **132**, 154104.
39. A. D. Becke, *Phys. Rev. A*, 1988, **38**, 3098-3100.
40. J. P. Perdew, *Phys. Rev. B*, 1986, **33**, 8822-8824.
41. A. Schäfer, C. Huber and R. Ahlrichs, *J. Chem. Phys.*, 1994, **100**, 5829-5835.
42. F. Weigend and R. Ahlrichs, *Phys. Chem. Chem. Phys.*, 2005, **7**, 3297-3305.
43. J. P. Perdew, A. Ruzsinszky, G. I. Csonka, L. A. Constantin and J. Sun, *Phys. Rev. Lett.*, 2009, **103**, 026403.
44. G. Luchini, J. Alegre-Requena, I. Funes-Ardoiz and R. Paton, *F1000Research*, 2020, **9**.
45. S. Grimme, *Chem. Eur. J.*, 2012, **18**, 9955-9964.

CHAPTER V

Chemodivergent nickel(0)-catalyzed arene C–F activation with alkynes: unprecedented C–F /C–H double insertion
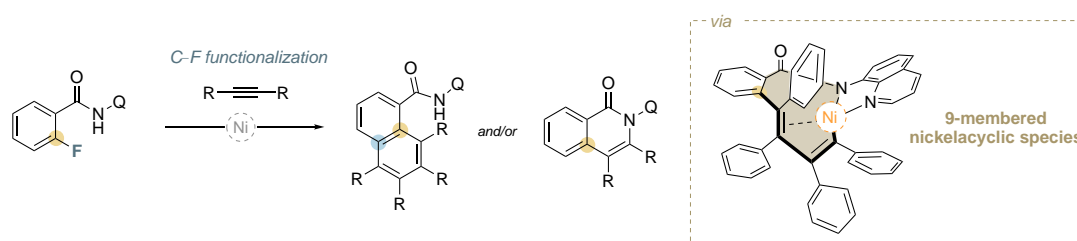
This Chapter corresponds to the following publication:

Reprinted with permission from ACS publications

For this publication L.C. synthesized and characterized the substrates, products and organometallic species. Moreover, L.C. performed either catalytic and stoichiometric experiments and optimization reactions. L.C. contributed in writing the manuscripts and was involved in all discussions.

Chemodivergent Nickel(0)-Catalyzed Arene C−F Activation with Alkynes: Unprecedented C−F/C−H Double Insertion

Lorena Capdevila,[†] Tjark H. Meyer,[‡] Steven Roldán-Gómez,[†] Josep M. Luis,[†] Lutz Ackermann,*,[‡] and Xavi Ribas*,[†]

[†]Institut de Química Computacional i Catàlisi (IQCC) and Dep. Química, Universitat de Girona, Campus de Montilivi, E-17003 Girona, Catalonia, Spain

[‡]Institut für Organische und Biomolekulare Chemie, Georg-August-Universität, Tammanstrasse 2, 37077 Göttingen, Germany

S *Supporting Information*

ABSTRACT: Nickel-catalyzed C−F activations enabled chemodivergent C−C formation with alkynes by chelation assistance. The judicious choice of the alkyne electronic properties allowed the selective synthesis of double-insertion aromatic homologation or alkyne monoannulation products by C−F/C−H activation. On the basis of the unambiguous crystallographic characterization of an unprecedented nine-membered nickelacyclic intermediate and extensive DFT studies, a plausible mechanistic rationale was established for the selective C−F activation and the chemodivergent catalysis.
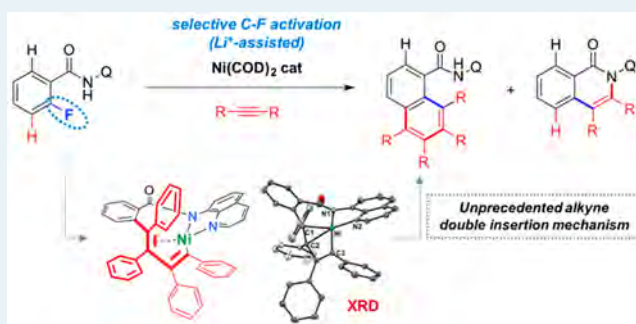
KEYWORDS: *nickel catalysis, C−F activation, aromatic homologation, directing group approach, DFT*

INTRODUCTION

Fluorinated compounds are key structural moieties in numerous areas of chemistry, with transformative applications to crop protection, catalysis, medicine, and material sciences.[1−4] The introduction of fluorinated motifs thus changes the physical, chemical and biological properties of a given molecule and, in the pharmaceutical industry context, improves the stability and lifetime of F-containing pharmaceuticals; 50% feature aryl fluorides. However, the stability is often too pronounced and the lead compound is frequently poorly biodegradable. Therefore, it is desirable to develop new sustainable methods for the functionalization of aromatic C−F bonds, as an enabling strategy to establish novel chemo- and regioselective transformation of fluorinated arenes. Transition-metal-catalyzed Ar−F functionalization is considerably more challenging than classical Ar−H or Ar−Hal (Hal = I, Br, Cl) activation, generally showing low selectivities and requiring electronically biased polyfluorinated substrates.[5−7] In particular, C−C formation reaction via C−F cleavage of fluoroarenes using a nickel catalyst has been reported for Kumada−Corriu,[8−16] Suzuki−Miyaura,[17−22] and Negishi[23] cross-coupling reactions. However, all of these methods use activated aryl nucleophiles, such as highly reactive Grignard reagents, zincates, and boronic acids, as the coupling partners for C−C formation via transmetalation (Scheme 1a). Alkyne insertion reactions have emerged as a powerful tool for the formation of cyclic compounds. Thus, several protocols through transition-metal-catalyzed C−H activation have been established with alkynes to form isoquinolones[24−28] or indoles.[29−32] The use of

an alkyne as a coupling partner can also lead to the direct formation of polysubstituted arenes.[33−36] In this context, Chatani[37] and Huang[38] recently reported a nickel-catalyzed[39] aromatic homologation reaction by a double C−H bond activation using 8-aminoquinoline as the directing group (Scheme 1b).

Taking into account the steadily increasing interest in the functionalization of the strongest bonds with carbon, we sought to develop new nickel(0)-catalyzed cyclizations of fluorinated arenes via alkyne insertion reactions.[40] Herein, we show that catalytic quantities of Ni(COD)$_2$ enable the chemodivergent C−F activation over C−H activation of fluoroarenes bearing either pyrimidin-2-amine[29,41] or 8-aminoquinoline[42] groups, toward isoquinolones and polysubstituted arenes. Mechanistic investigations were performed to clarify the parameters that control the chemoselectivity. Furthermore, the use of the 8-aminoquinoline group allowed us to isolate an unprecedented organometallic nickel(II) metallacycle featuring a doubly inserted acetylene, as the key intermediate in the aromatic homologation strategy (Scheme 1c).[43]

RESULTS

Role of N-Substitution Pattern. Initially, we probed the catalytic activation of the strong C−F bond by exploring the role of the directing group (DG) nature in the reaction with

Scheme 1. (a) Nickel-Catalyzed C−F Activation Reactions Using Highly Reactive, Preactivated R−M nucleophiles, (b) Alkyne Annulation via C−H Activation by Nickel Catalysts, and (c) Nickel-Catalyzed C−F Functionalization with Internal Alkynes
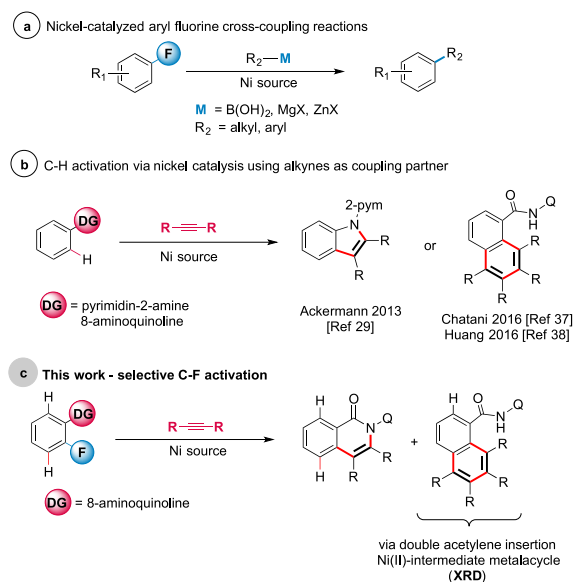
diphenylacetylene. To this end, we used substrates with two different well-studied directing groups, namely bidentate 8-aminoquinoline **1a** and monodentate pyrimidin-2-amine **1d** (Scheme 2). When the reaction was carried out with substrate

Scheme 2. Influence of N-Substitution on C−F Activation
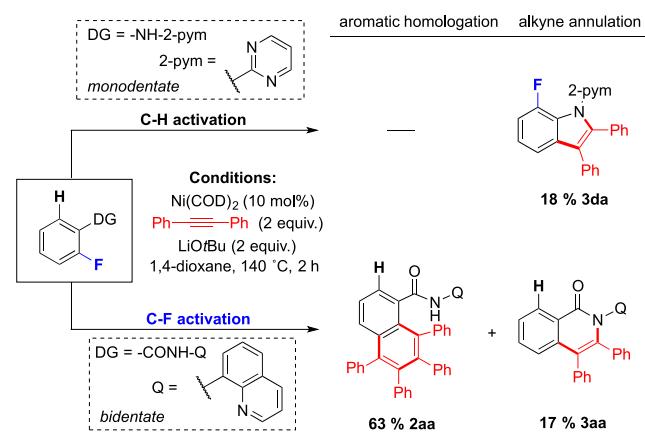
1d, a sluggish alkyne annulation reaction via C−H activation took place (**3da**, 18%), and the C−F bond remained intact. However, the use of 8-aminoquinoline as a bidentate directing group was crucial for the selective functionalization of the stronger C−F bond. On the basis of considerable optimization (Table S1), the alkyne monoannulation product (**3aa**) was obtained in a 17% yield, and the aromatic homologation product (**2aa**) was formed in a 63% yield (Scheme 2). This preliminary result clearly suggested that (a) the bidentate 8-AQ was ideal for the selective C−F cleavage whereas the monodentate DG only shows residual reactivity on C−H activation and (b) the insertion of two alkynes rendering the aromatic homologation product by dual C−F/C−H activation was here clearly favored over the alkyne monoannulation to

form isoquinolones. Thus, we became attracted to explore the parameters that govern this selectivity.

Influence of the Electronic Effect on the C−F Activation. With the optimal conditions for the C−F/C−H activation in hand, we then turned our attention toward the functionalization of the C−F bonds using different fluoroarene substrates. We performed a reaction using substrate **1b**, which has two fluorides at the ortho position of the arene (Table 1,

Table 1. C−F Functionalization Using Different Polyfluoroarenes
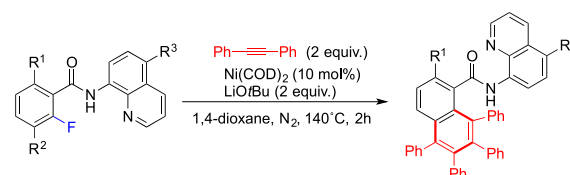
entry	R^1	R^2	R^3	yield (%) of 2xa[a]
1[b]	H	H	H	63 **2aa**
2	F	H	H	13 **2ba**
3[c]	F	H	H	34 **2ba**
4[d]	H	F	H	12 **2ca**
5[e]	H	H	NO_2	traces **2ea**

[a]Yield calculated from ^{1}H NMR of crude reaction mixture using 1,3,5-trimethoxybenzene as internal standard. [b]17% of alkyne annulation product **3aa**. [c]16 h. [d]Other minor products were detected. [e]Conversion 63%.

entry 2). In this case we could only obtain 13% of the homologation product **2ba** under otherwise identical conditions, suggesting that the presence of another electron-withdrawing F was not beneficial for the C−F functionalization reaction. The yield of the homologation product did not increase by adding different auxiliary ligands or changing the solvent. In addition, we synthesized substrate **1c**, which has two fluorides at the ortho and meta positions of the arene to explore the alkyne double insertion via C−F/C−F function-alization. Here, only 12% of the homologation product **2ca** was formed (Table 1, entry 4). Interestingly, using deactivated substrates, no alkyne annulation reaction took place and only aromatic homologation products were observed. The installa-tion of a nitro group at C5 of the quinolone moiety was not productive, and only decomposition products were obtained (Table 1, entry 5).

The formation of the two distinct products **2** and **3** led us to explore this reactivity further, changing the electronic proper-ties of the alkynes. Initial tests were performed using 1,2-di-*p*-tolylacetylene (Table 2, entry 2), and both products were also formed in a similar ratio (**2ab/3ab** ≈ 3), although with somewhat lower efficacy. In contrast, C−F activations with electron-deficient *p*-halo-substituted tolanes yielded an equal ratio of the two products (**2ax/3ax** ≈ 1, entries 3−5). This increment in the alkyne monoannulation products suggests that the presence of electron-withdrawing moieties favors the reductive elimination after the first alkyne insertion.[44−46] To address this point, we decided to study stronger electron-withdrawing groups (EWG), such as −C(O)Me and −CF$_3$, in the para position. To our delight, the aromatic homologation reaction was completely suppressed, exclusively giving the

Table 2. C−F Functionalization Using Different Symmetric Alkynes

entry	R′	yield (%) of 2ax[a]	yield (%) of 3ax[a]	total yield (%)
1[b]	H	63 2aa (60)	17 3aa (11)	80
2	Me	40 2ab (40)	14 3ab (6)	54
3	F	40 2ac (36)	43 3ac (34)	83
4	Cl	34 2ad (30)	39 3ad (29)	73
5	Br	37 2ae (25)	37 3ae (34)	74
6	MeC(O)	0 2af	36 3af (22)	36
7	CF₃	0 2ag	88 3ag (83)	88

[a]Yields calculated by ^{1}H NMR spectroscopy using 1,3,5-trimethoxybenzene as internal standard. Isolated yields are given in parentheses. [b]2 h.

alkyne monoannulation products in a 36% yield for **3af** (entry 6) and an 83% yield for **3ag** (entry 7), respectively.

The trend observed in Table 2 is clearly visualized in Scheme S2, plotting the observed **2ax/3ax** ratios versus the Hammett σ_p parameter. These findings showcase the aromatic homologation products being favored (**2ax**) when electron-donating groups are present, whereas the monoalkyne annulation products (**3ax**) are preferentially formed with electron-withdrawing substituents.

Study of the Steric Effect on C−F Activation. This reactivity was also studied using a set of unsymmetrically substituted alkynes. In all cases, both aromatic homologation and alkyne annulation reactions took place, with the former product being clearly preferred. A mixture of two (out of four) aromatic homologation regioisomers was formed (Table 3, entries 1−3). Yet, the alkyne monoannulation product was isolated with the aromatic motif being preferentially proximal to nitrogen.[47] Finally, when 4-octyne was used (Table 3, entry 4), the alkyne monoannulation product was not observed, and

Table 3. C−F Functionalization Using Alkyl−Aryl and Alkyl−Alkyl Acetylenes

entry	R¹	R²	yield (%) of 2ax[a]	ratio 2ax1:2ax2[b]
1[c]	Ph	Me	57 2ah (55)	1.6:1.0
2[c]	Ph	Et	70 2ai (49)	1.0:1.0
3[c,d]	Ph	Pr	85 2aj (41)	1.0:1.2
4[d,e]	Pr	Pr	53 2ak (41)	

[a]Yields determined by ^{1}H NMR spectroscopy using 1,3,5-trimethoxybenzene as internal standard. The yield of **2ax** = yield of **2ax1** + yield of **2ax2**. Isolated yields are given in parentheses. [b]Ratio calculated from NMR data. [c]Alkyne monoannulation products were formed in low quantities (see the Supporting Information). [d]8 h. [e]Only one aromatic homologation product is possible (**2ak**).

up to 53% of the aromatic homologation product, **2ak**, was formed instead. Thus, sterically congested alkyl groups disfavor the alkyne monoannulation product.

Isolation of Reaction Intermediates. To better understand the observed reactivity, a detailed ^{1}H NMR monitoring of the reaction of **1a** with diphenylacetylene was performed (Scheme S1). At the early stages (10 min), we observed the incipient formation of the products **2aa** and **3aa**. Additionally, we detected the formation of another minor species in the first 30 min of the reaction with a characteristic doublet at 9.06 ppm that subsequently faded away. The in situ ^{1}H NMR quantification of the intermediate species between 5 and 15 min accounted for over 80% of the total nickel content in the catalysis, indicating that this species belonged to the productive catalytic cycle.

Encouraged by the possibility of unraveling a key intermediate, we switched from catalytic to stoichiometric conditions and stopped the scaled reaction after 5 min. Upon chromatographic purification, a diamagnetic nickel complex was isolated in 23% yield (**INT4-E-H**). The compound was indeed very stable at room temperature, and high-quality crystals allowed unambiguous crystallographic analysis. Strikingly, the XRD structure revealed a square-planar nickel(II) complex with two alkynes being inserted toward a nine-membered nickelacyclic complex (Figure 1). Here, the terminal alkenyl moiety derived from the second inserted alkyne is trans to the anionic amide nitrogen. The square-planar geometry around the nickel(II) center features the π coordination of the alkene moiety corresponding to the initially inserted alkyne.[48] The latter nicely explains the extraordinary stability of such an intermediate species without the requirement of additional auxiliary ligands (see below). An analogous reaction with di-p-tolylacetylene afforded **INT4-E-Me**, which was likewise fully characterized by NMR spectroscopy. Furthermore, when the aromatic homologation reaction was performed using the analogous nonfluorinated substrate under the conditions reported by Huang, but at very short reaction times, the formation of the same **INT4-E-H** complex was also achieved (18% yield, Figure 1a and Figure S17).[38] This result suggests that this nine-membered nickelacyclic species is a common intermediate in aromatic homologation reactions, irrespective of being a C−F/C−H or a C−H/C−H activation route. In this line, a competition experiment using equimolar amounts of monofluorinated **1a** and the analogous nonfluorinated substrate shows a kinetically preferred C−F over C−H activation due to full consumption of **1a** in comparison to minimal conversion of the nonfluorinated substrate (Figure 1c). Indeed, a control experiment using only the nonfluorinated substrate under our catalytic conditions produced no aromatic homologation product and stilbene was detected as a byproduct, suggesting the implication of a Ni−hydride species (see below).[37,38]

Study of Isolated Ni(II) Intermediates in the Homologation Reaction. With intermediate **INT4-E-H** in hand, we investigated its evolution to the putative aromatic homologation product (**2aa**) under thermal conditions (Figure 2a), obtaining a modest 23% yield. Under these conditions (140 °C) and in the presence of 5 equiv of **1a** and base, a 41% yield of **2aa** was obtained. This is in line with the requirement of a second aminoquinoline (AQ) chelating unit inducing the m-C−H activation at the phenyl ring, which finally renders the aromatic homologation product **2aa** (Figure 2a). In addition, using 10 mol % of **INT4-E-H** under catalytic conditions, its full
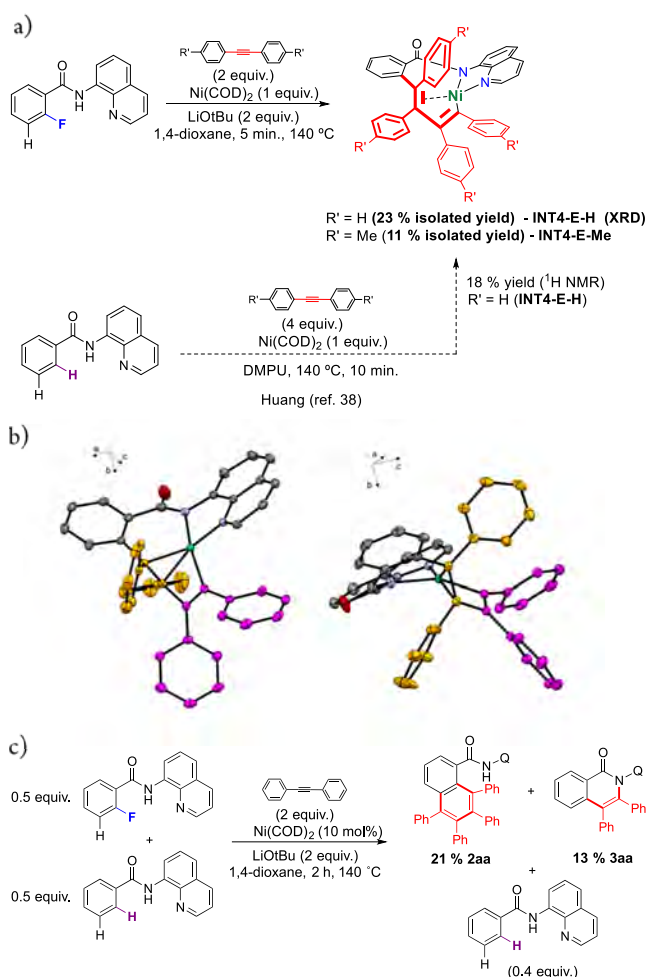
Figure 1. (a) Synthesis of the **INT4-E-H** complex via C−F/C−H (top) and via C−H/C−H activation previously reported by Huang (bottom) (yield 18%).[38] (b) Crystal structure of the **INT4-E-H** complex (CCDC 1891021). Selected bond distances (Å): Ni−C1 2.0411(19), Ni−C2 2.1060(17), Ni−C3 1.8946(16), Ni−N1 1.9209(16), Ni−N2 1.9011(16) (orange, first inserted alkyne in *E* conformation; magenta, second inserted alkyne in *Z* conformation; green, nickel(II) center). (c) Competition experiment with equimolar amounts of **1a** and the analogous nonfluorinated substrate, giving the products **2aa** and **3aa** mainly from C−F activation (**1a**, full conversion).

conversion to **2aa** was obtained (10% yield), although no catalytic turnover was achieved (Figure 2b). In sharp contrast, in the presence of PivOH, product **2aa** was not observed, while up to 46% of the linear alkenylation product **4aa** was obtained (Figure 2a), providing a new strategy toward molecular complexity by C−F activation.

Mechanistic Insight. On the basis of our findings and on the computational study detailed below, a full mechanistic proposal is depicted in Scheme 3. The coordination of deprotonated substrate **1a** with Ni(COD)₂ forms **INT1**, in which the strong C−F bond is cleaved via oxidative addition to generate the nickel(II) intermediate (**INT2**). A detailed DFT study on this step has been performed (Figure 3). The DFT geometry optimizations and frequency calculations have been carried out using the M06-L functional[49] and def2SVP basis set including solvent effects with the SMD model[50] and the dispersion with the Grimme GD3BJ approach. The Gibbs energies obtained were improved with single-point calculations
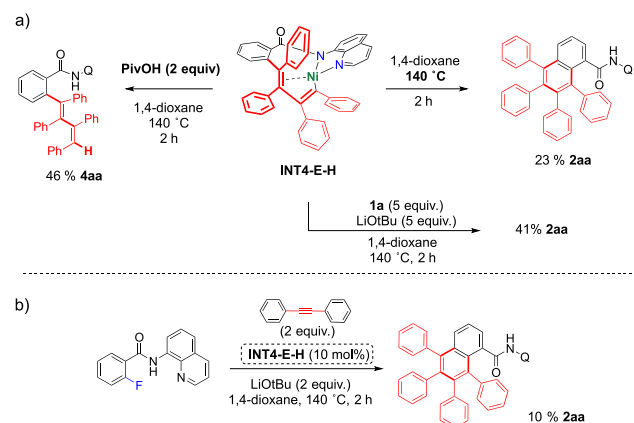
Figure 2. (a) Diverting reactivity pathways from **INT4-E-H**. (b) Reactivity using **INT4-E-H** as catalyst for the aromatic homologation transformation.

Scheme 3. Global Mechanistic Proposal[a]
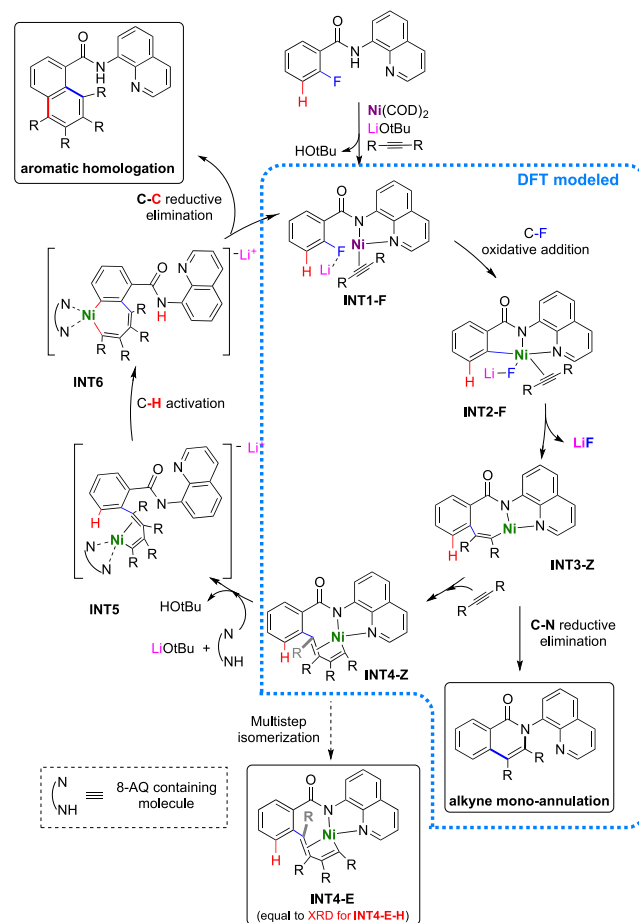
[a]Ni(0) is depicted in purple and Ni(II) in green.

at the M06-L/def2TZPV level including both the solvent and dispersion corrections. A complete description of the computational details of the DFT calculations is given in the Supporting Information. The results presented in Figure 3 show that the high selectivity of the oxidative addition step toward C−F activation over C−H activation is due to (a) a smaller energy barrier for Li⁺ Lewis acid assisted C−F activation in comparison to C−H activation by 4.6 kcal/mol, (b) the
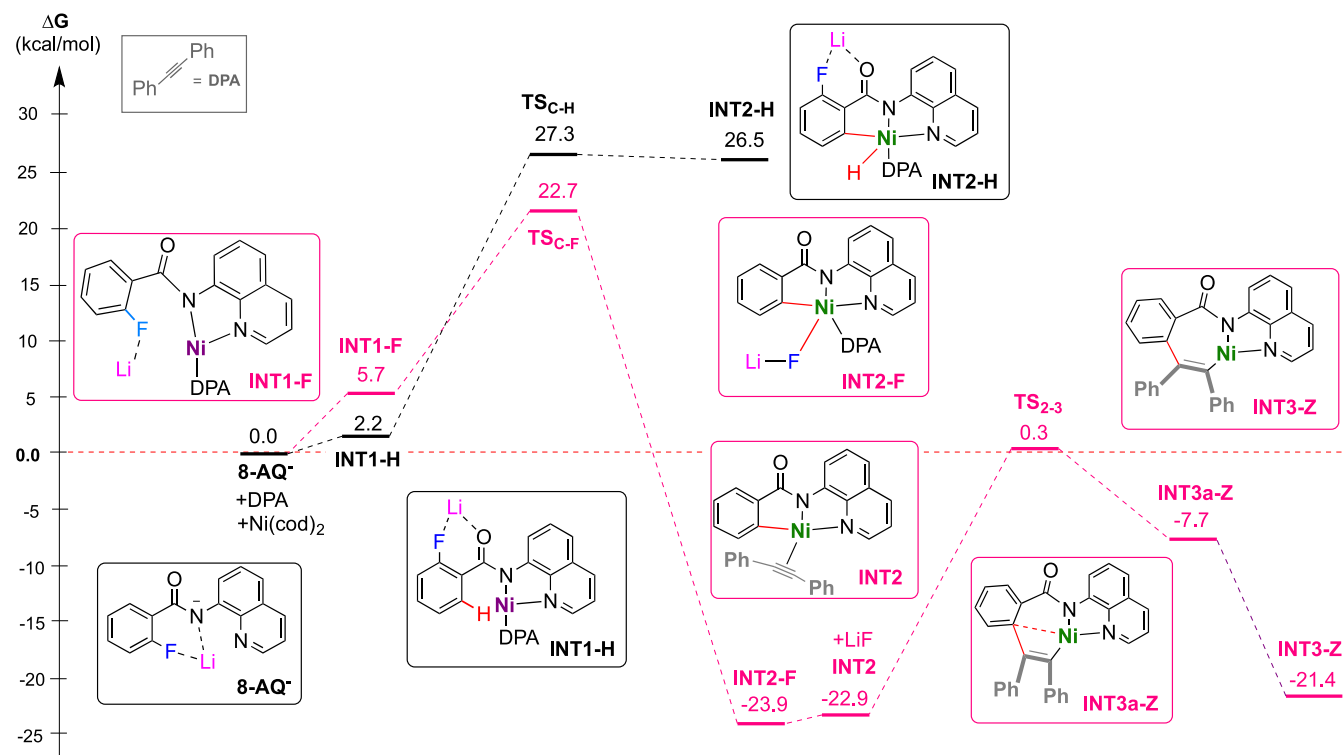
Figure 3. Gibbs energy profiles for the C−F (pink) versus C−H activation (black) through **INT2-F** and **INT2-H**, respectively, followed by the first DPA insertion at **INT2-F** to form **INT3-Z**. The reaction was modeled by DFT at the M06L/Def2TZVP//M06L/Def2SVP level of theory; energies are given in kcal/mol.

formation of the hydride-Ni(II) species (**INT2-H**) being strongly endergonic, and (c) the generation of a fluoride− Ni(II) species (**INT2-F**) being clearly exergonic (49.4 kcal/ mol more stable than **INT2-H**). Moreover, no alkene or H$_2$ is formed during the reaction, which is in line with the computational data.

The role of Li$^+$ is remarkable, since it facilitates the C−F oxidative addition, stabilizes the fluoride−Ni(II) species, and is ready to extrude LiF (see **TS$_{CF}$** in Figure 4), whose formation
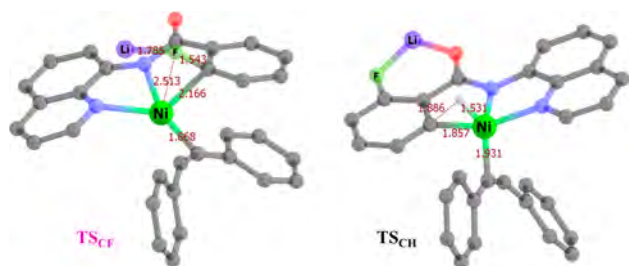
Figure 4. Optimized geometries of **TS$_{CF}$** and **TS$_{CH}$**.

is one of the driving forces of the reaction. Actually, the reaction does not proceed using *t*BuOK (potassium salt) as base. After the C−F oxidative addition step and extrusion of LiF, the first alkyne insertion (diphenylacetylene (DPA) was modeled) follows to form **INT3-Z**, with a barrier of 24.2 kcal/ mol (Figure 3). (DFT studies clearly indicate that the **INT3-Z** isomer is thermodynamically favored in comparison to **INT3-E**; see below and Figures 5 and 6.).

At this point, chemodivergent behavior can occur: either (i) the **INT3-Z** undergoes reductive elimination to form the alkyne monoannulation product **3** or (ii) a second alkyne
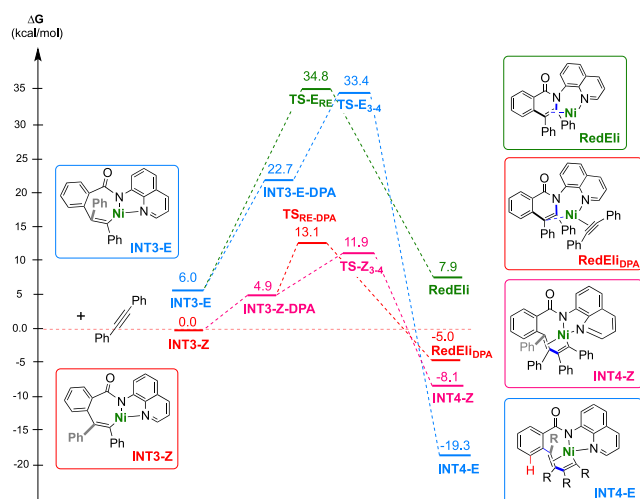
Figure 5. Gibbs energy profiles for the transition from the monoalkyne intermediates (**INT3-E** and **INT3-Z**) to the double-inserted alkyne compounds **INT4-E** (in blue) and **INT4-Z** (in pink), as well as the pathways for the intramolecular alkyne monoannulation from **INT3-E** (in green) and the annulation from **INT3-Z** with a second DPA coordinated to the metal (in red). The reaction was modeled by DFT at the M06L/Def2TZVP//M06L/Def2SVP level of theory; energies are given in kcal/mol.

insertion into a Ni−C bond proceeds toward **INT4-Z**. When the latter is formed, either this can isomerize to form **INT4-E** (equivalent to the isolated crystal structure **INT4-E-H**), which is more stable than **INT4-Z** (see below) or it can further react toward the synthesis of the homologation product. The experimental results suggest that the additional presence of 8-AQ motifs in either the substrate or the products facilitates
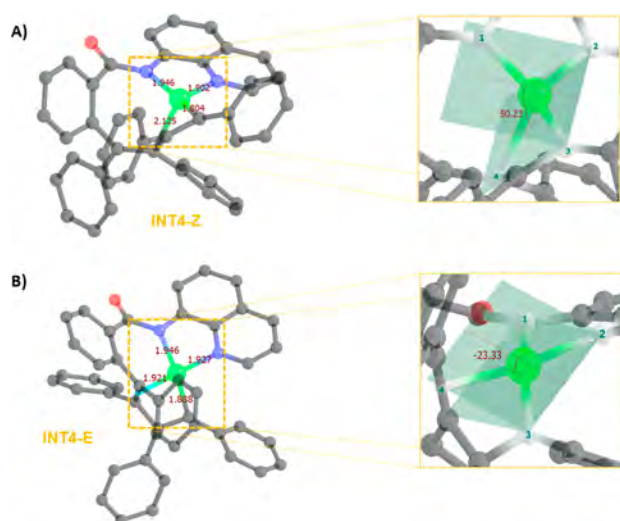
Figure 6. Optimized geometries of (a) **INT4-Z** and (b) **INT4-E**. The enlarged section highlights the distortion of the square planarity of the complex by measuring the dihedral angle N1N2C3C4. Atom color code: C, gray; N, blue; O, red; Ni, green. Hydrogen atoms have been omitted for clarity.

the activation of the *m*-C−H bond by stabilizing the nickel(II) center to give the final homologation products (**INT5** and **INT6**). The presence of an EWG on the alkyne triggers the chemodivergent transformation of **INT3-Z** to the alkyne monoannulation product, instead of the aromatic homologation product.

The insertion of the first alkyne may lead to two different **INT3** isomers, **INT3-Z** and **INT3-E** (Figure 5), which are differentiated by the stereochemistry of the C−C double bond from the first inserted alkyne in a *Z* (**INT3-Z**) or an *E* conformation (**INT3-E**).[51] The latter is 6.0 kcal/mol less stable than the former. The formation of **INT4-E** (−19.3 kcal/mol), which has exactly the same geometry as the crystal structure of **INT4-E-H** depicted in Figure 1, requires overcoming **TS-E$_{3-4}$** (33.4 kcal/mol). However, we found a far more kinetically favorable mechanism involving the first inserted alkyne in a *Z* conformation, whose transition state Gibbs energy (**TS-Z$_{3-4}$**) is 21.5 kcal/mol lower than **TS-E$_{3-4}$** (Figure 5). Importantly, the product obtained, **INT4-Z** (−8.1 kcal/mol), is 11.2 kcal/mol less stable than **INT4-E**. The experimental crystallization of **INT4-E-H** was mirrored by its strong thermodynamic stability found in the calculations, which is the driving force of a multistep isomerization of **INT4-Z** upon isolation as solid. In addition, a detailed analysis of the geometry of the Ni(II) center for optimized **INT4-Z** and **INT4-E** structures (by checking the dihedral angle between the atoms directly bonded to the metal) showed that the *E* isomer is significantly less distorted from square planarity (dihedral angle 23.3°) than the *Z* isomer (50.2°), thereby explaining the thermodynamic stability of **INT4-E** in comparison to **INT4-Z** (Figure 6).

The small energy barriers for the C−F oxidative addition, the first alkyne insertion, and the second alkyne insertion (<24 kcal/mol), together with the isolation of the double-alkyne-inserted nickelacyclic intermediate species, are in agreement with the rate-determining step being later than the insertion of the second alkyne.

Regarding the computed pathway leading to the alkyne monoannulation products (Figure 5), the most kinetically

favorable pathway involves a second molecule of acetylene coordinated to **INT3-Z**. It evolves through a reductive elimination transition state, **TS-Z$_{RE-DPA}$** (13.1 kcal/mol), which is only slightly above **TS-Z$_{3-4}$** by 1.2 kcal/mol (Figure 7). This small Gibbs energy difference is in agreement with the
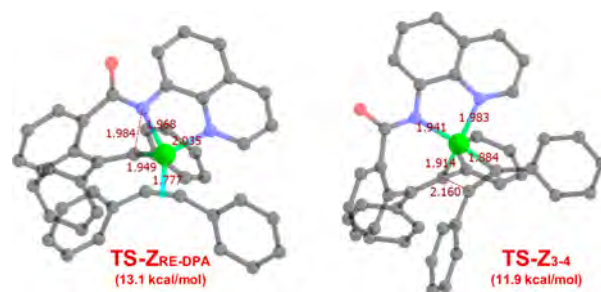
Figure 7. Optimized geometries of **TS-Z$_{RE-DPA}$** and **TS-Z$_{3-4}$**.

experimental formation of both aromatic homologation and alkyne monoannulation products, the former being preferred. When a *p*-CF$_3$-substituted alkyne is used, the Gibbs energy difference between the transition state of the second alkyne insertion, **CF$_3$-TS-Z$_{3-4}$** (13.4 kcal/mol), and the intramolecular reductive elimination, **CF$_3$-TS-Z$_{RE-DPA}$** (14.0 kcal/mol), is reduced to 0.6 kcal/mol, in agreement with the experimental trend observed when EWGs are present (see Figure S21).

■ CONCLUSIONS

In summary, we have developed a nickel-catalyzed C−F functionalization with internal alkynes to form either alkyne monoannulation or aromatic homologation products in a chemodivergent manner. The electronic properties of the fluoroarene and of the alkynes allowed us to selectively guide the reaction manifold. The selectivity for C−F over C−H activation is based on a lower transition state and exergonic step, as ascertained by DFT analysis, highlighting the crucial role of Li$^+$ in assisting the removal of the fluoride anion. A key unprecedented nickelacyclic species featuring a double-inserted alkyne was isolated and crystallized, unraveling the mechanistic pathway to the aromatic homologation product by challenging double C−F/C−H activation, which is also found for previously reported C−H/C−H aromatic homologations. These findings should prove instrumental as a mechanistic guidance for further transition-metal-catalyzed aromatic homologation reactions.

■ ASSOCIATED CONTENT

ⓢ Supporting Information

The Supporting Information is available free of charge on the ACS Publications website at DOI: 10.1021/acscatal.9b03620.

> Detailed spectroscopic characterization of all compounds, optimization details, experimental details of catalytic reactions, experimental details of stoichiometric reactions for the formation of **INT4-E-H** and **INT4-E-Me**, and computational details (PDF)
> Crystallographic data for **INT4-E-H** (CCDC-1891021)(CIF)

■ AUTHOR INFORMATION

Corresponding Authors
*E-mail for L.A.:lutz.Ackermann@chemie.uni-goettingen.de.

*E-mail for X.R.: xavi.ribas@udg.edu.

ORCID 🔘

Josep M. Luis: 0000-0002-2880-8680

Lutz Ackermann: 0000-0001-7034-8772

Xavi Ribas: 0000-0002-2850-4409

Notes

The authors declare no competing financial interest.

■ REFERENCES

(1) Böhm, H.-J.; Banner, D.; Bendels, S.; Kansy, M.; Kuhn, B.; Müller, K.; Obst-Sander, U.; Stahl, M. Fluorine in Medicinal Chemistry. *ChemBioChem* **2004**, *5*, 637−643.

(2) Müller, K.; Faeh, C.; Diederich, F. Fluorine in Pharmaceuticals: Looking Beyond Intuition. *Science* **2007**, *317*, 1881−1886.

(3) Purser, S.; Moore, P. R.; Swallow, S.; Gouverneur, V. Fluorine in medicinal chemistry. *Chem. Soc. Rev.* **2008**, *37*, 320−330.

(4) Wang, J.; Sánchez-Roselló, M.; Aceña, J. L.; del Pozo, C.; Sorochinsky, A. E.; Fustero, S.; Soloshonok, V. A.; Liu, H. Fluorine in Pharmaceutical Industry: Fluorine-Containing Drugs Introduced to the Market in the Last Decade (2001−2011). *Chem. Rev.* **2014**, *114*, 2432−2506.

(5) Sun, A. D.; Love, J. A. Cross coupling reactions of polyfluoroarenes via C−F activation. *Dalton Trans.* **2010**, *39*, 10362−10374.

(6) Amii, H.; Uneyama, K. C−F Bond Activation in Organic Synthesis. *Chem. Rev.* **2009**, *109*, 2119−2183.

(7) Ahrens, T.; Kohlmann, J.; Ahrens, M.; Braun, T. Functionalization of Fluorinated Molecules by Transition-Metal-Mediated C−F Bond Activation To Access Fluorinated Building Blocks. *Chem. Rev.* **2015**, *115*, 931−972.

(8) Kiso, Y.; Tamao, K.; Kumada, M. Effects of the nature of halides on the alkyl group isomerization in the nickel-catalyzed cross-coupling of secondary alkyl Grignard reagents with organic halides. *J. Organomet. Chem.* **1973**, *50*, C12−C14.

(9) Ackermann, L.; Born, R.; Spatz, J. H.; Meyer, D. Efficient Aryl−(Hetero)Aryl Coupling by Activation of C−Cl and C−F Bonds Using Nickel Complexes of Air-Stable Phosphine Oxides. *Angew. Chem., Int. Ed.* **2005**, *44*, 7216−7219.

(10) Yoshikai, N.; Mashima, H.; Nakamura, E. Nickel-Catalyzed Cross-Coupling Reaction of Aryl Fluorides and Chlorides with Grignard Reagents under Nickel/Magnesium Bimetallic Cooperation. *J. Am. Chem. Soc.* **2005**, *127*, 17978−17979.

(11) Yoshikai, N.; Matsuda, H.; Nakamura, E. Hydroxyphosphine Ligand for Nickel-Catalyzed Cross-Coupling through Nickel/Magnesium Bimetallic Cooperation. *J. Am. Chem. Soc.* **2009**, *131*, 9590−9599.

(12) Wang, J.-R.; Manabe, K. High Ortho Preference in Ni-Catalyzed Cross-Coupling of Halophenols with Alkyl Grignard Reagents. *Org. Lett.* **2009**, *11*, 741−744.

(13) Ackermann, L.; Wechsler, C.; Kapdi, A. R.; Althammer, A. Air-Stable Diaminophosphine Sulfides as Preligands for Nickel-Catalyzed Cross-Couplings of Unactivated Fluoro(hetero)arenes. *Synlett* **2010**, *2010*, 294−298.

(14) Nakamura, Y.; Yoshikai, N.; Ilies, L.; Nakamura, E. Nickel-Catalyzed Monosubstitution of Polyfluoroarenes with Organozinc Reagents Using Alkoxydiphosphine Ligand. *Org. Lett.* **2012**, *14*, 3316−3319.

(15) Guo, W.-J.; Wang, Z.-X. Cross-Coupling of ArX with ArMgBr Catalyzed by N-Heterocyclic Carbene-Based Nickel Complexes. *J. Org. Chem.* **2013**, *78*, 1054−1061.

(16) O'Neill, M. J.; Riesebeck, T.; Cornella, J. Thorpe−Ingold Effect in Branch-Selective Alkylation of Unactivated Aryl Fluorides. *Angew. Chem., Int. Ed.* **2018**, *57*, 9103−9107.

(17) Schaub, T.; Backes, M.; Radius, U. Catalytic C−C Bond Formation Accomplished by Selective C−F Activation of Perfluorinated Arenes. *J. Am. Chem. Soc.* **2006**, *128*, 15964−15965.

(18) Sun, A. D.; Love, J. A. Nickel-Catalyzed Selective Defluorination to Generate Partially Fluorinated Biaryls. *Org. Lett.* **2011**, *13*, 2750−2753.

(19) Tobisu, M.; Xu, T.; Shimasaki, T.; Chatani, N. Nickel-Catalyzed Suzuki−Miyaura Reaction of Aryl Fluorides. *J. Am. Chem. Soc.* **2011**, *133*, 19505−19511.

(20) Zhou, J.; Berthel, J. H. J.; Kuntze-Fechner, M. W.; Friedrich, A.; Marder, T. B.; Radius, U. NHC Nickel-Catalyzed Suzuki−Miyaura Cross-Coupling Reactions of Aryl Boronate Esters with Perfluorobenzenes. *J. Org. Chem.* **2016**, *81*, 5789−5794.

(21) Ho, Y. A.; Leiendecker, M.; Liu, X.; Wang, C.; Alandini, N.; Rueping, M. Nickel-Catalyzed Csp2−Csp3 Bond Formation via C−F Bond Activation. *Org. Lett.* **2018**, *20*, 5644−5647.

(22) Yu, D.; Shen, Q.; Lu, L. Selective Palladium-Catalyzed C−F Activation/Carbon−Carbon Bond Formation of Polyfluoroaryl Oxazolines. *J. Org. Chem.* **2012**, *77*, 1798−1804.

(23) Yu, D.; Wang, C.-S.; Yao, C.; Shen, Q.; Lu, L. Nickel-Catalyzed α-Arylation of Zinc Enolates with Polyfluoroarenes via C−F Bond Activation under Neutral Conditions. *Org. Lett.* **2014**, *16*, 5544−5547.

(24) Guimond, N.; Gouliaras, C.; Fagnou, K. Rhodium(III)-Catalyzed Isoquinolone Synthesis: The N−O Bond as a Handle for C−N Bond Formation and Catalyst Turnover. *J. Am. Chem. Soc.* **2010**, *132*, 6908−6909.

(25) Ackermann, L.; Lygin, A. V.; Hofmann, N. Ruthenium-Catalyzed Oxidative Annulation by Cleavage of C−H/N−H Bonds. *Angew. Chem., Int. Ed.* **2011**, *50*, 6379−6382.

(26) Shiota, H.; Ano, Y.; Aihara, Y.; Fukumoto, Y.; Chatani, N. Nickel-Catalyzed Chelation-Assisted Transformations Involving Ortho C−H Bond Activation: Regioselective Oxidative Cycloaddition of Aromatic Amides to Alkynes. *J. Am. Chem. Soc.* **2011**, *133*, 14952−14955.

(27) Cera, G.; Haven, T.; Ackermann, L. Iron-catalyzed C−H/N−H activation by triazole guidance: versatile alkyne annulation. *Chem. Commun.* **2017**, *53*, 6460−6463.

(28) Tian, C.; Massignan, L.; Meyer, T. H.; Ackermann, L. Electrochemical C−H/N−H Activation by Water-Tolerant Cobalt Catalysis at Room Temperature. *Angew. Chem., Int. Ed.* **2018**, *57*, 2383−2387.

(29) Song, W.; Ackermann, L. Nickel-catalyzed alkyne annulation by anilines: versatile indole synthesis by C−H/N−H functionalization. *Chem. Commun.* **2013**, *49*, 6638−6640.

(30) Stuart, D. R.; Bertrand-Laperle, M.; Burgess, K. M. N.; Fagnou, K. Indole Synthesis via Rhodium Catalyzed Oxidative Coupling of Acetanilides and Internal Alkynes. *J. Am. Chem. Soc.* **2008**, *130*, 16474−16475.

(31) Ackermann, L. Carboxylate-Assisted Ruthenium-Catalyzed Alkyne Annulations by C−H/Het−H Bond Functionalizations. *Acc. Chem. Res.* **2014**, *47*, 281−295.

(32) Shi, Z.; Zhang, C.; Li, S.; Pan, D.; Ding, S.; Cui, Y.; Jiao, N. Indoles from Simple Anilines and Alkynes: Palladium-Catalyzed C−H Activation Using Dioxygen as the Oxidant. *Angew. Chem., Int. Ed.* **2009**, *48*, 4572−4576.

(33) Le Bras, J.; Muzart, J. Dehydrogenative Heck Annelations of Internal Alkynes. *Synthesis* **2014**, *46*, 1555−1572.

(34) Fukutani, T.; Hirano, K.; Satoh, T.; Miura, M. Synthesis of Highly Substituted Acenes through Rhodium-Catalyzed Oxidative Coupling of Arylboron Reagents with Alkynes. *J. Org. Chem.* **2011**, *76*, 2867−2874.

(35) Pham, M. V.; Cramer, N. Aromatic Homologation by Non-Chelate-Assisted Rh[III]-Catalyzed C-H Functionalization of Arenes with Alkynes. *Angew. Chem., Int. Ed.* **2014**, *53*, 3484−3487.

(36) Martínez, Á. M.; Echavarren, J.; Alonso, I.; Rodríguez, N.; Gómez Arrayás, R.; Carretero, J. C. Rh[I]/Rh[III] catalyst-controlled divergent aryl/heteroaryl C−H bond functionalization of picolinamides with alkynes. *Chem. Sci.* **2015**, *6*, 5802−5814.

(37) Misal Castro, L. C.; Obata, A.; Aihara, Y.; Chatani, N. Chelation-Assisted Nickel-Catalyzed Oxidative Annulation via Double C−H Activation/Alkyne Insertion Reaction. *Chem. - Eur. J.* **2016**, *22*, 1362−1367.

(38) He, Z.; Huang, Y. Diverting C−H Annulation Pathways: Nickel-Catalyzed Dehydrogenative Homologation of Aromatic Amides. *ACS Catal.* **2016**, *6*, 7814−7823.

(39) Gandeepan, P.; Müller, T.; Zell, D.; Cera, G.; Warratz, S.; Ackermann, L. 3d Transition Metals for C−H Activation. *Chem. Rev.* **2019**, *119*, 2192.

(40) Eisenstein, O.; Milani, J.; Perutz, R. N. Selectivity of C−H Activation and Competition between C−H and C−F Bond Activation at Fluorocarbons. *Chem. Rev.* **2017**, *117*, 8710−8753.

(41) Ghorai, D.; Finger, L. H.; Zanoni, G.; Ackermann, L. Bimetallic Nickel Complexes for Aniline C−H Alkylations. *ACS Catal.* **2018**, *8*, 11657−11662.

(42) Grigorjeva, L.; Daugulis, O. Cobalt-Catalyzed, Aminoquinoline-Directed C(sp2)-H Bond Alkenylation by Alkynes. *Angew. Chem., Int. Ed.* **2014**, *53*, 10209−10212.

(43) Bennett, M. A.; Wenger, E. The Reactivity of Complexes of Nickel(0) and Platinum(0) Containing Benzyne and Related Small-Ring Alkynes. *Chem. Ber.* **1997**, *130*, 1029−1042.

(44) Johnson, J. B.; Rovis, T. More than Bystanders: The Effect of Olefins on Transition-Metal-Catalyzed Cross-Coupling Reactions. *Angew. Chem., Int. Ed.* **2008**, *47*, 840−871.

(45) Huang, C.-Y.; Doyle, A. G. Electron-Deficient Olefin Ligands Enable Generation of Quaternary Carbons by Ni-Catalyzed Cross-Coupling. *J. Am. Chem. Soc.* **2015**, *137*, 5638−5641.

(46) Yamamoto, T.; Yamamoto, A.; Ikeda, S. Organo (dipyridyl) nickel complexes. I. Stability and activation of the alkyl-nickel bonds of dialkyl (dipyridyl) nickel by coordination with various substituted olefins. *J. Am. Chem. Soc.* **1971**, *93*, 3350−3359.

(47) Meyer, T. H.; Oliveira, J. C. A.; Sau, S. C.; Ang, N. W. J.; Ackermann, L. Electrooxidative Allene Annulations by Mild Cobalt-Catalyzed C−H Activation. *ACS Catal.* **2018**, *8*, 9140−9147.

(48) Denninger, U.; Schneider, J. J.; Wilke, G.; Goddard, R.; Krömer, R.; Krüger, C. Transition metal complexes: VIII. An unusual rearrangement of a butadienyl ligand via cyclometallation. *J. Organomet. Chem.* **1993**, *459*, 349−357.

(49) Zhao, Y.; Truhlar, D. G. A new local density functional for main-group thermochemistry, transition metal bonding, thermochemical kinetics, and noncovalent interactions. *J. Chem. Phys.* **2006**, *125*, 194101.

(50) Marenich, A. V.; Cramer, C. J.; Truhlar, D. G. Universal solvation model based on solute electron density and on a continuum model of the solvent defined by the bulk dielectric constant and atomic surface tensions. *J. Phys. Chem. B* **2009**, *113*, 6378−6396.

(51) The possibility that a second AQ-containing substrate might coordinate at **INT3-Z** as proposed in the literature (see ref 37) was discarded due to the endergonic nature of the adduct formed with **1a-Li**, as ascertained by DFT calculations (see the Supporting Information).

CHAPTER VI

Nickel-catalyzed C$_{sp2}$–OMe functionalization for chemoselective aromatic homologation en route to nanographenes

This Chapter corresponds to the following publication:
Lorena Capdevila, Judith Sala, Lutz Ackermann, Xavi Ribas

Manuscript accepted for publication in Chem. Eur. J.
(doi.org/10.1002/chem.202200625)

Nickel-catalyzed C_{sp2}-OMe functionalization for chemoselective aromatic homologation en route to nanographenes

Lorena Capdevila, [a] Judith Sala, [a] Lutz Ackermann,[b] Xavi Ribas [a]*

[a] Institut de Química Computacional i Catàlisi (IQCC) and Dep. Química, Universitat de Girona, Campus de Montilivi, E-17003, Giro-na, Catalonia, Spain.
[b] Institut für Organische und Biomolekulare Chemie, Georg-August-Universität, Tammanstrasse 2, 37077 Göttingen, Germany.

Abstract

Here we report a Ni-catalyzed C_{sp2}−OMe *ortho*-functionalization methodology to form chemoselectively alkyne monoannulation or aromatic homologation products, as a novel protocol towards the valorisation of substrates containing C_{sp2}−OMe units. Double activation of C_{sp2}−OMe and C_{sp2}−F bonds is also demonstrated. Moreover, further use of aromatic homologation products towards the synthesis of nanographene-like compounds is described.

Introduction

Activation of C_{sp2}−O bonds of aryl ethers by transition metals is much more difficult than those of aryl halides, thus their use as electrophilic counterparts in cross coupling protocols is much more limited. This is probably due to the reluctance of the C–OMe bond towards oxidative addition and the lower propensity of the methoxy residue to act as a leaving group. However, among all transition metals, Ni^0-catalyzed C_{sp2}−O activation has become the methodology of choice to effect the cleavage of C_{sp2}−OR (R = Me, Ph) bonds.[1] Simple model C_{sp2}−OMe substrates have been used as electrophiles in Kumada,[2] Negishi[3] and Suzuki cross coupling catalysis (Figure 1a).[4] Also, the cleavage of C_{sp2}−OMe to C_{sp2}−H has also been achieved via reductive protocols with silanes[5] or in the presence of H_2.[6] On the other hand, C_{sp2}−OPh bond activation have been recently engaged into Ni-catalyzed C–O/N–H annulation of aromatic amides with alkynes for the production of isoquinolinones, by using C_{sp2}−OPh substrates bearing N-phenyl-benzamide Directing Groups (Figure 1b).[7] Concerning the mechanism of C_{sp2}−OMe activation, it is generally believed that oxidative addition at nickel(0) species is the key step in the process, although current knowledge is still limited.[8] In addition to the oxidative addition mechanism, non-classical modes of activation should be taken into account depending on the nature of the nucleophile and the ligand used.[1a] For instance, the involvement of in situ formed nickel(I) species has also been proposed in $Ni^0(COD)_2$/PCy_3-catalyzed reductive cleavage of aryl ethers using hydrosilane.[1c, 9] A very relevant raw source of C_{sp2}−OR moieties is lignin, which constitutes up to 30 wt% of wood-based biomass and is considered the largest source of renewable aromatics.[10] However, lignin decomposition is hampered by the difficulty in converting it into synthetically useful monomeric units by activation of the uniting C_{sp2}−OR (R = Me, Alkyl, Ar) and C–C bonds.[11] Nevertheless, the inert C_{sp2}−O bonds of aryl ethers contained in lignin remain in the monomers and new methodologies are needed to unlock this bottleneck of the lignin valorisation process.[12]

a) Nickel-catalyzed C$_{sp2}$–OMe funcionalization
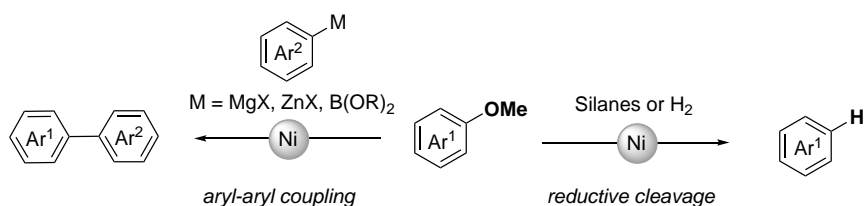
b) DG-assisted nickel-catalyzed C$_{sp2}$–OR funcionalization with alkynes

Figure 1. (a) Nickel-catalyzed C$_{sp2}$–OMe activation reaction using preactivated R–M nucleophiles to form C$_{sp2}$–C$_{sp2}$ coupling and reductive cleavage. (b) Directing group-assisted nickel-catalyzed C$_{sp2}$–OR functionalization with alkynes.

Recently we reported a nickel-catalyzed C$_{sp2}$−F functionalization with internal alkynes to form either alkyne monoannulation or aromatic homologation products in a chemodivergent manner, demonstrating the ability of the 8-aminoquinoline[13] directing group to activate the strong C$_{sp2}$−F bonds.[14] Here we report an analogous Ni-catalyzed methodology to form alkyne monoannulation or aromatic homologation products via the functionalization of strong C$_{sp2}$−OMe bonds, as a novel protocol towards the valorization of lignin monomers containing C$_{sp2}$−OMe units.

Results and discussion

We first focused on whether C$_{sp2}$−OMe could be functionalized with internal alkynes using a similar Ni^0-based methodology as for the C$_{sp2}$−F substrates recently reported by us. We screened as Directing Group (DG) the 8-aminoquinoline (8-AQ)[13, 15] (**1aa**), 2-pyridylisopropylamine (PIP)[16] (**1ba**) and 2-pyridylmethylamine (PM)[17] (**1ca**) units in *ortho*-position to the C$_{sp2}$−OMe substrate and diphenylacetylene (Scheme 1). Only positive outcome of the reaction was found for 8-AQ-containing substrate **1aa**, affording the aromatic homologation product **2aa** in 47% yield and the alkyne monoannulation product **3aa** in 27% yield. These results point out to the requirement of a rigid and bidentate DG for the reaction to proceed.
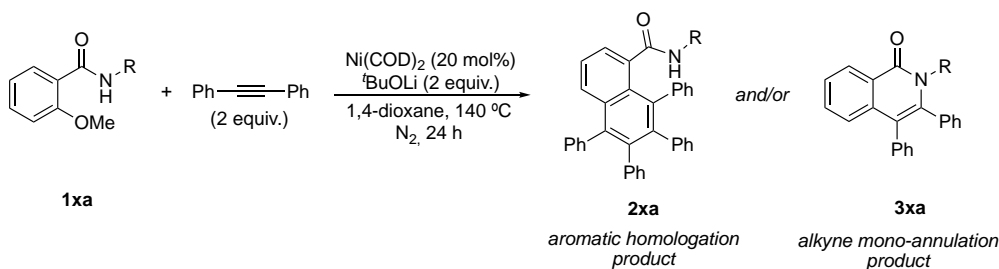
Scheme 1. Screening of effective DG for the Ni-catalyzed C_{sp2}–OMe functionalization with diphenylacetylene (in parenthesis: isolated yield; nd = not detected).

The **2aa/3aa** ratio of 1.7 obtained under these conditions was similar to the analogous C_{sp2}–F cleavage to obtain the same products (**2aa/3aa** ratio = 3.7),[14a] what suggested a similar mechanism of chemodivergent product formation. At this point, we pursued the optimization of the chemodivergence, and found that the **2aa/3aa** ratio could be completely reversed; if, additionally to the standard conditions, LiOTf (2 equiv.) was added, the aromatic homologation product **2aa** was maximized to a **2aa/3aa** ratio of 11.8 in a 59% yield (3h) (Scheme 2). However, when PPh₃ (2 equiv.) was added in lieu of LiOTf, a switch of chemoselectivity occurred and **3aa** was obtained in 64% yield within 3 h (**2aa/3aa** ratio = 1:2.6). It is worth to note that by increasing the reaction time up to 24 h, the alkyne monoannulation product **3aa** was obtained in an exclusive manner due to the decomposition of **2aa** under these conditions.

24 h – **38% 2aa** (7.6:1)
3h – **59% 2aa** (11.8:1)

24 h – **58% 3aa** (0:1)
3h – **64% 3aa** (1:2.5)
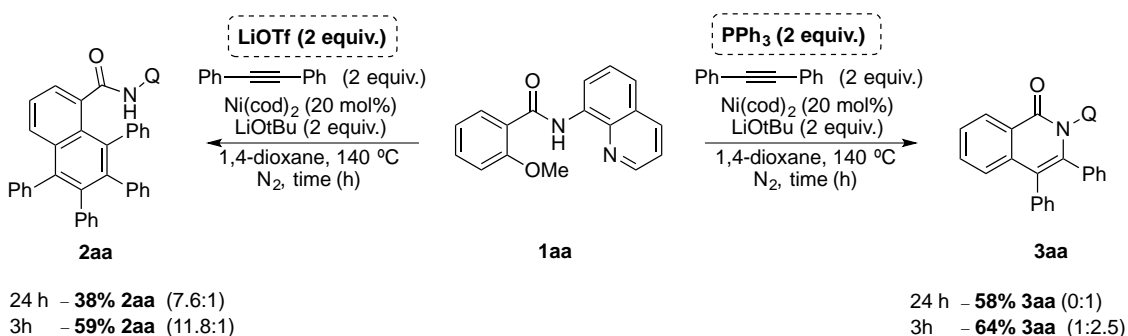
Scheme 2. Chemodivergent behavior towards the aromatic homologation and the alkyne monoannulation product (**2aa/3aa** ratio in parenthesis).

Then we turned our attention to substrates bearing a second –OMe group in *para-* (**1ab**) and *ortho-* (**1ac**) to the DG, in order to analyse the electronic and steric effects of the additional methoxy- group to the reaction outcome (Table 1). On the one hand, the yield for **2ab** (26%) and **3ab** (22%) decreased and the ratio **2ab/3ab** was ~ 1 when using substrate **1ab**. The same trend as in **1aa** was observed, and adding LiOTf, the formation of the aromatic homologation **2ab** was observed in a selective manner (32% in 24h).

Instead, adding PPh$_3$ the corresponding alkyne monoannulation product was formed in higher yields (70% in 3 h). The higher reactivity observed towards the formation of the alkyne monoannulation product suggested that the aromatic homologation reaction was impeded by the steric effect of the second –OMe group in *meta*. On the other hand, although no reactivity was observed using **1ac** under the standard conditions (Table 1, entry 7), full chemoselectivity for the aromatic homologation product **2ac** was regained (48% yield in 24 h, entry 8) when LiOTf was used as the additive.

Table 1. C$_{sp2}$–OMe functionalization using different methoxyarene substrates.

Entry	Substrate 1ax	Additives	Yield (%) of 2ax[a]	Yield (%) of 3ax[a]
1		without	47%	27%
2		LiOTf	38% (59%)	tr (tr)
3	**1aa**	PPh$_3$	tr (25%)	58% (64%)
4		without	26% (tr)	22% (tr)
5		LiOTf	32% (tr)	tr (tr)
6	**1ab**	PPh$_3$	tr (tr)	43%(70%)
7		without	tr	tr
8		LiOTf	48% (26%)	tr (tr)
9[b]	**1ac**	PPh$_3$	-	-

[a]Yield calculated from ^{1}H-NMR of crude reaction mixture using 1,3,5-trimethoxybenzene as internal standard (in parenthesis, yield at 3h); tr = traces. [b] Formation of product **4** in 25% yield.

Strikingly, substrate **1ac** afforded the double activation of both –OMe groups in *ortho* to the DG when PPh$_3$ was used, affording product **4** in 25% yield (29% using 50 mol% of Ni(COD)$_2$), featuring the aromatic homologation and the alkyne monoannulation simultaneously (Figure 2a). Gratifyingly, the crystal structure of **4** was obtained by slow evaporation of a CHCl$_3$ solution, and consisted of a racemic mixture of the two enantiomeric helical species that arise from the isoquinolinone formation at the monoannulation step (Figure 2b).

a) Double C$_{sp2}$–OMe functionalization

1ac

25% of 4
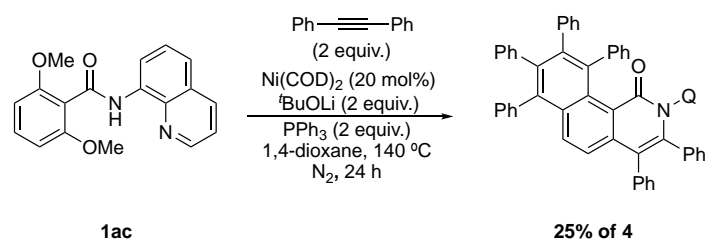
b) Crystal structure of **4**
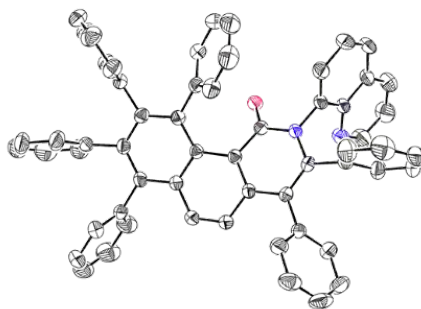
Figure 2. (a) Double C$_{sp2}$–OMe activation using substrate **1ac** to afford product **4** (yield based on alkyne). (b) Crystal structure of **4** (only shown one of the helical enantiomers of the racemic mixture).

We then focused our efforts in comparing the reactivity of the C$_{sp2}$–F and C$_{sp2}$–OMe groups. To this end, substrate **1ad** was synthesized bearing fluoride and methoxy groups in *ortho* to the amide motif (Scheme 3). Using the standard conditions and LiOTf, only the C$_{sp2}$–F moiety was activated to afford 44% of product **2ad**, with no traces of C$_{sp2}$–OMe activation. The intramolecular monoannulation product was not detected. Since we could achieve the simultaneous activation of two C$_{sp2}$–OMe bonds in *ortho* in **1ac**, and C$_{sp2}$–F was more reactive than C$_{sp2}$–OMe, we hypothesized that **1ad** could also undergo the simultaneous aromatic homologation and alkyne monoannulation to form **4**. Indeed, after optimization studies, we found that product **4** was formed, when employing both LiOTf and PPh$_3$.
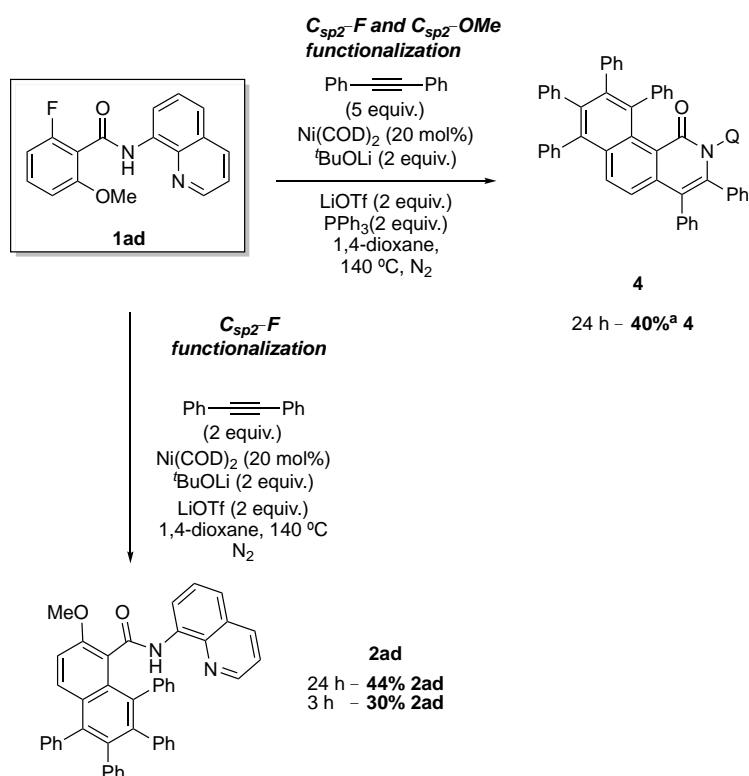
Scheme 3. Competition experiment between C_{sp2}–OMe vs C_{sp2}–F *ortho*-functionalization in **1ad** towards the formation of aromatic homologation and the simultaneous double functionalization. [a] Isolated yield.

At the current stage of this investigation, we envision an analogous mechanism for the C_{sp2}–OMe activation as the one described for C_{sp2}–F in our previous report.[14a] Indeed, when substrate **1ab** was reacted with diphenylacetylene under the aromatic homologation conditions for 3h, the square-planar nine-membered nickelacyclic intermediate complex **1ab-INT4-E-H** was selectively formed in a 91% NMR yield (Scheme 4). 2D NMR structural characterization clearly showed that **1ab-INT4-E-H** featured two alkynes inserted. The species **1ab-INT4-E-H** undergoes formation of the corresponding aromatic homologation product **2ab** in 32% yield after 24 h (Table 1, entry 5). This low yield compared to the almost quantitative accumulation of **1ab-INT4-E-H** might be related to the steric hindrance imposed by the -OMe group adjacent to the C–H activated in the aromatic homologation process, thus hampering the formation of **2ab**. As in the case of the C_{sp2}–F functionalization, the presence of lithium ions is crucial to stabilize the LiOMe as leaving group.
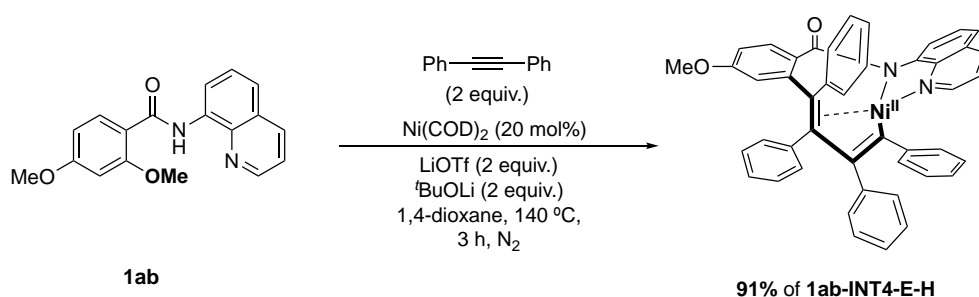
Scheme 4. Isolation of the **1ab-INT4-E-H** intermediate species. Yield calculated using 1,3,5-trimethoxybenzene as internal standard and based on the total Ni content.

Remarkably, the 1,2,3,4-tetraphenylnaphthalene unit in the homologation product **2aa** was envisioned as suitable to undergo Scholl or DDQ oxidative coupling to synthesize nanographene-like compounds (7-fused aromatic rings, pyrenoid type).[18] We first attempted the FeCl₃-mediated Scholl reaction, but inconclusive results were obtained. On the contrary, DDQ-based protocol afforded the oxidative fusion of the two phenyl moieties, along with in situ amide hydrolysis and esterification product **5** in 27% (Scheme 5). It is worth mentioning that a 9-fused ring compound was detected in the crude mixture (Figure S9), suggesting that it might also be accessible under modified experimental conditions. This type of transformation opens new opportunities in the use of these multi-ring products as starting scaffolds for bottom-up synthesis of unprecedented nanographene derivatives.[19] We are currently working on widening the scope of diphenylacetylene derivatives in order to expand the size of nanographenes.
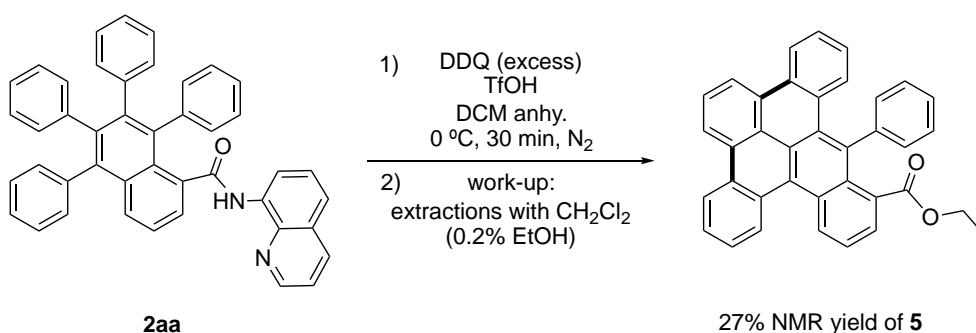
Scheme 5. Adjacent arene fusion reaction of **2aa** via DDQ-mediated oxidative coupling to form nanographene monofunctionalized derivatives **5**.

Conclusions

In summary, we have developed a novel Ni⁰-catalyzed methodology to achieve the C_{sp2}–OMe functionalization using internal alkynes, forming chemoselectively either aromatic homologation or intramolecular monoannulation products upon fine optimization of the reaction. This methodology stands as a new tool to activate C_{sp2}–OMe bonds showing the potential use of aryl-alkyl ethers as alternative electrophiles to aryl halides. Furthermore, aromatic homologation products are proven as valid precursors towards bottom-up nanographene-like synthesis, as a further diversification of the possible uses of these compounds.

Acknowledgments

References

[1]   a) M. Tobisu, N. Chatani, *Acc. Chem. Res.* **2015**, *48*, 1717-1726; b) T. B. Boit, A. S. Bulger, J. E. Dander, N. K. Garg, *ACS Catal.* **2020**, *10*, 12109-12126; c) J. Cornella, C. Zarate, R. Martin, *Chem. Soc. Rev.* **2014**, *43*, 8081-8097.
[2]   a) J. W. Dankwardt, *Angew. Chem. Int. Ed.* **2004**, *43*, 2428-2432; *Angew. Chem.* **2004**, *116*, 2482-2486; b) A. M. Borys, E. Hevia, *Angew. Chem. Int. Ed.* **2021**, *60* 24659-24667; *Angew. Chem.* **2021**, *133*, 24864-24872.
[3]   C. Wang, T. Ozaki, R. Takita, M. Uchiyama, *Chem. Eur. J.* **2012**, *18*, 3482-3485.

[4]   a) S. Z. Tasker, E. A. Standley, T. F. Jamison, *Nature* **2014**, *509*, 299-309; b) M. Tobisu, T. Shimasaki, N. Chatani, *Angew. Chem. Int. Ed.* **2008**, *47*, 4866-4869; *Angew. Chem.* **2008**, *120*, 4944- 4947; c) B. Zhao, T. Rogge, L. Ackermann, Z. Shi, *Chem. Soc. Rev.* **2021**, *50*, 8903-8953.

[5]   a) P. Álvarez-Bercedo, R. Martin, *J. Am. Chem. Soc.* **2010**, *132*, 17352-17353; b) M. Tobisu, K. Yamakawa, T. Shimasaki, N. Chatani, *Chem. Commun.* **2011**, *47*, 2946-2948.

[6]   A. G. Sergeev, J. F. Hartwig, *Science* **2011**, *332*, 439-443.

[7]   Y. Iyori, R. Ueno, A. Morishige, N. Chatani, *Chem. Sci.* **2021**, *12,* 1772-1777.

[8]   M. C. Schwarzer, R. Konno, T. Hojo, A. Ohtsuki, K. Nakamura, A. Yasutome, H. Takahashi, T. Shimasaki, M. Tobisu, N. Chatani, S. Mori, *J. Am. Chem. Soc.* **2017**, *139*, 10347-10358.

[9]   J. Cornella, E. Gómez-Bengoa, R. Martin, *J. Am. Chem. Soc.* **2013**, *135*, 1997-2009.

[10]   R. Rinaldi, R. Jastrzebski, M. T. Clough, J. Ralph, M. Kennema, P. C. A. Bruijnincx, B. M. Weckhuysen, *Angew. Chem. Int. Ed.* **2016**, *55*, 8164-8215; *Angew. Chem.* **2016**, *128*, 8296-8354.

[11]   a) H. Luo, E. P. Weeda, M. Alherech, C. W. Anson, S. D. Karlen, Y. Cui, C. E. Foster, S. S. Stahl, *J. Am. Chem. Soc.* **2021**, *143*, 15462-15470; b) S. Guadix-Montero, M. Sankar, *Top. Catal.* **2018**, *61*, 183-198; c) E. Subbotina, T. Rukkijakan, M. D. Marquez-Medina, X. Yu, M. Johnsson, J. S. M. Samec, *Nat. Chem.* **2021**, *13*, 1118-1125; d) J. Park, H. S. Cahyadi, U. Mushtaq, D. Verma, D. Han, K.-W. Nam, S. K. Kwak, J. Kim, *ACS Catal.* **2020**, *10*, 12487-12506.

[12]   M. Tobisu, N. Chatani, in *Organometallics for Green Catalysis* (Eds.: P. H. Dixneuf, J.-F. Soulé), Springer International Publishing, Cham, **2019**, pp 103-140.

[13]   L. Grigorjeva, O. Daugulis, *Angew. Chem. Int. Ed.* **2014**, *53,* 10209-10212; *Angew. Chem.* **2014**, *126*, 10373-10376.

[14]   a) L. Capdevila, T. H. Meyer, S. Roldán-Gómez, J. M. Luis, L. Ackermann, X. Ribas, *ACS Catal.* **2019**, *9*, 11074-11081; b) A. Das, N. Chatani, *ACS Catal.* **2021**, *11*, 12915-12930.

[15]   V. G. Zaitsev, D. Shabashov, O. Daugulis, *J. Am. Chem. Soc.* **2005**, *127*, 13154-13155.

[16]   F.-J. Chen, S. Zhao, F. Hu, K. Chen, Q. Zhang, S.-Q. Zhang, B.-F. Shi, *Chem. Sci.* **2013**, *4*, 4187-4192.

[17]   S. Inoue, H. Shiota, Y. Fukumoto, N. Chatani, *J. Am. Chem. Soc.* **2009**, *131*, 6898-6899.

[18]   M. Stępień, E. Gońka, M. Żyła, N. Sprutta, *Chem. Rev.* **2017,** *117*, 3479-3716.

[19]   A. Borissov, Y. K. Maurya, L. Moshniaha, W.-S. Wong, M. Żyła-Karwowska, M. Stępień, *Chem. Rev.* **2022,** *122*, 565-788.

CHAPTER VII

Silver(I)-catalyzed C–X, C–C, C–N and C–O cross-coupling using aminoquinoline directing group via elusive aryl-Ag(III) species
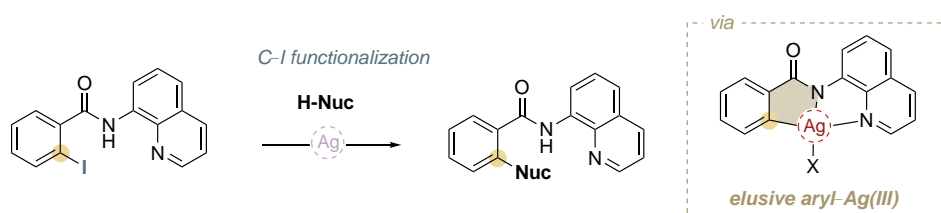
This Chapter corresponds to the following publication:

Reprinted with permission from ACS publications

For this publication L.C. synthesized and characterized the substrates and products. Moreover, L.C. performed all the optimization reactions and catalytic and stoichiometric experiments. L.C. contributed in writing the manuscripts and was involved in all discussions.

Silver(I)-Catalyzed C−X, C−C, C−N, and C−O Cross-Couplings Using Aminoquinoline Directing Group via Elusive Aryl-Ag(III) Species

Lorena Capdevila,[†] Erik Andris,[‡] Anamarija Briš,[‡,§] Màrius Tarrés,[†] Steven Roldán-Gómez,[†] Jana Roithová,*[‡,∥] and Xavi Ribas*[†]

[†]Institut de Química Computacional i Catàlisi (IQCC) and Departament de Química, Universitat de Girona, Campus de Montilivi, Girona, Catalonia E-17071, Spain

[‡]Department of Organic Chemistry, Faculty of Science, Charles University, Hlavova 2030/8, Prague 2 128 43, Czech Republic

[§]Ruđer Bošković Institute, Bijenička 54, Zagreb 10 000, Croatia

[∥]Institute for Molecules and Materials, Radboud University, Heyendaalseweg 135, Nijmegen 6525 AJ, Netherlands

ⓢ *Supporting Information*

ABSTRACT: Cross-coupling transformations are a powerful tool in organic synthesis. It is known that this kind of transformation undergoes 2-electron redox processes, and, for this reason, silver has been nearly forgotten as catalyst for cross-couplings because silver is mainly considered as a 1-electron redox metal. Herein, we disclose effective Ag(I)-catalyzed cross-coupling transformations using bidentate aminoquinoline as a directing group toward different nucleophiles to form C−C, C−N, and C−O bonds. DFT calculations indicate the feasible oxidative addition of **L₁-I** substrate via the Ag(I)/Ag(III) catalytic cycle. Furthermore, ion spectroscopy experiments suggest a highly reactive aryl-Ag(III) that in the absence of nucleophiles reacts to form an intermolecular cyclic product [**5d-Ag(I)-CH₃CN**], which in solution forms **5a**. This work proves that silver can undergo 2-electron redox processes in cross-coupling reactions like Pd and Cu.

KEYWORDS: silver, cross-coupling, two-electron redox catalysis, mass spectrometry, infrared photodissociation spectroscopy
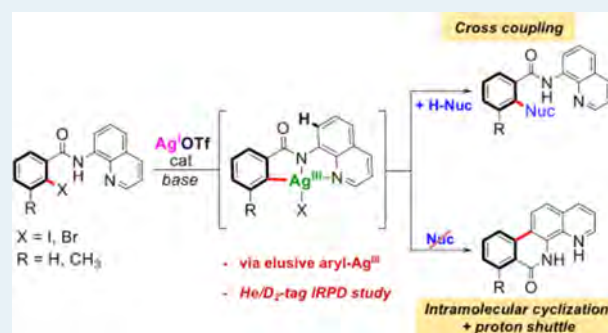
INTRODUCTION

The vast majority of C-heteroatom cross-coupling processes are governed by palladium (C−N, Buchwald−Hartwig) and copper (Ullmann-type) catalysis, constructing a myriad of scaffolds useful as pharmaceuticals, materials, etc.[1−5] However, there is a continuous need to discover new synthetic tools to have in hand versatile solutions for a given cross-coupling transformation. Silver has been completely forgotten in its use as a catalyst for cross-coupling,[6,7] which typically undergoes 2-electron redox processes, because it is generally believed that Ag only shows 1-electron redox chemistry.[8,9] Nevertheless, albeit scarce, there are reports showing that silver catalyzes Sonogashira-type couplings[10] and Ullmann-type C−N and C−O couplings,[11] although with complete lack of mechanistic understanding. In that respect, our group reported the unprecedented experimental evidence that 2-electron redox Ag(I)/Ag(III) catalysis can take place if the right coordination environment is provided to stabilize the key aryl-Ag(III) intermediate species (Scheme 1a−c).[9] It was shown that triazamacrocyclic aryl-Br substrates enforced an ideal square-planar environment to stabilize aryl-Ag(III) species formed through facile oxidative addition at Ag(I). Strikingly, the aryl-Ag(III) species reacted with O- and C-nucleophiles under mild

conditions via 2-electron reductive elimination, and the whole cross-coupling process could be engaged in a catalytic mode.

In the present work, we aim at transferring the Ag-catalyzed cross-coupling reactions into noncyclic aryl-halide substrates by using a bidentate aminoquinoline (AQ) directing group, thus exploring the limits of the transient stabilization of the putative aryl-Ag(III) in a nonconstrained system. To that end, we used **L₁-I** as a model substrate (see Figure 1) and investigated the silver catalysis for halide exchange reactions, Ullmann-type C−N and C−O couplings, and Hurtley-type C−C couplings with active methylene nucleophiles.[12−14] The implication of putative aryl-Ag(III) species has been analyzed by helium and D₂ tagging infrared photodissociation (IRPD) spectroscopy[15−19] and will be discussed in detail.

RESULTS AND DISCUSSION

We had previously shown that well-defined aryl-Ag(III) could undergo reductive elimination with different halides to effectively afford the halide exchange reaction within aryl-halide triazamacrocycles.[9] More importantly, the system was

Scheme 1. (a) Ag-Catalyzed Sonogashira-type Coupling; (b) Ag-Catalyzed Ullmann-type C–N and C–O Reaction; and (c) Ag-Catalyzed C–O and C–C Bond-Forming Cross-Coupling Reaction[9]

Figure 1. Macrocyclic model[9] and open model system were compared in the oxidative addition step.

Table 1. Ag-Catalyzed Halide Exchange Reactions

X = I, Br, Cl, F

entry	L$_1$-X	nBu$_4$NX	yield (%)^a (yield in CH$_3$CN)
1	L$_1$-I	nBu$_4$NCl	82% (95%) L$_1$-Cl
2^b			20% L$_1$-Cl
3		nBu$_4$NBr	74% (46%) L$_1$-Br
4^b			0% L$_1$-Br
5^c		nBu$_4$NF·3H$_2$O	0% L$_1$-F
6	L$_1$-Br	nBu$_4$NCl	78% L$_1$-Cl
7^b			0% L$_1$-Cl
8		nBu$_4$NI	0% (38%,^{d} 50%^{e}) L$_1$-I
9	L$_1$-Cl	NaI	0% L$_1$-I

^{a}Yield calculated from ^{1}H NMR of crude using trimethoxybenzene as internal standard. ^{b}The reaction was carried out without AgOTf. ^{c}Using 10 mol % of AgF. Side reaction was observed (34% yield of L$_1$-DMSO). ^{d}Using 20 mol % of AgOTf. ^{e}Using 20 mol % of AgOTf and 20 mol % of PPh$_3$.

The high reaction temperatures needed to achieve the halide exchange suggested a significantly higher energy barrier for the oxidative addition step in L$_1$-I than in the triazamacrocyclic aryl-I model substrate, where the reaction was conducted at room temperature (in agreement with DFT study, see below). When L$_1$-Br was used as substrate with nBu$_4$NX salts (X = Cl, I), the Br-to-Cl exchange was optimized in DMSO affording up to 78% yield. On the other hand, the Br-to-I exchange could only be optimized to afford a 38% yield in CH$_3$CN when 20 mol % of AgOTf was used as catalyst. This could be increased up to 50% when 20 mol % of PPh$_3$ was used as an additive (we also observed the beneficial use of PPh$_3$ as additive in cross-coupling catalysis using the triazamacrocyclic aryl-I substrate).[9] When L$_1$-Cl was used as substrate, no halide exchange reaction occurred, and L$_1$-Cl was fully recovered, presumably due to the unsurmountable energetic barrier for the oxidative addition under these conditions.

Given that the halide-exchange catalysis proved that the activation of aryl-I and aryl-Br was feasible via silver catalysis, we aimed at exploring the ability of generating C–N heteroatom bonds, using aliphatic amines as nucleophiles, as well as imidazole and anilines (Table 2). Under optimized conditions (DMSO as solvent and CsF as base), couplings with cyclohexanamine and cyclopentanamine afforded moderate yields of the coupling products (37−53% yield), as depicted in Table 2. Similarly, when imidazole was used, the coupling product **2c** was obtained in 59% yield. We then tested *para*-substituted anilines (NO$_2$- or MeO-), and they afforded a 79% yield of **2d** (NO$_2$) and a moderate 33% yield of **2f** (OMe). The beneficial electron-withdrawing effect of the NO$_2$ group suggested that the underlying mechanism for C–N couplings might be related to a facile deprotonation of the N-nucleophile.

We then explored the silver-catalyzed aryl-O cross-couplings with phenols bearing different *para*-substituents (R = H, Cl, OMe, NO$_2$) (Table 3). In this case, reactions were optimized in DMSO and tBuOK as a base. Good yields were obtained for phenol (73%, **3a**) and *p*-Cl-phenol (74%, **3b**), whereas low yield was obtained when electron-donating *p*-MeO-phenol was used (38%, **3c**). Surprisingly, the reaction was completely

catalytic in Ag(I) for the aryl-iodide to aryl-Br exchange. In this work, we started by analyzing the ability of Ag(I) to catalyze the halide exchange reactions using noncyclic aryl-halide substrates bearing an aminoquinoline bidentate directing group (DG), ligands L$_1$-X, L$_2$-X (X = I, Br, Cl, F; Figure 1). This noncyclic model substrate enforces a square-planar coordination upon oxidative addition at Ag(I), reduces from three to two the number of N-coordination sites as compared to the triazamacrocyclic substrates, and loses the macrocyclic effect.

Thus, we analyzed first the viability of this halide exchange catalysis using L$_1$-I with nBu$_4$NX salts (X = Cl, Br). After optimization, we found that the catalysis was effective at 100 °C for the coupling with Cl and Br using 10 mol % of Ag(I)OTf (see Table 1). The catalysis can be performed in CH$_3$CN or DMSO solvents, affording good-to-excellent yields.

Table 2. Ag-Catalyzed C−N Bond-Forming Reactions

Entry	Nuc.	Yield (%)[a]	Conv. (%)
1[b]	cyclohexyl-NH₂	53 % (51 %) 2a	>99 %
2[c]		0 % 2a	5 %
3[b]	cyclopentyl-NH₂	37 % (31 %) 2b	>99%
4	imidazole	59 % (54 %) 2c	71 %
5	O₂N-phenyl-NH₂	79 % (61 %) 2d	>99%
6[d]		85 % (59 %) 2e	>99 %
7[b]	MeO-phenyl-NH₂	33 % (30 %) 2f	86 %

[a]Yield calculated from ^{1}H NMR of crude using trimethoxybenzene as internal standard (isolated yield in parentheses). [b]Side reactions were observed: 18% of L_1-H and 19% of L_1-L_1 homocoupling (entry 1), 10% of L_1-H and 18% of L_1-L_1 homocoupling (entry 3), traces of L_1-H and 10% of L_1-L_1 homocoupling (entry 7). [c]The reaction was carried out without AgOTf. [d]Using L_2-I as a substrate.

Table 3. Ag-Catalyzed C−O Bond-Forming Reactions

Entry	Nuc.	Yield (%)[a]	Conv. (%)
1	Cl-phenyl-OH	74 % (73 %) 3a	73 %
2[b]		12 % 3a	19 %
3	phenyl-OH	73 % (60 %) 3b	94 %
4[c]	MeO-phenyl-OH	38 % (22 %) 3c	71 %
5	O₂N-phenyl-OH	0 % 3d	12 %
6[d]	H₃C-OH	12 % 3e	66 %
7[d]		21 % (13 %) 3e	73 %
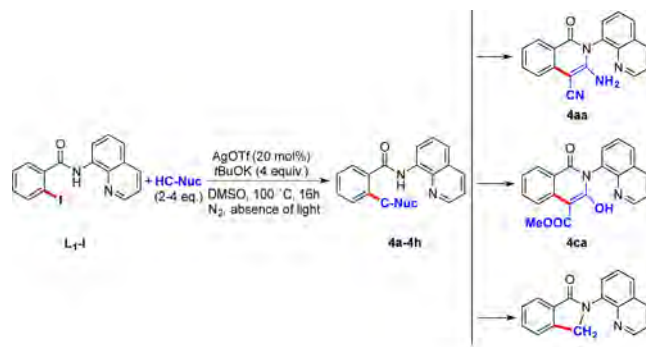
[a]Yield calculated from ^{1}H NMR of crude using trimethoxybenzene as internal standard (isolated yield in parentheses). [b]The reaction was carried out without AgOTf. [c]32% of L_1-H. [d]Using 2.5 mL of MeOH instead of DMSO; 10 mol % of AgOTf was used (entry 6).

ineffective when p-NO₂-phenol was used as nucleophile. These results suggest that deprotonation is not a key step in the C−O coupling reaction and that a correct electronic balance is needed to achieve the desired coupling products. We also attempted the cross-coupling catalysis with CH₃OH as nucleophile, but only stoichiometric amounts of the desired

3e coupling product were obtained when 10 and 20 mol % of AgOTf were used (CH₃OH as solvent and tBuOK as a base).

Finally, C−C cross-couplings were explored using activated methylene-type substrates (Hurtley-type couplings), nitromethane and p-MeO-phenylboronic acid (Table 4). Under

Table 4. Ag-Catalyzed C−C Bond-Forming Reactions

Entry	Nuc.	Yield (%)[a]	Conv.(%)
1	NC—CN	74 % (71 %) 4aa[b]	99 %
2[c]		0 % 4aa	16 %
3	EtO(O)—CN	48 % (41 %) 4b / 9 % 4ba	99 %
4[d]	MeO(O)(O)OMe	62 % 4ca	63 %
5[e]	diketone	0 % 4d	64 %
6	EtO(O)—NO₂	0 % 4e	19 %
7[e]	H₃C—NO₂	59 % (47 %) 4fa	99 %
8[f]	MeO-phenyl-B(OH)₂	20 % (15 %) 4g	57 %
9[f]	O₂N-phenyl-B(OH)₂	0 % 4h	71 %

[a]Yield calculated from ^{1}H NMR of crude using trimethoxybenzene as internal standard (isolated yield in parentheses). [b]90% of 4aa was obtained using CH₃CN as solvent. [c]The reaction was carried out without AgOTf. [d]The reaction was carried out using DMSO-d_6. [e]Side reactions were observed: 15% of L_1-H (entry 5) and 16% of L_1-DMSO (entry 7). [f]The reaction was carried out using 10 equiv of arylboronic acid at 120 °C.
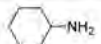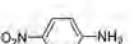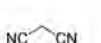
the optimized conditions (DMSO as solvent, tBuOK as a base, and 20 mol % AgOTf), malononitrile afforded a 74% yield of the coupling product 4aa, which consists of an initial C−C coupling and a subsequent cyclization by nucleophilic attack of the amide to one of the −CN groups (entry 1). The blank experiment did not afford 4aa (entry 2). The same product 4aa was obtained in 90% yield in CH₃CN, but some degree of decomposition of acetonitrile to form trimeric triazine-coupled product was observed,[20] and thus the solvent of choice was DMSO for the other C-nucleophiles. When ethyl 2-cyanoacetate was used, 48% yield of 4b was obtained (entry 3), which is the C−C coupling product without further intramolecular reorganization. In this case, only 9% yield of

4ba, the intramolecular cyclization product analogous to **4aa**, was obtained. On the other hand, dimethyl malonate afforded 62% yield of **4ca**, which corresponds to the cyclic product formed by a nucleophilic attack of the amide to one of the carbonyl groups (with loss of MeOH). In the case of acetylacetone and ethyl 2-nitroacetate, the catalysis was completely ineffective. Surprisingly, nitromethane worked well as nucleophile yielding a 59% yield of **4fa**, which bears an isoindolin-1-one formed after the loss of the nitro group. Also, 16% of **L₁-DMSO** is obtained (coupling of a deprotonated DMSO solvent molecule).

Finally, arylboronic acids were also tested due to the effective reductive elimination observed using the triazama-crocyclic aryl-Ag(III) species.[9] In the noncyclized substrate, only 20% yield of the biaryl C−C coupling product **4g** was obtained, suggesting that transmetalation and reductive elimination occurred but the system could not enter into catalytic turnover. When *p*-NO₂-phenylboronic acid was used, no coupling product was obtained, presumably because of the destabilizing effect of the electron-withdrawing group over the Ag(III) center.

Discarding Contamination of Other Metals. Given the unusual two-electron redox Ag(I)/Ag(III) reactivity, we analyzed two AgOTf commercial samples by ICP-MS searching the content of traces of other possibly active metals in cross-coupling reactions, specifically Pd and Cu. No traces of Pd were found, and 0.01% content of Cu was determined in two batches of AgOTf. We then reproduced three of the above coupling reactions using [Cu(CH₃CN)₄]OTf as catalyst at 0.002 mol % (the content of Cu traces when using a 20 mol % AgOTf). No significant product yields were found (Table 5).

Table 5. Comparison of Coupling Reactions Catalyzed by Ag or Cu Impurities

		Yield (Conv.)		
Entry	Nuc.	Ag(OTf) (20 mol%)	Cu(OTf)ᵃ (0.002%)	Cu(OTf)₂ (0.002%)
1	(cyclohexyl)−NH₂	53 % of **2a** (99%)	6 % of **2a** (6%)	9 % of **2a** (24%)
2	O₂N−(phenyl)−NH₂	79 % of **2d** (99 %)	24 % of **2d** (24 %)	−
3	NC⌒CN	74 % of **4aa** (99 %)	0 % of **4a/4aa** (36 %)	12% of **4aa** (37%)

ᵃUsing [Cu(CH₃CN)₄]OTf.

In addition, the coupling reactions were also tested in the presence of Cu(OTf)₂, which might have a role if Ag(0) was formed in situ and was reoxidized to Ag(I). Again, no significant yields were obtained. Therefore, yields obtained using 0.002 mol % [Cu(CH₃CN)₄]OTf or Cu(OTf)₂ in the coupling catalysis tested clearly discard any significant role of Cu and underline silver as the main catalyst (Table 5).

To further discard the activity of other impurities, small contents of HOTf, a typical impurity in triflate salts, were added in AgOTf-catalyzed halide exchange reactions. The reactions in Table 1, entries 3 and 6, were repeated using 10 mol % AgOTf and HOTf (5% with respect to AgOTf), and smaller yields were obtained in both cases (55% of **L₁-Br** and

68% of **L₁-Cl**, respectively), discarding any beneficial role of triflic acid impurities.

Computational Insight into the Mechanism of the Ag-Catalyzed Cross-Couplings. To gain insight into the role of silver in the catalysis mechanism, DFT studies (see the Supporting Information for details) were performed focusing on the I-to-Cl halide exchange reaction (Figure 2). We
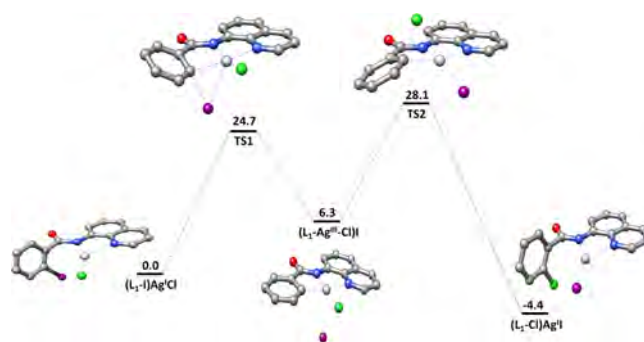
Figure 2. Gibbs energy profile of the oxidative addition and reductive elimination steps in the **L₁-I-to-L₁-Cl** halide exchange reaction.

determined that the aryl-I oxidative addition step (TS1) lies at 24.7 kcal mol⁻¹, rendering the key [**L₁-Ag(III)-Cl**](I) species. The latter shows a square-pyramidal geometry with I at the apical position (d_{Ag-I} = 3.7 Å), conforming to a d⁸ electronic configuration for Ag(III) in a manner analogous to that of well-defined aryl-Ag(III) species isolated in triazamacrocyclic scaffolds.[9] [**L₁-Ag(III)-Cl**](I) undergoes subsequent aryl-Cl reductive elimination (TS2 = 28.1 kcal mol⁻¹) to obtain the final (**L₁-Cl**)AgI compound. The barrier of 28.1 kcal mol⁻¹ agrees with the high temperature (100 °C) needed for the reaction to take place. It is noteworthy that the reverse reaction, formally the aryl-Cl oxidative addition, has a larger barrier (up to 32.5 kcal mol⁻¹) and conforms to the unobserved halide exchange when **L₁-Cl** is used as substrate.

Experimental IRPD-MS Analysis of Operando Catalysis. Aiming for direct experimental proof of aryl-Ag(III) active species, we applied high-resolution mass spectrometry (HRMS) and helium tagging infrared photodissociation (IRPD) spectroscopy to our system.[16−19] Initial HRMS analysis at short reaction times of the reactions using **L₁-I** and stoichiometric amounts of silver salt in CH₃CN (suitable solvent for the HRMS analysis) showed significant amounts of C−N homocoupling products. This result was a good indication of aryl-I activation but complicated the analysis. To simplify the reaction and the ulterior analysis, we designed the *o*Me-L₁-I (**L₂-I**) substrate to minimize the formation of homocoupling products by steric hindrance. For instance, using **L₂-I** as a substrate and *p*NO₂-aniline as a nucleophile for the silver-catalyzed C−N coupling affords 85% of **2e**. Focusing on the MS study, no nucleophile was added to the reaction to analyze only the putative [**L₂-Ag(III)**]⁺ species formed by aryl-I oxidative addition at Ag(I). The main peak observed at *m/z* 494.9088 presumably corresponded to [(**L₂-I**)Ag]⁺ (Figure S1). Noteworthy, a small peak at *m/z* 366.9987 was detected, tentatively assigned to [**L₂-Ag(III)**]⁺.

To identify the structure of the detected silver complexes, we have recorded their IRPD spectra. It turned out that the theoretically predicted IR spectrum of [(**L₂-I**)Ag]⁺ nicely reproduced the IRPD spectrum of the ions with *m/z* 495 (Figure 3).[21−26] It clearly confirmed that the detected *m/z* 495

Figure 3. (a) Helium tagging IRPD spectra of ions with m/z 495. (b) Theoretical IR spectrum (B3LYP[21−24]-D3BJ[25,26]/6-311+g(2d,p):SDD-(Ag,I)) of $[(\mathbf{L_2\text{-}I})\text{-}\mathbf{Ag(I)}]^+$. The scaling factor was 0.98 (below 2000 cm^{-1}) and 0.96 (above 2000 cm^{-1}). Predicted IR intensities above 2700 cm^{-1} were multiplied by 10.

Figure 4. (a) D$_2$ tagging IRPD spectra of ions with m/z 408. (b) Theoretical IR spectra (B3LYP-D3BJ/6-311+g(2d,p):SDD-Ag) of $[\mathbf{L_2}\text{-}\mathbf{Ag(III)}\text{-}\mathbf{CH_3CN}]^+$ and $[\mathbf{5d}\text{-}\mathbf{Ag(I)}\text{-}\mathbf{CH_3CN}]^+$. The harmonic IR spectra are in black; the scaling factor was 0.98 (below 2000 cm^{-1}) and 0.96 (above 2000 cm^{-1}). The anharmonic IR spectra (B3LYP-D3BJ/6-311+g(2d,p):SDD-Ag) are in red and were not scaled. Predicted IR intensities above 2700 cm^{-1} were multiplied by 10.

Scheme 2. Suggested Mechanism of the Formation of $[\mathbf{5a}\text{-}(\mathbf{Ag(I)}\text{-}\mathbf{CH_3CN})]$, the Experimentally Observed Intermediate

ion peak corresponds to the Ag(I) complexation to $\mathbf{L_2\text{-}I}$. The putative silver(III) intermediate (m/z 367) was detected as a complex with acetonitrile at softer ionization condition (m/z 408). We assumed that acetonitrile fills in the fourth coordination site of the silver(III) complex and therefore stabilizes this intermediate. However, the experimental IRPD spectrum of the ions with m/z 408 and the theoretical spectrum of the proposed $[\mathbf{L_2}\text{-}\mathbf{Ag(III)}\text{-}(\mathbf{CH_3CN})]^+$ intermedi-

ate did not agree. In particular, the theoretical spectrum of this Ag(III) complex did not contain any bands that could be attributed to the experimental peaks at 1110 and 2770 cm^{-1}. The search for alternative structures resulted in finding a series of more stable complexes with the same mass (see Figure S4). The theoretical IR spectrum for the complex [**5d-Ag(I)-CH$_3$CN**]$^+$ resulting from an intramolecular cyclization conformed to the experimental spectrum (Figure 4).

The formation of [**5d-Ag(I)-CH$_3$CN**]$^+$ was rationalized as depicted in Scheme 2. The first species formed is the coordination of Ag(I) to the substrate (m/z 495), which undergoes oxidative addition, formal loss of HI, and coordination of one CH$_3$CN molecule to transiently form the sought [**L$_2$-Ag(III)-(CH$_3$CN)**]$^+$. Because IRPD analysis discarded that m/z 408 corresponded to the latter species, [**5d-Ag(I)-CH$_3$CN**]$^+$ was formed in the gas phase as an intramolecular cyclization of the transient aryl-Ag(III) via formation of a Ag(I) complex bearing a cationic benzenylium moiety (a theoretical energy of 17 kcal mol^{-1} was calculated for this intermediate), which rapidly collapses to produce [**5d-Ag(I)-CH$_3$CN**]$^+$. In solution, further proton-shuttle affords [**5a-Ag(I)-CH$_3$CN**]$^+$, isolating 10-methylbenzo[c][1,10]-phenanthrolin-6(5H)-one (**5a**) as the final organic product.

To clarify whether [**5d-Ag(I)-CH$_3$CN**]$^+$ was only formed in the gas phase or if it was also formed in the reaction mixture, we repeated the reaction at ~0.1 g scale to isolate the products of the reaction of **L$_2$-I** and AgClO$_4$ in the presence of Na$_2$CO$_3$. Upon optimization (100 °C, 24 h), analysis by HRMS of the reaction crude indicated that a compound at m/z 261 appeared mixed with starting **L$_2$-I** and byproducts. After chromatographic purification of the 261 peak, NMR and HRMS characterization confirmed the formation of the intramolecular cyclization organic product (**5a**) (Scheme 3), which results from a tautomerization of tautomer of **5d**.

Global Mechanism. The mechanistic proposal depicted in Scheme 3 is derived from all of the experimental and theoretical results disclosed in this work. The initial step of the reaction conforms to an aryl-halide oxidative addition that converges into the key aryl-Ag(III) species. This species is at a crossroads depending on whether the nucleophile is present in the reaction mixture. If present, nucleophile coordination and reductive elimination affords the desired coupling product following a 2-electron Ag(I)/Ag(III) catalysis. If absent, the highly reactive aryl-Ag(III) species undergoes an intra-molecular cyclization reaction to form the experimentally characterized 10-methylbenzo[c][1,10]phenanthrolin-6(5H)-one (**5a**) species.

CONCLUSIONS

The ability of silver to undergo noncanonical 2-electron redox Ag(I)/Ag(III) cross-coupling catalysis for C−heteroatom and C−C bond formation has been successfully proven for a noncyclic substrate bearing an aminoquinoline bidentate DG (**L$_1$-I**). Contrary to the rigid triazamacrocyclic model first used to isolate a well-defined aryl-Ag(III) complex, the noncyclic **L$_1$-I** supports the same kind of intermediate species but is much more reactive. Despite our attempts to directly detect organometallic aryl-Ag(III) species, those remained elusive, although their existence is clearly inferred experimentally and theoretically in the four kinds of cross-coupling catalysis studied (halide exchange, C−N, C−O, and C−C couplings), and also in the IRPD-MS studies without nucleophile. The sharply enhanced reactivity of this species in noncyclic

Scheme 3. Global Mechanistic Proposal in Solution
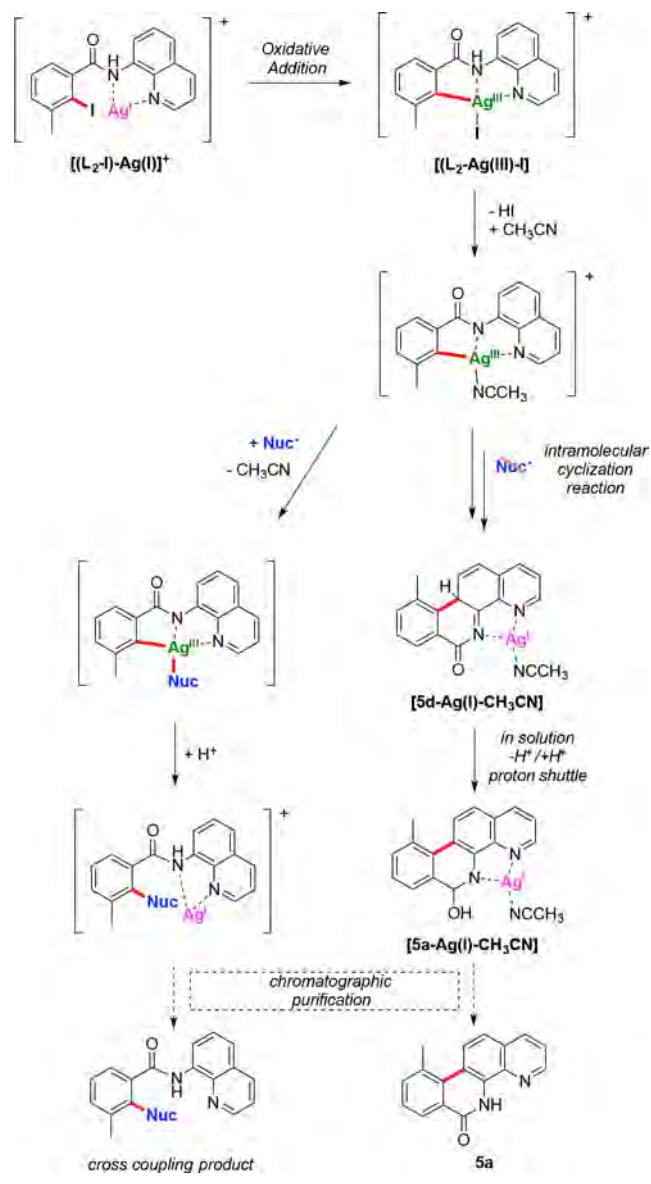
substrates as compared to macrocyclic substrates was also observed when studying Cu(III) intermediate species.[18] We envision that this work might trigger more research efforts on Ag-catalyzed cross-couplings, to further evaluate its use as an actual synthetic tool in organic synthesis, complementary to the well-known Pd(0)/Pd(II) and Cu(I)/Cu(III).

ASSOCIATED CONTENT

Ⓢ Supporting Information

The Supporting Information is available free of charge on the ACS Publications website at DOI: 10.1021/acscatal.8b03257.

Detailed spectroscopic characterization, computational DFT data, and technical details of the IRPD experiments (PDF)

AUTHOR INFORMATION

Corresponding Authors
*E-mail: jana.roithova@ru.nl.
*E-mail: xavi.ribas@udg.edu.

ORCID ⊙

Jana Roithová: 0000-0001-5144-0688

Xavi Ribas: 0000-0002-2850-4409

Notes

The authors declare no competing financial interest.

■ REFERENCES

(1) Hickman, A. J.; Sanford, M. S. High-valent organometallic copper and palladium in catalysis. *Nature* **2012**, *484*, 177−185.

(2) Wolfe, J. P.; Wagaw, S.; Marcoux, J.-F.; Buchwald, S. L. Rational Development of Practical Catalysts for Aromatic Carbon-Nitrogen Bond Formation. *Acc. Chem. Res.* **1998**, *31*, 805−818.

(3) Hartwig, J. F. Carbon-Heteroatom Bond-Forming Reductive Elimination of Amines, Ethers and Sulfides. *Acc. Chem. Res.* **1998**, *31*, 852−860.

(4) Casitas, A.; Ribas, X. The role of organometallic copper(III) complexes in homogeneous catalysis. *Chem. Sci.* **2013**, *4*, 2301−2318.

(5) Evano, G.; Blanchard, N. *Copper-Mediated Cross-Coupling Reactions*; John Wiley & Sons: Hoboken, 2014.

(6) Weibel, J.-M.; Blanc, A. l.; Pale, P. Ag-Mediated Reactions: Coupling and Heterocyclization Reactions. *Chem. Rev.* **2008**, *108*, 3149−3173.

(7) Font, M.; Ribas, X. Pincerlike Cyclic Systems for Unraveling Fundamental Coinage Metal Redox Processes. In *The Privileged Pincer-Metal Platform: Coordination Chemistry & Applications*, van Koten, G., Gossage, R. A., Eds.; Springer International Publishing: New York, 2016; Vol. 54, pp 269−306.

(8) Mijs, W. J.; Jong, C. R. H. I. d. *Organic Synthesis by Oxidation with Metal Complexes*; Plenum Press: New York, 1986.

(9) Font, M.; Acuña-Parés, F.; Parella, T.; Serra, J.; Luis, J. M.; Lloret-Fillol, J.; Costas, M.; Ribas, X. Direct observation of two-electron Ag(I)/Ag(III) redox cycles in coupling catalysis. *Nat. Commun.* **2014**, *5*, 4373.

(10) Li, P.; Wang, L. A Novel Silver Iodide Catalyzed Sonogashira Coupling Reaction. *Synlett* **2006**, *2006*, 2261−2265.

(11) Das, R.; Mandal, M.; Chakraborty, D. Silver-Nitrate-Catalyzed N-Arylation of Amines and O-Arylations of Phenols and Alcohols. *Asian J. Org. Chem.* **2013**, *2*, 579−585.

(12) Rovira, M.; Soler, M.; Güell, I.; Wang, M.-Z.; Gómez, L.; Ribas, X. Orthogonal Discrimination among Functional Groups in Ullmann-Type C−O and C−N Couplings. *J. Org. Chem.* **2016**, *81*, 7315−7325.

(13) Ribas, X.; Güell, I. Cu(I)/Cu(III) catalytic cycle involved in Ullmann-type cross-coupling reactions. *Pure Appl. Chem.* **2014**, *86*, 263−467.

(14) Rovira, M.; Font, M.; Ribas, X. Model Csp2-Csp3 Hurtley Coupling Catalysis that Operates through a Well-Defined Cu(I)/Cu(III) Mechanism. *ChemCatChem* **2013**, *5*, 687−691.

(15) Jašík, J.; Gerlich, D.; Roithová, J. Two-Color Infrared Predissociation Spectroscopy of C6H62+ Isomers Using Helium Tagging. *J. Phys. Chem. A* **2015**, *119*, 2532−2542.

(16) Jašík, J.; Žabka, J.; Roithová, J.; Gerlich, D. Infrared spectroscopy of trapped molecular dications below 4 K. *Int. J. Mass Spectrom.* **2013**, *354−355*, 204−210.

(17) Roithova, J. Characterization of reaction intermediates by ion spectroscopy. *Chem. Soc. Rev.* **2012**, *41*, 547−559.

(18) Rovira, M.; Jasikova, L.; Andris, E.; Acuna-Pares, F.; Soler, M.; Guell, I.; Wang, M.-Z.; Gomez, L.; Luis, J. M.; Roithova, J.; Ribas, X. A Cu(I)/Cu(III) prototypical organometallic mechanism for the deactivation of an active pincer-like Cu(I) catalyst in Ullmann-type couplings. *Chem. Commun.* **2017**, *53*, 8786−8789.

(19) Roithová, J.; Gray, A.; Andris, E.; Jašík, J.; Gerlich, D. Helium Tagging Infrared Photodissociation Spectroscopy of Reactive Ions. *Acc. Chem. Res.* **2016**, *49*, 223−230.

(20) Zhaoxiang, D.; Wenfeng, Q.; Weijia, L.; Yadong, L. Cyclo-trimerization of nitriles catalyzed by Li_3N. *Chin. Sci. Bull.* **2004**, *49*, 127−130.

(21) Becke, A. D. Density-functional thermochemistry. III. *J. Chem. Phys.* **1993**, *98*, 5648−5652.

(22) Lee, C.; Yang, W.; Parr, R. G. Development of the Colle-Salvetti correlation-energy formula into a functional of the electron density. *Phys. Rev. B: Condens. Matter Mater. Phys.* **1988**, *37*, 785−789.

(23) Miehlich, B.; Savin, A.; Stoll, H.; Preuss, H. Results obtained with the correlation energy density functionals of becke and Lee, Yang and Parr. *Chem. Phys. Lett.* **1989**, *157*, 200−206.

(24) Stephens, P. J.; Devlin, F. J.; Chabalowski, C. F.; Frisch, M. J. Ab Initio Calculation of Vibrational Absorption and Circular Dichroism Spectra Using Density Functional Force Fields. *J. Phys. Chem.* **1994**, *98*, 11623−11627.

(25) Grimme, S.; Antony, J.; Ehrlich, S.; Krieg, H. A consistent and accurate ab initio parametrization of density functional dispersion correction (DFT-D) for the 94 elements H-Pu. *J. Chem. Phys.* **2010**, *132*, 154104.

(26) Grimme, S.; Ehrlich, S.; Goerigk, L. Effect of the damping function in dispersion corrected density functional theory. *J. Comput. Chem.* **2011**, *32*, 1456−1465.

CHAPTER VIII

Results and Discussions

Unravelling the mechanistic details at molecular level is crucial to develop more efficient routes to construct C–C and C–Heteroatom bonds. It has already been demonstrated the stability offered by the macrocyclic model substrates to stabilize metals in a high oxidation state.[1, 2] A precise coordination environment and geometry around the metal center is crucial to stabilize the key intermediates and, therefore, it is essential to design the correct model substrate platform for the system to be studied. The use of triazamacrocyclic ligands allows the isolation of key intermediates in C–X and C–H activation transformations, shedding light in some fundamental steps such as the formation of the organometallic C–M bond, which is proposed as one of the initial steps of these reaction. Despite the progress done in unraveling the molecular mechanism of these transformations, the detailed understanding of the C–M bond cleavage and the concomitant functionalization step remains unclear due to the high reactivity of these intermediates. In the context of the chelation-assisted metal-catalyzed C–H functionalization reactions, the use of substrates bearing a directing group as a non-cyclic open model platform to trap key intermediates species in catalytic systems has received lots of interest. In addition, the activation of stronger bonds (C–F, C–O-alkyl and C–H) is a hot topic, since it opens the door to the development of new methodologies for the C–C and C–Heteroatom bonds.

In this framework, QBIS-CAT group has successfully employed triazamacrocyclic scaffolds for the isolation and characterization of high-valent metal species, which are catalytically competent intermediates in C–X and C–H transformations.[3-8] Therefore, we targeted the fundamental mechanistic understanding of cobalt-mediated aryl–N bond formation reactions using an arene-containing macrocyclic model substrate with organic azides as aminating reagent. Moreover, the directing group-assisted strategy was applied to achieve the Ni-catalyzed activation of strong bonds (C–F and C–OMe) in a regioselective manner. In addition, we developed novel Ag-based cross-coupling methodologies under a 2-electron redox regime.

In Chapter VIII.1 we describe the advances made in the recent years on Co-catalyzed cross-coupling reactions pointing out the potential use of cobalt to catalyze C–C and C–Heteroatom bond-forming transformations.

In Chapter VIII.2 we describe the reactivity of well-defined Oh aryl–Co(III) compounds towards inorganic and organic azides, focusing on the intramolecular aryl–N bond formation using aliphatic azides. A detailed mechanistic pathway for the C–H amination reaction mediated by high-valent Co(III) complex will be disclosed with crystallographic, spectroscopic and theoretical evidences. A thorough DFT study shows the stabilizing masking effect of the carboxylate moiety to the nitrenoid group, which is accompanied by a facile S_N2-like attack to render the aryl–N coupling product. This in-situ masking strategy guide the reaction to an efficient intramolecular C–N coupling, in contrast to the uncontrolled reactivity when no masking carboxylate is present.

In Chapter VIII.3 we describe the selective Ni-catalyzed C–F bond activation over the C–H bond assisted by 8-aminoquinoline as bidentate directing group. The use of internal alkynes as coupling partner renders either alkyne monoannulation or aromatic homologation product in a chemodivergent manner. The key removal of the fluoride anion assisted by Li^+ was supported by DFT studies, pointing out the crucial role of Li^+ in the catalytic turnover. We also report the crystallographic evidence of an unprecedented nickel acyclic intermediate species in aromatic homologation reactions.

Chapter VIII.4 describes the nickel-catalyzed C–OMe functionalization using alkynes and a directing group approach. The reaction shows in a selective manner the formation of aromatic homologation product adding LiOTf. In contrast, the presence of PPh_3 in the reaction switch the reactivity for the formation of alkyne monoannulation product. We

also report the synthesis of nanographene-like compound using the aromatic homologation product as a precursor, opening the door to further diversifications of these products.

Chapter VIII.5 discloses the Ag(I)-catalyzed cross-coupling reactions assisted by 8-aminoquinoline directing group. C–C and C–Heteroatom bond formation reactions has successfully achieved using different nucleophiles. Mechanistic investigations combining both DFT and IRDP-MS studies suggest a highly reactive aryl-Ag(III). In the absence of nucleophile, these species react intramolecularly to form a cyclic product observed experimentally.

<u>Note</u>: the numbering of metal complexes as well as the organic coupling compounds is in accordance within each chapter (VIII.2 to VIII.5) and refers to the numbering used in the corresponding original publications.

VIII.1. Cobalt-catalyzed cross-coupling reactions

This section corresponds to the content of the book chapter entitled "Cobalt-catalyzed cross-coupling reactions" by Lorena Capdevila and Xavi Ribas. In: Chemistry of organocobalt compounds; Ilan Marek and Corinne Gosmini (eds); Wiley & Sons 2022, DOI:10.1002/9780470682531.PAT0995, which can be found in Chapter III of this thesis.

In the past years, it has been demonstrated the potential of first-row transition metals to catalyze cross-coupling reactions. Since the first reports on Co-mediated homocoupling reactions by Gilman in 1939,[9] the use of Co catalyst has flourished and many examples have been reported. This chapter catch up on the important advances made in the field of cobalt-catalyzed cross-coupling transformations. This field is dominated by the construction of C–C bonds using organomagnesium reagents involving the activation of $C(sp^3)$–X, $C(sp^2)$–X and $C(sp)$–X bonds. In addition, different activated nucleophiles such as organozinc and organoboron reagents have also been used in these transformations. Additionally, this chapter also covers different mechanistic aspects concerning the redox chemistry of cobalt involved in the C–C bond formation processes. Finally, the last part is an update of the C–Heteroatom coupling reactions catalyzed by cobalt (C–N, C–O, C–S and C–P).

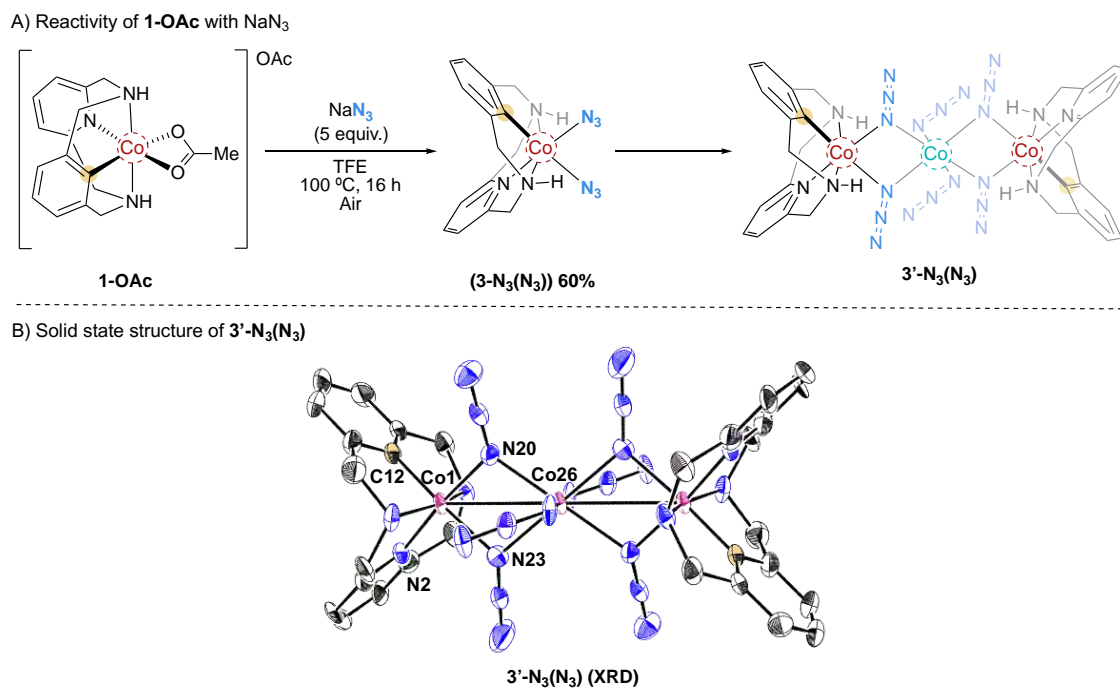## VIII.2. C$_{sp2}$–H amination reactions mediated by metastable Oh masked aryl–Co^{III}-nitrene species

This section corresponds to the content of the manuscript by Lorena Capdevila, Marc Montilla, Oriol Planas, Artur Brotons, Pedro Salvador, Vlad Martin-Diaconescu, Teodor Parella, Josep M. Luis, Xavi Ribas (submitted), which can be found in Chapter IV of this thesis.

Direct C–H functionalization approach has become a straightforward strategy for the construction of a variety of compounds. In this context, the development of high-valent Cobalt systems remained dormant until 2013, when Matsunaga and Kanai disclosed the first catalytic C–H functionalization using a high-valent cobalt catalyst.[10] However, in contrast to C–C bond formation reactions, direct C–N bond amination reactions using cobalt catalyst is less studied and few examples has been reported using Cp*Co(III)-based catalysts.[11-13] Although highly reactive Oh high valent M(V)=NR intermediate species are proposed, the operando mechanism of these transformation is still unclear, with no direct evidence of these key intermediates. With these considerations, the use of arene macrocyclic model system can shed light to the mechanism involved in C–H amination transformation mediated by high-valent Cobalt complexes.

Inspired by the results obtained by our group using a 12-membered macrocyclic model ligand, which is able to stabilize the aryl–Co(III) organometallic complex,[5, 6, 8] we decided to explore its reactivity towards inorganic and organic azides to pursue the C–N bond formation and to shed light to the plausible mechanism of the transformation. The **L-H** and **L-Me** ligands, the well-defined aryl–Co(III) complex (**1-OAc, 1-COOR and 1$_{Me}$-OAc**) and the analogous aryl–Rh(III) complex (**2-OAc and 2$_{Me}$-OAc**) were synthesized following the protocol previously reported by QBIS-CAT group.[5, 6, 14]

VIII.2.1 Reactivity of 1-OAc with NaN$_3$

The project started with the evaluation of the inner-sphere N-transfer reaction of the aryl–Co(III) complex (**1-OAc**). The stoichiometric reaction of **1-OAc** with and excess of sodium azide (NaN$_3$) in TFE at 100 °C renders the **3-N$_3$(N$_3$)** monomeric complex bearing two azide ligands as major product. The substitution of one acetate by one azide ligand (**3-N$_3$(OAc)**) was also observed as a minor complex. Crystals suitable for XRD analysis were obtained from **3-N$_3$(N$_3$)** in CH$_2$Cl$_2$ layered with pentane. Interestingly, the crystal structure shows stable trimeric [(L$_H$Co(III))$_2$Co(II)(N$_3$)$_2$(μ-N$_3$)$_4$] species **(3'-N$_3$(N$_3$)),** which co-crystalized with a [Co(II)(N$_3$)$_2$] unit as depicted in Scheme VIII.1. Light-induced activation of the azide was attempted, but neither with light irradiation (254 or 420 nm) nor heating could achieve the inner-sphere N-transfer processes, indicating the high stability of the **3-N$_3$(N$_3$)** organometallic complex.

A) Reactivity of **1-OAc** with NaN$_3$

1-OAc → NaN$_3$ (5 equiv.), TFE, 100 ºC, 16 h, Air → **(3-N$_3$(N$_3$)) 60%** → **3'-N$_3$(N$_3$)**

B) Solid state structure of **3'-N$_3$(N$_3$)**

3'-N$_3$(N$_3$) (XRD)

Scheme VIII.1. A) Formation of **3-N$_3$(N$_3$)** complex by reacting the aryl–Co(III) (**1-OAc**) with NaN$_3$. B) Solid state structure of **3'-N$_3$(N$_3$)**. Selected bond distances [Å] and angles [deg]: C(12)–Co(1) 1.853(11), Co(1)–N2 1.856(12), Co(1)–N(20) 1.955(12), Co(1)–N(23) 2.062, N(20)–Co(26) 2.175(9), N(23)–Co(26) 2.136(12), C(12)–Co(1)–N(20) 94.1(5), Co(1)–N(20)–Co(26) 101.5(4), Co(1)–N(23)–Co(26) 99.4(4), N(2)–Co(1)–N(23) 93.1(4).

VIII.2.2 Reactivity of 1-OAc with organic azides

Once we had explored the reactivity of the aryl–Co(III) complex with NaN$_3$, we decided to explore its reactivity towards aromatic and aliphatic azides. Initially, we subject the **1-OAc** with *p*-NO$_2$-phenyl azide, but only decomposition along with with non-identified products were detected. Better results were obtained using aliphatic azides. Initially, we explored the reactivity of **1-OAc** with benzyl azide (**a**) at 50 ºC in HFIP (or TFE) yielding the aryl-amine coupling complex **4a-OAc** in 46% yield (see Scheme VIII.2). The beneficial role of using fluorinated solvent (such as TFE and HFIP) for the aryl-N coupling was observed, as it has been demonstrated previously in these systems.[6] The **4a-OAc** was fully characterized by HRMS and 1D- and 2D-NMR where an indicative HMBC peak between the benzylic –CH$_2$ of the formal azide and the quaternary carbon of the aryl clearly proved the effective formation of the aryl–N bond.

1-OAc → Ph⌒N$_3$ (**a**) (2.1 equiv.), HFIP, 50 ºC, overnight, Air → **4a-OAc, 46%**
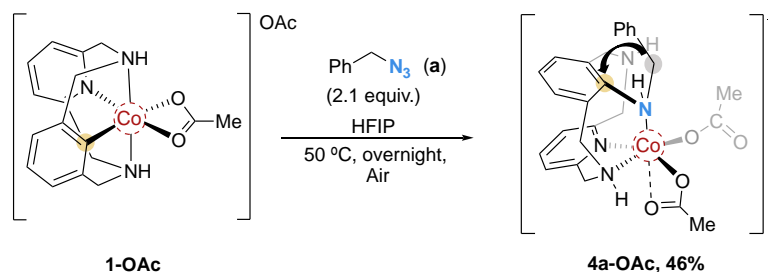
Scheme VIII.2. Reactivity of **1-OAc** with benzyl azide (**a**) to give the **4a-OAc** organometallic complex. The black arrow showcases the HMBC peak observed between the benzylic –CH$_2$ and the quaternary carbon of the aryl moiety.

Despite, **4a-OAc** complex is stable enough to be fully characterized by 1D- and 2D-NMR, it slowly evolves at room temperature to a more stable organometallic complex **5a-OAc** in quantitative yields, as shown in Figure VIII.1 in which the ^{1}H-NMR time-evolution is depicted.
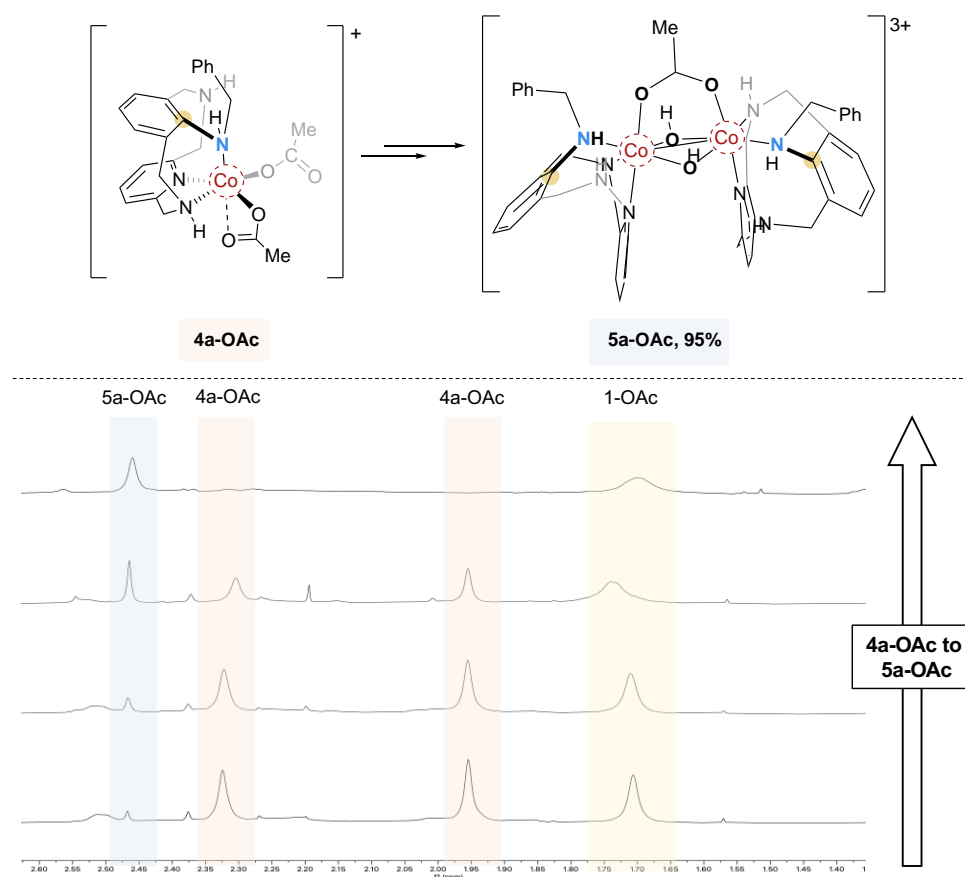
Figure VIII.1. ^{1}H-NMR spectra (acetate region) of **4a-OAc** crude mixture affording the **5a-OAc** complex.

Despite crystallographic analysis of the **4a-OAc** was unsuccessful, its evolution to **5a-OAc** complex allowed to obtain suitable crystals of the latter for XRD analysis from a CHCl$_3$ solution layered with pentane at -4 ºC. The solid state structure shows a distorted octahedral coordination environment at the Co(III) center with coordination to N$_{py}$, NH$_L$, NH$_{azide}$, one OAc and two µ-hydroxo bridging ligands as shown in Figure VIII.2.
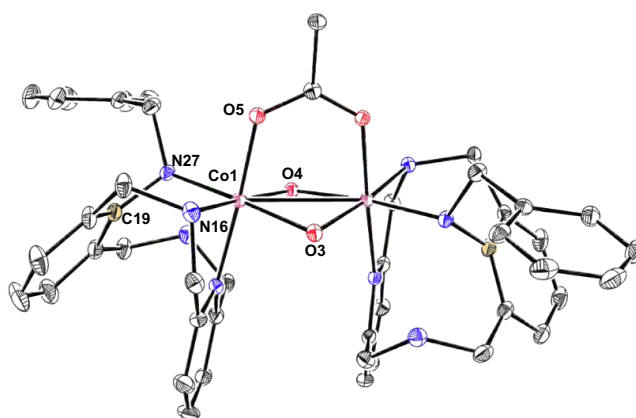
Figure VIII.2. Solid state structure of **5a-OAc.** Hydrogen-atoms, anions and solvent molecules have been omitted for clarity. Selected bond distances for [Å] and angles [deg]: C(19)–N(27) 1.441(16), N(27)–Co(1) 2.009(11), C(19)–N(27)–Co(1) 110.3(9), Co(1)–O(5) 1.924(9), Co(1)–N(16) 1.955(12), Co(1)–O(3) 1.932(9), Co(1)–O(4) 1.930 (9).

With these results, we decided to explore the reactivity of **1-OAc** with (2-azidoethyl)benzene **(b)** and (2-azidopropyl)benzene **(c)**. Subjection the **1-OAc** with an excess of the corresponding azide (**b** or **c**) affords the analogous aryl-amine complex in 26% (**4b-OAc**) and 25% yield (**4c-OAc**) (Scheme VIII.3). Furthermore, both organometallic complexes evolve to the corresponding dimer **5b-OAc** and **5c-OAc**, which were fully characterized by HRMS and 1D- and 2D NMR spectroscopy.

(4b-OAc) R = –CH₂Ph, **26%**
(4c-OAc) R = –CH₂CH₂Ph, **25%**

(5b-OAc) R = –CH₂Ph, **75%**
(5c-OAc) R = –CH₂CH₂Ph, **97%**

Scheme VIII.3. Reactivity of **1-OAc** with azides **b** and **c** yielding the corresponding **4x-OAc** species and its evolution to **5x-OAc** complexes.

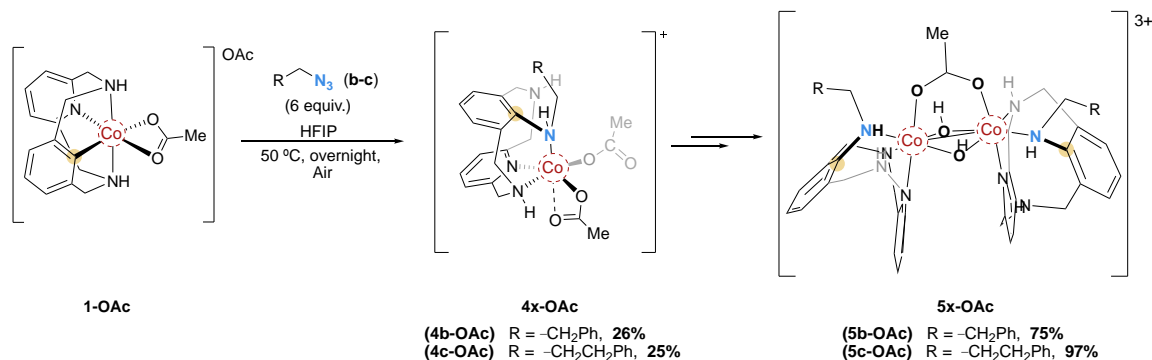Bearing in mind the formation of the aryl-amine complexes (**4x-OAc**), we explored the demetallation step to render the organic aminated product, which is predicted to be kinetically and thermodynamically disfavored.[15] We applied two different strategies to force the demetallation step based on the use of strong acids or thermolysis. Initially, HCl (2M) was added to a solution of **4a-OAc** in CHCl₃ and was stirred 16 h. Then, the crude mixture was basified and extracted, yielding the aminated product **P1** in 44% isolated yield. Applying the same conditions to a solution of **4b-OAc** and **4c-OAc** in CHCl₃, the desired aminated product **P2** and **P3** were obtained in 40% and 42% yield.

(P1) R = –Ph, **44%**
(P2) R = –(CH₂)Ph, **40%**
(P3) R = –(CH₂)₂Ph, **42%**
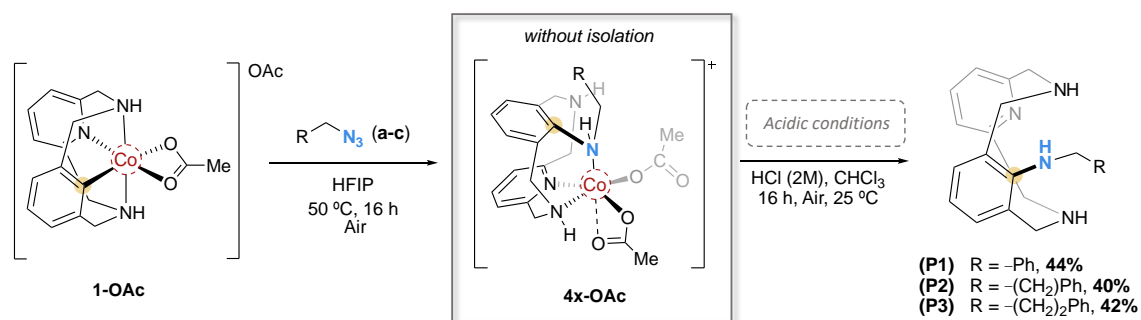
Scheme VIII.4 Synthesis of **P1-P3** aminated product from the **4x-OAc** complex by applying acidic conditions (isolated yields shown).

The demetallation step was also attempted by thermolysis. We subjected the **4a-OAc** to 100 ºC in HFIP during 16 h, and the formation of the cyclic product **P4** in 27% isolated yield was obtained (Scheme VIII.5), which was fully characterized by HRMS and 1D– and 2D–NMR spectroscopy. The formation of **P4** product was further confirmed by ¹³C-NMR, in which a signal in the typical imine region (165.0 ppm) was detected. Moreover, this signal HMBC-correlated to the two doublets at chemical shift of 4.33 and 4.04 ppm, which correspond to the –CH₂ of the pending amine, thus indicating the formation of the cyclic imine product. In contrast, **4b-OAc** and **4c-OAc** subjected to the same thermal conditions did not afford the desired cyclic product, confirming the crucial role of the benzylic position for the formation of the cyclic imine product.
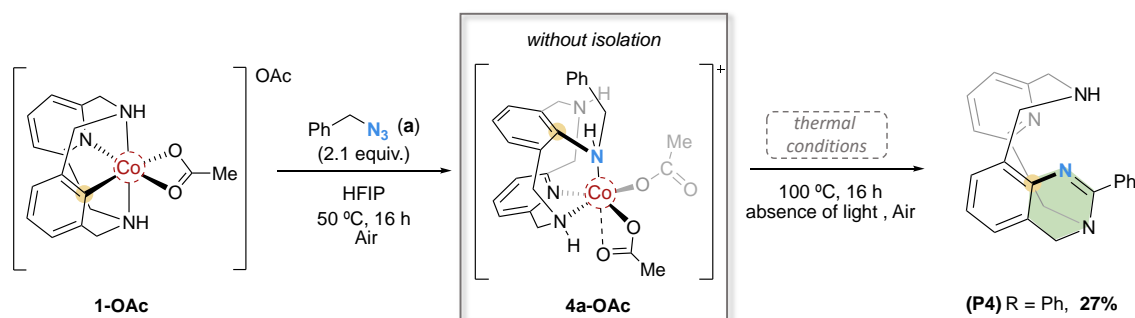
Scheme VIII.5 Synthesis of cyclic product **P4** from **4a-OAc** complex applying thermal conditions.

As mentioned above, the analogous cyclic product was not formed using **4b-OAc** and **4c-OAc** under thermal conditions. Instead, a new paramagnetic species in each case were detected. In order to promote the formation of this new paramagnetic species, **1-OAc** was mixed with 6 equivalents of the organic azide (**b**) in TFE under air at 100 °C. The new paramagnetic species turned out to be stable under inert atmosphere. Interestingly, applying the acidic conditions previously described to **6b-OAc** complex led to the formation of the **P2** product in 41% (based on **6b-OAc**) as depicted in Scheme VIII.6.
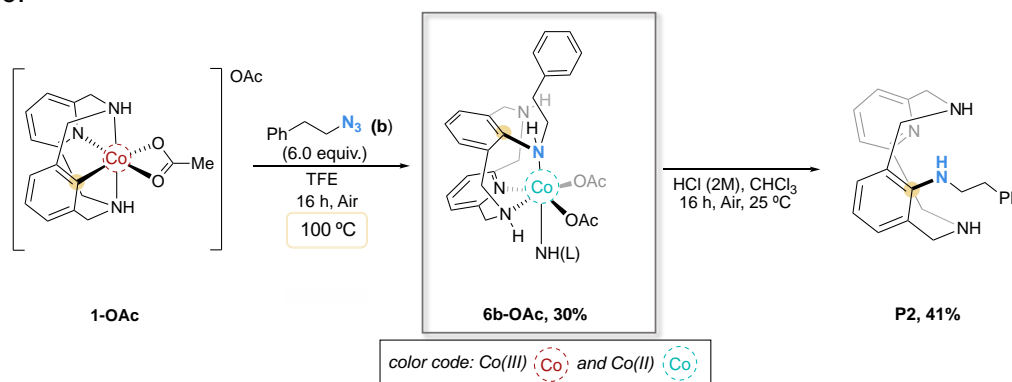
Scheme VIII.6. Reactivity of **1-OAc** with organic azide (**b**) at 100 °C. **P2** formation from **6b-OAc** under acidic conditions. Yield of **P2** is based on **6b-OAc**.

6b-OAc complex has been crystallographically and spectroscopically characterized (see Figure VIII.3) featuring a distorted octahedral geometry at Co(II) center, which is coordinated to a phenylethane-1-amine moiety (coupled to the aryl), N_{py}, two NH_L and two OAc. The Co(II) oxidation state of the **6b-OAc** was further confirmed by X-ray Absorption spectroscopy (analysis performed by Dr. Vlad Martin-Diaconescu, see Annex A.1 Figure S19) by contrasting to starting aryl-Co(III) complex **1-OAc** and the aryl-Co(III)-benzylamine complex (**7-OAc**), which was independently synthetized. In order to fully characterize the **6b-OAc**, the μ_{eff} was calculated using Evans' method[16] in CD_2Cl_2. A value of μ_{eff} = 4.22 MB was obtained suggesting a high spin Co(II)–d^7 electronic configuration. These results agree with the Co-ligand distances in the crystal structure (>2.1 Å). We hypothesized that the **6b-OAc** complex can be formed from a reductive elimination from a putative aryl-Co(IV)-imido complex, however the mechanism involved is unclear.
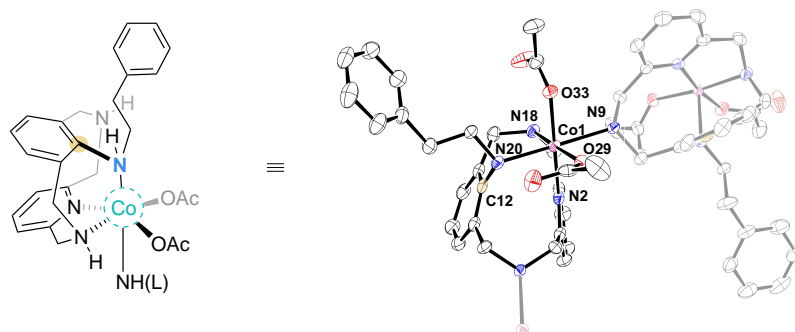
Figure VIII.3. Solid state structure of **6b-OAc** complex. Selected bond distances for [Å] and angles [deg]: C(12)–N(20) 1.439(5), N(20)–Co(1) 2.176(4), C(12)–N(20)–Co(1) 114.6(3), Co(1)–N(18) 2.127(4), Co(1)–N(9) 2.259(4), Co(1)–N(2) 2.255(4), Co(1)–O(33) 2.075(3), Co(1)–O(29) 2.056(3).

VIII.2.3 Mechanistic insights

To better understand the mechanism for the C–N bond formation system, several control experiments were performed. First of all, the role of the carboxylate anions was investigated (Scheme VII.7).

A) Evaluation of different carboxylate anions in **4a-OBzX** and **P1** product (50 ºC)
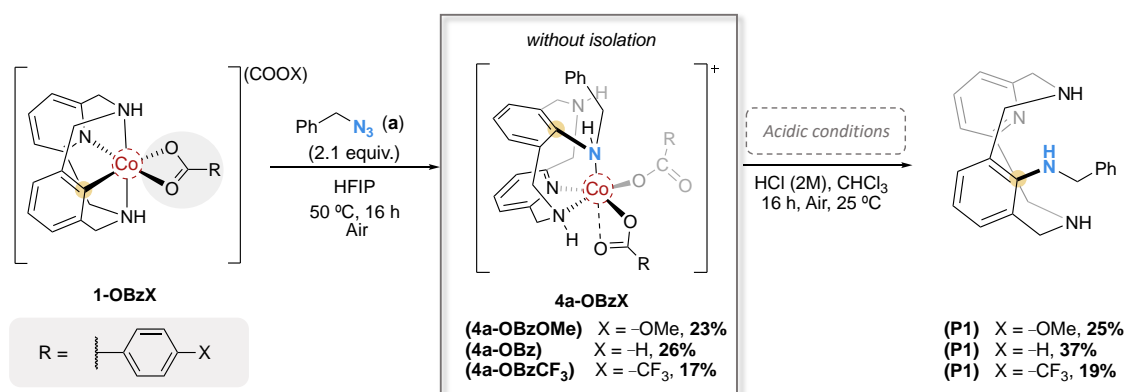
B) Evaluation of different carboxylate anions in **P4** product (100 ºC)

X	Yield of P4 (%)
OMe	42
Me	17
H	34
Cl	49
CF$_3$	23
CN	24
NO$_2$	16
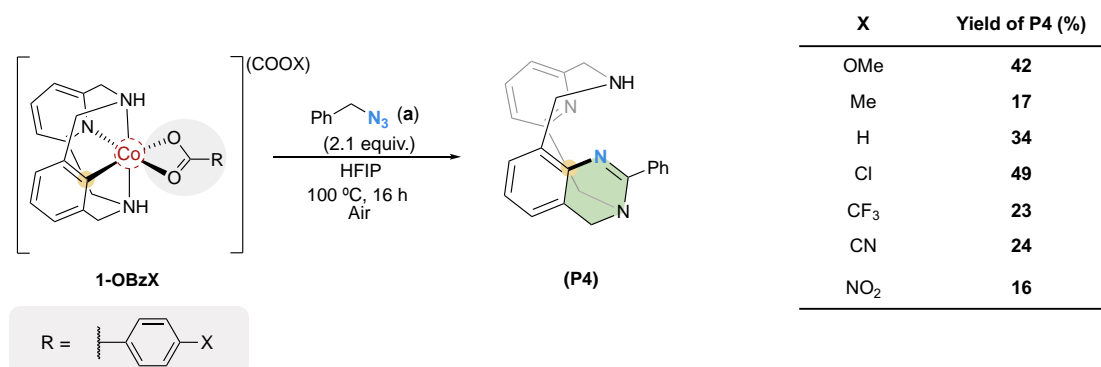
Scheme VIII.7. A) Evaluation of **1-OBzX** towards the formation of **4a-OBzX** and **P1** at 50 ºC. B) Evaluation of **1-OBzX** towards the **P4** formation. NMR yields using 1,3,5-trimethoxybenzene as internal standard.

We synthesized a set of aryl–Co(III) complexes bearing a *para*-substituted benzoate (**1-COOR**) as a carboxylate moiety. We evaluate how the electronic properties of the benzoate affect the formation of **4a-OBzX.** Thus, the **1-OBzOMe**, **1-OBz** and **1-OBzCF$_3$**

were subjected to the optimal conditions yielding the corresponding **4a-OBzX** in similar yields (see Scheme VIII.7.A). These results suggest us that the N_2 extrusion and the concomitant aryl–N coupling is not affected by the electronic properties of the benzoate moiety. Applying the acidic conditions to the **4a-OBzX** crude mixture renders the linear product **P1**. The formation of the cyclic **P4** product was also evaluated under thermal conditions using a set of **1-OBzX** complex as depicted in Scheme VIII.7.B. No correlation was observed in the formation of **P4** using different *para*-substituted benzoate complexes observing an improvement in terms of yield using **1-OBzOMe** (42%) and **1-OBzCl** (49%) compared to **1-OAc** (27%) (all yields are based on the corresponding **1-X** complex).

These results prompted us to explore the reactivity of the analogous aryl–Co(III) complex (**1-CH₃CN**) bearing two CH_3CN moieties instead of acetates (Scheme VIII.8) in order to evaluate the importance of the presence of a carboxylate-type ligand. Strikingly, the **1-CH₃CN** complex with benzyl azide (**a**) in HFIP at 50 ºC did not afford the analogous **4a-CH₃CN**. Thermal conditions (100 ºC) were also applied using this organometallic complex, however **P4** coupling product was not observed, either. In both conditions unknown paramagnetic species were detected as well as the formation of benzyl aldehyde as a side-product. These results highlight the importance of bearing carboxylate moiety to assist the desired aryl–N coupling. The importance of carboxylates will be further explored by DFT (see below), where its role is additionally confirmed suggesting the formation of a masked-Co(III)-nitrene for taming the reactivity of a highly reactive aryl–Co(III)-nitrene species.
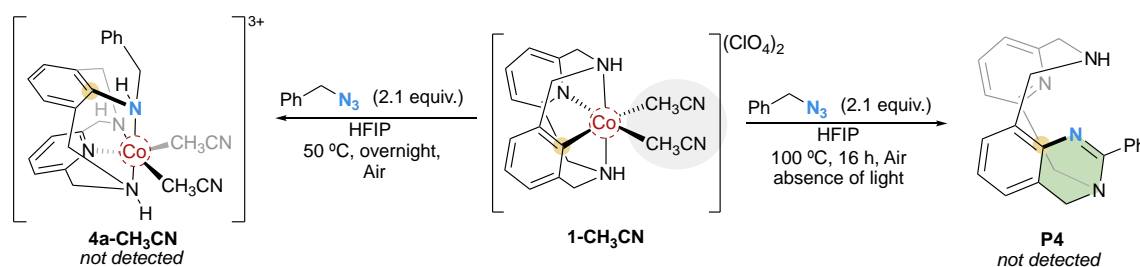
Scheme VIII.8. Reactivity of **1-CH₃CN** with benzyl azide at 50 ºC and 100 ºC.

We next explored the influence of TEMPO as a radical scavenger in the reaction. Subjecting the **1-OAc** and benzyl azide (**a**) together with 2 equivalents of TEMPO at 50 ºC, the **4a-OAc** complex was not detected. Instead, a MS peak tentatively matching with a Co(II) organometallic complex featuring a inserted imine, was detected (Scheme VIII.9). Performing the reaction at 100 ºC results in a decrease of **P4** yield from 27% to 7% NMR yield. A radical or non-radical mechanism cannot be postulated since we observed C–N coupling, albeit in low yield.

A) Reactivity of **1-OAc** with benzyl azide and TEMPO

1-OAc

m/z = 460.1312

4a-OAc *(not detected)*
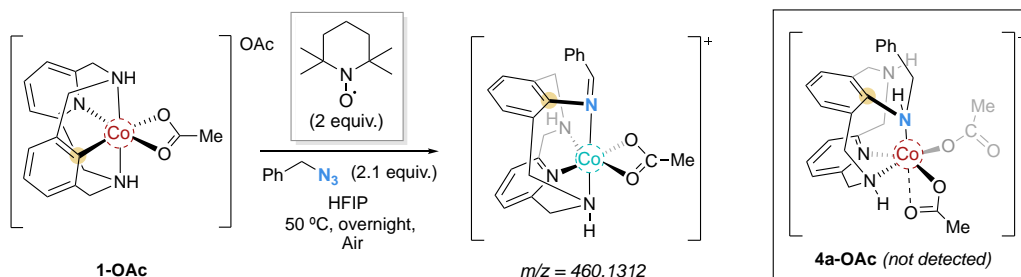
B) HRMS spectrum of crude mixture
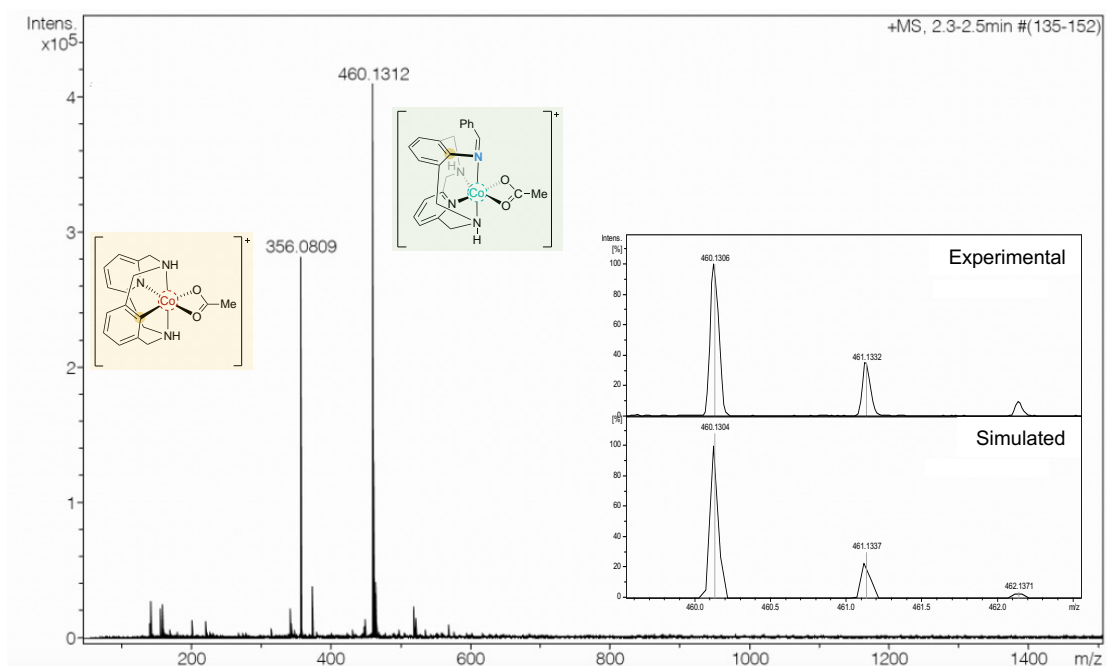
Scheme VIII.9. A) Evaluation of the addition of TEMPO in the reaction of **1-OAc** with benzyl azide at 50 ºC. B) HRMS spectrum obtained after reaction of **1-OAc** with benzyl azide and 2 equivalents of TEMPO showing a peak at *m/z = 460.1312,* which is tentatively assigned to Co(II) inserted imine complex.

To gain further insight on the underlying mechanism, DFT calculations were performed by Marc Montilla, Dr. Pedro Salvador and Dr. Josep M. Luis from IQCC at Universitat de Girona (see Annex 1 for the detailed DFT calculations performed). The interaction of aryl–Co(III) complex with benzyl azide followed by N_2 extrusion and the concomitant steps to render the aryl-N coupling were modeled by DFT (see Figure VIII.4). Firstly, the interaction between the aryl–Co(III) complex with benzyl azide rendering the intermediate **2** via N_2 extrusion, overcomes a 24.24 kcal mol^{-1} transition state (TS$_1$) which is the rate-limiting step of the reaction. In this context, some precedents in the literature postulated the formation of highly reactive Co(V)-imido via N_2 extrusion in C–H amidation processes catalyzed by Cp*Co(III) using TsN$_3$.To shed light into the characterization of this species **2**, wavefunction analysis of **2** together with effective oxidation state (EOS) analysis were performed. Both analysis describes **2** as a aryl–Co(III)=N-R nitrene species (Fischer-type) rather than aryl–Co(V)=N-R imido species (Schrock-type). Subsequently, the adjacent acetate attack to the N atom of the aryl–Co(III)-nitrene forming the more stable five-membered acetoxy(benzyl)amide ring, overcoming a very low barrier (<2 kcal·mol^{-1}). The description of intermediate **3** was also performed observing an increase of the bond distance (1.91 Å) with a decreased bond order (0.78), describing the **3** intermediate as a masked aryl-Co(III)-nitrene species. The enhanced electrophilic character of the N atom (in **2** (-0.74) vs **3** (-0.51)) explains the rapid

nucleophilic attack of the aryl moiety to the N atom forming Co(III) intermediate **4**, featuring the benzyl amine coupled to the aryl.
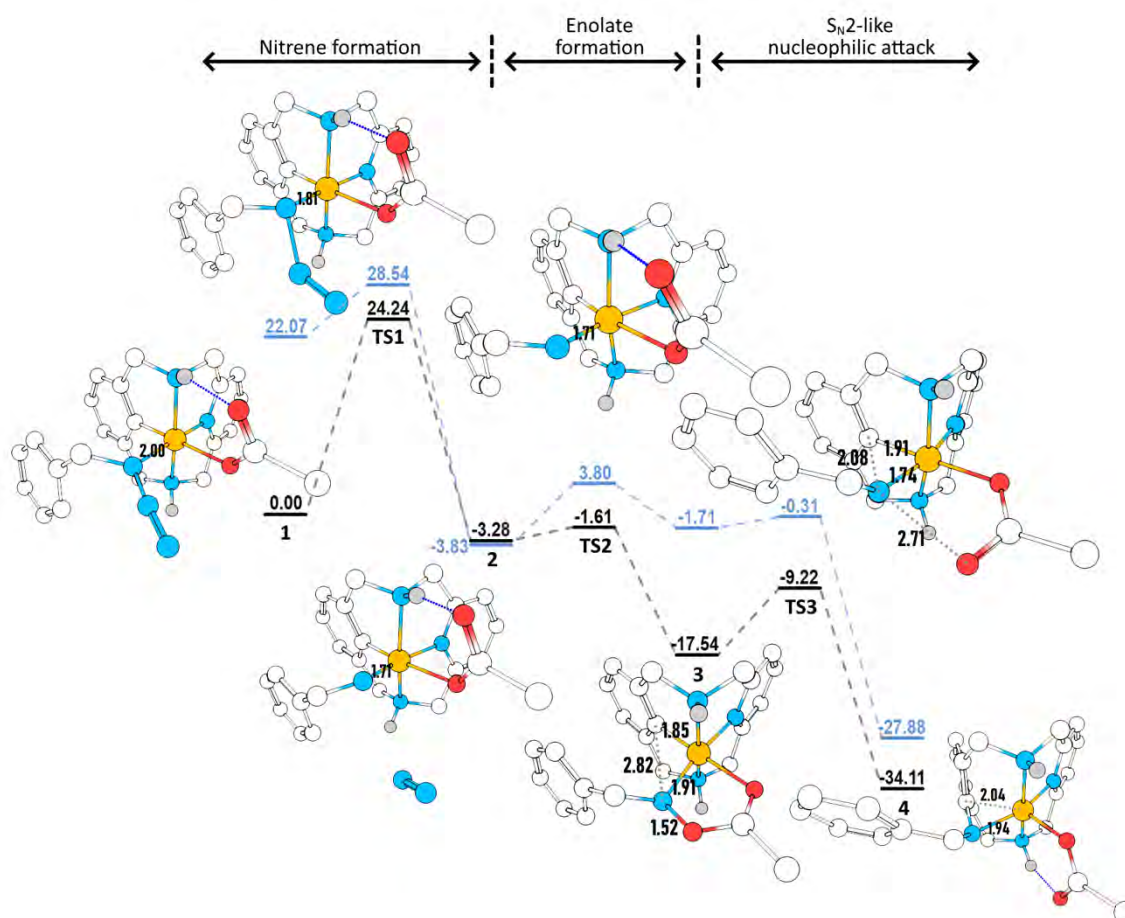
Figure VIII.4. RevTPSS-D3BJ/Def2TZVP//BP86-D3BJ/Def2SVP free energy profile for the studied reaction mechanism. Gibbs free energies (G, in kcal·mol^{-1}) are relative to 1. The pathway in black corresponds to the singlet species (S=0), while the blue pathway corresponds to the triplet species (S=1). Geometries for all S=0 intermediates and transition states are shown (nitrogen atoms are represented in blue, oxygens in red, cobalt in orange, carbon in white, and hydrogens in grey. Note that hydrogens bonded to carbon have been hidden for clarity). Relevant distances have also been included (in Å).

Combining experimental and computational experiments, the mechanism depicted in Scheme VIII.10 is proposed. It is highlighted the importance of the stabilizing masking effect of the carboxylate group to the aryl-Co(III) nitrene species guiding the reactivity to the formation of the aryl–N coupling. These results agree with the experimental results using **1-CH$_3$CN** where the putative aryl-Co imido/nitrene species formed is completely untamed due to the absence of the carboxylate.
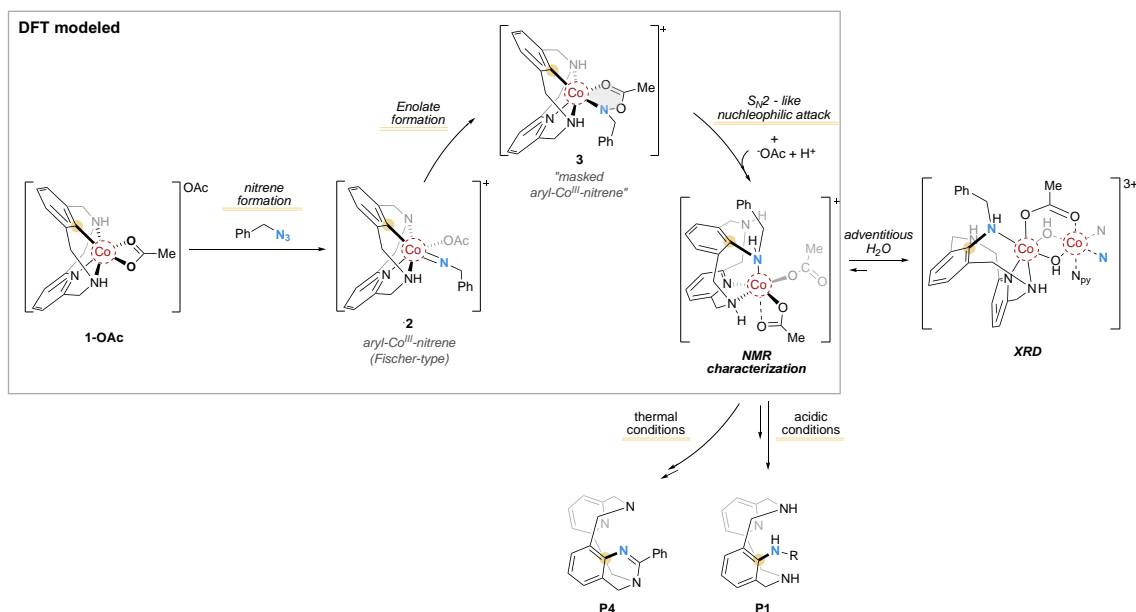
Scheme VIII.10. Proposed mechanism for the reaction of **1-OAc** and benzyl azide (**a**).

In order to highlight the singularity of Co over other Group 9 metals, we turned our attention to compare the reactivity observed exploring the analogous aryl–Rh(III) organometallic complex (**2-OAc**). To our delight, subjecting the **L-H** ligand with stoichiometric amounts of Rh(OAc)$_3$ with benzyl azide (**a**) in TFE at 100 ºC did not afford the desired aryl–N coupling product (**P4**). Hydrazine side-product was detected together with unreacted aryl–Rh(III) complex. The use of N-methylated ligand prevents the cyclization with the macrocyclic scaffold allowing us to gain insight into the different operando mechanism. For this reason, we synthesized the corresponding aryl–Co(III) and aryl–Rh(III) using N-methylated ligand (**L-Me**) (see Scheme VIII.11). **1$_{Me}$-OAc** organometallic complex did not react with 2 equivalent of benzyl azide (**a**) at 50 ºC in HFIP, suggesting that the N-H secondary amines are crucial for the aryl–N coupling. Interestingly, when we applied the same conditions using the **2$_{Me}$-OAc** (aryl–Rh(III) complex) in TFE, the organometallic complex **8a$_{Me}$-OAc** was obtained in 25% yield. The latter bears an iminoethyl phenyl moiety directly coordinated to the Rh(III) metal center. The analogous **8b$_{Me}$-OAc** using an excess of azide (**b**) was also obtained in 35% yield. These results highlight the different reactivity between first-row and second-row transition metals of the same group.
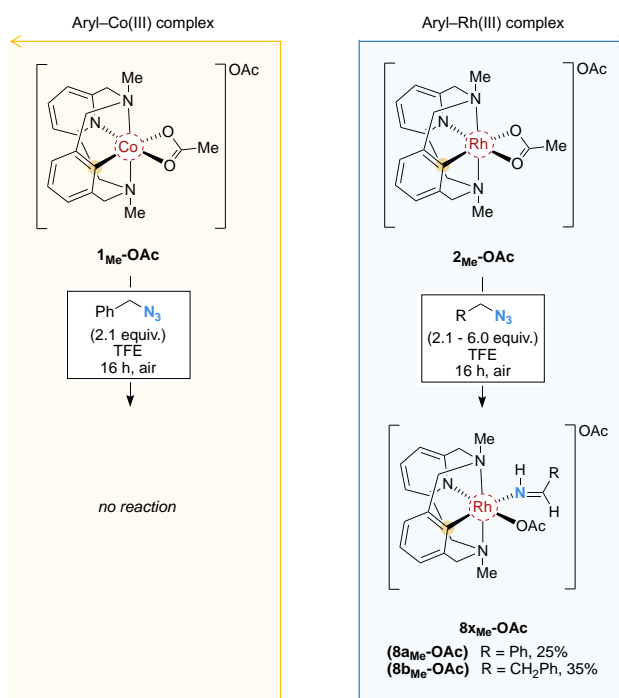
Scheme VIII.11. Different reactivity observed using **1_{Me}-OAc** (Co(III)) and **2_{Me}-OAc** (Rh(III)) with organic azides (**a-b**) at 50 ºC.

In summary, the intramolecular aryl–N bond formation was achieved using a well-defined Oh aryl–Co(III) complex and aliphatic azides as an aminating reagent. Thanks to the stabilizing effect offered by the model macrocyclic platform, we are able to trap the Co(III) species bearing the aryl–N bond formed (**4x-OAc**). This species evolves to form the corresponding **5x-OAc** dimeric species as a more stable species, for which crystallographic proof was obtained (**5a-OAc**). The use of **1-OAc** with azide **b** leads to the formation of a well-defined Co(II) complex bearing the aryl–N bond formed (**6b-OAc**). The crucial role of the carboxylate anions as a stabilizing masked effect was confirmed by the unproductive reactivity of the carboxylate-free **1-CH₃CN** complex and supported by DFT studies. A thorough wavefunction analysis clearly describes the formation of a Fischer-typer aryl-Co(III)-nitrene intermediate species instead of an aryl-Co(V)-imido complex, which rapidly evolves to the masked aryl–Co(III)-nitrene species. The increased electrophilicity on the N together with an increase of nucleophilicity on the aryl moiety substantiated the crucial role of the carboxylate to guide the reactivity toward the formation of the C–N bond.

VIII.3. Chemodivergent Nickel(0)-Catalyzed Arene C−F Activation with Alkynes: Unprecedented C−F/C−H Double Insertion

*This section corresponds to the content of the manuscript by Lorena Capdevila, Tjark H. Meyer, Steven Roldán-Gómez, Josep M. Luis, Lutz Ackermann and Xavi Ribas. ACS Catal. **2019**, 9,11074-11081, which can be found in Chapter V of this thesis.*

Aryl–F bonds are present in a wide range of compounds with applications in catalysis, medicine, and material sciences.[17-20] The introduction of Fluorine moieties changes the physical, chemical and biological properties of a F-containing compound. For example, its presence improves the stability of given pharmaceutical, which is important for a long-lasting activity of the drug. However, theses valuable compounds are poorly biodegradable due to the strength of its C–F bonds. Moreover, aryl fluorides are widely available representing an alternative electrophile for synthetic methodologies. For this reason, it is desirable to develop new methodologies for the aryl–F functionalization. Indeed, the C–C bond forming reaction via C–F cleavage using nickel catalyst is known, however most of them involve the use of preactivated nucleophiles as a coupling partner, such as Grignard reagents,[21-27] zincates,[28, 29] and boronic acids.[30-34] With these precedents in mind, we decided to explore nickel(0)-catalyzed cyclization reactions via aryl–F functionalization using alkynes as coupling partners.

VIII.3.1 Optimization of reaction conditions

The initial stages of this project involved the optimization of the selective activation of aryl–F bonds exploring the role of the directing group (DG) with diphenylacetylene. We studied this reaction using two well-known directing groups: 8-aminoquinoline (**1a**) and pyrimidin-2-amine (**1d**). First, we subject **1d** with diphenylacetylene using $Ni(cod)_2$ as a catalyst, LiO*t*Bu as a base in 1,4-dioxane at 140ºC during 2 h. With these reaction conditions, only sluggish alkyne monoannulation product **3da** was obtained via C–H activation reaction while the C–F bond remained intact. In contrast, when we subject **1a** to the catalytic conditions, the C–F functionalization was achieved forming the alkyne monoannulation product (**3aa**) in 17% yield and the aromatic homologation product (**2aa**) in 63% yield. These results suggested us that under these conditions, the use of 8-aminoquinoline as a bidentate directing group was essential to activate selectively the C–F bond. Furthermore, using the bidentate directing group, the insertion of two alkynes forming the aromatic homologation product (**2aa**) via C–F/C–H functionalization was favorable over the formation of the alkyne monoannulation product (**3aa**).
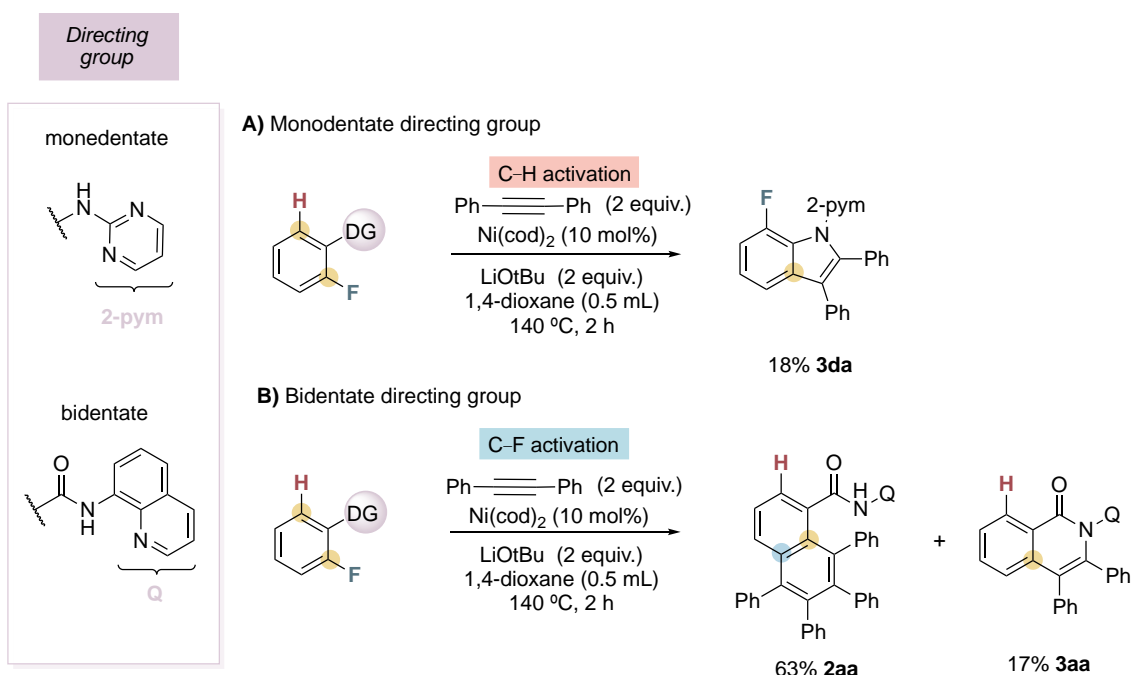
Scheme VIII.12. Role of the directing group in C–F vs C–H functionalization.

Encouraged by these results, the reaction conditions were further optimized in terms of additives, equivalents of alkyne, base and reaction time using **1a** as substrate (Table VIII.1). The increase of the equivalents of the alkyne from 2 to 5 equiv. was not beneficial for the functionalization of C-F bond, and the aromatic homologation product **2aa** was obtained in a low 32% of NMR yield (Entry 2). Different reaction times were then tested and neither increasing nor reducing the reaction time improved the **2aa** yield (Entries 4-7). When we subjected the substrate **1a** in the standard conditions adding an auxiliary ligand such as PCy$_3$ (Entry 9), the ratio between both products changed, favoring the formation of the alkyne monoannulation product **3aa**. With the best conditions, a variety of bases were investigated (Entries 9-12) and LiO^{t}Bu was found to be the best choice. It should be noted that the presence of Li$^+$ is crucial for the activation of the C–F bonds, which was demonstrated with the lack of products by using the same base ($^-$O^{t}Bu) with K$^+$ as countercation (Entry 10). Prompted by the selectivity observed to form the aromatic homologation product via C–F/C–H, we pursued to explore the parameters that enhanced this selectivity.
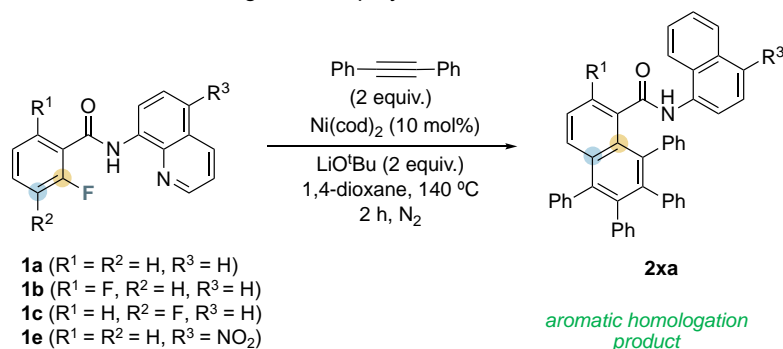
Table VIII.1. Optimization of the reaction conditions for the C–F functionalization.[a]

aromatic homologation product (2aa) + alkyne monoannulation product (3aa)
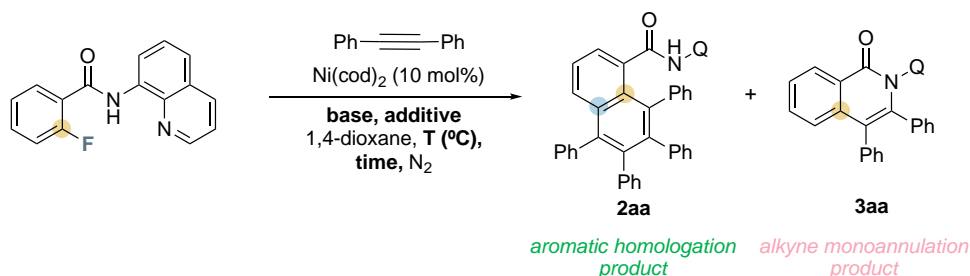
Entry	Alkyne (equiv.)	Base	Ni(cod)$_2$ (mol%)	Time	T (ºC)	Yield (%) of 2aa[b]	Yield (%) of 3aa[b]	Conv. (%)
1	2	^{t}BuOLi	10	16 h	140	50%	14%	99%
2	5	^{t}BuOLi	10	16 h	140	32%	tr	95%
3	2	^{t}BuOLi	-	16 h	140	0%	0%	19%
4	2	^{t}BuOLi	10	5 h	140	41%	20%	99%
5	**2**	**^{t}BuOLi**	**10**	**2 h**	**140**	**63%**	**17%**	**99%**
6	2	^{t}BuOLi	10	1 h	140	62%	16%	99%
7	2	^{t}BuOLi	10	30 min.	140	11%	4%	29%
8	2	^{t}BuOLi	10	2 h	130	36%	11%	95%
9[c]	2	^{t}BuOLi	10	2 h	140	43%	31%	95%
10[d]	2	^{t}BuOK	10	2 h	140	0%	0%	78%
11	2	Li$_2$CO$_3$	10	2 h	140	<10%	0%	8%
12	2	Cs$_2$CO$_3$	10	2 h	140	<10%	0%	27%

[a]Reaction conditions: aryl-F substrate (**1a**) (0.1 mmol), diphenylacetylene, Ni(cod)$_2$ (10 mol%), base (2 equiv.), additive (10 mol%), 0.5 mL 1,4-dioxane under N$_2$ atmosphere. [b] Yield calculated from ^{1}H-NMR of crude reaction using 1,3,5-trimethoxybenzene as internal standard. [c] 10mol% of PCy$_3$ was added. [d] Other unidentified products were detected.

## VIII.3.2. Study on the electronic and steric effects on the C–F activation

To get better understanding of the parameters that govern the preferential formation of **2aa**, we investigated the influence of the electronic properties of the substrate and the alkyne. To do so, we synthesized a variety of polyfluoroarenes substrates (**1b**, **1c** and **1e**) and we subjected them to the optimized catalytic system (Table VIII.2). When we performed the reaction using **1b** substrate, which has two fluorine atoms at the *ortho* position of the arene, only 13% of **2ba** was obtained (Entry 2). In this case, even after adding several auxiliary ligands, changing the solvent, or extending the reaction time the yield was not significantly improved (up to 34 % of **2ba**). These results suggested that the presence of an extra electro-withdrawing F group was not beneficial for the reaction. We also explored the double C–F functionalization using substrate **1c**, which presents two fluorine atoms at the *ortho* and *meta* position of the arene, however we could only achieve 12% of **2ca** product (Entry 3). It should be noted that in both cases the alkyne monoannulation reaction was suppressed. Furthermore, we investigated the C–F functionalization using **1e** substrate bearing a nitro group on the C5 position of the quinoline moiety. Unfortunately, both aromatic homologation and alkyne monoannulation product were not formed and only decomposition products were observed (Entry 4).

**Table VIII.2.** C–F functionalization using different polyfluoroarenes.[a]

1a ($R^1 = R^2 = H$, $R^3 = H$)
1b ($R^1 = F$, $R^2 = H$, $R^3 = H$)
1c ($R^1 = H$, $R^2 = F$, $R^3 = H$)
1e ($R^1 = R^2 = H$, $R^3 = NO_2$)

aromatic homologation product

Entry	R^1	R^2	R^3	Yield (%) of 2xa[b]
1[c]	H	H	H	63 % **2aa**
2	F	H	H	13 % (34 %)[d] **2ba**
3[e]	H	F	H	12 % **2ca**
4[f]	H	H	NO$_2$	traces **2ea**

[a]Reaction conditions: **1x** (0.1 mmol), diphenylacetylene (35.6 mg, 0.2 mmol), LiO^{t}Bu (16,0 mg, 0.2 mmol), Ni(cod)$_2$ (2,8 mg, 10 mol%), 1,4-dioxane (0.5 mL), N$_2$ atmosphere, 140 ºC, 2h. [b]Yields calculated from ^{1}H-NMR of crude reaction mixture using 1,3,5-trimethoxy benzene as internal standard. [c]17% of alkyne monoannulation product **3aa**. [d]16 h. [e]Other minor products were detected. [f]Conversion 63%.

Aiming to get further insight into the favorable formation of aromatic homologation product over the alkyne monoannulation one, we investigated the electronic properties of the alkyne partner. Initial assessments were carried out using 1,2-di-*p*-tolylacetylene (**b**), observing the formation of both product in a similar ratio (**2ab/3ab** ≈ 3) to the one obtained by using the di-phenylacetylene (**a**), although in a lower yield. Interestingly, when the substrate was subjected to different *p*-halo substituted tolanes, both products were formed in an equal ratio. This last result suggested that the presence of an electro-withdrawing group in the alkyne partner promotes the reductive elimination after the first alkyne inserted (Scheme VIII.13). To confirm this hypothesis, we investigated di-phenylacetylenes with stronger electro-deficient groups in *para* such as –C(O)Me and –CF$_3$. Surprisingly, in both cases only the alkyne monoannulation product was detected in a 36% of **3af** and 88% of **3ag** yields (NMR) and the aromatic homologation reaction was totally inhibited. We plotted the observed **2ax/3ax ratio** versus the Hammet σ_p parameter, showcasing a clear trend where the aromatic homologation product is preferentially favored when electro-donating groups are present, whereas the alkyne monoannulation products being favored with electro-deficient substituents (Annex 2, Scheme S2).
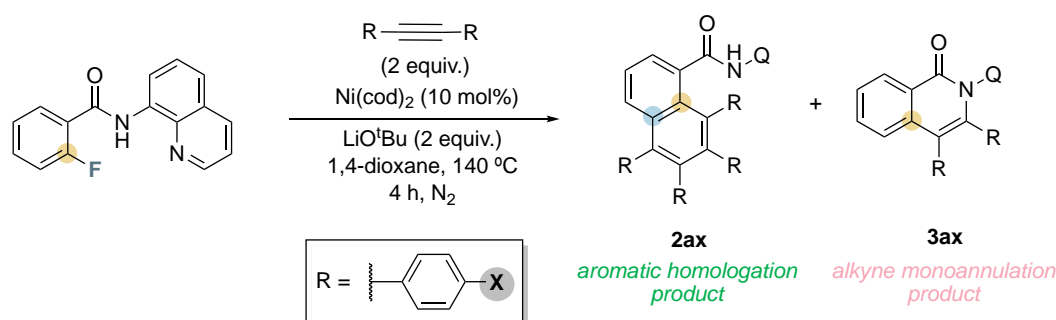
Products (Total Yield)[b]

X = Me (54)   X = H (80)[c]   X = F (83)   X = Cl (73)   X = Br (74)   X = MeC(O) (36)   X = CF$_3$ (88)
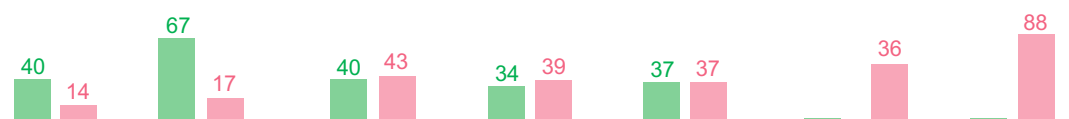
[a.] Reaction conditions: **1a** (0.1 mmol), alkyne (0.2 mmol), LiO^{t}Bu (16,0 mg, 0.2 mmol), Ni(cod)$_2$ (2,8 mg, 10 mol%), 1,4-dioxane (0.5 mL), N$_2$ atmosphere, 140 ºC, 4h. [b] Yields calculated from ^{1}H-NMR of crude reaction mixture using 1,3,5-trimethoxy benzene as internal standard. [c.] 2h.

Scheme VIII.13. C–F functionalization using different symmetric alkynes.[a]

Given the different reactivity observed changing the electronic properties of the alkyne, we decided to explore several unsymmetrical alkynes to study the influence of the sterics in the C–F functionalization. Three different unsymmetrical alkynes (**h-j**) were used, and in all the cases the aromatic homologation and the alkyne monoannulation reaction were obtained. The aromatic homologation product was formed as the major product, however two different regioisomers (out of four) were detected (**2ax1** and **2ax2**). It should be noted that in the case of the alkyne monoannulation product only one regioisomer was formed with the aromatic moiety being preferentially proximal to nitrogen. Finally, we explored the catalytic system using 4-octyne yielding aromatic homologation product (**2ak**) in 53% yield, whereas the alkyne monoannulation product was not observed. These results suggested that the sterically congested alkyl groups disfavor the alkyne monoannulation reaction.

Table VIII.3. C–F functionalization using alkyl-aryl and alkyl-alkyl acetylenes.[a]

Entry	R^1	R^2	Yield (%) of 2ax[b]	Ratio 2ax1:2ax2[c]
1[d]	Ph	Me	57% **2ah** (55)	1.6:1.0
2[d]	Ph	Et	70% **2ai** (49)	1.0:1.0
3[e]	Ph	Pr	85% **2aj** (41)	1.0:1.2
4[e,f]	Pr	Pr	53% **2ak** (41)	

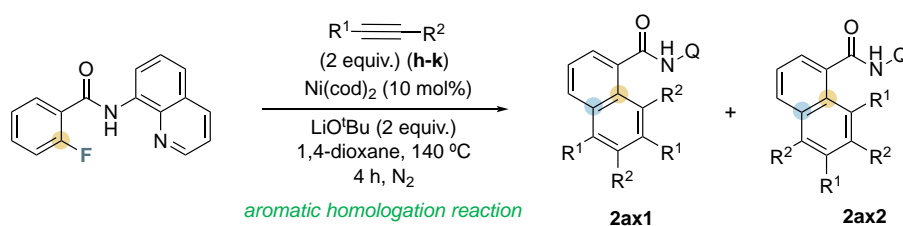[a]Reaction conditions: **1a** (0.1 mmol), alkyne (0.2 mmol), LiOtBu (16,0 mg, 0.2 mmol), Ni(cod)$_2$ (2,8 mg, 10 mol%), 1,4-dioxane (0.5 mL), N$_2$ atmosphere, 140 ºC, 4 h. [b]Yields calculated from ^{1}H-NMR of crude reaction mixture using 1,3,5-trimethoxy benzene as internal standard. The yield of **2ax** = yield of **2ax1** + yield of **2ax2**. Isolated yields are given in parentheses. [c]Ratio calculated from NMR data. [d]Alkyne monoannulation products were formed in low quantities (see the Supporting Information). [e]8 h. [f]Only one aromatic homologation product is possible (**2ak**).

## VIII.3.3. Mechanistic experiments

To better understand the observed reactivity, a set of competition experiments were performed. On one hand, the preferential activation of C–F over C–H bond was tested using equimolar amounts of monofluorinated **1a** and the analogous non-fluorinated substrate (Scheme VIII.14.A). The reaction showed total conversion of **1a** while insignificant consumption of the non-fluorinated substrate was detected. In this context, the single use of non-fluorinated substrate under the catalytic conditions did not proceed and stilbene formation was observed as side-product, indicating the involvement of Ni-hydride species. On the other hand, a competition experiment was carried out using an equimolar mixture of *para*-substituted phenylacetylene bearing an electron-withdrawing (–CF$_3$, **g**) and electron-donating group (–Me, **b**) as depicted in Scheme VIII.14.B. Interestingly, both alkynes reacted with the substrate. Under the reaction conditions, alkyne **b** reacted with the substrate **1a** forming exclusively the aromatic homologation product in a 31% yield (**2ab**). In contrast, alkyne **g** gives only the alkyne monoannulation product in 39% yield (**3ag**). These results also showcase how the electronic properties of the alkynes have an effect on the reactivity observed.

(**A**) Intermolecular competition between C–F and C–H activation
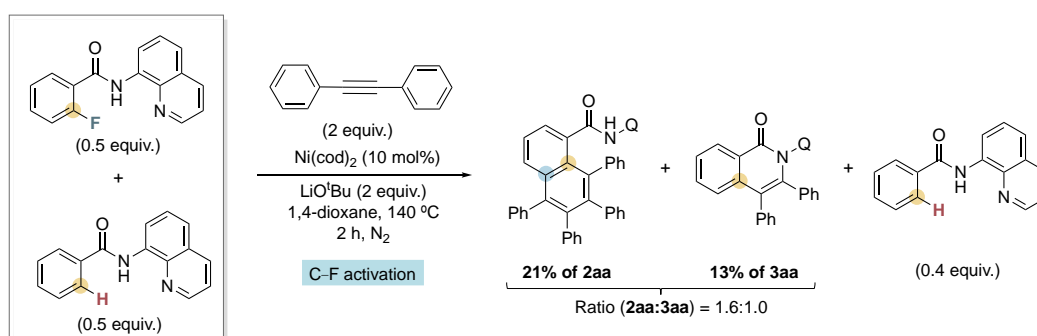
(**B**) *para*-substituted alkyene competition
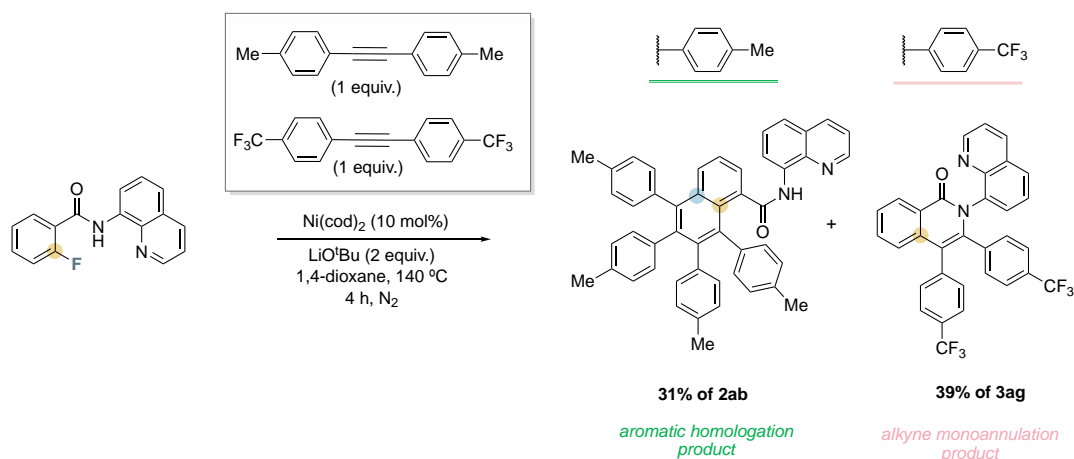
Scheme VIII.14. Competition experiments. (A) C–F vs C–H activation. (B) *para*-substituted alkyne bearing EDG and EWG.

To get more insight into the mechanism of the reaction, we analyzed by ^{1}H-NMR spectroscopy the reaction crude at several reaction times using **1a** and diphenylacetylene. This analysis shows the formation of both products at early stages of the reactions. Furthermore, a new set of peaks were detected, which after 30 minutes of reaction start to disappear, suggesting the transient formation of an intriguing nickel intermediate species (Figure VIII.5).
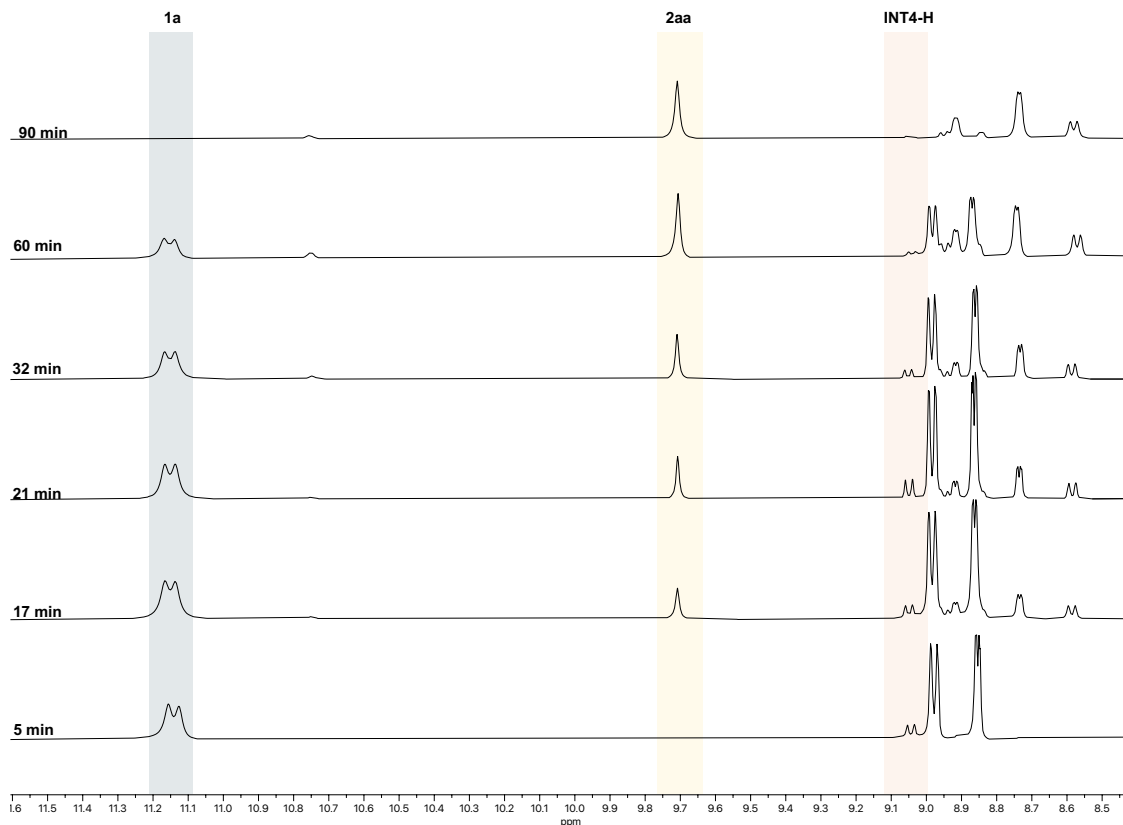

Figure VIII.5. ^{1}H-NMR analysis of the crude mixture at different reaction time.

In order to isolate and elucidate the structure of the mentioned intermediate species, we move to stoichiometric conditions stopping the reaction at 5 min. After submitting the reaction mixture through a column chromatography of the reaction mixture, we were able to isolate (23 % of **INT4-H**) and spectroscopically characterize the complex **INT4-H**, which structure was further confirmed by the XRD analysis (see Scheme VIII.15). Solid state structure revealed a distorted square-planar Ni(II)-complex where two alkynes are inserted forming a nine-membered nickelocycle complex. The high stability of the complex **INT4-H** is consistent with the π coordination of the alkene moiety derived from the first inserted alkyne. Additionally, the second inserted alkyne is *trans* to the amide nitrogen as shown in Scheme VIII.15. We observed 80% of the total nickel content in catalysis. In this line, when using di-*p*-tolylacetylene moiety, the corresponding Ni(II)-complex (**INT4-Me**) was formed; and attempts to crystalize the **INT4-Me** have been pursued without success due to the high solubility of the complex.

(**A**) Trapping the **INT4-R** intermediat under stoichiometric conditions
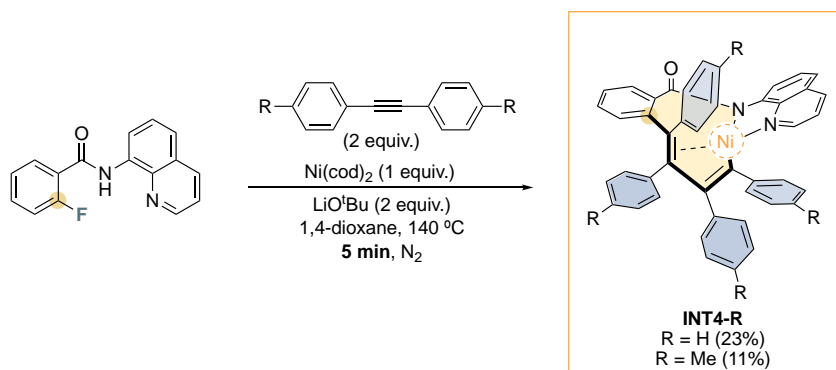
INT4-R
R = H (23%)
R = Me (11%)

(**B**) Solid state structure of **INT4-H**
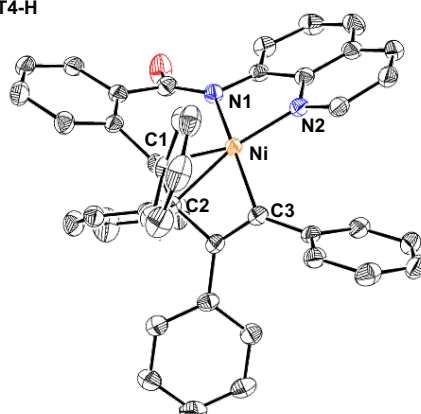
Scheme VIII.15. (A) Isolation of **INT4-R** organometallic complexes. (B) Solid state structure of **INT4-E-H** complex. Selected bond distances (Å): Ni−C1 2.0411(19), Ni−C2 2.1060(17), Ni−C3 1.8946(16), Ni−N1 1.9209(16), Ni−N2 1.9011(16).

Recently, Huang reported the aromatic homologation reaction via double C–H/C–H functionalization using $Ni(cod)_2$ as catalyst.[35] The isolation of the nickel(II)-complex prompted us to investigate whether **INT4-H** is a common intermediate in aromatic homologation reactions. This hypothesis was confirmed by summiting the non-fluorinated substrate to Huang's reaction conditions but at short reaction times, leading to the same the **INT4-H** in 18% yield as depicted in Scheme VIII.16.

INT4-H, 18%
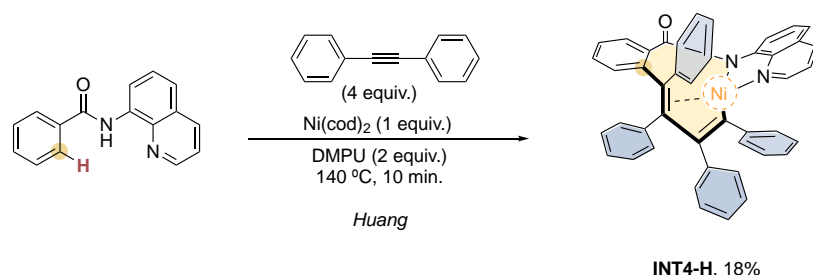
Scheme VIII.16. Formation of **INT4-H** using non-fluorinated substrates under Huang conditions.

Once we had been able to isolate and characterize **INT4-E-H**, the next goal was to evaluate its evolution to form the aromatic homologation product. Under thermal conditions (Figure VIII.6) only a 23% yield of **2aa** was achieved after 2 hours. The reaction was also monitored by ESI-MS showing an induction period as depicted in Figure VIII.6. This fact is attributed to the need of aminoquinoline (AQ) chelating unit which induces the *ortho* C–H activation at the phenyl ring (*meta* to the aminoquinoline-

DG) that finally renders the aromatic homologation product **2aa**. Indeed, as soon as the concentration of the product **2aa** starts to build up, the product itself allows for the accelerated evolution of **INT4-H** to addition product **2aa** in an autocatalytic fashion.
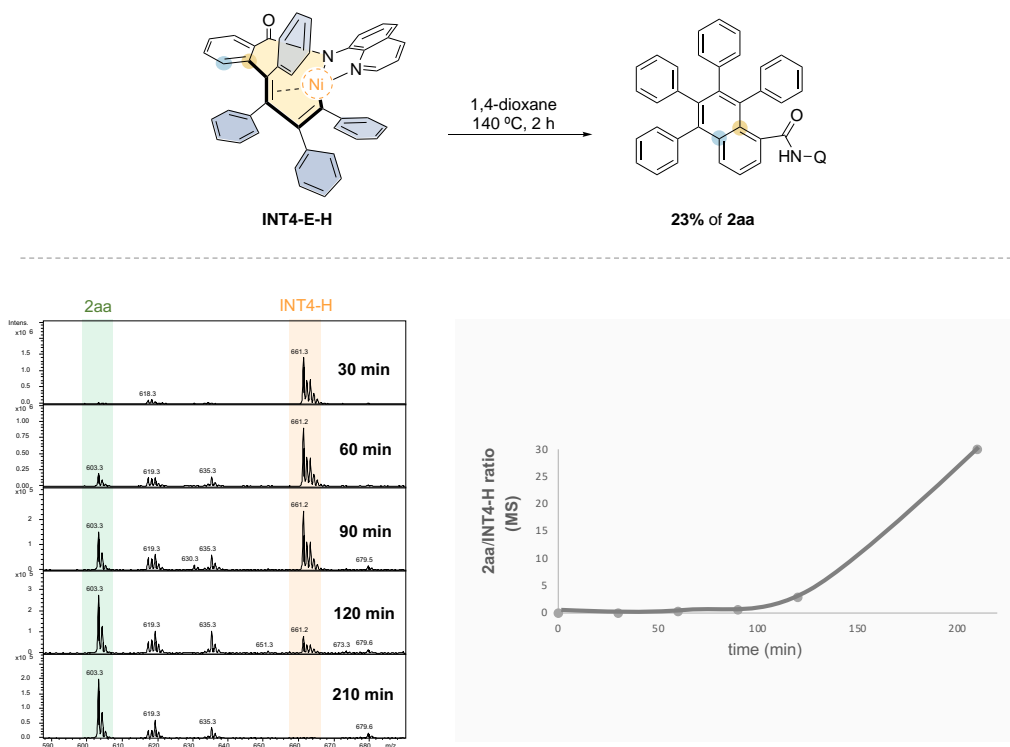
Figure. VIII.6. Evolution of **INT4-H** to the aromatic homologation product.

The requirement of a second AQ as a chelating moiety was confirmed by adding in the reaction 5 equiv. of **1a** and a base, yielding the product **2aa** in higher yield (41%), as depicted in Scheme VIII.17. Moreover, the linear alkenylation product was formed in 46% yield when we subject the **INT4-E-H** in the presence of PivOH under 140 ºC indicating a new potential C–F functionalization strategy. Later, we also explored the **INT4-E-H** (10 mol%) as a catalyst for our catalytic system, however no catalytic turnover was observed and only full conversion of **INT4-E-H** was achieved (10% yield of **2aa**).
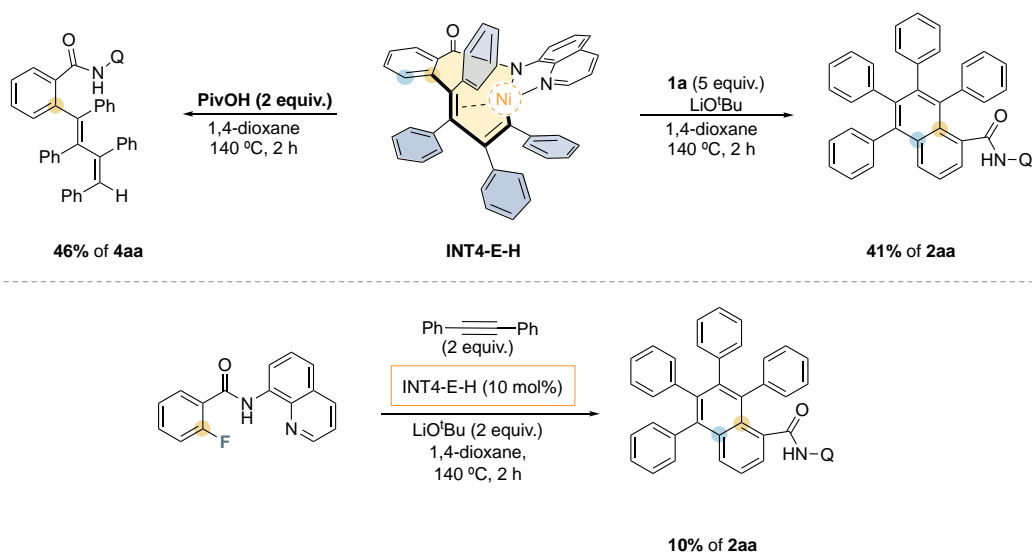
Scheme VIII.17. Diverting reactivity from **INT4-E-H** and reactivity using **INT4-E-H** as catalyst for the aromatic homologation transformation.

VIII.3.4. Theoretical studies and reaction mechanism

To get better understanding of the reactivity observed, DFT calculations were performed by Dr. Steven Roldán-Gómez and Dr. Josep M. Luis from IQCC at Universitat de Girona. (see Annex 2 for the detailed DFT calculation performed).

The first and the second alkyne insertion steps were deeply explored by DFT to get further insight in to the **INT4-H** intermediate isolated. In fact, the stereochemistry of the C–C double bond of the first inserted alkyne led to the formation of two **INT3** isomers (**INT3-Z** and **INT3-E**). The Z conformation is 6.0 kcal·mol^{-1} less stable than the analogous E conformation. The insertion of the second alkyne to both **INT3** isomers shows that the formation of **INT4-Z** is more kinetically favorable (TS–Z$_{3-4}$ is 21.5 kcal·mol^{-1} lower than TS–E$_{3-4}$). In contrast, the **INT4-Z** is 11.2 kcal·mol^{-1} less stable than the **INT4-E**. A deep analysis of the geometry of the Ni(II) center revealed that the **INT4-E** isomer is less distorted from square planarity (23.3º dihedral angle) than the **INT4-Z** isomer (50.2º). All these results suggest that the crystallization of the **INT4-E-H** occurs via a multistep isomerization of **INT4-Z**.
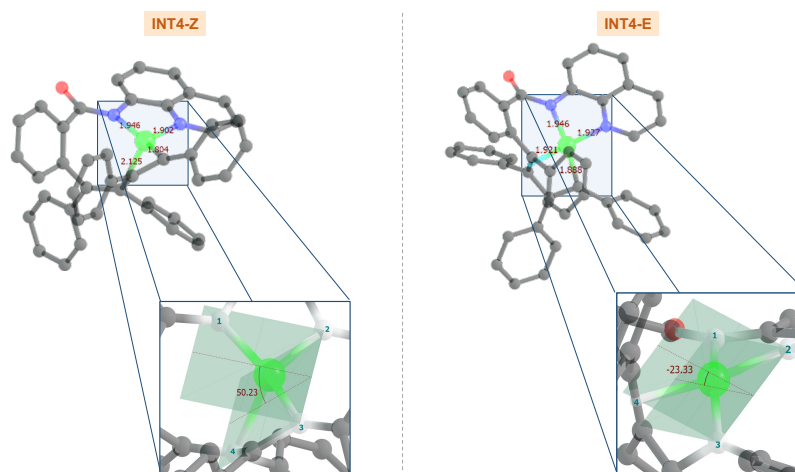

Figure VIII.7. Optimized geometries of **INT4-Z** and **INT4-E**. The distortion of the square planarity of the complex by measuring the dihedral angle N1N2C3C4 are highlighted.

To rationalize the formation of two different products (**2** and **3**) via C–F functionalization we proposed the mechanism depicted in Scheme VIII.18, which is supported by DFT calculations (see Annex 2 for the detailed DFT calculation performed).

The proposed mechanism pathway starts with the coordination of deprotonated substrate **1a** with Ni(cod)$_2$ forming **INT1**, followed by the C–F cleavage via oxidative addition to yield **INT2** (ΔG = 17 kcal·mol^{-1}). DFT calculations revealed the high selectivity of the oxidative addition step toward the C–F activation over C–H activation, which is assisted by Li$^+$. Indeed, the reaction does not proceed using KO^{t}Bu as base. Therefore, the presence of Li$^+$ stabilizes the fluoride–Ni(II) species and extracts the F$^-$ forming LiF; the formation of LiF is one of the driving forces of the reaction. At this point, the first alkyne is inserted (diphenylacetyelene (DPA)) forming the **INT3-Z** and from here a chemodivergent behavior can occur. On the one hand, the **INT3-Z** can reductively eliminate rendering the alkyne monoannulation product **3** (ΔG = 13.1 kcal·mol^{-1}). In contrast, a second alkyne insertion into a Ni–C bond proceeds giving **INT4-Z** (ΔG = 11.9 kcal·mol^{-1}), which can isomerize to form **INT4-E-H** (XRD) or it can react toward the synthesis of the homologation product **2**. In accordance to the experimental results, a second 8-AQ stabilize the Ni(II) center (**INT5**) to further functionalize the *meta* C–H bond (**INT6**) furnishing the final homologation product **2**. With these results in hand, we

suggested that the rate-determining step is one occurring after the insertion of the second alkyne. This is due to the small energy barriers (<24 kcal·mol^{-1}) for the C–F oxidative additions, the first and the second alkyne insertion and the isolation of the nickelcyclic intermediate. The formation of **2** and **3** as mixed products was explained by the small Gibbs energy difference observed between the reductive elimination transition state and the second insertion alkyne transition state where the former is above. The use of *p*-CF$_3$ substituted alkynes showed a reduction of the Gibbs energy difference between the transition state of the intramolecular reductive elimination (14.0 kcal·mol^{-1}) and the second alkyne insertion (13.4 kcal·mol^{-1}), which agrees with the experimental results observed using EWGs.
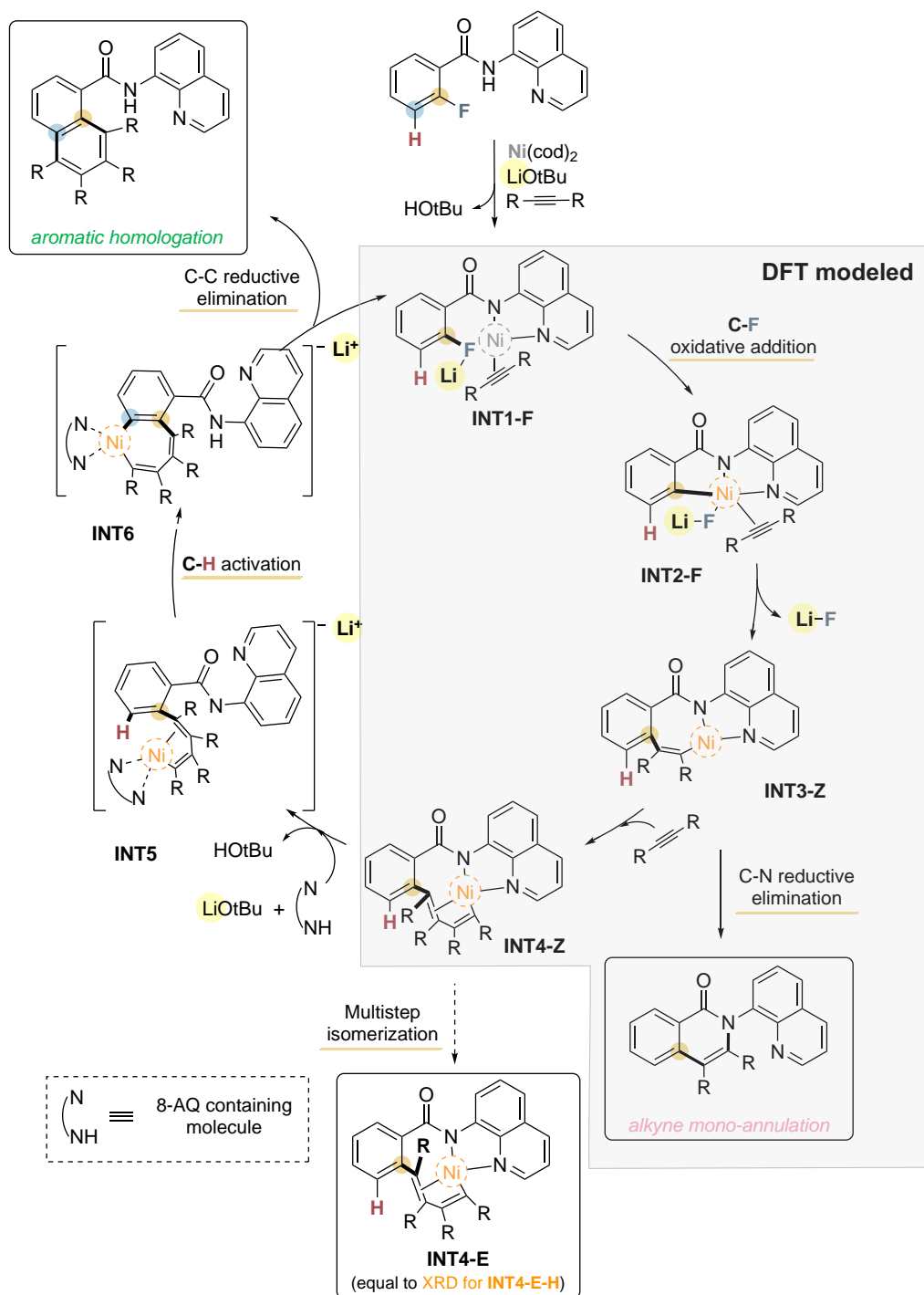
Scheme VIII.18. Proposed mechanism for the formation of the alkyne monoannulation and the aromatic homologation products via C–F activation.

In summary, the selective functionalization of C–F bond via nickel catalysis has been developed using chelated-assisted substrates. The formation of alkyne monoannulation and the aromatic homologation product in a chemodivergent manner was reported using internal alkynes. The electronic properties of fluoroarene and the alkynes allowed us to control the reaction products obtained. The selectivity towards the C– F activation over the C–H activation could be explained on a lower transition state and exergonic step where is assisted by the Li$^+$. Furthermore, an unprecedented nickelacyclic species bearing a double-inserted alkyne was isolated and crystallized, unravelling the mechanistic pathway for the aromatic homologation transformation. The nickel(II) organometallic complex was also isolated via C–H/C–H activation previously reported.

VIII.4. Nickel-catalyzed C_{sp2}–OMe functionalization for chemoselective aromatic homologation en route to nanographenes

This section corresponds to the content of the manuscript by Lorena Capdevila, Judith Sala, Lutz Ackermann, Xavi Ribas (Manuscript accepted for publication in Chem. Eur. J. (doi.org/10.1002/chem.202200625)) which can be found in Chapter IV of this thesis.

The direct functionalization of strong Ar–OMe bonds is highly desirable since it would represent to make available a raw material such as lignin, an aromatic polymer that constitute up to 30 wt% of wood-based biomass.[36] Lignin is considered the largest source of renewable aromatics, however, converting it into synthetically valuable monomeric units by activation of the aryl–OR (R = Me, alkyl, Aryl) is still underdeveloped.[37-41]

The use of aryl ethers remains limited due to the inertness of this bond. In this context, we reported a nickel-catalyzed Aryl–F functionalization using internal alkynes as coupling partner affording either alkyne monoannulation or aromatic homologation products (see Chapter VIII.3) The use of 8-aminoquinoline as directing group was crucial for the selective activation of the strong aryl–F bonds. With these precedents in mind, we decided to explore the nickel-catalyzed aryl–OMe functionalization assisted by 8-aminoquinoline directing group using alkynes as coupling partner.

VIII.4.1 Optimization of the reaction conditions

Initially, we attempted the aryl–OMe functionalization with internal alkynes using a similar Ni(0)-based protocol as for the aryl–F functionalization using different directing groups, i.e. 8-aminoquinoline (**1aa**), 2-pyridylisopropylamine (**1ba**) and 2-pyridylmethylamine (**1ca**) (Scheme VIII.19). Positive aryl–OMe functionalization was achieved using 8-aminoquinoline directing group yielding both the aromatic homologation product (**2aa**) in 47% yield and the alkyne monoannulation product (**3aa**) in 27% yield. On the contrary, no reactivity was observed by using 2-methylaminopyridine and 2-propan-2-aminopyridine, which suggested that the rigidity offered by the 8-aminoquinoline DG was crucial to achieve the aryl–OMe activation.
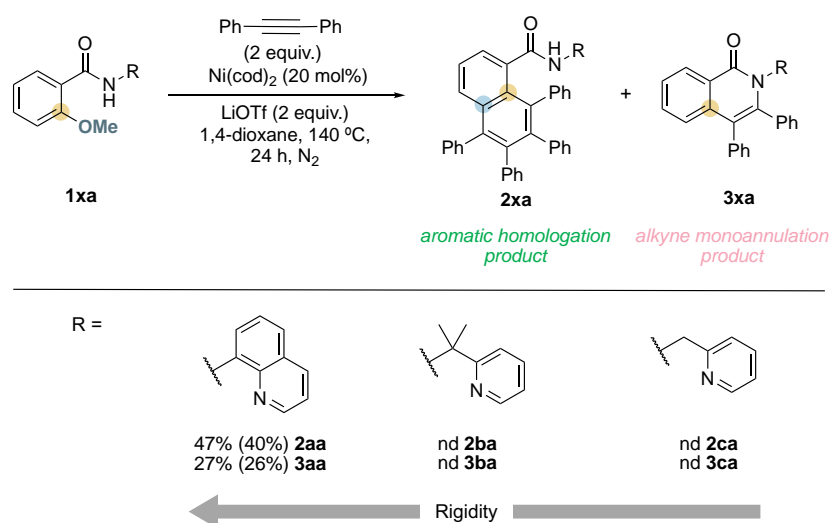
Scheme VIII.19. Directing group screening for the nickel-catalyzed aryl–OMe functionalization.

Using the standard conditions, we observed that the formation of the aromatic homologation product (**2aa**) is slightly favorable than the alkyne monoannulation (**3aa**)

2aa/3aa of 3.7). Thereafter, we attempted to optimize the aromatic homologation product in a higher ratio. Interestingly, an improvement of the chemodivergent behavior towards the formation of the aromatic homologation product (**2aa**) was observed by adding 2 equivalents of LiOTf (ratio **2aa/3aa** of 7.6). Furthermore, at lower reaction times (3 h instead of 24 h) better yield (59%) and selectivity (ratio **2aa/3aa** of 11.8) towards the formation of **2aa** were obtained. The improvement of the yield suggested that the aromatic homologation product decomposed over time under these conditions. After that, we investigated whether switching the selectivity towards the formation of the alkyne monoannulation product (**3aa**) over aromatic homologation was possible. Gratifyingly, we found that adding in the reaction PPh₃ as auxiliary ligand afforded the formation of **3aa** in a chemoselective manner in 58% yield after 24h.
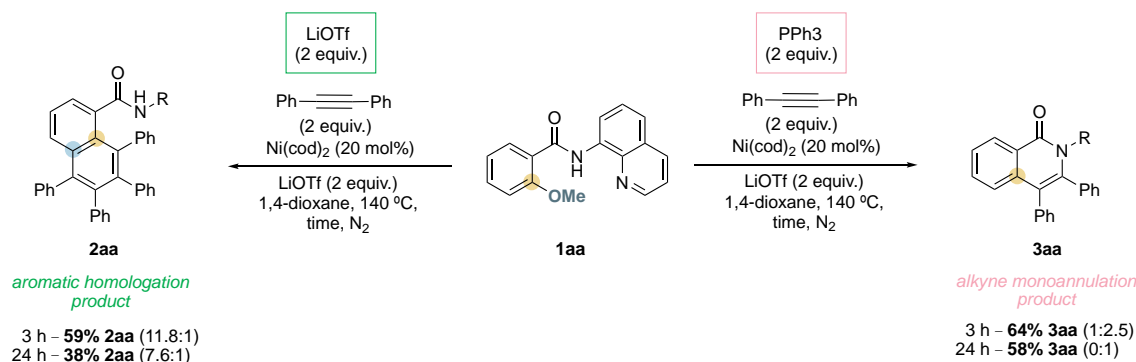
Scheme VIII.20. Nickel-catalyzed aryl–OMe functionalization yielding the aromatic homologation and the alkyne monoannulation product in a chemoselective manner.

## VIII.4.2 Exploring the use of different methoxyarenes

To get better understanding of the scope of the reaction, we explored different substrates bearing a second –OMe moiety in *para*- and *ortho*- to the DG in order to evaluate the influence of steric and electronic properties of substituents on the reactivity (Table VIII.4). We subject the substrates to the three different conditions tested above: a) without additives, b) adding 2 equivalents of LiOTf or c) adding 2 equivalents of PPh₃.

Using **1ab** substrate, which contains a -OMe group in *para*-position to the DG, a decrease of yield (26% of **2ab** and 22% of **3ab**) as well as a poorer selectivity was observed (**2ab/3ab** ratio ~1). Indeed, the aromatic homologation product **2ab** was formed in a chemoselective manner by adding 2 equivalents of LiOTf, albeit in low 32% yield. On the other hand, 43% yield of the alkyne monoannulation product **3ab** was observed adding 2 equivalents of PPh₃ after 24h. This product **3ab** was observed in a high 70% yield in shorter reaction time (3h), suggesting partial decomposition of the product over time under the reaction conditions. The higher yields observed towards the formation of the alkyne monoannulation product suggests that the close proximity of the second –OMe group can restrain the formation of the aromatic homologation product by steric effects. Then, we turned our attention to substrate **1ac**, bearing two –OMe groups to the *ortho*- position of the DG. The reaction did not proceed under standard conditions as neither the aromatic homologation product (**2ac**) nor the alkyne monnoannulation product (**3ac**) were detected, but exclusive formation of **2ac** (in 48% yield) was achieved when 2 equivalents of LiOTf were added. Interestingly, the addition of PPh₃ in the reaction afforded the activation of both –OMe groups forming the aromatic homologation and the alkyne monoannulation product simultaneously (25% of **4**). The structure of **4** was further confirmed by XRD (Figure VIII.8). Its solid-state structure confirmed the presence of a racemic mixture of the two enantiomeric helical-shaped products.

Table VIII.4. C–OMe functionalization using different methoxyarenes [a]

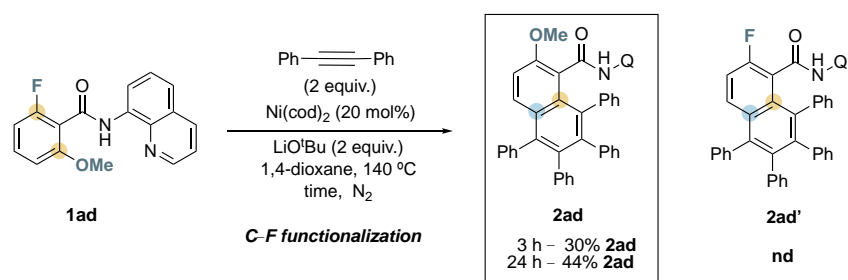|	Additives	Yield (%) of 2ax[b]	Yield (%) of 3ax[b]	Yield (%) of 4[b]
1aa	Without	47%	27%	-
	LiOTf	38% (59%)	tr (tr)	-
	PPh$_3$	tr (25%)	58% (64%)	-
1ab	Without	26% (tr)	22% (tr)	-
	LiOTf	32% (tr)	tr (tr)	-
	PPh$_3$	tr (tr)	43% (70%)	-
1ac	Without	tr	tr	-
	LiOTf	48% (26%)	tr	-
	PPh$_3$	-	-	25%[c]

[a.] Reaction conditions: **1aa** (0.1 mmol), alkyne (0.2 mmol), LiO^{t}Bu (16,0 mg, 0.2 mmol), additives (0.2 mmol), Ni(cod)$_2$ (5.6 mg, 20 mol%), 1,4-dioxane (0.5 mL), N$_2$ atmosphere, 140 ºC, 24 h. [b] Yields calculated from ^{1}H-NMR of crude reaction mixture using 1,3,5-trimethoxy benzene as internal standard (yields calculated at 3 h) .[c] Yield of **4** is based on alkyne.
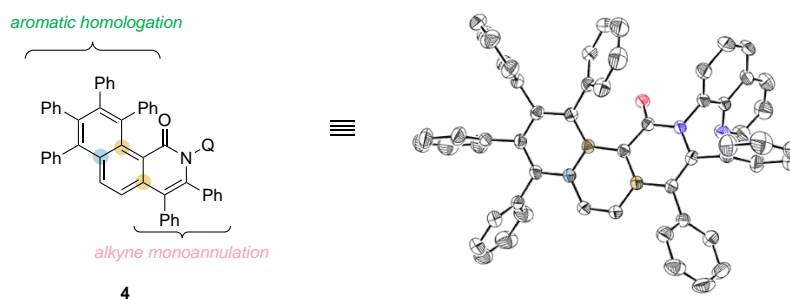
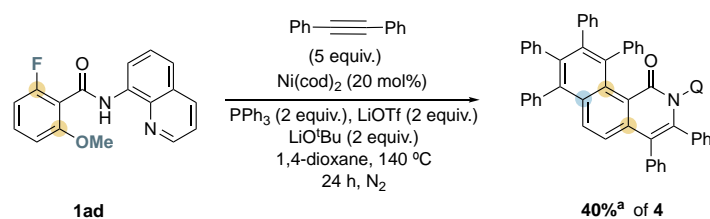**Figure VIII.8.** Solid state structure of product **4**.

VIII.4.3 Competition experiments and mechanistic insights

In order to compare the reactivity between aryl–F and aryl–OMe groups towards the formation of the aromatic homologation product and the alkyne monoannulation product, substrate **1ad** was synthesized (Scheme VIII.21). By subjecting it to the standard conditions in the presence of LiOTf, the aromatic homologation product **2ad** was formed in 44% yield via aryl–F activation, with no detection of aryl–OMe functionalization, thus indicating the high selectivity for aryl–F bond activation. Only traces of simultaneous formation of the aromatic homologation and the alkyne monoannulation product in the presence of 2 equivalents of PPh$_3$ were detected with this substrate. However, the yield of **4** could be increased up to 40% by adding 2 equivalents of LiOTf and 2 equivalent of PPh$_3$ and using 5 equivalents of diphenylacetylene.

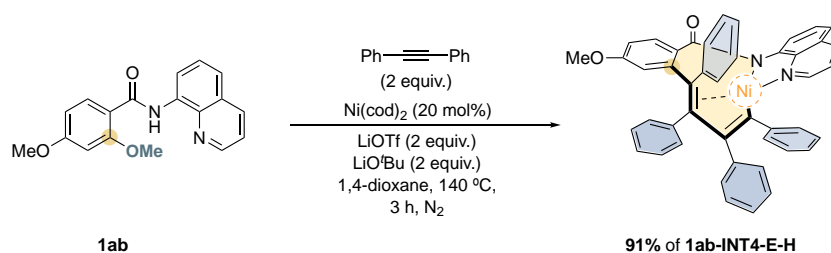**A**) Competition experiments between aryl–F and aryl–OMe activation

1ad

Ph————Ph
(2 equiv.)
Ni(cod)$_2$ (20 mol%)

LiO^{t}Bu (2 equiv.)
1,4-dioxane, 140 ºC
time, N$_2$

C–F functionalization

2ad

3 h – 30% **2ad**
24 h – 44% **2ad**

2ad'

nd

B) Double activation of both aryl–F and aryl–OMe bonds.

1ad

Ph————Ph
(5 equiv.)
Ni(cod)$_2$ (20 mol%)

PPh$_3$ (2 equiv.), LiOTf (2 equiv.)
LiO^{t}Bu (2 equiv.)
1,4-dioxane, 140 ºC
24 h, N$_2$

40%[a] of **4**

Scheme VIII.21. Competition experiments between C–OMe and C–F functionalization. A) Selective C–F functionalization over C–OMe. B) C–OMe and C–F functionalization in a simultaneous manner. [a] Isolated yield.

The similar reactivity observed for the aryl–OMe functionalization using diphenylacetylene and for the previous aryl–F project (Chapter VIII.3) suggests a similar operando mechanism. Actually, we isolated a square-planar Ni(II) intermediate complex bearing two alkynes inserted featuring a nine-membered nickelacyclic complex (**1ab-INT4-E-H**) at short reaction times (see Scheme VIII.22), which is analogous to **INT4-H** (see Scheme VIII.15). The detection of the **1ab-INT4-E-H** agrees with the slow reactivity observed using **1ab** substrate, which suggest a similar subsequent mechanism for the formation of the aromatic homologation product as for **INT4-H** (Scheme VIII.15.).

1ab

Ph———Ph
(2 equiv.)
Ni(cod)$_2$ (20 mol%)

LiOTf (2 equiv.)
LiO^{t}Bu (2 equiv.)
1,4-dioxane, 140 ºC,
3 h, N$_2$

91% of **1ab-INT4-E-H**

Scheme VIII.22. Detection of the analogous nickelacyclic **1b-INT4-E-H** complex.

VIII.4.3 Nanographene-like compounds

Given the high number of contiguous phenyl groups present in the products obtained, we decided to subject the 1,2,3,4-tetraphenylnaphtalene unit **2aa** to Scholl and DDQ oxidative coupling targeting the fusion of aromatic rings. In this context, several efforts have been recently done to develop new methodologies for the synthesis of nanographene-like compounds.[42] Initially, **2aa** was subjected to FeCl$_3$-mediated Scholl reaction, however the fused desired product was not detected. In contrast, applying the DDQ oxidative coupling conditions the oxidative fusion of the two phenyl moieties, along with in situ amide hydrolysis and esterification compound **5** was observed (Scheme VIII.23). It is worth to note that a 9-fused ring compound **6** was detected in the crude mixture (see Annex A.3 Figure S9). The nanographene-like derivative **5** was fully characterize by 1D and 2D NMR which agrees with the cleavage of one ring fusion together with amide hydrolysis and esterification during the reaction protocol.
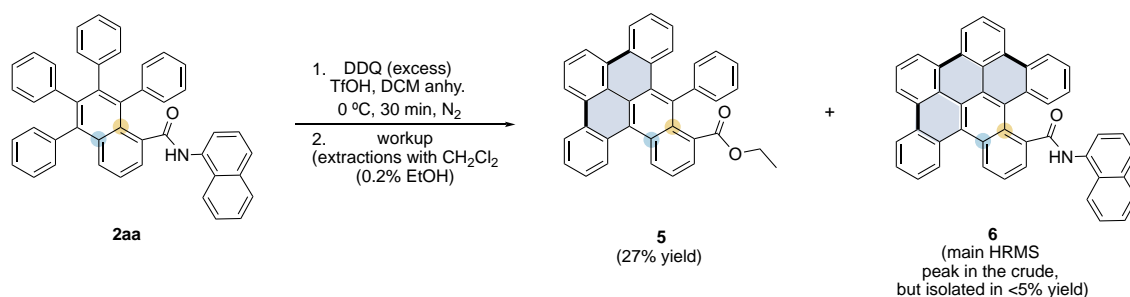
Scheme VIII.23. DDQ-mediated oxidative coupling of **2aa** to form nanographene derivatives **5** and **6**.

Summarizing this section, a new protocol for the synthesis of aromatic homologation and alkyne monoannulation products via Ni(cod)$_2$–catalyzed aryl–OMe functionalization has been developed. Furthermore, the addition of an excess of Li$^+$, particularly LiOTf, enhance the reactivity towards the formation of the aromatic homologation product in a selective manner. In contrast, the selective formation of alkyne monoannulation product was achieved by adding PPh$_3$, which blocks the insertion of the second alkyne. Moreover, the double functionalization was also achieved by activating two *ortho* C–OMe or one *ortho* C–OMe and one *ortho* C–F bonds, forming simultaneously the aromatic homologation and the alkyne monoannulation product. Finally, the aromatic homologation products are shown to be valid precursor towards nanographene-like derivative synthesis.

VIII.5 Silver(I)-Catalyzed C−X, C−C, C−N, and C−O Cross-Couplings Using Aminoquinoline Directing Group via Elusive Aryl-Ag(III) Species
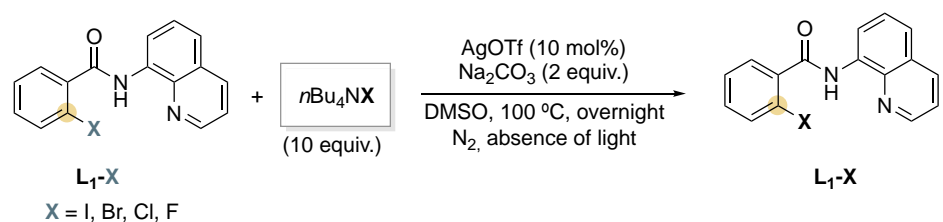
This section corresponds to the content of the manuscript by Lorena Capdevila, Erik Andris, Anamarija Briš, Màrius Tarrés, Steven Roldán-Gómez, Jana Roithová and Xavi Ribas. ACS Catal. ***2018****, 8, 10430-10436, which can be found in Chapter VII of this thesis.*

Continuous development of alternative strategies for the construction of molecular diversity via transition metal catalyzed cross coupling allows to increase the toolbox of redox metals to achieve a variety of transformations. In this context, silver salts are not regarded as 2-electron redox metals and are commonly used as co-catalyst or as additives in cross-coupling transformations. However, there are few examples of silver catalysis based on Sonogashira-type coupling[43] and Ullmann-type C–N and C–O coupling[44], but the mechanism of these reactions is still unclear. Our research group reported a well-defined macrocyclic aryl–Ag(III) complex and demonstrated for the first time the ability of silver to undergo two electron redox catalysis.[4] Indeed, the aryl–Ag(III) organometallic complex reacted with O– and C– nucleophiles affording the corresponding product under mild conditions. With these precedents in mind, we attempted to explore the silver(I) catalyzed cross-coupling reactions in a non-cyclic model substrate. We selected an aryl–X activation assisted by 8-aminoquinoline directing group using different nucleophiles to forge C–C and C–Heteroatom couplings.

VIII.5.1 Substrate scope

Prompted by the results obtained using the well-defined macrocyclic aryl–Ag(III), which reductively eliminate with different halides affording the halide exchange reaction within aryl-halide triazamacrocycle, we pursued to explore this transformation using the non-cyclic aryl-halide substrate bearing a 8-aminoquinoline (AQ) as directing group (Table VIII.5). Initially, we started exploring the viability of the halide exchange reactions using L_1-I substrates with nBu_4NX (X = Cl, Br) salts as halide source via silver catalysis. Thus, we optimized the reaction conditions observing that the catalysis was effective using an excess of the halide source (10 equiv.) and 10 mol% of AgOTf at 100 ºC in CH_3CN or DMSO. In both solvents, the L_1-Cl and L_1-Br products were obtained in good to excellent yields (entries 1 and 3). The Br-to-Cl exchange was also observed in good yield (78 % yield, Entry 6) using L_1-Br substrate in DMSO. In contrast, the Br-to-I exchange was not observed in the optimized conditions (Entry 7). However, increasing the amounts of AgOTf (20 mol%) in CH_3CN leads the L_1-I formation in 38% yield, and up to 50 % of L_1-I when 20 mol% of PPh_3 was used as additive. It is worth to know that using the triazamacrocyclic aryl-I substrate an improvement in the catalysis was also observed using PPh_3 as an additive.[4] Finally, we attempted the halide exchange reaction using L_1-Cl substrate, however we fully recovered the L_1-Cl substrate (Entry 9). The absence of halide exchange product agrees with a higher energy barrier for the aryl–Cl oxidative addition than the aryl–I and aryl–Br. The harsh conditions required for the halide exchange reactions using L_1-I and L_1-Br indicated a higher energy barrier for the oxidative addition step compared to the triazamocrocyclic aryl–X substrate, for which the catalysis proceeded at room temperature.[4]
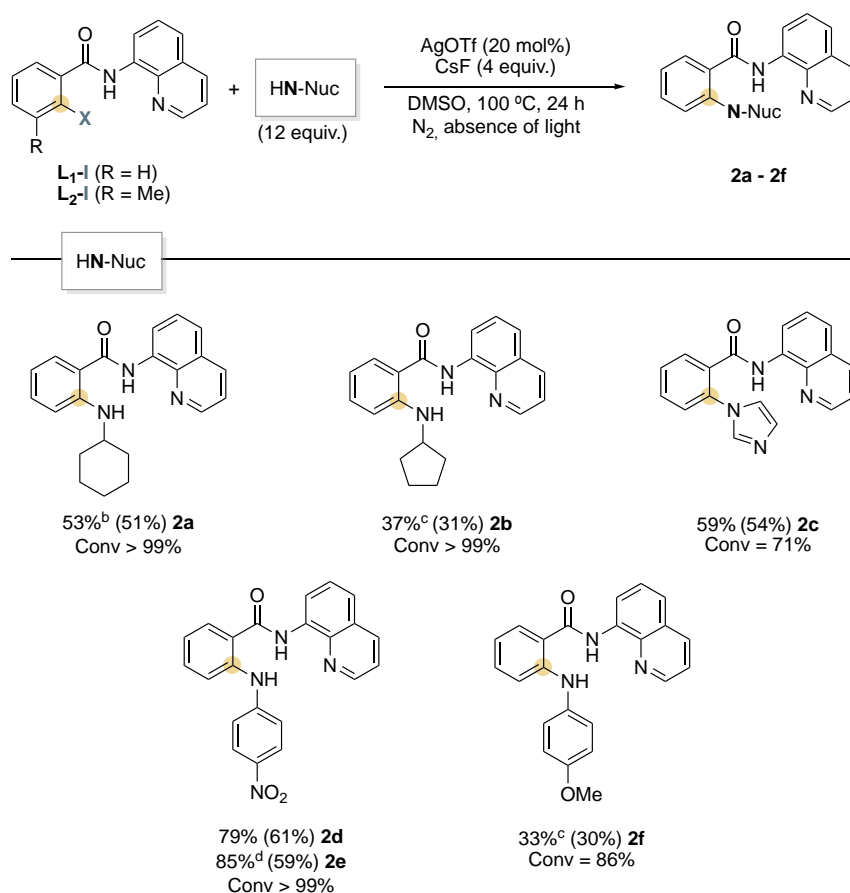
Table VIII.5. Ag-catalyzed halide exchange reactions.

Entry	L$_1$-X	nBu$_4$NX	Yield (%)^a (yield in CH$_3$CN)
1	L$_1$-I	nBu$_4$NCl	82 % (95 %) L$_1$-Cl
2^b		nBu$_4$NCl	20% L$_1$-Cl
3		nBu$_4$NBr	74 % (46 %) L$_1$-Br
4^b		nBu$_4$NBr	0 % L$_1$-Br
5^c		nBu$_4$NF·3H$_2$O	0 % L$_1$-F
6	L$_1$-Br	nBu$_4$NCl	78 % L$_1$-Cl
7^b		nBu$_4$NCl	0 % L$_1$-Cl
8		nBu$_4$NI	0 % (38 %^{d}, 50 %^{e}) L$_1$-I
9	L$_1$-Cl	NaI	0 % L$_1$-I

^{a}Yield calculated from ^{1}H-NMR of crude using 1,3,5-trimethoxybenzene as internal standard. ^{b} The reaction was carried out without AgOTf. ^{c} Using 10 mol% of AgF. Side reaction was observed (34% yield of L$_1$-DMSO). ^{d} Using 20 mol% of AgOTf. ^{e} Using 20 mol% of AgOTf and 20 mol% of PPh$_3$.
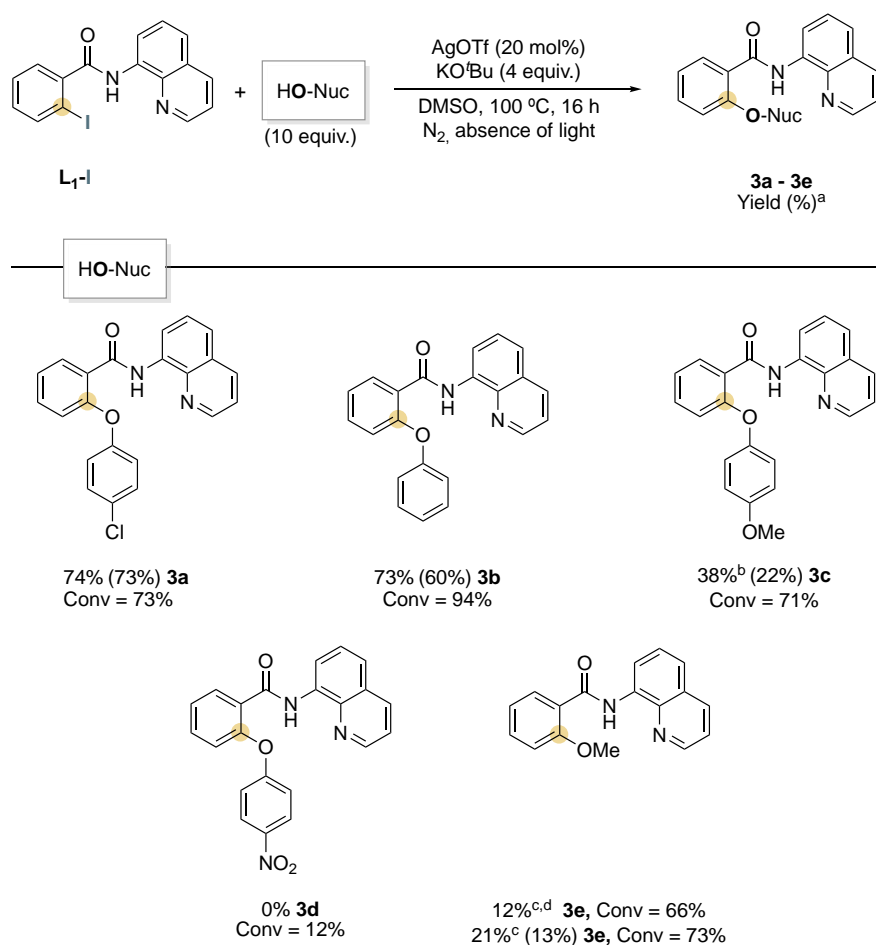
Given the reactivity observed in halide exchange transformation, which suggests a feasible aryl–I and aryl–Br oxidative addition, we envisioned to study cross-coupling reaction using silver. Thus, we turned our attention into the use of aliphatic amines, imidazole and anilines as nucleophiles for the construction of new C–N bonds (Table VIII.6). The first step was directed towards the optimization of the reactions using **L$_1$-I** and cyclohexylamine as N-nucleophile. The reaction was found to be more efficient using CsF as a base, DMSO as solvent and 20 mol% of AgOTf, affording the desired aryl–N coupling in 53% yield (**2a**). Then, we applied the optimized conditions using a set of N-nucleophiles such as cyclopentamine, where a lower yield was observed (37% of **2b**). The use of imidazole as nucleophile afforded the desired product **2c** in 59% yield. We also tested *para*-substituted anilines bearing electron-withdrawing (–NO$_2$) and electron-donating (–OMe) groups yielding 79% of **2d** and a 33% of **2f**, respectively. The higher yield obtained when using electron-withdrawing group is attributed to a more facile deprotonation of the N-nucleophile when compared with the corresponding aniline with the EDG.

Table VIII.6. C–N bond forming reactions under silver catalytic system.

53%[b] (51%) **2a**
Conv > 99%

37%[c] (31%) **2b**
Conv > 99%

59% (54%) **2c**
Conv = 71%

79% (61%) **2d**
85%[d] (59%) **2e**
Conv > 99%

33%[c] (30%) **2f**
Conv = 86%

[a]Yield calculated from ^{1}H-NMR of crude using trimethoxybenzene as internal standard (isolated yield in parentheses). Side reactions were observed [b]18% of **L$_1$-H** and 19% of **L$_1$-L$_1$** homocoupling. [c]10% of **L$_1$-H** and 18% of **L$_1$-L$_1$** homocoupling. [d] traces of **L$_1$- H** and 10% of **L$_1$-L$_1$** homocoupling. [d] Using **L$_2$-I** as a substrate.

To further expand the scope of the silver-catalyzed cross-coupling reaction we turned our attention to explore the formation of aryl–O bonds (Table VIII.7). We optimized the reaction conditions using **L$_1$-I** and phenol as O-nucleophile leading the desired product (**3b**) in 73% yield using DMSO as solvent and KO^{t}Bu as a base. With the optimized conditions in hand, we tested different *para*-substituted phenols. The use of *p*-Cl-phenol render the product **3a** in 74% yield, whereas the use of *p*-MeO-phenol yielded the product in low yield (38%, **3c**). Unproductive catalysis was observed using *p*-NO$_2$-phenol in contrast to the results obtained using *p*-NO$_2$-aniline as N-nucleophile. This result suggested that the deprotonation step is not a key step in the mechanism and the formation of C–O bond needs a correct electronic balance. Furthermore, cross-coupling reactions using CH$_3$OH as nucleophile was also explored using it as solvent and KO^{t}Bu as a base. The coupling product was observed indeed, although only stoichiometric amounts of **3e** was formed.
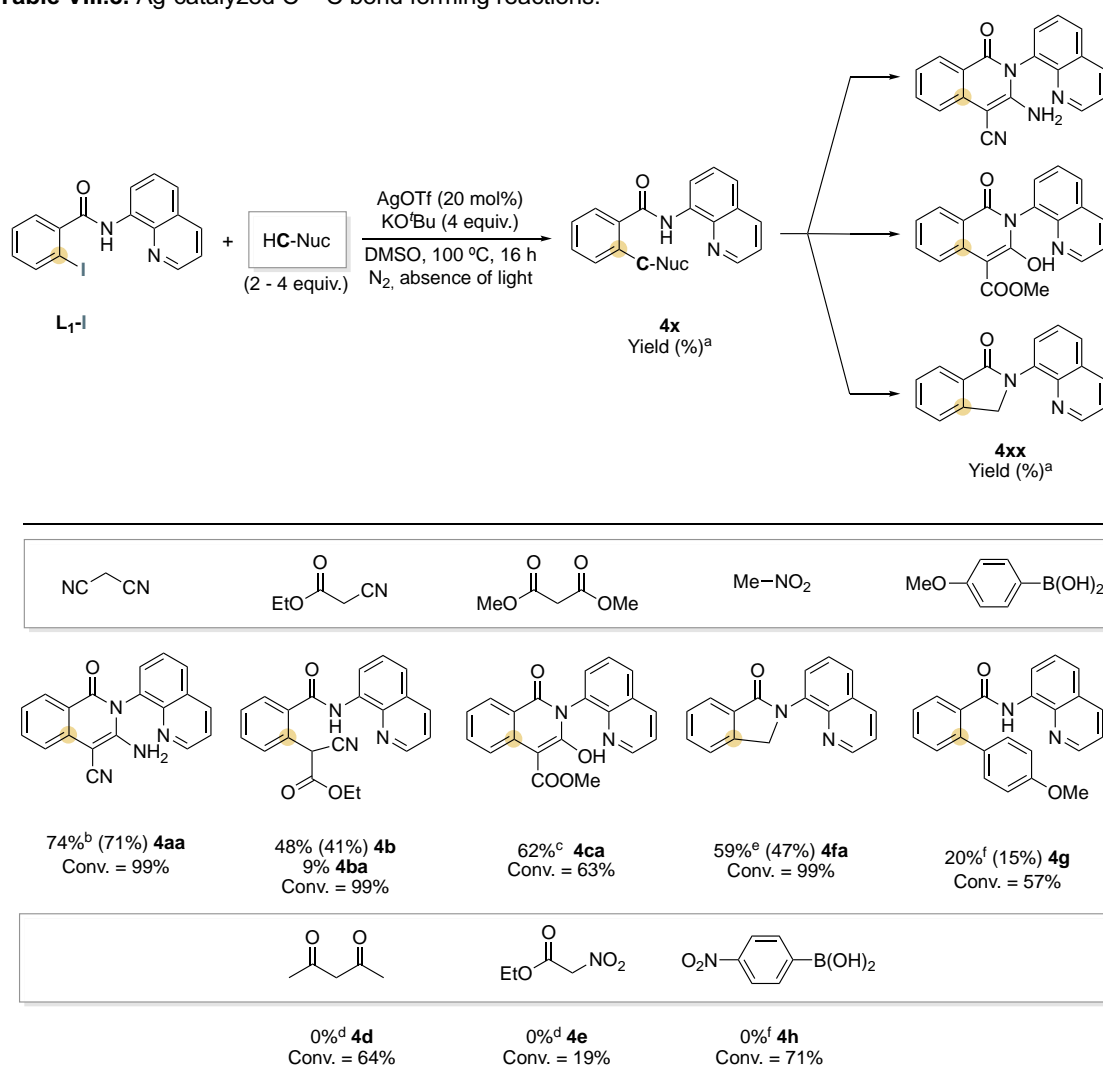
Table VIII.7. Ag-catalyzed C–O bond forming reactions.

L$_1$-I   +   HO-Nuc (10 equiv.)

AgOTf (20 mol%)
KO^{t}Bu (4 equiv.)
DMSO, 100 °C, 16 h
N$_2$, absence of light

3a - 3e
Yield (%)[a]

HO-Nuc

74% (73%) **3a**
Conv = 73%

73% (60%) **3b**
Conv = 94%

38%[b] (22%) **3c**
Conv = 71%

0% **3d**
Conv = 12%

12%[c,d] **3e**, Conv = 66%
21%[c] (13%) **3e**, Conv = 73%

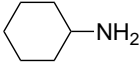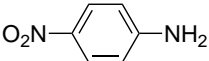[a]Yield calculated from ^{1}H-NMR of crude using trimethoxybenzene as internal standard (isolated yield in parentheses). [b] 32% of **L$_1$-H**. [c] Using 2.5 mL of MeOH instead of DMSO. [d] 10 mol% of AgOTf was used.

After demonstrating that we were able to construct C-N and C–O bonds via silver-catalyzed cross-coupling reactions, we attempted to explore the ability of this metal in C–C bond formation reactions (Table VIII.8). Activated methylene-type substrates such as malononitrile (Hurtley-type couplings), as well as nitromethane and boronic acids, were tested as C-coupling partner. The best results were observed using DMSO as solvent, KO^{t}Bu as base and AgOTf (20 mol%) as silver salt. When malononitrile was used, the coupling product **4aa** was obtained in a 74% yield, which is formed by an initial C–C coupling followed by nucleophilic attack of the amide to one of the –CN groups, forming the final cyclized product. It is worth to note that that highest yield was obtained when CH$_3$CN was used as solvent (90% of **4aa**), however decomposition of acetonitrile and formation of the trimeric triazine-coupled product was observed, and for this reason DMSO was selected as solvent. The key role of silver was further confirmed by the absence of product formation when the reaction was conducted without AgOTf. Using ethyl 2-cyanoacetate as substrate, the C–C coupling was achieved in 48% yield (**4b**) and only 9% of intramolecular cyclization product (**4ba**) was observed. Furthermore, dimethyl malonate was also subjected to the optimized conditions yielding the intramolecular cyclization product in 62% (**4ca**). In this case, the product was formed by a nucleophilic attack of the amide to one of the carbonyl groups, with MeOH as leaving molecule. The catalysis was completely suppressed using acetylacetone and ethyl 2-nitroacetate. On the other hand, the use of nitromethane as coupling counterpart led to the formation of the C–C product **4fa** in 59% yield, which features an isoindolin-1-one formed after the

loss of the nitro group. Furthermore, the coupling of a deprotonated DMSO solvent was observed as a side reaction in a 16% of **L₁-DMSO.** Prompted by these results, and given the previous reactivity observed using the triazamacrocyclic ary–Ag(III) complex,[4] we also explored the use of boronic acid as a C-counterpart. Contrariwise, only afforded 20% of **4g** desired product by using **L₁-I** as a substrate. Thus, the transmetallation and the reductive elimination occurred not in a catalytic but in a stoichiometric fashion. The destabilization effect of the Ag(III) center by the electron-withdrawing group could explain the absence of reactivity observed using the *p*-NO₂-phenylboronic acid.

Table VIII.8. Ag-catalyzed C – C bond forming reactions.

74%[b] (71%) **4aa**	48% (41%) **4b**	62%[c] **4ca**	59%[e] (47%) **4fa**	20%[f] (15%) **4g**
Conv. = 99%	9% **4ba**	Conv. = 63%	Conv. = 99%	Conv. = 57%
	Conv. = 99%			

| 0%[d] **4d** | 0%[d] **4e** | 0%[f] **4h** |
| Conv. = 64% | Conv. = 19% | Conv. = 71% |

[a]Yield calculated from ¹H-NMR of crude using trimethoxybenzene as internal standard (isolated yield in parentheses). [b] 90 % of **4aa** was obtained using CH_3CN as solvent. [c] the reaction was carried out using DMSO d₆. Side reactions were observed: [d] 15 % of **L₁-H**, [e] 16 % of **L₁-DMSO**. [f] The reaction was carried out using 10 equiv. of arylboronic acid at 120 ºC

To further confirm the role of the silver salt as a catalyst in the reaction, we prompted to analyze two AgOTf commercial samples by ICP-MS to search the content of traces of other metals, focusing especially on Pd and Cu due to their ability to catalyze cross-coupling reactions. We observed 0.01% content of Cu in both batches of AgOTf and no traces of Pd were found. With these results in hand, we subjected three of the coupling reactions, i.e. cyclohexylamine, *p*NO₂-aniline and malononitrile (see Table VIII.9) using [Cu(CH₃CN)₄]OTf as catalyst at 0.002 mol% (which corresponded to the content of Cu impurities using 20 mol% of AgOTf) and no significant yield of the desired product was

detected. Indeed, we also tested the addition of Cu(OTf)$_2$, which might be formed if Ag(0) was formed in situ and reoxidized to Ag(I), and again, only traces of the coupling products were detected. On the other hand, we explored the presence of other additives such as HOTf. The presence of both AgOTf and HOTf (5% respect to the AgOTf) in halide exchange reactions resulted in low product yields. These experiments confirmed the role of Ag(I) as catalyst for the unusual two-electron redox Ag(I)/Ag(III) reactivity in cross-coupling transformations.

Table VIII.9. Cross-coupling reactions catalyzed by Ag or Cu impurities.

Entry	Nucleophile	Yield (Conv.)[a]			
		AgOTf (20 mol%)	Cu(OTf)[b] (0.002 %)	Cu(OTf)$_2$ (0.002 %)	AgOTf + HOTf (10 mol% + 5 %)
1	⬡—NH$_2$	53 % of **2a** (99 %)	6 % of **2a** (6 %)	9 % of **2a** (24 %)	-
2	O$_2$N—⬡—NH$_2$	79 % of **2d** (99 %)	24 % of **2d** (24 %)	-	-
3	NC⌒CN	74 % of **4aa** (99 %)	0 % of **4a/4aa** (36 %)	12 % of **4aa** (37 %)	-
4	nBuN$_4$Br	74 %[c] of **L$_1$-Br**	-	-	55 %[d] of **L$_1$-Br**
5[c]	nBuN$_4$Cl	78 %[c] of **L$_1$-Cl**	-	-	68 %[d] of **L$_1$-Cl**

[a]Yield calculated form ^{1}H-NMR of crude using trimethoxybenzene as internal standard. [b] Using [Cu(CH$_3$CN)$_4$]OTf. [c] Using 10 mol% of AgOTf. [d] 5 % of HOTf respect to AgOTf.

VIII.5.2 Mechanistic experiments

To get better understanding of the role of silver in the mechanism, DFT studies were performed in collaboration with Dr. Steven Roldán-Gómez and Dr. Josep M. Luis from IQCC at Universitat de Girona. We modeled the I-to-Cl halide exchange reaction (see Annex 4 for DFT details). The calculation showed the formation of **[L$_1$-Ag(III)-Cl]** species overcoming a 24.7 kcal·mol^{-1} transition state (TS1) via Ag(I) oxidative addition at the aryl-I substrate. This species shows a square-pyramidal geometry with iodide moiety at the apical position (d$_{Ag-I}$ = 3.7 Å) (**[L$_1$-Ag(III)-Cl]**), featuring a d^8 electronic configuration for a Ag(III) as in the well-defined aryl–Ag(III) isolated species.[4] Afterwards, **[L$_1$-Ag(III)-Cl](I)** evolves to **(L$_1$-Cl)AgI** through reductive elimination (TS$_2$ = 28.1 kcal·mol^{-1}). The high temperature needed in the halide exchange reactions (100 ºC) is in agreement with the barrier of 28.1 kcal·mol^{-1}. The DFT studies showed a larger barrier up to 32.5 kcal·mol^{-1} for the aryl–Cl oxidative addition step which is in accordance with the lack of reactivity observed in the Cl-to-I transformation.
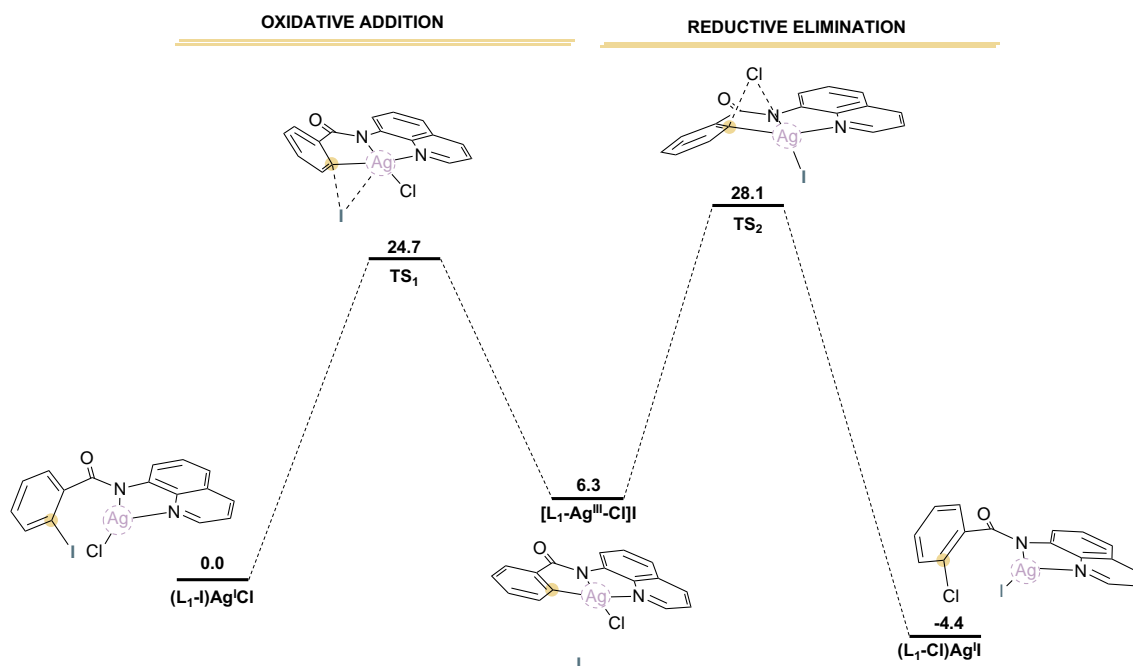
Figure VIII.9. Gibbs energy profile of the oxidative addition and reductive elimination steps in the **L₁-I** to **L₁-Cl** halide exchange reaction.

In order to get insight into the mechanism, we attempted the detection of aryl–Ag(III) active species using high-resolution mass spectrometry (HRMS) and helium tagging infrared photodissociation (IRPD) spectroscopy. These experiments were carried out in collaboration with Dr. Erik Andris, Anamarija Briŝ and Prof. Jana Roithová from Charles University - Prague.

Firstly, we analyzed the reaction mixture at short reaction times by HRMS using **L₁-I** and stoichiometric amounts of silver salt in CH_3CN, which is a suitable solvent for HRMS analysis. C–N homocoupling product was observed suggesting the activation of the aryl–I. To avoid the homocoupling undesired reaction, we designed the more sterically bulky substrate o-Me-L₁-I (**L₂-I**). As showed before the reaction using **L₂-I** and pNO₂-aniline as a nucleophile renders the C–N coupling in 85% **2e** (Table VIII.6)**.** In order to detect the putative **[L₂-Ag(III)]⁺** species, the reaction was carried out without the nucleophile and analyzed by HRMS. The analysis showed a main peak at m/z 495, tentatively assigned to **[(L₂-I)Ag]⁺**. In addition, a small peak at m/z 367 was detected presumably corresponding to **[L₂-Ag(III)]⁺.**
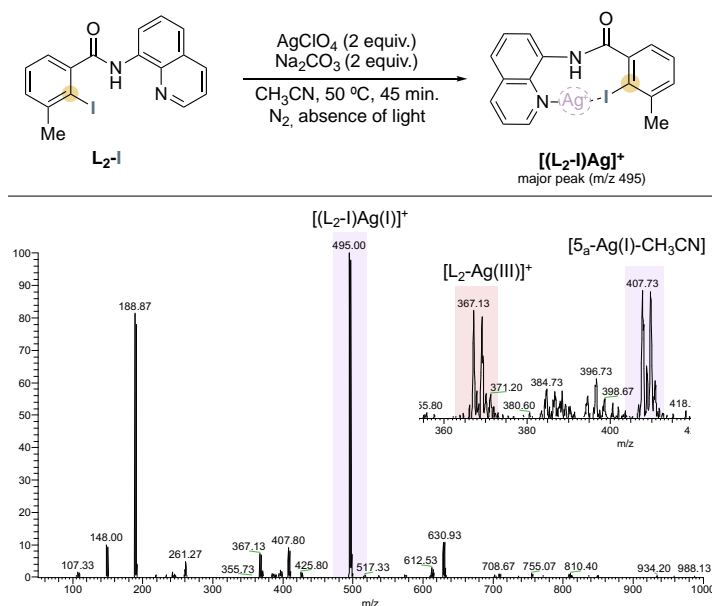
Figure VIII.10. ESI analysis of the crude mixture obtained for the ion spectroscopy experiments.

In order to identify the structure of the detected silver complexes we recorded their IRDP spectra (Figure VIII.11). Firstly, the major peak observed (*m/z* 495) was identified as the Ag(I) complexation to **L₂-I** substrate **[(L₂-I)Ag]⁺**, for which the theoretical IR spectrum reproduce the IRDP spectrum of the ion with *m/z* 495.
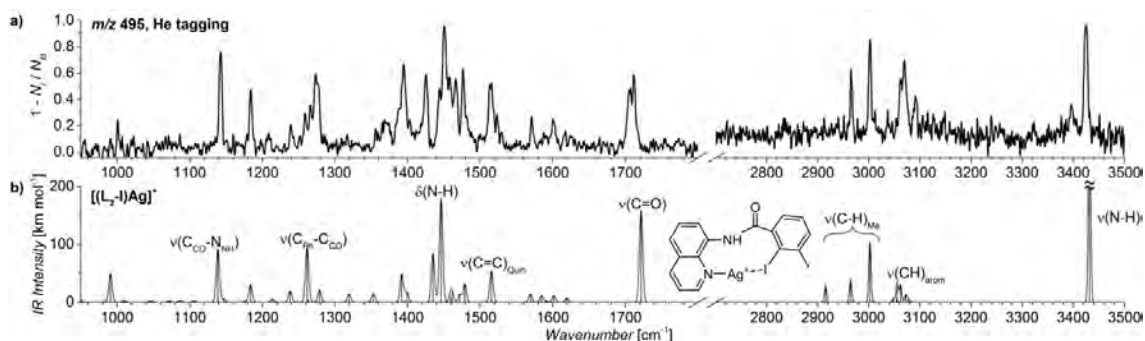

Figure VIII.11. a) Helium tagging IRPD spectra of ions with *m/z* 495. B) Theoretical IR spectrum (see SI for computational details). The scaling factor was 0.98 (below 2000 cm⁻¹) and 0.96 (above 2000 cm⁻¹). Predicted IR intensities above 2700 cm⁻¹ were multiplied by 10.

Then, we turned our attention to detect the putative Ag(III) intermediate (*m/z* 367). At softer ionization conditions we observed another peak with *m/z* = 408, which was presumably assigned as the proposed intermediate with an acetonitrile molecule that fills in the fourth coordination site and stabilizes the silver(III) complex. However, the theoretically spectrum did not fit with the IRPD spectrum recorded. A characteristic band at 1110 and 2770 cm⁻¹ on the IRPD spectrum prompted us to explore a set of alternatives structures with the same mass (Annex 4, Figure S4).

Finally, the theoretically predicted IR spectrum of **[5d-Ag(I)-CH₃CN]⁺** nicely reproduced the IRPD spectrum obtained confirming that the detected *m/z* 408 ion peak corresponds to the intramolecular cyclization conformer as depicted in Figure VIII.12. We proposed the mechanism in Scheme VIII.24 for the formation of **[5d-Ag(I)-CH₃CN]⁺**. After the formation of the **[(L₂-I)Ag]⁺** (*m/z* 495), the Ag(I) species undergoes oxidative addition followed the loss of HI and the coordination of one CH₃CN to fulfill the fourth coordination site forming the sought **[L₂-Ag(III)-(CH₃CN)]⁺**. Later, an intramolecular cyclization of the transient aryl-Ag(III) take place in the gas phase rendering a Ag(I) complex featuring a cationic benzenylium moiety which rapidly collapses to form **[5d-Ag(I)-CH₃CN]⁺**. Then,

subsequent proton-shuttle yields the **[5a-Ag(I)-CH₃CN]⁺**, isolating 10-methylbenzo[c]-[1,10]-phenanthrolin-6(5H)-one (**5a**) as a final organic product. To get further insight into the formation of **[5d-Ag(I)-CH₃CN]⁺,** we scale up the reaction (~ 0.1 g) in order to isolate and confirm the organic product detected. Upon mixing **L₂-I**, AgClO₄ and Na₂CO₃ at 100 ºC during 24 h, HRMS of the crude mixture showed a peak at *m/z* 261, which after chromatographic purification could be isolated and fully characterized by NMR and HRMS as the intramolecular cyclization product (**5a**), which resulted from the tautomerization of **5d.**
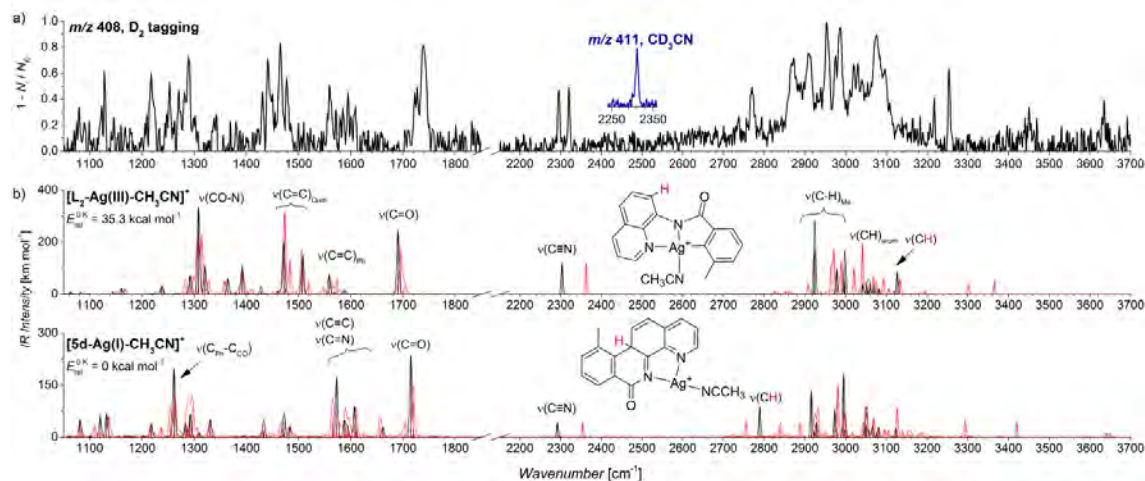
Figure VIII.12. a) D₂ tagging IRPD spectra of ions with *m/z* 408. b) Theoretical IR (B3LYP-D3BJ/6-311+g(2d,p):SDD-Ag) of **[L₂-Ag(III)-CH₃CN]⁺** and **[5d-Ag(I)-CH₃CN]⁺**.The harmonic IR spectra are in black; the scaling factor was 0.98 (below 2000 cm⁻¹) and 0.96 (above 2000 cm⁻¹). The anharmonic IR spectra (B3LYP-D3BJ/6-311+g(2d,p):SDD-Ag) are in red and were not scaled. Predicted IR intensities above 2700 cm⁻¹ were multiplied by 10.
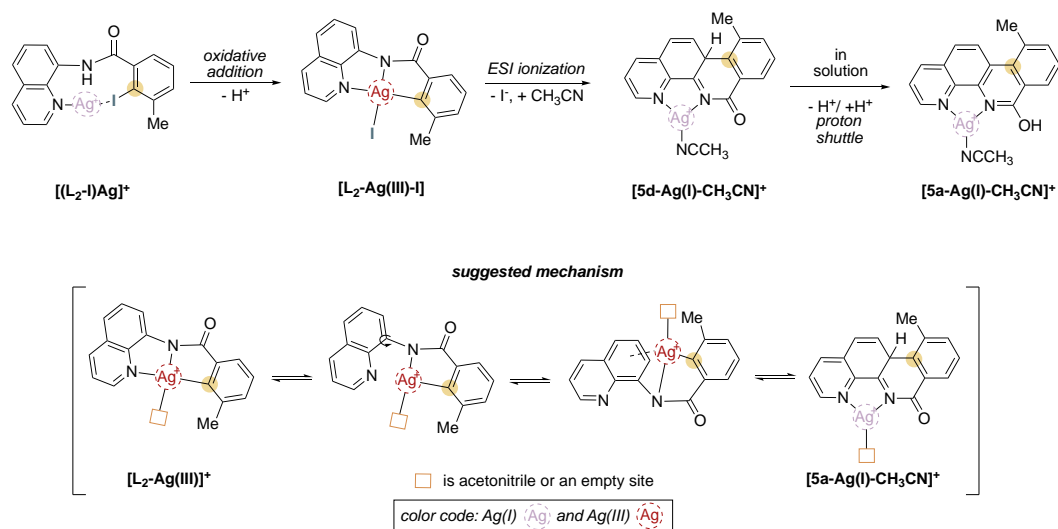
Scheme VIII.24. Suggested mechanism of the formation of **[5a-(Ag(I)-CH₃CN]**.

With all these results in hand, we proposed the following mechanism for the silver-catalyzed cross-coupling reaction, which is based both in experimental and theoretical evidences. Firstly, the Ag(I) is coordinated to the aminoquinoline DG, following oxidative addition that converges into the key aryl–Ag(III) species. At this point, if the nucleophile is present on the reaction mixture, nucleophile coordination and reductive elimination yields the coupling product. In contrast, the highly reactive aryl–Ag(III) species, in the absence of nucleophile, undergoes an intramolecular cyclization reaction to afford **5a** species, which was experimentally characterized.
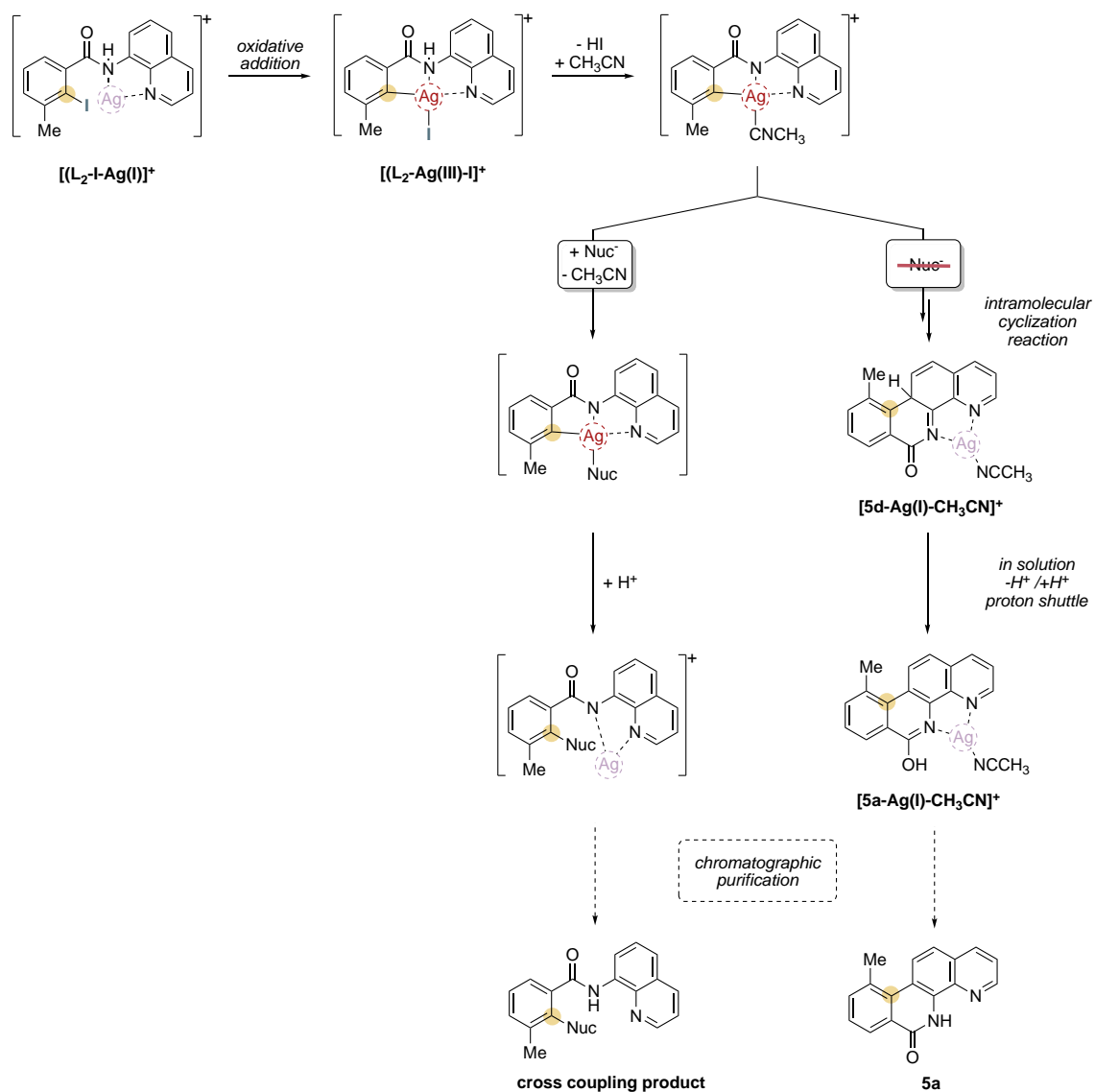
Scheme VIII.25. Proposed mechanism for the Ag(I)/Ag(III) cross-coupling system.

In summary, in this section we have been able to develop a new two-electron Ag(I)/Ag(III) cross-coupling catalysis with a non-cyclic aryl-X substrate. Furthermore, the protocol permits the use of different nucleophiles leading the formation of C–C and C–Heteroatom bonds, thus demonstrating that silver can become an alternative or a complementary catalyst for cross-coupling reactions. The direct detection of the aryl–Ag(III) using a non-cyclic substrate bearing a 8-aminoquinoline was unsuccessful, however the existence of this species was clearly suggested by DFT calculations, indicating a feasible oxidative addition of **L$_1$-I** substrate via Ag(I)/Ag(III) catalytic system. Moreover, ion spectroscopy experiments suggested a highly reactive aryl–Ag(III), which in the absence of nucleophile, reacted with itself to afford an intermolecular cyclic product.

VIII.6 References

[1]   Ribas, X.; Devillard, M. *Chem. Eur. J.* **2018,** *24*, 1222-1230.

[2]   Font, M.; Ribas, X., Pincerlike Cyclic Systems for Unraveling Fundamental Coinage Metal Redox Processes. In *The Privileged Pincer-Metal Platform: Coordination Chemistry & Applications*, van Koten, G.; Gossage, R. A., Eds. Springer International Publishing: Cham, 2016; pp 269-306.

[3]   Casitas, A.; King, A. E.; Parella, T.; Costas, M.; Stahl, S. S.; Ribas, X. *Chem. Sci.* **2010,** *1*, 326-330.

[4]   Font, M.; Acuña-Parés, F.; Parella, T.; Serra, J.; Luis, J. M.; Lloret-Fillol, J.; Costas, M.; Ribas, X. *Nat. Commun.* **2014,** *5*, 4373.

[5]   Planas, O.; Whiteoak, C. J.; Martin-Diaconescu, V.; Gamba, I.; Luis, J. M.; Parella, T.; Company, A.; Ribas, X. *J. Am. Chem. Soc.* **2016,** *138*, 14388-14397.

[6]   Planas, O.; Roldán-Gómez, S.; Martin-Diaconescu, V.; Parella, T.; Luis, J. M.; Company, A.; Ribas, X. *J. Am. Chem. Soc.* **2017,** *139*, 14649-14655.

[7]   Rovira, M.; Roldán-Gómez, S.; Martin-Diaconescu, V.; Whiteoak, C. J.; Company, A.; Luis, J. M.; Ribas, X. *Chem. Eur. J.* **2017,** *23*, 11662-11668.

[8]   Planas, O.; Roldán-Gómez, S.; Martin-Diaconescu, V.; Luis, J. M.; Company, A.; Ribas, X. *Chem. Sci.* **2018,** *9*, 5736-5746.

[9]   Gilman, H.; Lichtenwalter, M. *J. Am. Chem. Soc.* **1939,** *61*, 957-959.

[10]   Yoshino, T.; Ikemoto, H.; Matsunaga, S.; Kanai, M. *Angew. Chem. Int. Ed.* **2013,** *52*, 2207-2211.

[11]   Sun, B.; Yoshino, T.; Matsunaga, S.; Kanai, M. *Adv. Synth. Catal.* **2014,** *356*, 1491-1495.

[12]   Sun, B.; Yoshino, T.; Matsunaga, S.; Kanai, M. *Chem. Commun.* **2015,** *51*, 4659-4661.

[13]   Shah, T. A.; De, P. B.; Pradhan, S.; Banerjee, S.; Punniyamurthy, T. *J. Org. Chem.* **2019,** *84*, 16278-16285.

[14]   Planas, O.; Whiteoak, C. J.; Company, A.; Ribas, X. *Adv. Synth. Catal.* **2015,** *357*, 4003-4012.

[15]   Figg, T. M.; Park, S.; Park, J.; Chang, S.; Musaev, D. G. *Organometallics* **2014,** *33*, 4076-4085.

[16]   Evans, D. *J. Chem. Soc.* **1959**, 2003-2005.

[17]   Böhm, H.-J.; Banner, D.; Bendels, S.; Kansy, M.; Kuhn, B.; Müller, K.; Obst-Sander, U.; Stahl, M. *ChemBioChem* **2004,** *5*, 637-643.

[18]   Müller, K.; Faeh, C.; Diederich, F. *Science* **2007,** *317*, 1881-1886.

[19]   Purser, S.; Moore, P. R.; Swallow, S.; Gouverneur, V. *Chem. Soc. Rev.* **2008,** *37*, 320-330.

[20]   Wang, J.; Sánchez-Roselló, M.; Aceña, J. L.; del Pozo, C.; Sorochinsky, A. E.; Fustero, S.; Soloshonok, V. A.; Liu, H. *Chem. Rev.* **2014,** *114*, 2432-2506.

[21]   Ackermann, L.; Wechsler, C.; Kapdi, A.; Althammer, A. *Synlett* **2010,** *2010*, 294-298.

[22] Guo, W.-J.; Wang, Z.-X. *J. Org. Chem.* **2013,** *78*, 1054-1061.

[23] Kiso, Y.; Tamao, K.; Kumada, M. *J. Organomet. Chem.* **1973,** *50*, C12-C14.

[24] Ackermann, L.; Born, R.; Spatz, J. H.; Meyer, D. *Angew. Chem. Int. Ed.* **2005,** *44*, 7216-7219.

[25] Yoshikai, N.; Matsuda, H.; Nakamura, E. *J. Am. Chem. Soc.* **2009,** *131*, 9590-9599.

[26] Yoshikai, N.; Mashima, H.; Nakamura, E. *J. Am. Chem. Soc.* **2005,** *127*, 17978-17979.

[27] O'Neill, M. J.; Riesebeck, T.; Cornella, J. *Angew. Chem. Int. Ed.* **2018,** *57*, 9103-9107.

[28] Yu, D.-G.; Wang, C.-s.; Yao, C.; Shen, Q.; Lu, L. *Org. Lett.* **2014,** *16 21*, 5544-7.

[29] Nakamura, Y.; Yoshikai, N.; Ilies, L.; Nakamura, E. *Org. Lett.* **2012,** *14*, 3316-3319.

[30] Schaub, T.; Backes, M.; Radius, U. *J. Am. Chem. Soc.* **2006,** *128*, 15964-15965.

[31] Ho, Y. A.; Leiendecker, M.; Liu, X.; Wang, C.; Alandini, N.; Rueping, M. *Org. Lett.* **2018,** *20*, 5644-5647.

[32] Sun, A. D.; Love, J. A. *Org. Lett.* **2011,** *13*, 2750-2753.

[33] Tobisu, M.; Xu, T.; Shimasaki, T.; Chatani, N. *J. Am. Chem. Soc.* **2011,** *133*, 19505-19511.

[34] Zhou, J.; Berthel, J. H. J.; Kuntze-Fechner, M. W.; Friedrich, A.; Marder, T. B.; Radius, U. *J. Org. Chem.* **2016,** *81*, 5789-5794.

[35] He, Z.; Huang, Y. *ACS Catal.* **2016,** *6*, 7814-7823.

[36] Rinaldi, R.; Jastrzebski, R.; Clough, M. T.; Ralph, J.; Kennema, M.; Bruijnincx, P. C. A.; Weckhuysen, B. M. *Angew. Chem. Int. Ed.* **2016,** *55*, 8164-8215.

[37] Li, B.-J.; Yu, D.-G.; Sun, C.-L.; Shi, Z.-J. *Chem. Eur. J.* **2011,** *17*, 1728-1759.

[38] Zeng, H.; Qiu, Z.; Domínguez-Huerta, A.; Hearne, Z.; Chen, Z.; Li, C.-J. *ACS Catal.* **2017,** *7*, 510-519.

[39] Tobisu, M.; Chatani, N. *Acc. Chem. Res.* **2015,** *48*, 1717-1726.

[40] Yu, D.-G.; Li, B.-J.; Shi, Z.-J. *Acc. Chem. Res.* **2010,** *43*, 1486-1495.

[41] Tobisu, M.; Chatani, N., Metal-Catalyzed Aromatic C-O Bond Activation/Transformation. In *Organometallics for Green Catalysis*, Dixneuf, P. H.; Soulé, J.-F., Eds. Springer International Publishing: Cham, 2019; pp 103-140.

[42] Borissov, A.; Maurya, Y. K.; Moshniaha, L.; Wong, W.-S.; Żyła-Karwowska, M.; Stępień, M. *Chem. Rev.* **2021**.

[43] Li, P. *Cheminform* **2006,** *37*.

[44] Das, R.; Mandal, M.; Chakraborty, D. *Asian J. Org. Chem.* **2013,** *2*, 579-585.

CHAPTER IX

General Conclusions

Understanding the operando mechanism of a given transformation is crucial for the improvement of methodologies to construct complex molecules. In this context, the use of model substrate permits the stabilization of key intermediate species enabling their isolation and characterization. This information is vital for the design and development of new methodologies. The coordination environment offered by the 8-aminoquinoline bidentate directing group allows the correct geometry of the metal to effect the activation of an specific bond. This property allows both the stabilization and detection of intermediate species, and the improvement of the efficiency and selectivity of the catalytic process. In this thesis, an update in the field of cobalt-catalyzed cross-coupling reactions was covered in a review work (Chapter III), showing the potential of cobalt to catalyze these transformations. In this line, the reactivity of well-defined aryl–Co(III) complex towards the organic and inorganic azides have been described. Furthermore, several organometallic Co(III) and Co(II) complexes have been isolated and characterized gaining insight into the mechanism involved in C–H amination transformations mediated by high-valent cobalt system (Chapter IV). The use of 8-aminoquinoline-containing substrates as non-cyclic open model system to achieve the activation of strong C–X bonds (X = F, OMe) have been developed. Their reactivity towards C–F (Chapter V) and C–OMe (Chapter VI) functionalization have been tested with alkynes to form both aromatic homologation and alkyne monoannulation product. In the same line, arene substrates bearing 8-aminoquinoline has been explored for Ag(I)/Ag(III) catalyzed C-heteroatom cross coupling reactions (Chapter VII).

In **Chapter IV**, a 12-membered macrocyclic ligand is used as a model substrate to understand the mechanism involved in the C–N coupling mediated by Co(III). The reactivity of well-defined Oh aryl–Co(III) species with different organic and inorganic azides was explored. Using aliphatic azides, we provided spectroscopic and crystallographic evidences of organometallic Co(III) species bearing the aryl–N bond formed (**4x-OAc** and **5x-OAc**). Acidic conditions assist the demetallation step yielding the aryl–N coupling product with different azides. In contrast, an intramolecular cyclic product was observed under thermal conditions only by using benzyl azide (**a**), highlighting the importance of the benzylic position of the azide coupling partner. Furthermore, (2-azidoethyl)benzene (**b**) reacted with the aryl-Co(III) complex affording a well-defined Co(II) complex bearing the formed aryl–N bond. Experimental evidence indicated the crucial stabilizing masking effect of the carboxylate moiety on the reaction. Moreover, a thorough DFT study describes the formation of a transient aryl-Co(III)-nitrene intermediate species, which rapid evolves to a aryl-Co(III)-masked nitrene intermediate taming its reactivity and guiding the productive formation of the aryl–N bond. This in-situ masking strategy can be use as alternative protocol avoiding the use of stabilized nitrene sources such as dioxazolones in C–H amination reactions.

In **Chapter V**, we have reported a new nickel-catalyzed protocol for the C–F functionalization transformation assisted by the 8-aminoquinoline bidentate directing group. The protocol forms the aromatic homologation and the alkyne monoannulation products in a chemodivergent manner using internal alkynes. Furthermore, the methodology reported shows how the electronic properties of F-containing substrates and the alkynes direct the reactivity towards the aromatic homologation product or the alkyne mononannulation one. A DFT study indicated a lower transition state and exergonic step for the C–F activation over the C–H bond, which explained the observed selectivity for the former. Additionally, the key role of Li$^+$ in assisting the removal of the fluoride anion was reflected in both experimental and computational analysis. Finally, crystallographic evidence of 9-membered nickelacyclic species bearing a double-inserted alkyne provides important insights into the mechanism of the aromatic homologation reactions.

In **Chapter VI**, a new protocol for the synthesis of the aromatic homologation as well as the alkyne monoannulation product via aryl–OMe functionalization catalyzed by nickel was developed, which falls in the rising field of lignin valorisation. The key role of Li$^+$ observed in the previous Chapter V was further confirmed here, since its excess enhances the selectivity towards the aromatic homologation product. Furthermore, the chemoselectivity can be switched by adding PPh$_3$ in the reaction, affording the alkyne monoannulation product in a selective manner. Substrate bearing both C–F and C–OMe on the *ortho* position of the directing group was also used, showing the preferential activation of the C–F bonds over the C–OMe bonds. Furthermore, the presence of both C–F and C–OMe bonds at the *ortho*-positions permit us the one-step synthesis of a polycyclic aromatic hydrocarbons. In addition, this annulated products can be used in turn as precursors towards the nanographene-like synthesis.

In **Chapter VII**, we describe a protocol for silver(I)-catalyzed C–C and C–Heteroatom cross coupling, by using an arene-bearing non-cyclic substrate containing the 8-aminoquinoline directing group. The reactivity observed demonstrated the ability of silver to undergo two-electron redox Ag(I)/Ag(III) catalysis. In contrast to the use of triazamacrocyclic ligand, the detection of aryl–Ag(III) intermediate using the chelation system was indirect, which is in agreement with the higher reactivity observed in contrast to the triazamacrocyclic model substrate. DFT analysis together with IRPD-MS studies indicates the formation of the highly aryl–Ag(III) species. Indeed, the experiments done without the presence of nucleophile affords an intramolecular cyclic product. This work open the door towards the development of new Ag(I)/Ag(III) cross-coupling protocols.

ANNEX

Supporting Information

Supporting information for Chapter IV

C$_{sp2}$-H amination mediated by metastable Oh masked aryl-Co^{III}-nitrene species

Lorena Capdevila, Marc Montilla, Oriol Planas, Artur Brotons, Pedro Salvador, Vlad Martin-Diaconescu, Teodor Parella, Josep M. Luis,* Xavi Ribas*

Table of contents

1. General Considerations

Materials and methods

All reagents and solvents were purchased from Sigma Aldrich, Fisher Scientific or Fluorochem and used without further purification.^{1}H, ^{13}C{1H} and ^{19}F{H}-NMR spectra were recorded on Bruker 400 or 500 AVANCE spectrometer in the corresponding deuterated solvent (CDCl$_3$ or dmso d$_6$) and calibrated relative to the residual protons of the solvent. Quantification of reaction yields through integration of peaks was performed using an internal reference (1,3,5-trimethoxybenzene). High resolution mass spectra (HRMS) were recorded on a Bruker MicroTOF-Q IITM instrument using ESI source at Serveis Tècnics de Recerca, University of Girona. IR Spectra (FTIR) were recorded on a FT-IR Alpha spectrometer from Bruker with a PLATINUM-ATR attachment using OPUS software to process the data. The ligands **L-H**, **L-Me** and the **1-CH$_3$CN** complex have been synthesized according to the procedure described in the literature.[1-3]

XAS Data Acquisition and processing

Samples were run as solid powders diluted in boron nitride at the ALBA synchrotron CLAESS beamline. Data was collected in transmission mode, at liquid nitrogen temperatures (80K), using a Si311 double crystal monochromator. Data was averaged; normalized and calibrated using the Athena software.[4] The energy was calibrated to the first inflection point of Co foil taken as 7709.5 eV. The autobk algorithm was used for EXAFS spectra extraction having a spline in the 1 to 13 Å^{-1} region with an Rbkg of 1.1 for 1-OAc and 6b-OAc and R$_{bkg}$ of 1 for **7-OAc**. The FEFF6 code[5, 6] was used for scattering path generation, and k^3-weighted fits of the data were carried out in r-space over an r-range of 1-3.0 Å and a k-range of 2-12.0 Å^{-1} unless otherwise specified, using the Artemis software.[6] The S$_0^2$ value was set to 0.9, and a global E$_0$ was employed with the initial E$_0$ value set to the inflection point of the rising edge. Single scattering paths were fit in terms of a Δr_{eff} and σ^2 as previously described. To assess the goodness of the fits both the R$_{factor}$ (%R) and the reduced χ^2 (χ^2_v) were minimized, ensuring that the data was not over-fit. Pre-edge features were fit using a Gaussian-Lorentzian sum function with 50% Gaussian character.

Theoretical Calculations

All DFT calculations have been carried out using the GAUSSIAN16 program.[7] Geometry optimizations have been performed without any symmetry restrictions, considering the effect of the HFIP solvent (via the Self-Consistent Reaction Field –S1CRF– method using the SMD solvation model,[8] and also taking into account dispersion effects with the Grimme and coworkers DFT-D3BJ correction[9, 10] at the BP86-D3BJ(SMD)/Def2SVP level of theory.[11-14]

Note that the HFIP solvent is not implemented in GAUSSIAN16, so we performed those calculations using the *Solvent=Generic,Read* options for the *SCRF* keyword. The *Minnesota Solvent Descriptor Database*[15] explains that, using the universal solvation model as described by Cramer et al.,[16] one needs a set of descriptors which must be provided in order to use a custom/non-parameterized solvent using Gaussian's SCRF.

The required descriptors are:

ν	index of refraction at optical frequencies at 293K. Sometimes called n_{20}^D. Note that for this descriptor, the GAUSSIAN input requires the user to enter the square of this value, rather than the value itself.
α	Abraham's hydrogen bond acidity. In Abraham's notation: $\sum \alpha_2^H$
β	Abraham's hydrogen bond basicity. In Abraham's notation: $\sum \beta_2^H$
γ	Macroscopic surface tension at a liquid-air interface at 298K. In cal·mol^{-1}·Å^{-2}, but dimensionless. Note that 1 dyne/cm = 1.43932 cal·mol^{-1}·Å^{-2}.
ε	Dielectric constant at 298K.
ϕ	Aromaticity: out of all non-hydrogen atoms, fraction which are aromatic carbons.
ψ	Electronegative halogenicity: out of all non-hydrogen atoms, fraction which are F, Cl, or Br.
ν_{25}	same as n, but at 298K.

And the corresponding values for HPIF are:

ν	1.275 [17]
α	0.77 [18]
β	0.10 [19]
γ	23.23 [20]
ε	16.7 [21]
ϕ	0.000
ψ	0.600
ν_{25}	-

After optimization of the geometries with this procedure, analytical frequency calculations have been performed at the same level of theory, to evaluate enthalpy and entropy corrections at 298.15K, and to ensure that all frequencies were positive for the minima, while having only one negative frequency for the transition states (corresponding with the expected atom displacement for the chemical process). All points in the reaction pathway have been connected via IRC.

Single point calculations on the equilibrium geometries, including the solvent and dispersion effects (E_{sp}), have been carried out at the RevTPSS-D3BJ(SMD)/Def2TZVP level of theory.[22] Note that the D3BJ parameters for the RevTPSS functional are not currently implemented in GAUSSIAN16, so they were included using the corresponding IOp keywords: *IOp(3/174=1000000) IOp(3/175=1402300) IOp(3/177=442600) IOp(3/178=4472300)*.[dft-11]

Then, the total Gibbs Energy values (G) are given by:

$$G = E_{sp} + G_{corr.} + G^{°/*} \quad (1)$$

where the Gibbs Energy correction ($G_{corr.}$) has been obtained from the thermodynamical analysis at the optimization level of theory, but corrected using the GoodVibes code[23] so that frequencies below 100 are not treated with the Harmonic Approximation, but rather with the Quasi-Harmonic Approximation as described by Grimme.[24] Finally, the additional correction term $G^{°/*}$ accounts for the transition from the standard state concentration (gas phase, pressure of 1 atm) to the concentrations used experimentally.

Effective oxidation state (EOS) analysis

The concept of oxidation state (OS) is unavoidably related to the electron distribution around the atoms, which can nowadays be described to an unprecedented precision with modern electronic structure methods. The effective oxidation state (EOS) analysis introduced by Ramos-Cordoba et al. is formally applicable to any molecular system and wavefunction on equal footing.[25] The scheme uses Mayer's effective fragment orbitals (EFOs) and their occupation numbers (λ), obtained independently for each atom/ligand and for each spin case. These spin-resolved EFOs are sorted by decreasing occupation number and individual electrons are assigned to them until the total number of electrons is reached. This procedure leads to an effective configuration of each ligand/atom, and hence its OS. The difference in the occupation between the last occupied (LO) and first unoccupied (FU) EFOs indicates to which extent the electron distribution can be pictured as a discrete ionic model. A simple reliability index, R (%) = min (R_α, R_β), can be introduced for each spin case σ as

$$R_\sigma(\%) = 100 \cdot \min(1, max(0, \lambda_{LO}^\sigma - \lambda_{FU}^\sigma + 1/2)). \tag{2}$$

The OS assignment is considered as undisputable when the difference in occupation of the frontier EFOs exceeds half electron, leading to R = 100. When the two frontier EFOs from different fragments exhibit the same occupation number, two different equally plausible OS distributions are present with R = 50.

Besides the OS assignation and the associated R value, the visual inspection of the EFOs is also useful in order to determine which atom/ligand orbitals hold the individual electrons (or electron pairs). For each formal bond between two fragments, one finds one (and only one) pair of complementary EFOs on each of them representing the dangling valence of the split bond with occupations that add approximately to one for each spin channel.

In order to obtain the EFOs, an underlying atomic partitioning scheme is necessary. The shape of the EFOs is rather insensitive to partitioning, while the occupation numbers may vary. The partial ionic character of the bonds is better captured by schemes such as QTAIM or topological fuzzy Voronoi cells (TFVC), as compared to Mulliken's or Hirshfeld's schemes, and therefore QTAIM and TFVC schemes are better suited for OS assignation.

2. Synthesis of aryl-Co^{III}-X complexes (1-X)
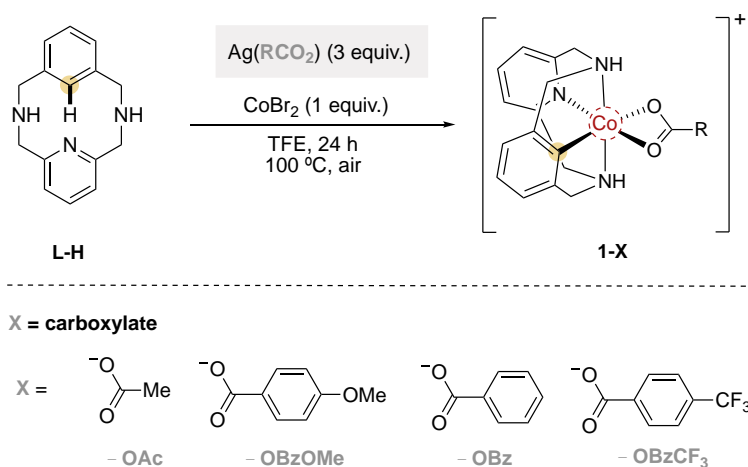
Scheme S1. Synthesis of aryl-Co^{III}-X complexes (**1-X**).
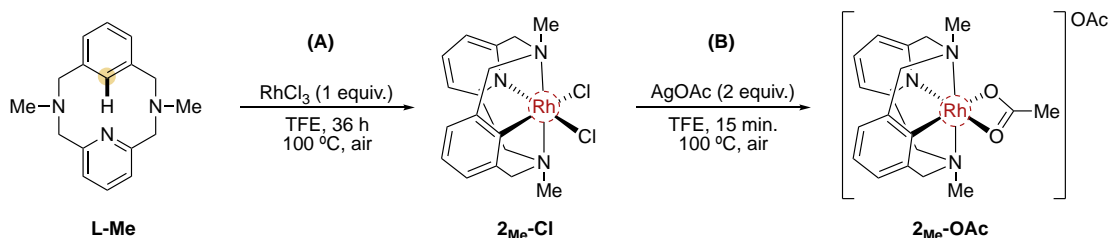
The **1-X** complexes have been synthesized according to the procedure described in the literature.[2, 3] To a solution of **L-H** ligand (50 mg, 0.21 mmol) in a 10 mL vial, Ag(RCOO$_2$) (0.63 mmol) and CoBr$_2$ (45.9 mg, 0.21 mmol) were mixed in TFE (2.5 mL). The vial was sealed with a septum and warmed up to 100 ºC. After 24 h, the solvent was removed, and the mixture was dissolved in CHCl$_3$ and layered with pentane at 4 ºC. The resulting oil was dried under vacuum during 6 h affording the corresponding **1-X** organometallic complex. Recrystallization with CHCl$_3$ layered with pentane gave the corresponding complex **1-X**, which was characterized by NMR and X-Ray spectroscopy.

The NMR data of **1-OAc***,* **1-OBzOMe** and **1-OBz** was in agreement with the previous reports. [2, 3]

Aryl-Co^{III}-(OBz-CF$_3$)$_2$ – **(1-OBzCF$_3$)**
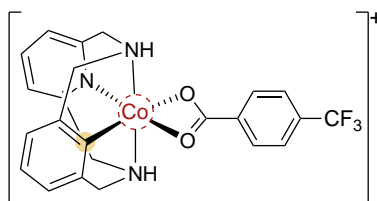
Red foam (74%, 105.2 mg). **^{1}H NMR** (400 MHz, CHCl$_3$, 298 K) δ (ppm): 8.24 (bs, 2H), 7.73 (d, ^3J = 7.7 Hz, 2H), 7.52 (m, 3H), 7.36 (d, ^3J = 7.7 Hz, 2H), 7.19 (bs, 2H), 7.06 (t, ^3J = 7.0 Hz, 1H), 7.00 – 6.94 (m, 4H), 5.01 (dd, ^2J = 16.7 Hz, ^3J = 7.0 Hz, 2H), 4.92 (dd, ^2J = 15.4 Hz, ^3J = 6.7 Hz, 2H), 3.95 – 3.88 (m, 4H). **^{13}C {1H} NMR** (100 MHz, CHCl$_3$, 298 K) δ (ppm): 174.7 (1C), 169.4 (1C), 161.7 (2C), 148.5 (2C), 138.8 (1C), 137.5 (1C), 131.5 (1C), 129.2 (2C), 124.6 (1C), 124.4 (2C), 124.3 (CF3), 120.7 (2C), 118.7 (2C), 62.5 (2C), 62.2(2C). **^{19}F-NMR** (400 MHz, CDCl3, 298 K) δ (ppm): -62.6, -62.8. **HRMS** (ESI) calc. for C$_{23}$H$_{20}$F$_3$CoN$_3$O$_2^+$ [M – (OBzCF$_3$)]$^+$: 486.0834; found 486.0828.

## 3. Synthesis of aryl-Rh^{III}-X complexes (2$_{Me}$-X)

Scheme S2. Synthesis of **2$_{Me}$-OAc** from **L-Me** ligand.

(A) The **2$_{Me}$-Cl** complex has been synthesized according to the procedure described in the literature.[2] **L-Me** (100 mg, 0.37 mmol) and RhCl$_3$ (77.4 mg, 0.37 mmol) were mixed in TFE (2.5 mL). The crude mixture was heated up to 100 ºC during 36 h. The solvent was then removed, and the crude mixture was dissolved in a mixture 1:1 CH$_3$CN/CH$_3$OH and layered with ether. Yellow crystals of **2$_{Me}$-Cl** were obtained after 24 h at 4 ºC. The NMR data was in agreement with the previous report.

(B) In a 10 mL vial, **2$_{Me}$-Cl** (20 mg, 0.045 mmol) and AgOAc (18.4 mg, 0.11 mmol, 2.5 equiv.) were mixed in TFE and heated over 15 min at 100 ºC. Then, the solvent was removed observing a quantitative formation of **2$_{Me}$-OAc** and was used without purification.

^{1}H NMR (400 MHz, CHCl$_3$, ppm): 7.43 (t, ^3J = 7.6 Hz, 1H), 6.89 (d, ^3J = 7.6 Hz, 2H), 6.72 – 6.67 (m, 3H), 4.95 (d, ^2J = 14.6 Hz, 4H), 3.92 (d, ^2J = 15.7 Hz, 2H), 3.81 (d, ^2J = 14.6 Hz, 2H), 3.12 (s, 6H), 1.95 (s, 3H). **^{13}C {1H} NMR** (100 MHz, CHCl$_3$, 298 K) δ (ppm): 178.3 (1C), 167.3 (1C), 159.2 (2C), 142.2 (2C), 136.9 (1C), 123.0 (1C), 119.7 (2C), 118.4 (1C), 75.4 (2C), 73.8 (2C), 51.7 (2C), 24.6 (1C). **HRMS** (ESI) calc. for C$_{19}$H$_{23}$RhN$_3$O$_2^+$ [M – OAc]$^+$: 428.0840; found: 428.0839.

4. Reactivity of 1-OAc with NaN$_3$
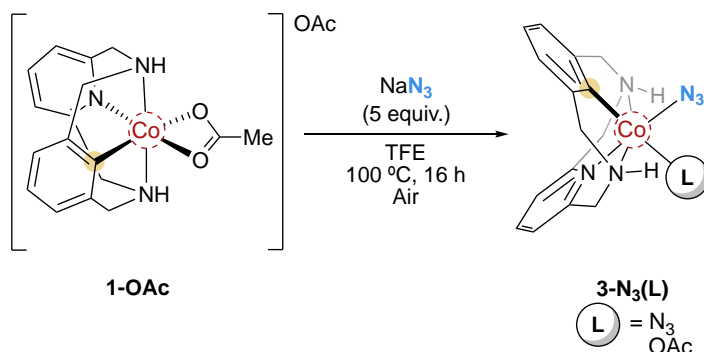
Scheme S3. Formation of **1-N$_3$(L)** organometallic complex.

In a 2 mL vial, **1-OAc** (20 mg, 0,048 mmol) and NaN$_3$ (5 equiv.) were mixed in TFE (1.5 mL) and the vial was sealed. The mixture was heated at 100 °C during 16 h. The solvent was then removed, and the crude mixture was analyzed by ^{1}H-NMR and HRMS observing the formation of **3-N$_3$(N$_3$)** and **3-N$_3$(OAc)** organometallic complexes.
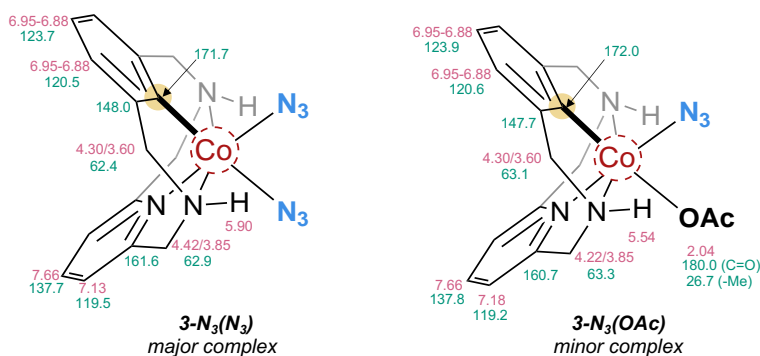
The **3-N$_3$(N$_3$) and 3-N$_3$(OAc)** complexes were synthetized according to the procedure described above in a 60% NMR yield.

3-N$_3$(N$_3$): **^{1}H NMR** (400 MHz, dmso d$_6$, 298 K) δ (ppm): 7.65 (t, 1H), 7,13 (d, ^3J = 7.9 Hz, 1H), 6.95-6.88 (m, 3H), 5.90 (t, ^3J = 6.9 Hz, 1H) 4.42 (m, 1.4H), 4.44-4.22 (m, 4H), 3.80 (d ^2J = 16.8 Hz, 2H), 3.72-3.66 (m, 2H), **^{13}C {1H} NMR** (100 MHz, CHCl$_3$, 298 K) δ (ppm): 171.7, 161.6, 148.0, 137.7, 123.7, 119.5, 62.9, 62.4.

3-N$_3$(OAc): **^{1}H NMR** (400 MHz, dmso d$_6$, 298 K) δ (ppm): 7.65 (t, 1H), 7.18 (d, 7.18 ^3J = 7.9 Hz, 1H), 6.95-6.88 (m, 3H), 5.54 (t ^3J = 6.9 Hz, 1H), 4.44-4.22 (m, 4H), 3.80 (d ^2J = 16.8 Hz, 2H), 3.72-3.66 (m, 2H), 2.04 (s, 1,94H, OAc). **^{13}C {1H} NMR** (100 MHz, CHCl$_3$, 298 K) δ (ppm): 180.0, 172.0, 160.7, 147.7, 137.8, 123.9, 120.6, 119.2, 63.3, 63.1, 26.7.

HRMS (ESI) calc. for C$_{15}$H$_{16}$CoN$_6^+$ [M]$^+$: 339.0763, found 339.0760. **IR (ATR):** υ (cm^{-1}) = 3419, 3269, 3177, 2936, 2873, 2119, 2066, 1688, 1637, 1561, 1412, 1275, 1141, 1092, 945, 826, 762, 661.

5. Detection and isolation of reaction intermediates using 1-OAc and organic azides (a-c)
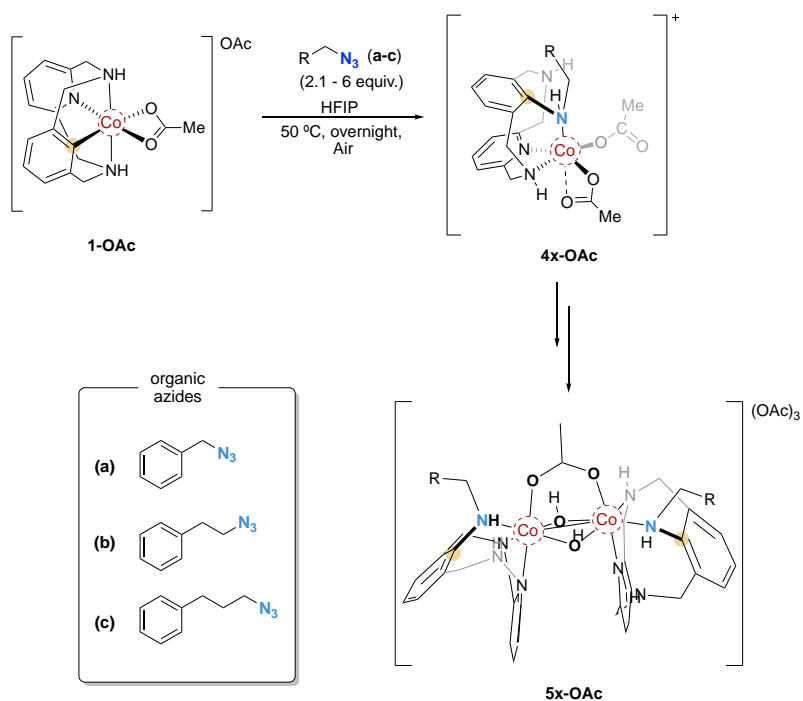
Scheme S4. Detection of **4x-OAc** and isolation of the corresponding **5x-OAc**.

In a 2 mL vial, **1-OAc** (20 mg, 0,048 mmol) and organic azide **a-c** (2.1 - 6 equiv.) were mixed in HFIP (1 mL) and the vial was sealed. The mixture was heated at 50 ºC overnight. The crude was concentrated under vacuum line until the initial volume was reduced to two-thirds. The crude mixture was analyzed by ^{1}H-NMR (CDCl$_3$) and HRMS observing the formation of the reaction intermediates (**4x-OAc**). Then, recrystallization with CHCl$_3$ layered with pentane under air the corresponding dimeric species (**5x-OAc**) was slowly formed which were characterized by NMR.
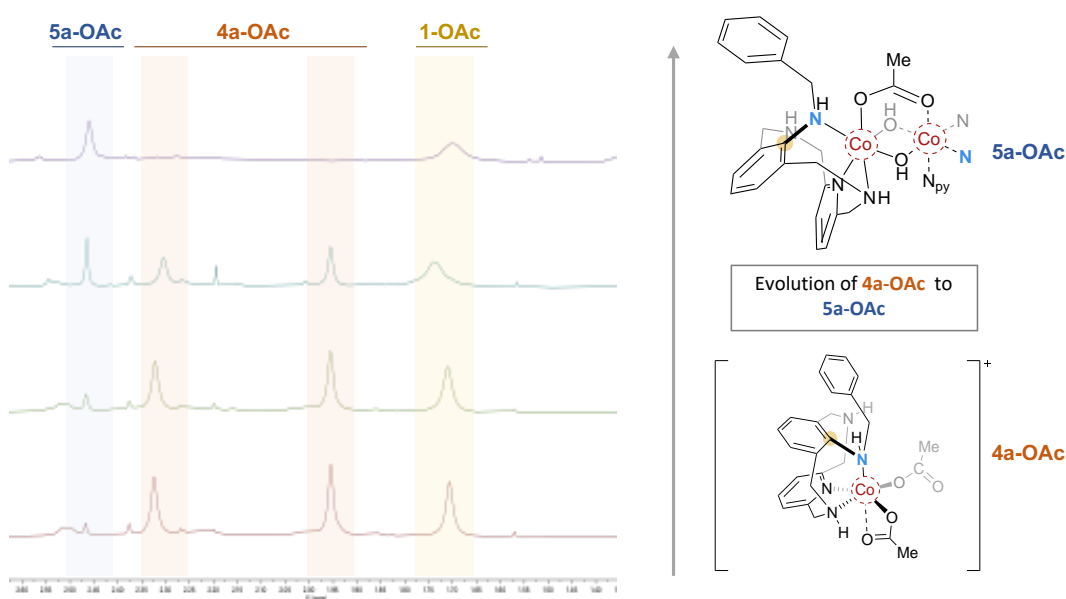
Figure S1. ^{1}H-NMR spectra (acetate region) of **4a-OAc** crude mixture yielding the **5a-OAc** complex.

5.1 Characterization of 4x-OAc
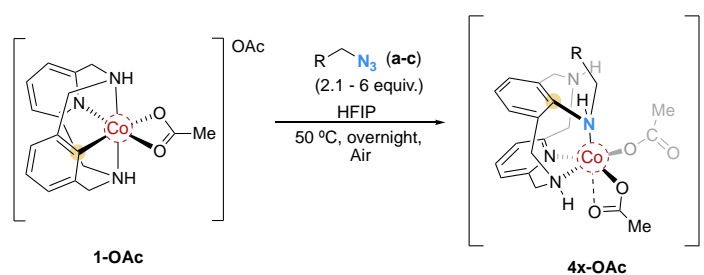
Scheme S5. Formation of **4x-OAc** from **1-OAc** and organic azide (**a-c**)

Aryl-(NHCH₂Ph)-Co^{III} – (4a-OAc)
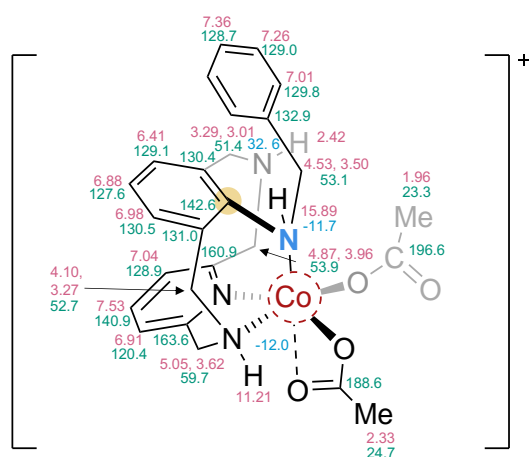
The **4a-OAc** complex was synthetized according to the procedure described above using 2.1 equivalents of benzyl azide (**a**) in a 46 % NMR yield. ^{1}**H NMR** (500 MHz, CHCl₃, 298 K) δ (ppm): 15.89 (d, ^3J = 8.9 Hz, 1H), 11.21 (s, 1H), 7.53 (t, ^3J = 7.6 Hz, 1H), 7.36 (1H), 7.26 (1H), 7.04 (d, ^3J = 7.6 Hz, 1H), 7.01 (d, ^3J = 7.6 Hz, 2H), 6.98 (1H), 6.91 (d, ^3J = 8.0 Hz, 1H), 6.88 (t, ^3J = 7.6 Hz, 1H), 6.41 (d, ^3J = 7.6 Hz, 1H). 5.05 (dd, ^2J = 16.4 Hz, ^3J = 6.7 Hz, 1H), 4.87 (d, ^2J = 14.3 Hz, 1H), 4.53 (d, ^2J = 13.0 Hz, 1H), 4.10 (1H), 3.96 (d, ^2J = 14.2 Hz, 1H), 3.62 (d, ^2J = 16.2 Hz, 1H), 3.50 (1H), 3.29 (d, ^2J = 14.8 Hz, 1H), 3.27 (d, ^2J = 14.8 Hz, 1H), 3.01 (d, ^2J = 14.6 Hz, 1H), 2.42 (bs, 1H), 2.33 (s, 3H), 1.96 (s, 3H). ^{13}**C {1H} NMR** (125 MHz, CHCl₃, 298 K) δ (ppm): 196.6, 188.6, 163.6, 160.9, 142.6, 140.9, 132.9, 131.0, 130.4, 129.8, 129.1, 129.0, 128.9, 128.7, 127.6, 120.4, 59.7, 53.9, 52.7, 51.4, 24.7, 23.3. ^{15}**N-NMR** (50.7 MHz): -12.0, -11.7, 32.6. **HRMS** (ESI) calc. for C₂₆H₃₀CoN₄O₄$^+$ [M – OAc]$^+$: 521.1594, found 521.1598.
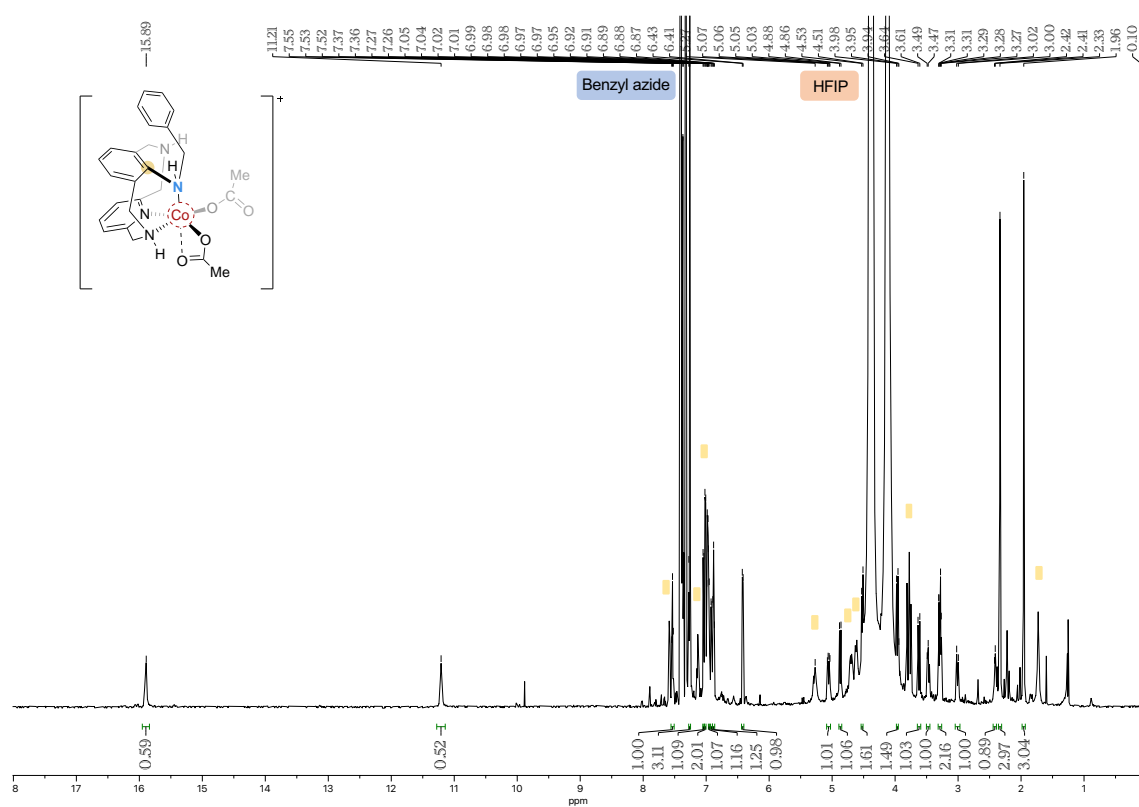
Figure S2. 500 MHz ^{1}H NMR spectra of **4a-OAc** crude mixture in CHCl$_3$, 298 K. In yellow was depicted the unreactive **1-OAc**.
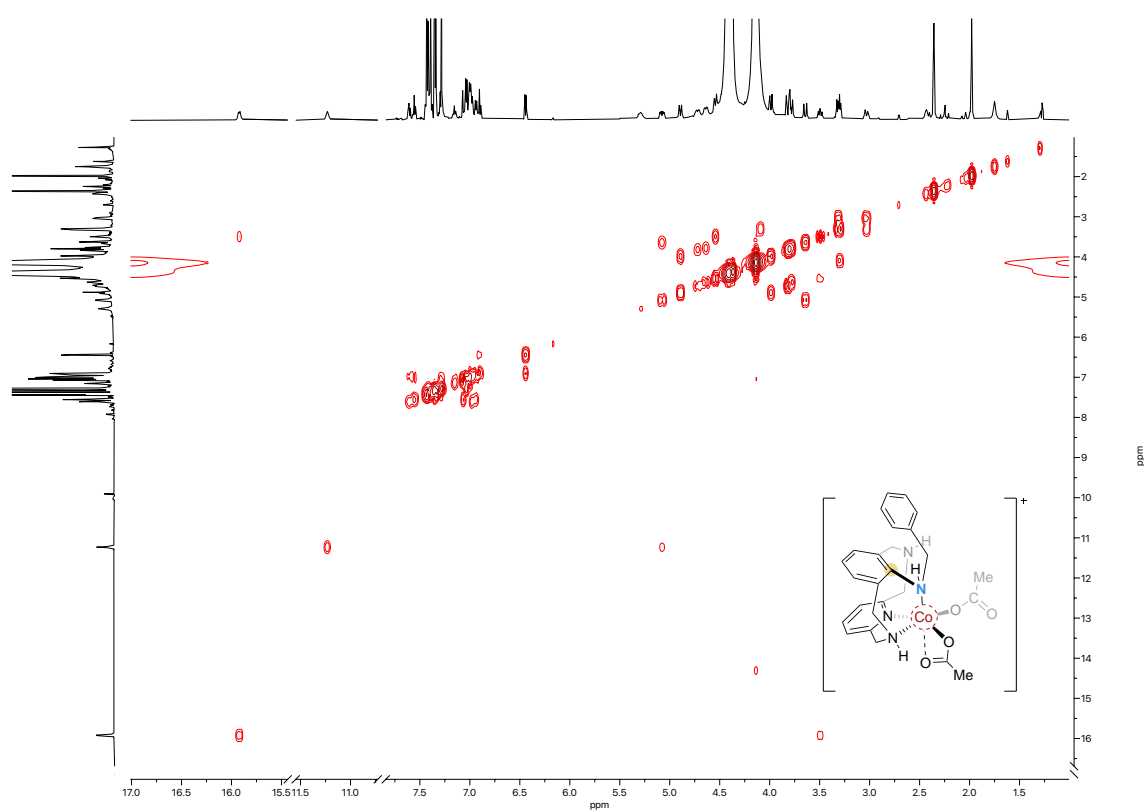

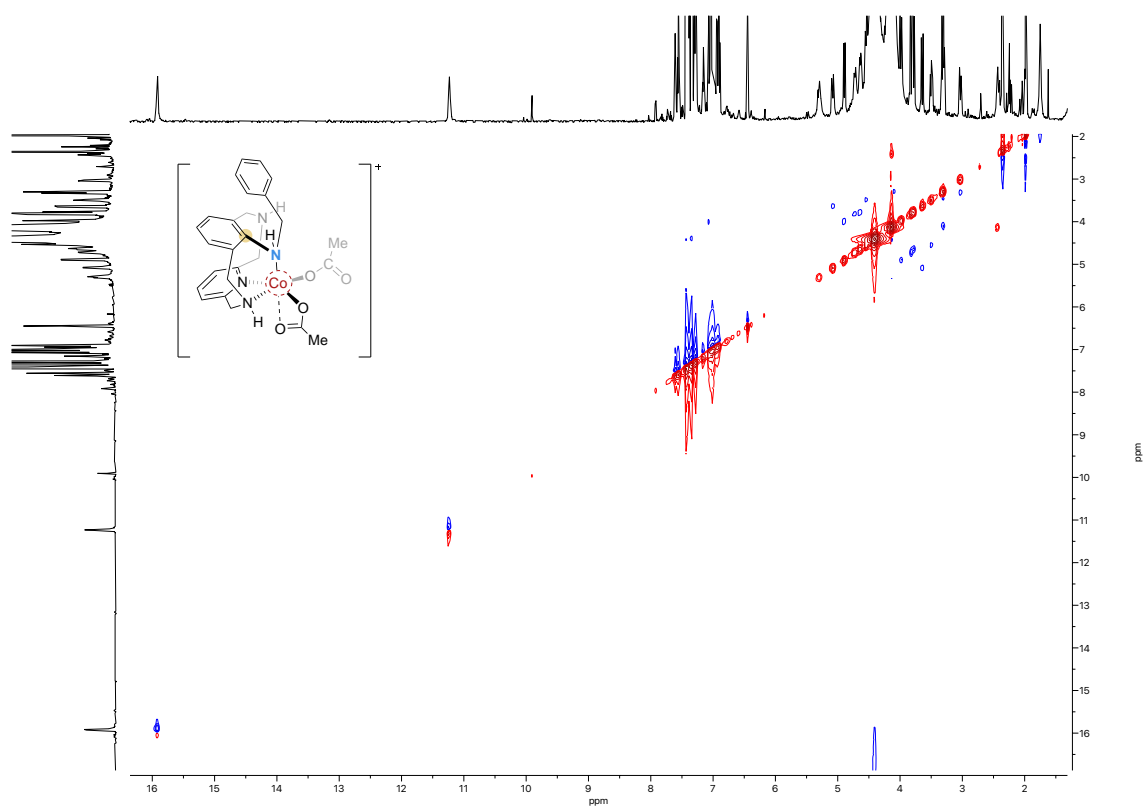**Figure S3**. 500 MHz ^{1}H-^{1}H COSY spectrum of **4a-OAc** crude mixture in CHCl$_3$, 298 K.

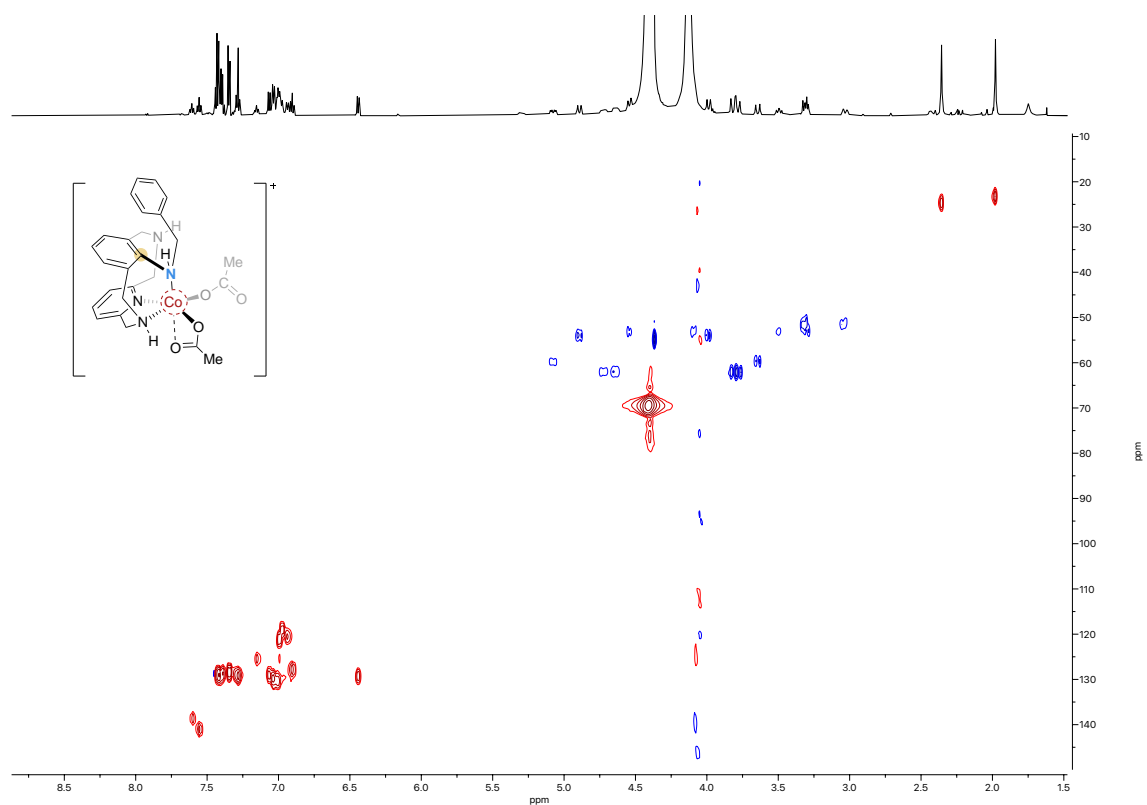**Figure S4**. 500 MHz ^{1}H-^{1}H NOESY spectrum of **4a-OAc** crude mixture in CHCl$_3$, 298 K.

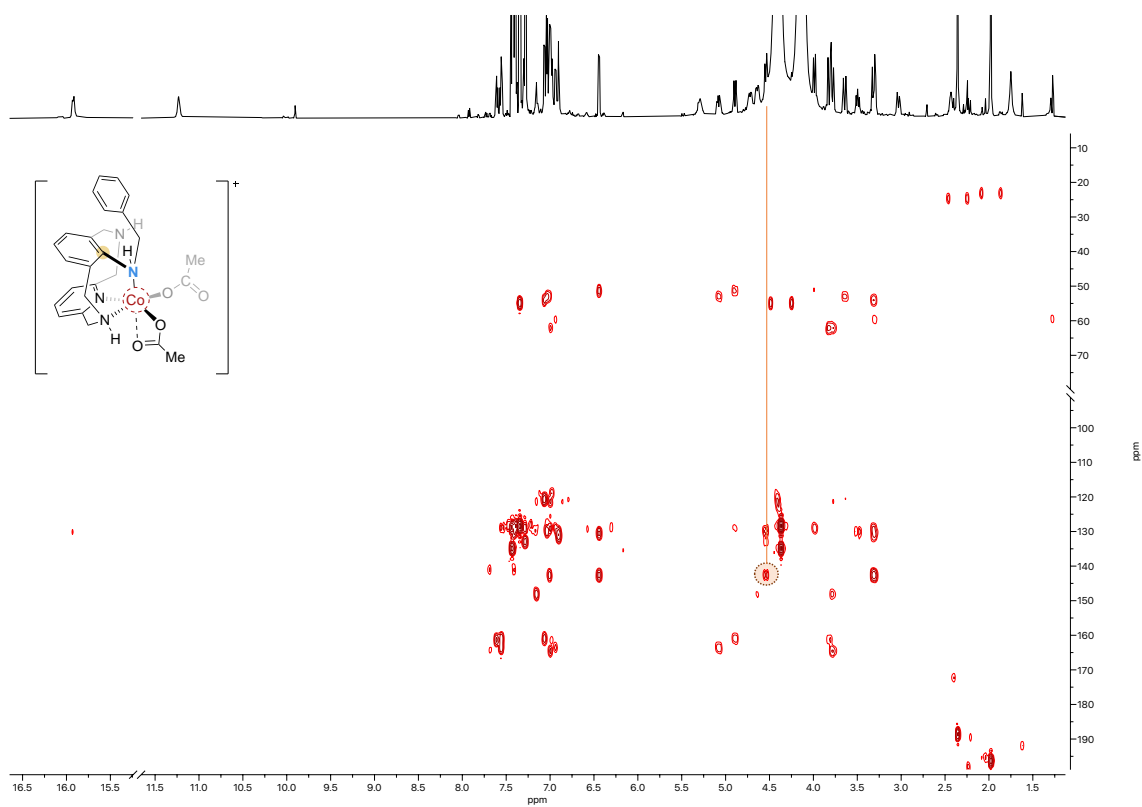**Figure S5**. 500 MHz ^{1}H-^{13}C HSQC spectrum of **4a-OAc** crude mixture in CHCl$_3$, 298 K.

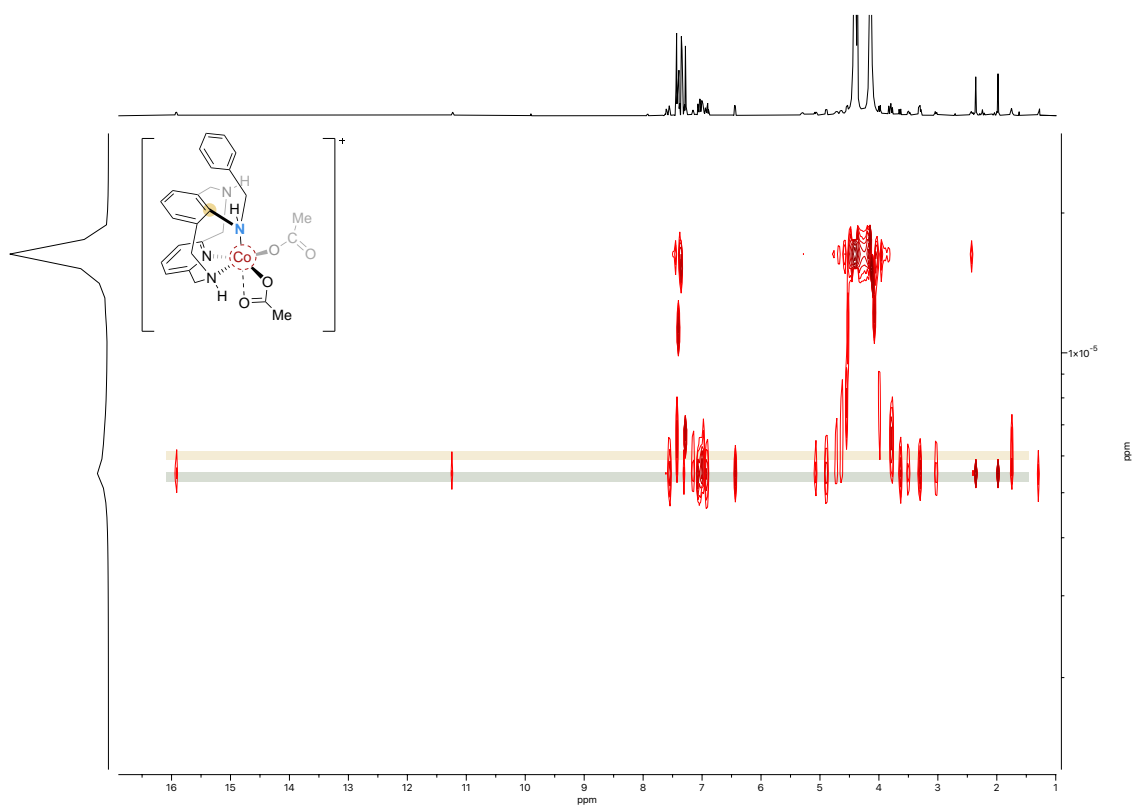**Figure S6.** 500 MHz ^{1}H-^{13}C HMBC spectrum of **4a-OAc** crude mixture in CHCl$_3$, 298 K.

Figure S7. 500 MHz DOSY spectrum of **4a-OAc** crude mixture in CHCl$_3$, 298 K. In yellow was depicted the unreactive **1-OAc**.
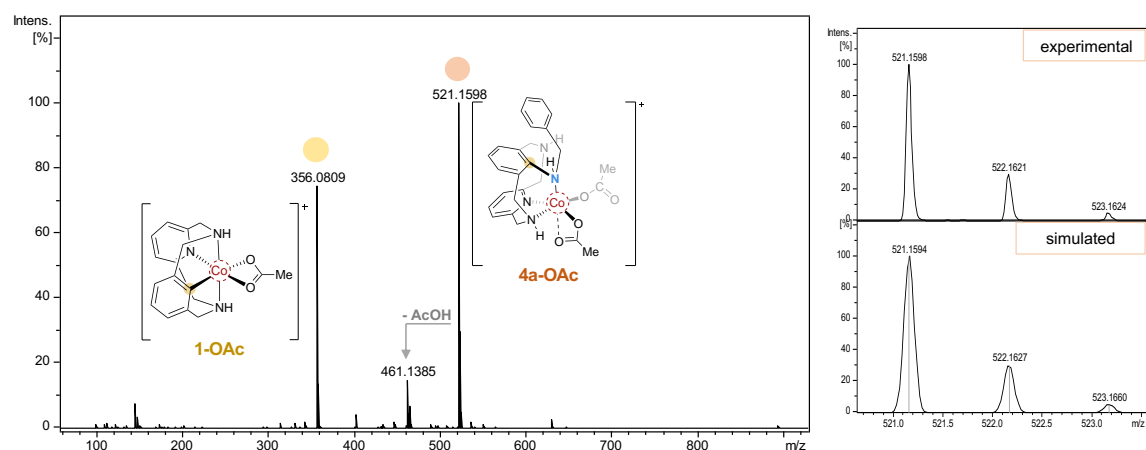
Figure S8. HRMS spectrum of **4a-OAc** crude mixture showing a peak at *m/z* = 521.1598.

Aryl-(NH(CH$_2$)$_2$Ph)-Co^{III} – **(4b-OAc)**

The excess of azide (**b**) needed (6 equiv.) in the reaction using **1-OAc**, makes the characterization of the **4b-OAc** complex crude difficult. The –NH and the –OAc peaks were in agreement with the analogous **4a-OAc** complex. Furthermore, the formation of **4b-OAc** was further confirmed by HRMS (see figure 9 and 10).
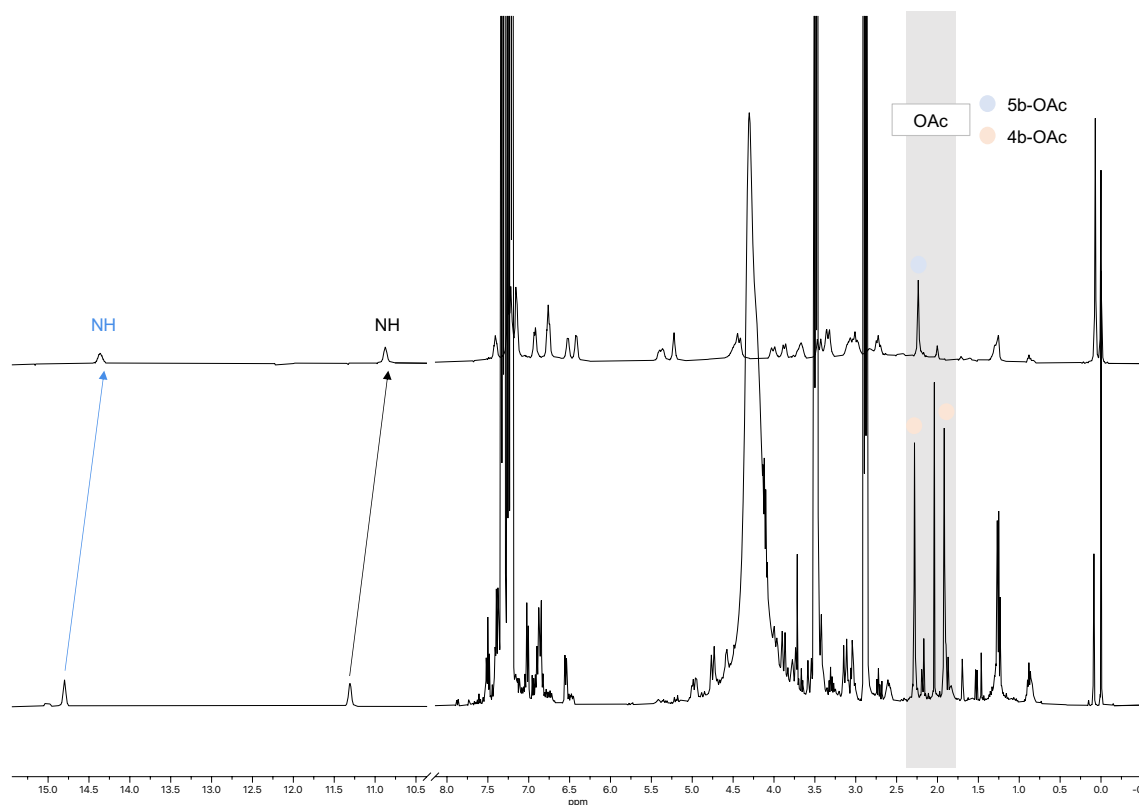

Figure S9. ^{1}H-NMR spectra obtained after reaction of **1-OAc** with organic azide, 400 MHz, 298 K (**b**) showing the formation of **4b-OAc** (bottom) and its evolution to form the **5b-OAc** (top).
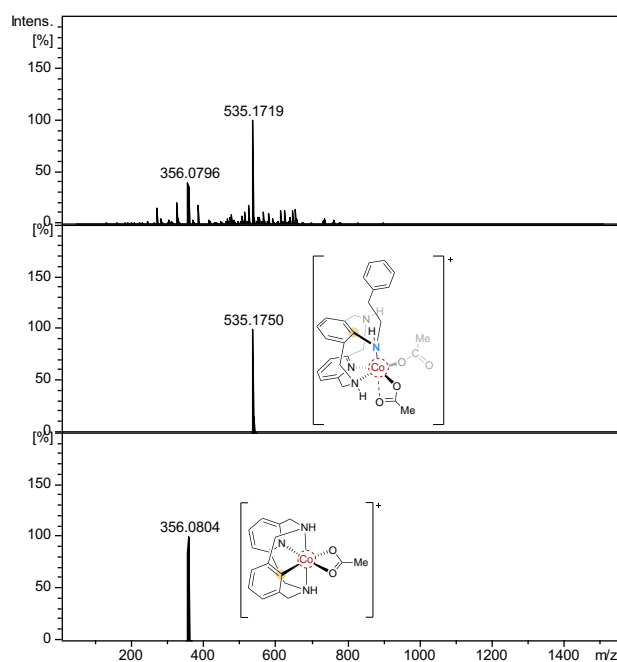
Figure S10. HRMS obtained after reaction of **1-OAc** with organic azide (**b**). Mass analysis show a peak at m/s = 535.1719 which corresponds to **4b-OAc**.

Aryl-(NH(CH$_2$)$_3$Ph)-Co^{III} – **(4c-OAc)**

As in the case of using azide (b), the excess of azide (**c**) used (6 equiv.) in the reaction using **1-OAc** makes the characterization of the **4c-OAc** complex crude difficult. The –NH and the –OAc peaks were in agreement with the analogous **4a-OAc** complex. Furthermore, the formation of **4c-OAc** was further confirmed by HRMS (see Figure 11 and 12).
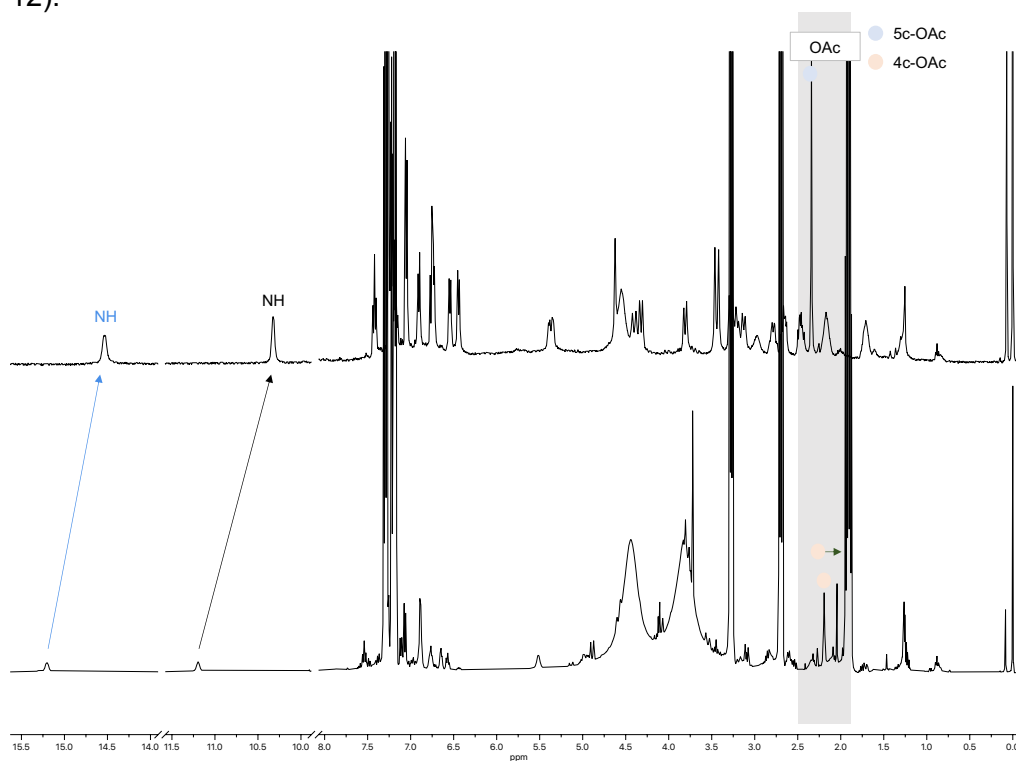

Figure S11. ^{1}H-NMR obtained after reaction of **1-OAc** with organic azide, 400 MHz, 298 K (**c**) showing the formation of **4c-OAc** (bottom) and its evolution to form the **5c-OAc** (top)

Figure S12. HRMS obtained after reaction of **1-OAc** with organic azide (**c**). Mass analysis show a peak at m/z = 549.1910 which corresponds to **4c-OAc**.

5.2 Characterization of 5x-OAc

Scheme S6. Formation of **5x-OAc** from **4x-OAc**

[Aryl-(NHCH$_2$Ph)-Co^{III}]$_2$ – **(5a-OAc)**

Red oil (9.6 mg, 0.0089 mmol, 81% based on **4a-OAc**; 95% NMR yield based on **4a-OAc**). **^{1}H NMR** (500 MHz, CHCl$_3$, 298 K) δ (ppm): 15.02 (bs, 2H), 10.60 (bs, 2H), 7.33 (t, ^3J = 7.6 Hz, 2H), 7.23-7.22 (m, 6H), 7.13 (m, 4H), 6.96 (d, ^3J = 7.2 Hz, 2H), 6.73 (d, ^3J = 7.4 Hz, 2H), 6.68 (t, ^3J = 7.2 Hz, 2H), 6.42 (d, ^3J = 7.6 Hz, 2H), 6.15 (d, ^3J = 7.2 Hz, 2H), 5.52 (dd, ^3J = 6.7 Hz, ^3J = 17.4 Hz, 2H), 5.14 (s, 2H), 6.61 (m, 4H), 3.90 (m, 2H), 3.84 (m, 2H), 3.51 (m, 4H), 3.03 (m, 2H), 2.96 (s, 4H), 2.70 (bs, 2H), 2.44 (s, 3H). **^{13}C {1H} NMR** (125 MHz, CHCl$_3$, 298 K) δ (ppm): 190.3 (2C), 165.9 (2C), 161.6 (2C), 144.4 (2C), 139.8 (2C), 135.3 (2C), 132.4 (2C),

219

130.8 (2C), 130.6 (4C), 130.0 (2C), 128.6 (2C), 128.5 (6C), 127.2 (2C), 126.4 (2C), 120.1 (2C), 59.5 (2C), 53.4 (2C), 52.3 (2C), 51.9 (2C), 50.9 (2C), 24.6 (1C). **HRMS** (ESI) calc. for $C_{50}H_{59}Co_2N_8O_8^+$ [M-OAc]$^+$: 1017.3119; found: 1017.3121.


[Aryl-(NH(CH₂)₂Ph)- Co^{III}]₂ – **(5b-OAc)**
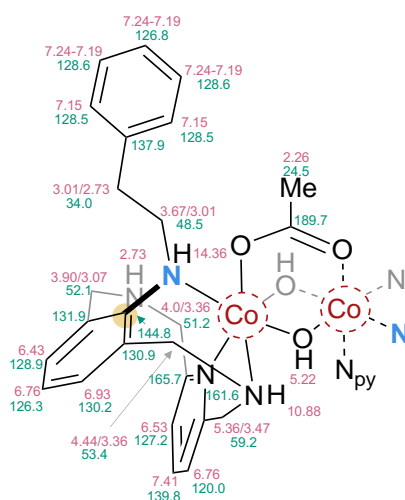
Red oil (4.8 mg, 0.0043 mmol, 70% based on **4b-OAc**; 75% NMR Yield based on **4b-OAc**). **¹H NMR** (400 MHz, CHCl₃, 298 K) δ (ppm): 14.36 (bs, 2H), 10.88 (bs, 2H), 7.41 (t, ^3J = 7.1 Hz, 2H), 7.24-7.19 (m, 6H), 7.15 (m, 4H), 6.93 (d, ^3J = 7.1 Hz, 2H), 6.76 (m, 4H), 6.53 (d, ^3J = 7.1 Hz, 2H), 6.43 (d, ^3J = 7.1 Hz, 2H), 5.36 (m, 2H), 5.22 (s, 2H), 4.44 (m, 2H), 4.03 (d, ^3J = 15.2 Hz, 2H), 3.90 (d, ^3J = 12.1 Hz, 2H), 3.67 (m, 2H), 3.47 (d, ^3J = 17.2 Hz, 2H), 3.36 (m, 4H), 3.07-3.01 (m, 6H), 2.83 (bs, 2H), 2.73 (m, 2H), 2.24 (s, 3H). **¹³C {1H} NMR** (100 MHz, CHCl₃, 298 K) δ (ppm): 189.7, 165.7, 161.6, 144.8, 139.8, 137.9, 131.9, 130.9, 130.2, 128.9, 128.6, 128.5, 127.2, 126.8, 126.3, 120.0, 59.2, 53.4, 52.2, 51.2, 48.5, 34.0, 24.5. **HRMS** (ESI) calc. for $C_{52}H_{63}Co_2N_8O_8^+$ [M-OAc]$^+$: 1045.3427; found: 1045.3440.


[Aryl-(NH(CH₂)₃Ph)- Co^{III}]₂ – **(5c-OAc)**
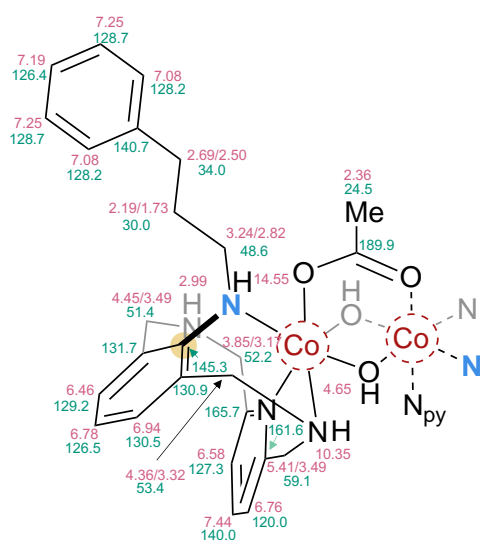
Red oil (5.0 mg, 0.0044 mmol, 73% based on **4c-OAc**; 97% NMR Yield based on **4c-OAc**). **¹H NMR** (400 MHz, CHCl₃, 298 K) δ (ppm): 14.55 (bs, 2H), 10.35 (bs, 2H), 7.44 (t, ^3J = 7.2 Hz, 2H), 7.25 (m, 4H), 7.19 (m, 2H), 7.08 (d, ^3J = 7.4 Hz, 4H), 6.94 (d, ^3J = 7.2 Hz, 2H), 6.78 (t, ^3J = 7.7 Hz, 2H), 6.76 (d, ^3J = 7.4 Hz, 2H), 6.58 (d, ^3J = 7.2 Hz, 2H), 6.46 (d, ^3J = 7.2 Hz, 2H), 5.40 (dd, ^2J = 17.3 Hz, ^3J = 7.2. Hz, 2H), 4.05 (s, 2H), 4.45 (d, ^2J = 15.6 Hz, 2H), 4.36 (d, ^2J = 14.3 Hz, 2H), 3.85 (d, ^2J = 13.1 Hz, 2H), 3.49 (d, ^2J = 17.3 Hz, 2H), 3.32 (bs, 2H), 3.24 (bs, 2H), 3.17 (d, ^2J = 13.9 Hz, 2H), 2.99 (bs, 2H), 2.82 (bs, 2H), 2.69 (bs, 2H), 2.50 (bs, 2H), 2.36 (s, 3H), 2.19 (bs, 2H). **¹³C {1H} NMR** (100 MHz, CHCl₃, 298 K) δ (ppm): 189.8, 165.7, 145.3, 140.7, 140.0, 131.7, 130.9, 130.5, 129.2, 128.7, 128.2, 127.3, 126.5, 126.4, 120.0, 59.1, 53.4, 52.2, 51.4, 48.6, 34.0, 30.0, 24.5. **HRMS** (ESI) calc. for $C_{54}H_{67}Co_2N_8O_8^+$ [M-OAc]$^+$: 1073.3740, found 1073.3792.

6. C-N bond formation reactions

6.1 Reactivity of 1-OAc with organic azides at 50 ºC
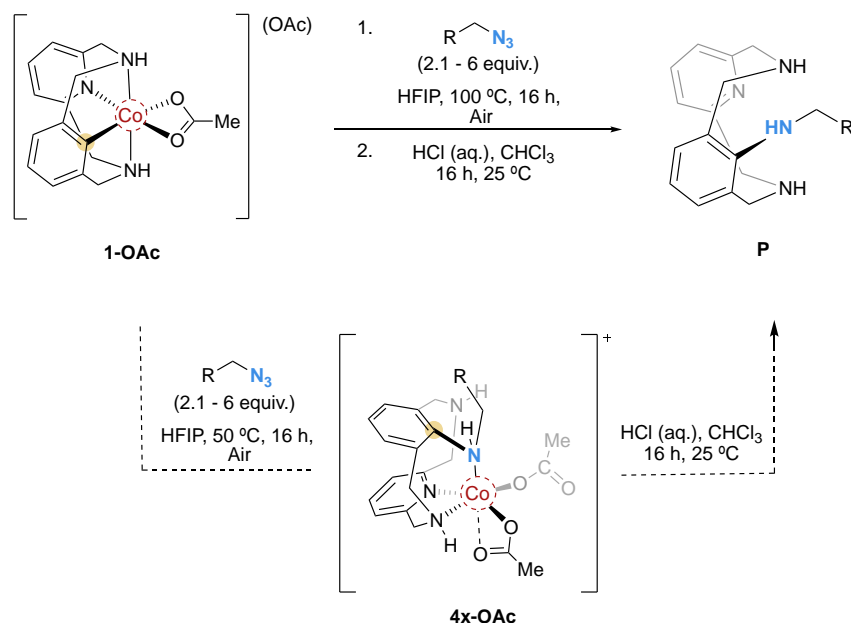
Scheme S7. Formation of lineal **P1**, **P2** and **P3** product.

In a 2 mL vial, **1-OAc** (20 mg, 0,048 mmol) and organic azide **a-c** (2.1 – 6 equiv.) were mixed in HFIP (1 mL) and the vial was sealed. The mixture was heated at 50 ºC overnight. The crude was concentrated under vacuum line until the initial volume was reduced to two-thirds. Then, the crude mixture was dissolved in CHCl$_3$ and HCl (3 mmol, 2M) was added. After stirring overnight, the crude was basified until pH 14 and extracted with CHCl$_3$. Products were purified using neutral alumina column chromatography (CHCl$_3$, then CHCl$_3$/MeOH 8:2) and characterized by NMR techniques.

P1
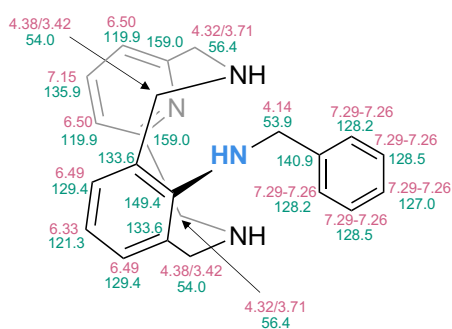
Yellow solid (7.3 mg, 0.021 mmol, 44%). **^{1}H NMR** (400 MHz, CHCl$_3$, 298 K) δ (ppm): 7.29-7.26 (m, 5H), 7.15 (t, ^3J = 7.7 Hz, 1H), 6.50 (d, ^3J = 7.6 Hz, 2H), 6.49 (d, ^3J = 7.4 Hz, 2H), 6.33 (t, ^3J = 7.4 Hz, 2H), 4.38 (d, ^2J = 14.5 Hz, 2H), 4.32 ((d, ^2J = 15.4 Hz, 2H), 4.14 (s, 2H), 3.71 (d, ^2J = 15.4 Hz, 2H), 3.42 (d, ^2J = 14.5 Hz, 2H). **^{13}C {1H} NMR** (100 MHz, CHCl$_3$, 298 K) δ (ppm): 159.0 (2C), 149.4 (1C), 140.9 (1C), 135.9 (1C), 133.6 (2C), 129.4 (2C), 128.5 (2C), 128.3 (2C), 127.0 (1C), 121.3 (1C), 119.9 (2C), 56.4 (2C), 54.1 (2C), 53.9 (1C).

**HRMS** (ESI) calc. for C$_{22}$H$_{24}$N$_4$ [M+H]$^+$: 345.2074; found: 345.2075.

P2
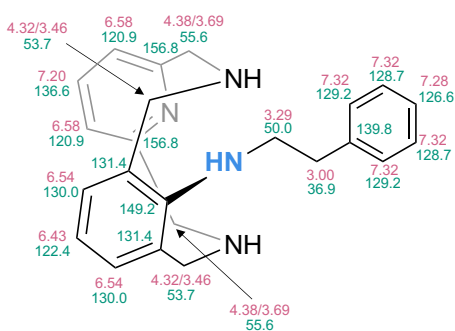
Yellow solid (6.8 mg, 0.019 mmol, 40%). **^{1}H NMR** (400 MHz, CHCl$_3$, 298 K) δ (ppm): 7.35-7.28 (m, 5H), 7.20 (t, ^3J = 7.7 Hz, 1H), 6.58 (d, ^3J = 7.9 Hz, 2H), 6.54 (d, ^3J = 7.9 Hz, 2H), 6.43 (t, ^3J = 7.30, 1H), 4.38 (d, ^2J = 15.3 Hz, 2H), 4.32 (d, ^2J = 14.6 Hz, 2H), 3.69 (d, ^2J = 3.7 Hz, 2H), 3.46 (d, ^2J = 14.6 Hz, 2H), 3.29 (t, ^3J = 6.9 Hz, 2H), 3.0 (t, ^3J = 6.9 Hz, 2H). **^{13}C {1H} NMR** (100 MHz, CHCl$_3$, 298 K) δ (ppm): 156.8 (2C), 149.2, 139.8, 136.6, 131.4 (2C), 130.0 (2C), 129.2 (2C), 128.7 (2C), 126.6, 122.4, 120.9 (2C), 55.6 (2C), 53.7 (2C), 50.0, 36.9. **HRMS** (ESI) calc. for C$_{23}$H$_{26}$N$_4$ [M+H]$^+$: 359.2230; found: 359.2234.

P3
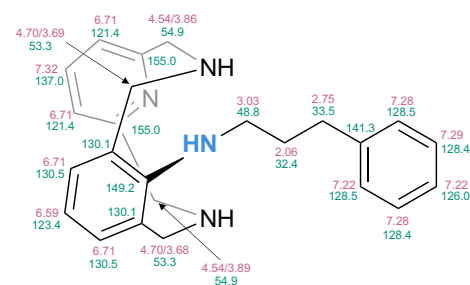

Yellow solid (7.7 mg, 0.020 mmol, 42%). **^{1}H NMR** (400 MHz, CHCl$_3$, 298 K) δ (ppm): 7.32-7.28 (m, 3H), 7.23-7.20 (m, 3H), 6.72-6.70 (m, 4H), 6.59 (t, ^3J = 7.3 Hz, 1H), 4.70 (d, ^2J = 14.4 Hz, 2H), 4.54 (d, ^2J = 15.5 Hz, 2H), 3.86 (d, ^2J = 15.5 Hz, 2H), 3.69 (d, ^2J = 14.4 Hz, 2H), 3.03 (t, ^3J = 7.7 Hz, 2H), 2.75 (t, ^3J = 7.5 Hz, 2H), 2.06 (quint, ^3J = 7.1 Hz, 2H). **^{13}C {1H} NMR** (100 MHz, CHCl$_3$, 298 K) δ (ppm): 155.0, 149.2, 141.3, 137.0, 130.5, 130.1, 128.5, 128.4, 126.0, 123.4, 121.5, 54.9, 53.4, 48.8, 33.5, 32.4. **HRMS** (ESI) calc. for C$_{24}$H$_{28}$N$_4$ [M+H]$^+$: 373.2387; found: 373.2394.

6.2 Reactivity of 1-OAc with organic azides at 100 ºC

6.2.1 Using benzyl azide (a)
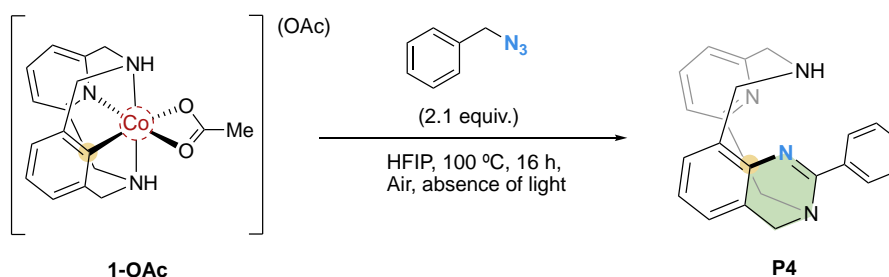
Scheme S8. Reactivity of **1-OAc** and benzyl azide to form **P4** product.

In a 2 mL vial, **1-OAc** (20 mg, 0,048 mmol) and organic azide **a** (2.1 equiv.) were mixed in HFIP (1 mL) and the vial was sealed and heated at 100ºC during 16 h in the absence of light. Then, after removal of the solvent, the product was purified using neutral alumina column chromatography (CHCl$_3$, then CHCl$_3$/MeOH 8:2) and characterized by NMR.
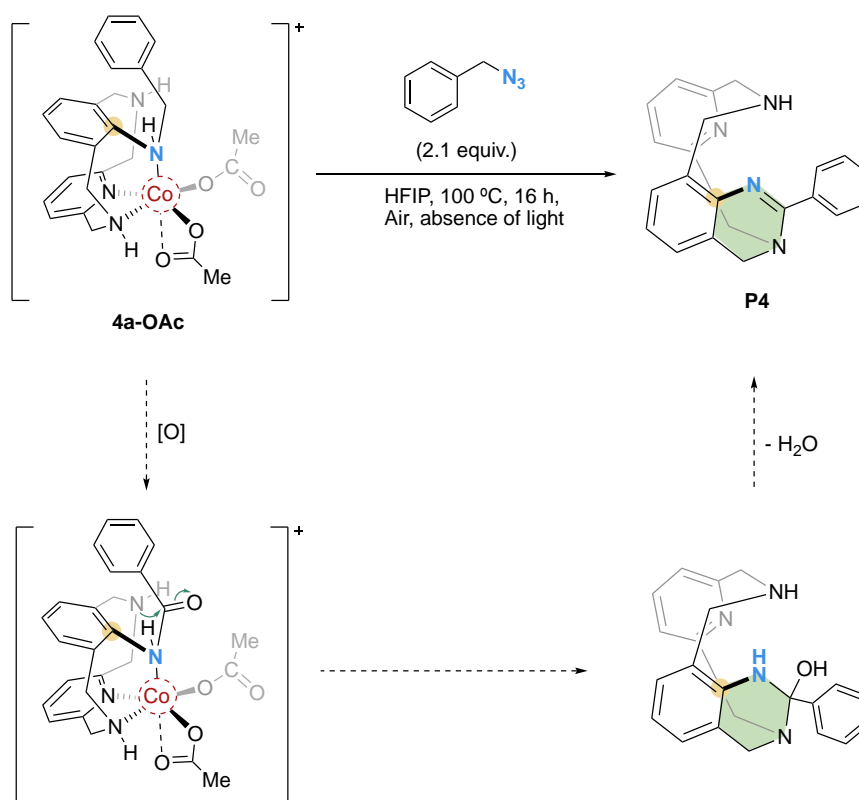
Scheme S9. Proposed mechanism for the intramolecular cyclization to form the **P4** product.

**Table S1.** Reaction of **1-OAc** with benzyl azide (**a**) using different conditions.

Entry	Solvent	Atmosphere	Yield of P4 (%)[a]
2	TFE	Air	34% (31 %)
7	HFIP	Air	(27%)
8	HFIP	O_2	28%
9	HFIP	N_2	5%[b]

[a]Yields are calculated using 1,3,5-trimethoxybenzene as internal standard. Isolated yield in parenthesis. [b] Reaction was performed using Schlenck flask.

P4
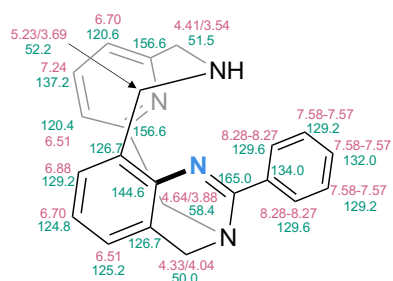
Yellow solid (4.4 mg, 0.013 mmol, 27%). **^{1}H NMR** (400 MHz, CHCl$_3$, 298 K) δ (ppm): 8.28-8.27 (m, 2H), 7.58-7.57 (m, 3H), 7.24 (t, ^3J = 7.2 Hz, 1H), 6.88 (d, ^3J = 7.3 Hz, 1H), 6.74-6.69 (m, 2H), 6.52-6.50 (m, 2H), 5.23 (d, ^2J = 13.6 Hz, 1H), 4.64 (d, ^2J = 15.1 Hz, 1H), 4.41 (d, ^2J = 16.9 Hz, 1H), 4.33 (d, ^2J = 15.6 Hz, 1H), 4.04 (d, ^2J = 15.6 Hz, 1H), 3.88 (d, ^2J = 15.1 Hz, 1H), 3.69 (d, ^2J = 13.6 Hz, 1H), 3.54 (d, ^2J = 16.9 Hz, 1H). **^{13}C {1H} NMR** (100 MHz, CHCl$_3$, 298 K) δ (ppm): 165.0 (1C), 156.6 (2C), 144.6 (1C), 137.2 (1C), 134.0 (1C), 132.0 (1C), 129.6 (2C), 129.2 (3C), 126.7 (2C), 125.2 (1C), 124.8 (1C), 120.6 (1C), 120.4 (1C), 58.4 (1C), 52.2 (1C), 51.5 (1C), 50.0 (1C). **HRMS** (ESI) calc. for C$_{22}$H$_{20}$N$_4$ [M+H]$^+$: 341.1761, found 341.1751.

6.2.2 Using (2-azidoethyl)benzene (b)
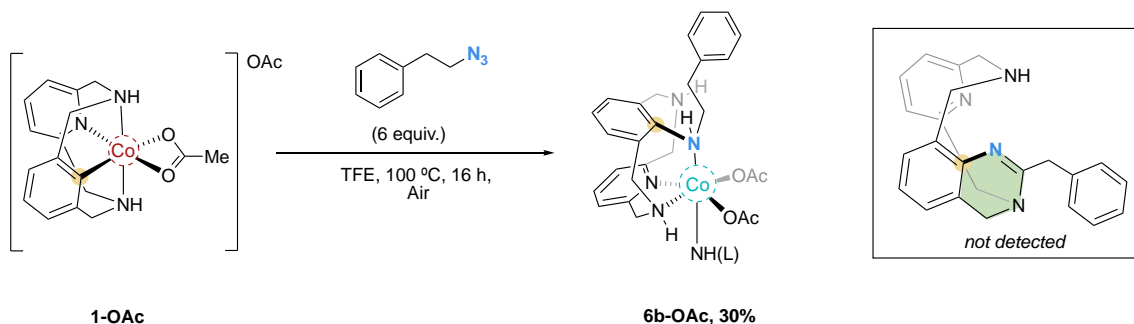
Scheme S10. *Reaction of 1-OAc with organic azide (b) forming the **6b-OAc** complex*

In a 2 mL vial, **1-OAc** (20 mg, 0,048 mmol) and organic azide **b** (6 equiv.) were mixed in TFE (1 mL) and the vial was sealed and heated at 100 ºC during 16 h. Then, the solvent was removed and suitable crystals of **6b-OAc** were grown by pentane diffusion in a concentrated solution in CH$_2$Cl$_2$ anhydrous under inert atmosphere.

^{1}H NMR (400 MHz, CHCl$_3$, 298 K) δ (ppm): 225.98, 204.88, 196.48, 51.77, 49.45, 44.92.
HRMS (ESI) calc. for C$_{25}$H$_{29}$CoN$_4$O$_2$ $^+$ [M-OAc]$^+$: 476.1617, found 476.1618.
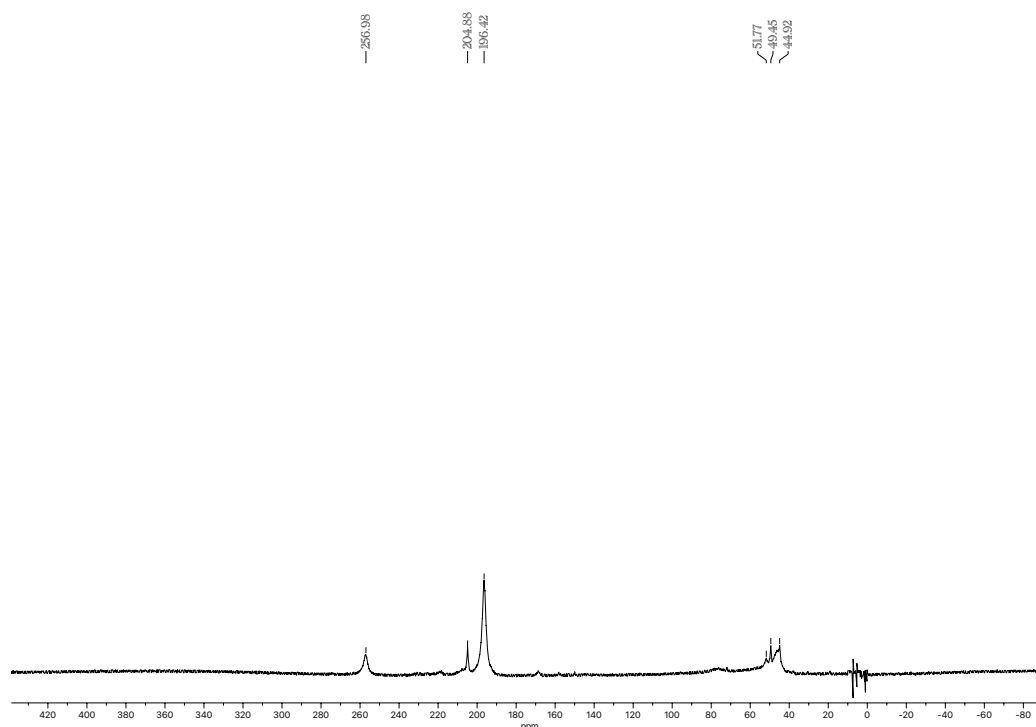

Figure S13. 400 MHz ^{1}H-NMR spectrum of **6b-OAc** in CDCl$_3$, 298 K.
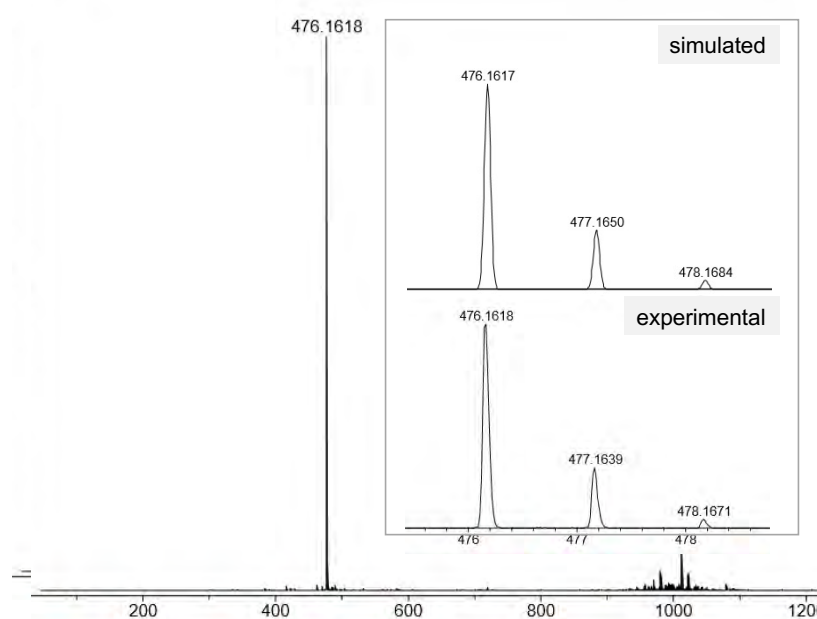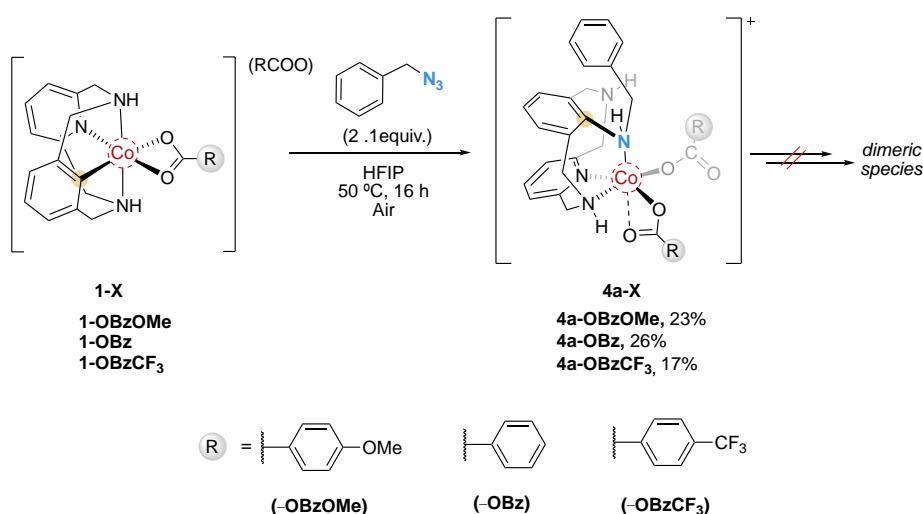
Figure S14. HRMS spectrum of **6b-OAc** showing a peak at *m/z* = 476.1618.

6.3 Evaluation of different carboxylate anions

6.3.1 *4a-X* complexes

Scheme S11. Formation of **4a-X** complexes. NMR yields are calculated using 1,3,5-trimethoxybenzene as internal standard.

In a 2 mL vial, **1-X** (0.048 mmol) and benzyl azide (**a**) (0.1 mmol, 2.1 equiv.) were mixed in HFIP (1 mL) and the vial was sealed. The mixture was heated at 50 ºC overnight. The crude was concentrated under vacuum line until the initial volume was reduced to two-thirds. The crude mixture was analyzed by ^{1}H-NMR and HRMS observing the formation of the corresponding **4a-X** complex. Faster decomposition was observed compared to the analogous **4a-OAc** complex and no dimeric species was detected.
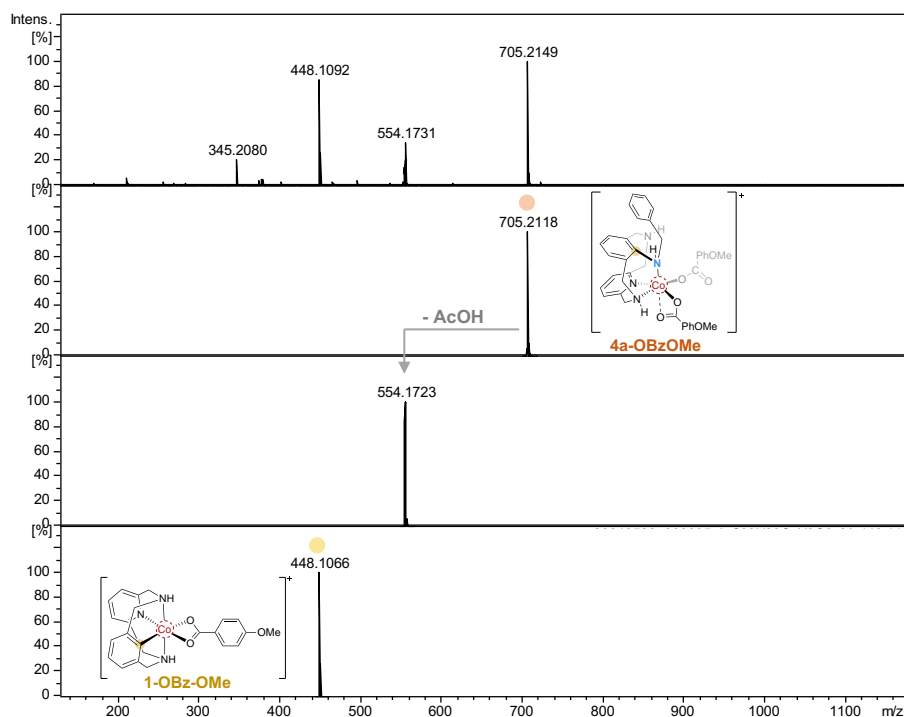
Figure S15. HRMS obtained after reaction of **1-OBzOMe** with benzyl azide (**a**). Mass analysis show a peak at *m/z* = 705.2149 which corresponds to **4a-OBzOMe** complex.
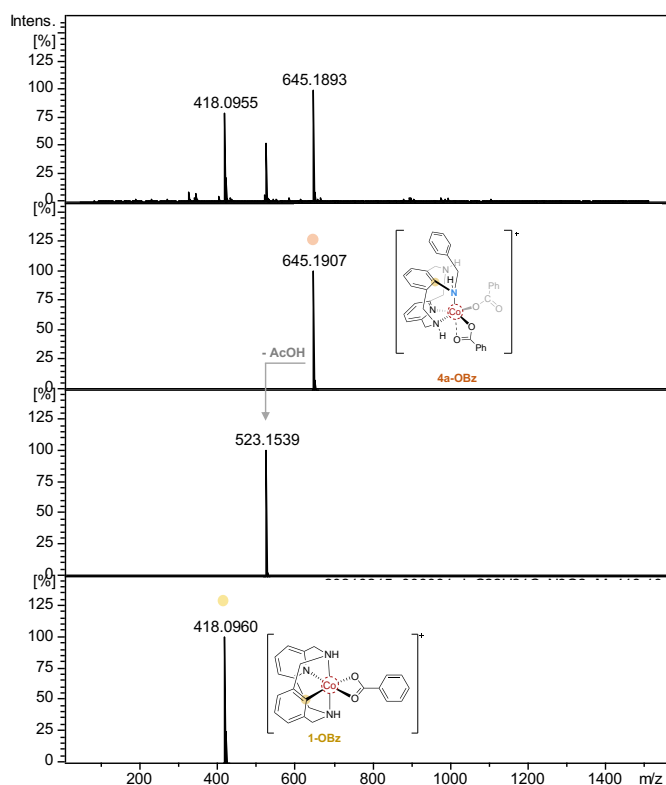

Figure S16. HRMS obtained after reaction of **1-OBz** with benzyl azide (**a**). Mass analysis show a peak at *m/z* = 645.1893 which corresponds to **4a-OBz** complex.
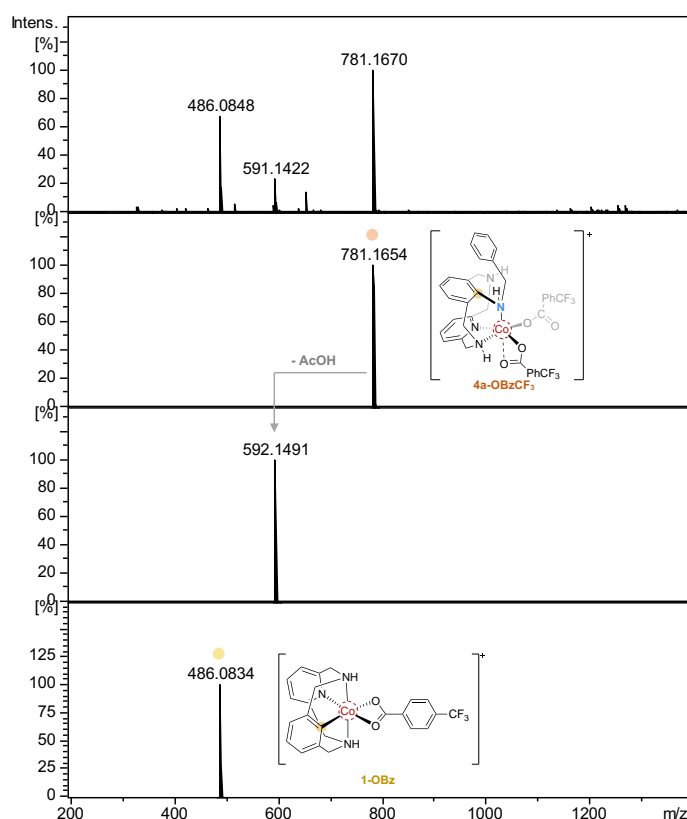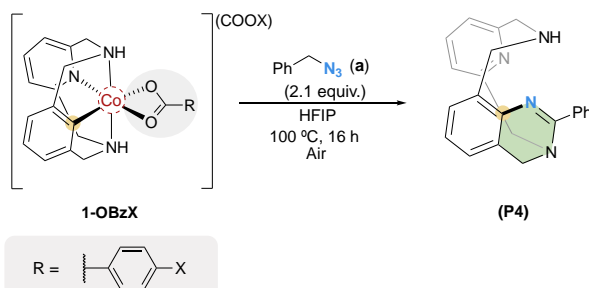
Figure S17. HRMS obtained after reaction of **1-OBzCF₃** with benzyl azide (**a**). Mass analysis show a peak at *m/z* = 781.1670 which corresponds to **4a-OBzCF₃** complex.

6.3.2 **P4** formation using **1-X** complexes

Scheme S12. Evaluation of different carboxylate anions in **P4** formation.

Procedure A: In a 2 mL vial, **1-X** (0.048 mmol) and benzyl azide (**a**) (0.1 mmol, 2.1 equiv.) were mixed in HFIP (1 mL) and the vial was sealed and heated at 100ºC during 16 h in the absence of light. Then, after removal of the solvent, the product was purified using neutral alumina column chromatography (CHCl₃, then CHCl₃/MeOH 8:2) and analyzed by NMR using 1,3,6-trimethoxybenzene as internal standard.

via 4a-COOR
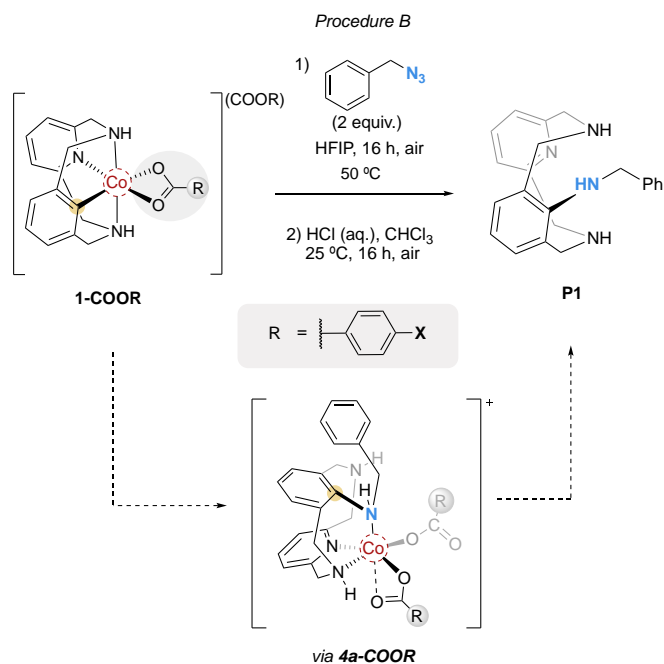
Scheme S13. Evaluation of different carboxylate anions in **P1** formation reaction at 50ºC.

Procedure B: In a 2 mL vial, **1-X** (0.048 mmol) and benzyl azide (**a**) (0.1 mmol, 2.1 equiv.) were mixed in HFIP (1 mL) and the vial was sealed. The mixture was heated at 50 ºC overnight. The crude was concentrated under vacuum line until the initial volume was reduced to two-thirds. Then, the crude mixture was dissolved in 1 mL of CHCl₃ and HCl (3 mmol, 2M) was added. After stirring overnight, the crude was basified until pH 14 and extracted with CHCl₃. Products were purified using neutral alumina column chromatography (CHCl₃, then CHCl₃/MeOH 8:2) and characterized by NMR techniques.

7. Mechanistic insights

7.1 Inhibitory effect with TEMPO in 1-OAc and benzyl azide reaction
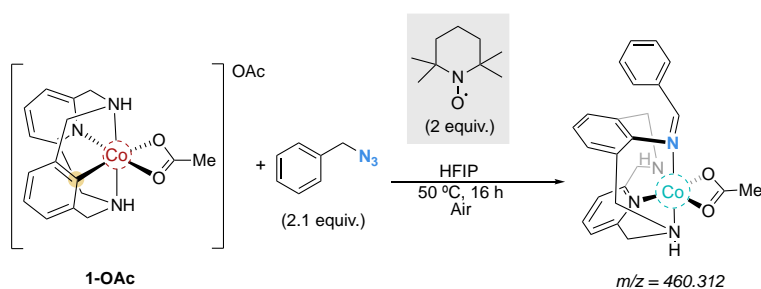
Scheme S14. Addition of TEMPO in the reaction of **1-OAc** with benzyl azide at 50 ºC.
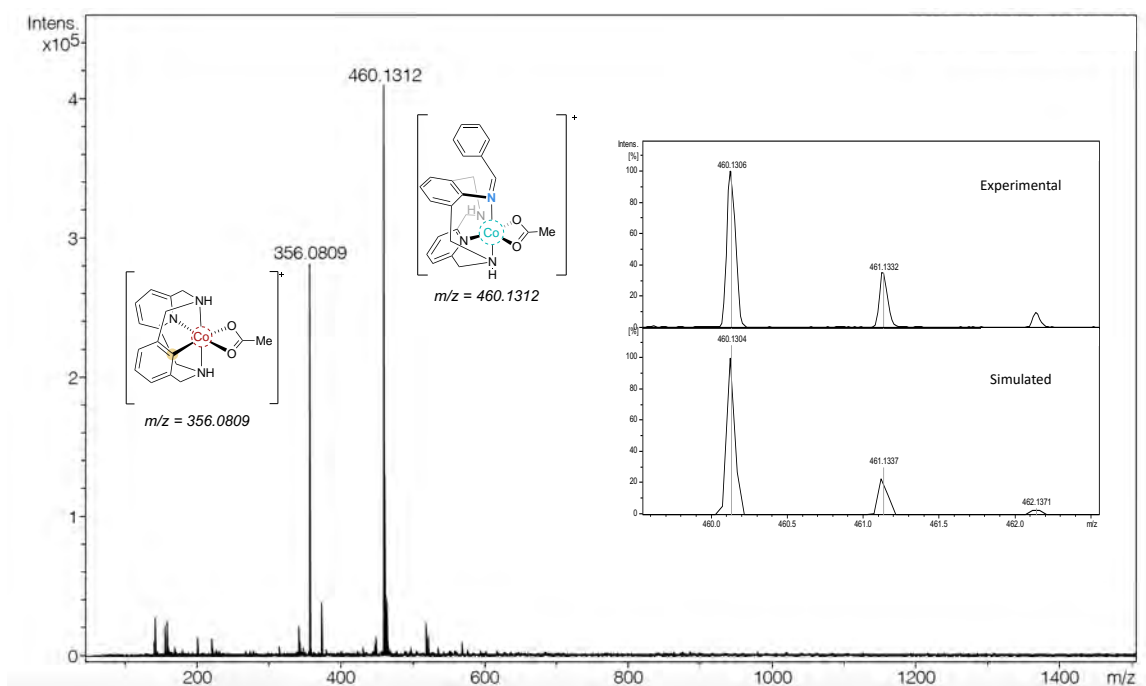
Figure S18. HRMS obtained after reaction of **1-OAc** with organic azide (**a**) and TEMPO. Mass analysis show a peak at *m/z* = 460.1312 which is tentatively assigned to Co[II] inserted imine complex.

7.2 Reactivity of 1-OAc and benzyl azide with xanthene
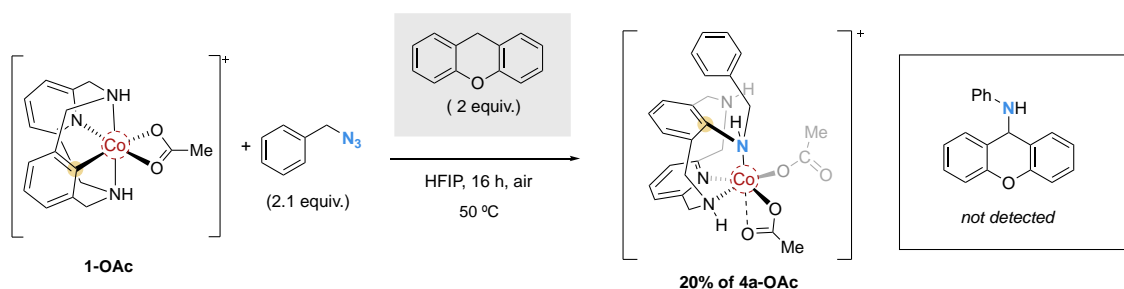
Scheme S15. Reaction of **1-OAc** and benzyl azide (**a**) with xanthene

In a 2 mL vial, **1-OAc** (0.048 mmol), benzyl azide (**a**) (0.1 mmol, 2.1 equiv.) and xanthene (0.096, 2 equiv.) were mixed in HFIP (1 mL). The vial was sealed and stirred under air over 16 h at 50 ºC. The crude mixture was concentrated under vacuum line until the initial volume was reduced to two-thirds. Then, the reaction crude was analyzed by ^{1}H-NMR and HRMS observing the formation of the inserted Co[III] complex in 20% NMR yield using 1,3,5-trimethoxybenzene as internal standard. The intermolecular imido transfer was not observed using xanthene as an external substrate.

7.3 Evaluation of demetallation sources
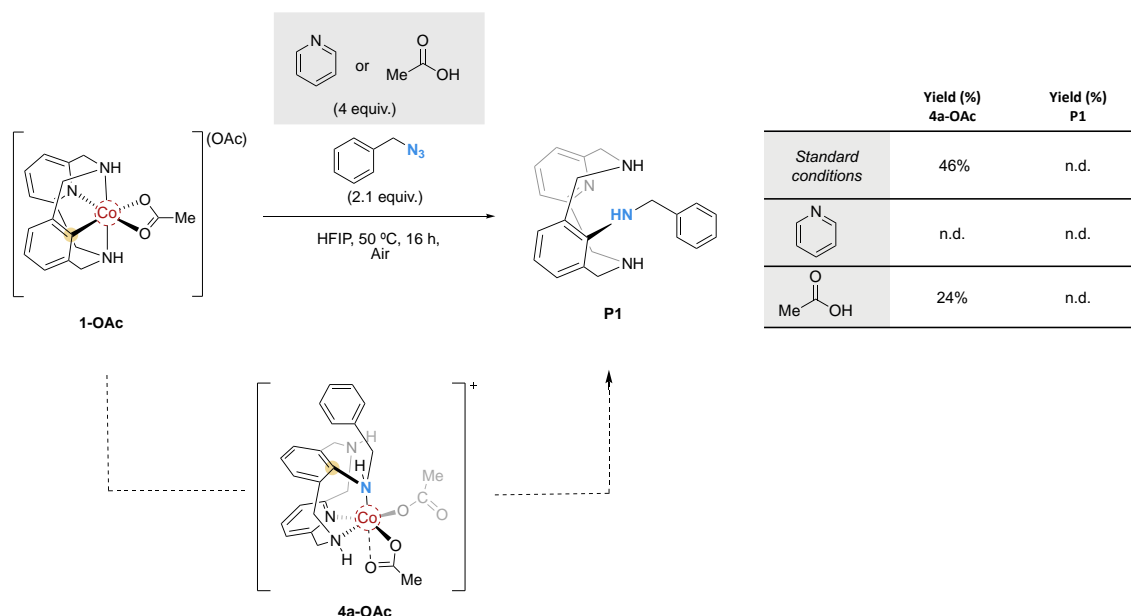
Scheme S16. Evaluation of different additive in the **P1** formation

In a 2 mL vial, **1-OAc** (0.048 mmol), benzyl azide (**a**) (0.1 mmol, 2.1 equiv.) and the corresponding additive (0.192 mmol, 4 equiv.) were mixed in HFIP (1 mL). The vial was sealed and stirred under air over 16 h at 50 ºC. The crude mixture was concentrated under vacuum line until the initial volume was reduced to two-thirds. Then, the reaction crude was analyzed by ^{1}H-NMR and HRMS using 1,3,5-trimethoxybenzene as internal standard.

The presence of pyridine in the reaction quenches the reactivity due to the coordination of the pyridine to the Co^{III} complex starting material. On the other hand, in the presence of acetic acid lower yield of **4a-OAc** (24%) was observed. However, no **P1** product was detected, and traces amounts of **L-H** ligand were observed in HRMS analysis.

7.4 Reactivity of 1-OAc with benzyl amine to form 7-OAc
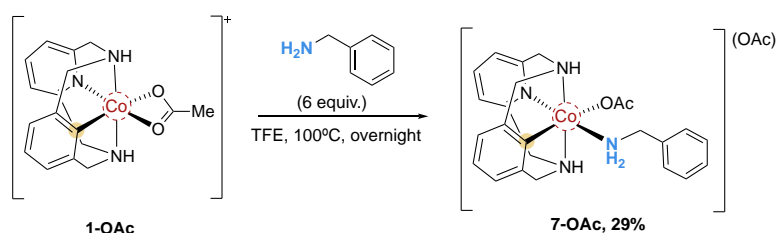
Scheme S17. Formation of **7-OAc** by reacting **1-OAc** complex with benzyl amine.

In a 2 mL vial, **1-OAc** (20 mg, 0.048 mmol) and benzyl amine (6 equiv.) were mixed in TFE and the vial was sealed and heated at 100 ºC. After stirring overnight, the solvent was removed and ether diffusion over CHCl$_3$ give the **7-OAc** organometallic complex, which was characterized by NMR, HRMS and X-Ray spectroscopy.

Mixture of two conformers were observed. **^{1}H NMR** (400 MHz, CHCl$_3$, 298 K) δ (ppm): 8.35 (bs, 1H), 7.60 (m, 2H), 7.23 (m, 6H), 7.14-7.00 (m, 10H), 6.95 (d, ^3J = 7.7 Hz, 2H), 6.89 (d, ^3J = 7.4 Hz, 2H), 4.82 (m, 3H), 4.70 (d, ^2J = 16.6 Hz, 2H), 4.57 (d, ^2J = 16.0 Hz, 2H), 4.33 (bs, 1H), 4.21 (d, ^2J = 16.6 Hz, 2H), 3.81-3.77 (m, 4H), 3.71 (d, ^2J = 16.9 Hz, 2H), 3.61 (d, ^2J = 16.9 Hz, 2H), 2.89 (bs, 2H), 2.76 (bs, 2H), 2.20 (s, 6H), 1.95 (s, 6H). **^{13}C {1H} NMR** (100 MHz, CHCl$_3$, 298 K) δ (ppm): δ 207.7, 179.9, 169.0, 168.6, 161.2, 161.1, 161.0, 160.8, 148.0, 147.9, 147.8, 147.7, 138.3, 138.2, 138.1, 138.0, 128.7, 128.6, 128.1, 128.0, 127.8, 127.8, 125.1, 125.0, 121.3, 121.0, 119.2, 119.1, 63.5, 63.4, 63.3, 63.2, 63.1, 63.0, 47.8, 47.4, 47.0, 46.9, 31.2, 25.5. **HRMS** (ESI) calc. for C$_{24}$H$_{28}$CoN$_4$O$_2^+$ [M – OAc]$^+$: 463.1537, found 463.1539.

7.5 Reactivity of 1-CH$_3$CN with benzyl azide (a)
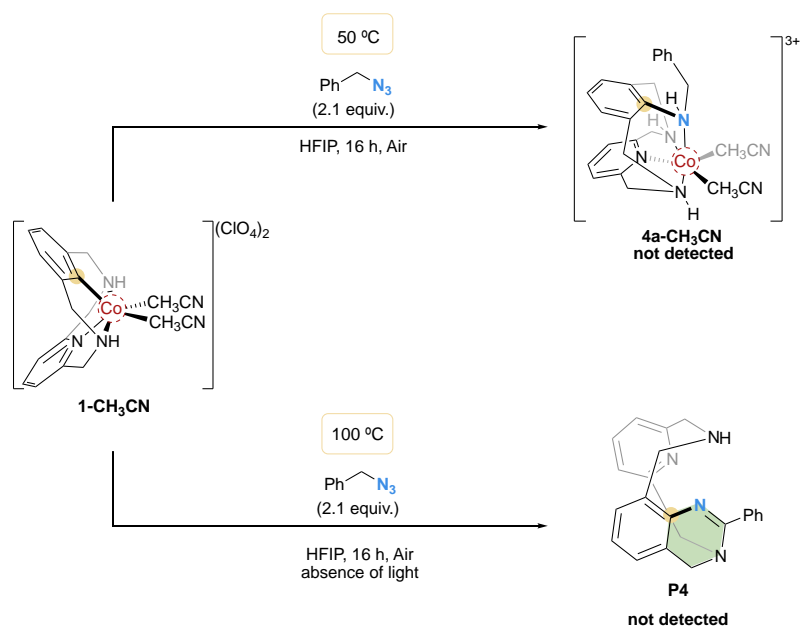
Scheme S18. Unproductive reactivity of **1-CH$_3$CN** complex with benzyl azide at 50 ºC and 100 ºC.

Procedure A: In a 2 mL vial, **1-CH$_3$CN** (27.7 mg, 0.048 mmol) and organic azide **a** (2.1 equiv.) were mixed in HFIP (1 mL) and the vial was sealed. The mixture was heated at 50 ºC overnight. The crude was concentrated under vacuum line until the initial volume was reduced to two-thirds. The crude mixture was analyzed by ^{1}H-NMR but no traces of aryl-amine coupling complex **4a-CH$_3$CN** was observed. The broad ^{1}H-NMR spectrum indicated the presence of unknown paramagnetic species.

Procedure B: In a 2 mL vial, **1-CH$_3$CN** (27.7 mg, 0.048 mmol) and organic azide **a** (2.1 equiv.) were mixed in HFIP (1 mL) and the vial was sealed and heated at 100ºC during 16 h in the absence of light. Then, after removal of the solvent, the crude mixture was analyzed by ^{1}H-NMR observing the total conversion, however neither the **4a-CH$_3$CN** nor final **P4** were detected. Moreover, 17% of benzaldehyde was observed together with unknown paramagnetic species.

8. Reactivity of 1_{Me}-OAc (Co^{III}) and 2_{Me}-OAc (Rh^{III}) complex with organic azides

a) Using 1_{Me}-OAc (Co^{III})

b) Using 2_{Me}-OAc (Rh^{III})

1_{Me}-OAc

2_{Me}-OAc

$8x_{Me}$-OAc
(8a$_{Me}$-OAc) R = Ph, 25%
(8b$_{Me}$-OAc) R = CH$_2$Ph, 35%
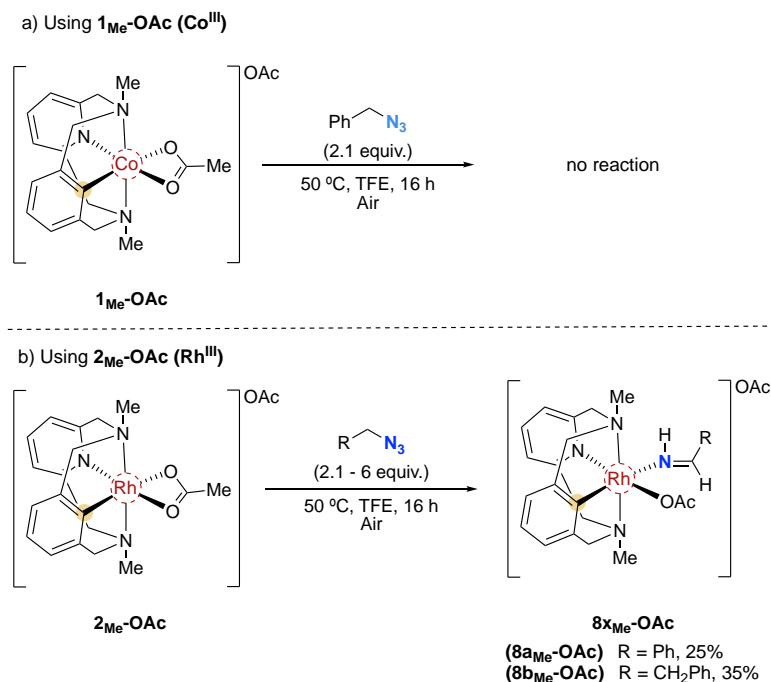
Scheme S19. Exploring the reactivity of N-methylated complex with organic azides. a) Using 1_{Me}-OAc (Co^{III}) and b) Using 2_{Me}-OAc (Rh^{III}) to afford the $8x_{Me}$-OAc complexes.

Using the N-methylated ligand (**L-Me**) no reactivity was observed for the Co^{III} complex using 2 equiv. of benzyl azide in HFIP at 50 °C, recovering the starting 1_{Me}-OAc complex. In contrast, the Rh-based 2_{Me}-OAc complex led to the formation of $8a_{Me}$-OAc complex in 25% yield, featuring an imine moiety directly coordinated to the Rh^{III} center.[26-28] Furthermore, the complex $8b_{Me}$-OAc bearing an iminoethyl phenyl was also obtained (35% yield) using an excess of azide **b** (6 equiv.) in TFE at 50 °C.

Procedure followed for the formation of $8x_{Me}$-OAc:

2_{Me}-Cl (20 mg, 0.045 mmol) and AgOAc (18.4 mg, 0.11 mmol, 2.5 equiv.) were mixed in TFE and heated over 15 min at 100 °C. The crude was cooled down to room temperature and filtered and the corresponding organic azide was added. After heating for 16 h at 50 °C, the crude was concentrated under vacuum line until the initial volume was reduced to two-thirds. The mixture was dissolved in CHCl$_3$ and layered with pentane or ether at 4 °C giving the corresponding $8x_{Me}$-OAc complex which was characterized by NMR and HRMS.

Aryl-Rh^{III}-(NHCHPh) – (8a$_{Me}$-OAc)
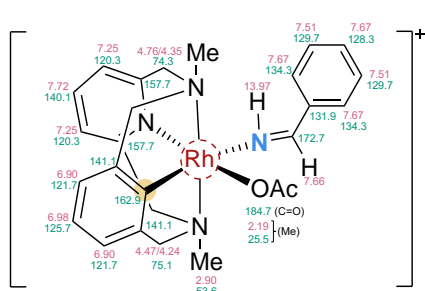
8a$_{Me}$-OAc was synthesized using 2.1 equivalents of azide **a** affording the organometallic complex as yellow oil (25 % NMR Yield). **¹H NMR** (400 MHz, CHCl$_3$, 298 K) δ (ppm): 13.97 (d, ^3J = 21.2 Hz, 1H), 7.72 (t, ^3J = 7.9 Hz, 1H), 6.67 (b, 1H), 7.64-7.58 (m, 3H), 7.51 (m, 2H), 7.25 (d, ^3J = 7.9 Hz, 2H), 6.98 (m, 1H), 6.90 (m, 2H), 4.76 (d, ^2J = 16.0 Hz, 2H), 4.47 (b, 2H), 4.35 (d, ^2J = 16.0 Hz, 2H), 4.24 (d, ^2J = 16.1 Hz, 2H), 2.90 (s, 6H), 2.s9 (s, 3H). **¹³C {1H} NMR**

(100 MHz, CHCl$_3$, 298 K) δ (ppm): 184.6 (1C), 172.7 (1C), 162.9 (1C), 157.7 (2C), 141.1 (2C), 140.1 (1C), 134.3 (2C), 131.9 (1C), 129.7 (2C), 128.3 (1C), 125.7 (1C), 121.7(2C), 120.3 (2C), 75.1 (2C), 74.3 (2C), 53.6 (2C), 25.5 (1C). **HRMS** (ESI) calc. for C$_{26}$H$_{30}$RhN$_4$O$_2^+$ [M – OAc]$^+$: 533.1418, found 533.1424.

Aryl-Rh(III)-(NHCHCH$_2$Ph) – (8b$_{Me}$-OAc)
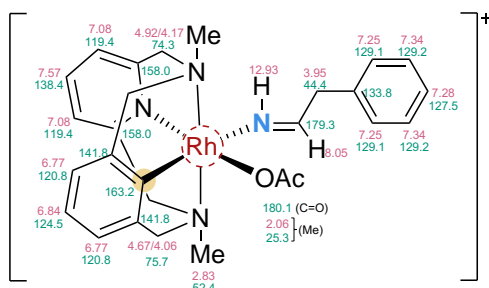
8b$_{Me}$-OAc was synthesized using 6 equivalents of azide **b** affording the organometallic complex as yellow oil (35 % NMR Yield). **^{1}H NMR** (400 MHz, CHCl$_3$, 298 K) δ (ppm): 12.93 (d, ^3J = 20.3 Hz, 1H), 8.05 (dt, ^3J = 20.3 Hz, ^3J = 5.6 Hz, 1H), 5.57 (t, ^3J = 7.9 Hz, 1H), 6.34 (m, 2H), 7.28 (m, 1H), 7.25 (m, 2H), 7.08 (d, ^3J = 7.9 Hz, 2H), 6.84 (m, 1H), 6.77 (m, 2H), 4.92 (d, ^2J = 15.6 Hz, 2H), 4.67 (d, ^2J = 15.6 Hz, 2H), 4.17 (d, ^2J = 15.6 Hz, 2H), 4.06 (d, ^2J = 15.6 Hz, 2H), 3.95 (d, d, ^3J = 5.6 Hz, 2H), 2.83 (s, 6H), 2.06 (s, 3H). **^{13}C {1H} NMR** (100 MHz, CHCl$_3$, 298 K) δ (ppm): 180.1 (1C), 179.3 (1C), 163.2 (1C), 158.0 (2C), 141.8 (2C), 138.4 (1C), 133.8 (1C), 129.2 (2C), 129.1 (2C), 124.5 (1C), 120.8 (2C), 119.4 (2C), 75.7 (2C), 74.3 (2C), 52.4 (2C), 44.4 (1C), 25.3 (1C). **HRMS** (ESI) calc. for C$_{27}$H$_{32}$RhN$_4$O$_2^+$ [M – OAc]$^+$: 547.1575, found 547.1567.

9. XAS analysis of 1-OAc, 6b-OAc and 7-OAc complexes

1-OAc and **7-OAc** exhibit rising edges centered around 7720 eV at half-height. Together with the intense pre-edge region with a maximum at 7711.5 eV this is consistent with the previously reported aryl-Co^{III} species having Co-C bonds.[1, 2] The slightly lower rising edge energy and pre-edge intensity of **7-OAc** relative to **1-OAc** indicates a more negative effective charge on the metal center and a lass covalent interaction with the surrounding ligands. EXAFS analysis shows both species consist of a six-coordinate environment having 2 N/O/C scattering atoms at 1.86 A and 3 N/O scattering atoms centered around 2.0 A, consistent with the reported crystal structures (Fig. S19).[1, 2] Therefore the differences in the XANES features must arise from the differences in surrounding ligands, where the pi-accepting nature of the acetonitrile ligands, evidenced in the crystal structure of **1-OAc**[1] result in an ever so slightly effectively more oxidized metal center, leading to a slight increase in the rising edge energy. Furthermore, the pi-backbonding in **1-OAc** is also expected to increase metal p-character mixing into the Co d-manifold resulting in a slightly more intense pre-edge feature with respect to **7-OAc**. **6b-OAc** on the other hand has a similar rising edge profile to the previously reported Co^{II} species from the same family of complexes.[1] Coupled with EXAFS analysis of the bond distances, which are significantly larger than for the +3 analogues with 2 N/O scattering
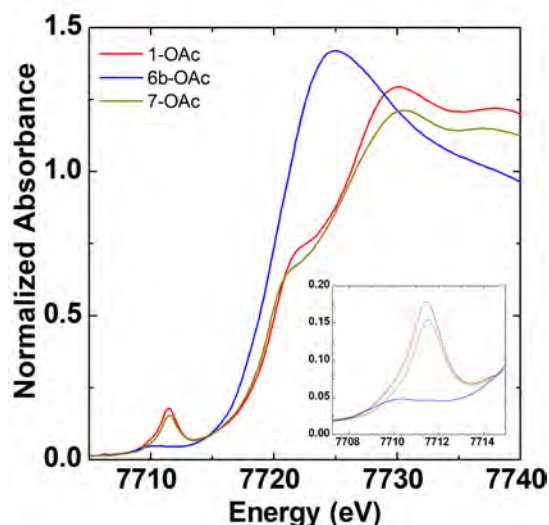
Figure S19: XANES region XAS spectra highlighting the rising edges for **1-OAc**, **6b-OAc** and **7-OAc**, with inset showing the pre-edge region due to 1s-3d transitions.

atoms at 2.01 A and 4 N/O scattering atoms at 2.14 A, all lead to characterizing this species as having a +2 metal oxidation state. Lastly, the small scattering intensity in the Fourier transformed EXAFS spectra above 2 A, and the need of only including 2 C scattering atoms at 2.95 A for **6b-OAc** suggests, in stark contrast to the Co[III] analogues, a more disordered metal coordination environment in the bulk sample as opposed to what might be expected from the crystal structure.

Table S2: X-ray absorption spectroscopy parameters at the Co K-edge.

SAMPLE	OXIDATION STATE	E_0' (eV)[1]	$E_0^{1/2}$ (eV)[2]	Pre-edge Energy (eV)	Pre-edge Area
3c-OAc[3]	2.0	7719.8	7718.5	7709.8	0.12
1-OAc	3.0	7720.1	7720.0	7711.5	0.30
6b-OAc	2.0	7719.9	7718.8	7710.1	0.11
7-OAc	3.0	7719.6	7719.8	7711.5	0.27

(1) E0' values at were taken as the maximum infection point of the first derivative
(2) $E0_{1/2}$ values were taken at the half-height ie. 0.5 normalized intensity units of the rising edge
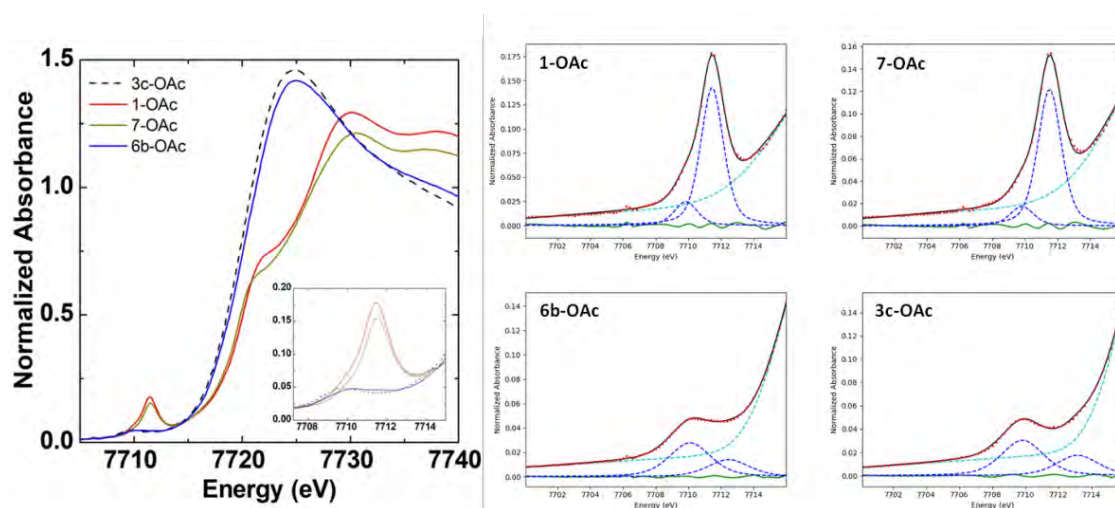(3) J. Am. Chem. Soc. 2016, 138, 14388–14397

Figure S20: Co K-edge XANES spectra and pre-edge fits.

Panel S1:Summary of EXAFS analysis at the Co[III]complex 1-OAc: k^3-weighted fits carried out in r-space over a k-range of 3-12 Å using a Hanning window (dk 1), and an $S_0 = 0.9$ was chosen. Bond distances and disorder parameters (Δr_{eff} and σ^2) were allowed to float having initial values of 0.0 Å and 0.003 Å^2 respectively, with a universal E_0 and $\Delta E_0 = 0$ eV. Plotted is the best fit (bottom of the table), σ^2 values reported as x 10^3 Å^2.

| SAMPLE	Δk	Δr	Var.	R$_{FACTOR}$	χ^2_v	ΔE$_0$	M-N/C/O N	r(Å)	σ²	M-N/C/O N	r(Å)	σ²	M-C N	r(Å)	σ²	M--C-N--M N	r(Å)	σ²	M--C-N^{MeCN}--M N	r(Å)	σ²
	2-12	1-3	5	0.0247	116.8	2.2	2	1.88	5	3	1.99	5	6	2.81	4	8	2.99	4	3	3.15	5
	2-12	1-3	5	0.0248	116.6	2.3	1	1.86	6	4	1.97	6	6	2.81	4	8	2.99	4	3	3.16	6
	2-12	1-3	5	0.0139	65.4	2.0	1	1.86	8	5	1.97	8	6	2.81	4	8	2.99	4	3	3.15	8
1-OAc	2-12	1-3	5	0.0174	82.2	2.2	3	1.90	6	3	2.01	6	6	2.81	4	8	2.99	4	3	3.16	6
	2-12	1-3	5	0.0254	119.8	1.8	2	1.87	7	4	1.98	7	6	2.81	4	-	-	-	3	3.15	7
	2-12	1-3	5	0.0246	116.3	3.6	2	1.88	7	4	1.99	7	6	2.82	4	8	3.00	4	-	-	-
	2-12	1-3	5	0.0127	59.6	1.8	2	1.87	7	4	1.98	7	6	2.81	4	8	2.99	4	3	3.16	7

*Although EXAFS can not differentiate between O/N/C scattering paths, chemical intuition was used for description; M is the absorber element in this case Mn
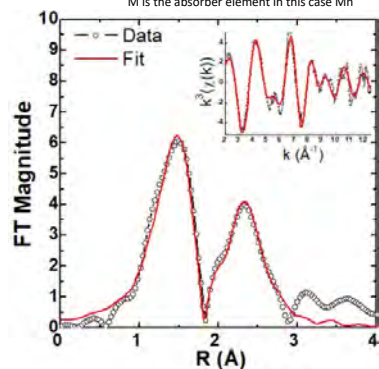
Panel S2: Summary of EXAFS analysis of 6b-OAc: k^3-weighted fits carried out in r-space over a k-range of 3-11.5 Å using a Hanning window (dk 1), and an S_0 = 0.9 was chosen. Bond distances and disorder parameters (Δr_{eff} and σ^2) were allowed to float having initial values of 0.0 Å and 0.003 Å^2 respectively, with a universal E_0 and ΔE_0 = 0 eV. Plotted is the best fit (bottom of the table)), σ^2 values reported as x 10^3 Å^2.

SAMPLE	Δk	Δr	Var.	R_{FACTOR}	χ^2_v	ΔE_0	M-N/C/O N	r(Å)	σ^2	M-N/C/O N	r(Å)	σ^2	M-N/C/O N	r(Å)	σ^2	M-C N	r(Å)	σ^2
	2-11.5	1-3	3	0.0313	139.5	1.6	1	2.03	7	4	2.13	7	-	-	-	2		7
	2-11.5	1-3	3	0.0279	124.6	1.9	2	2.05	7	3	2.15	7	-	-	-	2	2.97	7
6b-OAc	2-11.5	1-3	3	0.0184	82.3	1.7	4	2.07	9	2	2.17	9	-	-	-	2	2.99	9
	2-11.5	1-3	3	0.0303	135.0	1.4	2	2.02	5	2	2.13	5	2	2.21	5	-	-	-
	2-11.5	1-3	3	0.0177	79.2	1.6	2	2.02	5	2	2.13	5	2	2.21	5	2	2.94	5
	2-11.5	1-3	3	0.0140	62.5	1.3	2	2.04	8	4	2.14	8	-	-	-	2	2.96	8

*Although EXAFS can not differentiate between O/N/C scattering paths, chemical intuition was used for description;
M is the absorber element in this case Mn
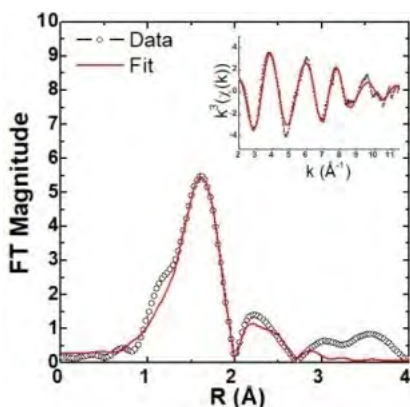
Panel S3: Summary of EXAFS analysis at the 7-OAc: k^3-weighted fits carried out in r-space over a k-range of 3-12 Å using a Hanning window (dk 1), and an S_0 = 0.9 was chosen. Bond distances and disorder parameters (Δr_{eff} and σ^2) were allowed to float having initial values of 0.0 Å and 0.003 Å^2 respectively, with a universal E_0 and ΔE_0 = 0 eV. Plotted is the best fit (bottom of the table)), σ^2 values reported as x 10^3 Å^2.

SAMPLE	Δk	Δr	Var.	R_{FACTOR}	χ^2_v	ΔE_0	M-N/C/O N	r(Å)	σ^2	M-N/C/O N	r(Å)	σ^2	M-C N	r(Å)	σ^2	M-C N	r(Å)	σ^2
	2-12	1-3	4	0.0381	225.7	-1.2	2	1.87	2	3	2.01	2	4	2.81	2	2	2.94	2
	2-12	1-3	4	0.0359	212.6	0.0	1	1.87	2	4	2.01	6	4	2.8	2	2	2.94	2
7-OAc	2-12	1-3	4	0.0362	214.5	-1.1	2	1.87	3	4	2.01	4	4	2.81	3	2	2.94	3
	2-12	1-3	4	0.0394	235.7	-0.1	2	1.87	3	4	2.01	4	4	2.81	3	2	2.94	3
	2-12	1-3	4	0.0544	322.0	-1.7	2	1.87	5	4	2.02	5	6	2.81	5	-	-	-
	2-12	1-3	4	0.0256	152.0	-1.4	2	1.86	3	4	2.01	4	4	2.8	3	2	2.94	3

*Although EXAFS can not differentiate between O/N/C scattering paths, chemical intuition was used for description;
M is the absorber element in this case Mn

M--C-N--M N	r(Å)	σ^2	M--C-O/N--M N	r(Å)	σ^2
4	3.01	2	4	3.16	2
4	3.00	2	4	3.16	2
-	-	-	-	-	-
8	3.01	3	-	-	-
4	3.01	5	4	3.16	5
4	3.00	3	4	3.16	3
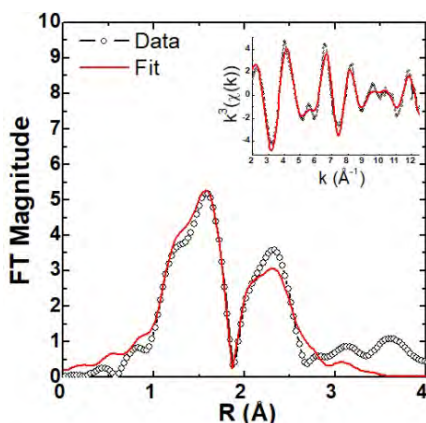
10. Crystallographic data information

Crystallographic data for compounds **1-OBzOMe** (CCDC-2097543), **1-OBzOCF₃** (CCDC-2097542), **3'-N₃(N₃)** *(CCDC-2097541), **5a-OAc** *(CCDC-2097546), **6b-OAc** *(CCDC-*2097544), **7-OAc** *(CCDC-*2097545) can be obtained free of charge from the Cambridge Crystallographic Data Centre via www.ccdc.cam.ac.uk/data_request/cif. Moreover, the corresponding CIF files have been included in the Supplementary Digital Material included in the attached CD.
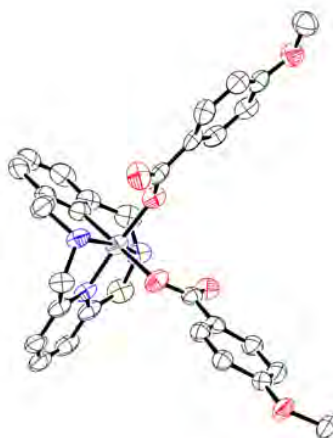
10.1 X-Ray structure of 1-OBzOMe

Figure S21. X-Ray crystal structure of **1-OBzOMe** at 50% probability level. H-atoms and solvent molecules have been omitted for clarity.

Orange-pink needle of $(C_{31}H_{28}CoN_3O_6)_2$, $7H_2O$, were grown from a $CHCl_3$ solution layered with pentane, and used for low temperature (100(2) K) X-ray structure determination. The X-ray intensity data were measured on a Bruker D8 QUEST ECO system equipped with a doubly curved silicon crystal Bruker Triumph monochromator and a Mo Kalpha sealed X-ray tube (λ = 0.71073 Å). A total of 540 frames were collected. The total exposure time was 12.50 hours. The frames were integrated with the Bruker SAINT software package using a narrow-frame algorithm. The integration of the data using a monoclinic unit cell yielded a total of 43919 reflections to a maximum θ angle of 27.54° (0.77 Å resolution), of which 6956 were independent (average redundancy 6.314, completeness = 99.5%, R_{int} = 10.94 %, R_{sig} = 7.97%) and 4543 (65.31%) were greater than $2\sigma(F^2)$. The final cell constants of $\underline{a}$ = 12.9753(10) Å, $\underline{b}$ = 14.8245(14) Å, $\underline{c}$ = 16.6220(14) Å, β = 108.367(2)°, volume = 3034.4(5) Å³, are based upon the refinement of the XYZ centroids of 9909 reflections above 20 $\sigma(I)$ with 5.496° < 2θ < 54.82°. Data were corrected for absorption effects using the MultiScan method (SADABS). The ratio of minimum to maximum apparent transmission was 0.643. The calculated minimum and maximum transmission coefficients (based on crystal size) are 0.8340 and 0.9810. The structure was solved and refined using the Bruker SHELXTL Software Package, using the space group P 1 21/n 1, with Z = 2 for the formula unit, $C_{62}H_{70}Co_2N_6O_{19}$. The final anisotropic full-matrix least-squares refinement on F^2 with 433 variables converged at R1 = 5.85%, for the observed data and wR2 = 16.10% for all data. The goodness-of-fit was 1.049. The largest peak in the final differences electron density synthesis was 0.606 e⁻/Å³ and the largest hole was -0.694 e⁻/Å³ with an RMS deviation of 0.087 e⁻/Å³. On the basis of the final model, the calculated density was 1.446 g/cm³ and F(000), 1380 e⁻.

Table S3. Crystallographic parameters for **1-OBzOMe**.

| Chemical formula	$(C_{31}H_{28}CoN_3O_6)_2$, $7H_2O$	
Formula weight	1321.10 g/mol	
Temperature	100(2) K	
Wavelenght	0.71073 Å	
Crystal size	0.030 x 0.040 x 0.300 mm	
Crystal system	Monoclinic	
Space group	P 1 21/n 1	
Unit cell dimensions	a = 12.9753(10) Å	α = 90°
	b = 14.8245(14) Å	β = 108.367(2)°
	c = 16.6220(14) Å	γ = 90°
Volume	3034.4(5) Å^3	
Density (calculated)	1.446 g/cm^3	
Absorption coefficient	0.627 mm^{-1}	
Final R indices	4543 data; I>2σ(I)	R1 = 0.0585, wR2 = 0.1363
	all data	R1 = 0.1062, wR2 = 0.1610

10.2   X-Ray structure of 1-OBzCF₃
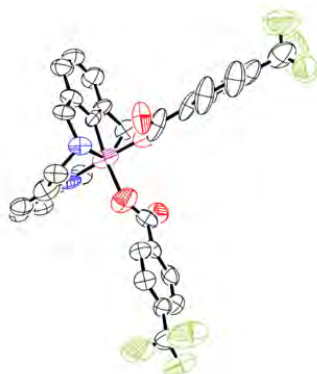
Figure S22. X-Ray crystal structure of **1-OBzCF₃** at 50% probability level. H-atoms and solvent molecules have been omitted for clarity.

Red-pink block of $C_{31}H_{24}CoF_6N_3O_4$, $(C_8H_5F_3O_2)$, H_2O were grown from a CHCl$_3$ solution layered with pentane, and used for low temperature (100(2) K) X-ray structure determination. The X-ray intensity data were measured on a Bruker D8 QUEST ECO system equipped with a doubly curved silicon crystal Bruker Triumph monochromator and a Mo Kalpha sealed X-ray tube (λ = 0.71076 Å). A total of 1452 frames were collected. The total exposure time was 21.65 hours. The frames were integrated with the Bruker SAINT software package using a narrow-frame algorithm. The integration of the data using a monoclinic unit cell yielded a total of 84160 reflections to a maximum θ angle of 28.37° (0.75 Å resolution), of which 9346 were independent (average redundancy 9.005, completeness = 99.5%, R$_{int}$ = 3.16 %, R$_{sig}$ = 1.85%) and 7955 (85.12%) were greater than 2σ(F^2). The final cell constants of $\underline{a}$ = 14.30(2) Å, $\underline{b}$ = 14.84(2) Å, $\underline{c}$ = 17.70(3) Å, β = 93.35(3)°,volume = 3750.(10) Å^3, are based upon the refinement of the XYZ centroids of 9921 reflections above 20 σ(I) with 5.945° < 2θ < 56.39°.Data were corrected for absorption effects using the MultiScan method (SADABS). The ratio of minimum to maximum apparent transmission was 0.921. The calculated minimum and maximum transmission coefficients (based on crystal size) are 0.9210 and 0.9460. The structure was solved and refined using the Bruker SHELXTL Software Package, using the space group P 1 21/c 1, with Z = 4 for the formula unit, $C_{39}H_{31}CoF_9N_3O_7$. The final anisotropic full-matrix least-squares refinement on F^2 with 813 variables converged at R1 = 7.33%, for the observed data and wR2 = 17.75% for all data. The goodness-of-fit was 1.092. The largest peak in the final differences electron density synthesis was 0.685 e$^-$/Å^3 and the largest hole was -1.074 e$^-$/Å^3 with an RMS deviation of 0.066 e$^-$/Å^3. On the basis of the final model, the calculated density was 1.565 g/cm^3 and F(000), 1800 e$^-$.

Table S4. Crystallographic parameters for **1-OBzCF₃**.

|	
Chemical formula	$C_{31}H_{24}CoF_6N_3O_4$, $(C_8H_5F_3)$, H_2O
Formula weight	883.60 g/mol
Temperature	100(2) K
Wavelenght	0.71076 Å
Crystal size	0.100 x 0.100 x 0.150 mm
Crystal system	Monoclinic
Space group	P 1 21/c 1
Unit cell dimensions	a = 14.30(2) Å α = 90°
	b = 14.84(2) Å β = 93.35(3)°
	c = 17.70(3) Å γ = 90°
Volume	3750.(10) Å³
Density (calculated)	1.565 g/cm³
Absorption coefficient	0.558 mm⁻¹
Final R indices	7955 data; I>2σ(I) R1 = 0.0733, wR2 = 0.1694
	all data R1 = 0.0850, wR2 = 0.1775

10.3 X-Ray structure of 3'-N₃(N₃)
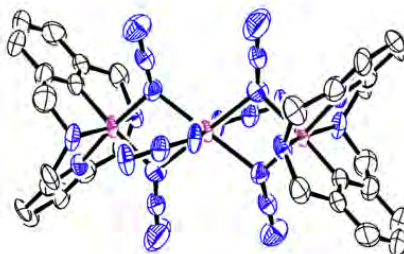
Figure S23. X-Ray crystal structure of **3'-N₃(N₃)** at 50% probability level. H-atoms and solvent molecules have been omitted for clarity.

Brown-red block-like of $C_{30}H_{32}Co_3N_{24}$, $(CH_2Cl_2)_2$, were grown from a CH_2Cl_2 solution layered with pentane, and used for low temperature (100(2) K) X-ray structure determination. The X-ray intensity data were measured on a Bruker D8 QUEST ECO system equipped with a doubly curved silicon crystal Bruker Triumph monochromator and a Mo Kalpha sealed X-ray tube (λ = 0.71076 Å). A total of 720 frames were collected. The total exposure time was 20.00 hours. The frames were integrated with the Bruker SAINT software package using a narrow-frame algorithm. The integration of the data using a monoclinic unit cell yielded a total of 15531 reflections to a maximum θ angle of 24.58° (0.85 Å resolution), of which 2750 were independent (average redundancy 5.648, completeness = 78.5%, R_{int} = 9.60 %, R_{sig} = 6.89%) and 1946 (70.76%) were greater than $2\sigma(F^2)$. The final cell constants of <u>a</u> = 10.22(2) Å, <u>b</u> = 14.49(3) Å, <u>c</u> = 14.19(3) Å, β = 96.99(3)°,volume = 2086.(8) Å³, are based upon the refinement of the XYZ centroids of 2857 reflections above 20 σ(I) with 5.922° < 2θ < 48.79°. Data were corrected for absorption effects using the MultiScan method (SADABS). The ratio of minimum to maximum apparent transmission was 0.719. The calculated minimum and maximum transmission coefficients (based on crystal size) are 0.8410 and 0.8770. The structure was solved and refined using the Bruker SHELXTL Software Package, using the space group P 1 21/c 1, with Z = 2 for the formula unit, $C_{32}H_{36}Cl_4Co_3N_{24}$. The final anisotropic full-matrix least-squares refinement on F^2 with 280 variables converged at R1 = 9.16%, for the observed data and wR2 = 28.07% for all data. The goodness-of-fit was 1.136. The largest peak in the final differences electron density synthesis was 1.299 e⁻/Å³ and the largest hole was -1.387 e⁻/Å³ with an RMS deviation of 0.181 e⁻/Å³. On the basis of the final model, the calculated density was 1.712 g/cm³ and F(000), 1090 e⁻.

Table S5. Crystallographic parameters for **3'-N$_3$(N$_3$)**.

|		
Chemical formula	C$_{30}$H$_{32}$Co$_3$N$_{24}$, (CH$_2$Cl$_2$)$_2$	
Formula weight	1175.44.60 g/mol	
Temperature	100(2) K	
Wavelenght	0.71076 Å	
Crystal size	0.090 x 0.100 x 0.1200 mm	
Crystal system	Monoclinic	
Space group	P 1 21/c 1	
Unit cell dimensions	a = 10.22(2) Å	α = 90°
	b = 14.49(2) Å	β = 96.99(5)°
	c = 14.19(3) Å	γ = 90°
Volume	2086.(8) Å^3	
Density (calculated)	1.712 g/cm^3	
Absorption coefficient	1.495 mm^{-1}	
Final R indices	1946 data; I>2σ(I)	R1 = 0.0916, wR2 = 0.2483
	all data	R1 = 0.1280, wR2 = 0.2807

10.4 X-Ray structure of 5a-OAc
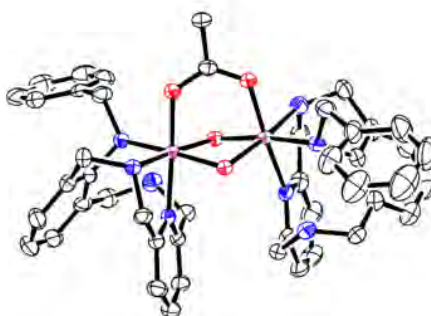
Figure S24. X-Ray crystal structure of **5a-OAc** at 50% probability level. H-atoms and solvent molecules have been omitted for clarity.

Needle-like of C$_{46}$H$_{53}$Co$_2$N$_8$O$_4$, (C$_3$H$_2$F$_6$O)$_3$, (C$_2$H$_3$O$_2$)$_4$ were grown from slow CHCl$_3$ solution layered with pentane at -4 ºC , and used for low temperature (100(2) K) X-ray structure determination. The X-ray intensity data were measured on a Bruker D8 QUEST ECO system equipped with a doubly curved silicon crystal Bruker Triumph monochromator and a Mo Kalpha sealed X-ray tube (λ = 0.71076 Å). A total of 277 frames were collected. The total exposure time was 9.23 hours. The frames were integrated with the Bruker SAINT software package using a narrow-frame algorithm. The integration of the data using a monoclinic unit cell yielded a total of 39050 reflections to a maximum θ angle of 18.79° (1.10 Å resolution), of which 5512 were independent (average redundancy 7.085, completeness = 99.5%, R$_{int}$ = 36.10 %, R$_{sig}$ = 20.13%) and 3026 (54.90%) were greater than 2σ(F^2). The final cell constants of $\underline{a}$ = 21.20(4) Å, $\underline{b}$ = 11.96(2) Å, $\underline{c}$ = 29.59(4) Å, β = 108.90(4)°,volume = 7098.(19) Å^3, are based upon the refinement of the XYZ centroids of 1009 reflections above 20 σ(I) with 6.502° < 2θ < 37.65°. Data were corrected for absorption effects using the MultiScan method (SADABS). The ratio of minimum to maximum apparent transmission was 0.727. The calculated minimum and maximum transmission coefficients (based on crystal size) are 0.9180 and 0.9880. The structure was solved and refined using the Bruker SHELXTL Software Package, using the space group P 1 21/c 1, with Z = 4 for the formula unit, C$_{63}$H$_{71}$Cl$_0$Co$_2$F$_{19}$N$_9$O$_{15}$. A considerable amount of electron density attributable to three C$_3$H$_2$F$_6$O and two C$_2$H$_3$O$_2$ heavyly disordered solvent molecules was removed with the SQUEEZE option of PLATON.[29] Those solvent molecules are, however, included in the reported chemical formula and derived values (e.g. formula weight, F(000), etc). The final anisotropic full-matrix least-squares refinement on F^2 with 406 variables converged

at R1 = 8.84%, for the observed data and wR2 = 24.85% for all data. The goodness-of-fit was 1.024. The largest peak in the final differences electron density synthesis was 0.41 e$^-$/Å^3 and the largest hole was -0.46 e$^-$/Å^3 with an RMS deviation of 0.231 e$^-$/Å^3. On the basis of the final model, the calculated density was 1.534 g/cm^3 and F(000), 2132 e$^-$

Table S6. Crystallographic parameters for **5a-OAc**.

| Chemical formula	$C_{46}H_{53}Co_2N_8O_4$, $(C_3H_2F_6O)_3$, $(C_2H_3O_2)_4$	
Formula weight	1640.13 g/mol	
Temperature	100(2) K	
Wavelenght	0.71076 Å	
Crystal size	0.020 x 0.020 x 0.150 mm	
Crystal system	Monoclinic	
Space group	P 1 21/c 1	
Unit cell dimensions	a = 21.20(4) Å	α = 90°
	b = 11.96(2) Å	β = 108.90(4)°
	c = 29.59(4) Å	γ = 90°
Volume	7098.(19) Å^3	
Density (calculated)	1.534 g/cm^3	
Absorption coefficient	0.583 mm^{-1}	
Final R indices	3026 data; I>2σ(I)	R1 = 0.0884, wR2 = 0.2073
	all data	R1 = 0.1530 wR2 = 0.2485

10.5 X-Ray structure of 6b-OAc
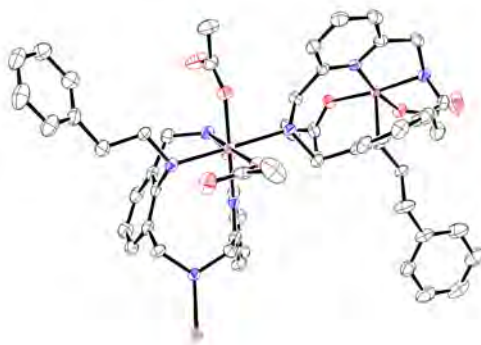
Figure S25. X-Ray crystal structure of **6b-OAc** at 50% probability level. H-atoms and solvent molecules have been omitted for clarity.

Pink needle of $(C_{27}H_{32}CoN_4O_4)_2$, $(CH_2Cl_2)_2$, H_2O were grown from pentane diffusion in a concentrated solution in CH_2Cl_2 anhydrous under inert atmosphere and used for low temperature (100(2) K) X-ray structure determination. The X-ray intensity data were measured on a Bruker D8 QUEST ECO system equipped with a doubly curved silicon crystal Bruker Triumph monochromator and a Mo Kalpha sealed X-ray tube (λ = 0.71073 Å). A total of 910 frames were collected. The total exposure time was 22.75 hours. The frames were integrated with the Bruker SAINT software package using a narrow-frame algorithm. The integration of the data using a monoclinic unit cell yielded a total of 76818 reflections to a maximum θ angle of 27.55° (0.77 Å resolution), of which 6608 were independent (average redundancy 11.625, completeness = 99.7%, R_{int} = 4.94%, R_{sig} = 2.34%) and 5442 (82.35%) were greater than 2σ(F^2). The final cell constants of a = 14.830(12) Å, b = 11.908(10) Å, c = 16.675(12) Å, β = 103.06(2)°,volume = 2869.(4) Å^3, are based upon the refinement of the XYZ centroids of 9796 reflections above 20 σ(I) with 6.068° < 2θ < 54.93°. Data were corrected for absorption effects using the MultiScan method (SADABS). The ratio of minimum to maximum apparent transmission was 0.880. The calculated minimum and maximum transmission coefficients (based on crystal size) are 0.7890 and 0.9140. The structure was solved and refined using the Bruker SHELXTL Software Package, using the space group P 1 21/n 1, with Z = 2 for the formula unit,

$C_{56}H_{70}Cl_4Co_2N_8O_9$. The final anisotropic full-matrix least-squares refinement on F^2 with 375 variables converged at R1 = 7.78%, for the observed data and wR2 = 24.18% for all data. The goodness-of-fit was 1.087. The largest peak in the final differences electron density synthesis was 2.371 $e^-/Å^3$ and the largest hole was -2.035 $e^-/Å^3$ with an RMS deviation of 0.167 $e^-/Å^3$. On the basis of the final model, the calculated density was 1.457 g/cm^3 and F(000), 1312 e^-.

Table S7. Crystallographic parameters for **6b-OAc.**

Chemical formula	$(C_{27}H_{32}CoN_4O_4)_2$, $(CH_2Cl_2)_2$, H_2O	
Formula weight	1258.86 g/mol	
Temperature	100(2) K	
Wavelenght	0.71073 Å	
Crystal size	0.110 x 0.110 x 0.300 mm	
Crystal system	Monoclinic	
Space group	P 1 21/n 1	
Unit cell dimensions	a = 14.830(12) Å	α = 90°
	b = 11.908(10) Å	β = 103.06(2)°
	c = 16.675(12) Å	γ = 90°
Volume	2869.(4) $Å^3$	
Density (calculated)	1.457 g/cm^3	
Absorption coefficient	0.828 mm^{-1}	
Final R indices	5442 data; I>2σ(I)	R1 = 0.0778, wR2 = 0.2251
	all data	R1 = 0.0932, wR2 = 0.2418

10.6 X-Ray structure of 7-OAc
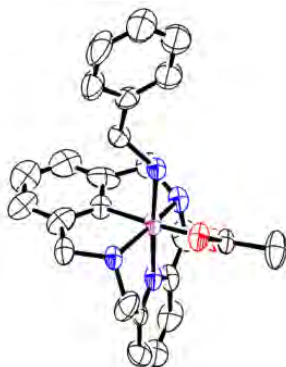
Figure S26 X-Ray crystal structure of **7-OAc** at 50% probability level. H-atoms and solvent molecules have been omitted for clarity.

Pink-red prism-like specimen of $(C_{24}H_{28}CoN_4O_4)_2$, $(CH_2Cl_2)_2$, $(C_2H_3O_2)_2$, $(H_2O)_3$ were grown from slow CH_2Cl_2 solution layered with pentane and used for low temperature (100(2) K) X-ray structure determination. The X-ray intensity data were measured on a Bruker D8 QUEST ECO system equipped with a doubly curved silicon crystal Bruker Triumph monochromator and a Mo Kalpha sealed X-ray tube (λ = 0.71073 Å). A total of 707 frames were collected. The total exposure time was 19.64 hours. The frames were integrated with the Bruker SAINT software package using a narrow-frame algorithm. The integration of the data using a triclinic unit cell yielded a total of 113544 reflections to a maximum θ angle of 26.48° (0.80 Å resolution), of which 12127 were independent (average redundancy 9.363, completeness = 99.6%, R_{int} = 9.33%, R_{sig} = 5.37%) and 8266 (68.16%) were greater than 2σ(F^2). The final cell constants of <u>a</u> = 11.4024(5) Å, <u>b</u> = 13.8632(6) Å, <u>c</u> = 18.7203(8) Å, α = 87.4460(10)°, β = 86.1440(10)°, γ = 84.8130(10)°, volume = 2938.2(2) $Å^3$, are based upon the refinement of the XYZ centroids of 9994 reflections above 20 σ(I) with 5.906° < 2θ < 52.70°. Data were corrected for absorption

effects using the MultiScan method (SADABS). The ratio of minimum to maximum apparent transmission was 0.906. The calculated minimum and maximum transmission coefficients (based on crystal size) are 0.8140 and 0.9570. The structure was solved and refined using the Bruker SHELXTL Software Package, using the space group P -1, with Z = 2 for the formula unit, $C_{54}H_{70}Cl_6Co_2N_8O_{11}$. The final anisotropic full-matrix least-squares refinement on F^2 with 706 variables converged at R1 = 9.61%, for the observed data and wR2 = 26.68% for all data. The goodness-of-fit was 1.028. The largest peak in the final differences electron density synthesis was 1.684 e$^-$/Å^3 and the largest hole was -1.319 e$^-$/Å^3 with an RMS deviation of 0.137 e$^-$/Å^3. On the basis of the final model, the calculated density was 1.512 g/cm^3 and F(000), 1388 e$^-$.

Table S8. Crystallographic parameters for **7-OAc**.

Chemical formula	$(C_{24}H_{28}CoN_4O_4)_2$, $(CH_2Cl_2)_2$, $(C_2H_3O_2)_2$, $(H_2O)_3$	
Formula weight	1337.74 g/mol	
Temperature	100(2) K	
Wavelenght	0.71073 Å	
Crystal size	0.050 x 0.100 x 0.240 mm	
Crystal system	Monoclinic	
Space group	P -1	
Unit cell dimensions	a = 11.4024(5) Å	α = 87.4460(10)°
	b = 13.8632(6) Å	β = 86.1440(10)°
	c = 18.7203(8) Å	γ = 84.8130(10)°
Volume	2938.2(2) Å^3	
Density (calculated)	1.512 g/cm^3	
Absorption coefficient	0.896 mm^{-1}	
Final R indices	8266 data; I>2σ(I)	R1 = 0.0961, wR2 = 0.2308
	all data	R1 = 0.1408, wR2 = 0.2667

11. Computational studies

11.1 EOS (Effective oxidation state) analysis

*Nitrene **2***

The occupation of the EFOs showed in Figure S27 and in the EOS analysis presented in Table S9 clearly stablish that **2** can be described as an aryl-Co^{III}=N-R (R = -CH$_2$Ph) nitrene species (Fischer-type). The low R(%) value of the OS assignation is due to highly covalent character of the Co-aryl bond.

Table S9. For the nitrene **2**, effective oxidation state of each fragment, as well as occupations of the last occupied and first unoccupied EFOs.

Fragment	EOS	Last occ.	First unocc.
1 (Co)	3	0.618	0.483
2 (N$_2$)	0	0.969	0.007
3 (Carboxylate)	-1	0.858	0.017
4 (PhCH$_2$N)	0	0.655	0.343
5 (Aryl)	-1	0.485	0.063

Reliability Index R(%) = 50.2%

Masked nitrene 3

The results of the EOS analysis indicating that **3** can be describe as a Co^{III} nitrene:

Table S10. For the masked nitrene **3**, effective oxidation state of each fragment, as well as occupations of the last occupied and first unoccupied EFOs.

Fragment	EOS	Last occ.	First unocc.
1 (Co)	3	0.817	0.419
2 (Ring)	-1	0.741	0.045
3 (Aryl)	-1	0.542	0.095

Reliability Index R(%) = 62.21%

11.2. Analysis of the EFOs (Effective fragment orbitals)

For the nitrene **2**, a pair of EFOs can be found corresponding to the Co-N π bond. These two EFOs (one for the Co, and one on the N atom in the PhCH$_2$N fragment) are obtained separately and independently. The former has an occupation of 0.62, and the latter an occupation of 0.34, so they agree with the description of **2** as an aryl-Co^{III}=N-R nitrene with a significant back-donation from the Co to the N.

PhCH$_2$N EFO (occupation = 0.34)   *Co EFO (occupation = 0.62)*
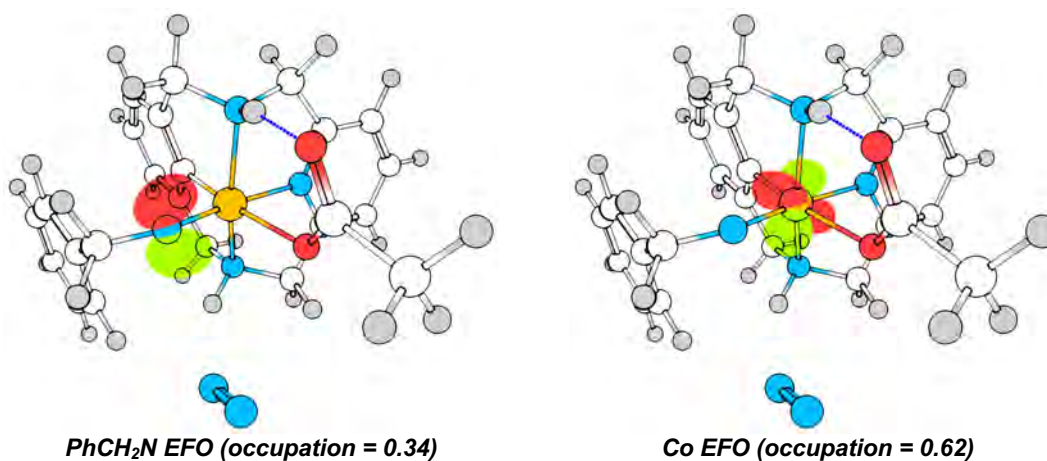
Figure S27. The complementary EFOs of Co and N corresponding to the Co-N π bond.

A pair of EFOs describing the sigma bond can also be identified. The Co has an occupation of 0.40, with the N having an occupation of 0.66:

PhCH₂N EFO (occupation = 0.66)   *Co EFO (occupation = 0.40)*
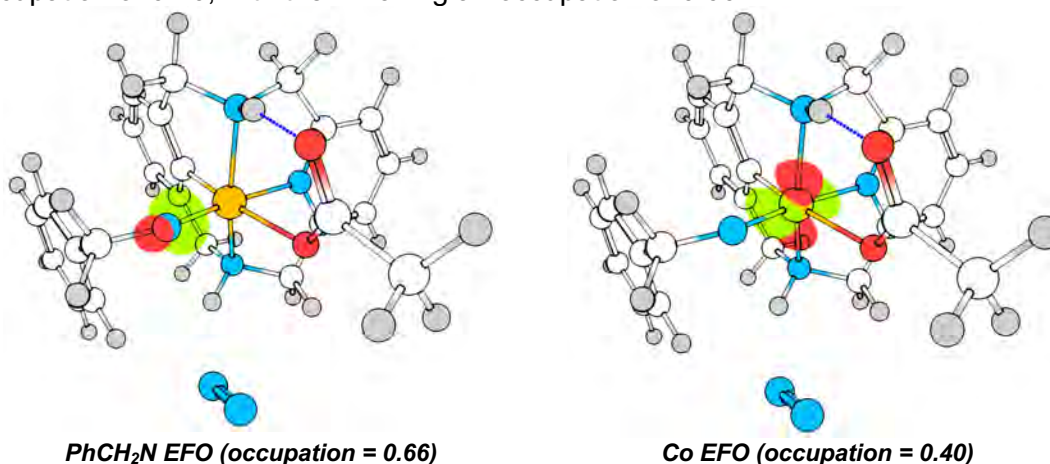
Figure S28. The complementary EFOs of Co and N corresponding to the Co-N sigma bond.

For the masked nitrene **3**, the sigma Co-N bond can easily be identified, with an occupation of 0.31 for the Co, and 0.74 for the N, which agrees with the description of **3** as a masked Co^{III} nitrene:

PhCH₂N EFO (occupation = 0.31)   *Co EFO (occupation = 0.74)*
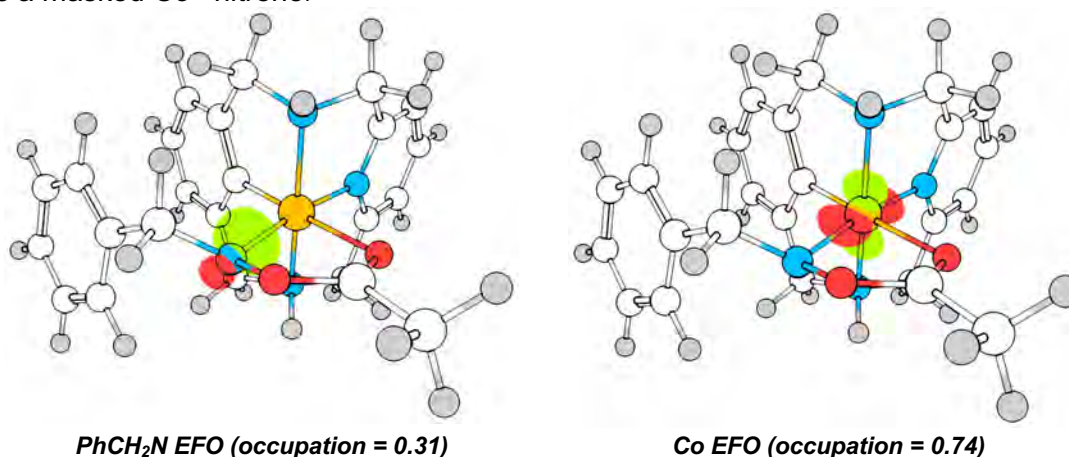
Figure S29. The complementary EFOs of Co and N corresponding to the Co-N sigma bond.

In this case there's no π bond (the bond order is only 0.51), but we can find the lone pair on the nitrogen, with an occupation of 0.96:
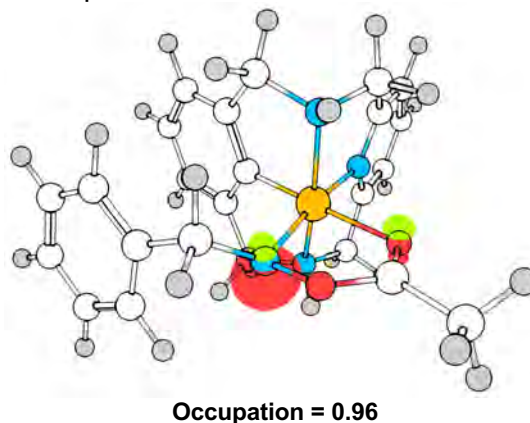
Occupation = 0.96

Figure S30. EFO of the ring fragment corresponding mostly to the lone pair on N.

As for the EFOs of the aryl ligand, for each of the two geometries we can find the aryl contribution to the sigma Co-aryl bond. The occupations of this EFOs are useful to compare the nucleophilic character of the aryl in the *nitrene 2* and *masked nitrene 3* (Figure S32). The former has an occupation of 0.49, while for the latter it's 0.54, indicating that the nucleophilic character of the aryl increases when the masked nitrene **3** is formed.

occupation = 0.49   **occupation = 0.54**
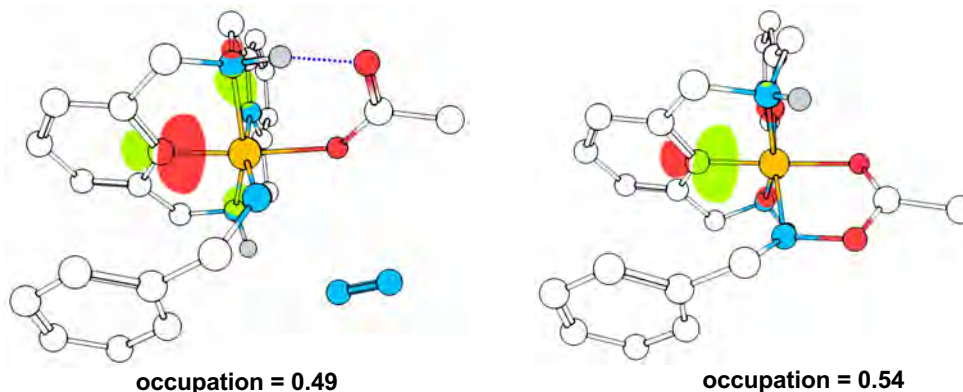
Figure S31. Comparison of the aryl EFO in the nitrene **2** (left) and masked nitrene **3** (right) geometries.

11.3 Analysis of the MO-LCAO coefficients for nitrene 2

Visual representation of the MOs

HOMO-11   LUMO
MO #116   MO #128
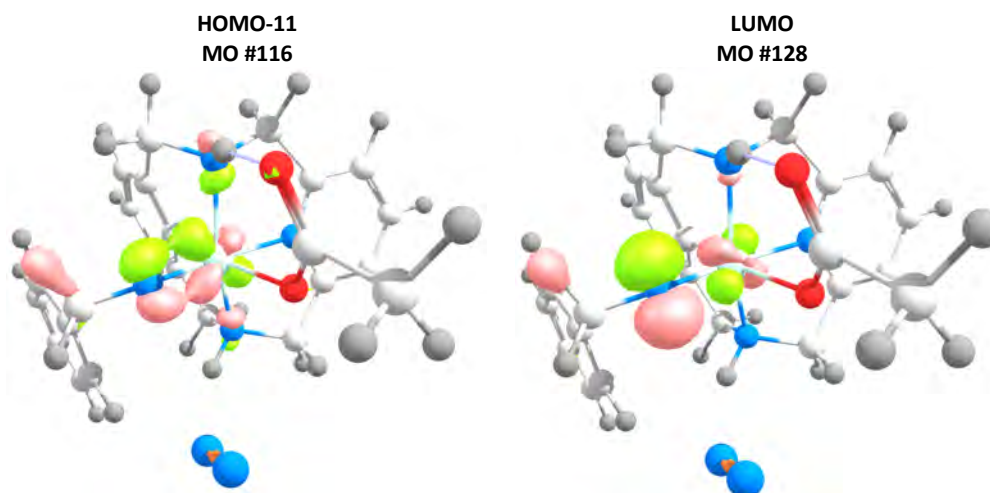
Figure S32. BP86-D3BJ(SMD)/Def2SVP MOs (level of theory used for the geometry optimizations).

The **HOMO-11** is a π bonding molecular orbital formed by the overlapping of the d_{yz} orbital of the metal, and the p_z of the nitrogen (bonding interaction). As it can be seen in Table S11, the major contribution to the **HOMO-11** is due to the d orbitals of Co, which agrees with the fact that for very high values of the isosurfaces the **HOMO-11** is only localized on Co.[30] The **LUMO,** on the other hand, is the corresponding π anti-bonding molecular orbital. The major contribution to the **LUMO** is given by the p_z orbital of the N, which agrees with the fact that for very high values of the isosurfaces the **LUMO** is only localized on the N. Therefore, the analysis of the canonical MOs is in complete agreement with the EOS method description of **2** as aryl-Co^{III}=N-R nitrene.

Table S11. MO-LCAO coefficients of **HOMO-11** and **LUMO** for the Co *d* atomic orbitals and the N of the nitrenoid *p* atomic orbitals (left), and the corresponding squared (right) for nitrene **2**.

	AO #	MO #	116 HOMO-11	128 LUMO	116 HOMO-11	128 LUMO
Cobalt *d* atomic orbitals	43	9D 0	0.317	-0.278	0.100	0.077
	44	9D+1	0.246	-0.141	0.060	0.020
	45	9D-1	-0.060	0.215	0.004	0.046
	46	9D+2	0.125	-0.262	0.016	0.069
	47	9D-2	0.139	-0.171	0.019	0.029
	48	10D 0	0.132	-0.100	0.017	0.010
	49	10D+1	0.104	-0.051	0.011	0.003
	50	10D-1	-0.022	0.077	0.000	0.006
	51	10D+2	0.048	-0.095	0.002	0.009
	52	10D-2	0.055	-0.062	0.003	0.004
Nitrenoid *p* atomic orbitals	438	4PX	0.007	0.042	0.000	0.002
	439	4PY	0.116	0.265	0.014	0.070
	440	4PZ	0.218	0.410	0.047	0.168
	441	5PX	-0.004	-0.025	0.000	0.001
	442	5PY	-0.088	-0.209	0.008	0.044
	443	5PZ	-0.165	-0.312	0.027	0.097

11.4 Study of the S=1 and S=2 states

Table S12. Electronic Energy differences for the triplet and quintuplet BP86-D3BJ/Def2SVP single point calculations at the singlet equilibrium geometry with respect to the singlet electronic energy (in kcal/mol).

	ΔE (Triplet – Singlet)	ΔE (Quintuplet – Singlet)
Reactant complex	32.75	79.59
TS1 (N$_2$ release)	14.35	54.15
Nitrene	4.93	47.49
TS2 (Nitrene to Ring)	1.61	45.16
Ring	31.66	80.45
TS3 (C-N coupling)	18.34	48.85
Coupled	17.12	44.03

11.5 Analysis of the triplet Nitrene 2

For the nitrene **2**, the singlet → triplet spin-crossing involves a beta electron of the lone pair of the N atom in the nitrene. This is evidenced by the spin density, which is located around this nitrogen, as can be seen from its isosurface plot, and the integrated atomic values:
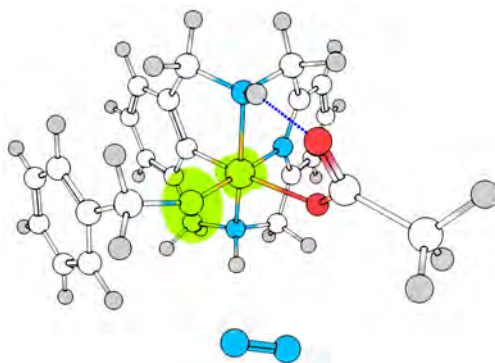
Figure S33. Spin density isosurface (isovalue = 0.03). It can be seen that the major contribution is located around the nitrogen atom.

Table S13. Atomic spin densities for this triplet nitrene **2**. For both the real-space partitioning, and the Hilbert-space one, the spin density is mostly located on the nitrogen.

	Co spin density	**N spin density**
TFVC (Real space)	0.5617	1.1976
Mulliken (Hilbert space)	0.5119	1.3348

The results of the EOS analysis for the triplet also shed light into the electronic structure of the triplet state. For the Co-N sigma interaction (see figure S34), the picture is similar to that of the singlet species. The sigma-type EFO on the N atom has a much larger occupation than the complementary d-type EFO on Co. Some spin polarization can be observed (the occupation of the alpha and beta EFOs differ), but both alpha and beta electrons (essentially the electron pair) is assigned to the sigma-donating N moiety.

The Co-N π interaction is the one affected by the singlet $\rightarrow$ triplet transition. The EOS analysis for the singlet species revealed the presence of a lone pair on N and a single π Co-N bond polarized towards the Co. For the S=0 state, the overall electron count for the N moiety results in an electron pair for the sigma part and a lone electron pair, thus four valence electrons.

| Alpha EFO (Occ = 0.723; occupied) | Alpha EFO (Occ = 0.361; unoccupied) |
| Beta EFO (Occ = 0.762; occupied) | Beta EFO (Occ = 0.314; unoccupied) |
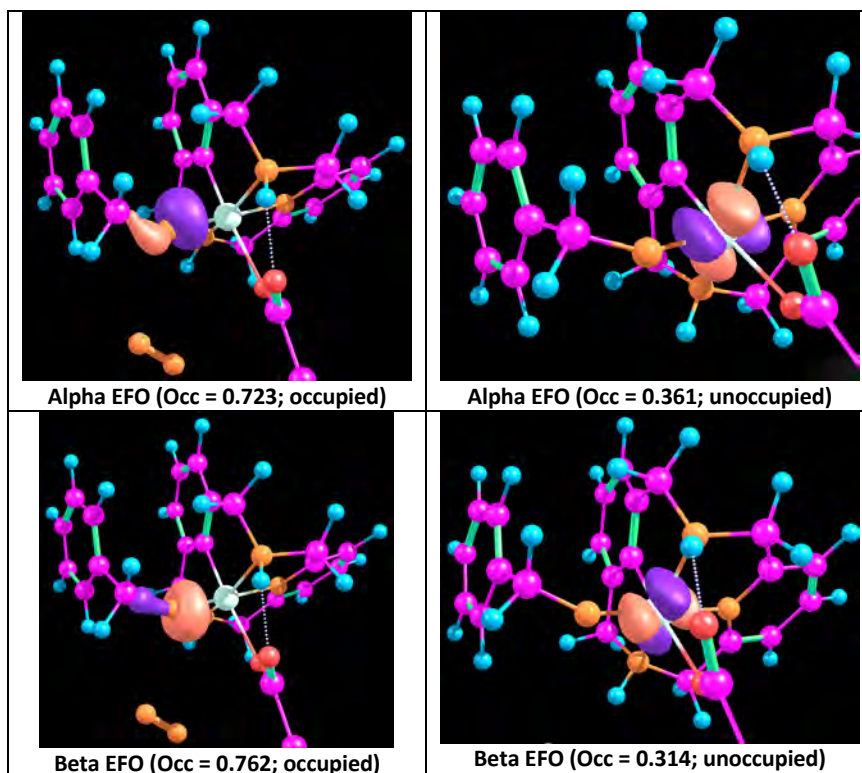
Figure S34. EFOs involved in Co-N sigma interaction in triplet Nitrene **2**.

The beta electron of the lone pair of the singlet is transferred (as alpha) to a formally empty p-type EFO on the N, resulting in a triplet state with two alpha p-type nonbonding electrons (see figure S35). At the same time a second π bond is established between Co-N involving the beta electrons (see figure S36). Both π bonds of the beta spin channels are polarized towards the Co moiety, as evidenced by the EFO occupations of Figure S36. The overall electron count for the N moiety results in an electron pair for the sigma part and two alpha non-bonding pi electrons, giving a total of four valence electrons, like for the singlet state. Hence, the nitrene character of the species is retained for both the singlet and triplet states.

Alpha EFO (Occ = 0.943; occupied) Alpha EFO (Occ = 931, occupied)
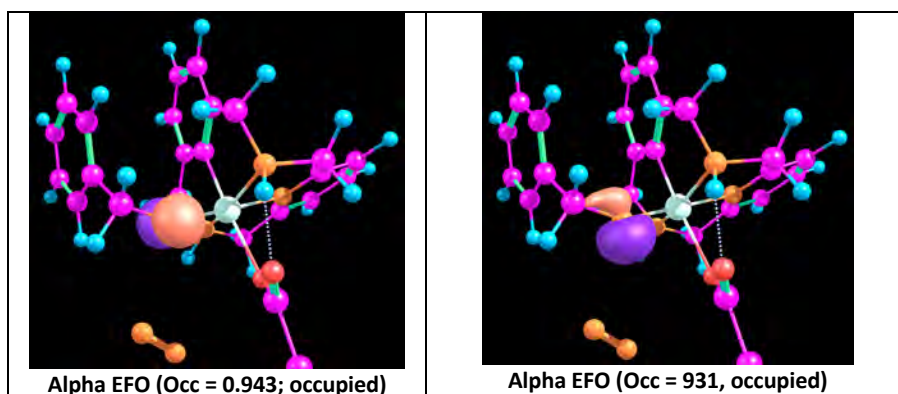
Figure S35. Alpha EFOs involved in Co-N π interaction in triplet Nitrene **2**.

Beta EFO (Occ = 0.237; unoccupied) Beta EFO (Occ = 0.685; occupied)

Beta EFO (Occ = 0.255; unoccupied) Beta EFO (Occ = 0.674; occupied)
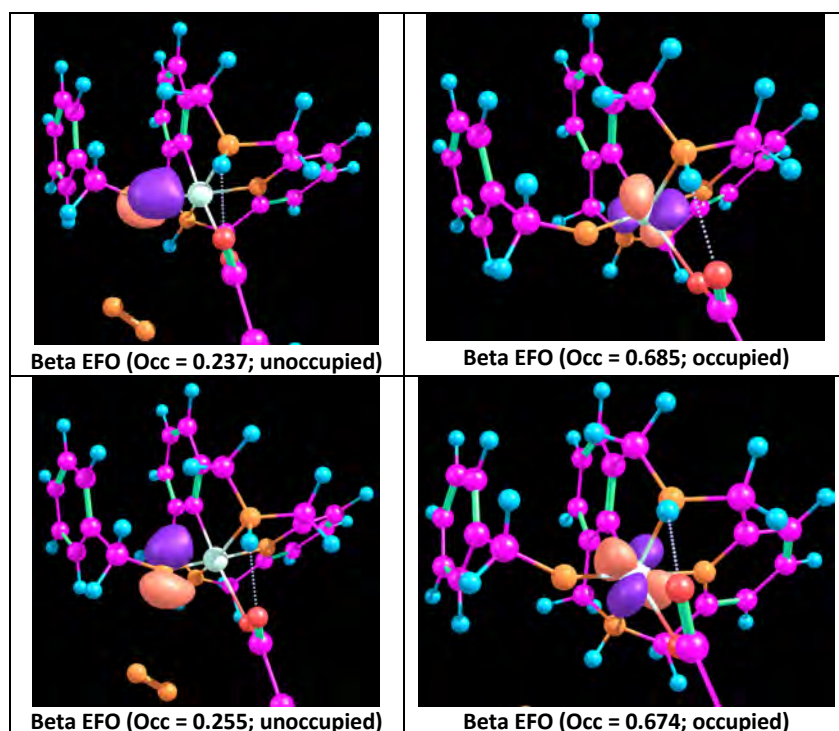
Figure S36. Beta EFOs involved in Co-N π interaction in triplet Nitrene **2**.

11.6 Attempts to find a stable penta-coordinated intermediate for Nitrene 2

Several relaxed PES scans were performed to look for a penta-coordinated intermediate for singlet Nitrene **2**. Reference image for the numbered atoms, which will be relevant for the scans below:
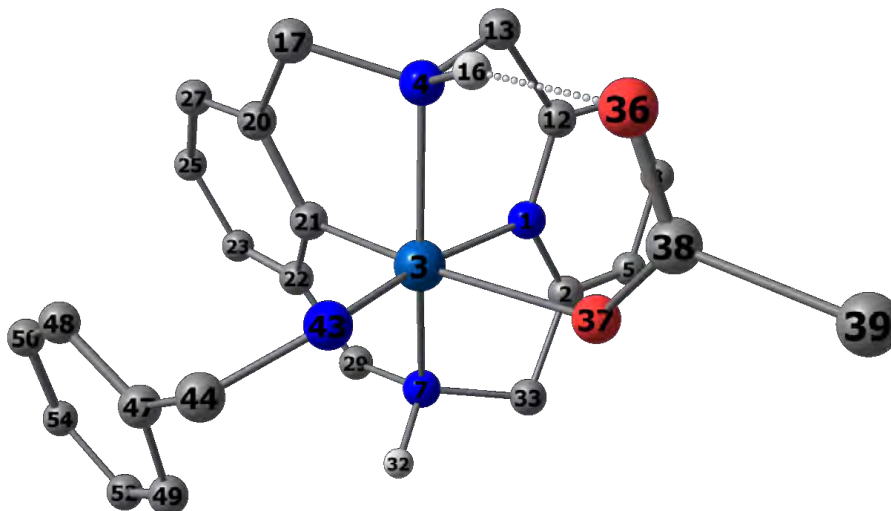
Figure S37. Numbered atoms for the Nitrene **2** geometry. The labels are used in the following discussion.

a. Scanning along Co-N distances

Bond 3-1: energy increase.
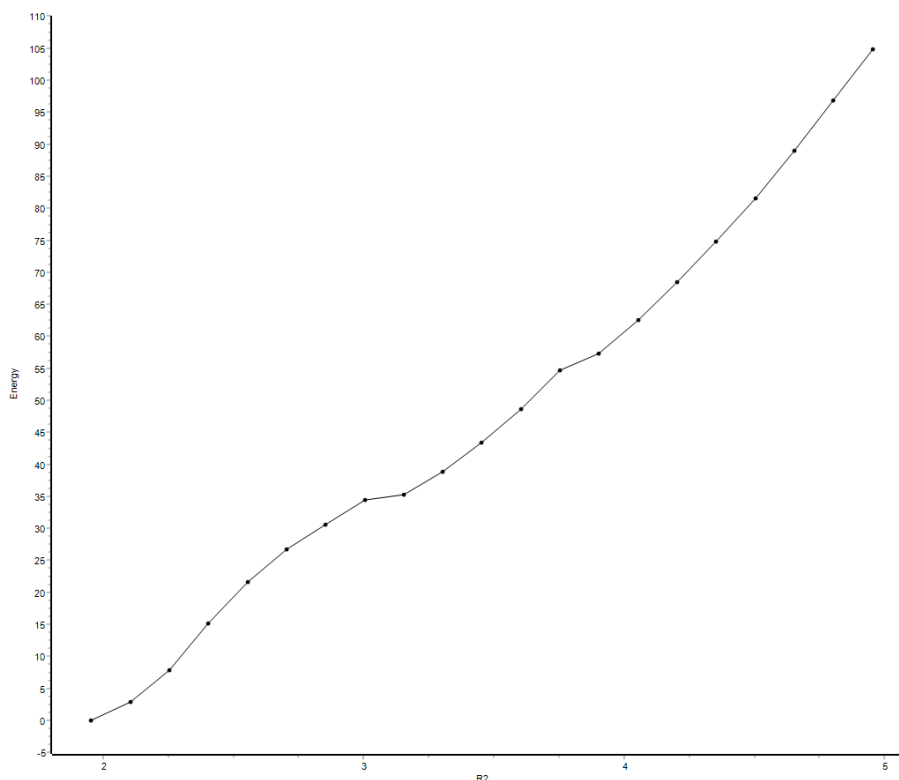
Figure S38. Relaxed PES scan along the Co-N (3,1) bond length.

Bond 3-4: energy increase.
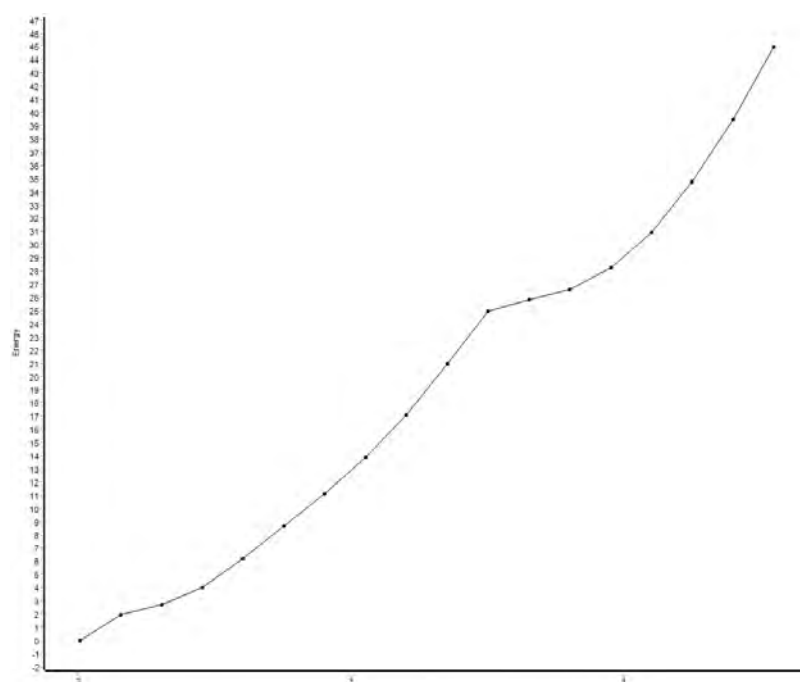
Figure S39. Relaxed PES scan along the Co-N (3,4) bond length.

Bond 3-7: energy increase. After some steps, the geometry is distorted to the point that the final product is formed (C-N bond coupling), leading to a decrease in energy. The barrier, of course, is much higher than the one of the mechanism shown in the manuscript.
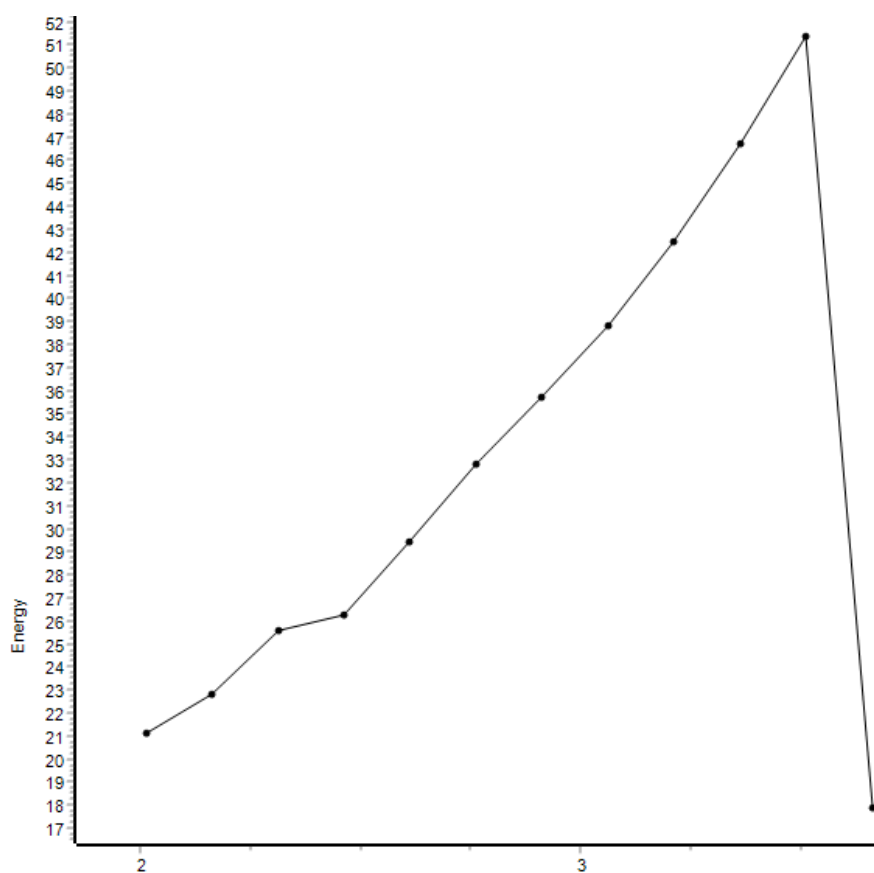
Figure S40. Relaxed PES scan along the Co-N (3,7) bond length.

b. Scans along N-C-C-N (4-13-12-1) dihedral

Both the positive and negative directions for the change of this dihedral were explored:

Positive direction: energy increase.
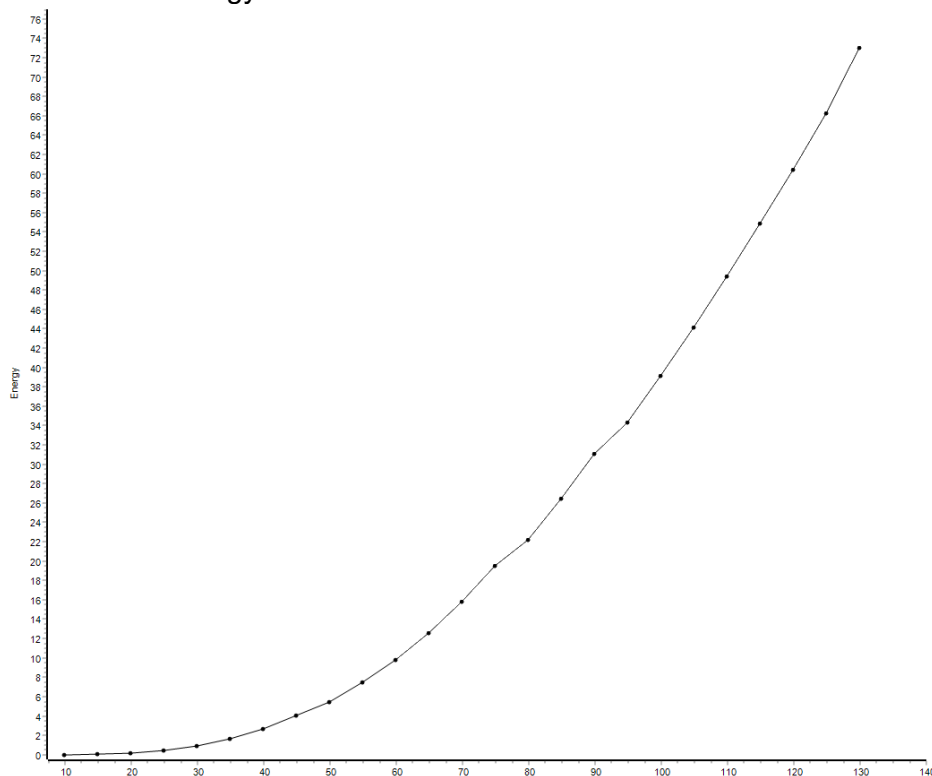
Figure S41. Relaxed PES scan along the N-C-C-N (4,13,12,1) dihedral angle.

Negative direction: energy increase. After some steps, the O-N bond (36-43) is formed, leading to the masked nitrene **3**. Thus, the search is stopped because it's not going to lead to possible alternative stable nitrene **2** intermediates. Once again, the barrier observed here is much higher than the barrier for the ring formation in our proposed mechanism.
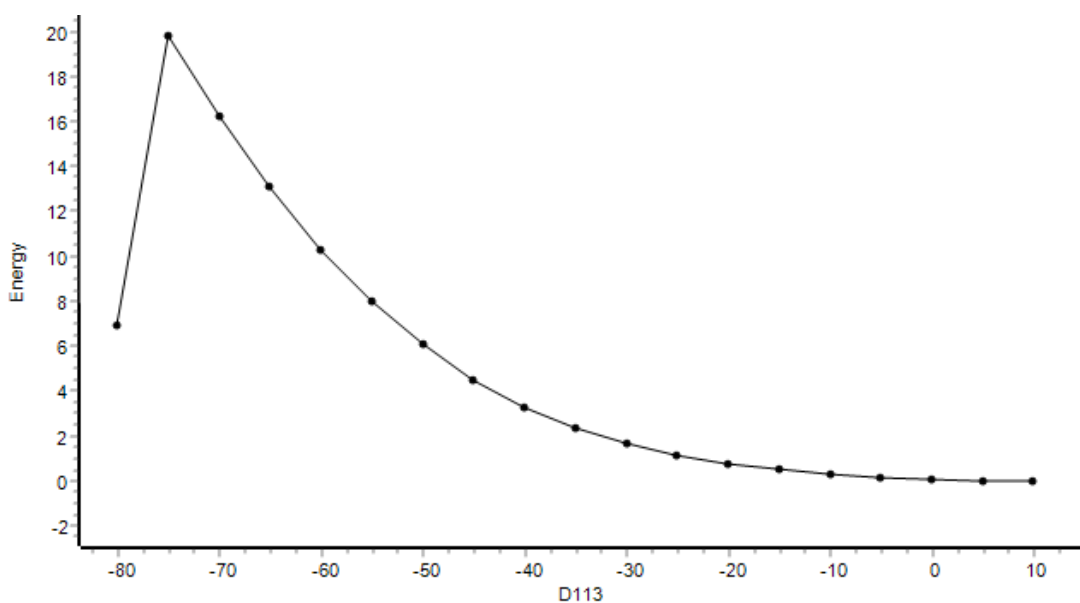
Figure S42. Relaxed PES scan along the N-C-C-N (4,13,12,1) dihedral, negative direction.

c. Designs of penta-coordinated intermediates

Penta-coordinated geometries were designed where the pyridine moiety is no longer coordinating (what we would have expected from the scans in subsections *a* and *b*, if such an intermediate existed).

Since the disconnected pyridine could rotate toward two different directions, two geometries were designed. Both geometries were optimized using two approaches: direct optimization, or step-wise optimization (first relaxing everything while the 3-1 bond was frozen, and then optimizing the resulting geometry). In all cases, the final optimized geometry was the same as Figure S37. For the triplet state, the geometries also optimized back to the original geometry, not leading to new alternative penta-coordinated intermediates.

12. DFT XYZ coordinates of geometry optimized structures

The optimized XYZ Cartesian coordinates for all the structures can be found in the following database link, in a very convenient format and allowing easy visualization and extraction of the XYZ file if needed: https://doi.org/10.19061/iochem-bd-4-29

13. Selected Original NMR and HRMS Spectra
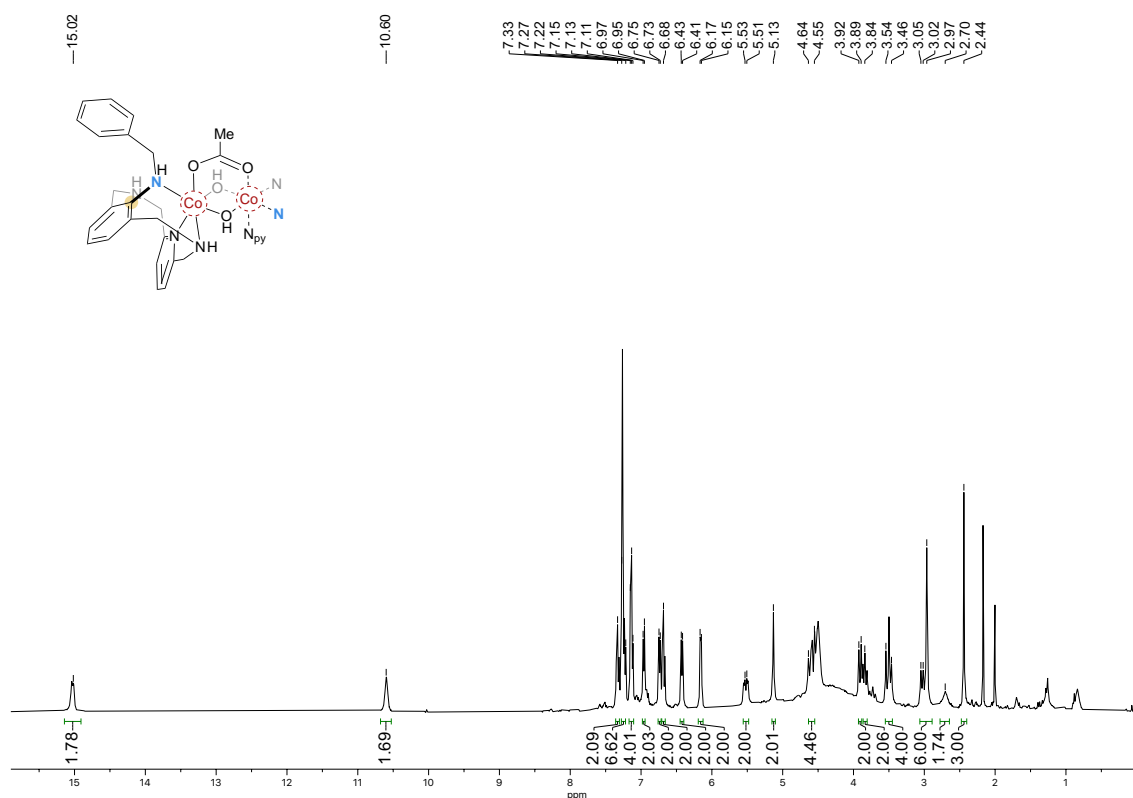
Figure S43. 500 MHz, ^{1}H NMR spectrum of **5a-OAc** in CDCl$_3$, 298 K.
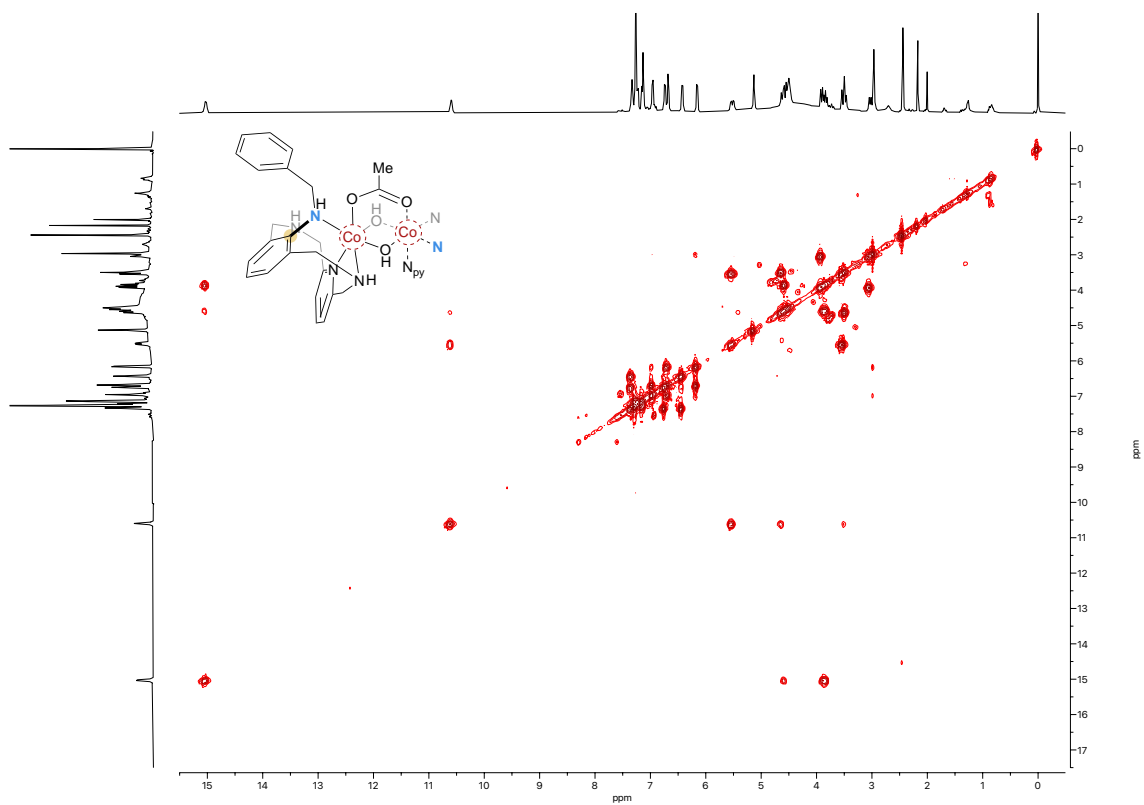
Figure S44. 500 MHz, ^{1}H-^{1}H COSY NMR spectrum of **5a-OAc** in CDCl$_3$, 298 K.
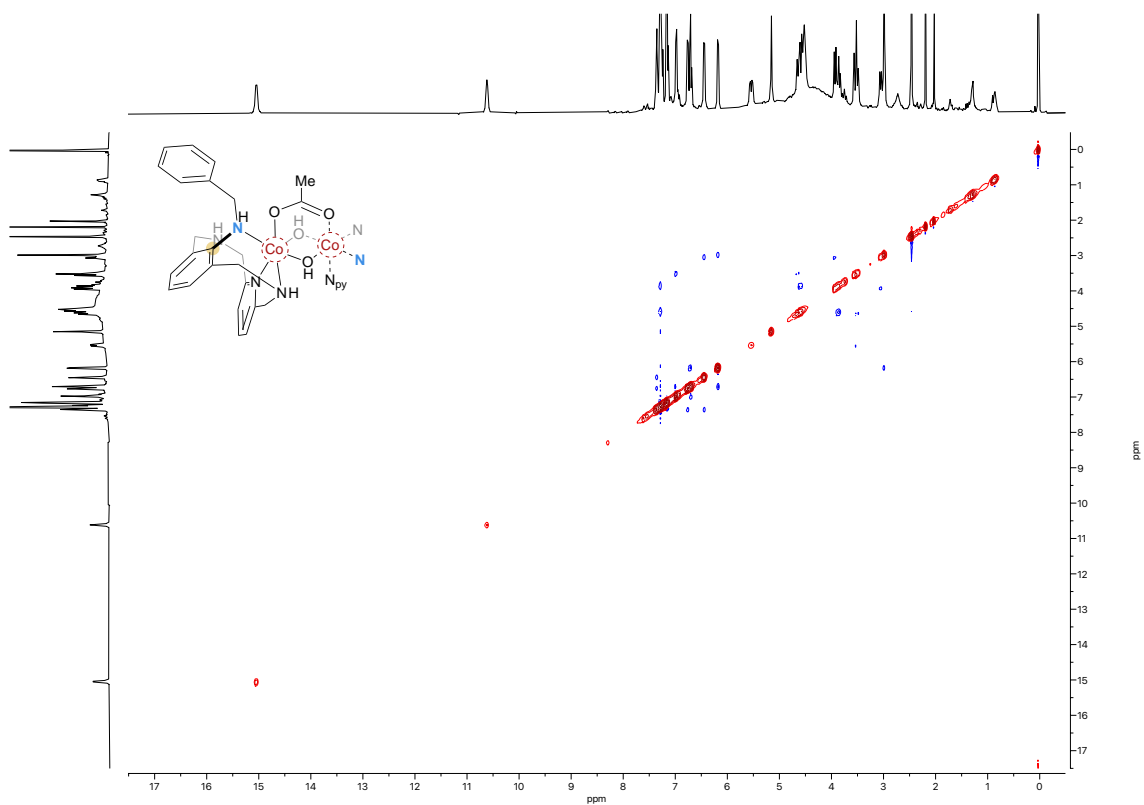
Figure S45. 500 MHz, ^{1}H-^{1}H NOESY NMR spectrum of **5a-OAc** in CDCl$_3$, 298 K.
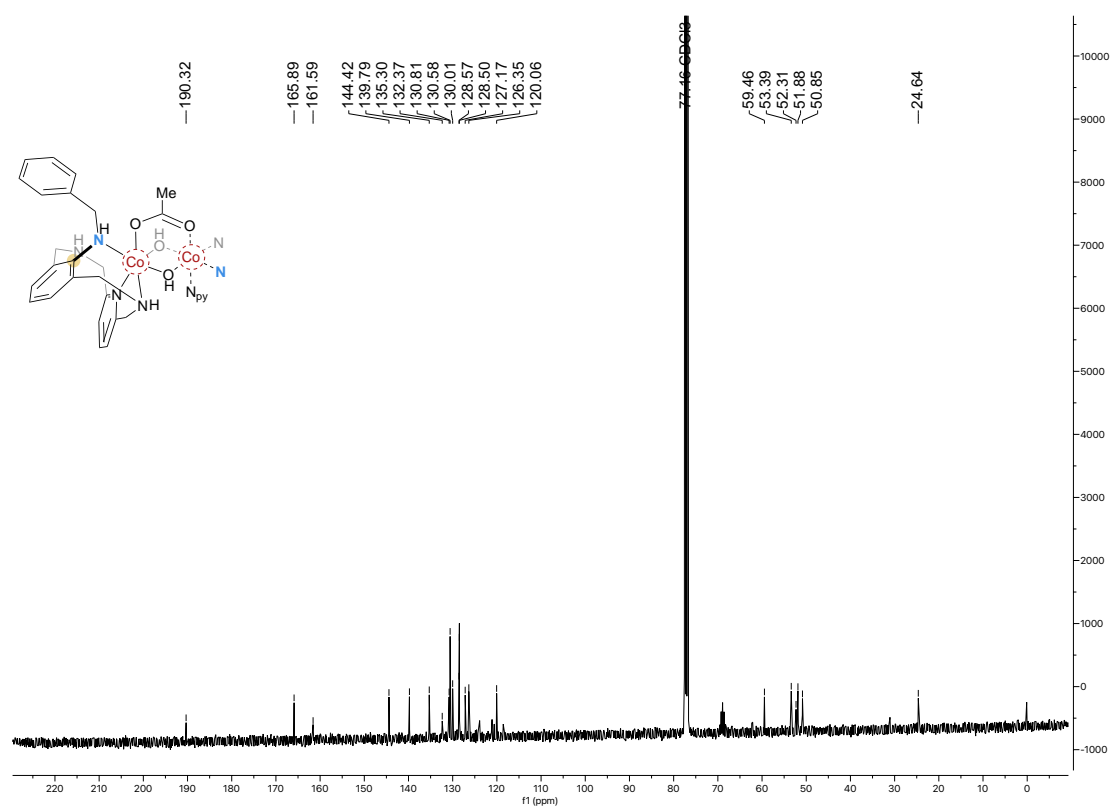
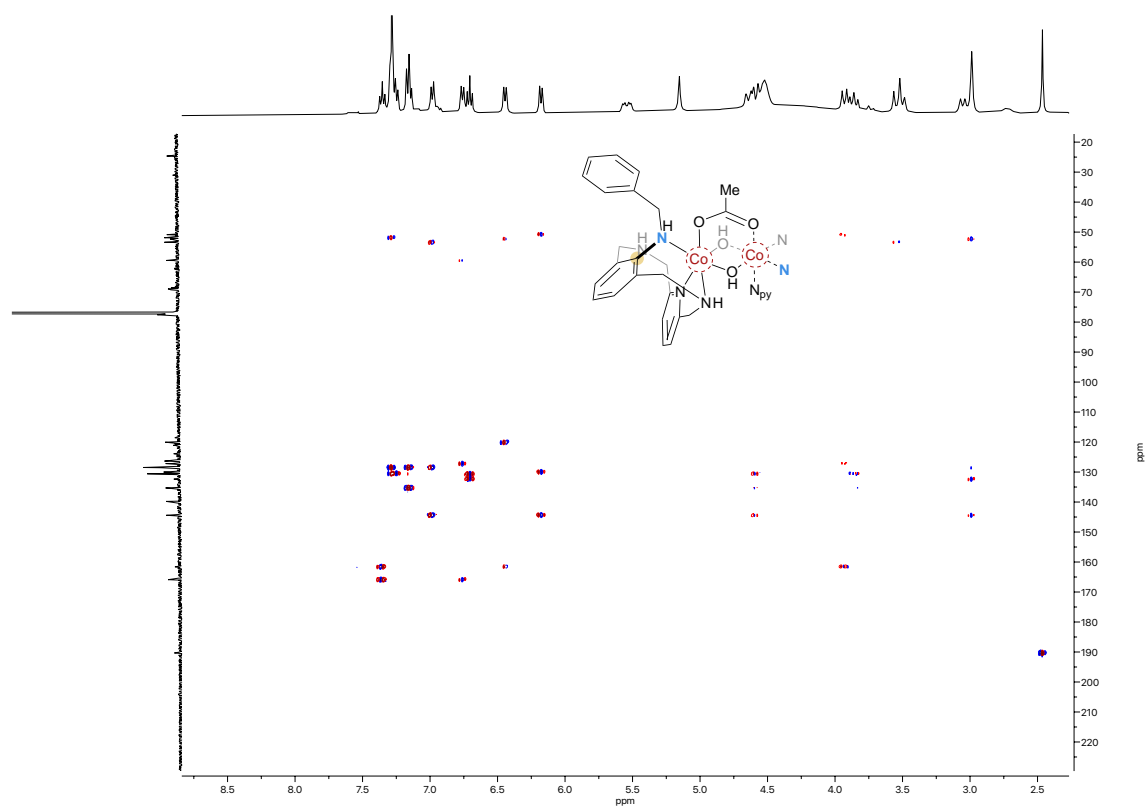**Figure S46.** 125 MHz, $^{13}C\{^1H\}$ NMR spectrum of **5a-OAc** in CDCl$_3$, 298 K.

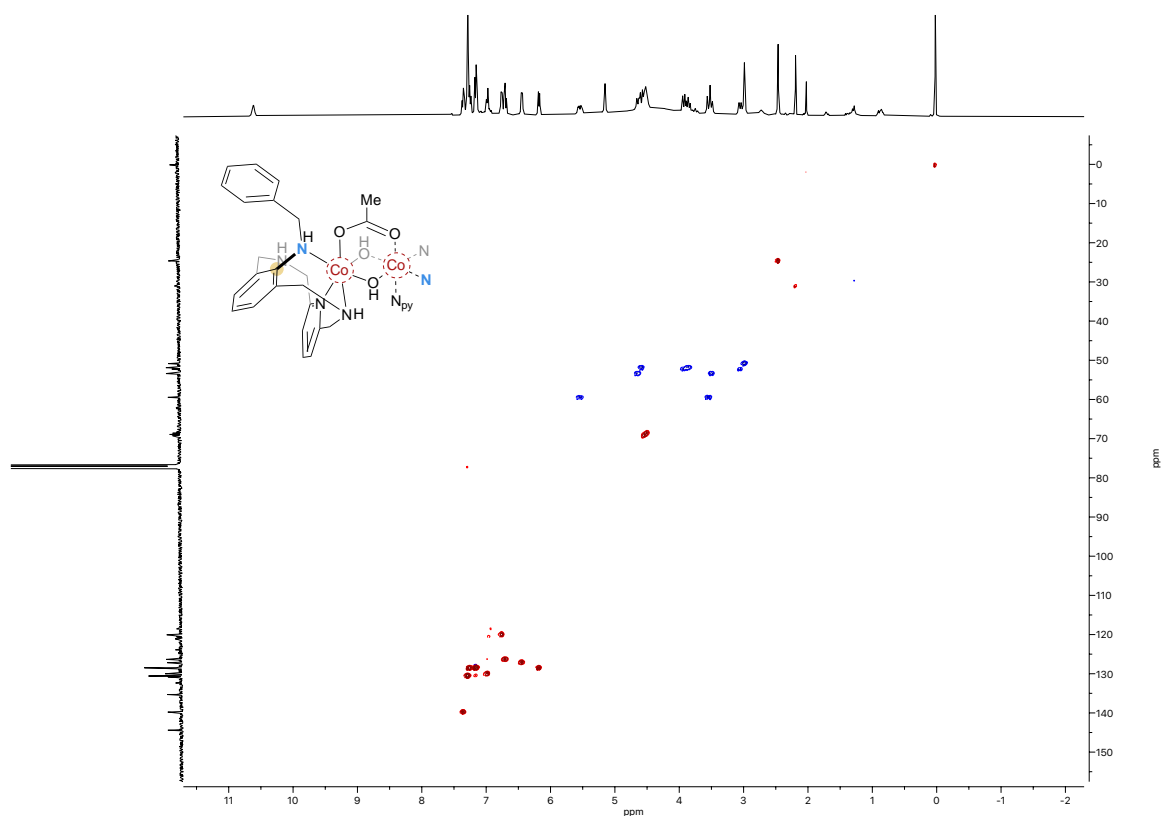**Figure S47.** 500 MHz, ^1H-^{13}C HMBC NMR spectrum of **5a-OAc** in CDCl$_3$, 298 K.

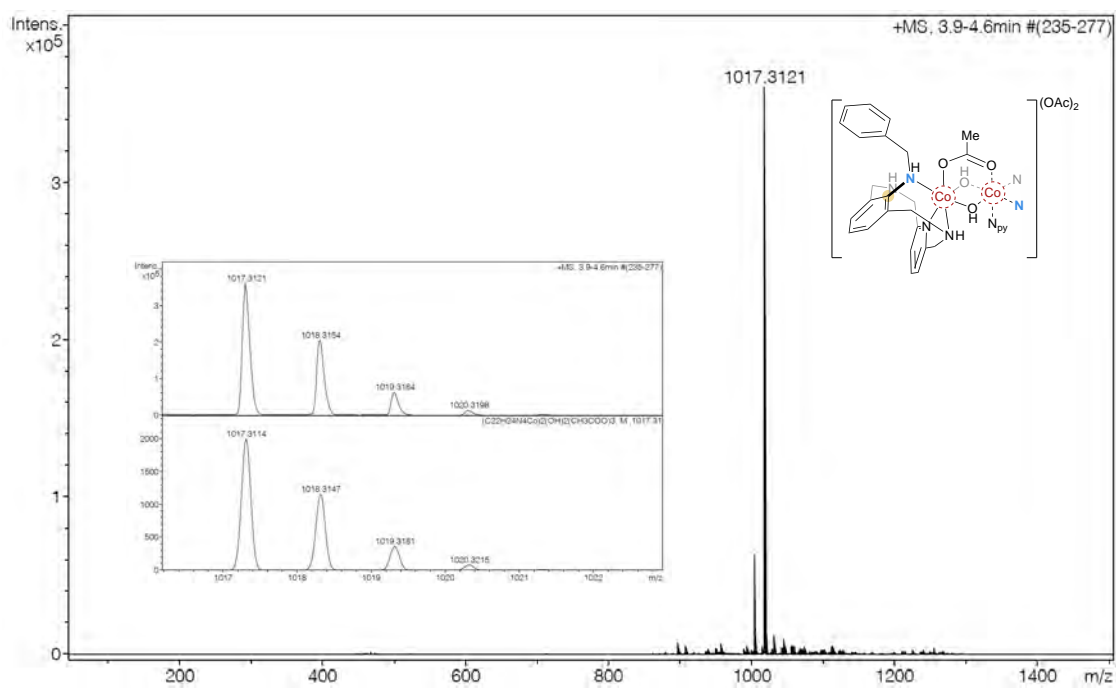**Figure S48.** 500 MHz, ^{1}H-^{13}C HSQC NMR spectrum of **5a-OAc** in CDCl$_3$, 298 K.

Figure S49. HRMS spectrum of **5a-OAc** showing a peak at *m/z* = 1017.3121. Inset: up, experimental spectrum; down, simulated spectrum.
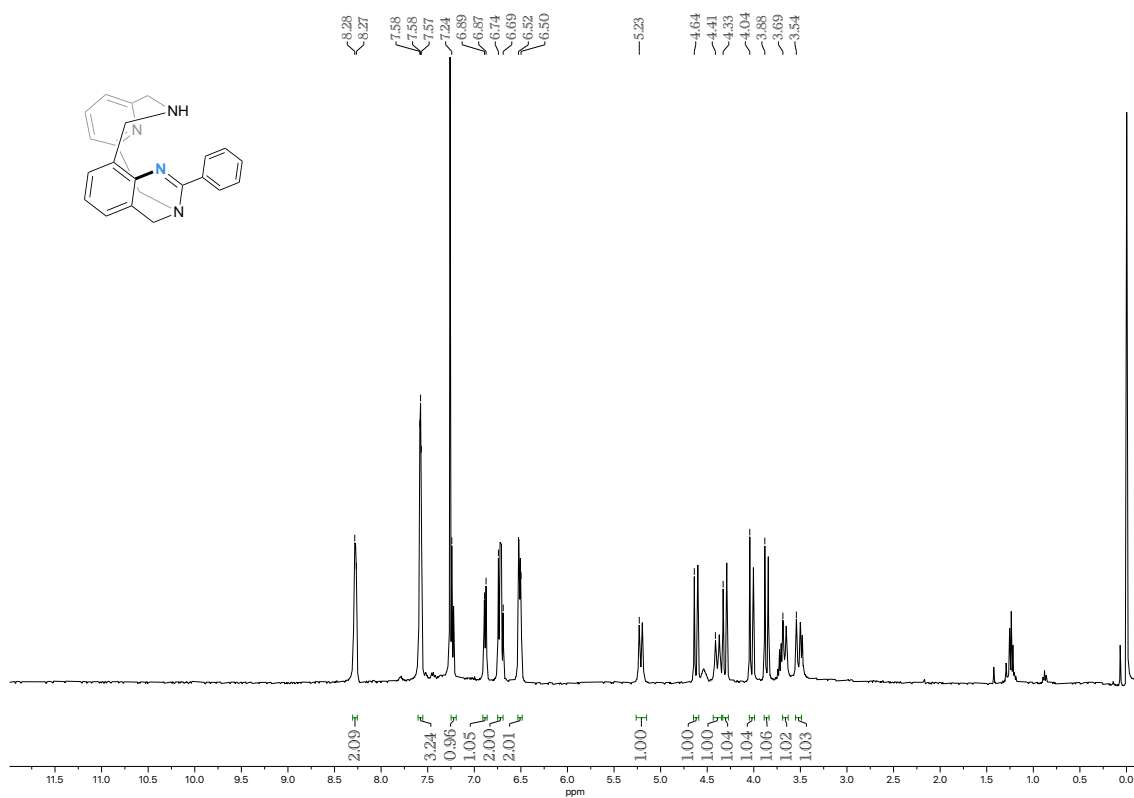
Figure S50. 400 MHz, ^{1}H NMR spectrum of **P4** in CDCl$_3$, 298 K.
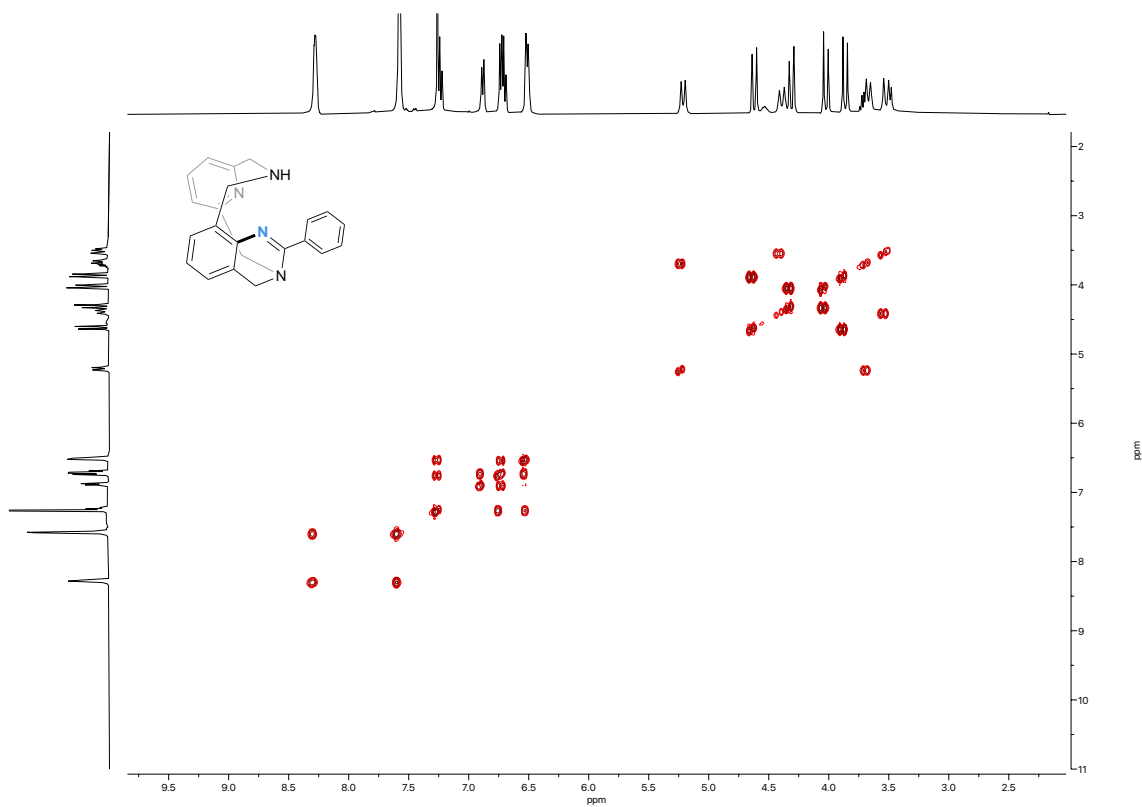
Figure S51. 400 MHz, ^{1}H-^{1}H COSY NMR spectrum of **P4** in CDCl$_3$, 298 K.
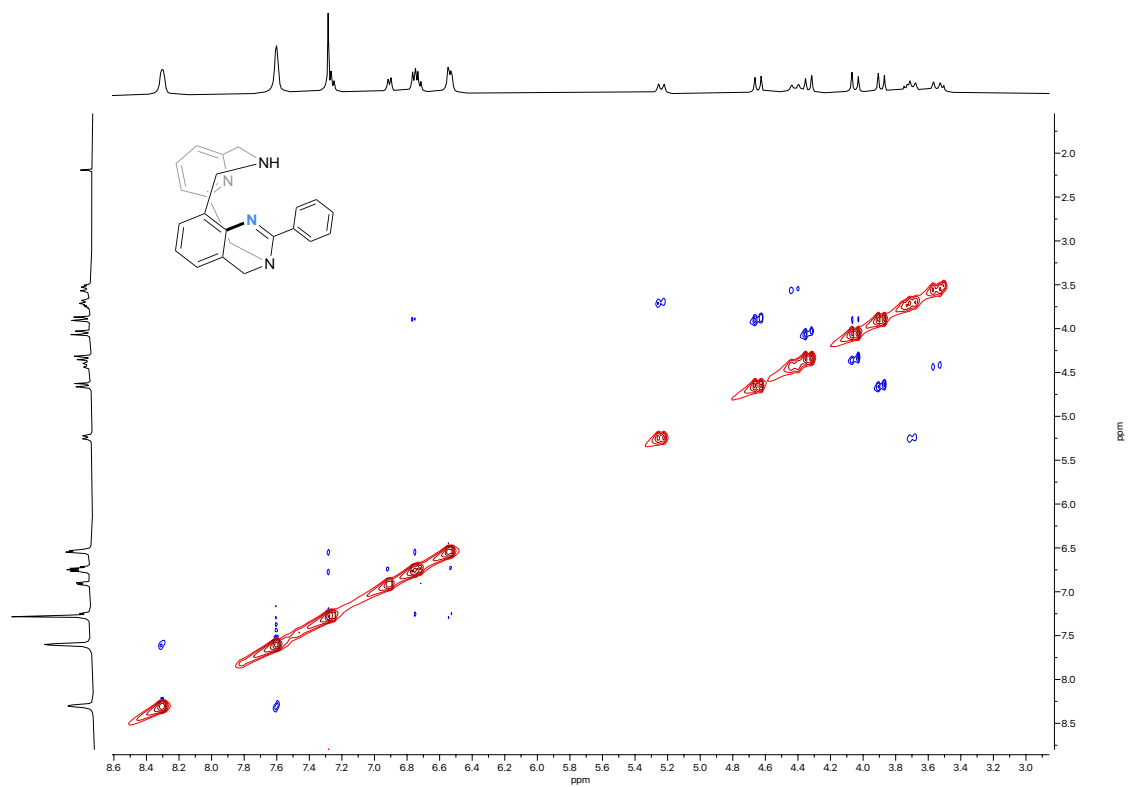
Figure S52. 400 MHz, ^{1}H-^{1}H NOESY NMR spectrum of **P4** in CDCl$_3$, 298 K.
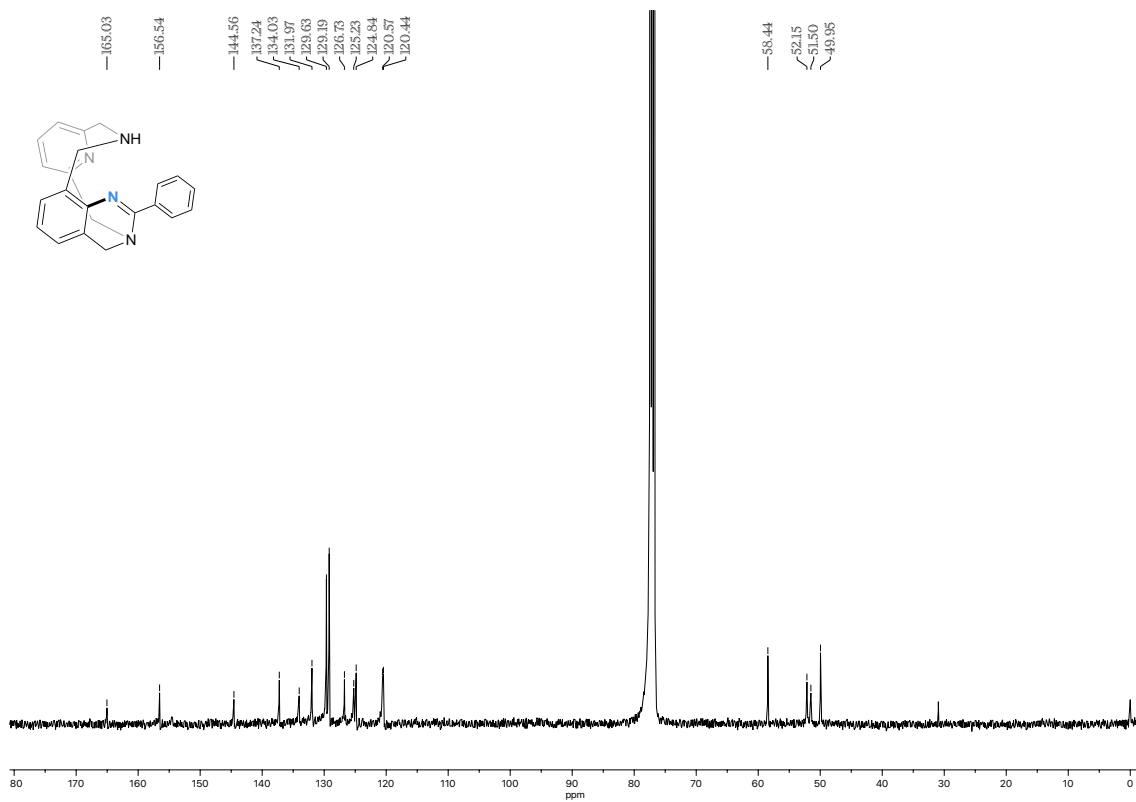
Figure S53. 100 MHz, ^{13}C {^{1}H} NMR spectrum of **P4** in CDCl$_3$, 298 K.
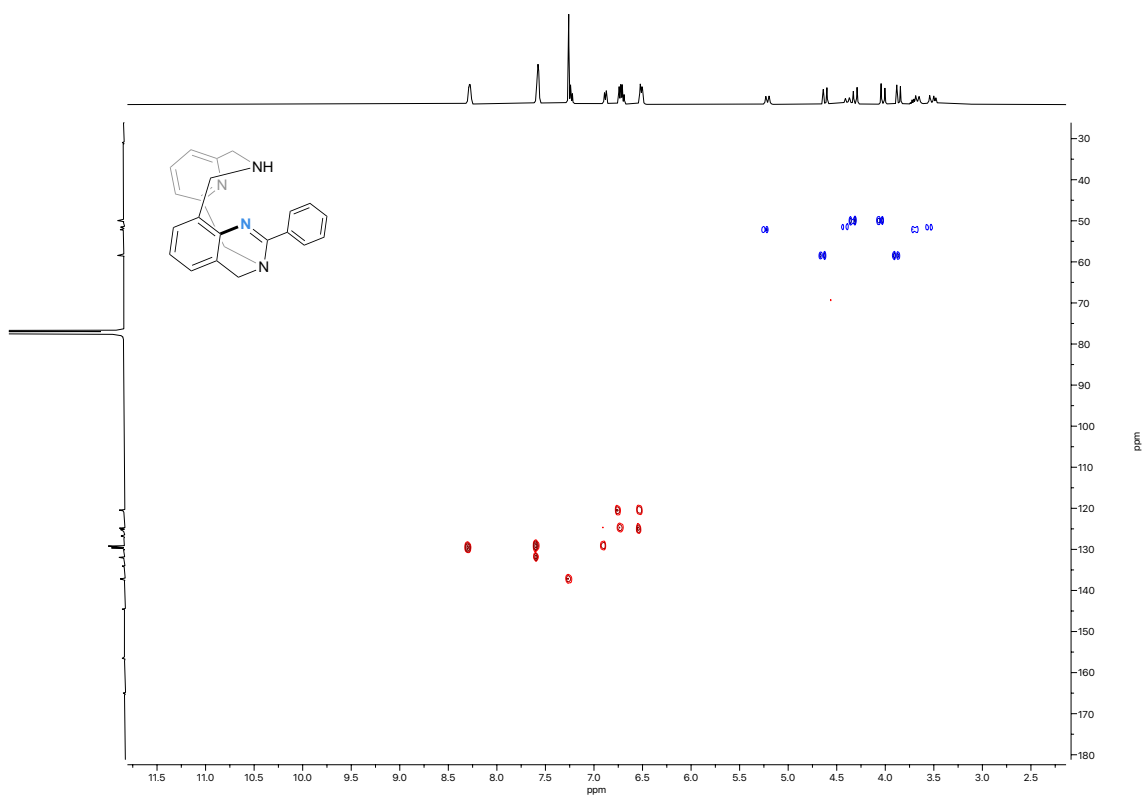
Figure S54. 400 MHz, ^{1}H-^{13}C HSQC NMR spectrum of **P4** in CDCl$_3$, 298 K.
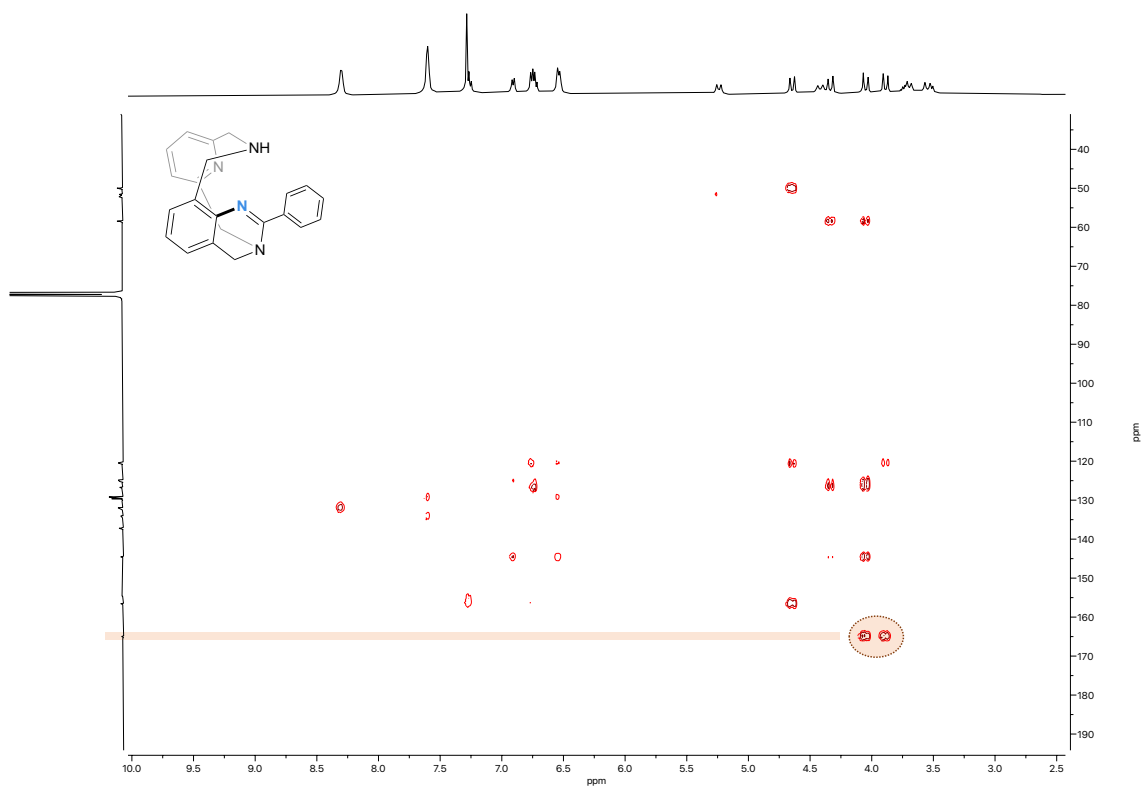

Figure S55. 400 MHz, ^{1}H-^{13}C HMBC NMR spectrum of **P4** in CDCl$_3$, 298 K.
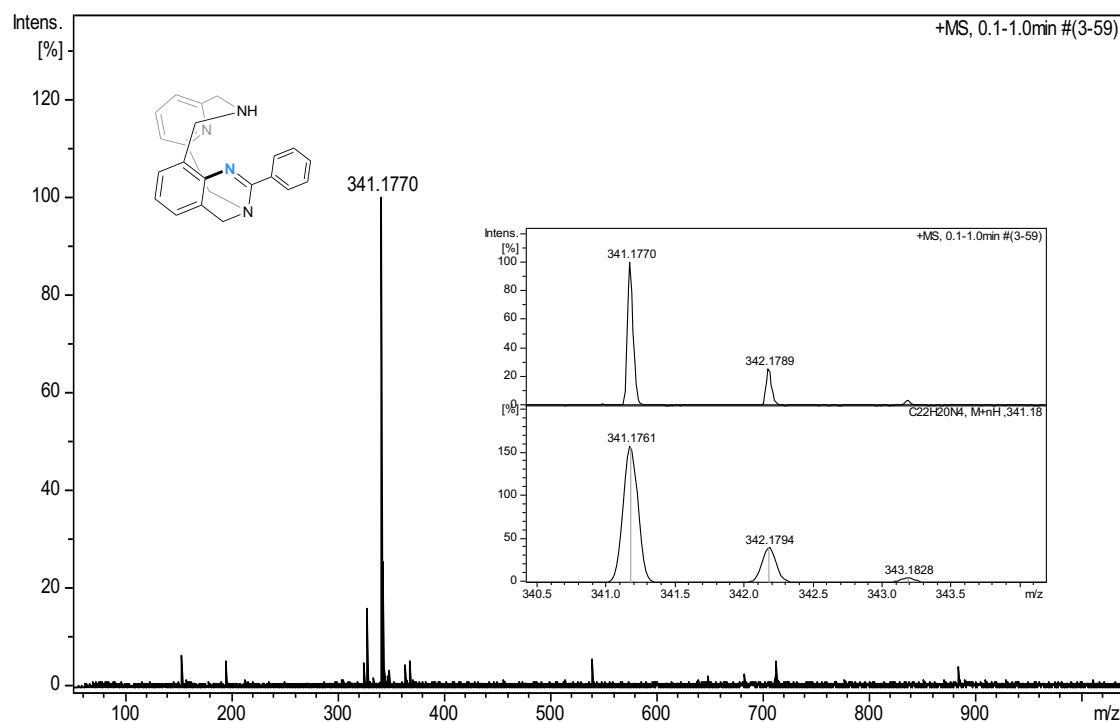
Figure S56. HRMS spectrum of **P4** showing a peak at *m/z* = 341.1770. Inset: up, experimental spectrum; down, simulated spectrum.

14. References

[1]   Planas, O.; Whiteoak, C. J.; Martin-Diaconescu, V.; Gamba, I.; Luis, J. M.; Parella, T.; Company, A.; Ribas, X. *J. Am. Chem. Soc.* **2016**, *138*, 14388-14397.

[2]   Planas, O.; Roldán-Gómez, S.; Martin-Diaconescu, V.; Parella, T.; Luis, J. M.; Company, A.; Ribas, X. *J. Am. Chem. Soc.* **2017,** *139*, 14649-14655.

[3]   Planas, O.; Roldán-Gómez, S.; Martin-Diaconescu, V.; Luis, J. M.; Company, A.; Ribas, X. *Chem. Sci.* **2018,** *9*, 5736-5746.

[4]   Ravel, B.; Newville, M. *J. Synchrotron Rad.* **2005,** *12*, 537-541.

[5]   Rehr, J. J.; Albers, R. C. *Rev. Modern Phys.* **2000,** *72*, 621-654.

[6]   Newville, M. *J. Synchrotron Rad.* **2001,** *8*, 96-100.

[7]   Frisch, M. J. T., G. W.; Schlegel, H. B.; Scuseria, G. E.; Robb, M. A.; Cheeseman, J. R.; Scalmani, G.; Barone, V.; Petersson, G. A.; Nakatsuji, H.; Li, X.; Caricato, M.; Marenich, A. V.; Bloino, J.; Janesko, B. G.; Gomperts, R.; Mennucci, B.; Hratchian, H. P.; Ortiz, J. V.; Izmaylov, A. F.; Sonnenberg, J. L.; Williams-Young, D.; Ding, F.; Lipparini, F.; Egidi, F.; Goings, J.; Peng, B.; Petrone, A.; Henderson, T.; Ranasinghe, D.; Zakrzewski, V. G.; Gao, J.; Rega, N.; Zheng, G.; Liang, W.; Hada, M.; Ehara, M.; Toyota, K.; Fukuda, R.; Hasegawa, J.; Ishida, M.; Nakajima, T.; Honda, Y.; Kitao, O.; Nakai, H.; Vreven, T.; Throssell, K.; Montgomery, J. A., Jr.; Peralta, J. E.; Ogliaro, F.; Bearpark, M. J.; Heyd, J. J.; Brothers, E. N.; Kudin, K. N.; Staroverov, V. N.; Keith, T. A.; Kobayashi, R.; Normand, J.; Raghavachari, K.; Rendell, A. P.; Burant, J. C.; Iyengar, S. S.; Tomasi, J.; Cossi, M.; Millam, J. M.; Klene, M.; Adamo, C.; Cammi, R.; Ochterski, J. W.; Martin, R. L.; Morokuma, K.; Farkas, O.; Foresman, J. B.; Fox, D. J. *Gaussian 16, Revision A.03*, Gaussian Inc.: Wallingford CT, 2016.

[8]   Marenich, A. V.; Cramer, C. J.; Truhlar, D. G. *J. Phys. Chem. B* **2009,** *113*, 6378-6396.

[9]   Grimme, S.; Ehrlich, S.; Goerigk, L. *J. Comput. Chem.* **2011,** *32*, 1456-1465.

[10] Grimme, S.; Antony, J.; Ehrlich, S.; Krieg, H. *J. Chem. Phys.* **2010,** *132*, 154104.
[11] Becke, A. *D. Phys. Rev. A* **1988,** *38*, 3098-3100.
[12] Perdew, J. P. *Phys. Rev. B* **1986,** *33*, 8822-8824.
[13] Weigend, F.; Ahlrichs, R. *Phys. Chem. Chem. Phys.* **2005,** *7*, 3297-3305.
[14] Schäfer, A.; Huber, C.; Ahlrichs, R. *J. Chem. Phys.* **1994,** *100*, 5829-5835.
[15] https://comp.chem.umn.edu/solvation/mnsddb.pdf.
[16] Hawkins, G. D.; Cramer, C. J.; Truhlar, D. G. *J. Phys. Chem. B* **1998,** *102*, 3257-3271.
[17] https://www.chemicalbook.com/ChemicalProductProperty_EN_CB3251829.htm.
[18] Abraham, M. H. *J. Phys. Org. Chem.* **1993,** *6*, 660-684.
[19] Berkessel, A.; Adrio, J. A. *J. Am. Chem. Soc.* **2006,** *128*, 13412-13420.
[20] Mayans, E.; Ballano, G.; Sendros, J.; Font-Bardia, M.; Campos, J. L.; Puiggalí, J.; Cativiela, C.; Alemán, C. *ChemPhysChem* **2017,** *18*, 1888-1896.
[21] Goerigk, L.; Hansen, A.; Bauer, C.; Ehrlich, S.; Najibi, A.; Grimme, S. *Phys. Chem. Chem. Phys.* **2017,** *19*, 32184-32215.
[22] Perdew, J. P.; Ruzsinszky, A.; Csonka, G. I.; Constantin, L. A.; Sun, J. *Phys. Rev. Lett.* **2009,** *103*, 026403.
[23] Luchini, G.; Alegre-Requena, J.; Funes-Ardoiz, I.; Paton, R. *F1000Research* **2020,** *9*.
[24] Grimme, S. *Chem. Eur. J.* **2012,** *18*, 9955-9964.
[25] Ramos-Cordoba, E.; Postils, V.; Salvador, P. *J. Chem. Theor. Comput.* **2015,** *11*, 1501-1508.
[26] Lee, J. H.; Gupta, S.; Jeong, W.; Rhee, Y. H.; Park, J. *Angew. Chem. Int. Ed.* **2012,** *51*, 10851-10855.
[27] Albertin, G.; Antoniutti, S.; Baldan, D.; Castro, J.; García-Fontán, S. *Inorg. Chem.* **2008,** *47*, 742-748.
[28] Kim, H.; Chang, S. *Angew. Chem. Int. Ed.* **2017,** *56*, 3344-3348.
[29] Spek, A. *Acta Cryst. C* **2015,** *71*, 9-18.
[30] Kuijpers, P. F.; van der Vlugt, J. I.; Schneider, S.; de Bruin, B. *Chem. Eur. J.* **2017,** *23*, 13819-13829.

Supporting Information for Chapter V

Chemodivergent Nickel(0)-Catalyzed Arene C–F Activation with alkynes: Unprecedented C–F/ C–H Double Insertion

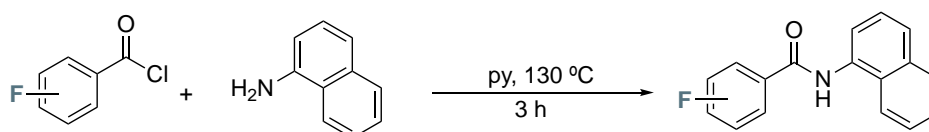Lorena Capdevila, Tjark H. Meyer, Steven Roldán-Gómez, Josep M. Luis, Lutz Ackermann,* and Xavi Ribas*

Table of contents

1. General considerations

All reagents and solvents were purchased from Sigma Aldrich, Fisher Scientific or Fluorochem and used without further purification. Internal alkynes **a-g**[1-2], *N*-(2-Fluorophenyl)pyrimidin-2-amine **1d**,[3] and N-(quinolin-8-yl)benzamide **1f** [4] were synthesized according to previously described methods. [1]H, ^{13}C{^{1}H} and ^{19}F{H}-NMR spectra were recorded on Bruker 400 AVANCE spectrometer in the corresponding deuterated solvent (CDCl$_3$ and d_6-DMSO) and calibrated relative to the residual protons of the solvent. Quantification of reaction yields through integration of peaks was performed using an internal reference (1,3,5-trimethoxybenzene). High resolution mass spectra (HRMS) were recorded on a Bruker MicroTOF-Q IITM instrument using ESI source at Serveis Tècnics de Recerca, University of Girona. IR Spectra (FTIR) were recorded on a FT-IR Alpha spectrometer from Bruker with a PLATINUM-ATR attachment using OPUS software to process the data. All reactions were carried out in a N$_2$ drybox with O$_2$ and H$_2$O concentrations <1 ppm.

## 2. Synthesis and characterization data for substrates

The substrates have been synthesized according to the procedure described in the literature from 8-aminoquinoline and the corresponding acyl chloride.[4] To a solution of 8-aminquinoline (0.81 g, 5.66 mmol) in pyridine (16 mL), acyl chloride (5.66 mmol) was added. The reaction was heated to 130 ºC and stirred for 3 hours. After the reaction time, the mixture was left to cool to 70 ºC and poured over 40 mL of ice-cold water. The resulting mixture was extracted with dichloromethane (3 x 20 mL) and the combined organic layers were dried over MgSO$_4$. The solvent was removed in vacuo. Purification by column chromatography afforded a crystalline solid.

2-Fluoro-*N*-(quinoline-8-yl)benzamide (1a):
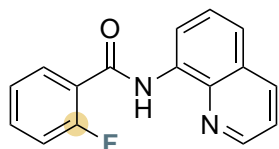
Prepared in accordance to the general procedure described above: 8-aminquinoline (0.81 g, 5.66 mmol), 2-fluorobenzoyl chloride (0.89 g, 5.66 mmol). Purification by column chromatography in dichloromethane afforded **1a** as a crystalline white solid. (0.92 g, **61%**). **^{1}H-NMR** (400 MHz, CDCl$_3$, 298 K) δ (ppm): 11.17 (bs, 1H), 8 .98 (dd, *J* = 7.1 Hz, 2.1 Hz, 1H), 8.88 (dd, *J* = 4.3 Hz, 1.7 Hz, 1H), 8.26-8.17 (m, 2H), 7.63-7.51 (m, 3H), 7.48 (dd, *J* = 8.2 Hz, 4.2 Hz, 1H), 7.37-7.22 (m, 2H). **^{13}C-NMR** (100 MHz, CDCl$_3$, 298K) δ (ppm): 161.8 (d, *J*$_{C-F}$ = 3.6 Hz),160.7 (d, *J*$_{C-F}$ = 249.2 Hz), 148.6, 138.9, 136.4, 135.0, 133.7 (d, *J*$_{C-F}$ = 8.9 Hz), 132.2 (d, *J*$_{C-F}$ = 2.5 Hz), 128.2, 127.6, 125.0 (d, *J*$_{C-F}$ = 4.0 Hz),122.3 (d, *J*$_{C-F}$ = 11.3 Hz), 122.2, 121.8, 117.4, 116.5 (d, *J*$_{C-F}$ = 24.3 Hz). **^{19}F-NMR** (400 MHz, CDCl$_3$, 298K) δ (ppm): -112.14 ppm. **HRMS** (ESI, m/z): Calculated for C$_{16}$H$_{11}$FN$_2$O [M+Na]$^+$ 289.0748, Found 289.0742. **R$_f$**: 0.58 (EtOAC:hexane (3:7)).
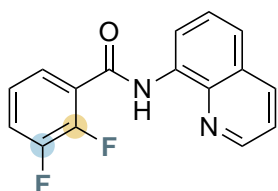
2,6-Difluoro-*N*-(quinolin-8-yl)benzamide (1b):
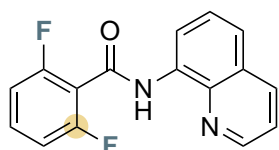
Prepared in accordance to the general procedure described above: 8-aminoquinoline (0.81 g, 5.66 mmol), 2,6-difluorobenzoyl chloride (1.0 g, 5.66 mmol). Purification by column chromatography in dichloromethane afforded **1b** as a crystalline white solid. (0.90 g, **56%**) **^{1}H-NMR** (400 MHz, CDCl$_3$, 298K) δ

(ppm): 10.34 (s, 1H), 8.94 (dd, J = 6.7 Hz, 2.7 Hz, 1H), 8.78 (dd, J = 4.4 Hz, 1.9 Hz, 1H), 8.14 (dd, J = 8.3 Hz, 2.4 Hz, 1H), 7.60-7.54 (m, 2H), 7.43-7.40 (m, 2H), 7.02-7.00 (m, 2H). ^{13}**C-NMR** (100 MHz, CDCl$_3$, 298K) δ (ppm): 160.3 (d, J_{C-F} = 253.5 Hz),160.2 (d, J_{C-F} = 253.5 Hz), 158.6, 148.5, 138.5, 136.4, 134.2, 132.1 (t, J_{C-F} = 10.6 Hz), 128.0, 127.4, 122.5, 121.8, 117.1,114.9 (t, J_{C-F} = 19.9 Hz), 112.4-112.2 (m, 2C). ^{19}**F-NMR** (400 MHz, CDCl$_3$, 298K) δ (ppm):-111.69 ppm. **HRMS** (ESI, m/z): Calculated for C$_{16}$H$_{10}$F$_2$N$_2$O [M+Na$^+$] 307.0653, Found 307.0661. *Rf*: 0.60 (CH$_2$Cl$_2$).

2,3-Difluoro-*N*-(quinolin-8-yl)benzamide (1c):

Prepared in accordance to the general procedure described above: 8-aminquinoline (0.81 g, 5.66 mmol), 2,3-difluorobenzoyl chloride (0.7 mL , 5.66 mmol) was added. Purification by column chromatography in dichloromethane afforded **1c** as a crystalline white solid. (0.91 g, **56%**). ^{1}**H-NMR** (400 MHz, CDCl$_3$, 298K) δ (ppm): 11.07 (bs, 1H), 8.93 (dd, J = 6.2 Hz, 2.6 Hz, 1H), 8.86 (dd, J = 4.4 Hz, 2.1 Hz, 1H), 8.17 (dd, J = 8.1 Hz, 1.6 Hz, 1H), 7.95 (m, 1H), 7.60–7.54 (m, 2H), 7.47 (dd, J = 8.3 Hz, 4.4 Hz, 1H), 7.40–7.33 (m, 1H), 7.28-7.22 (m, 1H). ^{13}**C-NMR** (100 MHz, CDCl$_3$, 298K) δ (ppm): 160.7 (t, J_{C-F} = 3 Hz), 150.7 (dd, J_{C-F} = 248.9 Hz, 14.1 Hz), 148.6, 148.5 (dd, J_{C-F} = 251.6 Hz, 14.1 Hz), 138.8, 136.4, 134.7, 128.1, 127.5, 126.5 (d, J_{C-F} = 3.3 Hz), 124.7 (dd, J_{C-F} = 6.7 Hz, 4.6 Hz), 124.5 (d, J_{C-F} = 8.8 Hz), 122.5, 121.9, 120.5 (d, J_{C-F} = 14.7 Hz), 117.4. ^{19}**F-NMR** (400 MHz, CDCl$_3$, 298K) δ (ppm): -137.4 (d, J = 21.2 Hz, 1F), -138.3 (d, J = 21.2 Hz, 1F). **HRMS** (ESI, m/z): Calculated for C$_{16}$H$_{10}$F$_2$N$_2$O [M+Na$^+$] 307.0653, Found 307.0665.

2-Fluoro-*N*-(5-nitroquinolin-8-yl)benzamide (1e):
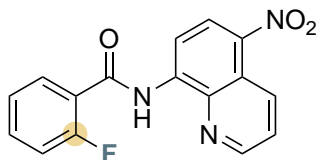
The substrate **1e** has been synthesized according to the procedure described in the literature.[4] **1a** (133.0 mg, 0.5 mmol), Co(NO$_3$)$_2$·6H$_2$O (29.1 mg, 20 mol %), ^{t}BuONO (267 μL, 90%, 2 mmol) were mixed in acetic acid (3.5 mL) at 25 °C for four hours. The crude mixture was extracted with ethyl acetate (3 x 10 mL) and the organic layers were dried over MgSO$_4$ and the solvent was removed under reduced pressure. Purification by column chromatography in dichloromethane afforded **1e** as a crystalline yellow solid. (51.6 mg, **33%**). ^{1}**H-NMR** (400 MHz, CDCl$_3$, 298K) δ (ppm): 11.55 (bs, 1H), 9.30 (dd, J = 8.9 Hz, 1.4 Hz, 1H), 9.06 (d, J = 8.8 Hz, 1H), 8.99 (dd, J = 4.2 Hz, 1.3 Hz, 1H), 8.61 (d, J = 8.8 Hz, 1H), 8.24 (td, J = 7.9 Hz, 1.8 Hz, 1H), 7.76 (dd, J = 8.9 Hz, 4.2 Hz, 1H), 7.64-7.58 (m, 1H), 7.38 (t, J = 7.7 Hz, 1H), 7.31-7.28 (m, 1H). ^{13}**C-NMR** (100 MHz, CDCl$_3$, 298K) δ (ppm): 162.3, 160.9 (d, J_{C-F} = 248.6 Hz), 149.4, 141.3, 139.2, 138.1, 134.6 (d, J_{C-F} = 9.3 Hz), 133.4, 132.4 (d, J_{C-F} = 1.5 Hz), 127.9, 125.3 (d, J_{C-F} = 3.2 Hz), 124.8, 121.9, 121.4 (d, J_{C-F} = 11.6 Hz), 116.7 (d, J_{C-F} = 24.4 Hz), 114.6. ^{19}**F-NMR** (400 MHz, CDCl$_3$, 298K) δ (ppm): -111.69 ppm. **HRMS** (ESI, m/z): Calculated for C$_{16}$H$_{10}$N$_3$O$_3$F [M+Na]$^+$ 334.0598, Found 334.0601.

3. Reaction optimization

General procedure for the optimization experiments

1a (26.6 mg, 0.1 mmol), diphenylacetylene, LiOtBu (16.0 mg, 0.2 mmol, 2 equiv.) and catalytic amounts of Ni(cod)$_2$ (2.8 mg, 0.01 mmol, 10 mol %) with 1,4-dioxane (0.5 mL) were added to a glass vial under inert-atmosphere, and the vial was sealed. The reaction mixture was heated at different temperatures at different reaction time. The resulting crude mixture was extracted with dichloromethane (3 x 10 mL) and the organic layers were combined and dried over MgSO$_4$. The solvent was then removed under reduced pressure. The crude mixture was analysed by ^{1}H-NMR spectroscopy (CDCl$_3$) using 1,3,5-trimethoxybenzene as an internal standard.

Table S1. Optimization of Reaction Conditions
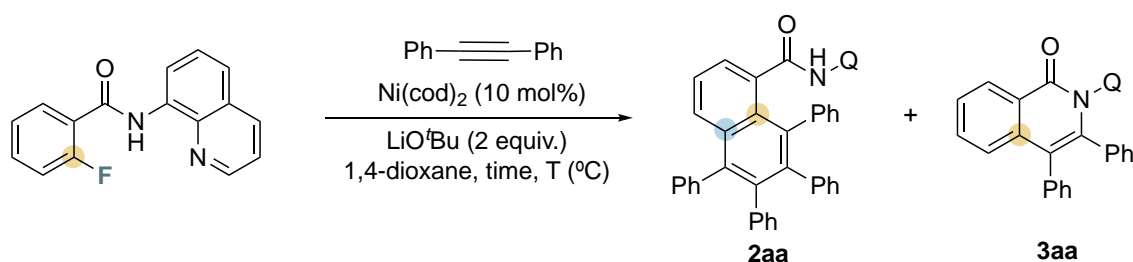
Entry	Ni source	Additive (10 mol%)	Alkyne (equiv.)	Base	Time	T (ºC)	Yield (%) of 2aa[a]	Yield (%) of 3aa[a]	Conv (%)
1	Ni(cod)$_2$	-	2	LiO^{t}Bu	16 h	140	50%	14%	99%
2	Ni(cod)$_2$	-	5	LiO^{t}Bu	16 h	140	32%	tr	95%
3	-	-	2	LiO^{t}Bu	16 h	140	0%	0%	19%
4	Ni(cod)$_2$	-	2	LiO^{t}Bu	5 h	140	41%	20%	99%
5	**Ni(cod)$_2$**	**-**	**2**	**LiO^{t}Bu**	**2 h**	**140**	**63%**	**17%**	**99%**
6	Ni(cod)$_2$	-	2	LiO^{t}Bu	1 h	140	62%	16%	99%
7	Ni(cod)$_2$	-	2	LiO^{t}Bu	30 min	140	11%	4%	29%
8	Ni(cod)$_2$	-	2	LiO^{t}Bu	2 h	130	36%	11%	95%
9	Ni(cod)$_2$	PCy$_3$	2	LiO^{t}Bu	2 h	140	43%	31%	95%
10[b]	Ni(cod)$_2$	-	2	KO^{t}Bu	2 h	140	-	-	78%
11	Ni(cod)$_2$	-	2	Li$_2$CO$_3$	2 h	140	< 10%	-	8%
12	Ni(cod)$_2$	-	2	Cs$_2$CO$_3$	2 h	140	< 10%	-	27%

[a] Yield calculated from ^{1}H-NMR of crude reaction mixture using 1,3,5-trimethoxybenzene as internal standard. [b] Other unidentified products were detected.

4. Mechanistic insights

4.1. NMR spectroscopic study

General procedure for NMR experiments

1a (26.6 mg, 0.1 mmol), diphenylacetylene (36.0 mg, 0.2 mmol, 2 equiv.), LiOtBu (16.0 mg, 0.2 mmol, 2 equiv.) and catalytic amounts of Ni(cod)$_2$ (2.8 mg, 0.01 mmol, 10 mol %), with 1,4-dioxane (0.5 mL) were added to a glass vial under inert-atmosphere, and the vial was sealed. The reaction mixture was stirred at 140 ºC at different reaction time. The resulting crude reaction mixture was extracted with dichloromethane (3 x 10 mL)

and the organic layers were combined and dried over $MgSO_4$. The solvent was removed under reduced pressure. The crude mixture was analysed by ^{1}H-NMR spectroscopy ($CDCl_3$) using 1,3,5-trimethoxybenzene as an internal standard.
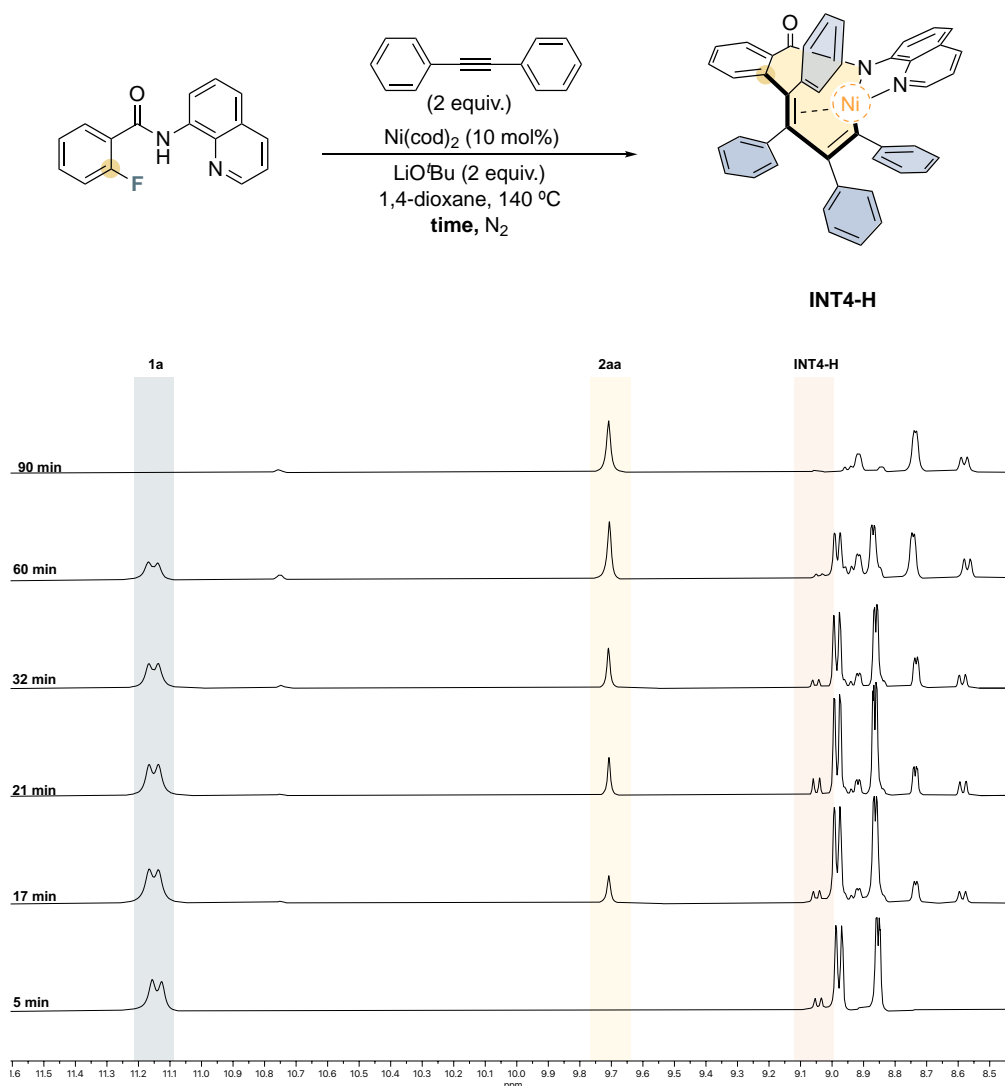

Scheme S1. ^{1}H-NMR spectra of the reaction of the reaction crude during the time. Up to 80% yield of the **INT4-H** with respect to total nickel content at 5 min of the catalytic reaction.

4.2. Isolation and characterization of the intermediates

*General procedure for isolation of **INT4-E-X (X = H, CH₃)** intermediates*

1a (26.6 mg, 0.1 mmol), alkyne (0.2 mmol, 2 equiv.), LiOtBu (16.0 mg, 0.2 mmol, 2 equiv.) and Ni(cod)$_2$ (28.0 mg, 0.1 mmol, 1 equiv.) with 1,4-dioxane (0.5 mL) were added to a glass vial under inert-atmosphere, and the vial was sealed. The reaction mixture was stirred at 140 ºC for 5 min. The resulting crude was extracted with dichloromethane (3 x 10 mL) and the organic layers were combined and dried over $MgSO_4$. The solvent was then removed under reduced pressure. The product was purified using a column chromatography using CH_2Cl_2/EtOAc (starting from 10:0 to 0:10).
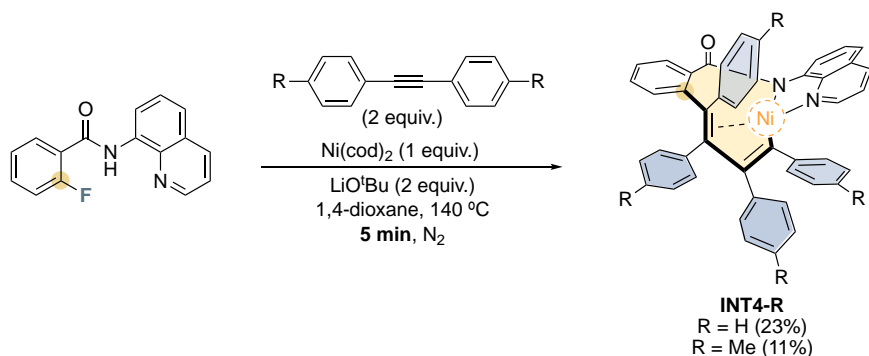
INT4-E-H

Prepared in accordance to the general synthesis described above: **1a** (26.6 mg, 0.1 mmol) was converted to **INT4-H** (15.2 mg, 23%) as orange solid. **^{1}H-NMR** (400 MHz, CDCl$_3$, 298K) δ (ppm): 9.05 (dd, J = 8.0 Hz, 1.0 Hz, 1H), 8.28 (d, J = 7.4 Hz, 2H), 8.12 (dd, J = 8.2 Hz, 1.2 Hz, 1H), 8.03–8.01 (m, 1H), 7.60–7.58 (m, 2H), 7.55 (t, J = 7.9 Hz, 1H), 7.42–7.28 (m, 6H), 7.24–7.18 (m, 2H), 7.11-7.03 (m, 3H), 7.03-6.98 (m, 8H), 6.81 (dd, J = 8.2 Hz, 5.1 Hz, 1H), 6.28-6.26 (m, 2H). **^{13}C-NMR** (100 MHz, CDCl$_3$, 298K) δ (ppm): 169.5, 161.1, 150.5, 148.3, 147.7, 145.5, 140.9, 140.2, 139.4, 138.9, 138.4, 137.9, 135.3, 131.6(2C), 131.1, 130.9, 130.2, 129.5 (2C), 129.1, 128.9 (2C), 128.6 (2C), 127.9, 127.8(3C), 127.6 (2C), 127.5, 127.3 (2C), 126.8, 126.6, 125.8, 125.7 (2C), 120.6, 120.2, 117.6, 109.5, 94.4. **HRMS** (ESI, m/z): Calculated for C$_{44}$H$_{30}$NiN$_2$O [M+Na]$^+$ 683.1604, Found 683.1608. **IR (ATR):** υ (cm^{-1}) = 3056, 2922, 2853, 1661, 1524, 1459, 1377, 1327, 820, 738, 696, 551, 483.
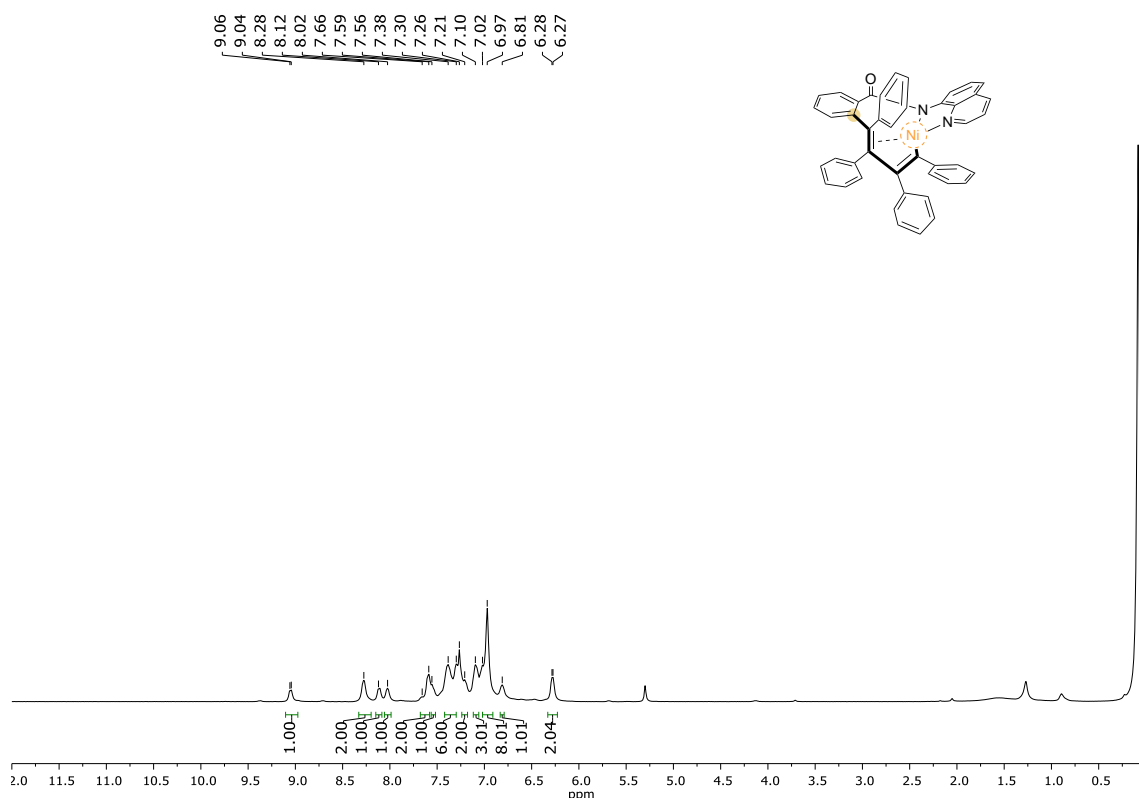

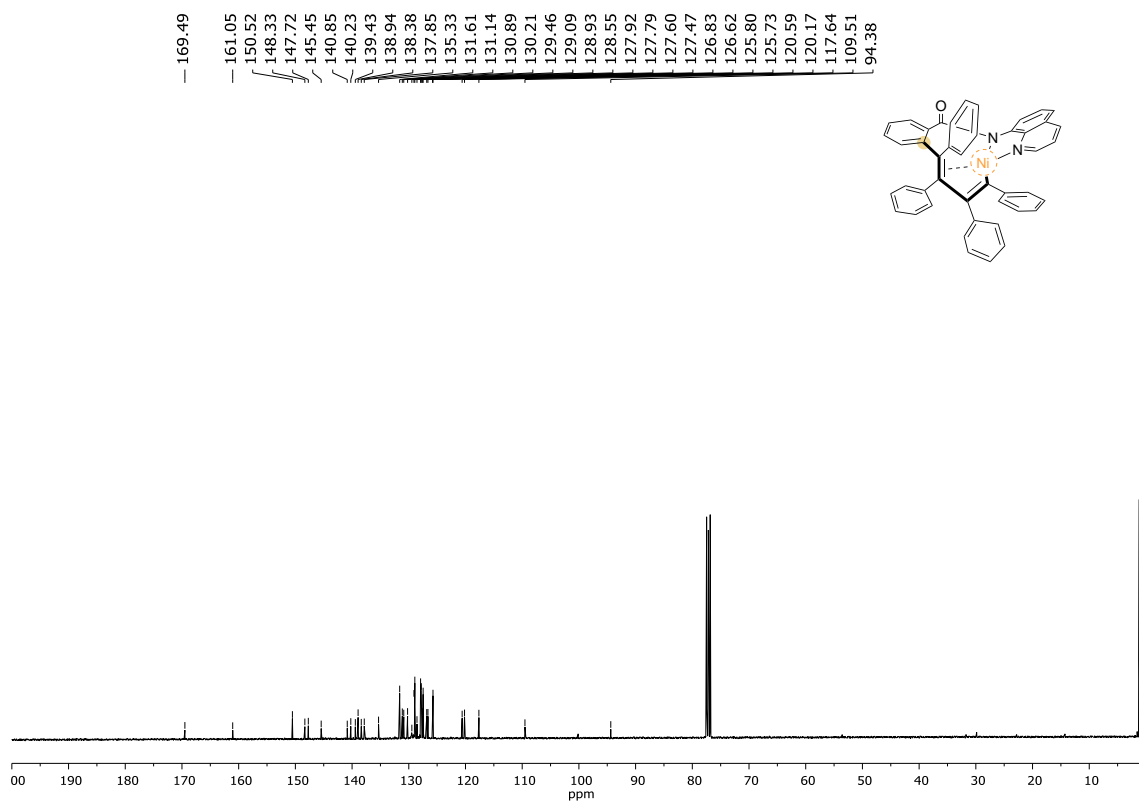**Figure S1**. 400 MHz ^{1}H-NMR spectrum of **INT4-E-H** in CDCl$_3$, 298 K.

169.49
161.05
150.52
148.33
147.72
145.45
140.85
140.23
139.43
138.94
138.38
137.85
135.33
131.61
131.14
130.89
130.21
129.46
129.09
128.93
128.55
127.92
127.79
127.60
127.47
126.83
126.62
125.80
125.73
120.59
120.17
117.64
109.51
94.38

Figure S2. 100 MHz ^{13}C-NMR spectrum of **INT4-E-H** in CDCl$_3$, 298 K.
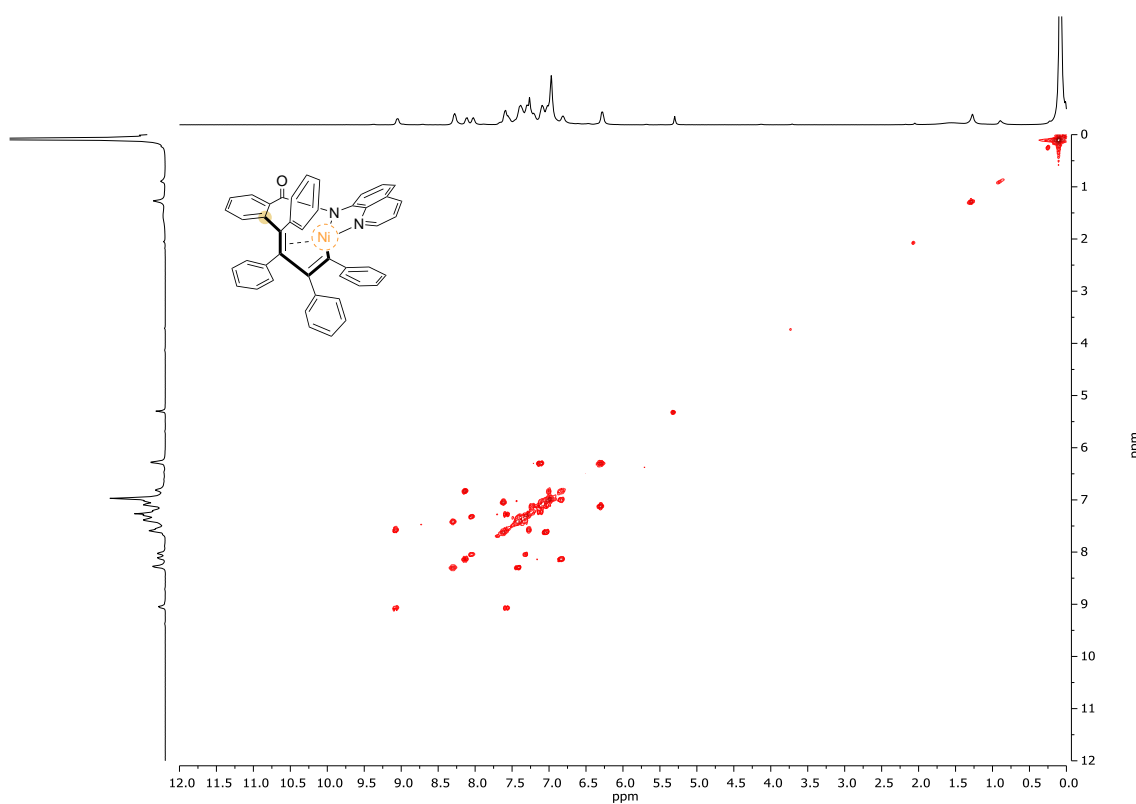

Figure S3. 400 MHz ^{1}H-^{1}H COSY NMR spectrum of **INT4-E-H** in CDCl$_3$, 298 K.
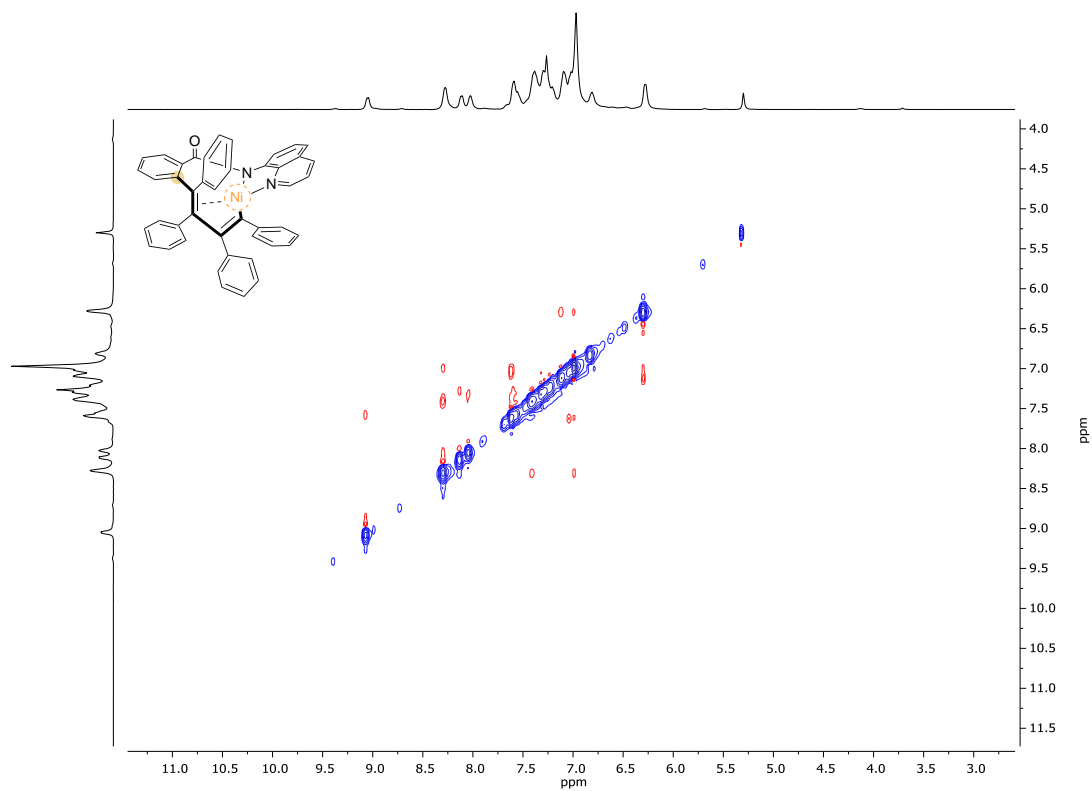
Figure S4. 400 MHz ^{1}H-^{1}H NOESY NMR spectrum of **INT4-E-H** in CDCl$_3$, 298 K.
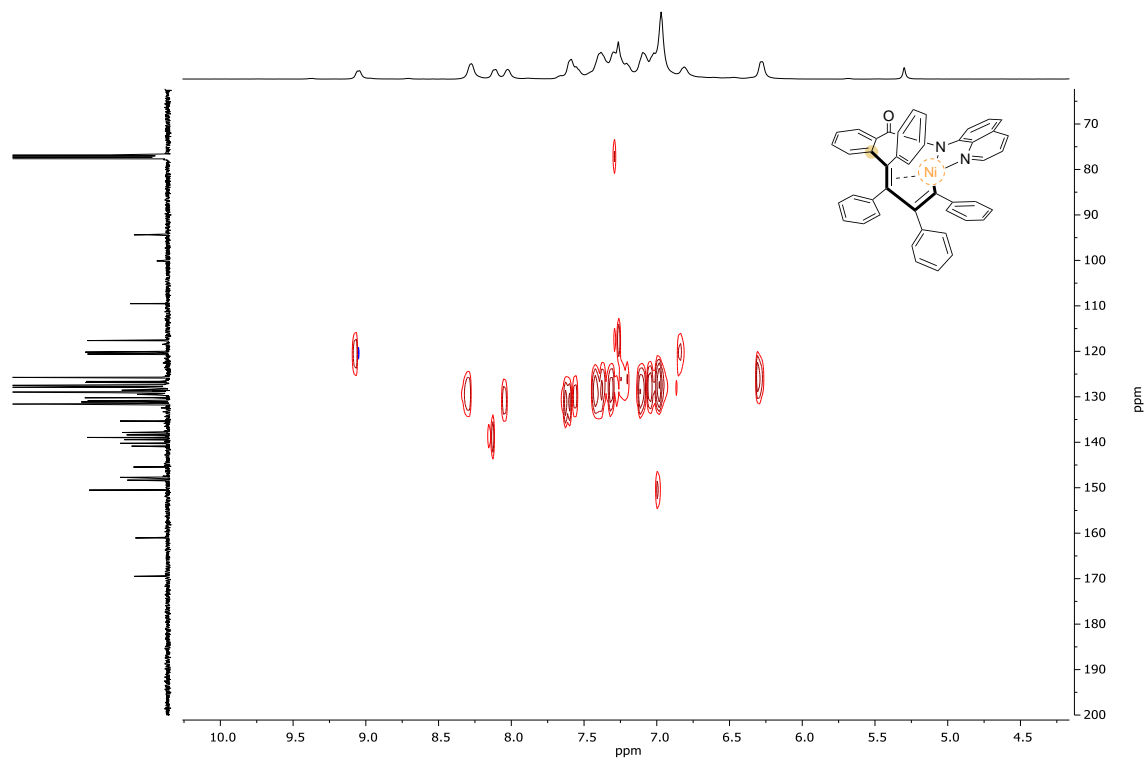

Figure S5. 400 MHz ^{1}H-^{13}C HSQC NMR spectrum of **INT4-E-H** in CDCl$_3$, 298 K.
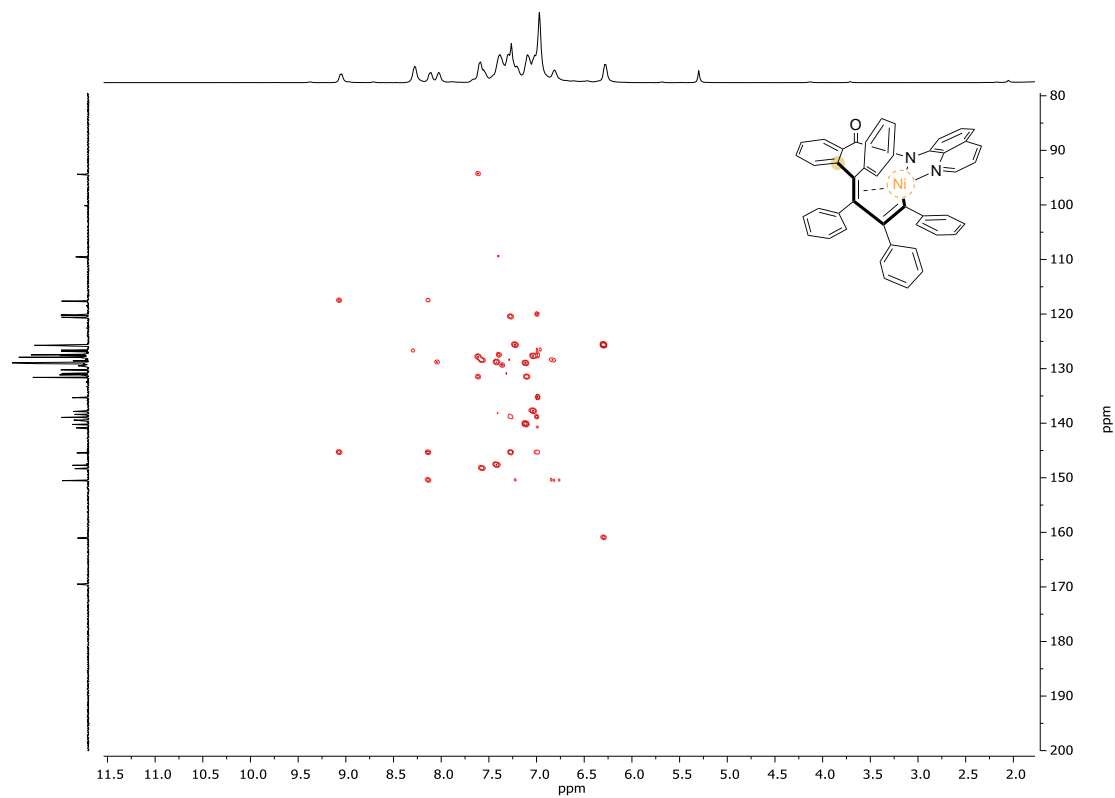
Figure S6. 400 MHz ^{1}H-^{13}C HMBC NMR spectrum of **INT4-E-H** in CDCl$_3$, 298 K.

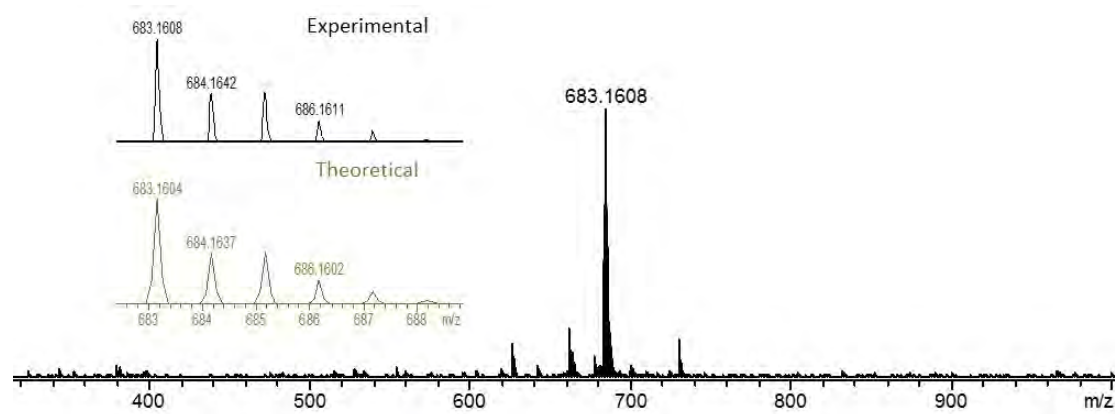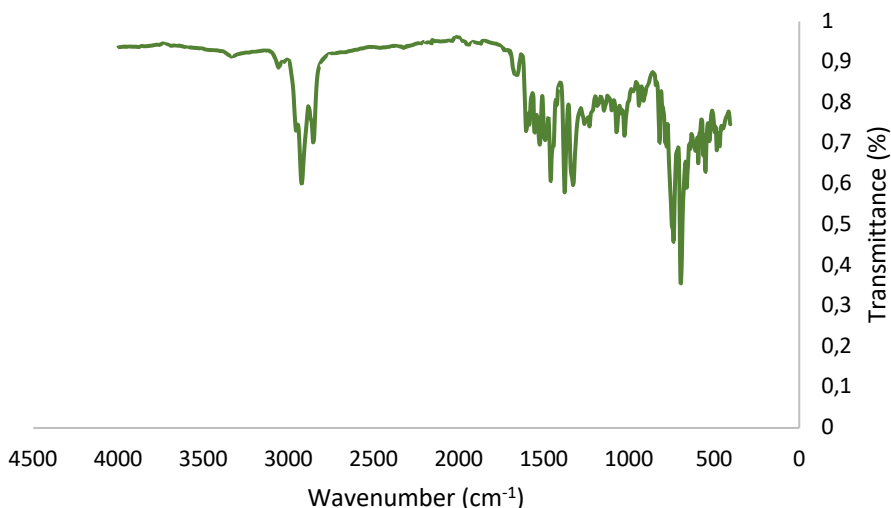**Figure S7.** MS spectrum of **INT4-E-H** (m/z = 683.1608)**.**

Figure S8. IR spectrum of **INT4-E-H.**

INT4-E-Me

Prepared in accordance to the general synthesis described above: **1a** (26.6 mg, 0.1 mmol) was converted to **INT4-E-Me** (7.9 mg, 11%), as an orange solid. **^{1}H-NMR** (400 MHz, CDCl$_3$, 298K) δ (ppm): 9.05 (dd, J = 8.1 Hz, 1.2 Hz, 1H), 8.11–8.09 (m, 3H), 8.04–8.02 (m, 1H), 7.54 (t, J = 7.8 Hz, 1H), 7.42 (d, J = 8.1 Hz, 2H), 7.38–7.36 (m, 1H), 7.30–7.27 (m, 2H), 7.25–7.23 (m, 1H), 7.18 (d, J = 8.3 Hz, 2H), 7.04 (dd, J = 5.3 Hz, 1.4 Hz, 1H), 6.91 (d, J = 7.7 Hz, 2H), 6.83–6.77 (m, 7H), 6.17 (d, J = 8.1 Hz, 2H), 2.40 (s, 3H), 2.23 (s, 3H), 2.14 (s, 3H), 2.13 (s, 3H). **^{13}C-NMR** (100 MHz, CDCl$_3$, 298K) δ (ppm): 169.5, 160.1, 150.5, 148.4, 145.5, 145.2, 140.9, 140.0, 138.7 (2C), 138.2, 137.3, 137.1, 136.2, 136.0, 135.3, 135.1, 132.9, 131.4 (2C), 131.2, 131.0, 130.1, 129.8 (2C), 129.5 (2C), 129.3 (3C), 128.8, 128.6 (2C), 128.5, 127.4 (2C), 127.3, 125.8 (2C), 120.6, 120.1, 117.5, 109.0, 94.3, 21.6 (2C), 21.5, 21.2. **HRMS** (ESI, m/z): Calculated for C$_{48}$H$_{38}$NiN$_2$O [M+Na]$^+$ 739.2230, Found 739.2237. **IR (ATR):** υ (cm^{-1}) = 3022, 2961, 2922, 2855, 1604, 1555, 1499, 1461, 1378, 1336, 1260, 1078, 1018, 906, 801, 727, 522.
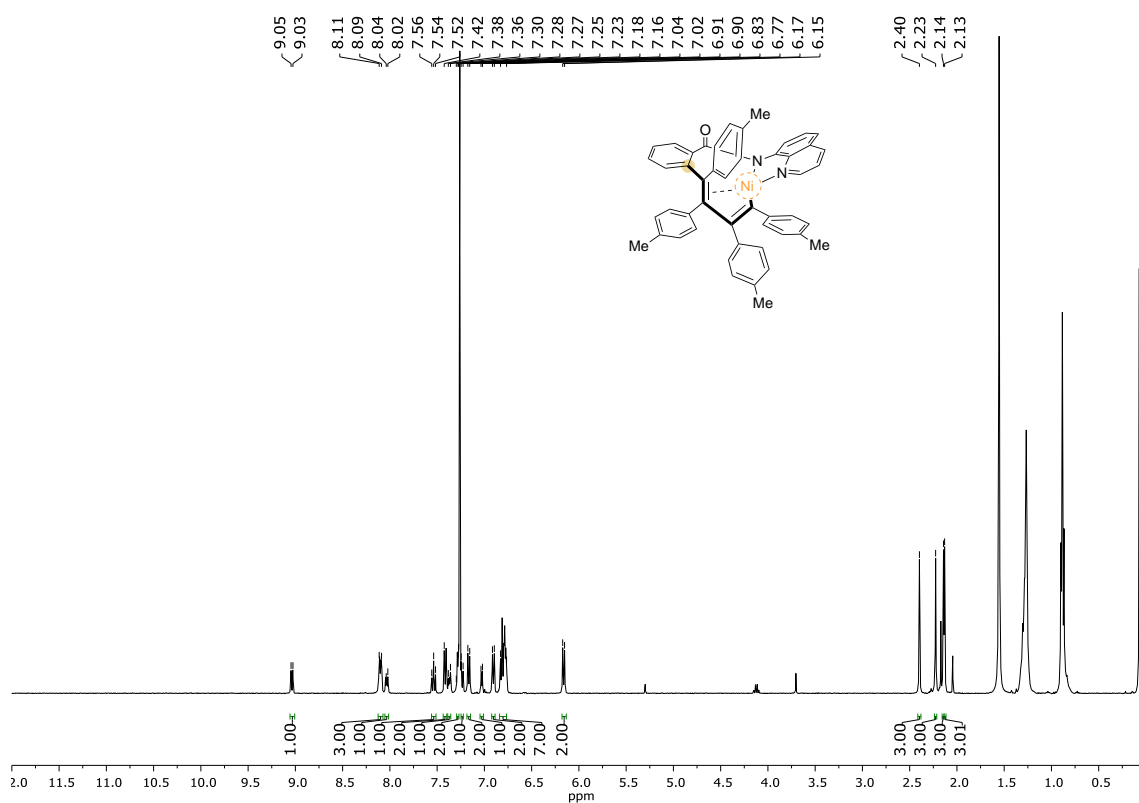
Figure S9. 400 MHz ^{1}H-NMR spectrum of **INT4-E-Me** in CDCl$_3$, 298 K.
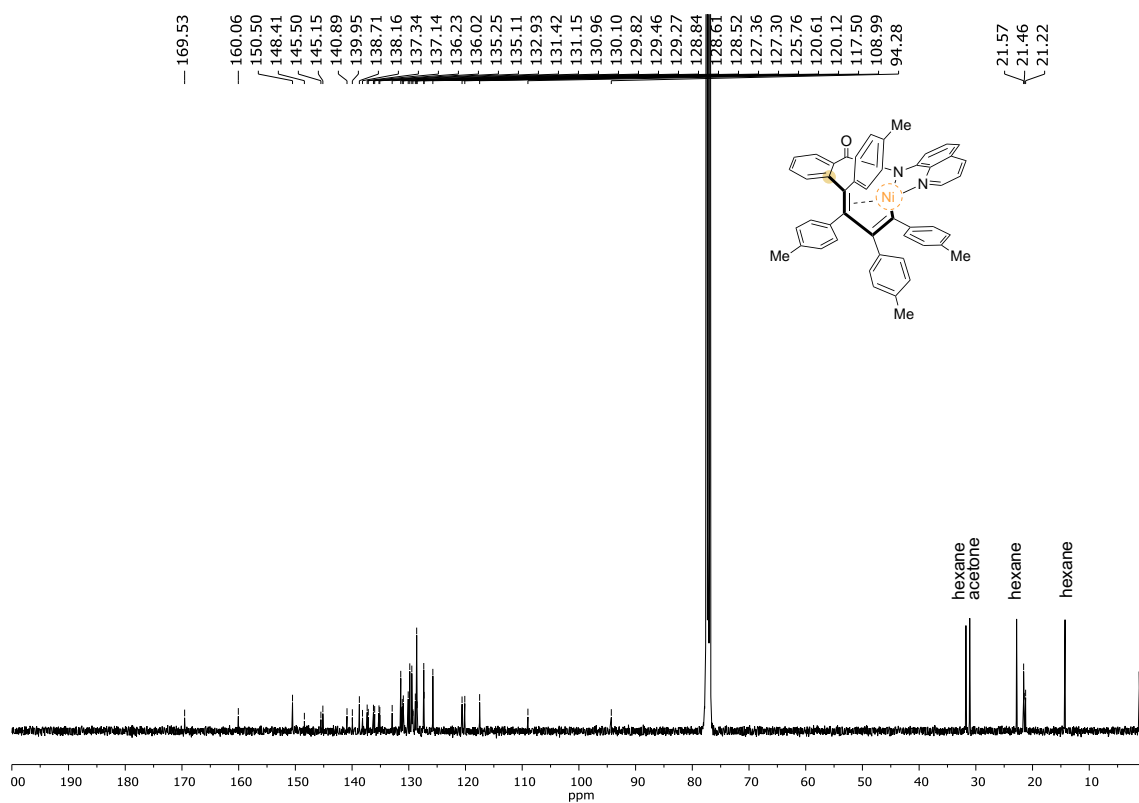
Figure S10. 100 MHz ^{13}C-NMR spectrum of **INT4-E-Me** in CDCl$_3$, 298 K
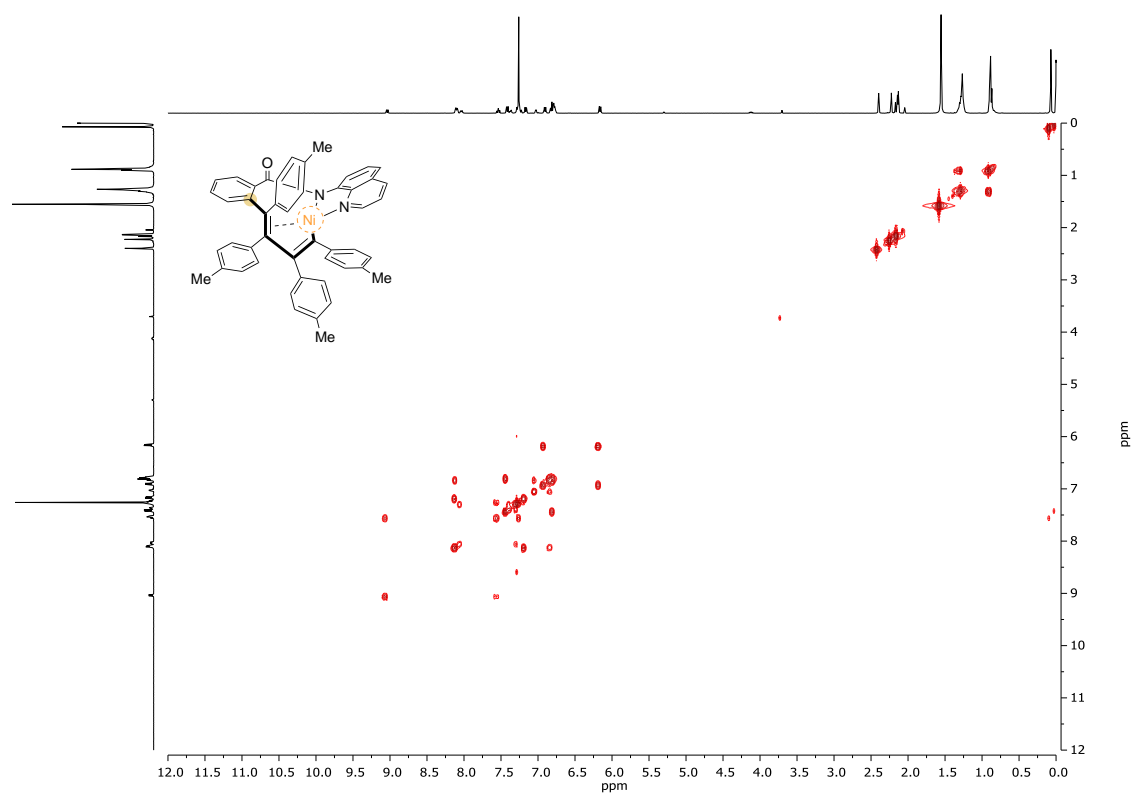
Figure S11. 400 MHz ^{1}H-^{1}H COSY NMR spectrum of **INT4-E-Me** in CDCl$_3$, 298 K.
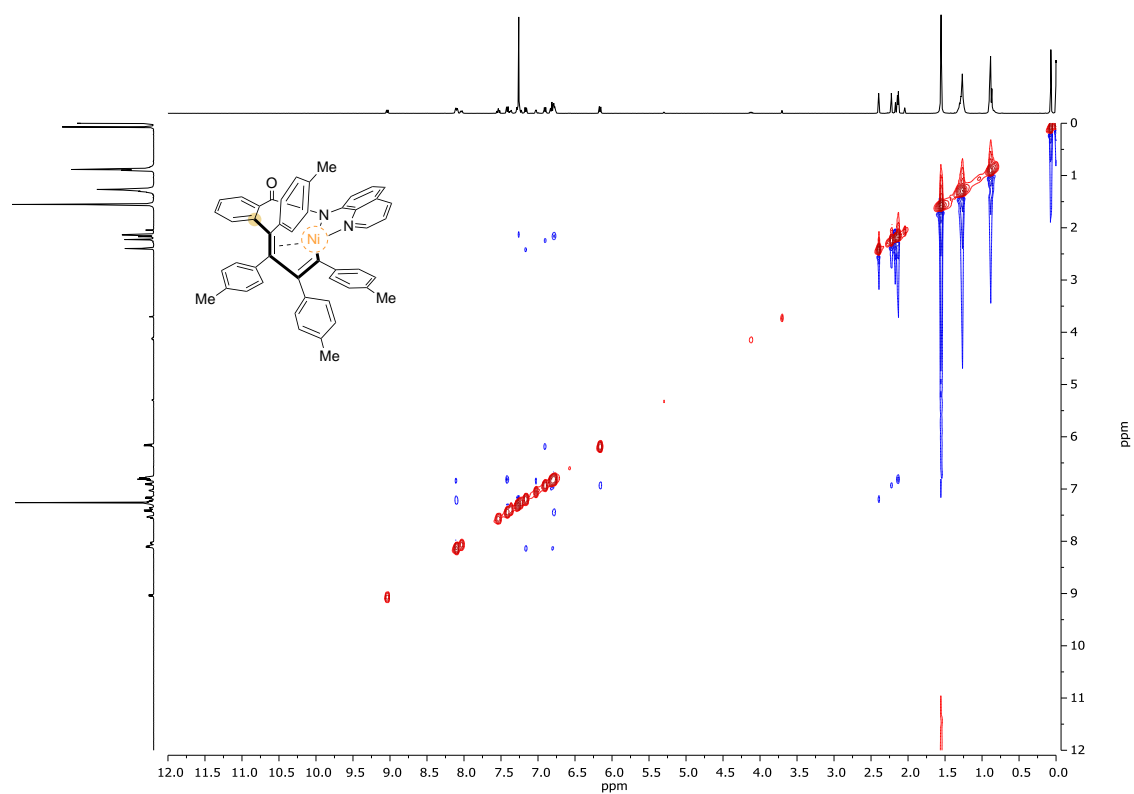
Figure S12. 400 MHz ^{1}H-^{1}H NOESY NMR spectrum of **INT4-E-Me** in CDCl$_3$, 298 K.

Figure S13. 400 MHz ^{1}H-^{13}C-HSQC NMR spectrum of **INT4-E-Me** in CDCl$_3$, 298 K.

Figure S14. 400 MHz ^{1}H-^{13}C HMBC NMR spectrum of **INT4-E-Me** in CDCl$_3$, 298 K.
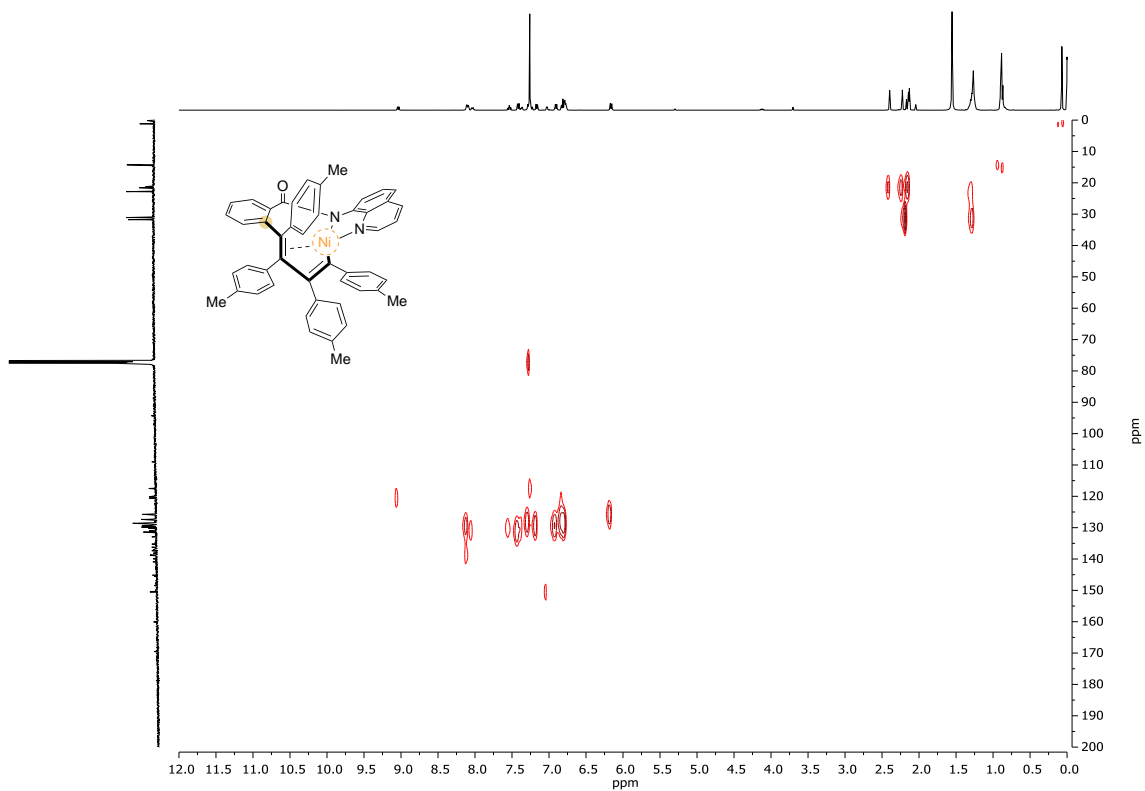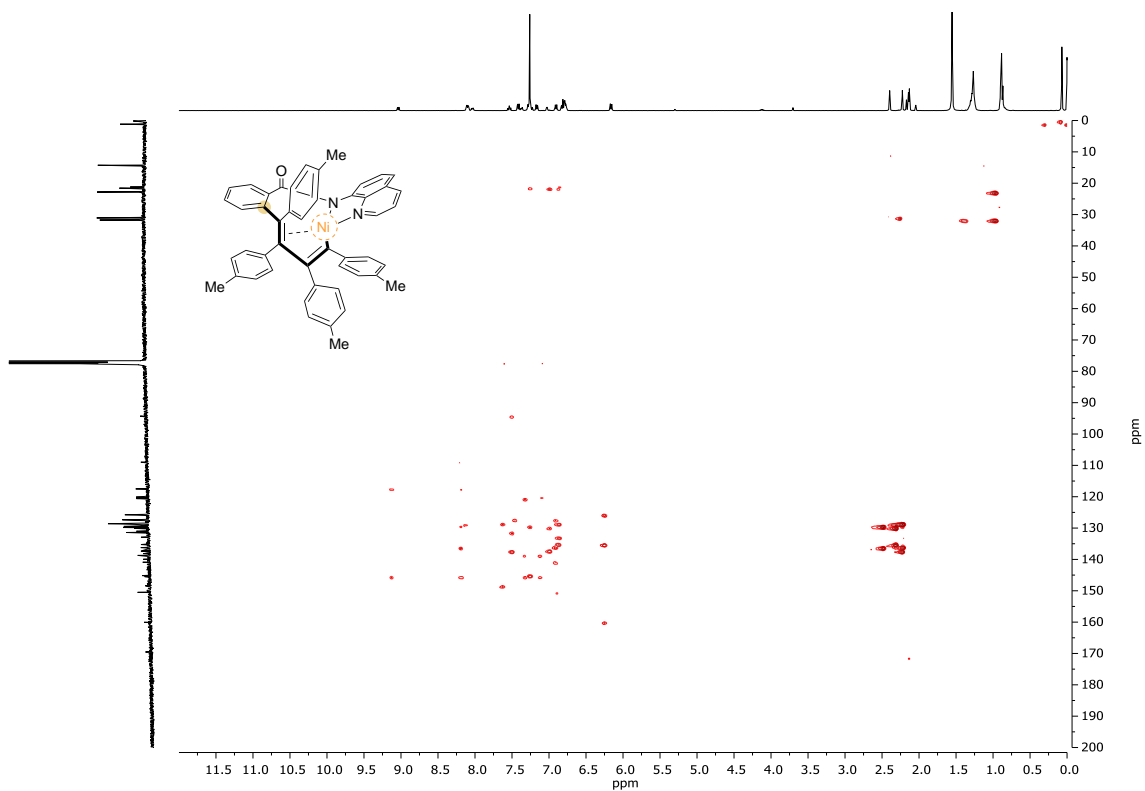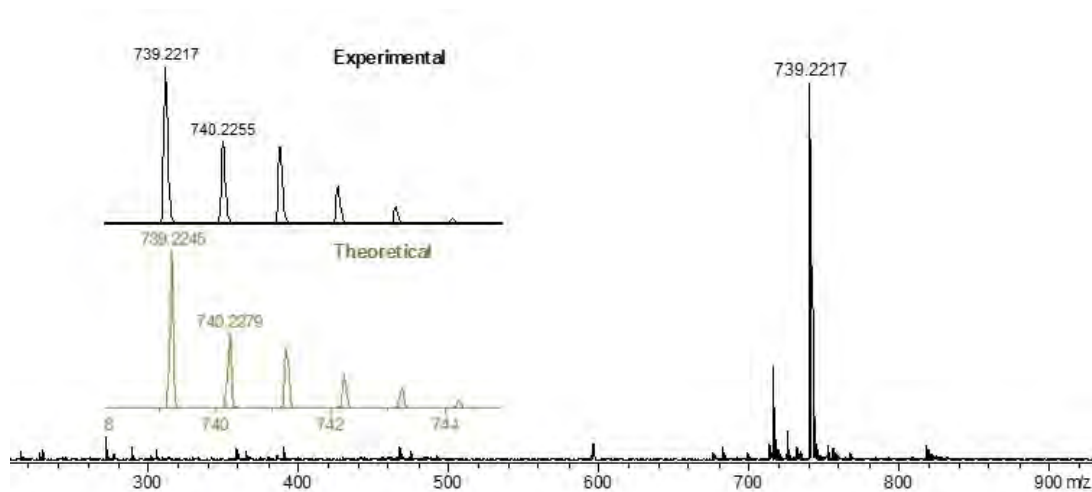
Figure S15. MS spectrum of **INT4-E-Me** (m/z = 739.2217)**.**
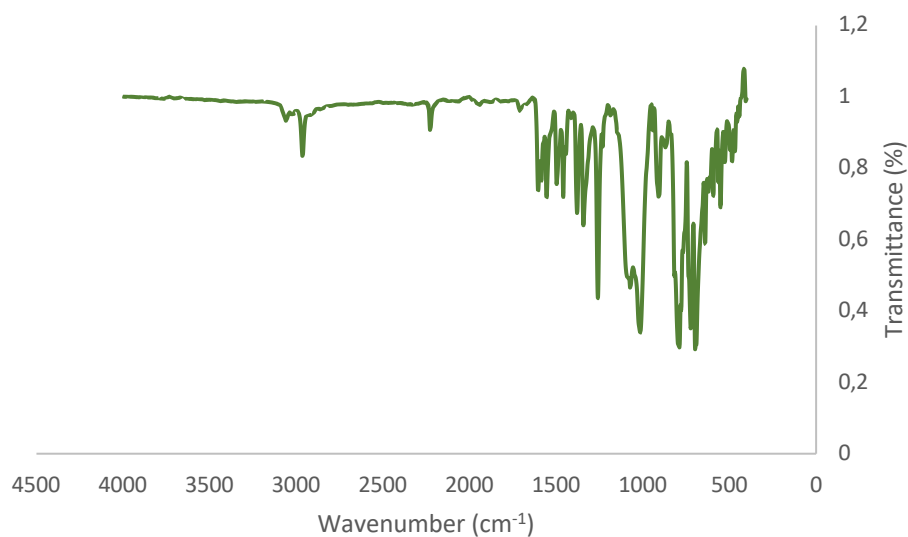
Figure S16. IR spectrum of INT4-E-Me.

4.3. Competition experiments with differently substituted alkynes

31% of 2ab   **39% of 3ag**
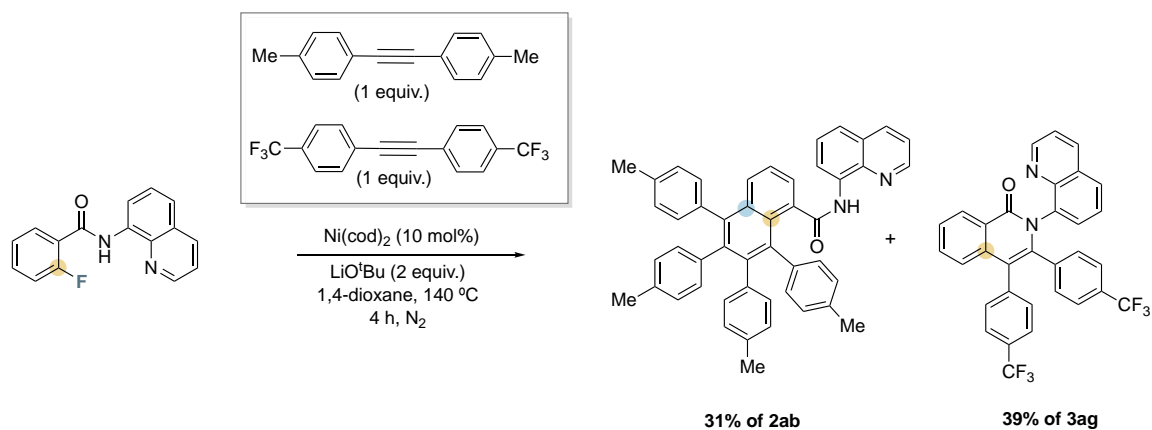
1a (26.6 mg, 0.1 mmol), 1,2-di-p-tolyacetylene (20.6 mg, 0.1 mmol, 1 equiv.), 1,2-bis(4-(trifluoromethyl)phenyl)ethyne (31,4 mg, 0.1 mmol, 1 equiv), LiOtBu (16.0 mg, 0.2 mmol, 2 equiv.) and catalytic amounts of Ni(cod)$_2$ (2.8 mg, 0.01 mmol, 10 mol %) with 1,4-dioxane (0.5 mL) were added to a glass vial under inert-atmosphere, and the vial was sealed. The reaction mixture was heated at 140ºC during 4 hours. The crude mixture was extracted with dichloromethane (3 x 10 mL) and the organic layers were combined and dried over MgSO$_4$. The solvent was then removed under reduced pressure. The crude mixture was analysed by ^{1}H-NMR spectroscopy (CDCl$_3$) using 1,3,5-trimethoxybenzene as an internal standard.
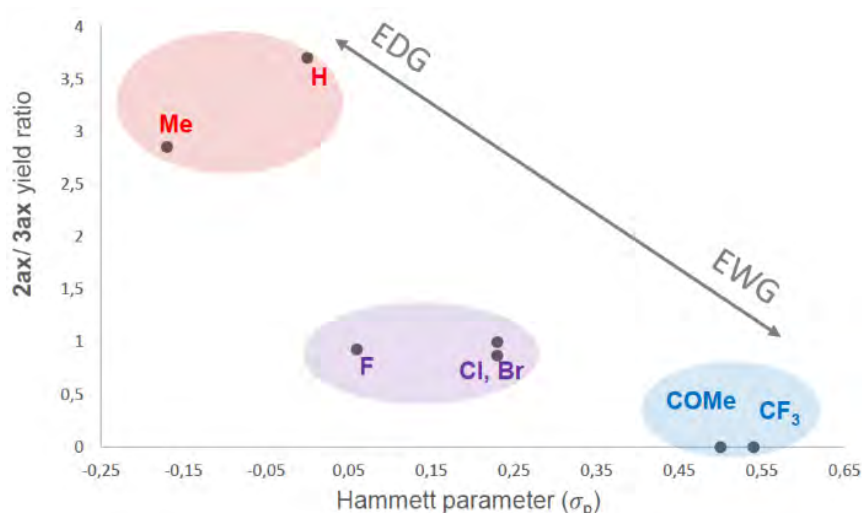
Scheme S2. Electronic influence on the aromatic homologation (**2ax**) *versus* alkyne mono-annulation (**3ax**) products (Hammett analysis).

4.4. Study of the Reactivity of INT4-E-H

a) *Heating of* **INT4-E-H**
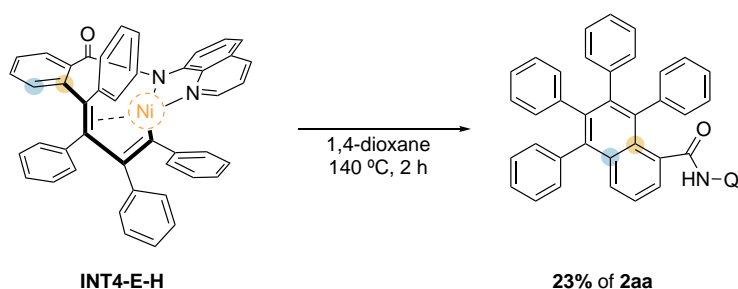
A solution of **INT4-E-H** (6.6 mg, 0.01 mmol) in 1,4-dioxane (0.2 mL) was heated to 140 ºC and stirred for 2 hours. After the reaction time, the mixture was left to cool down and extracted with dichloromethane (3 x 5 mL). The combined organic layers were dried over MgSO$_4$ and the solvent was removed under reduced pressure. The crude mixture was analysed by ^{1}H-NMR spectroscopy (CDCl$_3$) using 1,3,5-trimethoxybenzene as internal standard.

b) *Heating of* **INT4-E-H** *with PivOH*

INT4-E-H

PivOH (2 equiv.)
1,4-dioxane
140 ºC, 2 h

46% of **4aa**
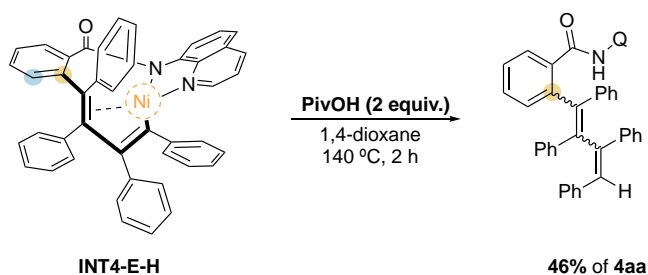
To a solution of **INT4-H** (47.3 mg, 0.07 mmol) in 1,4-dioxane (0.5 mL), PivOH (14.6 mg, 0.14 mmol, 2 equiv.) was added. The crude mixture was heated to 140 ºC and stirred for 2 hours. After the reaction time, the mixture was left to cool down and extracted with dichloromethane (3 x 5 mL). The combined organic layers were dried over MgSO$_4$ and the solvent was removed under reduced pressure. The crude mixture was analyzed by ^{1}H-NMR spectroscopy (CDCl$_3$) using 1,3,5-trimethoxybenzene as internal standard.

c) *Formation of* **INT4-H** *via C-H/C-H funcionalization*

(4 equiv.)
Ni(cod)$_2$ (1 equiv.)
DMPU (2 equiv.)
140 ºC, 10 min.

Huang

INT4-H
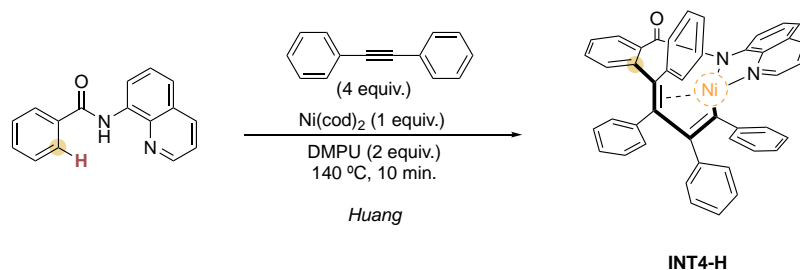
Non-fluorinated **1f** (31.0 mg, 0.125 mmol), alkyne (89.1 mg, 0.5 mmol, 4 equiv.) and Ni(cod)$_2$ (34.0 mg, 0.125 mmol, 1 equiv.) with DMPU (1 mL) were added to a glass vial under inert-atmosphere, and the vial was sealed. The reaction mixture was stirred at 140 ºC for 10 min. The resulting crude was extracted with dichloromethane (3 x 10 mL) and the organic layers were combined and dried over MgSO$_4$. The solvent was then removed under reduced pressure. The crude mixture was purified using a column chromatography using CH$_2$Cl$_2$/AcOEt (starting from 10:0 to 0:10). The crude mixture was analyzed by ^{1}H-NMR (yield 18%) and HRMS.

Figure S17. 400 MHz ^{1}H-NMR spectrum of crude mixture of **INT4-E-H** using non-fluorinated **1f** substrate (top) compared to isolated **INT4-E-H** species (bottom) in CDCl$_3$, 298 K.

Figure S18. MS spectrum of crude mixture of **INT4-E-H** using non-fluorinated **1f** substrate (m/z = 661.1)**.**

5. X-Ray diffraction data
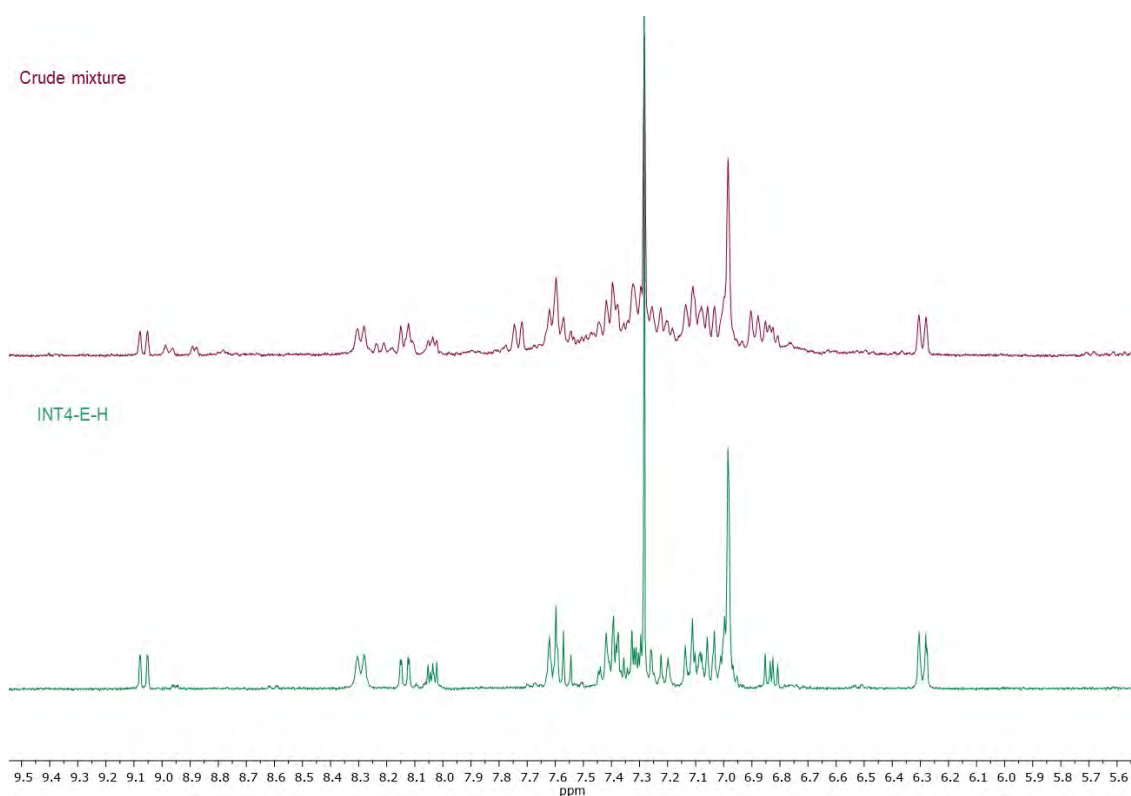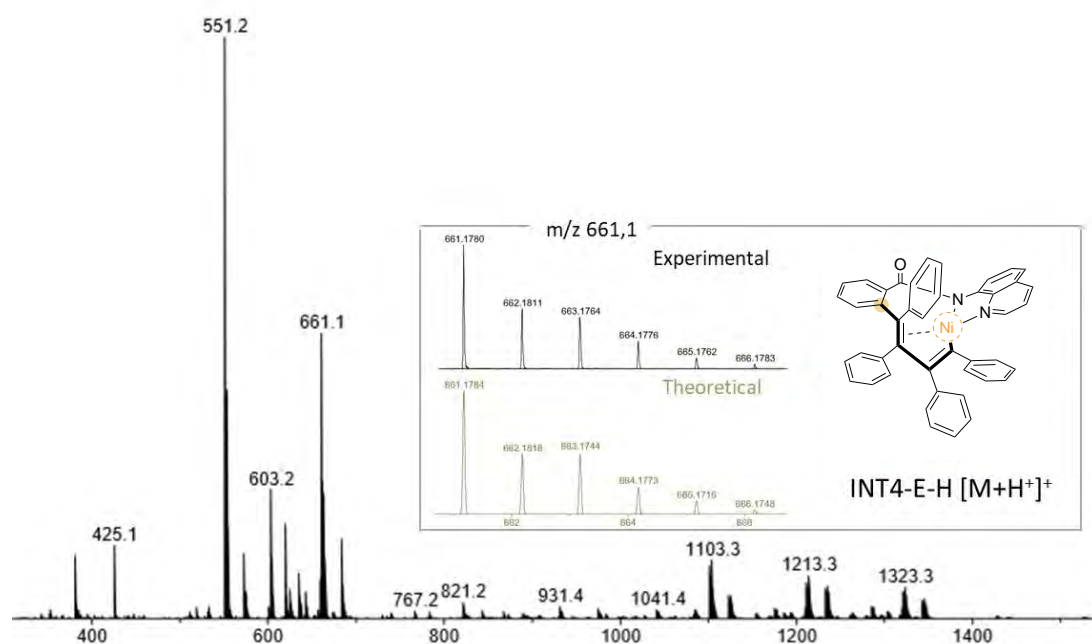
Crystallographic data for compounds **INT4-E-H** (CCDC-1891021) can be obtained free of charge from the Cambridge Crystallographic Data Centre via www.ccdc.cam.ac.uk/data_request/cif. Moreover, the corresponding CIF files have been included in the Supplementary Digital Material included in the attached CD.

5.1 X-Ray structure of INT4-E-H
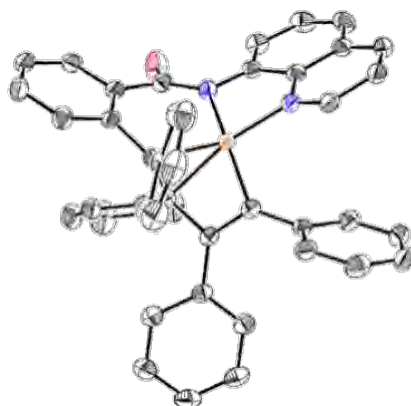
Figure S19. X-Ray crystal structure of **INT4-E-H** at 50% probability level. H atoms and solvent molecules have been omitted for clarity.

Dark red crystals of $C_{44}H_{30}NiN_2O$, $CHCl_3$, were grown from double layer of hexane and a chloroform solution of the compound, and used for low temperature (100(2) K) X-ray structure determination. The X-ray intensity data were measured on a Bruker D8 QUEST ECO system equipped with a doubly curved silicon crystal Bruker Triumph monochromator and a Mo Kalpha sealed X-ray tube (λ = 0.71076 Å). A total of 642 frames were collected. The total exposure time was 1.78 hours. The frames were integrated with the Bruker SAINT[5] software package using a wide-frame algorithm. The integration of the data using a monoclinic unit cell yielded a total of 91838 reflections to a maximum θ angle of 27.50° (0.77 Å resolution), of which 9082 were independent (average redundancy 10.112, completeness = 99.8%, R_{int}= 3.70%, R_{sig} = 1.80%) and 7848 (86.41%) were greater than $2\sigma(F^2)$. The final cell constants of <u>a</u> = 15.600(11) Å, <u>b</u> = 15.771(11) Å, <u>c</u> = 16.342(10) Å, β = 99.93(3)°, volume = 3960.(5) $Å^3$, are based upon the refinement of the XYZ-centroids of 190 reflections above 20 σ(I) with 7.358° < 2θ < 44.44°. Data were corrected for absorption effects using the Multi-Scan method (SADABS).[6] The ratio of minimum to maximum apparent transmission was 0.870. The calculated minimum and maximum transmission coefficients (based on crystal size) are 0.6690 and 0.9440. The structure was solved and refined using the Bruker SHELXTL Software Package,[7] using the space group P 1 21/n 1, with Z = 4 for the formula unit, $C_{45}H_{31}Cl_3N_2NiO$. The final anisotropic full-matrix least-squares refinement on F^2 with 497 variables converged at R1 = 2.87%, for the observed data and wR2 = 7.44% for all data. The goodness-of-fit was 1.029. The largest peak in the final difference electron density synthesis was 0.352 $e^-/Å^3$ and the largest hole was -0.319 $e^-/Å^3$ with an RMS deviation of 0.047 $e^-/Å^3$. On the basis of the final model, the calculated density was 1.309 g/cm^3 and F(000), 1608 e^-.

Table S2. Crystallographic parameters for **INT4-E-H** (CCDC-1891021).

Chemical formula	$C_{45}H_{31}Cl_3N_2NiO$
Formula weight	780.78 g/mol
Temperature	100(2) K
Wavelength	0.71076 Å
Crystal size	0.080 x 0.420 x 0.600 mm
Crystal habit	intense red-black plate
Crystal system	monoclinic
Space group	P 1 21/n 1
Unit cell dimensions	a = 15.600(11) Å α = 90°
	b = 15.771(11) Å β = 99.93(3)°
	c = 16.342(10) Å γ = 90°
Volume	3960.(5) Å³
Z	4
Density (calculated)	1.309 g/cm³
Absorption coefficient	0.728 mm⁻¹
F(000)	1608
Diffractometer	Bruker D8 QUEST ECO
Radiation source	sealed X-ray tube, Mo Kalpha
Theta range for data collection	2.84 to 27.50°
Index ranges	-20<=h<=20, -20<=k<=20, -21<=l<=21
Reflections collected	91838
Independent reflections	9082 [R(int) = 0.0370]
Coverage of independent reflections	99.8%
Absorption correction	Multi-Scan
Max. and min. transmission	0.9440 and 0.6690
Structure solution technique	direct methods
Structure solution program	SHELXT 2014/5 (Sheldrick, 2014)
Refinement method	Full-matrix least-squares on F^2
Refinement program	SHELXL-2016/6 (Sheldrick, 2016)
Function minimized	$\Sigma\ w(F_o^2 - F_c^2)^2$
Data / restraints / parameters	9082 / 0 / 497
Goodness-of-fit on F^2	1.029
Δ/σ$_{max}$	0.001
Final R indices	7848 data; R1 = 0.0287, wR2 = 0.0693 I>2σ(I)
	all data R1 = 0.0371, wR2 = 0.0744
Weighting scheme	$w=1/[\sigma^2(F_o^2)+(0.0299P)^2+2.8503P]$ where $P=(F_o^2+2F_c^2)/3$
Largest diff. peak and hole	0.352 and -0.319 eÅ⁻³
R.M.S. deviation from mean	0.47 ⁻³

6. DFT modelling of the double alkyne insertion an alkyne monoannulation

6.1 Computational details

All DFT calculations were performed with the Gaussian 09 Revision E.01 program.[8] Geometry optimizations were carried out using the M06L functional[9] along with the def2SVP basis set and its respective density fitting basis set (w06).[10-11]. To check the reliability of the chosen funcitonal, some calculations with B3LYP[12-15] were also done, along with the def2SVP basis set. Grimme's Dispersion model with Becke-Johnson damping function, GD3BJ[16], was added to the B3LYP functional to improve accuracy. Solvation effects were included as a Polarizable Continuum using the SMD model.[17] Subsequently, we performed frequency calculations to each of the optimized structures to ensure that all local minima have only real frequencies and all transition states have only one imaginary frequency. To calculate the Gibbs energy (**ΔG**), i.e., to evaluate the entropic and enthalpic corrections, we used the python program Goodvibes (developed by Funes-Ardoiz and Paton).[18] The Gibbs energies were computed using the quasi-harmonic treatment (developed by Truhlar)[19] with a frequency scale factor of 1.0, a frequency cut-off value of 50 cm^{-1} and a temperature value of 413.15 K (140 ℃). The free energy correction associated with the change from a standard-state gas phase pressure of 1 atm to a standard state gas phase concentration of the different reactants was also included in the final Gibbs energy differences.

We also performed IRC calculations (using the LQA algorithm)[20-21] to verify that the transition states were connected with their respective reactants and products. Finally, single point energy calculations on the equilibrium geometries, including solvent effects, were computed with the more flexible basis set defTZPV[10-11] and their respective functional (M06L or B3LYP).

Therefore, the values of **ΔG** reported in the manuscript are calculated at M06L/def2TZVP//M06L/def2SVP, including solvent effects (SMD), using the vibrational quasi-harmonic model (frequency cut-off 50 cm-1 & scale factor 1.0), assuming a temperature of 413.15 K, and a concentration of 0.02 M for the Ni catalyst, 0.2 for the 8AQ and 0.4 M for DPA.

The xyz coordinates can be found in the Supplementary Digital Material included in the attached CD.

6.2 Additional B3LYP calculations

The same Energy profile showed in Figure 4 of the Manuscript was calculated using B3LYP funtional. The comparison of Figures 4 (main text) and S20 show that both functionals lead to the same conclussions: i) **INT3-Z** is more stable than **INT3-E** while **INT4-E** is more stable than **INT4-Z**; ii) The double-insertion is kinetically more favorable than the mono insertion; iii) The transition states connected to **INT3-Z** have a far lower energy than their counterparts conneted to **INT3-E**.
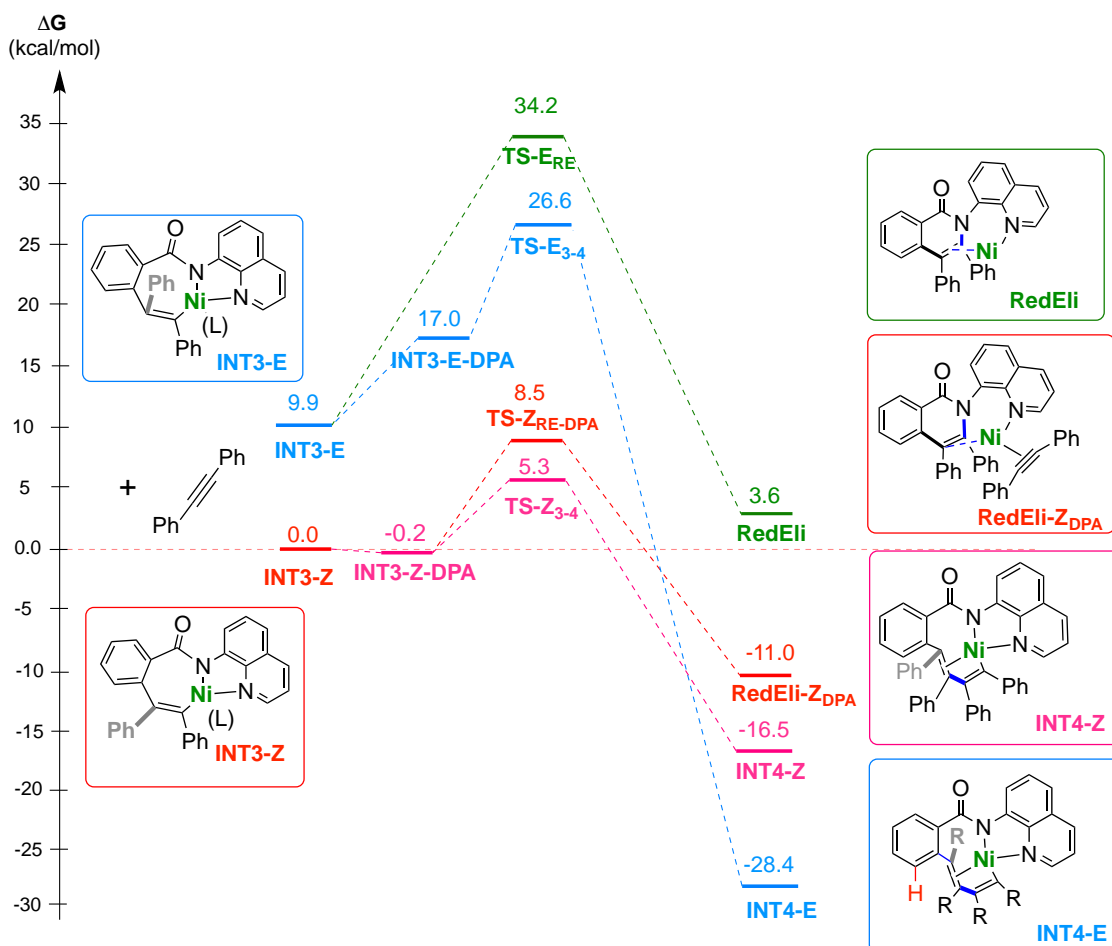
Figure S20. Gibbs Energy profiles for the transition from the monoalkyne intermediates (**INT3-E** or **INT3-Z**) to the double inserted alkyne compounds **INT4-E** (in blue) or **INT4-Z** (in pink), as well as the pathways for the intramolecular alkyne mono-annulation from **INT3-E** (in green) and from **INT3-Z** with a second DPA coordinated to the metal (in red). The reaction was modeled at B3LYP-GD3BJ/Def2TZVP//B3LYP-GD3BJ/Def2SVP level of theory; energies given in kcal/mol

6.3 Effect of the p-CF₃ (EWG) substituent on the DPA.
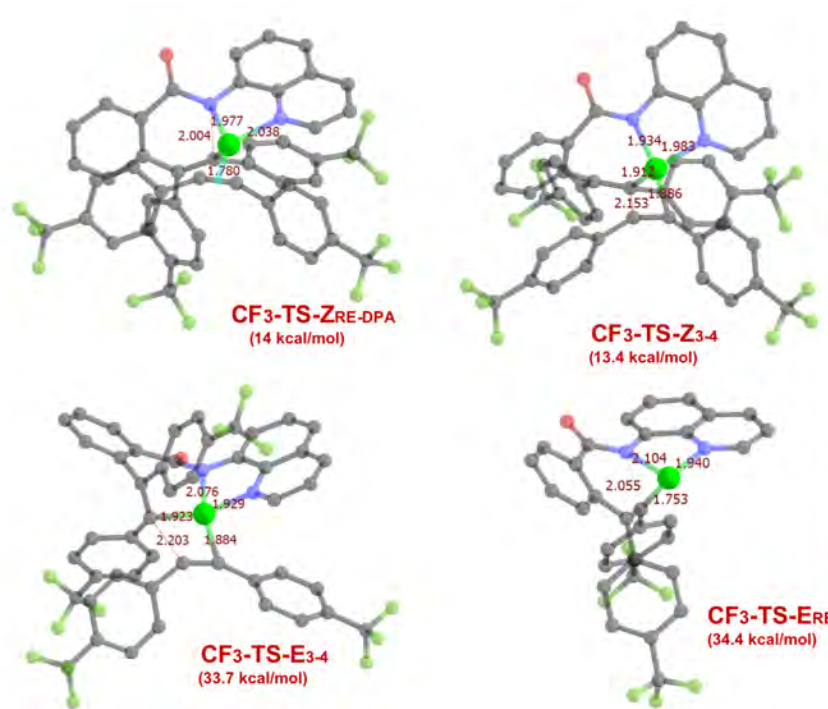
Figure S21. Optimized geometries of **CF₃-TS-E$_{RE}$, CF₃-TS-E$_{3-4}$, CF₃-TS-Z$_{RE-DPA}$** and **CF₃-TS-Z$_{3-4}$** calculated at M06L/def2TZVP//M06L/def2SVP level.

For the CF₃ *p*-substituted DPA, we have also calculated **CF₃-TS-E$_{RE}$, CF₃-TS-E$_{3-4}$, CF₃-TS-Z$_{RE-DPA}$** and **CF₃-TS-Z$_{3-4}$** at M06L/def2TZVP//M06L/def2SVP level. As mentioned in the manuscript, the diference in energy between the CF₃-TS-Z$_{3-4}$ and CF₃-TS-Z$_{RE-DPA}$ is just 0.6 kcal/mol, smaller by half than the one from the unsubstituted DPA Transition states (1.2 kcal/mol).

Table S3. Gibbs Energy values in kcal/mol for the optimized transition states of the second alkyne insertion and the reductive elimination (alkyne mono-annulation) for the DPA and the *p*-CF₃-DPA. The zero of energy is asumme as the energy of the **INT3** + respective DPA at infinite distance.

Alkyne	TS-Z$_{RE-DPA}$	TS-Z$_{3-4}$	TS-E$_{RE}$	TS-E$_{3-4}$
DPA	13.1	11.9	34.8	33.4
p-CF₃-DPA	14.0	13.4	34.4	33.7

6.4 The insertion of a second 8-aminoquinoline coordinated to INT3

The **INT3-Z** and **INT3-E** have a ligand vacancy created by the formation of LiF. We have studied if the insertion of a second 8-AQ to **INT3-Z** is thermodynamically favorable at at M06L/def2TZVP//M06L/def2SVP level, considering the two posible forms of 8-AQ (i.e. amino-protonated and amino-deprotonared, in the latter case we included in the calculations a Li⁺ to compensate the charge negative of the molecule). The results shown in the Table S4 clearly show that the insertion of a second 8-AQ is not favourable.

Table S4. Reletive Gibbs energy values in kcal/mol of the possible complexes that **INT3-Z** can form with the additional AQ-containing substrate.

Adduct/Intermediate	Isomer Z
INT3-Z	**0.0**
INT3-Z-AQH	7.3
INT3-Z-AQ	12.5
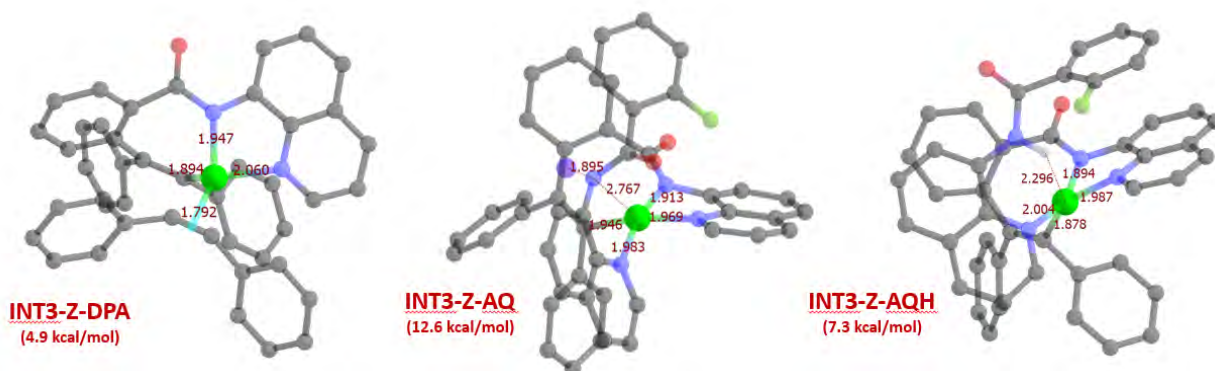
Figure S22. Optimized geometries of **INT3-Z-DPA, INT3-Z-AQ** and **INT3-Z-AQH** optimized at M06L/def2TZVP//M06L/def2SVP level.

7. Characterization data

General Procedure

1a-1d (0.1 mmol), alkyne **a-k** (2 equiv.), LiOtBu (16.0 mg, 0.2 mmol, 2 equiv.) and catalytic amounts of Ni(cod)$_2$ (2.8 mg, 0.01 mmol, 10 mol %) with 1,4-dioxane (0.5 mL) were added to a glass vial under inert-atmosphere, and the vial was sealed. The reaction mixture was heated at 140 ºC at different reaction times (2 – 8 h). The resulting crude mixture was extracted with dichloromethane (3 x 10 mL) and the organic layers were combined and dried over MgSO$_4$. The solvent was then removed under reduced pressure and purified using column chromatography.

5,6,7,8-Tetraphenyl-*N*-(quinolin-8-yl)-1-naphthamide (2aa):
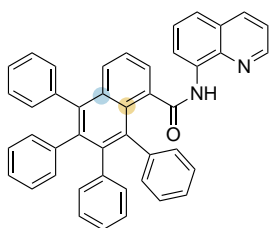
Prepared in accordance to the general synthesis described above: **1a** (26.6 mg, 0.1 mmol) and **a** (35.6 mg, 0.2 mmol) afforded **2aa** (37.8 mg, 60%) as a yellow solid. **^{1}H-NMR** (400 MHz, CDCl$_3$, 298 K) δ (ppm): 9.73 (s, 1H), 8.75 (dd, *J* = 4.3 Hz, 1.7 Hz, 1H), 8.21 (dd, *J* = 7.5 Hz, 1.6 Hz, 1H), 8.15 (dd, *J* = 8.3 Hz, 1.7 Hz, 1H), 7.81 (dd, *J* = 8.6 Hz, 1.4 Hz, 1H), 7.75 (dd, *J* = 7.1 Hz, 1.4 Hz, 1H), 7.48-7.36 (m, 4H), 7.27-7.19 (m, 5H), 7.02-6.91 (bs, 1H), 6.88-6.82 (m, 6H), 6.77-6.73 (m, 6H), 6.52 (tt, *J* = 7.5 Hz, 1.4 Hz, 1H), 6.12 (bs, 1H). **^{13}C-NMR** (100 MHz, CDCl$_3$, 298 K) δ (ppm): 168.8, 147.1, 141.4, 140.4, 139.8, 139.6, 139.4, 139.0, 138.4, 137.6, 136.9, 136.3, 134.5, 133.5, 131.3, 131.2, 131.1, 129.7, 128.3, 127.7, 127.6, 127.6, 127.2, 126.6, 126.5, 126.4, 126.0, 125.4, 125.2, 124.9, 121.3, 121.2, 116.8. **HRMS** (ESI, m/z): Calculated for C$_{44}$H$_{30}$N$_2$O [M+H]$^+$

603.2431, Found 603.2394. **R$_f$**: 0.81 (EtOAc/Hexane (1:1)) This compound is known and the data described is in agreement with the previous reports.[22-23]

3,4-Diphenyl-2-(quinolin-8-yl)isoquinolin-1(2H)-one (3aa):

Prepared in accordance to the general synthesis described above: **1a** (26.6 mg, 0.1 mmol) and **a** (35.6 mg, 0.2 mmol) afforded **3aa** (4.9 mg, 11%) as a pale yellow solid. **^{1}H-NMR** (400 MHz, CDCl$_3$, 298 K) δ (ppm): 8.93 (dd, J = 4.3 Hz, 1.7 Hz, 1H), 8.58 (m, 1H), 8.06 (dd, J = 8.4 Hz, 1.7 Hz, 1H), 7.67-7.49 (m, 4H), 7.39-7.35 (m, 3H), 7.25-7.24 (m, 2H), 7.17-7.15 (m, 3H), 6.97 (dt, J = 7.7 Hz, 1.3 Hz, 1H), 6.83 (td, J = 7.6 Hz, 0.8 Hz, 1H), 6.76-6.70 (m, 2H), 6.49 (td, J = 7.7 Hz, 0.8 Hz, 1H). **^{13}C-NMR** (100 MHz, CDCl$_3$, 298 K) δ (ppm): 162.9, 150.9, 144.9, 142.0, 138.3, 137.9, 136.7, 136.1, 135.0, 132.6, 132.0, 131.8, 131.0, 130.9, 129.9, 128.9, 128.7, 128.6, 124.1, 127.9, 127.3, 126.9, 126.8, 126.7, 126.5, 125.9, 125.8, 125.7, 121.6, 118.7. **HRMS** (ESI-MS): Calculated for C$_{30}$H$_{20}$N$_2$O [M+H]$^+$ 425.1648, Found 425.1636. **R$_f$**: 0.33 (EtOAc/Hexane (1:1)). This compound is known and the data described is in agreement with the previous reports.[24]
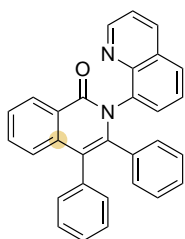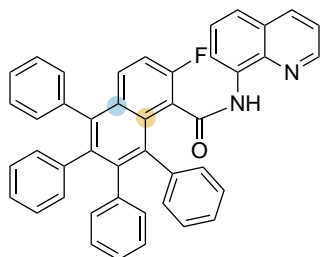
2-Fluoro-5,6,7,8-tetraphenyl-*N*-(quinolin-8-yl)-1-naphthamide (2ba):

Prepared in accordance to the general synthesis described above: **1b** (28.4 mg, 0.1 mmol) and **a** (35.6 mg, 0.2 mmol) afforded **2ba** as a white solid (34% calculated by ^{1}H-NMR of crude). **^{1}H-NMR** (400 MHz, CDCl$_3$, 298 K) δ (ppm): 9.72 (s, 1H), 8.75 (dd, J = 4.2 Hz, 1.7 Hz, 1H), 8.24 (dd, J = 7.6 Hz, 1.4 Hz, 1H), 8.15 (dd, J = 7.3 Hz, 1.7 Hz, 1H), 7.79 (dd, J = 9.3 Hz, 6.1 Hz, 1H), 7.47-7.41 (m, 2H), 7.37 (t, J = 7.8 Hz, 1H), 7.25-7.20 (m, 6H), 6.96-6.63 (m, 13H), 6.44 (t, J = 7.6 Hz, 1H), 6.03 (t, J = 7.1 Hz, 1H). **^{13}C-NMR** (100 MHz, CDCl$_3$, 298 K) δ (ppm): 163.3, 158.8 (d, J_{C-F} = 246 Hz), 148.1, 142.8, 140.3 (d, J_{C-F} = 6.1 Hz), 139.4, 139.2, 139.1, 138.4, 138.3, 137.8 (d, J_{C-F} = 6.1 Hz), 136.4, 134.3, 133.3, 131.9, 131.7, 131.6, 131.5, 131.2, 130.9, 130.3, 129.3 (d, J_{C-F} = 4.2 Hz), 127.8, 127.7, 127.3, 126.9, 126.8, 126.7, 126.6, 126.5, 126.4, 126.3, 125.9, 125.6 (d, J_{C-F} = 24.7 Hz), 121.5, 121.4, 117.1, 115.9 (d, J_{C-F} = 26.6 Hz). **^{19}F-NMR** (400 MHz, CDCl$_3$, 298 K) δ (ppm): -114.11 ppm. **HRMS** (ESI-MS): Calculated for C$_{44}$H$_{29}$N$_2$OF [M+Na]$^+$ 643.2156, Found 643.2141. **R$_f$**: 0.75 (CH$_2$Cl$_2$). This compound is known and the data described is in agreement with the previous reports.[22]

N-(Quinolin-8-yl)-5,6,7,8-tetra-*p*-tolyl-1-naphthamide (2ab):
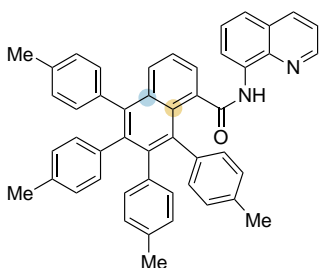
Prepared in accordance to the general synthesis described above: **1a** (26.6 mg, 0.1 mmol) and **b** (41.3 mg, 0.2 mmol) afforded **2ab** (26.6 mg, 40%) as a pale yellow solid. **^{1}H-NMR** (400 MHz, CDCl$_3$, 298 K) δ (ppm): 9.65 (s, 1H), 8.75 (dd, J = 4.2 Hz, 1.8 Hz, 1H), 8.25 (dd, J = 5.6 Hz, 3.5 Hz, 1H), 8.15 (dd, J = 8.3 Hz, 1.8 Hz, 1H), 7.76 (dd, J = 8.6 Hz, 1.3 Hz, 1H), 7.70 (dd, J = 7.0 Hz, 1.4 Hz, 1H), 7.44-7.40 (m, 5H), 7.16-7.14 (m, 2H), 7.12-7.06 (m, 4H), 6.70-6.65 (m, 5H), 6.58 (bs, 3H), 5.85 (bs, 1H), 2.37 (s, 3H), 2.33 (s, 3H), 2.09 (s, 3H), 2.03 (s, 3H). **^{13}C-NMR** (100 MHz, CDCl$_3$, 298 K) δ (ppm): 169.2, 148.0, 141.6, 140.0, 138.9, 138.5, 138.3, 137.7, 137.7, 137.6, 137.0, 136.7, 136.3, 135.9, 135.7, 134.9, 134.5, 134.3, 133.8, 131.6, 131.0, 129.8, 129.2, 128.9, 128.7, 128.4, 127.9, 127.5, 127.4, 127.3, 127.2, 124.6,

121.8, 121.4, 121.1, 120.5, 116.7, 21.4, 21.2, 21.1, 20.8. **HRMS** (ESI, m/z): Calculated for $C_{48}H_{38}N_2O$ [M+Na]$^+$ 681.2876, Found 681.2866. R_f : 0.90 (EtOAc:hexane (8:2)). This compound is known and the data described is in agreement with the previous reports.[22]

2-(Quinolin-8-yl)-3,4-di-*p*-tolulisoquinolin-1(*2H*)-one (3ab):

Prepared in accordance to the general synthesis described above: **1a** (26.6 mg, 0.1 mmol) and **b** (41.3 mg, 0.2 mmol) afforded **3ab** (2.6 mg, 6%) as a pale orange solid. **1H-NMR** (400 MHz, CDCl$_3$, 298 K) δ (ppm): 8.93 (dd, *J* = 4.0 Hz, 1.7 Hz, 1H), 8.57 (dd, *J* = 8.1 Hz, 1.7 Hz, 1H), 8.07 (dd, *J* = 8.3 Hz, 1.9 Hz, 1H), 7.68 (dd, *J* = 8.1 Hz, 1.6 Hz, 1H), 7.60-7.44 (m, 3H), 7.39-7.34 (m, 2H), 7.31-7.28 (m, 1H), 7.14 (dd, *J* = 7.6 Hz, 1.5 Hz, 1H), 7.06-7.03 (m, 2H), 6.99-6.96 (d, *J* = 7.8 Hz, 1H), 6.86 (dd, *J* = 7.9 Hz, 1.9 Hz, 1H), 6.62 (td, *J* = 8.2 Hz, 1.9 Hz, 2H), 6.28 (d, *J* = 7.9 Hz, 1H), 2.28 (s, 3H), 1.95 (s, 3H). **13C-NMR** (100 MHz, CDCl$_3$, 298 K) δ (ppm): 162.9, 150.8, 145.0, 142.1, 138.6, 138.1, 136.8, 136.2, 136.1, 133.8, 132.4, 132.3, 131.8, 131.6, 131.0, 130.8, 129.7, 128.9, 128.9, 128.6, 128.5, 128.4, 127.5, 127.3, 126.6, 125.9, 125.8, 125.7, 121.5, 118.6, 21.3, 21.2. **HRMS** (ESI, m/z): Calculated for $C_{32}H_{24}N_2O$ [M+Na]$^+$ 475.1781, Found 475.1787. R_f: 0.35 (EtOAc:hexane (8:2)). This compound is known and the data described is in agreement with the previous reports.[25]

5,6,7,8-Tetrakis(4-fluorophenyl)-N-(quinolin-8-yl)-1-naphthamide (2ac):
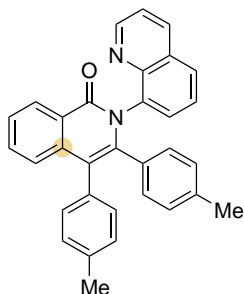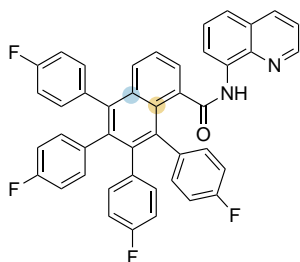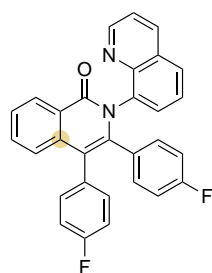
Prepared in accordance to the general synthesis described above: **1a** (26.6 mg, 0.1 mmol) and **c** (42.8 mg, 0.2 mmol) afforded **2ac** (24.0 mg, 36%) as a pale orange solid. **1H-NMR** (400 MHz, CDCl$_3$, 298 K) δ (ppm): 9.75, (s, 1H), 8.74 (dd, *J* = 4.1, 1.4 Hz, 1H), 8.26 (dd, *J* = 7.5 Hz, 0.9 Hz, 1H), 8.18 (dd, *J* = 8.4 Hz, 1.2 Hz, 1H), 7.77-7.74 (m, 2H), 7.51-7.43 (m, 4H), 7.19-7.15 (m, 3H), 6.99 (t, *J* = 8.6 Hz, 2H), 6.75-6.72 (m, 3H), 6.65 (t, *J* = 8.5 Hz, 5H), 6.54-6.50 (m, 3H). **13C-NMR** (100 MHz, CDCl$_3$, 298 K) δ (ppm): 168.6, 161.7 (d, J_{C-F} = 246.3 Hz), 161.3 (d, J_{C-F} = 246.3 Hz), 160.8 (d, J_{C-F} = 245.1 Hz), 160.6 (d, J_{C-F} = 244.4 Hz), 148.0, 140.6, 139.01, 138.5, 138.2, 137.2, 136.8, 136.5, 136.01, 136.0, 135.9, 135.1, 135.08, 135.0, 134.9, 134.2, 133.6, 132.7, 132.4, 132.3, 132.2, 129.4, 128.5, 127.85, 127.2, 125.4, 121.6, 121.5, 116.6, 115.0, 114.8, 114.12, 113.9, 113.7. **19F-NMR** (400 MHz, CDCl$_3$, 298 K) δ (ppm): -115.2, -116.0, -116.3, -116.6. **HRMS** (ESI-MS): Calculated for $C_{44}H_{26}F_4N_2O$ [M+H]$^+$ 675.2054, Found 675.2053. R_f: 0.58 (EtOAc/Hexane (3:7)). This compound is known and the data described is in agreement with the previous reports.[22]

3,4-Bis(4-fluorophenyl)-2-(quinolin-8-yl)isoquinolin-1(*2H*)-one (3ac):

Prepared in accordance to the general synthesis described above: **1a** (26.6 mg, 0.1 mmol) and **c** (42.8 mg, 0.2 mmol) afforded **3ac** (15.6 mg, 34 %) as a pale brown solid. **1H-NMR** (400 MHz, CDCl$_3$, 298 K) δ (ppm): 8.91 (dd, *J* = 4.3 Hz, 1.8 Hz, 1H), 8.57 (ddd, *J* = 8.1 Hz, 1.5 Hz, 0.6 Hz, 1H), 8.07 (dd, *J* = 8.6 Hz, 1.8 Hz, 1H), 7.70 (dd, *J* = 8.5 Hz, 1.5 Hz, 1H), 7.62 (ddd, *J* = 8.1 Hz, 6.9 Hz, 1.5 Hz, 1H), 7.56-7.50 (m, 2H), 7.43-7.36 (m, 2H), 7.27 (m, 1H), 7.18-7.13 (m, 2H), 6.97-6.88 (m, 3H), 6.76-7.72 (m, 1H),6.55 (td, *J* = 8.2 Hz, 2.6 Hz, 1H), 6.21 (td, *J* = 8.2 Hz, 2.6 Hz, 1H). **13C-NMR** (100 MHz, CDCl$_3$, 298 K) δ (ppm): 162.8, 161.8, (d, J_{C-F} =

246.3 Hz), 161.6 (d, $J_{C\text{-}F}$ = 247.8 Hz), 150.9, 144.7, 141.3, 138.1, 137.6, 136.2, 133.5 (d, $J_{C\text{-}F}$ = 7.9 Hz), 133.3 (d, $J_{C\text{-}F}$ = 7.6 Hz), 132.8, 132.5 (d, $J_{C\text{-}F}$ = 8.7 Hz), 132.4, 131.8 (d, $J_{C\text{-}F}$ = 8.2 Hz), 131.0, 130.9, 129.0, 128.9, 128.7, 127.1, 125.9, 125.8, 125.5, 121.7, 117.9, 115.3 (d, $J_{C\text{-}F}$ = 21.3 Hz), 115.2 (d, $J_{C\text{-}F}$ = 20.8 Hz), 114.1 (d, $J_{C\text{-}F}$ = 21.9 Hz), 113.8 (d, $J_{C\text{-}F}$ = 22.0 Hz).**^{19}F-NMR** (400 MHz, CDCl$_3$, 298 K) δ (ppm): -113.8, -115.6. **IR (ATR):** υ (cm^{-1}) = 3065, 2962, 2919, 1719, 1655, 1603, 1504, 1327, 1260, 1219, 1156, 1015, 908, 818, 725, 618, 542, 520. **HRMS** (ESI-MS): Calculated for $C_{30}H_{18}F_2N_2O$ [M+H]$^+$ 461.1460, Found 461.1452. **R$_f$:** 0.11 (EtOAc/Hexane (3:7)).

5,6,7,8-Tetrakis(4-chlorophenyl)-N-(quinolin-8-yl)-1-naphthamide (2ad):

Prepared in accordance to the general synthesis described above: **1a** (26.6 mg, 0.1 mmol) and **d** (49.4 mg, 0.2 mmol) afforded **2ad** (22.5 mg, 30 %) as a pale yellow solid. **^{1}H-NMR** (400 MHz, CDCl$_3$, 298 K) δ (ppm): 9.73 (s, 1H), 8.75 (dd, J = 4.3 Hz, 1.6 Hz, 1H), 8.22-8.18 (m, 2H), 7.77 (dd, J = 7.0 Hz, 1.2 Hz, 1H), 7.71 (dd, J = 8.5 Hz, 1.2 Hz, 1H), 7.51-7.44 (m, 5H), 7.29 (d, J = 8.0 Hz, 3H), 7.13 (d, J = 8.2 Hz, 3H), 6.91 (d, J = 8.0 Hz, 3H), 6.82 (d, J = 7.5 Hz, 2H), 6.71 (d, J = 7.5 Hz, 2H), 6.59 (bs, 2H). **^{13}C-NMR** (100 MHz, CDCl$_3$, 298 K) δ (ppm): 168.5, 148.1, 140.0, 138.5, 138.4, 138.3, 138.3, 138.2, 137.6, 137.4, 137.2, 136.9, 136.6, 134.2, 133.6, 133.2, 133.0, 132.6, 132.5, 132.4, 132.3, 132.2, 132.1, 132.0, 129.5, 128.5, 128.4, 128.1, 128.0, 127.6, 127.5, 127.3, 125.7, 121.9, 121.6, 116.9. **IR (ATR):** υ (cm^{-1}) = 3340, 3044, 2961, 2927, 1674, 1594, 1519, 1483, 1423, 1383, 1325, 1261, 1087, 1014, 895, 790, 772, 732, 575, 512. **HRMS** (ESI, m/z): Calculated for $C_{44}H_{26}Cl_4N_2O$ [M+Na]$^+$ 763.0670, Found 763.0657. **R$_f$:** 0.88 (EtOAc/Hexane (1:1)).
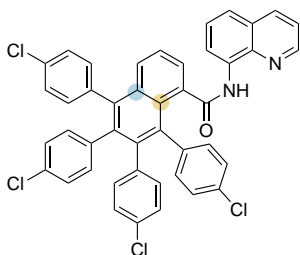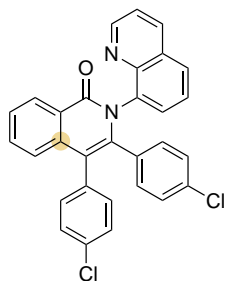
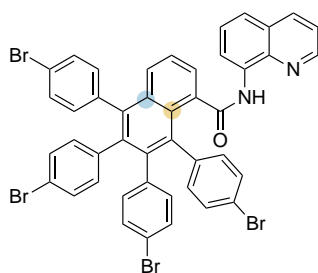## 3,4-Bis(4-chlorophenyl)-2-(quinolin-8-yl)isoquinolin-1(2H)-one (3ad):

Prepared in accordance to the general synthesis described above: **1a** (26.6 mg, 0.1 mmol) and **d** (49.4 mg, 0.2 mmol) afforded **3ad** (14.2 mg, 29%) as a yellow solid. **^{1}H-NMR** (400 MHz, CDCl$_3$, 298 K) δ (ppm): 8.90 (dd, J = 4.3 Hz, 1.8 Hz, 1H), 8.58 (dd, J = 7.9 Hz, 1.6 Hz, 1H), 8.09 (dd, J = 8.4 Hz, 1.8Hz, 1H), 7.72 (dd, J = 8.4 Hz, 1.5 Hz, 1H), 7.64-7.61 (m, 1H), 7.57-7.49 (m, 2H), 7.41 (t, J = 7.8 Hz, 1H), 7.38 (dd, J = 4.3 Hz, 8.4 Hz, 1H), 7.25-7.18 (m, 3H), 7.15-7.11 (m, 2H), 6.89 (dd, J = 8.4 Hz, 2.3 Hz, 1H), 6.85 (dd, J = 8.4 Hz, 2.3 Hz, 1H), 6.71 (dd, J = 84. Hz, 2.3 Hz, 1H), 6.51 (dd, J = 8.4 Hz, 2.3 Hz, 1H). **^{13}C-NMR** (100 MHz, CDCl$_3$, 298 K) δ (ppm): 162.7, 151.0, 144.7, 141.0, 137.8, 137.4, 136.3, 134.9, 133.6, 133.3, 133.2, 133.1, 133.0, 132.8, 132.0, 131.2, 130.9, 129.1, 129.0, 128.7, 128.7, 128.5, 127.3, 127.2, 127.1, 125.9, 125.8, 125.5, 121.8, 117.6. **HRMS** (ESI, m/z): Calculated for $C_{30}H_{18}Cl_2N_2O$ [M+Na]$^+$ 515.0688, Found 515.0686. **R$_f$:** 0.33 (EtOAc/Hexane (1:1)). This compound is known and the data described is in agreement with the previous reports.[25]

5,6,7,8-Tetrakis(4-bromophenyl)-*N*-(quinolin-8-yl)-1-naphthamide (2ae):

Prepared in accordance to the general synthesis described above: **1a** (26.6 mg, 0.1 mmol) and **e** (67.2 mg, 0.2 mmol) afforded **2ae** (22.6 mg, 25%) as a yellow solid. **^{1}H-NMR** (400 MHz, CDCl$_3$, 298 K) δ (ppm): 9.73 (s, 1H), 8.74 (dd, *J* = 4.2 Hz, 1.6 Hz, 1H), 8.23-8.18 (m, 2H), 7.76 (dd, *J* = 6.9 Hz, 1.2 Hz, 1H), 7.69 (dd, *J* = 8.5 Hz, 1.2 Hz, 1H), 7.51-7.43 (m, 8H), 7.07-7.05 (m, 4H), 7.00-6.97 (m, 3H), 6.65-6.63 (m, 3H), 6.57-6.53 (m, 2H).**^{13}C-NMR** (100 MHz, CDCl$_3$, 298 K) δ (ppm): 168.3, 148.0, 139.6, 138.6, 138.5, 138.2, 138.2, 138.1, 137.9, 137.7, 137.0, 136.8, 136.5, 134.0, 133.4, 132.7, 132.6, 132.5, 132.4, 131.2, 131.0, 130.3, 130.1, 129.4, 128.3, 128.0, 127.9, 127.5, 125.6, 121.8, 121.5, 121.3, 121.3, 120.4, 120.1, 116.9. **IR (ATR):** υ (cm^{-1}) = 3332, 3043, 2961, 2848, 1669, 1519, 1483, 1386, 1325, 1261, 1070, 1010, 906, 789, 755, 728, 507. **HRMS** (ESI, m/z): Calculated for C$_{44}$H$_{26}$Br$_4$N$_2$O [M+Na]$^+$ 940.8636, Found 940.8641. **R$_f$:** 0.60 (EtOAc/Hexane (7:3)).
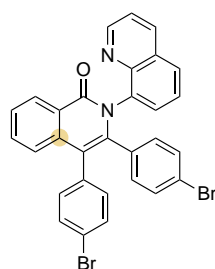
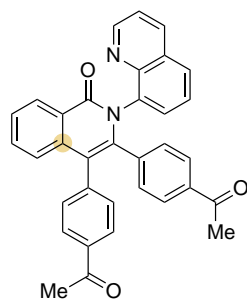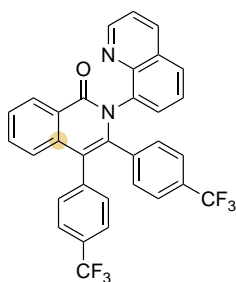**3,4-Bis(4-bromophenyl)-2-(quinolin-8-yl)isoquinolin-1(*2H*)-one (3ae):**

Prepared in accordance to the general synthesis described above: **1a** (26.6 mg, 0.1 mmol) and **e** (67.2 mg, 0.2 mmol) afforded **3ae** (19.9 mg, 34%) as a yellow solid. **^{1}H-NMR** (400 MHz, CDCl$_3$, 298 K) δ (ppm): 8.90 (dd, *J* = 4.1 Hz, 1.4 Hz, 1H), 8.57 (dd, *J* = 7.9 Hz, 1.1 Hz, 1H), 8.08 (dd, *J* = 8.3 Hz, 1.8 Hz, 1H), 7.72 (dd, *J* = 8.2 Hz, 1.3 Hz, 1H), 7.62 (ddd, *J* = 8.2 Hz, 7.0 Hz, 1.5 Hz, 1H), 7.54 (ddd, *J* = 8.2 Hz, 7.2 Hz, 1.3 Hz, 1H), 7.49 (dd, *J* = 7.2 Hz, 1.4 Hz, 1H), 7.43-7.34 (m, 4H), 7.25-7.23 (m, 1H), 7.09-7.05 (m, 2H), 7.00 (dd, *J* = 8.2 Hz, 1.7 Hz, 1H), 6.84 (dd, *J* = 8.5 Hz, 1.8 Hz, 1H), 6.68-6.62 (m, 2H).**^{13}C-NMR** (100 MHz, CDCl$_3$, 298 K) δ (ppm): 162.7, 151.0, 144.7, 140.9, 137.7, 137.4, 136.3, 135.4, 133.7, 133.5, 133.3, 132.8, 132.3, 131.6, 131.5, 131.4, 130.9, 130.3, 130.0, 129.1, 129.0, 128.7, 127.2, 126.0, 125.8, 125.5, 122.0, 121.8, 121.4, 117.6. **IR (ATR):** υ (cm^{-1}) = 3061, 2926, 2853, 1655, 1608, 1485, 1389, 1325, 1069, 1011, 906, 804, 725, 595, 515. **HRMS** (ESI, m/z): Calculated for C$_{30}$H$_{18}$Br$_2$N$_2$O [M+Na]$^+$ 604.9660, Found 604.9656. **R$_f$:** 0.1 (EtOAc/Hexane (7:3)).

Dimethyl 4,4'-(1-oxo-2-(quinolin-8-yl)-1,2-dihydroisoquinoline-3,4-diyl)dibenzoate (3af):

Prepared in accordance to the general synthesis described above: **1a** (26.6 mg, 0.1 mmol) and **f** (52.5 mg, 0.2 mmol) afforded **3af** (11.1 mg, 22%) as a pale brown solid. **^{1}H-NMR** (400 MHz, CDCl$_3$, 298 K) δ (ppm): 8.95 (dd, *J* = 4.2 Hz, 1.6 Hz, 1H), 8.62 (dd, *J* = 7.8 Hz, 1.6 Hz, 1H), 8.10 (dd, *J* = 8.4 Hz, 1.6 Hz, 1H), 7.87 (dd, *J* = 7.8 Hz, 1.8 Hz, 1H), 7.82 (dd, *J* = 7.8 Hz, 1.4 Hz, 1H), 7.72 (dd, *J* = 8.3 Hz, 1.6 Hz, 1H), 7.65 (dd, *J* = 7.8 Hz, 2.1 Hz, 1H), 7.61 (dd, *J* = 7.8 Hz, 1.2 Hz, 1H), 7.55 (dd, *J* = 7.4 Hz, 1.5 Hz, 1H), 7.47-7.39 (m, 3H), 7.38-7.31 (m, 2H), 7.25 (d, *J* = 7.9 Hz, 1H), 7.14-7.10 (m 2H), 7.92 (dd, *J* = 8.3 Hz, 1.5 Hz, 1H), 2.57 (s, 3H), 2.33 (s, 3H). **^{13}C-NMR** (100 MHz, CDCl$_3$, 298 K) δ (ppm): 197.8, 197.4, 162.6, 151.1, 144.7, 141.6, 141.0, 139.4, 137.4, 137.2, 136.3, 135.9, 135.8, 132.9, 132.2, 132.1, 131.1, 131.0, 130.3, 129.2, 129.0, 128.8, 128.4, 128.2, 127.4, 127.0, 126.8, 126.0, 125.9, 125.4, 121.9, 117.7, 26.7, 26.5. **IR (ATR):** υ (cm^{-1}) = 3048, 2962, 2920, 2856, 2095, 1779, 1661, 1595, 1520, 1482, 1329,

1260, 1157, 1090, 1015, 790, 703, 617, 543. **HRMS** (ESI, m/z): Calculated for $C_{34}H_{24}N_2O_3$ [M+Na]$^+$ 531.1685, Found 531.1572. **R$_f$**: 0.16 (EtOAc:Hexane, 1:1).

3,4-Bis(4-trifluoromethylphenyl)-2-(quinolin-8-yl)isoquinolin-1(*2H*)-one (3ag):
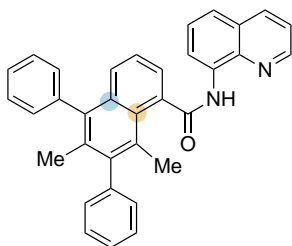
Prepared in accordance to the general synthesis described above: **1a** (26.6 mg, 0.1 mmol) and **g** (62.8 mg, 0.2 mmol) afforded **3ag** (46.4 mg, 83%) as a yellow solid. **^{1}H-NMR** (400 MHz, CDCl$_3$, 298 K) δ (ppm): 8.91 (dd, *J* = 4.2 Hz, 1.7 Hz, 1H), 8.60 (ddd, *J* = 8.0 Hz, 1.6 Hz, 0.6 Hz,1H), 8.08 (dd, *J* = 8.3 Hz, 1.7 Hz, 1H), 7.71 (dd, *J* = 8.3 Hz, 1.5 Hz, 1H), 7.66-7.62 (m, 1H), 7.60-7.56 (m, 1H), 7.53-7.47 (m, 3H), 7.42-7.32 (m, 4H), 7.21 (ddd, *J* = 8.1 Hz, 1.4 Hz, 0.7 Hz, 1H), 7.14-7.10 (m, 2H), 6.91 (d, *J* = 8.3 Hz, 1H), 6.78 (d, *J* = 7.9 Hz, 1H). **^{13}C-NMR** (100 MHz, CDCl$_3$, 298 K) δ (ppm): 162.6, 151.1, 144.6, 140.8, 140.2, 138.2, 137.4, 137.1, 136.3, 133.0, 132.3, 132.1, 131.1, 131.0, 130.3, 129.7, 129.6, 129.4, 129.3, 129.0, 128.8, 127.5, 125.9, 125.3,125.2, 124.9, 124.0, 123.7, 122.2, 121.9, 117.5. **^{19}F-NMR** (400 MHz, CDCl$_3$, 298 K) δ (ppm): -62.7, -62.9, -63.1. **HRMS** (ESI, m/z): Calculated for $C_{32}H_{18}F_6N_2O$ [M+Na]$^+$ 583.1216, Found 583.1234. **R$_f$**: 0.60 (EtOAc:Hexane (8:2)). This compound is known and the data described is in agreement with the previous reports.[25]
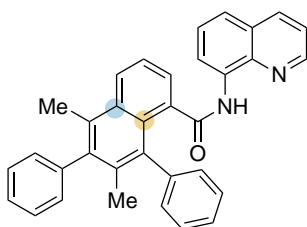
6,8-Dimethyl-5,7-diphenyl-*N*-(quinolin-8-yl)-1-naphtamide (2ah1)

Prepared in accordance to the general synthesis described above: **1a** (26.6 mg, 0.1 mmol) and **h** (23.2 mg, 0.2 mmol) afforded a mixture of two isomers **2ah1:2ah2** (25.8 mg, 55%**,** 1.6:1.0 mixture of isomers were separated by column chromatography). **^{1}H-NMR** (400 MHz, CDCl$_3$, 298 K) δ (ppm): 10.21 (s, 1H), 8.98 (dd, *J* = 7.4 Hz, 1.6 Hz, 1H), 8.76 (dd, *J* = 4.3 Hz, 1.6 Hz, 1H), 8.19 (dd, *J* = 8.4 Hz, 2.3 Hz, 1H), 7.75 (dd, *J* = 6.9 Hz, 1.4 Hz, 1H), 7.62-7.51 (m, 5H), 7.47-7.43 (m, 2H), 7.41-7.29 (m, 6H), 7.23 (bs, 1H), 7.21 (bs, 1H), 2.42 (s, 3H), 1.85 (s, 3H). **^{13}C-NMR** (100 MHz, CDCl$_3$, 298 K) δ (ppm): 171.0, 148.4, 143.1, 142.3, 140.7, 138.8, 137.5, 136.5, 135.7, 134.9, 133.7, 133.1, 131.4, 130.6, 129.8, 129.5, 128.7, 128.6, 128.2, 127.6, 127.2, 126.9, 126.4, 124.2, 122.0, 121.8, 116.8, 20.3, 20.2. **HRMS** (ESI, m/z): Calculated for $C_{34}H_{26}N_2O$ [M+Na]$^+$ 501.1937, Found 501.1940. **R$_f$** : 0.61 (CH$_2$Cl$_2$).[23]

5,7-Dimethyl-6,8-diphenyl-*N*-(quinolin-8-yl)-1-naphtamide (2ah2)

Prepared in accordance to the general synthesis described above: **1a** (26.6 mg, 0.1 mmol)) and **h** (23.2 mg, 0.2 mmol) afforded a mixture of two isomers **2ah1:2ah2** (25.8 mg, 55%, 1.6:1.0 mixture of isomers separated by column chromatography). **^{1}H-NMR** (400 MHz, CDCl$_3$, 298 K) δ (ppm): 9.59 (s, 1H), 8.72 (dd, *J* = 4.2 Hz, 1.5 Hz, 1H), 8.27 (dt, *J* = 8.3 Hz, 1.3 Hz, 2H), 8.17 (dd, *J* = 8.4 Hz, 1.5 Hz, 1H), 7.67 (dd, *J* = 6.8 Hz, 1.3 Hz, 1H), 7.58 (dd, *J* = 8.4 Hz, 6.9 Hz, 1H), 6.48-7.36 (m, 8H), 7.25-7.24 (m, 2H), 7.00 (bs, 1H), 6.78 (tt, *J* = 7.4 Hz, 1.3 Hz, 1H), 6.33 (bs, 1H), 2.48 (s, 3H), 1.72 (s, 3H). **^{13}C-NMR** (100 MHz, CDCl$_3$, 298 K) δ (ppm): 169.4, 148.0, 142.3, 141.2, 140.3, 138.5, 137.0, 136.4, 136.2, 135.1, 134.7, 132.4, 132.3, 131.6, 131.3, 129.5, 128.6, 128.5, 127.8, 127.3, 126.9, 126.8, 126.6, 124.4, 121.4, 121.2, 116.9, 20.5, 17.7. **IR (ATR):** υ (cm^{-1}) = 3350, 3052, 3022, 2953, 2924, 2854, 1678, 1520, 1483, 1384, 1326,

790, 701. **HRMS** (ESI, m/z): Calculated for $C_{34}H_{26}N_2O$ [M+Na]$^+$ 501.1937, Found 501.1940. **R$_f$**: 0.47 (CH_2Cl_2).

4-Methyl-3-phenyl-2-(quinolin-8-yl)isoquinolin-1(*2H*)-one (3ah)

Prepared in accordance to the general synthesis described above: **1a** (26.6 mg, 0.1 mmol) and **h** (23.2 mg, 0.2 mmol) afforded **3ah** (5.6 mg, 12%) as major isomer (6.0:1.0, inseparables by column chromatography) as a pale yellow solid. **¹H-NMR** (400 MHz, CDCl$_3$, 298 K) δ (ppm): 8.90 (dd, *J* = 4.5 Hz, 1.8 Hz, 1H), 8.57 (d, *J* = 8.2 Hz, 1H), 8.05 (dd, *J* = 8.5 Hz, 1.8 Hz, 1H), 7.83-7.76 (m, 2H), 7.65 (dd, *J* = 8.2 Hz, 1.2 Hz, 1H), 7.56 (ddd, *J* = 8.2 Hz, 6.6 Hz, 1.9 Hz, 1H), 7.44-7.42 (m, 1H), 7.38-7.34 (m, 2H), 7.18-7.11 (m, 2H), 6.97 (tt, *J* = 7.8 Hz, 1.4 Hz, 1H), 6.86 (d, *J* = 7.8 Hz, 1H), 6.73 (t, *J* = 7.8 Hz, 1H), 2.12 (s, 3H). **¹³C-NMR** (100 MHz, CDCl$_3$, 298 K) δ (ppm): 162.8, 151.0, 141.0, 138.3, 138.1, 136.1, 132.9, 132.7, 132.4, 131.0, 130.5, 129.4, 128.9, 128.6, 128.4, 127.9, 127.5, 127.3, 126.7, 126.1, 125.9, 123.7, 121.6, 110.3, 15.0. **HRMS** (ESI, m/z): Calculated for $C_{25}H_{18}N_2O$ [M+Na]$^+$ 385.1311, Found 385.1307. **R$_f$**: 0.15 (EtOAc:Hexane, 4:6). This compound is known and the data described is in agreement with the previous reports.[26]

6,8-Diethyl-5,7-diphenyl-N-(quinolin-8-yl)-1-naphthamide (2ai1)
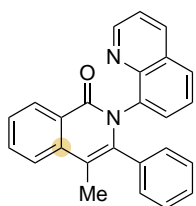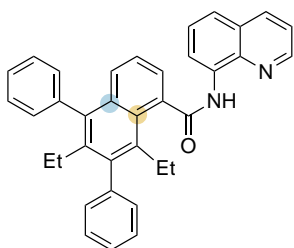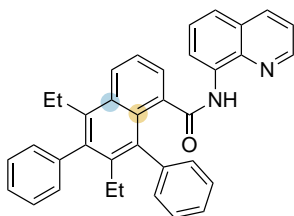
Prepared in accordance to the general synthesis described above: **1a** (26.6 mg, 0.1 mmol) and **i** (26.0 mg, 0.2 mmol) afforded a mixture of two isomers **2ai1:2ai2** (24.9 mg, 49%, 1.0:1.0 mixture of isomers separated by column chromatography). **¹H-NMR** (400 MHz, CDCl$_3$, 298 K) δ (ppm): 10.22 (s, 1H), 8.97 (dd, *J* = 7.4 Hz, 1.6 Hz, 1H), 8.74 (dd, *J* = 4.3 Hz, 1.8 Hz, 1H), 8.19 (dd, *J* = 8.4 Hz, 1.8 Hz, 1H), 7.67 (dd, *J* = 6.9 Hz, 1.5 Hz, 1H), 7.60 (d, *J* = 7.6 Hz, 1H), 7.55-7.53 (m, 1H), 7.52-7.49 (m, 2H), 7.48-7.43 (m, 4H), 7.38-7.35 (m, 4H), 7.32-7.28 (m, 3H), 2.95-2.90 (m, 2H), 2.26 (q, *J* = 7.5 Hz, 2H), 0.90 (t, *J* = 6.9 Hz, 3H), 0.70 (t, *J* = 6.9 Hz, 3H). **¹³C-NMR** (100 MHz, CDCl$_3$, 298 K) δ (ppm): 171.1, 148.4, 142.2, 141.4, 140.4, 139.4, 138.7, 138.4, 137.3, 136.5, 135.5, 135.0, 134.6, 130.7, 130.1, 130.0, 128.4, 128.2, 127.9, 127.6, 126.3, 127.2, 126.8, 126.7, 126.5, 124.0, 122.0, 121.8, 116.8, 25.2, 24.9, 16.4, 15.4. **HRMS** (ESI, m/z): Calculated for $C_{36}H_{30}N_2O$ [M+Na]$^+$ 529.2250, Found 529.2257. **R$_f$**: 0.71 (CH_2Cl_2). This compound is known and the data described is in agreement with the previous reports.[23]

5,7-Diethyl-6,8-diphenyl-N-(quinolin-8-yl)-1-naphthamide (2ai2)

Prepared in accordance to the general synthesis described above: **1a** (26.6 mg, 0.1 mmol) and **i** (26.0 mg, 0.2 mmol) afforded a mixture of two isomers **2ai1:2ai2** (24.9 mg, 49%, 1.0:1.0 mixture of isomers separated by column chromatography). **¹H-NMR** (400 MHz, CDCl$_3$, 298 K) δ (ppm): 9.58 (s, 1H), 8.72 (dd, *J* = 4.3 Hz, 1.6 Hz, 1H), 8.27 (ddd, *J* = 7.2 Hz, 5.6 Hz, 1.5 Hz, 2H), 8.17 (dd, *J* = 8.3 Hz, 1.6 Hz, 1H), 7.62 (dd, *J* = 7.0 Hz, 1.3 Hz, 1H), 7.54 (dd, *J* = 8.4 Hz, 7.0 Hz, 1H), 7.49-7.39 (m, 7H), 7.32 (d, *J* = 7.2 Hz, 2H), 7.22 (bs, 1H), 7.06 (bs, 1H), 6.73 (tt, *J* = 7.6 Hz, 1.2 Hz, 1H), 6.32 (bs, 1H), 2.87 (q, *J* = 7.6 Hz, 2H), 2.18 (m, 2H), 1.20 (t, *J* = 7.6 Hz, 3H), 0.60 (t, *J* = 7.6 Hz, 3H). **¹³C-NMR** (100 MHz, CDCl$_3$, 298 K) δ (ppm): 169.5, 148.0, 141.4, 141.1, 140.3, 139.5, 138.5, 138.4, 137.5, 136.4, 136.1, 134.8, 131.3, 129.8, 129.2, 129.0,

128.1, 127.9, 127.3, 127.1, 127.0, 126.8, 126.6, 124.4, 121.4, 121.2, 116.9, 25.1, 23.9, 15.7, 15.3. **IR (ATR):** υ (cm^{-1}) = 3350, 3054, 2969, 2930, 2873, 1676, 1519, 1483, 1423, 1384, 1326, 1264, 734, 703. **HRMS** (ESI, m/z): Calculated for $C_{36}H_{30}N_2O$ [M+Na]$^+$ 529.2250, Found 529.2257. **R$_f$:** 0.50 (CH$_2$Cl$_2$).

4-Ethyl-3-phenyl-2-(quinolin-8-yl)isoquinolin-1(2*H*)-one (3ai)

Prepared in accordance to the general synthesis described above: **1a** (26.6 mg, 0.1 mmol) and **i** (26.0 mg, 0.2 mmol) afforded **3ai** (5.3 mg, 14%) as major isomer (11.5:1.0, inseparables by column chromatography), as a pale brown solid. **^{1}H-NMR** (400 MHz, CDCl$_3$, 298 K) δ (ppm): 8.89 (dd, *J* = 4.2 Hz, 1.8 Hz, 1H), 8.58 (dd, *J* = 8.1 Hz, 1.7 Hz, 1H), 8.04 (dd, *J* = 8.2 Hz, 1.8 Hz, 1H), 7.86 (d, *J* = 7.8 Hz, 1H), 7.78 (dd, *J* = 7.1 Hz, 1.5 Hz, 1H), 7.64 (dd, *J* = 8.2 Hz, 1.5 Hz, 1H), 7.54 (ddd, *J* = 8.2 Hz, 7.1 Hz, 1.2 Hz, 1H), 7.45 (dd, *J* = 7.3 Hz, 1.5 Hz, 1H), 7.37-7.33 (m, 2H), 7.20 (dt, *J* = 7.6 Hz, 1.3 Hz, 1H), 7.12 (td, *J* = 7.6 Hz, 1.0 Hz, 1H), 6.97 (tt, *J* = 7.3 Hz, 1.3 Hz, 1H), 6.89 (dt, *J* = 7.8 Hz, 1.3 Hz, 1H), 6.72 (td, *J* = 7.8 Hz, 1.0 Hz, 1H), 2.60-2.47 (m, 2H), 1.15 (t, *J* = 7.6 Hz, 3H). **^{13}C-NMR** (100 MHz, CDCl$_3$, 298 K) δ (ppm): 162.7, 150.9, 144.9, 141.0, 138.1, 137.2, 136.0, 135.4, 132.6, 131.1, 130.3, 129.2, 129.1, 128.9, 128.6, 127.9, 127.4, 127.2, 126.5, 126.4, 125.8, 123.6, 121.5, 116.4, 21.8, 15.0. **HRMS** (ESI, m/z): Calculated for $C_{26}H_{20}N_2O$ [M+Na]$^+$ 399.1468, Found 399.1480. **R$_f$:** 0.17 (EtOAc:Hexane, 1:1).This compound is known and the data described is in agreement with the previous reports.[25]
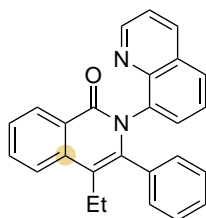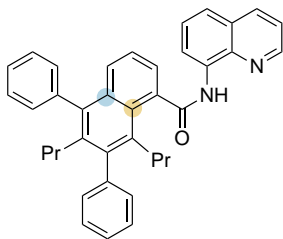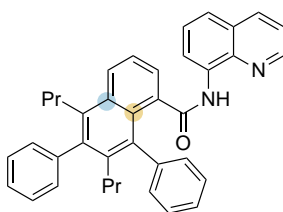
5,7-Diphenyl-6,8-dipropyl-*N*-(quinolin-8-yl)-1-naphtahamide (2aj1)

Prepared in accordance to the general synthesis described above: **1a** (26.6 mg, 0.1 mmol) and **j** (28.8 mg, 0.2 mmol) afforded a mixture of two isomers **2aj1:2aj2** (21.7 mg, 41%, 1.0:1.2 mixture of isomers separated by column chromatography). **^{1}H-NMR** (400 MHz, CDCl$_3$, 298 K) δ (ppm): 10.25 (s, 1H), 9.00 (d, *J* = 7.5 Hz, 1H), 8.74 (m, 1H), 8.19 (dd, *J* = 8.4 Hz, 0.8 Hz, 1H), 7.66-7.31 (m, 16H), 2.84-2.80 (m, 2H), 2.17-2.13 (m, 2H), 1.44-1.38 (m, 2H), 1.18-1.12 (m, 2H), 0.39-0.33 (m, 6H). **^{13}C-NMR** (100 MHz, CDCl$_3$, 298 K) δ (ppm): 171.2, 148.3, 142.5, 141.5, 140.5, 138.7, 138.4, 137.5, 137.0, 136.4, 135.5, 134.4, 130.8, 130.3, 130.1, 130.0, 128.4, 128.2, 127.9, 127.6, 127.3, 127.1, 126.9, 126.8, 126.5, 126.0, 125.9, 124.5, 124.0, 122.0, 121.8, 116.8, 34.5, 34.2, 25.6, 24.4, 14.6, 14.3. **IR (ATR):** υ (cm^{-1}) = 3342, 3053, 2958, 2869, 1672, 1597, 1517, 1479, 1423, 1384, 1324, 1262, 1204, 1150, 1068, 824, 791, 736, 703. **HRMS** (ESI, m/z): Calculated for $C_{38}H_{34}N_2O$ [M+Na]$^+$ 557.2563, Found 557.2568. **R$_f$:** 0.73 (CH$_2$Cl$_2$).

6,8-Diphenyl-5,7-dipropyl-*N*-(quinolin-8-yl)-1-naphthamide (2aj2)

Prepared in accordance to the general synthesis described above: **1a** (26.6 mg, 0.1 mmol) and **j** (28.8 mg, 0.2 mmol) afforded a mixture of two isomers **2aj1:2aj2** (21.7 mg, 41%, 1.0:1.2 mixture of isomers separated by column chromatography). **^{1}H-NMR** (400 MHz, CDCl$_3$, 298 K) δ (ppm): 9.58 (s, 1H), 8.71 (dd, *J* = 4.1 Hz, 1.6 Hz, 1H), 8.28 (dd, *J* = 7.5 Hz, 1.5 Hz, 1H), 8.23 (dd, *J* = 8.5 Hz, 1.1 Hz, 1H), 8.17 (dd, *J* = 8.3 Hz, 1.6 Hz, 1H), 7.61 (dd, *J* = 6.8 Hz, 1.1 Hz, 1H), 7.54-7.37 (m, 9H), 7.29-7.27 (m, 2H), 7.04 (bs, 1H), 6.73 (t,

J = 7.8 Hz, 1H), 6.31 (bs, 1H), 2.80-2.76 (m, 2H), 2.13-1.98 (m, 2H), 1.69-1.59 (m, 2H), 1.14-0.96 (m, 2H), 0.89 (t, *J* = 7.4 Hz, 3H), 0.25 (t, *J* = 7.4 Hz, 3H). **^{13}C-NMR** (100 MHz, CDCl$_3$, 298 K) δ (ppm): 169.5, 148.0, 141.5, 140.6, 140.1, 139.6, 138.5, 137.4, 137.1, 136.4, 136.1, 134.8, 131.6, 129.8, 129.1, 128.9, 128.0, 127.9, 127.5, 127.3, 127.0, 126.9, 126.8, 126.6, 124.2, 121.4, 121.2, 116.9, 34.4, 33.2, 24.8, 24.3, 14.9, 14.5. **IR (ATR):** υ (cm^{-1}) = 3345, 3053, 3022, 2958, 2929, 2870, 1674, 1519, 1482, 1423, 1384, 1325, 1263, 825, 790, 735, 702. **HRMS** (ESI, m/z): Calculated for C$_{38}$H$_{34}$N$_2$O [M+Na]$^+$ 557.2563, Found 557.2568. **R$_f$:** 0.57 (CH$_2$Cl$_2$).

3-Phenyl-4-propyl-2-(quinolin-8-yl)isoquinolin-1(*2H*)-one (3aj)

Prepared in accordance to the general synthesis described above: **1a** (26.6 mg, 0.1 mmol) and **j** (28.8 mg, 0.2 mmol) afforded **3aj** (3.20 mg, 8%) as a white solid. **^{1}H-NMR** (400 MHz, CDCl$_3$, 298 K) δ (ppm): 8.89 (dd, *J* = 4.2 Hz, 1.7 Hz, 1H), 8.58 (dd, *J* = 7.8 Hz, 1.2 Hz, 1H), 8.05 (dd, *J* = 8.2 Hz, 1.7 Hz, 1H), 7.83-7.73 (m, 2H), 7.65 (dd, *J* = 8.2 Hz, 1.6 Hz, 1H), 7.53 (ddd, *J* = 8.2 Hz, 6.8 Hz, 1.2 Hz, 1H), 7.43 (dd, *J* = 7.3 Hz 1.6 Hz, 1H), 7.38-7.33 (m, 2H), 7.19-7.09 (m, 2H), 6.99 (tt, *J* = 7.6 Hz, 1.2 Hz, 1H), 6.88 (d, *J* = 7.3 Hz, 1H), 6.71 (t, *J* = 8.6 Hz, 1H), 2.49-2.41 (m, 2H), 1.64-1.59 (m, 2H), 0.86-0.82 (m, 3H). **^{13}C-NMR** (100 MHz, CDCl$_3$, 298 K) δ (ppm): 162.6, 150.8, 144.9, 141.2, 138.1, 137.5, 136.1, 135.4, 132.6, 131.1, 130.4, 129.3, 129.0, 128.8, 128.5, 127.9, 127.3, 127.1, 126.5, 126.4, 125.8, 123.7, 121.5, 115.2, 31.0, 23.8, 14.6. **HRMS** (ESI, m/z): Calculated for C$_{27}$H$_{22}$N$_2$O [M+Na]$^+$ 413.1624, Found 413.1630. **R$_f$:** 0.21 (EtOAc:Hexane, 1:1).This compound is known and the data described is in agreement with the previous reports.[25]

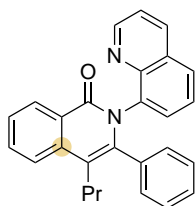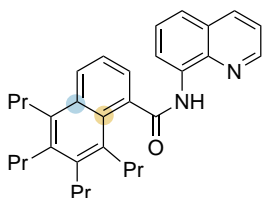## 5,6,7,8-Tetrapropyl-*N*-(quinolin-8-yl)-1-naphthamide (2ak)

Prepared in accordance to the general synthesis described above: **1a** (26.6 mg, 0.1 mmol) and **k** (22.0 mg, 0.2 mmol) afforded **2ak** (18.6 mg, 41%) as a colorless oil. **^{1}H-NMR** (400 MHz, CDCl$_3$, 298 K) δ (ppm): 10.15 (s, 1H), 9.04 (dd, *J* = 7.6 Hz, 1.3 Hz, 1H), 8.68 (dd, *J* = 4.20 Hz, 1.6 Hz, 1H), 8.19-8.14 (m, 2H), 7.66-7.55 (m, 3H), 7.45-7.41 (m, 2H), 3.08-3.00 (m, 4H), 2.78-2.70 (m, 4H), 1.77-1.68 (m, 2H), 1.66-1.50 (m, 6H), 1.16 (t, *J* = 7.30 Hz, 3H), 1.12 (t, *J* = 7.3 Hz, 3H), 1.03 (t, *J* = 7.3 Hz, 3H), 0.67 (t, *J* = 7.3 Hz, 3H). **^{13}C-NMR** (100 MHz, CDCl$_3$, 298 K) δ (ppm): 171.6, 148.3, 138.9, 138.7, 138.1, 136.4, 135.7, 135.2, 134.8 (2C), 132.5, 128.2, 128.1, 127.7, 127.0, 126.2, 123.4, 121.8, 121.7, 116.7, 33.0, 32.9, 32.7, 31.9, 25.8, 25.2, 25.0, 24.8, 15.2, 15.1, 15.0, 14.6. **HRMS** (ESI, m/z): Calculated for C$_{32}$H$_{38}$N$_2$O [M+Na]$^+$ 489.2882, Found 489.2879. **R$_f$:** 0.52 (EtOAc:Hexane (1:9)). This compound is known and the data described is in agreement with the previous reports.[22]

7-Fluoro-2,3-diphenyl-1-(pyrimidin-2-yl)-1*H*-indole (3da)
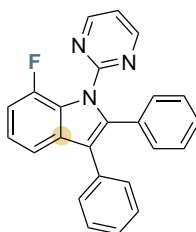
Prepared in accordance to the general synthesis described above: **1d** (18.9 mg, 0.1 mmol) and **a** (35.6 mg, 0.2 mmol) afforded **3da** as white solid. **^{1}H-NMR** (400 MHz, CDCl$_3$, 298 K) δ (ppm): 8.71 (d, *J* = 4.8 Hz, 2H), 7.52 (dd, *J* = 7.6 Hz, 0.8 Hz, 1H), 7.36-7.29 (m, 5H), 7.23 (t, *J* = 4.8 Hz, 1H), 7.19-7.11 (m, 6H), 6.97 (ddd, *J* = 12.4 Hz, 7.9 Hz, 0.8 Hz, 1H). **^{13}C-NMR** (100 MHz, CDCl$_3$, 298 K) δ (ppm): 158.4, 158.3, 149.9 (d, *J*$_{C-F}$ = 245.0 Hz), 138.0, 134.2, 132.1 (d, *J*$_{C-F}$ = 3.8 Hz), 131.3, 130.9, 130.4, 128.4, 128.1, 127.8, 126.6, 125.0 (d, *J*$_{C-F}$ = 10.4 Hz), 121.7 (d, *J*$_{C-F}$ = 6.7 Hz),

119.6, 118.8 (d, J_{C-F} = 2.1 Hz), 115.8 (d, J_{C-F} = 4.1 Hz), 109.5 (d, J_{C-F} = 17.9 Hz). **^{19}F-NMR** (400 MHz, CDCl$_3$, 298 K) δ (ppm): -127.9 ppm. **HRMS** (ESI, m/z): Calculated for C$_{24}$H$_{16}$FN$_3$ 388.1220, Found 388.1226. This compound is known and the data described is in agreement with the previous reports.[27]

N-(Quinolin-8-yl)-2-(1,2,3,4-tetraphenylbuta-1,3-dien-1-yl)benzamide (4aa):
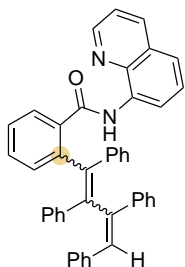
Prepared in accordance to the general synthesis described above: **INT4-H** (47.3 mg, 0.07 mmol) was converted to **4aa** (17.8 mg, 42%) as a yellow solid. **^{1}H-NMR** (400 MHz, CDCl$_3$, 298 K) δ (ppm): 10.26 (s, 1H), 8.90 (dd, *J* = 7.2 Hz, 1.4 Hz, 1H), 8.68 (dd, *J* = 4.1 Hz, 1.8 Hz, 1H), 8.17 (dd, *J* = 8.2 Hz, 1.6 Hz, 1H), 7.65 (dd, *J* = 7.8 Hz, 1.4 Hz, 1H), 7.58-7.53 (m, 2H), 7.43 (dd, *J* = 8.2 Hz, 4.1, Hz, 1H), 7.31-7.28 (m, 2H), 7.19 (ddd, *J* = 8.9 Hz, 7.6 Hz, 1.2 Hz, 1H), 7.13-7.11 (m, 2H), 7.09-7.06 (m, 2H), 7.02-6.87 (m, 12H), 6.81-6.77 (m, 2H), 6.58-6.55 (m, 3H). **^{13}C-NMR** (100 MHz, CDCl$_3$, 298 K) δ (ppm): 167.7, 148.0, 144.8, 143.9, 143.3, 143.0, 142.9, 140.9, 140.4, 138.7, 137.6, 137.5, 136.3, 135.3, 135.2, 132.0, 131.7 (2C), 131.5 (2C), 129.9, 129.8 (2C), 129.1 (2C), 128.1, 127.8, 127.7 (2C), 127.6 (3C), 127.5 (2C), 127.4 (2C), 127.1, 126.5, 126.4, 126.3, 126.2, 121.7, 121.5, 116.4. **IR (ATR):** υ (cm^{-1}) = 3348, 3055, 3021, 2961, 2925, 2854, 1670, 1596, 1576, 1521, 1486, 1443, 1424, 1384, 1326, 1260, 1074, 1024, 906, 824, 791, 758, 728, 695, 647, 628, 595. **HRMS (ESI, m/z):** Calculated for C$_{44}$H$_{32}$N$_2$O [M+Na]$^+$ 627.2407, Found 627.2382.

8. References

[1]   Mio, M. J.; Kopel, L. C.; Braun, J. B.; Gadzikwa, T. L.; Hull, K. L.; Brisbois, R. G.; Markworth, C. J.; Grieco, P. A. *Org. Lett.* **2002,** *4*, 3199-3202.
[2]   Mei, R.; Zhang, S.-K.; Ackermann, L. *Synlett* **2017,** *28*, 1715-1718.
[3]   Ackermann, L.; Lygin, A. V. *Org. Lett.* **2012,** *14*, 764-767.
[4]   Whiteoak, C. J.; Planas, O.; Company, A.; Ribas, X. *Adv. Synth. Catal.* **2016,** *358*, 1679-1688.
[5]   Bruker Advanced X-ray Solutions. SAINT +, Version 6.36A, **2001**.
[6]   Sheldrick, G. M. *Empirical Absorption Correction Program,* Universität Göttingen, **1996**.
[7]   Sheldrick, G. M*., Program for Crystal Structure Refinement,* Universität Göttingen, **1997**
[8]   Frisch, M. J. T., G. W.; Schlegel, H. B.; Scuseria, G. E.; Robb, M. A.; Cheeseman, J. R.; Scalmani, G.; Barone, V.; Petersson, G. A.; Nakatsuji, H.; Li, X.; Caricato, M.; Marenich, A. V.; Bloino, J.; Janesko, B. G.; Gomperts, R.; Mennucci, B.; Hratchian, H. P.; Ortiz, J. V.; Izmaylov, A. F.; Sonnenberg, J. L.; Williams-Young, D.; Ding, F.; Lipparini, F.; Egidi, F.; Goings, J.; Peng, B.; Petrone, A.; Henderson, T.; Ranasinghe, D.; Zakrzewski, V. G.; Gao, J.; Rega, N.; Zheng, G.; Liang, W.; Hada, M.; Ehara, M.; Toyota, K.; Fukuda, R.; Hasegawa, J.; Ishida, M.; Nakajima, T.; Honda, Y.; Kitao, O.; Nakai, H.; Vreven, T.; Throssell, K.; Montgomery, J. A., Jr.; Peralta, J. E.; Ogliaro, F.; Bearpark, M. J.; Heyd, J. J.; Brothers, E. N.; Kudin, K. N.; Staroverov, V. N.; Keith, T. A.; Kobayashi, R.; Normand, J.; Raghavachari, K.; Rendell, A. P.; Burant, J. C.; Iyengar, S. S.; Tomasi, J.; Cossi, M.; Millam, J. M.; Klene, M.; Adamo, C.; Cammi, R.; Ochterski, J. W.; Martin, R. L.; Morokuma, K.; Farkas, O.; Foresman, J. B.; Fox, D. J. *Gaussian*, Gaussian Inc.: Wallingford CT, 2016.
[9]   Zhao, Y.; Truhlar, D. G. *J. Chem. Phys.* **2006,** *125*, 194101.
[10]   Weigend, F.; Ahlrichs, R. *Phys. Chem. Chem. Phys.* **2005,** *7*, 3297-3305.
[11]   Weigend, F. *Phys. Chem. Chem. Phys.* **2006,** *8*, 1057-1065.
[12]   Becke, A. D. *J. Chem. Phys.* **1993**, *98*, 1372.
[13]   Lee, C.; Yang, W.; Parr, R. G. *Phys. Rev. B* **1988**, *37*, 785–789.
[14]   Vosko, S. H.; Wilk, L.; Nusair, M. *Can. J. Phys.* **1980**, *58*, 1200–1211.
[15]   Stephens, P. J.; Devlin, F. J.; Chabalowski, C. F.; Frisch, M. J. *J. Phys. Chem.* **1994**, *98*, 11623–11627.
[16]   Grimme, S.; Antony, J.; Ehrlich, S.; Krieg, H. *J. Chem. Phys.* **2010**, *132*, 154104.

[17]   Marenich, A. V.; Cramer, C. J.; Truhlar, D. G. *J. Phys. Chem. B* **2009,** *113*, 6378-6396.
[18]   Luchini, G.; Alegre-Requena, J. V.; Funes-Ardoiz, I.; Paton, R. S. F1000Research, **2020**, *9*, 291
[19]   Ribeiro, R. F.; Marenich, A. V.; Cramer, C. J.; Truhlar, D. G. *J. Phys. Chem. B* **2011**, *115*, 14556-14562.
[20]   Page, M.; Jr., J. W. M. *J. Chem. Phys.* **1988,** *88*, 922-935.
[21]   Page, M.; Doubleday, C.; Jr., J. W. M. *J. Chem. Phys.* **1990,** *93*, 5634-5642.
[22]   He, Z.; Huang, Y. *ACS Catal.* **2016,** *6*, 7814-7823.
[23]   Misal-Castro, L. C.; Obata, A.; Aihara, Y.; Chatani, N. *Chem. Eur. J.* **2016,** *22*, 1362-1367.
[24]   Grigorjeva, L.; Daugulis, O. *Org. Lett.* **2014,** *16*, 4684-4687.
[25]   Allu, S.; Swamy, K. C. K. *J. Org. Chem.* **2014,** *79*, 3963-3972.
[26]   Grigorjeva, L.; Daugulis, O. *Angew. Chem. Int. Ed.* **2014,** *53*, 10209-10212.
[27]   Song, W.; Ackermann, L. *Chem. Commun.* **2013,** *49*, 6638-6640.

Supporting Information for Chapter VI

Nickel-catalyzed C$_{sp2}$-OMe functionalization for chemoselective aromatic homologation en route to nanographenes

Lorena Capdevila, Judith Sala, Lutz Ackermann, Xavi Ribas*

Table of contents

1. General Considerations

All reagents and solvents were purchased from Sigma Aldrich, Fisher Scientific or Fluorochem and used without further purification. ^{1}H, ^{13}C{1H} and ^{19}F{H}-NMR spectra were recorded on Bruker 400 AVANCE spectrometer in the corresponding deuterated solvent (CDCl$_3$) and calibrated relative to the residual protons of the solvent. Quantification of reaction yields through integration of peaks was performed using an internal reference (1,3,5-trimethoxybenzene). High resolution mass spectra (HRMS) were recorded on a Bruker MicroTOF-Q IITM instrumentusing ESI source at Serveis Tècnics de Recerca, University of Girona. IR Spectra (FTIR) were recorded on a FT-IR Alpha spectrometer from Bruker with a PLATINUM-ATR attachment using OPUS software to process the data. All reactions were carried out in a N$_2$ drybox with O$_2$ and H$_2$O concentrations <1 ppm.

2. Synthesis of substrates

Substrates **1aa-1ac**[1] and **1ba-1ca**[2,3] were synthesized according to the previously described methods.

Preparation of 2-fluoro-6-methoxy-N-(quinoline-8-yl)benzamide (**1ad**)
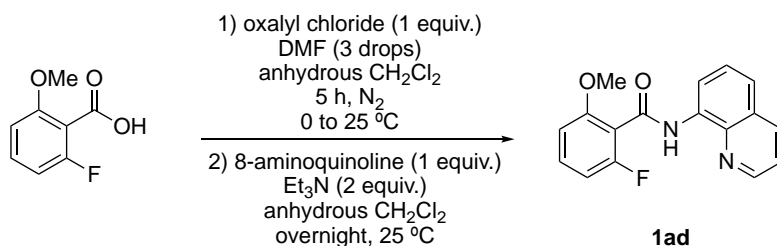
Scheme S1. Synthesis of **1ad** substrate

To a solution of 2-fluoro-6-methoxybenzoic acid (640.0 mg, 3.8 mmol, 1 equiv.), DMF (3 drops) in anhydrous CH$_2$Cl$_2$ (20 mL), oxalyl chloride (0.4 mL, 4.6 mmol, 1.2 equiv.) was added dropwise at 0 ºC under N$_2$ atmosphere. The mixture was heated at room temperature for 5 hours and the solvent was then removed under reduced pressure. To a solution of 8-aminoquinoline (714.0 mg, 4.9 mmol, 1.3 equiv.), Et$_3$N (1.1 mL, 7.9 mmol, 2.1 equiv.) in anhydrous CH$_2$Cl$_2$ (20 mL), the acid chloride dissolved in 5 mL of anhydrous CH$_2$Cl$_2$ was added dropwise at 0 ºC. The crude mixture was stirred at room temperature overnight. After that, the crude was quenched with NaHCO$_3$ (15 mL) and extracted with CH$_2$Cl$_2$. The combined organic layers were washed with aqueous HCl (1M), brine and dried over MgSO$_4$. The solvent was removed under reduced pressure and purified by column chromatography using CH$_2$Cl$_2$ as eluent affording the pure compound **1ad** in 74% isolated yield as white solid.
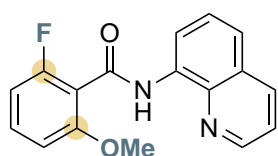
^{1}H-NMR (400 MHz, CDCl$_3$, 298 K) δ (ppm): 10.43 (s, 1H), 9.00 (dd, J = 7.5 Hz, 1.5 Hz, 1H), 8.81 (dd, J = 4.1 Hz, 1.5 Hz, 1H), 8.20 (dd, J = 7.9 Hz, 1.5 Hz, 1H), 7.63-7.55 (m, 2H), 7.45 (dd, J = 8.3 Hz, 4.1 Hz, 1H), 7.37 (m, 1H), 6.86.6.82 (m, 2H), 3.94 (s, 3H). **^{13}C-NMR** (100 MHz, CDCl$_3$, 298 K) δ (ppm): 161.3, 160.9 (d, J_{C-F} = 250.9 Hz), 158.1 (d, J_{C-F} = 7.1 Hz), 148.2, 138.6, 136.3, 134.7, 131.6 (d, J_{C-F} = 10.6 Hz), 128.0, 127.5, 121.9, 121.6, 117.0, 115.1 (d, J_{C-F} = 17.6 Hz), 108.8 (d, J_{C-F} = 21.7 Hz), 107.1 (d, J_{C-F} = 2.9 Hz), 56.4. **^{19}F-NMR** (400 MHz, CDCl$_3$, 298 K) δ (ppm): -114.62. **HRMS** (ESI, m/z): Calculated for C$_{17}$H$_{13}$FN$_2$O$_2$ [M+H]$^+$ 297.1034, Found

297.1033. **IR (ATR):** υ (cm^{-1}) = 3349, 3069, 3013, 2841, 1674, 1615, 1579, 1522, 1482, 1386, 1327, 1264, 1238, 1084, 898, 822, 783, 737, 666, 595, 484. **R$_f$** = 0.54 (CH$_2$Cl$_2$).

3. Reaction optimization

3.1 Concentration screening

Scheme S2. Optimization of conditions for C–OMe functionalization.

1aa (27.8 mg, 0.1 mmol, 1 equiv.), diphenylacetylene (36,0, mg, 0.2 mmol, 2 equiv.), LiOtBu (16.0 mg, 0.2 mmol, 2 equiv.) and Ni(cod)$_2$ (5.6 mg, 0.02 mmol, 20 mol %) with 1,4-dioxane (0.25 – 1.0 mL) were mixed in a glass vial under inert-atmosphere, and the vial was sealed. The reaction mixture was stirred at 140 ºC After 24 h, the crude mixture was extracted with dichloromethane (3 x 10 mL) and the organic layers were combined and dried over MgSO$_4$. The solvent was removed under reduced pressure and the crude mixture was analyzed by ^{1}H-NMR spectroscopy (CDCl$_3$) using 1,3,6-trimethoxybenzene as internal standard.

Table S1. Optimization of concentration for C–OMe functionalization.

Entry	1,4 –dioxane (mL)	2aa yield (%)[a]	3aa yield (%)[a]	Total yield (%)[a]	Ratio 2aa:3aa
1	0.25	38	15	53	2.5 :1
2	**0.5**	**47**	**27**	**74**	**1.7 :1**
3	1	0	0	0	-

[a] Yield calculated from ^{1}H-NMR of crude mixture using 1,3,5-trimethoxybenzene as internal standard.

3.2 Base screening

The same procedure was applied as described for the concentration studies, except 0.5 mL of 1,4-dioxane was used and the base was varied.

Table S2. Optimization of base for C–OMe functionalization.

Entry	Base (2 equiv.)	Additive (2 equiv.)	2aa yield (%)[a]	3aa yield (%)[a]	Total yield (%)[a]	Ratio 2aa:3aa
1	LiO^{t}Bu	-	47	27	74	1.7:1
2	Li$_2$CO$_3$	-	0	0	0	-
3	KO^{t}Bu	-	0	0	0	-
4	KO^{t}Bu	LiOTf	53	30	83	1.8:1

[a] Yield calculated from ^{1}H-NMR of crude mixture using 1,3,5-trimethoxybenzene as internal standard.

3.3 Equivalent of base and alkyne optimization

The effect of equivalents of base and alkyne was studied applying the optimized procedure.

Table S3. Optimization of the base and alkyne equivalents for C–OMe functionalization.

Entry	Eq. base	Eq. alkyne	2aa yield (%)[a]	3aa yield (%)[a]	Total yield (%)[a]	Ratio 2aa:3aa
1	2	2	47	27	74	1.7 :1
2	2	4	13	0	13	1:0
3	4	2	42	18	60	2.3 :1
4	2	1	35	10	45	3.5 :1

[a] Yield calculated from ^{1}H-NMR of crude mixture using 1,3,5-trimethoxybenzene as internal standard.

3.4 Role of Lewis acid

The effect of additives was studied using the optimized conditions.

Table S4. The role of the additives for C–OMe functionalization.

Entry	Additive (2 eq.)	2aa yield (%)[a]	3aa yield (%)[a]	Total yield (%)[a]	Ratio 2aa:3aa
1	-	47	27	74	1.7:1
2	Mg(OTf)$_2$	41	6	47	6.8:1
3	Zn(OTf)$_2$	0	0	0	-
4	LiOTf	38	5	43	7.6:1

[a] Yield calculated from ^{1}H-NMR of crude mixture using 1,3,5-trimethoxybenzene as internal standard.

3.5 Time study

The effect of variation of time was studied using the optimized conditions.

Table S5. Optimization of the time for C–OMe functionalization.

Entry	Eq. of LiOTf	Time (h)	2aa yield (%)[a]	3aa yield (%)[a]	Total yield (%)[a]	Ratio 2aa:3aa
1	-	24	47	27	74	1.7:1
2	2	24	38	5	43	7.6:1
3	2	5	49	4	53	12.3:1
4	2	3	59	5	64	11.8:1
5	2	2	27	4	31	6.8:1
6	2	1	31	8	39	3.9:1
7	2	30 min	11	3	14	3.7:1
8	4	24	51	5	56	10.2:1
9	4	3	38	2	4	19:1

[a] Yield calculated from ^{1}H-NMR of crude mixture using 1,3,5-trimethoxybenzene as internal standard.

3.6 Role of phosphine ligand and time study

The effect phosphine was studied using the optimized conditions at different reaction time.

Table S6. Optimization of the phosphine and reaction time for C–OMe functionalization.

Entry	PR$_3$ (2 equiv.)	Time (h)	2aa yield (%)[a]	3aa yield (%)[a]	Total yield (%)[a]	Ratio 2aa:3aa
1	-	24	47	27	74	1.7:1
2	PCy$_3$	24	0	0	0	-
3	PPh$_3$	24	tr	58	58	0:1
4	PPh$_3$	3	25	64	89	1:2.5

[a] Yield calculated from ^{1}H-NMR of crude mixture using 1,3,5-trimethoxybenzene as internal standard.

3.7 Control experiments

Control experiments were performed using the optimized conditions described above.

Table S7. Control experiments for C–OMe functionalization.

Entry	Additive (2 eq.)	Ni(COD)$_2$ (mol %)	Time (h)	2aa yield (%)[a]	3aa yield (%)[a]	Total yield (%)[a]
1	-	10	24	30	9	39
2	-	20	24	47	27	74
3	-	-	24	0	0	0
4	LiOTf	-	24	0	0	0
5	PPh$_3$	-	24	0	0	0

[a] Yield calculated from ^{1}H-NMR of crude mixture using 1,3,5-trimethoxybenzene as internal standard.

4. Reaction optimization for the formation of 4
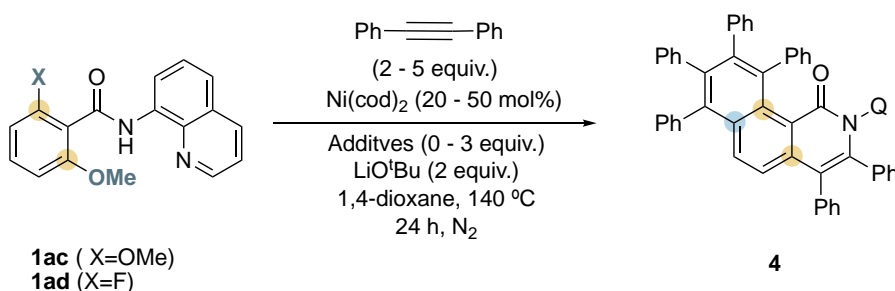
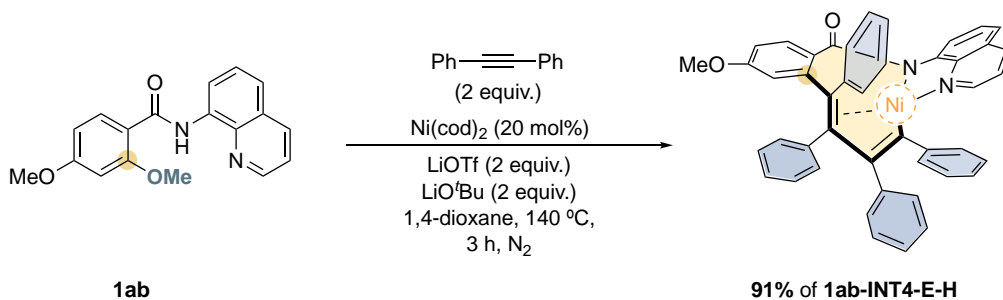**Scheme S3.** Optimization of reaction conditions to form **4**.

1ax (0.1 mmol, 1 equiv.), diphenylacetylene (2 - 5 equiv.), LiOtBu (16.0 mg, 0.2 mmol, 2 equiv.), LiOTf (0 - 2 equiv.), PPh$_3$ (1 - 3 equiv.) and Ni(cod)$_2$ (20 - 50 mol%) with 1,4-dioxane (0.5 mL) were mixed in a glass vial under inert-atmosphere, and the vial was sealed. The reaction mixture was stirred at 140 ºC After 24 h, the crude mixture was extracted with ethyl acetate (3 x 10 mL) and the organic layers were combined and dried over MgSO$_4$. The solvent was removed under reduced pressure. The product was purified by preparative layer using EtOAc/Hexane (3:7) as eluent and was analyzed by ^{1}H-NMR spectroscopy (CDCl$_3$) using 1,3,6-trimethoxybenzene as internal standard.

Table S8. Optimization of the formation of **4** using **1ac** and **1ad** substrates.

Entry	1ax	Alkyne (equiv.)	LiOTf (equiv.)	PPh$_3$ (equiv.)	Ni(cod)$_2$ (mol%)	4 yield (%)[a]
1		2	-	2	20	25%[b]
2		2	-	2	50	29%[b]
3	**1ac**	3	-	2	20	<10%
4		3	-	2	50	18%
5		5	-	2	20	<10%
6		5	2	2	20	-
7		2	2	2	20	<10%
8		5	2	3	20	<10%
9	**1ad**	5	2	2	10	<10%
10		5	2	2	20	(40%)[c]
11		5	2	1	20	27%
12		5	2	2	50	19%

[a] Yield calculated from ^{1}H-NMR of crude mixture after the preparative layer using 1,3,5-trimethoxybenzene as internal standard. [b] Yield based on the equivalents of alkyne. [c] Isolated yield.

5. Detection and isolation of 1ab-INT4-E-H

Scheme S4. Reaction conditions to synthesize **1ab-INT4-E-H**.

1ab (30.8 mg, 0.1 mmol, 1 equiv.), diphenylacetylene (36,0, mg, 0.2 mmol, 2 equiv.), LiOtBu (16.0 mg, 0.2 mmol, 2 equiv.), LiOTf (31.2 mg, 0.2 mmol, 2 equiv.) and Ni(cod)$_2$ (5.6 mg, 0.02 mmol, 20 mol %) with 1,4-dioxane (0.50 mL) were mixed in a glass vial under inert-atmosphere, and the vial was sealed. The reaction mixture was stirred at 140 ºC. After 3 h, the crude mixture was extracted with dichloromethane (3 x 10 mL) and the organic layers were combined and dried over MgSO$_4$. The solvent was removed under reduced pressure and the crude mixture was analyzed by ^{1}H-NMR spectroscopy (CDCl$_3$) using 1,3,6-trimethoxybenzene as internal standard. Purification by flash column chromatography afforded **1ab-INT4-E-H** as orange solid (91% based on Ni content).

^{1}H-NMR (400 MHz, CDCl$_3$, 298 K) δ (ppm): 9.06 (dd, J = 7.9 Hz, 0.9Hz, 1H), 8.28 (d, J = 7.3 Hz, 2H), 8.14 (dd, J = 8.4 Hz, 1,1 Hz, 1H), 8.01 (d, J = 8.6 Hz, 1H), 6.68 (m, 2H), 7.58 (t, J = 8.1 Hz, 1H), 7.42-7.38 (m, 2H), 7.36(m, 1H), 7.27 (d, J = 7.8 Hz, 1H), 7.13-7.04 (m, 6H), 6.99-6.95 (m, 6H), 6.91 (d, J = 2.4 Hz, 1H), 6.85-6.81 (m, 2H), 6.28 (d, J = 6.95 Hz, 2H), 3.80(s, 3H). **^{13}C-NMR** (100 MHz, CDCl$_3$, 298 K) δ (ppm): 169.2, 161.0, 159.9, 150.3, 148.4, 147.4, 145.4, 141.0, 140.7, 140.1, 138.8, 137.8, 135.2, 133.1, 131.3, 130.1, 128.9, 128.8, 128.4, 127.8, 127.7, 127.6, 127.3, 126.7, 126.5, 125.6, 125.5, 120.5, 120.0, 117.3, 116.8, 111.9, 108.8, 94.2, 55.3. **HRMS (ESI, m/z):** Calculated for C$_{45}$H$_{32}$NiN$_2$O$_2$ [M+H]$^+$ 691.1890, Found 691.1876. **IR (ATR):** υ (cm^{-1}) = 3053, 2954, 2921, 2851, 1593, 1552, 1498, 1460, 1376, 1324, 1274, 1216, 1074, 1027, 907, 822, 727, 694, 584, 470. **R$_f$**: 0.35 (EtOAc/Hexane (1:1)).
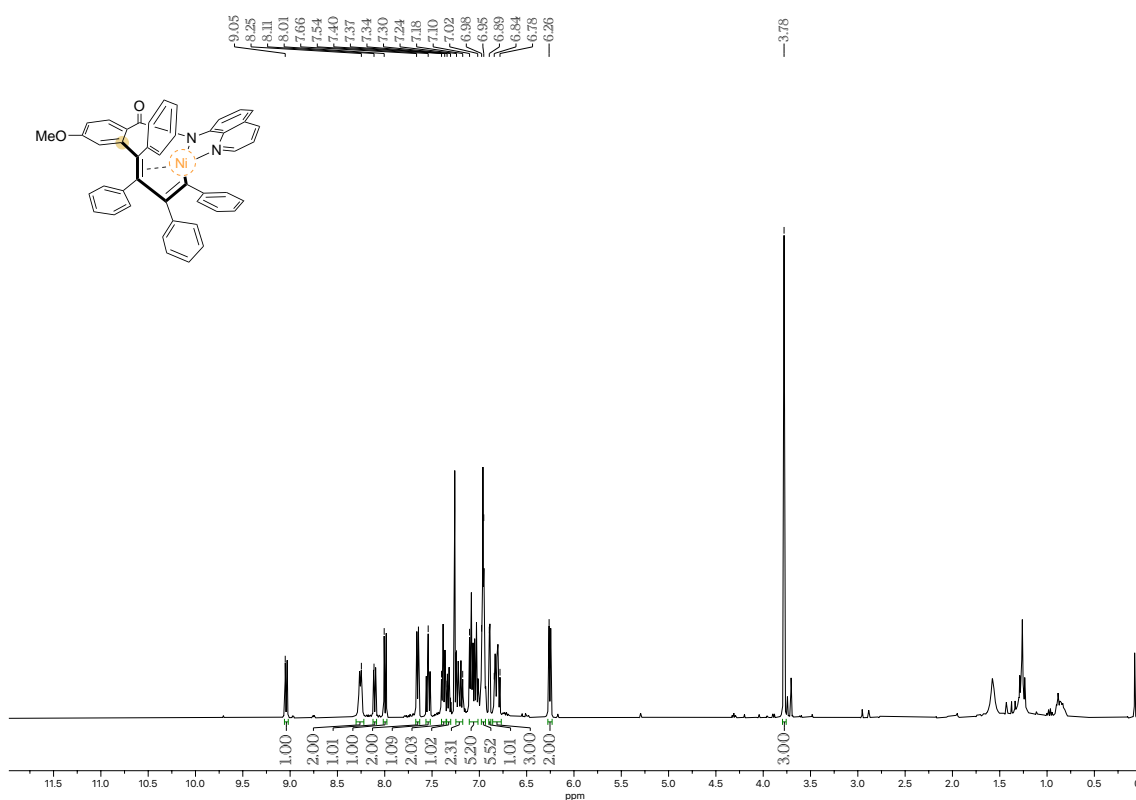

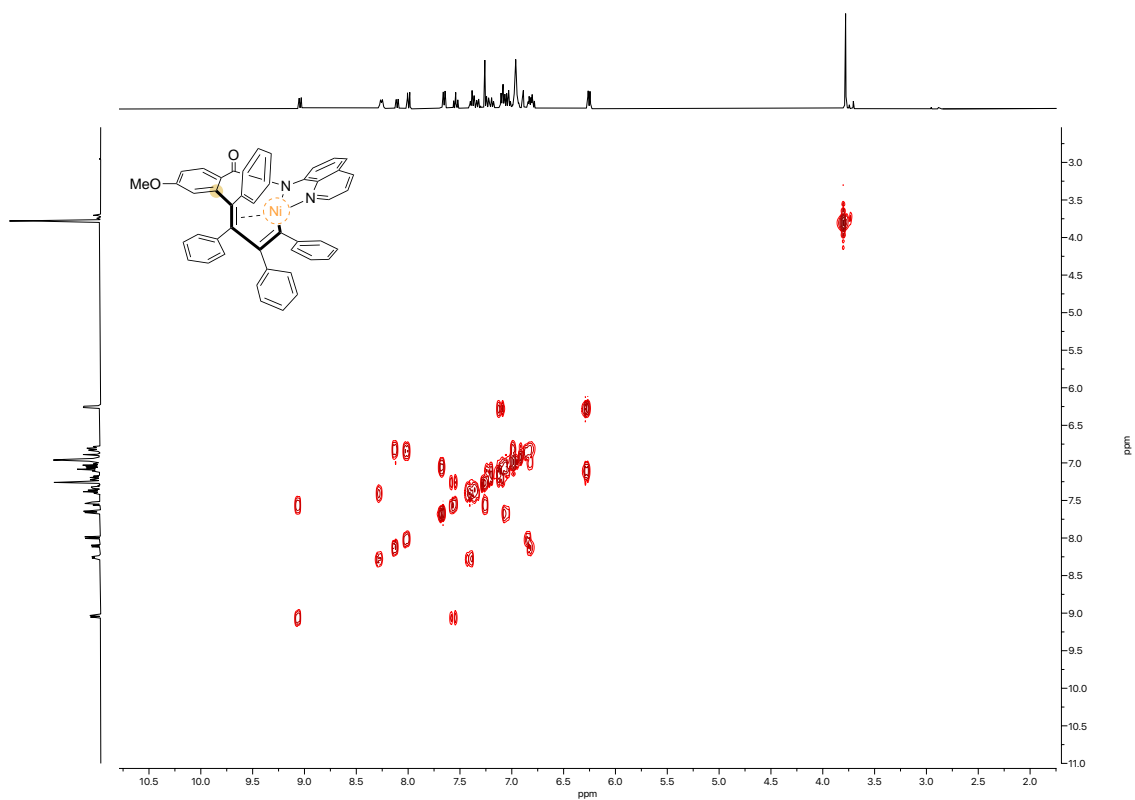**Figure S1.** 400 MHz ^{1}H-NMR spectrum of **1ab-INT4-E-H** in CDCl$_3$, 298K.

Figure S2. 400 MHz ^{1}H-^{1}H COSY NMR spectrum of **1ab-INT4-E-H** in CDCl$_3$, 298K.
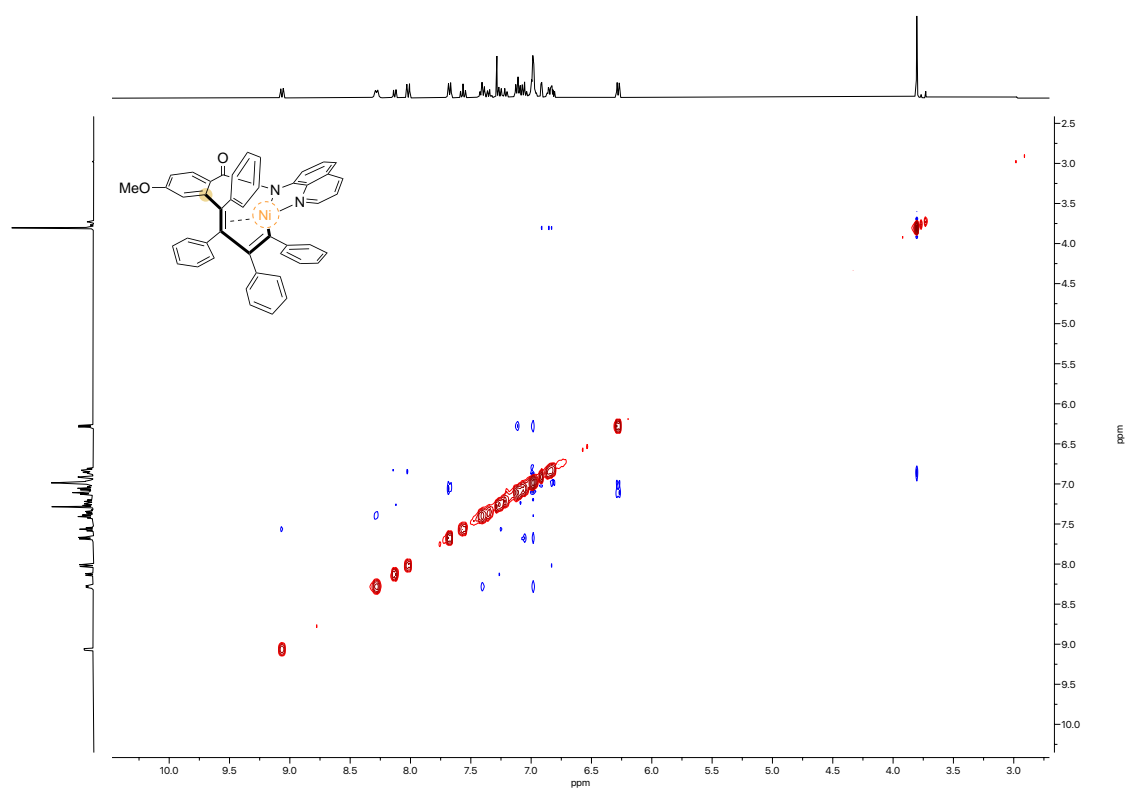

Figure S3. 400 MHz ^{1}H-^{1}H NOESY NMR spectrum of **1ab-INT4-E-H** in CDCl$_3$, 298K.
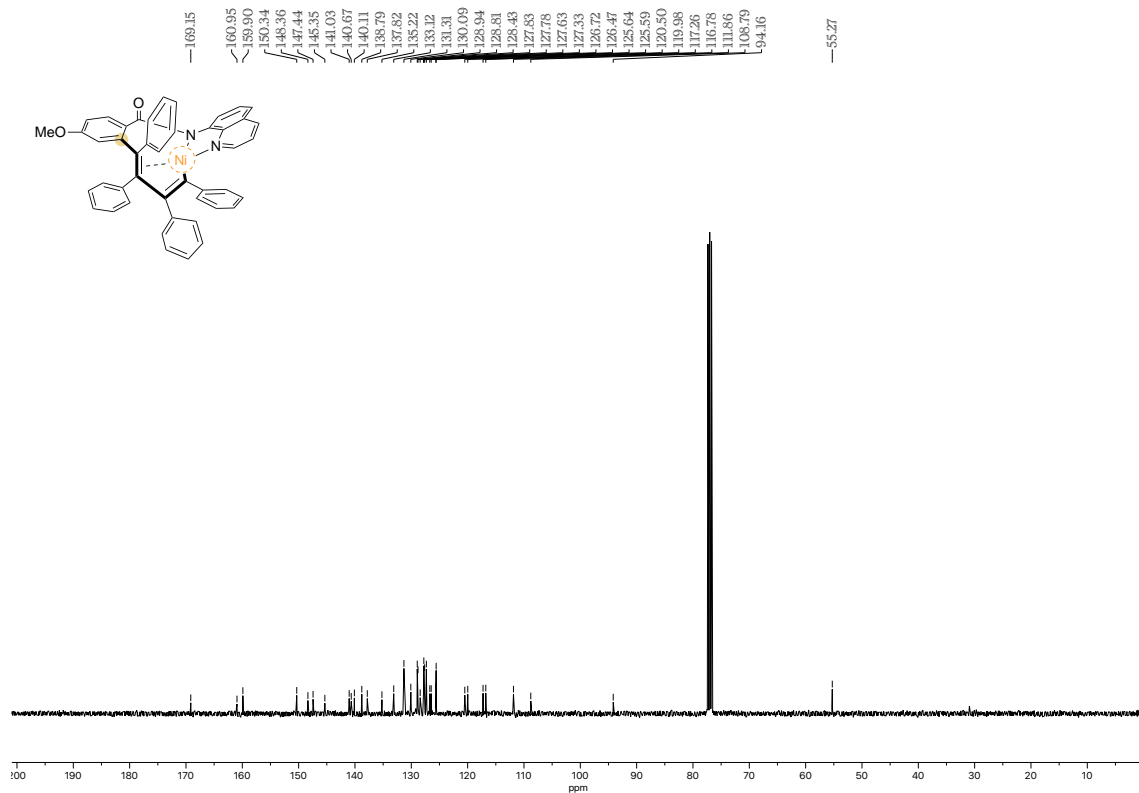
Figure S4. 100 MHz ^{13}C-NMR spectrum of **1ab-INT4-E-H** in CDCl$_3$, 298K.
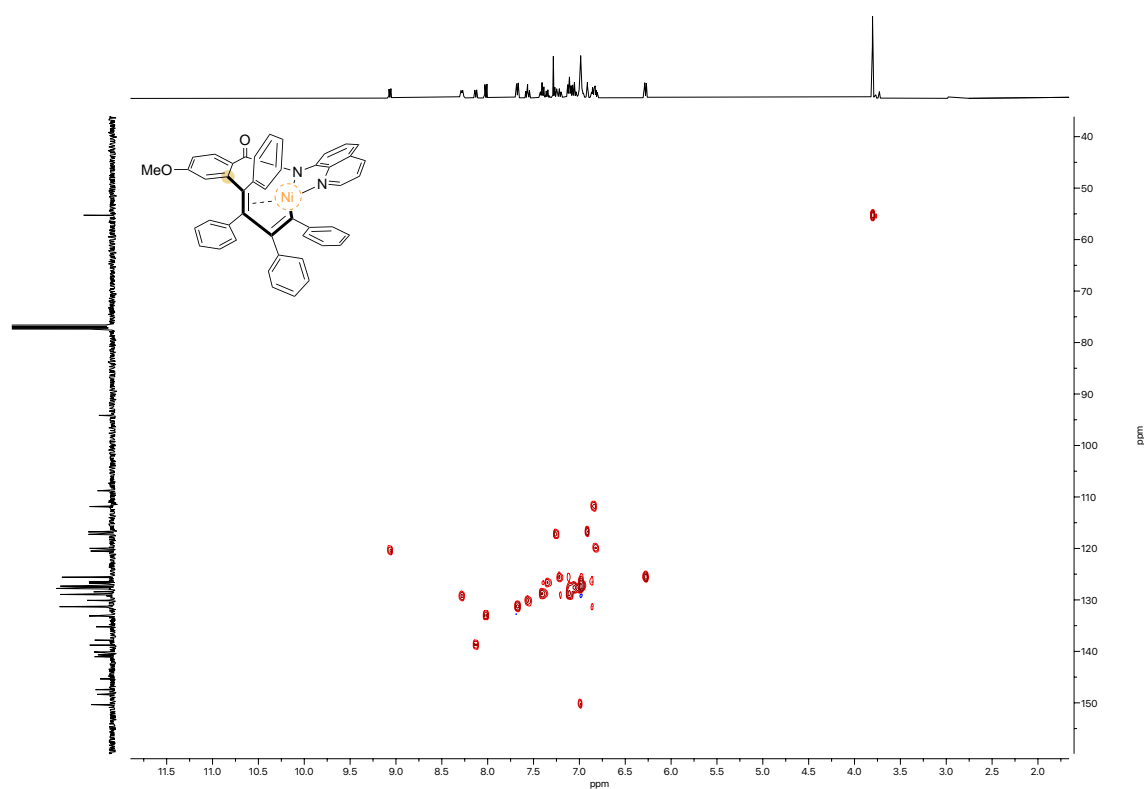

Figure S5. 400 MHz ^{1}H-^{13}C HSQC NMR spectrum of **1ab-INT4-E-H** in CDCl$_3$, 298K.
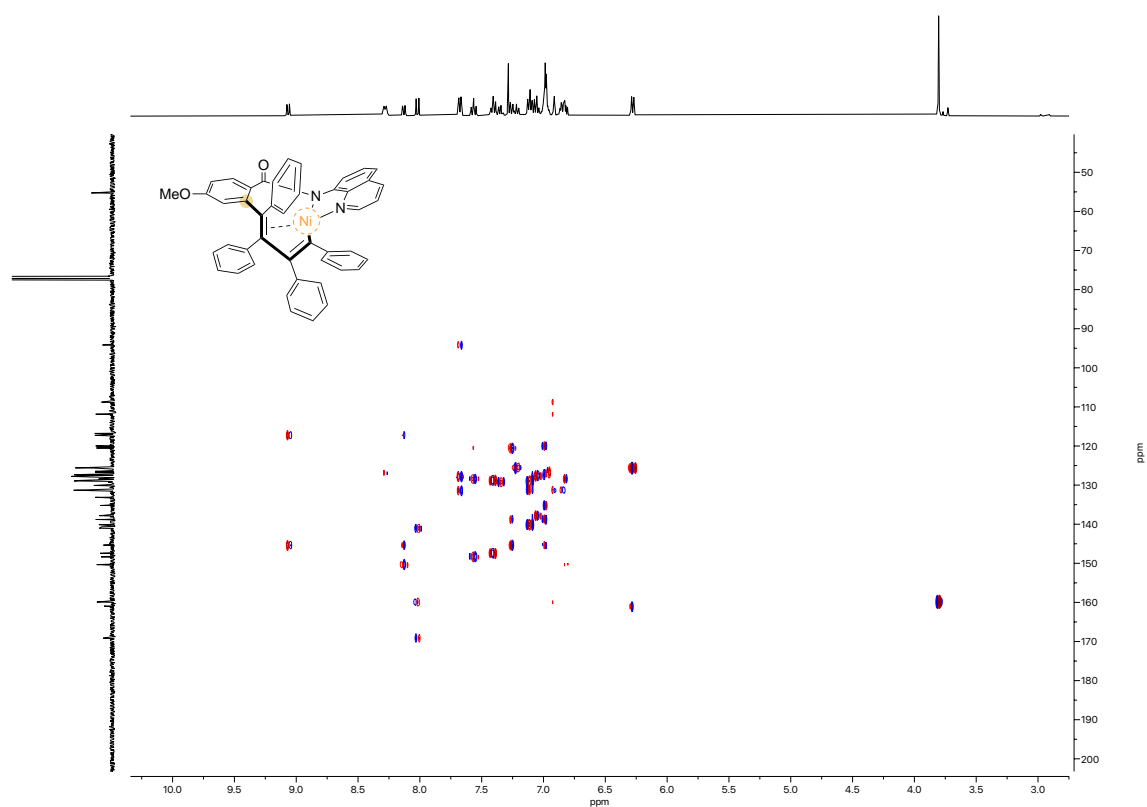
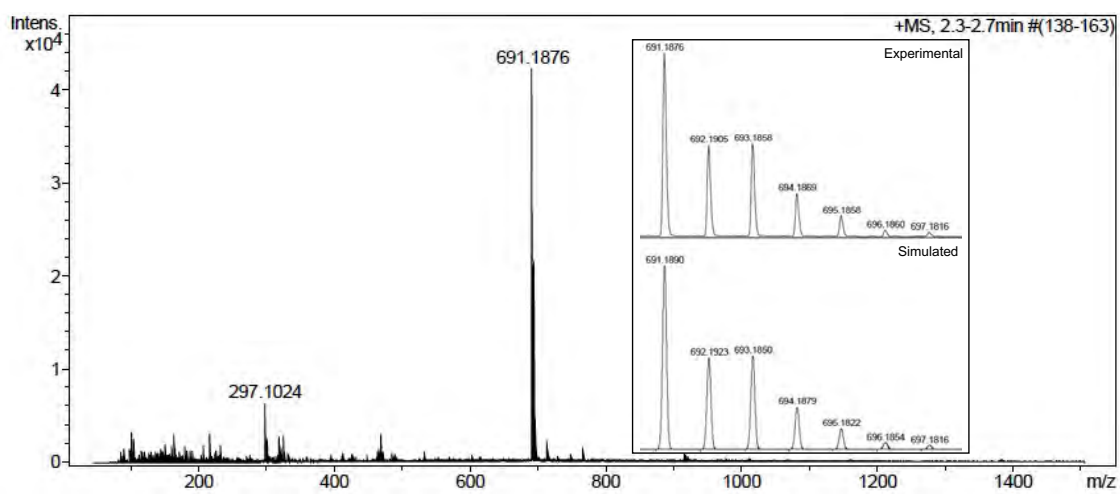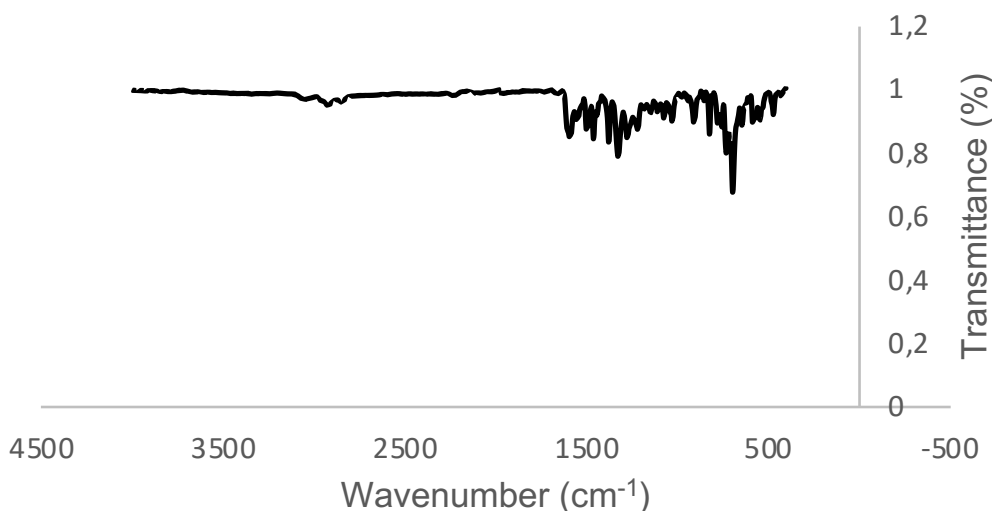**Figure S6.** 400 MHz ^{1}H-^{13}C HMBC NMR spectrum of **1ab-INT4-E-H** in CDCl$_3$, 298K
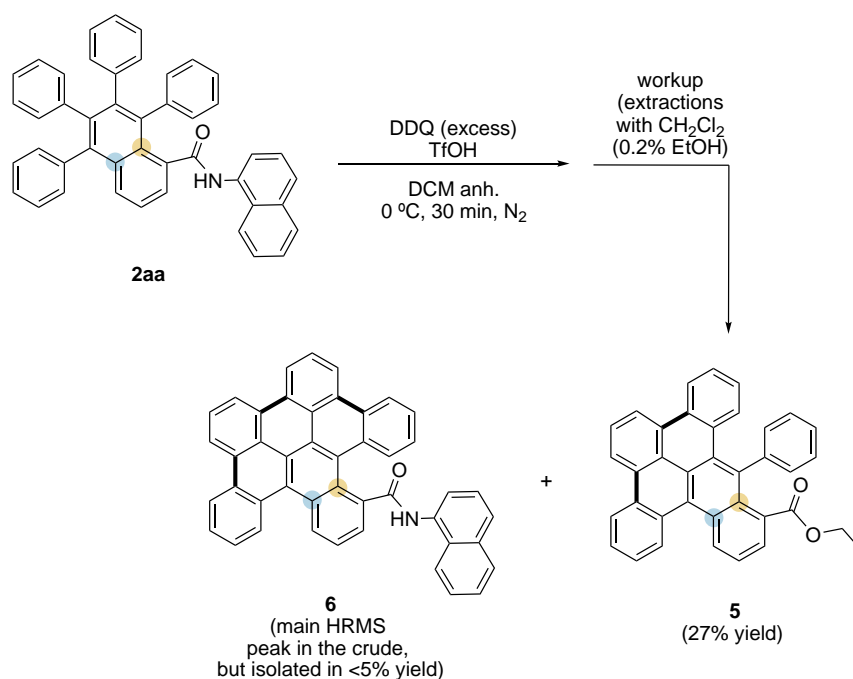

Figure S7. MS spectrum of **1ab-INT4-E-H.**

Figure S8. IR spectrum of **1ab-INT4-E-H**.

6. DDQ-oxidative coupling

Scheme S5. Synthetic protocol for the synthesis of compounds **5** and **6** from **2aa**.

2aa (40 mg, 0.066 mmol, 1 equiv.) was dissolved in anhydrous CH_2Cl_2 (50 mL) under N_2 atmosphere. The solution was cooled to 0 ºC and DDQ (749.1 mg, 3.30 mmol, 50 equiv.) was added in one portion. After, the TfOH (2.5 mL) was added dropwise, and the crude mixture was stirred during 30 minutes under N_2 bubbling. After that, the reaction is quenched with H_2O and extracted with CH_2Cl_2 (0.2% EtOH as stabilizer). The combined organic layers dried over $MgSO_4$ and the solvent was then removed under reduced pressure. The crude mixture was analyzed by HRMS and NMR spectroscopy.
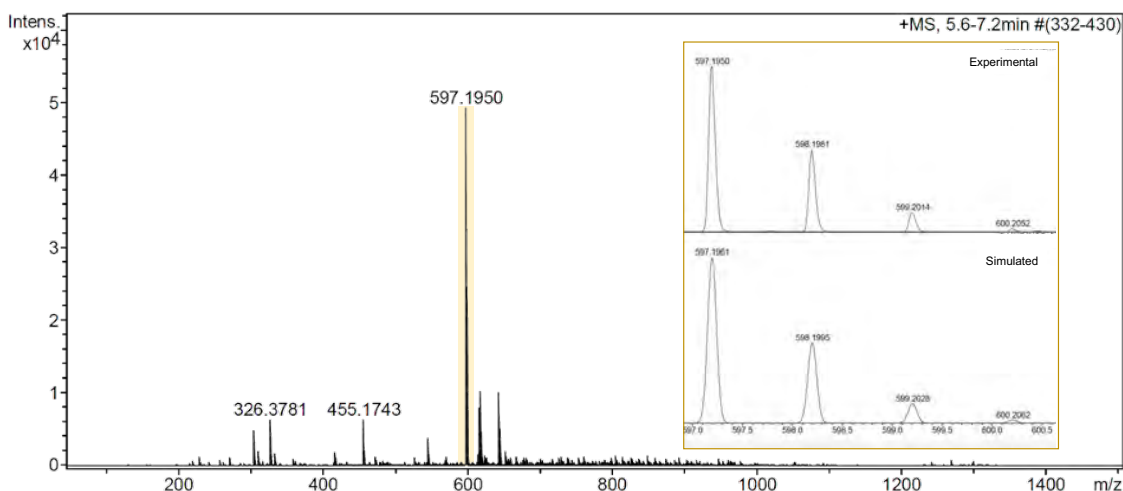
Figure S9. HRMS of the crude mixture obtained after reaction of **2aa** with DDQ and TfOH. Mass analysis shows a peak at *m/z* = 597.1950 which may correspond to the fully-fused compound bearing the 8-AQ group (see image). Compound **5** is not observable due to its neutral character, unless it is purified (C$_{37}$H$_{24}$O$_2$ [M+K]$^+$ 539.1614).

Ethyl 16-phenylbenzo[*fg*]naphtho[1,2,3-*op*]tetracene-1-carboxylate (5)
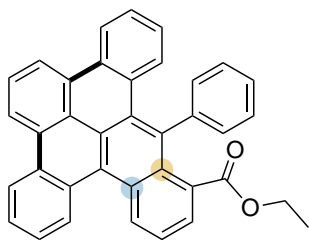
Prepared following the procedure detailed above: **2aa** (40.0 mg, 0.066 mmol) was converted to **6** as yellow solid (27% NMR yield). **^{1}H-NMR** (400 MHz, CDCl$_3$, 298 K) δ (ppm): 8.95 (m, 1H), 8.80 (m, 1H), 8.67 (dd, *J* = 7.9 Hz, 1.6 Hz, 1H), 8.62 (d, *J* = 8.2 Hz, 1H), 8.26 (d, *J* = 7.5 Hz, 1H), 8.14 (d, *J* = 7.5 Hz, 1H), 8.05 (dd, *J* = 7.9 Hz, 1.3 Hz, 1H), 7.95 (d, *J* = 7.5 Hz, 1H), 7.84-7.79 (m, 2H), 7.77 (t, *J* = 7.6 Hz, 1H), 7.65 (t, *J* = 8.1 Hz, 1H), 7.59-7.50 (m, 2H), 7.00 (m, 2H), 6.88 (tt, *J* = 7.3 Hz, 1.1 Hz, 1H), 6.80(m, 2H), 2.88 (dq, *J* = 8.5 Hz, 6.9 Hz, 1H), 2.58 (dq, *J* = 8.5 Hz, 6.9 Hz, 1H), 0.45 (t, *J* = 6.9 Hz, 3H). **^{13}C-NMR** (100 MHz, CDCl$_3$, 298 K) δ (ppm): 170.3, 152.1, 134.2, 133.2, 132.2, 131.8, 131.6, 131.4, 130.9, 130.8, 130.7, 130.3, 130.0, 129.7, 129.6, 129.2, 128.6, 128.5, 127.9, 127.85, 127.80, 127.7, 127.4, 126.5, 125.7, 124.9, 123.6, 122.7, 122.2, 122.0, 120.5, 59.6, 15.0. **HRMS** (ESI, m/z): Calculated for C$_{37}$H$_{24}$O$_2$ [M+K]$^+$ 539.1408, Found 539.1614. **IR (ATR):** υ (cm^{-1}) = 3059, 2962, 2923, 2870, 2854, 1765, 1484, 1459, 1446, 1260, 1061, 1017, 963. **R$_f$** = 0.70 (CH$_2$Cl$_2$).
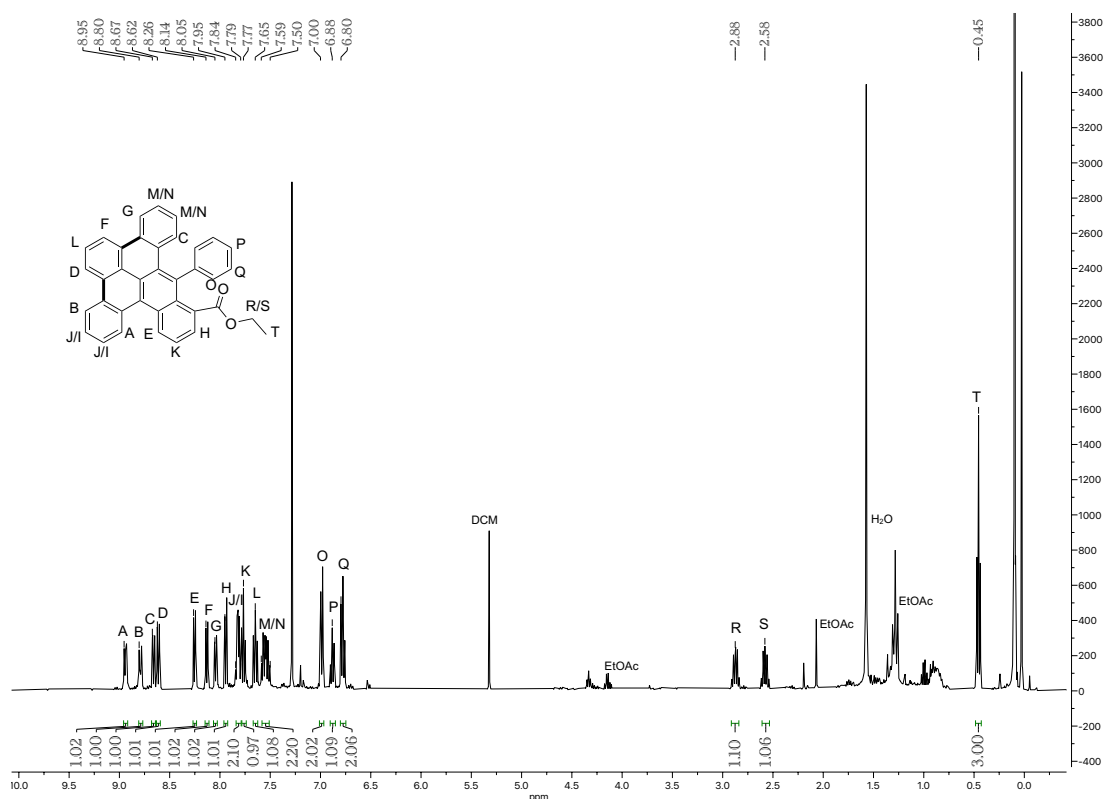
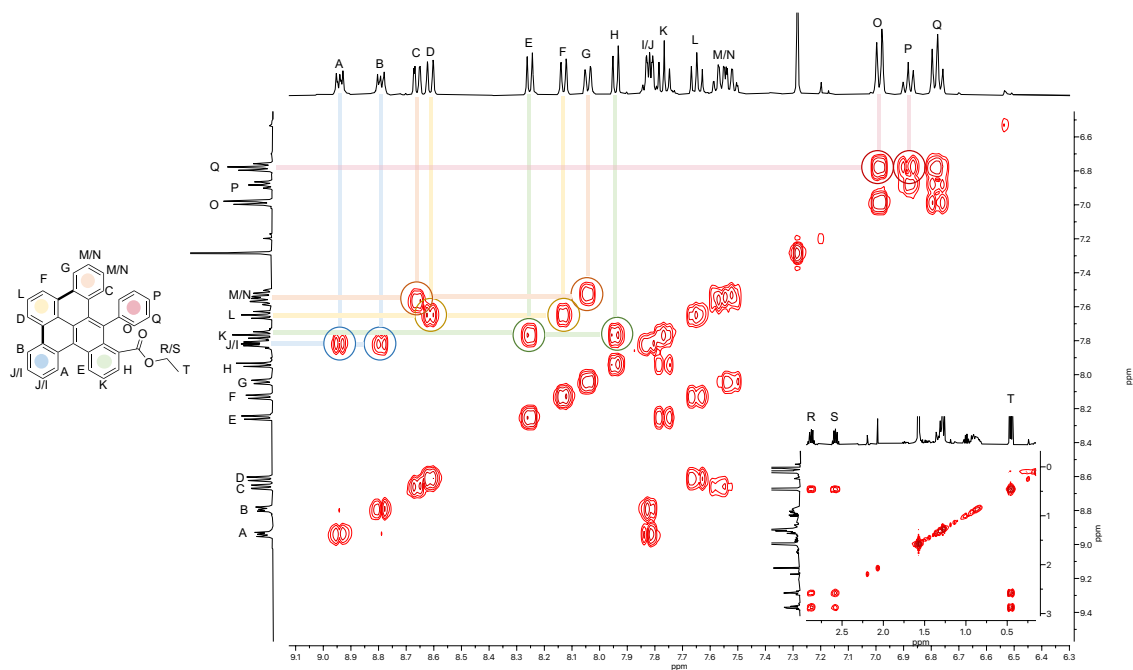**Figure S10.** 400 MHz ^{1}H-NMR spectrum of **5** in CDCl$_3$, 298K.
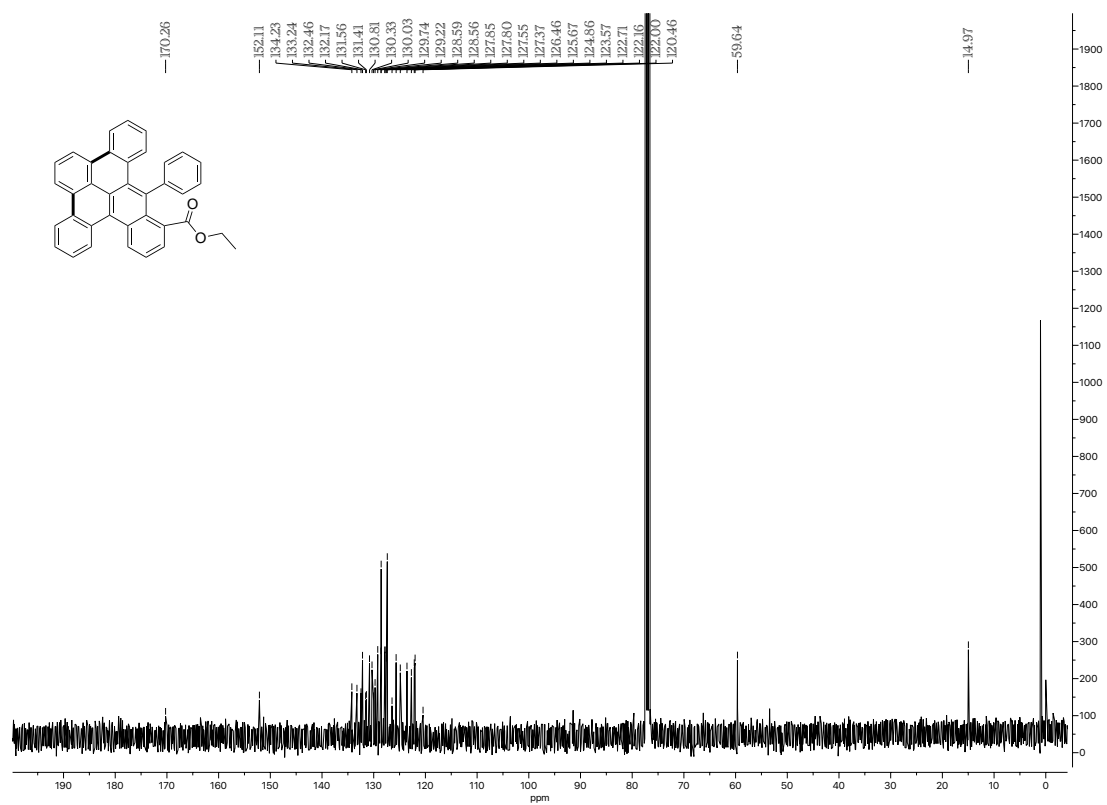

Figure S11. 400 MHz ^{1}H-^{1}H COSY NMR spectrum of **5** in CDCl$_3$, 298K.

Figure S12. 400 MHz ^{1}H-^{1}H NOESY NMR spectrum of **5** in CDCl$_3$, 298K.

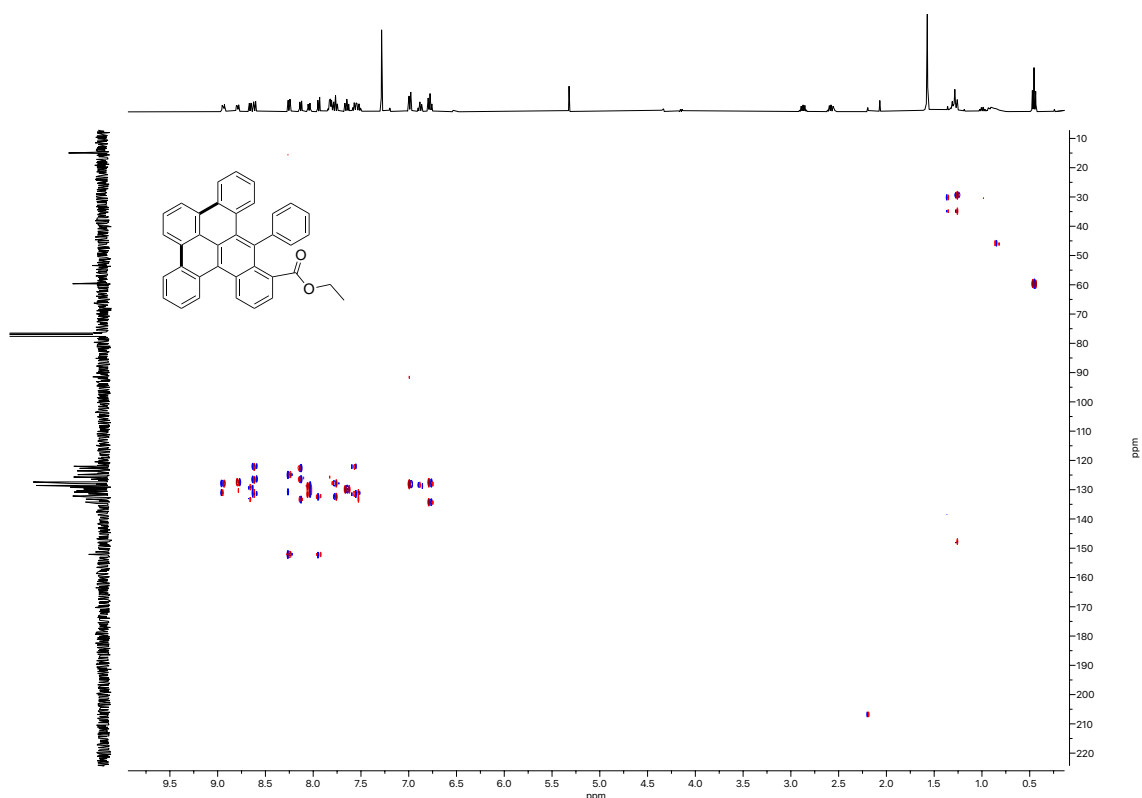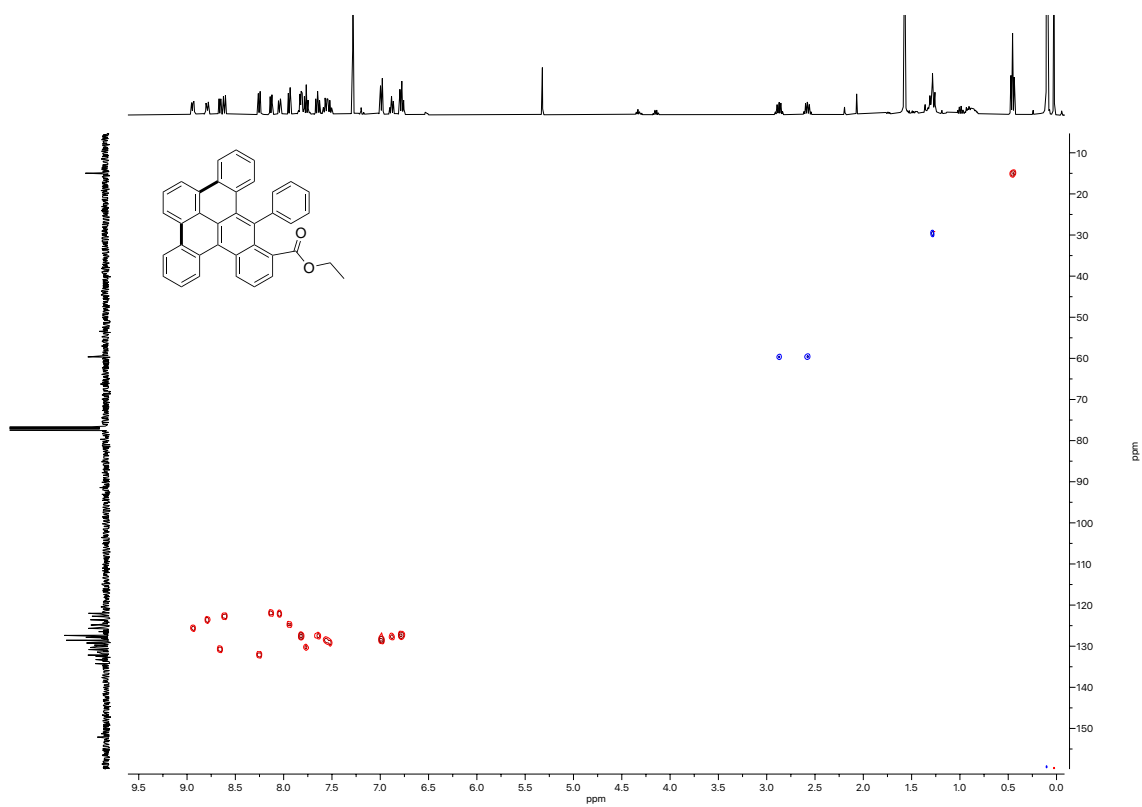**Figure S13.** 100 MHz ^{13}C-NMR spectrum of **5** in CDCl$_3$, 298K.

Figure S14. 400 MHz ^{1}H-^{13}C HSQC NMR spectrum of **5** in CDCl$_3$, 298K.

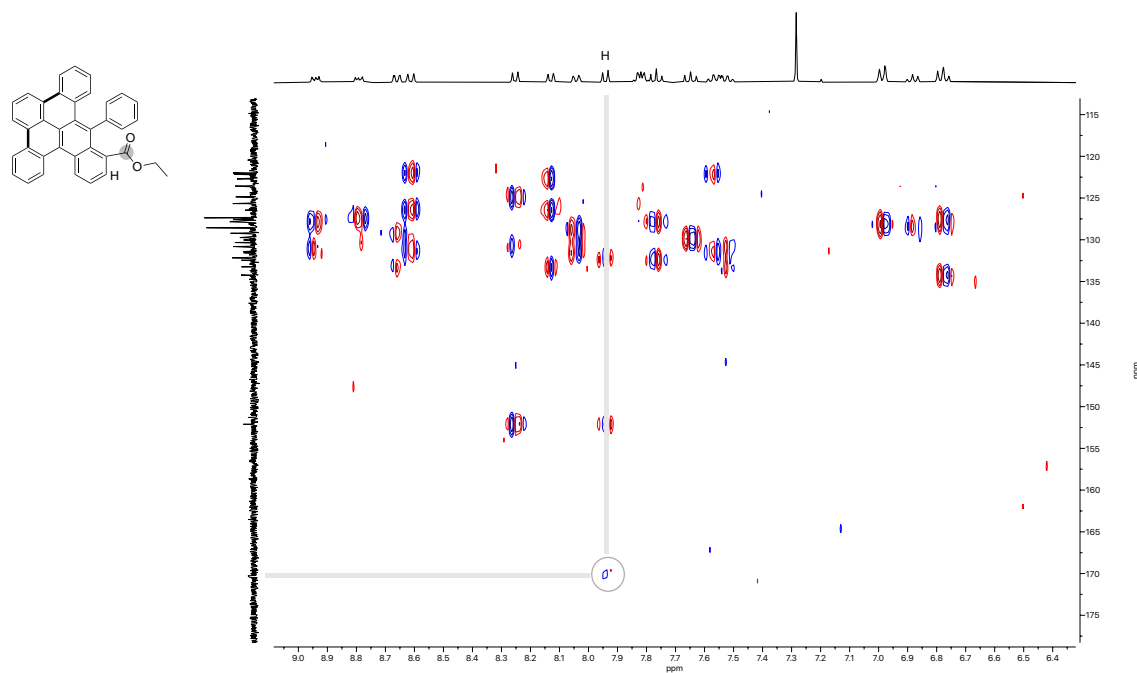**Figure S15.** 400 MHz ^{1}H-^{13}C HMBC NMR spectrum of **5** in CDCl$_3$, 298K
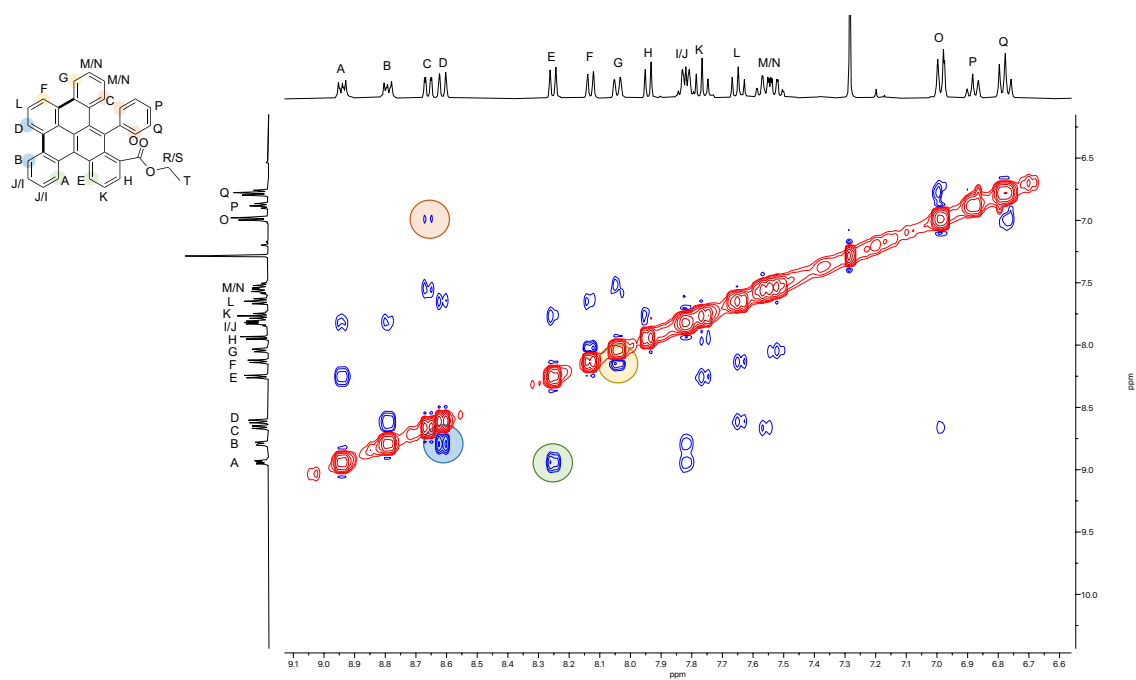
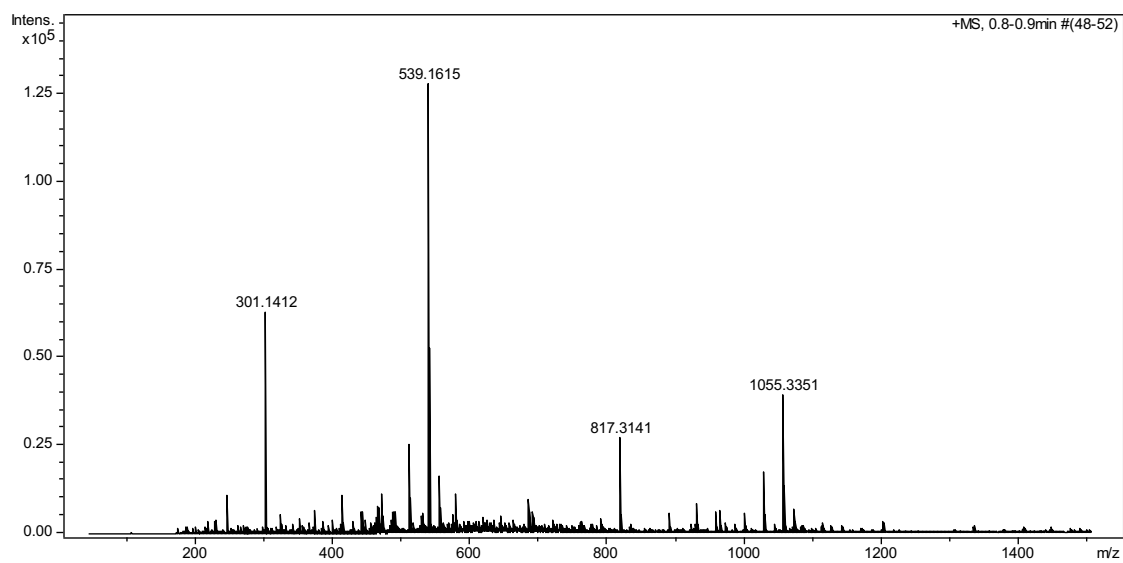**Figure S16.** 400 MHz ^{1}H-^{13}C HMBC NMR spectrum of **5** in CDCl$_3$, 298K

Figure S17. HRMS spectrum of **5** showing a peak at m/z = 539.1615 ([M+K]$^+$).
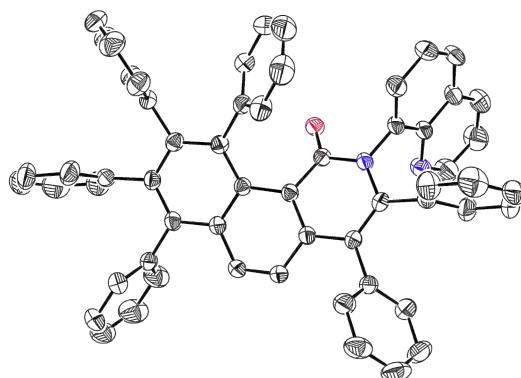
7. X-Ray diffraction data

Figure S18. X-Ray crystal structure of **4** at 50% probability level. H-atoms and solvent molecules have been omitted for clarity.

A yellow prism-like specimen of $C_{60}H_{40}Cl_6N_2O$, were grown from evaporation of $CDCl_3$ at 25 °C, and used and used for the X-ray crystallographic analysis. The X-ray intensity data were measured on a D8 QUEST ECO three-circle diffractometer system equipped with a Ceramic x-ray tube (Mo Kα, λ = 0.71076 Å) and a doubly curved silicon crystal Bruker Triumph monochromator. A total of 728 frames were collected. The total exposure time was 4.04 hours. The frames were integrated with the Bruker SAINT software package using a narrow-frame algorithm. The integration of the data using a triclinic unit cell yielded a total of 27558 reflections to a maximum θ angle of 8.46° (0.75 Å resolution), of which 12259 were independent (average redundancy 2.248, completeness = 98.0%, R_{int} = 1.54%, R_{sig} = 2.19%) and 10388 (84.74%) were greater than $2\sigma(F^2)$. The final cell constants of <u>a</u> = 11.659(5) Å, <u>b</u> = 15.370(6) Å, <u>c</u> = 15.900(8) Å, α = 73.74(2)°, β = 72.33(2)°, γ = 68.40(2)°, volume = 2478.(2) Å^3, are based upon the refinement of the XYZ-centroids of 9925 reflections above 20 σ(I) with 5.968° < 2θ < 56.37°. Data were corrected for absorption effects using the Multi-Scan method (SADABS). The ratio of minimum to maximum apparent transmission was 0.937. The calculated minimum and maximum transmission coefficients (based on crystal size) are 0.6989 and 0.7457. The structure was solved and refined using the Bruker SHELXTL Software Package, using the space group P -1, with Z = 2 for the formula unit, $C_{60}H_{40}Cl_6N_2O$. The final anisotropic full-matrix least-squares refinement on F^2 with 622 variables converged at R1 = 4.35%, for the observed data and wR2 = 11.42% for all data. The goodness-of-fit was 1.035. The largest peak in the final difference electron density synthesis was 0.822 e$^-$/Å^3 and the largest hole was -0.764 e$^-$/Å^3 with an RMS deviation of 0.048 e$^-$/Å^3. On the basis of the final model, the calculated density was 1.364 g/cm^3 and F(000), 1048 e.

Table S9. Crystallographic parameters for **4**.

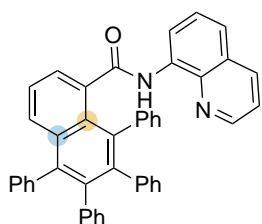| Chemical formula	$C_{60}H_{40}Cl_6N_2O$
Formula weight	1017.64 g/mol
Temperature	150(2) K
Wavelength	0.71076 Å
Crystal size	0.080 x 0.100 x 0.230 mm
Crystal habit	yellow prism
Crystal system	triclinic
Space group	P -1
Unit cell dimensions	a = 11.659(5) Å α = 73.74(2)°
	b = 15.370(6) Å β = 72.33(2)°
	c = 15.900(8) Å γ = 68.40(2)°
Volume	2478.(2) Å^3
Z	2
Density (calculated)	1.364 g/cm^3
Absorption coefficient	0.392 mm^{-1}
F(000)	1048

## 8. Characterization data

General Procedures
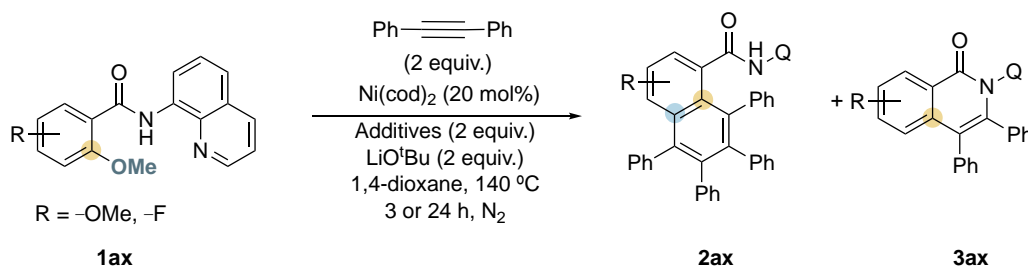
Procedure A (aromatic homologation product): **1ax** (0.1 mmol), diphenylacetylene (36.0, mg, 0.2 mmol, 2 equiv.), LiO*t*Bu (16.0 mg, 0.2 mmol, 2 equiv.), LiOTf (31.2 mg, 0.2 mmol, 2 equiv.) and Ni(cod)$_2$ (5.6 mg, 0.02 mmol, 20 mol %) with 1,4-dioxane (0.5 mL) were mixed in a glass vial under inert-atmosphere, and the vial was sealed. The reaction mixture was stirred at 140 ºC at different reaction times (3 or 24 h). After that, the crude mixture was extracted with dichloromethane (3 x 10 mL) and the organic layers were combined and dried over MgSO$_4$. The solvent was removed under reduced pressure and purified using column chromatography.

Procedure B (alkyne mono-annulation product): **1ax** (0.1 mmol), diphenylacetylene (36,0, mg, 0.2 mmol, 2 equiv.), LiO*t*Bu (16.0 mg, 0.2 mmol, 2 equiv.), PPh$_3$ (52.4 mg, 0.2 mmol, 2 equiv.) and Ni(cod)$_2$ (5.6 mg, 0.02 mmol, 20 mol %) with 1,4-dioxane (0.5 mL) were mixed in a glass vial under inert-atmosphere, and the vial was sealed. The reaction mixture was stirred at 140 ºC at different reaction times (3 or 24 h). After that, the crude mixture was extracted with dichloromethane (3 x 10 mL) and the organic layers were combined and dried over MgSO$_4$. The solvent was removed under reduced pressure and purified using column chromatography.
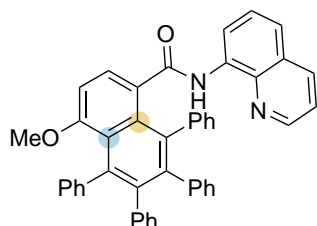
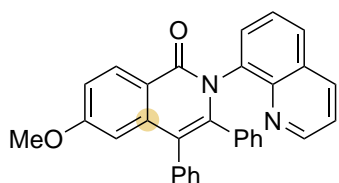### 5,6,7,8-tetraphenyl-*N*-(quinolin-8-yl)-1-naphthamide (2aa)

Prepared in accordance to the general synthesis A described above during 3 hours: **1aa** (27.8, 0.1 mmol) was converted to **2aa**, 29.6 mg of a yellow solid (**49 %**). **^{1}H-NMR** (400 MHz, CDCl$_3$, 298 K) δ (ppm): 9.75 (s, 1H), 8.78 (dd, J = 4.2 Hz, 1.7 Hz, 1H), 8.23 (dd, J = 7.6 Hz, 1.3 Hz, 1H), 8.18 (dd, J = 8.4 Hz, 1.6 Hz, 1H), 7.83 (dd, J = 8.5 Hz, 1.3 Hz, 1H), 7.78 (dd, J = 7.0 Hz, 1.3 Hz, 1H), 7.50-7.44 (m, 3H), 7.40 (t, J = 8.1 Hz, 1H), 7.32-7.21 (m, 6H), 7.02-6.84 (m, 7H), 6.80-6.74 (m, 5H), 6.54 (t, J = 7.40 Hz, 1H), 6.14 (bs, 1H). **^{13}C-NMR** (100 MHz, CDCl$_3$, 298 K) δ (ppm): 168.9, 147.9, 141.4, 140.4, 139.8, 139.6, 139.4, 139.0, 138.4, 137.6, 136.9, 136.3, 134.5, 133.5, 131.3, 131.2, 131.1, 129.7, 128.3, 127.7, 127.6, 127.2, 126.6, 126.5, 126.4, 126.0,125.4, 125.2, 24.9, 121.3, 121.2, 116.8. **HRMS** (ESI, m/z): Calculated for C$_{44}$H$_{30}$N$_2$O [M+H]$^+$ 603.2431, Found 603.2425. **R$_f$** = 0.80 (EtOAc:Hexane 1:1)). This compound is known and the data described is in agreement with the previous reports.[4]

### 3,4-diphenyl-2-(quinolin-8-yl)isoquinolin-1(2*H*)-one (3aa)
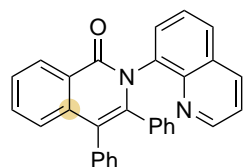
Prepared in accordance to the general synthesis B described above during 24 hours: **1aa** (27.8, 0.1 mmol) was converted to **3aa**, 23.8 mg of a yellow solid (**56 %**). **^{1}H-NMR** (400 MHz, CDCl$_3$, 298 K) δ (ppm): 8.96 (dd, *J* = 4.2 Hz, 1.7 Hz, 1H), 8.62 (dd, *J* = 8.0 Hz, 1.0 Hz, 1H), 8.08 (dd, *J* = 8.3 Hz, 1.7 Hz, 1H), 7.69 (dd, *J* = 8.2 Hz, 1.0 Hz, 1H), 7.63 (td, *J* = 8.1 Hz, 1.8 Hz, 1H), 7.57-7.51 (m, 2H), 7.42-7.37 (m, 2H), 7.34 (d, *J* = 8.1 Hz, 1H), 7.28-7.26 (m, 2H), 7.22-7.17 (m, 3H), 7.00 (m, 1H), 6.88-6.84 (m, 1H), 6.79-6.73 (m, 2H), 6.51 (t, *J* = 7.6 Hz, 1H). **^{13}C-NMR** (100 MHz, CDCl$_3$, 298 K) δ (ppm): 162.7, 150.8, 144.8, 141.9, 138.2, 137.8, 136.6, 136.0, 134.9, 132.4, 131.9, 131.7, 131.4, 130.9, 130.8, 129.8, 128.8, 128.6, 128.4, 128.0, 127.8, 127.2, 126.8, 126.7, 126.6, 126.5, 126.4, 125.7, 125.7, 121.5, 118.5. **HRMS** (ESI, m/z): Calculated for C$_{30}$H$_{20}$N$_2$O [M+H]$^+$ 425.1648 Found 425.1645. **R$_f$** = 0.33 (EtOAc/Hexane (1:1))**.** This compound is known and the data described is in agreement with the previous reports.[5]

4-methoxy-5,6,7,8-tetraphenyl-*N*-(quinolin-8-yl)-1-naphthamide (2ab)

Prepared in accordance to the general synthesis A described above during 24 hours: **1ab** (30.8 mg, 0.1 mmol) was converted to **2ab**, 19,9 mg of a pale pink solid (**31 %**).**^{1}H-NMR** (400 MHz, CDCl$_3$, 298 K) δ (ppm): 9.69 (s, 1H), 8.79 (dd, *J* = 4.2 Hz, 1.7 Hz, 1H), 8.20 (dd, *J* = 7.7 Hz, 1.7 Hz, 1H), 8.15 (dd, *J* = 8.2 Hz, 1.7 Hz, 1H), 7.75 (d, *J* = 8.0 Hz, 1H), 7.47-7.44 (m, 2H), 7.30 (t, *J* = 8.0 Hz, 1H), 7.13-7.11 (m, 4H), 7.07-7.03 (m, 3H), 6.86-6.80 (m, 4H), 6.78-6.74 (m, 6H), 6.68-6.66 (m,2H), 6.55-6.51 (t, *J* = 7.4 Hz, 1H), 3.44 (s, 3H). **^{13}C-NMR** (100 MHz, CDCl$_3$, 298 K) δ (ppm): 168.9, 158.7, 147.9, 143.9, 141.5, 140.6, 140.5, 140.4, 139.7, 138.5, 137.4, 136.9, 136.3, 134.6, 132.4, 131.3, 131.0, 130.9, 130.0, 129.7, 128.5, 127.7, 127.2, 126.3, 126.2, 126.1, 125.8, 125.3, 125.0, 124.8, 121.3, 121.0, 116.6, 55.7. **HRMS** (ESI, m/z): Calculated for C$_{45}$H$_{32}$N$_2$O$_2$ [M+H]$^+$ 633.2537, Found 633.2561. **R$_f$** = 0.56 (CH$_2$Cl$_2$). This compound is known and the data described is in agreement with the previous reports.[4]

## 6-methoxy-3,4-diphenyl-2-(quinolin-8-yl)isoquinolin-1(2*H*)-one (3ab)

Prepared in accordance to the general synthesis B described above during 3 hours: **1ab** (30.8 mg, 0.1 mmol) was converted to **3ab**, 30.1 mg of a pale yellow solid (**66 %**).**^{1}H-NMR** (400 MHz, CDCl$_3$, 298 K) δ (ppm): 8.93 (dd, J = 4.2 Hz, 1.7 Hz, 1H), 8.52 (d, J = 8.9 Hz, 1H), 8.05 (dd, J = 8.3 Hz, 1.6 Hz, 1H), 7.66 (dd, J = 8.1 Hz, 1.0 Hz, 1H), 7.50 (dd, J = 7.3 Hz, 1.2 Hz, 1H), 7.38-7.34 (m, 2H), 7.25-7.22 (m, 2H), 7.17-7.13 (m, 3H), 7.11 (dd, J = 8.9 Hz, 2.7 Hz, 1H), 6.97 (d, J = 7.5 Hz, 1H), 6.82 (t, J = 7.5 Hz, 1H), 6.75-6.67 (m, 3H), 6.48 (t, J = 7.7 Hz, 1H), 3.75 (s, 3H). **^{13}C-NMR** (100 MHz, CDCl$_3$, 298 K) δ (ppm): 163.0, 162.4, 150.7, 144.9, 142.5, 140.3, 137.8, 136.6, 136.0, 135.0, 131.8, 131.6, 131.0, 130.7, 130.6, 129.8, 128.7, 128.5, 128.0, 127.8, 127.2, 126.8, 126.6, 126.4, 125.7, 121.4, 119.6, 118.2, 115.3, 107.6, 55.3. **HRMS** (ESI, m/z): Calculated for C$_{32}$H$_{22}$N$_2$O$_2$ [M+H]$^+$ 455.1754, Found 455.1751. **R$_f$:** 0.64 (EtOAc). This compound is known and the data described is in agreement with the previous reports.[6]

2-methoxy-5,6,7,8-tetraphenyl-*N*-(quinolin-8-yl)-1-naphthamide (2ac)
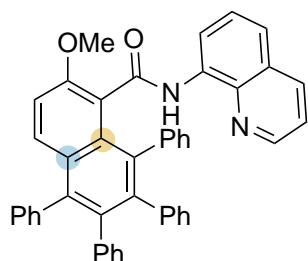
Prepared in accordance to the general synthesis A described above: **1ac** (30.8 mg, 0.1 mmol) was converted to **2ae**, 28.2 mg of a pale pink solid (**45 %**). **^{1}H-NMR** (400 MHz, CDCl$_3$, 298 K) δ (ppm): 9.67 (s, 1H), 8.76 (dd, J = 4.2 Hz, 1.8 Hz, 1H), 8.26 (dd, J = 7.6 Hz, 1.3 Hz, 1H), 8.16 (dd, J = 8.2 Hz, 1.6 Hz, 1H), 7.81 (d, J = 9.4 Hz, 1H), 7.46-7.36 (m, 3H), 7.31(m, 1H), 7.27-7.24 (m, 5H), 6.93-6.66 (m, 13H), 6.44 (tt, J = 7.5 Hz, 1.2 Hz, 1H), 6.02 (t, J = 6.5, 1H), 3.91 (s, 3H). **^{13}C-NMR** (100 MHz, CDCl$_3$, 298 K) δ (ppm): 166.0, 155.6, 147.7, 142.3, 140.6, 140.1, 139.8, 138.8, 138.6, 138.4, 137.6, 136.8, 136.2, 134.7, 133.4, 132.0, 131.5, 131.2, 130.8, 129.4, 128.4, 127.7, 127.6, 127.2, 126.5, 126.4, 126.1, 125.8, 125.6, 125.2, 125.0, 122.7, 121.1, 120.8, 116.9, 113.1, 57.0. **HRMS** (ESI, m/z): Calculated for C$_{45}$H$_{32}$N$_2$O$_2$ [M+H]$^+$ 633.2537, Found 633.2530 **IR (ATR):** υ (cm^{-1}) = 3399, 3052, 2986, 1635, 1523, 1472, 1392, 1264, 1015, 730, 700. **R$_f$:** 0.49 (CH$_2$Cl$_2$).

3,4,7,8,9,10-hexaphenyl-2-(quinolin-8-yl)benzo[*h*]isoquinolin-1(2*H*)-one (4)
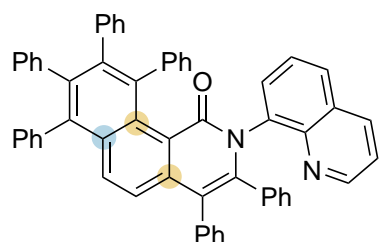
Prepared following the procedure detailed hereafter: **1ad** (29.6mg, 0.1 mmol), diphenylacetylene (36,0, mg, 0.2 mmol, 2 equiv.), LiOtBu (16.0 mg, 0.2 mmol, 2 equiv.), LiOTf (31.2 mg, 0.2 mmol, 2 equiv.), PPh$_3$ (52.4 mg, 0.2 mmol, 2 equiv.) and Ni(cod)$_2$ (5.6 mg, 0.02 mmol, 20 mol %) with 1,4-dioxane (0.5 mL) were mixed in a glass vial under inert-atmosphere, and the vial was sealed. The reaction mixture was stirred at 140 ºC during 24 h. After that, the crude mixture was extracted with ethyl acetate (3 x 10 mL) and the organic layers were combined and dried over MgSO$_4$. The solvent was removed under reduced pressure and purified using preparative layer using EtOAc/Hexane as eluent (3:7) affording the product **4** in 40% yield. **^{1}H-NMR** (400 MHz, CDCl$_3$, 298 K) δ (ppm): 8.78 (dd, J = 4.1 Hz, 1.7 Hz, 1H), 7.91 (dd, J = 8.4 Hz, 1.7 Hz, 1H), 7.60 (d, J = 9.3 Hz, 1H), 7.53-7.51 (m, 2H), 7.27-7.06 (m, 14H), 6.93-6.80 (m, 14H), 6.75-6.71 (m, 2H), 6.67(tt, J = 7.6 Hz, 1.4 Hz, 1H), 6.59 (d, J = 7.0 Hz, 1H), 6.43 (bs, 1H). **^{13}C-NMR** (400 MHz, CDCl$_3$, 298 K) δ (ppm): 161.1, 150.0, 144.8, 143.9, 143.4, 140.6, 140.6, 140.4, 140.3, 140.3, 139.5, 139.4, 139.3, 138.6, 137.7, 137.6, 136.9, 135.6, 134.7, 132.6, 132.1, 131.8, 131.7, 131.2, 131.1, 130.9, 130.8, 130.6, 130.4, 128.6, 128.5, 128.2, 127.9, 127.7,

127.5, 127.4, 126.9, 126.7, 126.6, 126.5, 126.47, 126.4, 126.3, 126.0, 125.4, 125.3, 125.2, 124.9, 123.2, 122.0, 121.0, 117.0. **HRMS** (ESI, m/z): Calculated for $C_{58}H_{38}N_2O$ [M+H]$^+$ 779.3057, Found 779.3067. **IR (ATR):** υ (cm^{-1}) = 3054, 3021, 2961, 2919, 2850, 1655, 1595, 1488, 1440, 1328, 1259, 1204, 1149, 1091, 1065, 1018, 798, 758, 695. **R$_f$** = 0.29 (EtOAc).

9. References

[1] Singh, B. K.; Jana, R. *J. Org. Chem.* **2016,** *81*, 831-841.
[2] Li, B.; Liu, B.; Shi, B.-F. *Chem. Commun.* **2015,** *51*, 5093-5096.
[3] Omer, H. M.; Liu, P.; Brummond, K. M. *J. Org. Chem.* **2020,** *85*, 7959-7975.
[4] He, Z.; Huang, Y. *ACS Catal.* **2016,** *6*, 7814-7823.
[5] Grigorjeva, L.; Daugulis, O. *Angew. Chem. Int. Ed.* **2014,** *53*, 10209-10212.
[6] Kalsi, D.; Dutta, S.; Barsu, N.; Rueping, M.; Sundararaju, B. *ACS Catal.* **2018,** *8*, 8115-8120.

Supporting Information for Chapter VII

Silver(I)-catalyzed C–X, C–C, C–N and C–O cross couplings using aminoquinoline directing groups via elusive aryl-Ag(III) species

Lorena Capdevila, Erik Andris, Anamarija Briš, Màrius Tarrés, Steven Roldán-Gómez, Jana Roithová*, Xavi Ribas*

Table of contents

1. General considerations

All reagents and solvents were purchased from Sigma Aldrich, Fisher Scientific or Fluorochem and used without further purification. ^{1}H and ^{13}C {^{1}H} NMR spectra were recorded on Bruker 400 AVANCE spectrometer in the corresponding deuterated solvent (CDCl$_3$ and d$_6$-DMSO) and calibrated relative to the residual protons of the solvent. Quantification of reaction yields through integration of peaks was performed using an internal reference (1,3,5-trimethoxybenzene). High resolution mass spectra (HRMS) were recorded on a Bruker MicroTOF-Q IITM instrument using ESI source at Serveis Tècnics, University of Girona. IR Spectra (FTIR) were recorded on a FT-IR Alpha spectrometer from Bruker with a PLATINUM-ATR attachment using OPUS software to process the data. All reactions were carried out in a N$_2$ drybox with O$_2$ and H$_2$O concentrations <1 ppm.

2. Synthesis and characterization data for substrates

2-iodo-*N*-(quinolin-8-yl)benzamide (L$_1$-I)
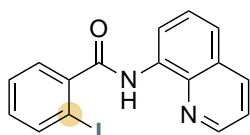
This substrate has been synthesized according to the procedure described in the literature from 8-aminoquinoline and the benzoyl chloride:[1] To a solution of 8-aminoquinoline (0.50 g, 3.47 mmol), 2-iodobenzoyl chloride (0.92 g, 3.47 mmol) in pyridine (10 mL), was heated to 130 ºC and stirred for 1 hour. After the reaction time, the mixture was left to cool to 70 ºC and poured into 50 mL of ice-cold water. The resulting crude mixture was extracted with dichloromethane (3 x 20 mL) and the organic layers were combined, dried over magnesium sulfate and the solvent removed under reduced pressure. Purification by column chromatography in dichloromethane afforded a crystalline solid (1.03 g, 80 % of a pale yellow solid). ^{1}**H-NMR** (CDCl$_3$, 400MHz, 298 K) δ (ppm): 10.15 (s, 1H), 8.95 (dd, *J* = 7.2 Hz, 1.6 Hz, 1H), 8.78 (dd, *J* = 4.2 Hz, 1.6 Hz, 1H), 8.18 (dd, *J* = 8.3 Hz, 1.6 Hz, 1H), 7.97 (dd, *J* = 8.0 Hz, 0.8, 1H), 7.64-7.56 (m, 3H), 7.49-7.44 (m, 2H), 7.18 (ddd, *J* = 8.0 Hz, 7.2 Hz, 1.6 Hz, 1H). ^{13}**C-NMR** (CDCl$_3$, 100 MHz, 298K) δ (ppm): 167.5, 148.4, 142.3, 140.3, 138.6, 136.4, 134.3, 131.4, 128.5, 128.3, 128.0, 127.4, 122.2, 121.7, 116.9, 92.8. **HRMS** (ESI, m/z): Calculated for C$_{16}$H$_{11}$IN$_2$O [M+H]$^+$ 374.9989, Found 374.9984. **R$_f$**: 0.64 (dichloromethane). This compound is known and the data described are in agreement with the previous reports.[2]

2-bromo-*N*-(quinolin-8-yl)benzamide (L$_1$-Br)
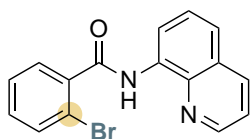
This substrate was prepared according to the general procedure described above for the synthesis of substrate L$_1$-I. 8-Aminoquinoline (0.50 g, 3.47 mmol), 2-bromobenzoyl chloride (0.76 g, 3.47 mmol) were used (0.88 g, 78 % of a white solid). ^{1}**H-NMR** (CDCl$_3$, 400 MHz, 298K) δ (ppm): 10.29 (s, 1H), 8.95 (dd, *J* = 7.2 Hz, 1.6 Hz, 1H), 8.79 (dd, *J* = 4.4 Hz, 2.0 Hz, 1H), 8.19 (dd, *J* = 8.4 Hz, 1.6 Hz, 1H), 7.73-7.69 (m, 2H), 7.63-7.57 (m, 2H), 7.48-7.43 (m, 2H), 7.35 (ddd, *J* = 7.9 Hz, 7.2 Hz, 1.6 Hz, 1H). ^{13}**C-NMR** (CDCl$_3$, 100 MHz, 298 K) δ (ppm): 166.0, 148.4, 138.7, 138.4, 136.4, 134.3, 133.7, 131.5, 129.6, 128.0, 127.7, 127.4, 122.2, 121.7, 119.7, 116.8. **HRMS** (ESI, m/z): Calculated for C$_{16}$H$_{11}$BrN$_2$O [M+H]$^+$ 327.0128, Found 327.0132. **R$_f$**: 0.55 (dichloromethane). This compound is known and the data described are in agreement with the previous reports.[3]

2-chloro-*N*-(quinolin-8-yl)benzamide (**L₁-Cl**)
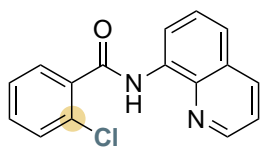
This substrate was prepared according to the general procedure described above for the synthesis of substrate **L₁-I**. 8-Aminoquinoline (0.50 g, 3.47 mmol), 2-chlorobenzoyl chloride (0.61 g, 3.47 mmol) were used (0.73 g, 75 % of white solid). **¹H-NMR** (CDCl₃, 400 MHz, 298 K) δ (ppm): 10.49 (s, 1H), 8.96 (dd, *J* = 7.2 Hz, 1.6 Hz, 1H), 8.80 (dd, *J* = 4 Hz, 1.6 Hz, 1H), 8.19 (dd, *J* = 8.4 Hz, 1.6 Hz, 1H), 7.82 (dd, *J* = 6.8 Hz, 2.4 Hz, 1H), 7.63-7.56, (m, 2H), 7.52-7.39 (m, 4H). **¹³C-NMR** (CDCl₃, 1 00 MHz, 298 K) δ (ppm): 164.9, 148.4, 138.7, 136.4, 135.9, 134.5, 131.5, 131.5, 130.6, 130.1, 128.0, 127.4, 127.2, 122.2, 121.7, 116.9. **HRMS** (ESI, m/z): Calculated for $C_{16}H_{11}ClN_2O$ [M+H]⁺ 283.0633, Found 283.0643. **R_f**: 0.56 (dichloromethane). This compound is known and the data described are in agreement with the previous reports.[4]

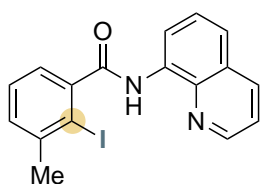## 2-iodo-3-methyl-*N*-(quinolin-8-yl)benzamide (**L₂-I**)

This substrate has been synthesized according to the procedure described in the literature from 8-aminoquinoline and the benzoic acid.[5] Oxalyl chloride (0.4 mL, 1.2 equiv., 4.57 mmol) was added dropwise to a solution of 2-iodo-3-methylbenzoic acid (1 g, 3.81 mmol), DMF (3 drops) in anhydrous CH_2Cl_2 (15 mL) at 0ºC under N₂ atmosphere. The mixture was allowed to warm to room temperature and stirred during 5 h and then the solvent was removed. To a solution of 8-aminoquinoline (0.71 g, 1.3 equiv., 4.93 mmol), Et₃N (1.0 mL, 2.0 equiv., 7.62 mmol) and anhydrous CH_2Cl_2 (20 mL) were added. Acid chloride in anhydrous CH_2Cl_2 (5 mL) was added dropwise at 0ºC, and the solution was stirred overnight at room temperature. The resulting crude mixture was quenched with NaHCO₃ (15 mL) and the organic layer was separated. The aqueous layer was extracted with CH_2Cl_2 (2 x 15 mL) and the combined organic layers were washed with aqueous HCl (15 mL, 1M), and brine (5 mL), dried over magnesium sulfate, filtered and evaporated under reduced pressure. The crude mixture was purified by column chromatography on silica gel (eluent: dichloromethane) to afford the desired compound (0.46 g, 31 % of a white solid). **¹H-NMR** (CDCl₃, 400MHz, 298 K) δ (ppm): 10.07 (s, 1H), 8.95 (dd, *J* = 7.3 Hz, *J* = 2.0 Hz, 1H), 8.77 (dd, J = 4.2 Hz, 1.7 Hz, 1H), 8.19 (dd, *J* = 8.3 Hz, 1.7 Hz, 1H), 7.64-7.55 (m, 2H), 7.46 (dd, *J* = 8.2 Hz, 4.3 Hz, 1H), 7.35 (s, 3H), 2.55 (s, 3H). **¹³C-NMR** (CDCl₃, 100 MHz, 298K) δ (ppm): 168.7, 148.5, 144.2, 143.3, 138.7, 136.5, 134.5, 130.9, 128.4, 128.2, 127.6, 125.4, 122.3, 121.9, 117.1, 99.7, 29.4. **IR (ATR)**: υ (cm⁻¹) = 3339, 1669, 1567, 1519, 1483, 1421, 1385, 1325, 1278, 1150, 1009, 931, 821, 783, 763, 735, 715, 671, 610, 497, 443. **HRMS** (ESI, m/z): Calculated for $C_{17}H_{13}IN_2O$ [M+Na]⁺ 410.9965 , Found 410.9956. **R_f** : 0.68 (dichloromethane).

3. Silver-catalyzed cross-coupling reactions

3.1 Optimization of halide exchange reactions

General procedure for the optimization experiments

37.4 mg of **L₁-I** (0.1 mmol), *n*Bu₄NCl, base (2 equiv., 0.2 mmol), AgOTf (2.6 mg, 10 mol%, 0.01 mmol) with 2.5 mL of solvent were added to a glass vial under an inert-atmosphere, and the vial sealed and covered with aluminum foil. The reaction mixture was stirred overnight at specified temperature. The crude mixture was extracted with ethyl acetate (3 x 10 mL) and the combined organic layers were dried over magnesium sulfate. The solvent was removed under reduced pressure. The crude reaction was analyzed by ¹H-NMR spectroscopy (CDCl₃) using 1,3,5-trimethoxybenzene as internal standard.

**Table S1**. Optimization of halide exchange catalysis
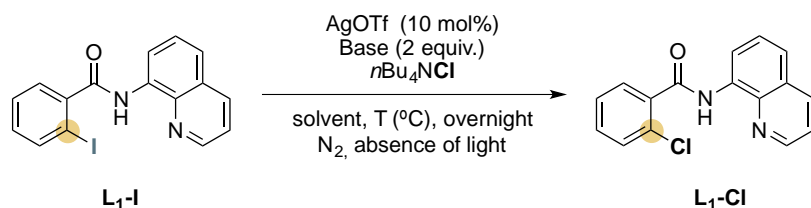
Entry	Base	Equiv. of *n*Bu4NCl	T (°C)	Solvent	AgOTf (mol %)	Yield (%) of L1-Cl[a]
1	-	10	100	CH_3CN	10	0
2	NaOAc	10	100	CH_3CN	10	12
3	K_3PO_4	10	100	CH_3CN	10	11
4	K_2CO_3	10	100	CH_3CN	10	0
5	**Na_2CO_3**	**10**	**100**	**CH_3CN**	**10**	**95**
6	Na_2CO_3	5	100	CH_3CN	10	48
7	Na_2CO_3	1	100	CH_3CN	10	0
8	Na_2CO_3	10	70	CH_3CN	10	33
9	Na_2CO_3	10	50	CH_3CN	10	25
10	Na_2CO_3	10	r.t.	CH_3CN	10	0
11	**Na_2CO_3**	**10**	**100**	**DMSO**	**10**	**82**
12	Na_2CO_3	10	100	DMSO	-	20
13	Na_2CO_3	10	100	CH_3CN	-	0

[a]Yield calculated from ^{1}H-NMR of crude reaction mixture using 1,3,5-trimethoxybenzene as internal standard.

3.2 Optimization of C-N bond formation reactions

General procedure for the optimization experiments

37.4 mg of **L1-I** (0.1 mmol), cyclohexanamine, base and catalytic amounts of AgOTf with 1 mL of solvent were added to a glass vial under an inert-atmosphere, and the vial was sealed and covered with aluminum foil. The reaction mixture was stirred at 100 °C for 24 hours. The resulting crude mixture was extracted with ethyl acetate (3 x 10 mL) and the organic layers were combined and dried over magnesium sulfate. The solvent was removed under reduced pressure. The crude reaction was analyzed by ^{1}H-NMR spectroscopy (CDCl$_3$) using 1,3,5-trimethoxybenzene as internal standard.

**Table S2**. Optimization of C-N bond formation catalysis using cyclohexanamine as nucleophile
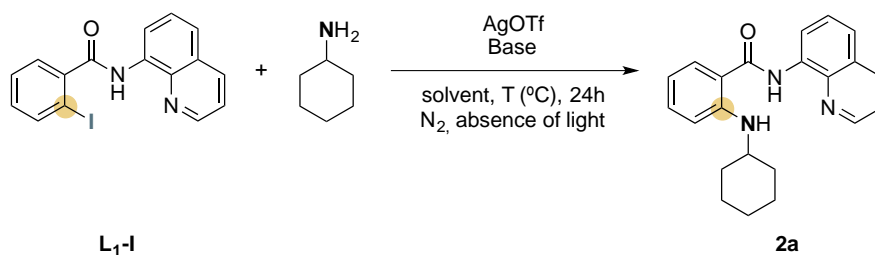
Entry	Equiv. of cyclohexanamine	Base	Equiv. of base	Solvent	AgOTf (mol%)	Yield (%) of 2a[a]
1	4	CsF	2	THF	10	17
2	4	KOAc	2	THF	10	9
3	4	CsOPiv	2	THF	10	17
4	4	Na$_2$CO$_3$	2	THF	10	tr
5	4	^{t}BuOK	2	THF	10	0
6	4	CsF	2	Toluene	10	13
7	4	CsF	2	CH$_3$CN	10	tr
8	4	CsF	2	DMSO	10	21
9	4	CsF	4	DMSO	10	23
10	4	CsF	6	DMSO	10	20
11	**12**	**CsF**	**4**	**DMSO**	**20**	**53**
12	12	CsF	4	DMSO	-	0

[a]Yield calculated from ^{1}H-NMR of crude using 1,3,5-trimethoxybenzene as internal standard.

3.3 Optimization of C-O bond formation reactions

General procedure for the optimization experiments

37.4 mg of **L$_1$-I** (0.1 mmol), phenol, base and AgOTf (5.1 mg, 20 mol%, 0.02 mmol) with 1 mL of solvent were added to a glass vial under an inert atmosphere, and the vial was sealed and covered with aluminum foil. The reaction mixture was stirred at 100 ºC overnight. The crude reaction mixture was extracted with ethyl acetate (3 x 10 mL) and the organic layers were combined and dried over magnesium sulfate and the solvent was then removed under reduced pressure. The crude reaction mixture was analyzed by ^{1}H-NMR spectroscopy (CDCl$_3$) using 1,3,5-trimethoxybenzene as internal standard.

Table S3. Optimization of C-O bond formation catalysis using phenol as nucleophile.
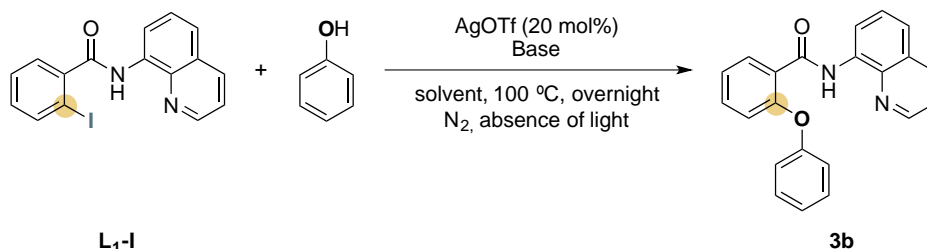
Entry	Equiv. of phenol	Base	Equiv. of base	Solvent	AgOTf (mol%)	Yield (%) of 3b[a]
1	10	KO^{t}Bu	2	DMSO	20	55
2	10	CsF	2	DMSO	20	30
3	10	Na$_2$CO$_3$	2	DMSO	20	21
4	**10**	**KO^{t}Bu**	**4**	**DMSO**	**20**	**73**
5	10	KO^{t}Bu	4	CH$_3$CN	20	59

[a] Yield calculated from ^{1}H-NMR of crude using 1,3,5-trimethoxybenzene as internal standard.

3.4 Optimization of C-C bond formation reactions

3.4.1 Activated methylene

General procedure for the optimization experiments

37.4 mg of **L₁-I** (0.1 mmol), malononitrile, base (4 equiv., 0.4 mmol) and catalytic amounts of AgOTf with 2.5 mL of solvent were added to a glass vial under an inert-atmosphere, and the vial sealed and covered with aluminum foil. The reaction mixture was stirred at 100 ºC overnight. The resulting crude mixture was extracted with ethyl acetate (3 x 10 mL) and the organic layers were combined and dried over magnesium sulfate. The solvent was removed under reduced pressure. The crude reaction mixture was analyzed by ¹H-NMR spectroscopy (CDCl₃) using 1,3,5-trimethoxybenzene as internal standard.

Table S4. Optimization of C-C bond formation catalysis using malononitrile as nucleophile.
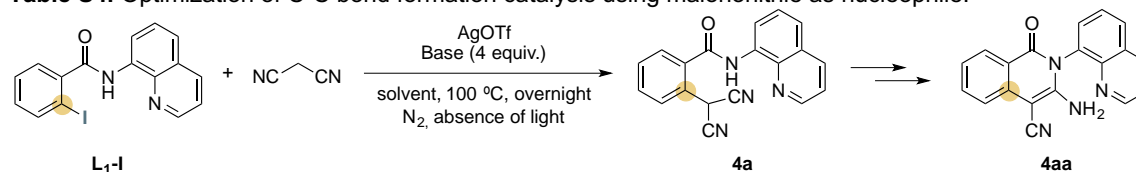

Entry	Base	Equiv. of malononitrile	T (ºC)	Solvent	AgOTf (mol%)	Yield (%) of 4aa[a]
1	Na₂CO₃	2	100	CH₃CN	10	0
2	KO^{t}Bu	2	100	CH₃CN	10	45
3	KO^{t}Bu	2	100	CH₃OH	10	18
4	KO^{t}Bu	2	100	Toluene	10	0
5	KO^{t}Bu	2	100	DMSO	10	65
6	KO^{t}Bu	2	100	DMSO	20	74
7	**KO^{t}Bu**	**2**	**100**	**CH₃CN**	**20**	**90**
8	KO^{t}Bu	2	100	DMSO	-	0

[a] Yield calculated from ¹H-NMR of crude using 1,3,5-trimethoxybenzene as internal standard.

3.4.2 Arylboronic acids

General procedure for the optimization experiments

37.4 mg of **L₁-I** (0.1 mmol), (4-methoxyphenyl)boronic acid, base (4 equiv., 0.4 mmol), AgOTf (5.1 mg, 20 mol%, 0.02 mmol) with 1 mL of solvent were added to a glass vial under an inert-atmosphere, and the vial was sealed and covered with aluminum foil. The reaction mixture was stirred overnight at the specified temperature. The resulting crude mixture was extracted with ethyl acetate (3 x 10 mL) and the organic layers were combined and dried over magnesium sulfate. The solvent was then removed under reduced pressure and the resulting crude was analyzed by ¹H-NMR spectroscopy (CDCl₃) using 1,3,5-trimethoxybenzene as internal standard.

Table S5. Optimization of C-C bond formation catalysis using 4-methoxyphenylboronic acid as nucleophile.
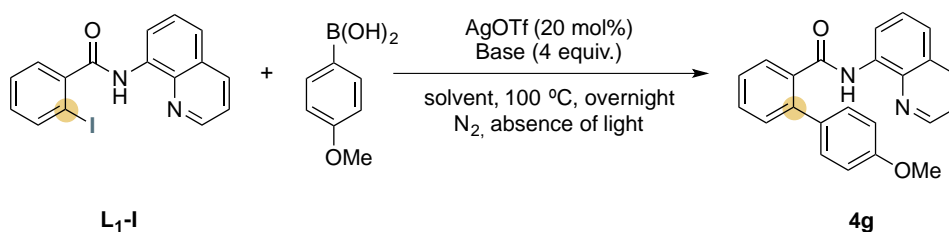
Entry	Base	Equiv. of (4-methoxyphenyl) boronic acid	T (ºC)	Solvent	AgOTf (mol%)	Yield (%) of 4g[a]
1	KO^{t}Bu	4	100	DMSO	20	10
2	KO^{t}Bu	10	100	DMSO	20	15
3	**KO^{t}Bu**	**10**	**120**	**DMSO**	**20**	**20**
4	KO^{t}Bu	10	120	CH$_3$CN	20	7
5[b]	KO^{t}Bu	10	120	CH$_3$CN/MeOH	20	0
6	Na$_2$CO$_3$	10	120	DMSO	20	11
7	CsF	10	120	DMSO	20	11
8	KO^{t}Bu	10	120	DMSO	-	0

[a] Yield calculated from ^{1}H-NMR of crude using 1,3,5-trimethoxybenzene as internal standard. [b] The reaction was performed using a mixture of CH$_3$CN/MeOH (1:1).

4. Mechanistic studies

4.1 DFT calculations

We carried out all calculations with Gaussian 09 program.[6] Geometry optimizations were obtained using the Becke three-parameter functional with the Becke 88 exchange functional and the Lee, Yang, and Parr correlation functional (B3LYP)[7, 8,9, 10] along with a modified combination of basis sets and functions. This basis set was composed in the following manner: 6-311+G* [11-16] for **C, H, N, O, Cl**; SSD basis set[17, 18] with its corresponding Effective Core Potential (ECP) for **Ag** and **I** with the addition of 4 extra functions for **I** (*s, p, d* functions from aug-cc-pVDZ[19] to add diffusion and a *d* function from 6-311+G* to add polarization) and 4 extra functions for **Ag** (*s, p, d* functions from aug-cc-pVDZ to add diffusion and a *d* function from cc-pVDZ-PP to add polarization).

Empirical dispersion was added using the D3 version of Grimme's model with Becke-Johnson damping function (**GD3BJ**)[20] along with solvation effects in dimethyl sulfoxide simulated by the SMD method developed by Truhlar *et al.*[21] Subsequent frequency calculations at the same level of theory were performed to evaluate enthalpy and entropy corrections at 298.15 K (**G$_{corr.}$**) and ensured that all local minima had only real frequencies while a single imaginary frequency confirmed the presence of transition states. All the transition states were connected to the corresponding reactants and products by IRC calculations. Also, Single Point Energy (SPE) calculations under the same conditions but with a more flexible basis set were performed. In this case, for **C, H, N, O, Cl,** we used May-cc-pPVTZ[22]; for **Ag** and **I**, we used a modified version of aug-cc-pVTZ (we just removed the 2 largest angular momenta from the basis set to make it more comparable to May-cc-pVTZ) with its respective ECP (**aug-cc-pVTZPP**). Finally, standard state gas-phase concentration correction from 1 atm to 1 Molar was applied to all Final Gibbs energy values.[23]

The xyz coordinates for all the structures can be found in the Supplementary Digital Material included in the attached CD.

4.2 Ion spectroscopy experiments

General procedure for the ion spectroscopy experiments

L$_2$-I (0.0388 g, 0.1 mmol), AgClO$_4$ (0.041 g, 0.2 mmol) and Na$_2$CO$_3$ (0.021 g, 0.2 mmol) were dissolved in 1 mL of acetonitrile under nitrogen and covered with aluminum foil. The reaction mixture was stirred at 50 °C for 45 minutes. For the ion spectroscopy measurements, an aliquot of the reaction mixture was diluted 100 times in acetonitrile (acetonitrile-d$_3$). The diluted solutions were kept at −30 °C during measurements.

The ions were transferred to the gas phase by electrospray ionization (ESI). The diluted solution was pushed from a glass vial by 1 psi pressure of nitrogen to the ESI ion source through 100 μm (i. d.) fused-silica capillary at a rate approximately 0.1 mL hr^{-1}. The spraying voltage of 2.5 kV was connected to the solution in the vial by a 0.3 mm stainless steel wire. The sheath gas pressure was 10 psi and the heated capillary was kept at 170 °C. Two different ionization conditions were used: soft (20 V capillary voltage, 140 V tube lens voltage) and hard (100 V capillary voltage, 250 V tube lens voltage). The hard conditions were optimized to maximize the IR attenuation at 1740 cm^{-1} peak.

IR spectra were measured with the ISORI instrument.[24, 25] The ions generated ions in the ESI ion source were mass selected and trapped and thermalized by helium (or helium with 10 % D$_2$) buffer gas in the wire-quadrupole ion trap at 3 K and 20 K, respectively. In the process, some ions attach He atom (D$_2$ molecule) to form weakly-bound clusters. The trapped ions were irradiated for 900 ms by the pulsed IR laser (OPO/OPA system from LaserVision) and then extracted by lowering the exit electrode potential, mass analyzed by a quadrupole and counted by a Daly-type detector. Photodissociation spectra were constructed as a frequency-dependent reduced signal (1 − N_i/N_{i0}), where N_i and N_{i0} are the numbers of the He- (D$_2$-) tagged ions extracted from the trap in the cycles with (N_i) and without (N_{i0}) laser irradiation. The pulse sequence of one cycle is shown in Figure S2.
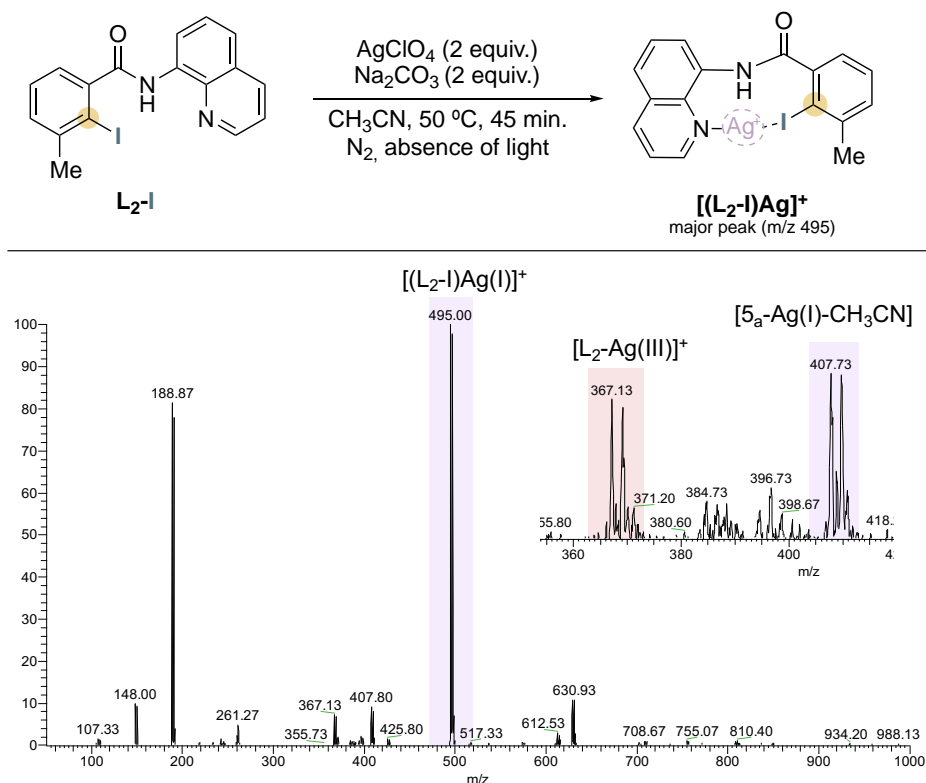

Figure S1. ESI analysis of the crude mixture obtained for the ion spectroscopy experiments

Computational details

The density functional theory (DFT) calculations were performed with the Gaussian 16 rev. A.03 package.[6] We have used the B3LYP[8, 10, 26, 27] functional with D3BJ[28, 29] corrections for the dispersion interactions. The basis set was 6-311+g(2d,p) for C, H, N and O atoms and SDD for the Ag and I atoms. The vibrational analysis provided the harmonic frequencies and confirmed the structures as minima on the potential energy surface. We also performed anharmonic VPT2 analysis[30, 31] to calculate anharmonic IR spectra with the default setting in the Gaussian 16 package. Optimized geometries can be found in the Supplementary Digital Material included in the attached CD.
.
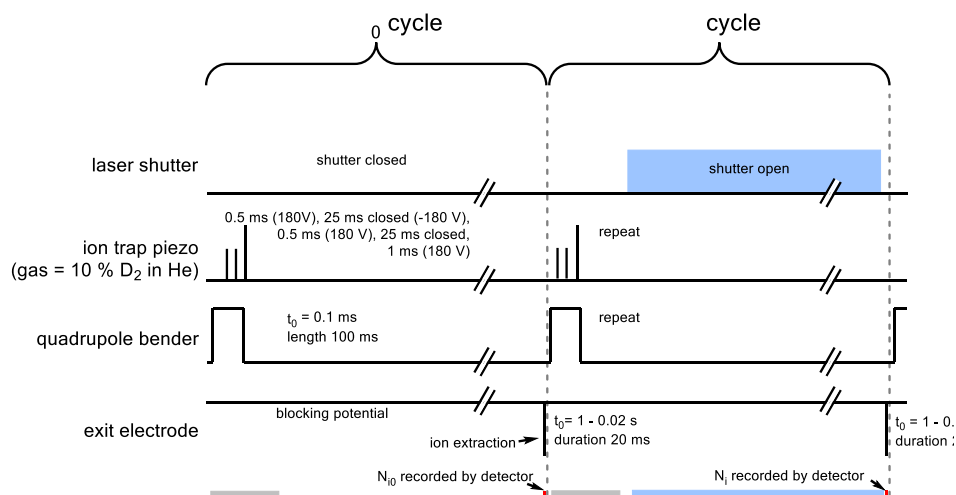
Figure S2. Timing sequence used during the acquisition of the IRPD spectra with the ISORI instrument.
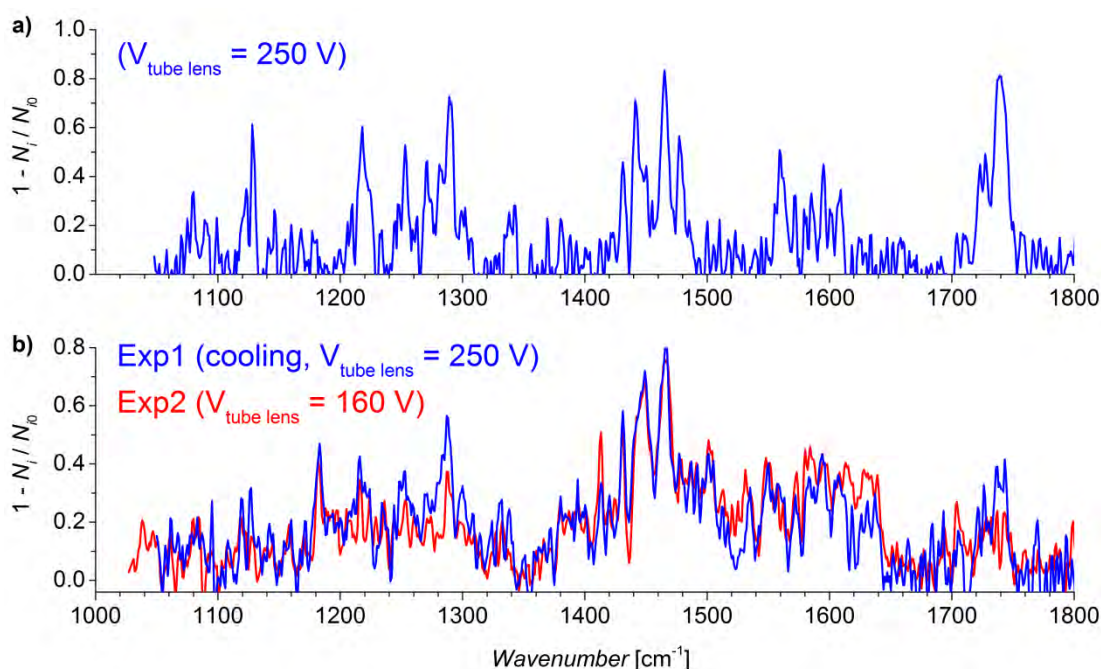

Figure S3. a) D_2-IRPD spectrum of *m/z* 408 ions. b) He-IRPD spectra of *m/z* 408 ions. The blue spectrum was obtained at higher potential in the ion-transfer range (harder ionization conditions), the reaction mixture was cooled to -30 °C. The red spectrum was obtained at softer ionization conditions.
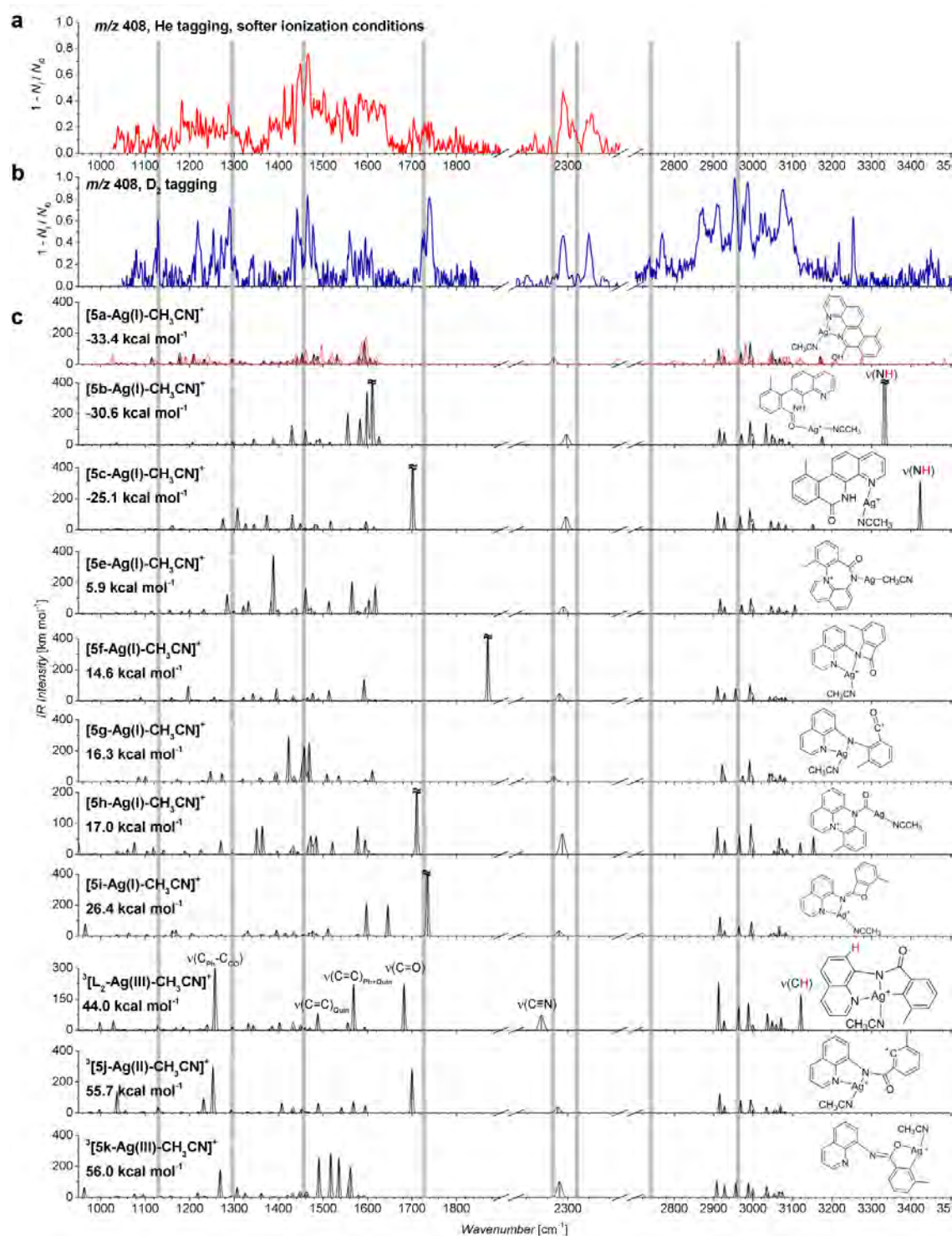
Figure S4. a) Helium tagging IRPD spectra of *m/z* 408 ions acquired with softer ionization conditions (see Experimental Details). b) D₂ tagging IRPD spectra of ions with *m/z* 408. b) IR spectra of different isomers with *m/z* 408 calculated at B3LYP-D3BJ/6-311+G(2d,p) :SDD(Ag) level (black lines). Frequency scaling factors are $0.98 < 2000$ cm⁻¹, $0.96 > 2000$ cm⁻¹. Energies given are enthalpies at 0 K. The anharmonic IR spectra (B3LYP-D3BJ/6-311+g(2d,p):SDD-Ag) are in red and were not scaled. All predicted IR intensities above 2700 cm⁻¹ were multiplied by 10.

5. Characterization data

5.1 C-N bond formation reactions

All the C-N bond formation products were synthesized using the optimized reaction conditions from section 3.2.
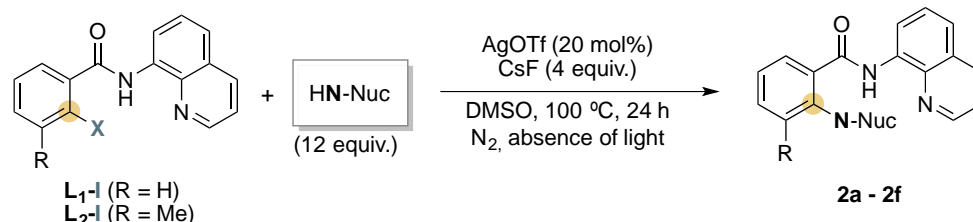
**Scheme S1**. Silver-catalyzed C–N bond formation reactions.

L$_1$-I, (0.1 mmol/0.25 mmol), AgOTf (20 mol%), CsF (4 equiv.), amine (12 equiv.) and 1 - 2.5 mL of dimethylsulfoxide were added to a glass vial under inert atmosphere and the vial was sealed. The resulting mixture was stirred at 100 ºC for 24 h. The resulting crude mixture was extracted with ethyl acetate (3 x 10 mL) and the organic layers were combined and dried over magnesium sulfate. The solvent was removed under reduced pressure and the product was purified using column chromatography.

2-(cyclohexylamino)-*N*-(quinolin-8-yl)benzamide (2a)
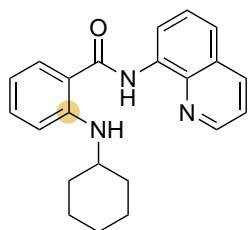
Prepared in accordance to the general synthesis described for above: **L$_1$-I** (37.4 mg, 0.1 mmol in 1 mL of DMSO) as converted to **2a**; 17.7 mg as a pale yellow solid (51 %). **^{1}H-NMR** (CDCl$_3$, 400 MHz, 298 K) δ (ppm): 10.61 (s, 1H), 8.84-8.82 (m, 2H), 8.17 (dd, *J* = 8.1 Hz, 1.8 Hz, 1H), 7.85 (bs, 1H), 7.80 (dd, *J* = 8.0 Hz, 1.4 Hz, 1H), 7.60-7.50 (m, 2H), 7.46 (dd, *J* = 4.9 Hz, 1H), 7.34 (ddd, *J* = 6.7 Hz, 1.9 Hz, 1H), 6.79 (d, *J* = 8.1 Hz, 1H), 6.68 (ddd, *J* = 8.0 Hz, 7.2 Hz, 1.1 Hz, 1H), 3.41 (s, 1H), 2.09-2.06 (m,2H), 1.82-1.78 (m, 2H), 1.66-1.56 (m, 2H), 1.46-1.30 (m, 4H). **^{13}C-NMR** (CDCl$_3$, 100 MHz, 298 K) δ (ppm): 168.5, 149.7, 148.3, 139.0, 136.5, 135.1, 133.3, 128.4, 128.2, 127.6, 121.8, 121.4, 116.4, 115.0, 114.4, 112.4, 50.9, 33.1, 26.1, 25.0. **IR (ATR):** υ (cm^{-1}) = 3335, 2922, 2848, 1646, 1574, 1510, 1483, 1453, 1421, 1386, 1324, 1249, 1165, 894, 822, 791, 752, 694, 922, 522, 461, 439. **HRMS** (ESI, m/z): Calculated for C$_{22}$H$_{23}$N$_3$O [M+H]$^+$ 346.1914, Found 346.1921. **R$_f$** : 0.77 (dichloromethane).

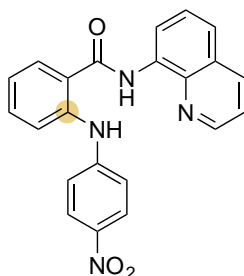## 2-(cyclopentylamino)-N(quinolin-8-yl)benzamide (2b)
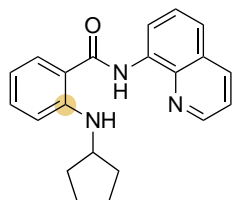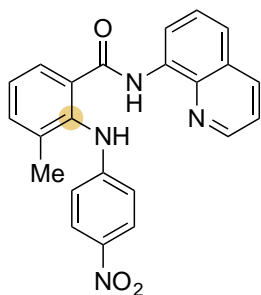

Prepared in accordance to the general synthesis described above: **L$_1$-I** (37.4 mg, 0.1 mmol in 1 mL of DMSO) was converted to **2b**; 10.2 mg as a pale yellow solid (31 %). ^{1}H-NMR (CDCl$_3$, 400 MHz, 298 K) δ (ppm): 10.61 (bs, 1H), 8.84-8.81 (m, 1H), 8.17 (dd, J = 8.3 Hz, 1.8 Hz), 7.85 (d, *J* =4.6 Hz, 1H), 7.79 (dd, *J* = 7.9 Hz, 1.6 Hz, 1H), 7.60-7.50 (m, 2H), 7.47 (dd, *J* = 8.3 Hz, 3.9 Hz, 1H), 7.36 (ddd, *J* = 8.3 Hz, 7.0 Hz, 1.6 Hz, 1H), 6.79 (dd, *J* = 8.3 Hz, 1.1 Hz, 1H), 6.70 (ddd, *J* = 7.9 Hz, 7.2 Hz, 1.1 Hz, 1H), 3.89 (m, 1H), 2.09-2.04 (m, 2H), 1.81-1.76 (m, 2H), 1.65-1.61 (m, 4H). **^{13}C-NMR** (CDCl$_3$, 100 MHz, 298 K) δ (ppm): 168.5, 150.2, 148.3, 139.1, 136.5, 135.1, 133.3, 128.3, 128.2, 127.6, 121.8, 121.4, 116.4, 115.2, 114.6, 112.8, 54.0, 33.7, 24.3. **IR (ATR):** υ (cm^{-1}) = 3352, 2953, 1642, 1579, 1413, 1483, 1420, 1381, 1323, 1239, 1164, 894, 826, 791, 763, 735, 669, 601, 525. **HRMS** (ESI, m/z): Calculated for C$_{21}$H$_{20}$N$_3$O [M+Na]$^+$ 354.1577, Found 354.1581. **R$_f$** : 0.47 (dichloromethane).

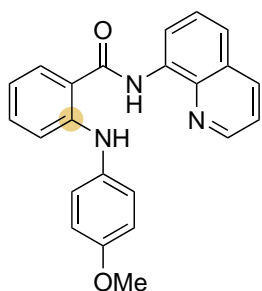## 2-(1*H*-imidazol-1-yl)-*N*-(quinolin-8-yl)benzamide (2c)
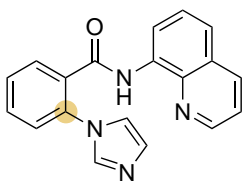
Prepared in accordance to the general synthesis described above: **L$_1$-I** (93.5 mg, 0.25 mmol in 2.5 mL of DMSO) was converted to **2c**; 42.3 mg as white solid (54 %). **^{1}H-NMR** (CDCl$_3$, 400 MHz, 298 K) δ (ppm): 9.97 (s, 1H), 8.77 (m, 1H), 8.68 (dd, *J* = 4.2 Hz, 1.7 Hz, 1H), 8.13 (dd, *J* = 6.6 Hz, 1.6 Hz, 1H), 7.92 (dd, *J* = 7.5 Hz, 1.6 Hz, 1H), 7.82 (s, 1H), 7.65-7.56 (m, 2H), 7.54-7.51 (m, 2H), 7.44-7.40 (m, 2H), 7.24 (s, 1H), 7.05 (s, 1H). **^{13}C-NMR** (CDCl$_3$, 100 MHz, 298 K) δ (ppm): 164.6, 148.3, 138.4, 137.5, 136.4, 134.9, 134.1, 133.0, 131.8, 130.2, 129.9, 129.0, 128.0, 127.2, 126.7, 122.4, 121.9, 120.7, 116.8. **IR (ATR):** υ (cm^{-1}) = 2919, 1669, 1545, 1504, 1423, 1371, 1321, 1237, 1058, 911, 824, 794, 782, 753, 730, 657, 597, 537, 491, 446. **HRMS** (ESI, m/z): Calculated for C$_{19}$H$_{14}$N$_4$O [M+H]$^+$ 315.1240, Found 315.1239. **R$_f$**: 0.65 (dichloromethane).

2-((4-chlorophenyl)amino)-*N*-(quinolin-8-yl)benzamide (2d)

Prepared in accordance to the general synthesis described above: **L$_1$-I** (93.5 mg, 0.25 mmol in 2.5 mL of DMSO) was converted to **2d**; 59.0 mg as a yellow solid (61 %). **^{1}H-NMR** (CDCl$_3$, 400 MHz, 298 K) δ (ppm): 10.75 (s, 1H), 9.96 (s, 1H), 8.85-8.83 (m, 2H), 8.21 (dd, *J* = 8.4 Hz, 1.9 Hz, 1H), 8.16 (d, *J* = 9.1 Hz, 2H), 7.94 (dd, *J* = 8.4 Hz, 1.9 Hz, 1H), 7.63-7.60 (m, 3H), 7.53-7.49 (m, 2H), 7.24-7.15 (m, 3H), 7.19-7.15 (m, 1H). **^{13}C-NMR** (CDCl$_3$, 100 MHz, 298 K) δ (ppm): 167.3, 148.6, 148.5, 142.4, 141.0, 138.9, 136.7, 134.3, 132.7, 128.5, 128.2, 127.5, 126.1, 122.6, 122.4, 122.0, 121.9, 118.9, 116.8, 116.6. **HRMS** (ESI, m/z): Calculated for C$_{22}$H$_{16}$N$_4$O$_3$ [M+H]$^+$ 385.1295, Found 385.1288. **R$_f$** = 0.80 (dichloromethane). This compound is known and the data described are in agreement with the previous reports.[32]

## 3-methyl-2-((4-nitrophenyl)amino)-N-(quinolin-8-yl)benzamide (2e)

Prepared in accordance to the general synthesis described above: **L$_2$-I** (38.9 mg, 0.1 mmol in 1 mL of DMSO) was converted to **2e**; 23.3 mg as yellow solid (59 %). **^{1}H-NMR** (CDCl$_3$, 400 MHz, 298 K) δ (ppm): 10.68 (s, 1H), 8.80 (dd, J = 5.8 Hz, 3.1 Hz, 1H), 8.75 (dd, J = 4.3 Hz, 1.7 Hz, 1H), 8.37 (s, 1H), 8.16 (dd, J = 8.3 Hz, 1.7 Hz, 1H), 8.06-8.03 (m, 2H), 7.81 (dd, J = 7.8 Hz, 1.7 Hz, 1H), 7.55-7.53 (m, 2H), 7.48-7.43 (m, 2H), 7.34 (t, J = 7.6 Hz, 1H), 6.65-6.61 (m, 2H), 2.22 (s, 3H).). **^{13}C-NMR** (CDCl$_3$, 100 MHz, 298 K) δ (ppm): 166.7, 151.0, 148.5, 140.0, 138.7, 138.0, 136.6, 135.9, 134.8, 134.4, 131.0, 128.1, 127.4, 126.5, 126.0, 125.9, 122.4, 121.9, 116.9, 114.5, 19.1. **IR (ATR):** υ (cm^{-1}) = 3323, 1654, 1596, 1518, 1483, 1321, 1178, 1109, 825, 790, 751. **HRMS** (ESI, m/z): Calculated for C$_{23}$H$_{19}$N$_4$O$_3$ [M+Na]$^+$, 421. 1271, Found 421.1261. **R$_f$** = 0.65 (EtOAc/Hexane(6:4)).

2-((4-methoxyphenyl)amino)-N-(quinolin-8-yl)benzamide (2f)

Prepared in accordance to the general synthesis described above: **L₁-I** (93.5 mg, 0.25 mmol in 2.5 mL of DMSO) was converted to **2f**; 28.1 mg as yellow solid (30 %). **¹H-NMR** (CDCl₃, 400 MHz, 298 K) δ (ppm): 10.73 (s, 1H), 9.46 (s, 1H), 8.88-8.84 (m, 2H), 8.18 (dd, J = 8.3 Hz, 1.7 Hz, 1H), 7.85 (dd, J = 7.9 Hz, 1.3 Hz, 1H), 7.61-7.52 (m, 2H), 7.48 (dd, J = 7.9 Hz, 4.2 Hz, 1H), 7.29 (ddd, J = 8.4 Hz, 7.1 Hz, 1.3 Hz, 1H), 7.23-7.19 (m, 2H), 7.14 (dd, J = 8.4 Hz, 1.3 Hz, 1H), 6.93-6.89 (m, 2H), 6.84 (ddd, J = 8.1 Hz, 7.1 Hz, 1.3 Hz, 1H), 3.82 (s, 3H). **¹³C-NMR** (CDCl₃, 100 MHz, 298 K) δ (ppm): 168.2, 156.3, 148.4, 139.0, 136.5, 134.8, 134.2, 132.9, 128.2, 128.1, 127.5, 125.1, 121.8, 121.7, 117.0, 116.9, 116.4, 114.8, 114.6, 55.6. **HRMS** (ESI, m/z): Calculated for $C_{23}H_{19}N_3O_2$ [M+H]⁺ 370.1550, Found 370.1546. **R_f** : 0.79 (CH₂Cl₂). This compound is known and the data described are in agreement with the previous reports.[32]

5.2. C-O bond formation reactions

All the C-O bond formation products were synthesized using the optimized reaction conditions from section 3.3.
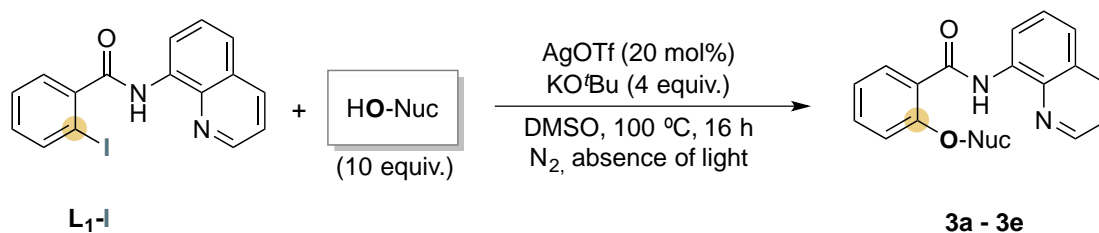
**Scheme S2**. Silver-catalyzed C–O bond formation reactions.

L₁-I, (0.1 mmol), AgOTf (5.2 mg, 20 mol%, 0.02 mmol), ᵗBuOK (45.0 mg, 4 equiv., 0.4 mmol), phenol (a-d) (10 equiv., 1.0 mmol) and 1 mL of dimethylsulfoxide were added to a glass vial under inert atmosphere and the vial was sealed. The resulting mixture was stirred at 100 ºC overnight. The resulting crude mixture was extracted with ethyl acetate (3 x 10 mL) and the organic layers were combined, cleaned with NaOH (2M) and dried over magnesium sulfate. The solvent was removed under reduced pressure and the product was purified using column chromatography.

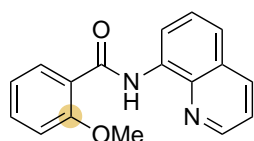## 2-(4-chlorophenoxy)-*N*-(quinolin-8-yl)benzamide (3a)
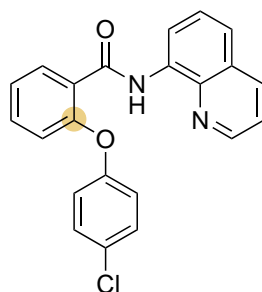
Prepared in accordance to the general synthesis described above: **L₁-I** (37.4 mg, 0.1 mmol) was converted to **3a**; 27.2 mg as white solid (73 %). **¹H-NMR** (CDCl₃, 400 MHz, 298 K) δ (ppm): 12.09 (s, 1H), 8.98 (dd, J = 8.3 Hz, 1.3 Hz, 1H), 8.59 (dd, J = 4.2 Hz, 1.6 Hz, 1H), 8.39 (dd, J = 7.8 Hz, 1.7 Hz, 1H), 8.13 (dd, J = 8.3 Hz, 1.6 Hz, 1H), 7.57 (t, J = 8.3 Hz, 1H), 7.52-7.46 (m, 2H), 7.40 (dd, J = 8.4 Hz, 4.1 Hz, 1H), 7.38-7.35 (m, 2H), 7.31 (ddd, J = 8.4 Hz, 7.8 Hz, 1.1 Hz, 1H), 7.21-7.17 (m, 2H), 7.02 (dd, J = 8.0 Hz, 0.8 Hz, 1H). **¹³C-NMR** (CDCl₃, 100 MHz, 298 K) δ (ppm):163.0, 155.0, 154.8, 148.2, 139.2, 136.3,135.4, 133.2, 132.7, 130.1, 129.5, 128.1, 127.6, 125.3, 124.3, 121.8, 121.7, 120.9, 118.7, 117.3. **IR (ATR)**: υ (cm⁻¹) = 3296, 2919, 2850, 1663, 1524, 1474, 1385, 1325, 1280, 1224, 1097, 905, 868, 823, 792, 750, 701, 685, 662, 594, 520, 489, 442. **HRMS** (ESI, m/z): Calculated for $C_{22}H_{15}ClN_2O_2$ [M+Na]⁺ 397.0714, Found 397.0707. **R_f** : 0.69 (EtOAc/Hexane (3:7)).

2-phenoxy-*N*-(quinoline-8-yl)benzamide (3b)
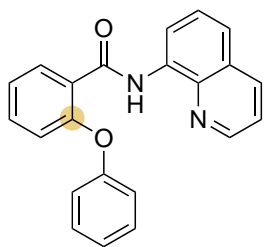
Prepared in accordance to the general synthesis described above: **L₁-I** (37.4 mg, 0.1 mmol) was converted to **3b**; 20.4 mg as a pale yellow solid (60 %). **¹H-NMR** (CDCl₃, 400 MHz, 298 K) δ (ppm): 12.23 (s, 1H), 9.00 (dd, *J* = 7.9 Hz, 1.3 Hz, 1H), 8.57 (dd, *J* = 4.0 Hz, 1.8 Hz, 1H), 8.40 (dd, *J* = 7.7 Hz, 1.9 Hz, 1H), 8.11 (dd, *J* = 8.3 Hz, 1.8 Hz, 1H), 7.57 (t, *J* = 7.9 Hz, 1H), 7.51-7.40 (m, 4H), 7.37 (dd, *J* = 8.1 Hz, 4.1 Hz, 1H), 7.30-7.26 (m, 4H), 7.19 (t, *J* = 7.2 Hz, 1H), 7.03 (d, *J* = 8.7 Hz, 1H). **¹³C-NMR** (CDCl₃, 100 MHz, 298 K) δ (ppm): 163.3, 156.1, 155.6, 148.2, 139.3, 136.2, 135.6, 133.1, 132.5, 130.0, 128.1, 127.6, 125.1, 124.4, 123.8, 121.7, 121.6, 119.8, 118.6, 117.3. **IR (ATR):** υ (cm⁻¹) = 3286, 3042, 2962, 2923, 1652, 1597, 1527, 1474, 1328, 1259, 1226, 1095, 1016, 906, 867, 789, 748, 683, 594, 520, 467. **HRMS** (ESI, m/z): Calculated for $C_{22}H_{16}N_2O_2$ [M+Na]⁺ 363.1104, Found 363.1102. **R_f** : 0.50 (CH₂Cl₂).

## 2-(4-methoxyphenoxy)-*N*-(quinolin-8-yl)benzamide (3c)
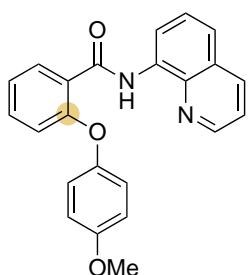
Prepared in accordance to the general synthesis described above: **L₁-I** (37.4 mg, 0.1 mmol) was converted to **3c**; 8.3 mg as a yellow solid (22 %). **¹H-NMR** (CDCl₃, 400 MHz, 298 K) δ (ppm): 12.31 (s, 1H), 9.01 (dd, *J* = 7.6 Hz, 1.1 Hz, 1H), 8.56 (dd, *J* = 4.3 Hz, 1.8 Hz, 1H), 8.38 (dd, *J* = 7.9 Hz, 1.8 Hz, 1H), 8.11 (dd, *J* = 8.2 Hz, 1.8 Hz, 1H), 7.57-7.55 (m, 1H), 7.51-7.49 (m, 1H), 7.42 (ddd, *J* = 8.2 Hz, 7.3 Hz, 1.8 Hz, 1H), 7.37 (dd, *J* = 8.2 Hz, 4.3 Hz, 1H), 7.25-7.20 (m, 3H), 6.98-6.95 (m, 3H), 3.84 (s, 3H). **¹³C-NMR** (CDCl₃, 100 MHz, 298 K) δ (ppm): 163.4, 156.6, 149.1, 148.2, 139.3, 136.2, 135.7, 133.0, 132.5, 129.0, 128.1, 127.6, 124.3, 123.1, 121.6, 121.6, 121.4, 117.3, 117.2, 115.1, 55.8. **IR (ATR):** υ (cm⁻¹) = 3259, 3044, 3002, 2954, 1654, 1597, 1530, 1503, 1389, 1328, 1285, 1219, 1153, 1102, 1029, 908, 846, 825, 792, 746, 684, 595, 518, 484. **HRMS** (ESI, m/z): Calculated for $C_{23}H_{18}N_2O_3$ [M+Na]⁺ 393.1210, Found 393.1203. **R_f** : 0.75 (CH₂Cl₂).

2-methoxy-N-(quinolin-8-yl)benzamide (3e)

Prepared in accordance to the general synthesis described above: **L₁-I** (37.4 mg, 0.1 mmol in 1 mL of CH₃OH) was converted to **3e** 3.50 mg as a pale yellow solid (13 %). **¹H-NMR** (CDCl₃, 400 MHz, 298 K) δ (ppm): 12.35 (s, 1H), 9.04 (dd, J = 7.6 Hz, 1.6 Hz, 1H), 8.89 (dd, J = 4.2 Hz, 1.6 Hz, 1H), 8.36 (dd, J = 7.8 Hz, 1.8 Hz, 1H), 8.18 (dd, J = 8.2 Hz, 1.6 Hz, 1H), 7.59 (t, J = 8.2 Hz, 1H), 7.54- 7.50 (m, 2H), 7.47 (dd, J = 8.2 Hz, 3.7 Hz, 1H), 7.15 (t, J = 7.8 Hz, 1H), 7.09 (d, J = 8.2 Hz, 1H), 4.22 (s, 3H). **¹³C-NMR** (CDCl₃, 100 MHz, 298 K) δ (ppm): 163.7, 157.8, 148.3, 139.3, 136.3, 135.8, 133.1, 132.4, 128.1, 127.6, 122.4, 121.5, 121.4, 121.3, 117.4, 111.6, 56.2. **HRMS** (ESI, m/z): Calculated for $C_{17}H_{14}N_2O_2$ [M + Na]⁺ 301.0947, Found 301.0948. **R_f** : 0.47 (CH₂Cl₂). This compound is known and the data described are in agreement with the previous reports.[33]

5.3. C-C bond formation reactions

The C-C coupling products using activated methylene substrates were synthesized using the optimized reaction conditions from section 3.4.1.
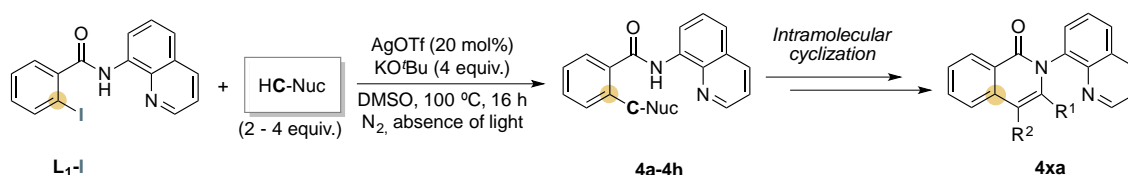
**Scheme S3**. Silver-catalyzed C–C bond formation reactions.

L₁-I, (0.10 mmol), AgOTf (5.2 mg, 20 mol%, 0.02 mmol), ᵗBuOK (45.0 mg, 4 equiv., 0.40 mmol), activated methylene (2 equiv. of **a** and 4 equiv. of **b-f**) and 2.5 mL of dimethylsulfoxide were added to a glass vial under inert atmosphere and the vial was sealed. The resulting mixture was stirred at 100 ºC overnight. The resulting crude mixture was extracted with ethyl acetate (3 x 10 mL) and the organic layers were combined and dried over magnesium sulfate. The solvent was removed under reduced pressure and the product was purified using column chromatography.

3-amino-1-oxo-2-(quinolin-8-yl)-1,2-dihydroisoquinoline-4-carbonitrile (4aa)
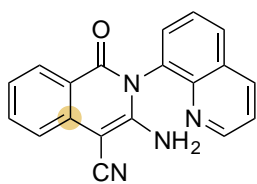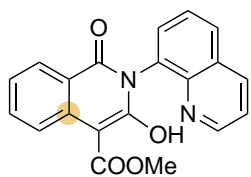
Prepared in accordance to the general synthesis described above: **L₁-I** (37.4 mg, 0.10 mmol) was converted to **4aa**; 22.1 mg of a pale orange solid (71 %). This compound was isolated by precipitation using dichloromethane as solvent. ^{1}**H-NMR** (DMSO d$_6$, 400 MHz, 298 K) δ (ppm): 8.82 (dd, J = 4.2 Hz, 1.7 HZ, 1H), 8.51 (dd, J = 8.3 Hz, 1.7 Hz, 1H), 8.17 (dd, J = 8.3 Hz, 1.4 Hz, 1H), 7.92 (dd, J = 8.01 Hz, 1.0 Hz, 1H), 7.84 (dd, J = 7.1 Hz, J = 1.4 Hz, 1H), 7.76 (t, J = 7.6 Hz, 1H), 7.67 (ddd, J = 8.5 Hz, 7.3 Hz, 1.5 Hz, 1H), 7.60 (dd, J = 8.3 Hz, 4.2 Hz, 1H), 7.42 (d, J = 8.0 Hz, 1H), 7.14 (ddd, J = 8.1 Hz, 7.1 Hz, 1.0 Hz, 1H), 6.74 (bs, 2H). ^{13}**C-NMR** (DMSO d$_6$, 100 MHz, 298 K) δ (ppm): 161.6, 155.3, 151.0, 143.8, 137.5, 136.6, 134.1, 132.9, 131.2, 130.1, 129.4, 128.0, 126.9, 122.1, 122.0, 120.5, 118.5, 118.1, 63.9. **IR (ATR):** υ (cm^{-1}) = 3414, 3058, 2195, 1672, 1624, 1544, 1493, 1429, 1386, 1323, 1161, 992, 889, 843, 824, 786, 771, 754, 690, 634, 511, 467. **HRMS** (ESI, m/z): Calculated for C$_{19}$H$_{12}$N$_4$O [M+H]$^+$ 313.1084, Found 313.1089.
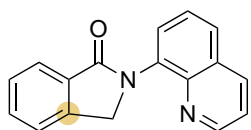
Ethyl (S)-2-cyano-2-(2-(quinolin-8-ylcarbamoyl)phenyl)acetate (4b)
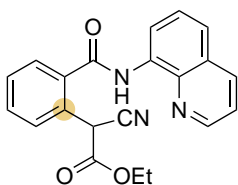
Prepared in accordance to the general synthesis described above: **L₁-I** (37.4 mg, 0.10 mmol) was converted to **4b**; 15.1 mg as lightless orange liquid (42 %). ^{1}**H-NMR** (CD$_3$Cl, 400 MHz, 298 K) δ (ppm): 10.52 (s, 1H), 8.88-8.83 (m, 1H), 8.81 (dd, J = 4.2 Hz, 1.6 Hz, 1H), 8.20 (dd, J = 8.3 Hz, 1.6 Hz, 1H), 7.92 (dd, J = 7.3 Hz, 1.6 Hz, 1H), 7.77 (dd, J = 7.5 Hz, 1.6 Hz, 1H), 7.65- 7.57 (m, 4H), 7.48 (dd, J = 8.2 Hz, 4.3 Hz, 1H), 6.16 (s, 1H), 4.22 (qd, J = 7.2 Hz, 2.6 Hz, 2H), 1.19 (t, J = 7.2 Hz, 3H). ^{13}**C-NMR** (CDCl$_3$, 100 MHz, 298 K) δ (ppm): 166.5, 165.2, 148.6, 138.7, 136.6, 134.9, 134.4, 131.8, 130.4, 130.2, 129.7, 128.1, 127.9, 127.5, 122.5, 122.0, 116.9, 116.2, 63.3, 40.3, 13.9. **HRMS** (ESI, m/z): Calculated for C$_{21}$H$_{17}$N$_3$O$_3$ [M+H]$^+$ 360.1343, Found 360.1358. **R$_f$**: 0.56 (CH$_2$Cl$_2$). This compound is known and the data described is in agreement with the previous reports.[34]

Methyl 3-hydroxy-1-oxo-2-(quinolin-8-yl)-1,2-dihydroisoquinoline-4-carboxylate (4ca)

Prepared in accordance to the general synthesis described above: L₁-I (37.4 mg, 0.1 mmol) was converted to 4ca. This product could not be isolated and the yield was calculated from crude mixture using trimethoxybenzene as internal standard (62 %). **¹H-NMR** (DMSO-d_6, 400 MHz, 298 K) δ (ppm): 8.74 (dd, J = 4.1 Hz, 1.6 Hz, 1H), 8.40 (m, 2H), 7.95 (dd, J = 8.1 Hz, 1.1 Hz, 1H), 7.87 (dd, J = 7.8 Hz, 1.1 Hz, 1H), 7.65 (m, 1H), 7.49 (m, 2H), 7.33 (ddd, J = 8.6 Hz, 6.9 Hz, 1.6 Hz, 1H), 6.78 (m, 1H), 3.71 (s, 3H). **HRMS** (ESI, m/z): Calculated for $C_{20}H_{14}N_2O_4$ [M+H]⁺ 347.1026, Found 347.1024.

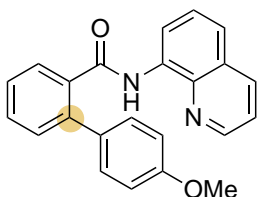## 2-(quinolin-8-yl)isoindolin-1-one (4fa)

Prepared in accordance to the general synthesis described above: **L₁-I** (37.4 mg, 0.10 mmol) was converted to **4f**; 12.3 mg as pale orange solid (47 %). **¹H-NMR** (CDCl₃, 400 MHz, 298 K) δ (ppm): 8.88 (dd, J = 4.2 Hz, 1.7 Hz, 1H), 8.21 (dd, J = 8.3 Hz, 1.7 Hz, 1H), 8.01 (dt, J = 7.6 Hz, 1.1 Hz, 1 H), 7.94 (dd, J = 7.4 Hz, 1.4 Hz, 1H), 7.83 (dd, J = 8.3 Hz, 1.4 Hz, 1H), 7.66-7.59 (m, 2H), 7.54-7.50 (m, 2H), 7.43 (dd, J = 8.3 Hz, 4.2 Hz, 1H), 5.30 (s, 2H). **¹³C-NMR** (CDCl₃, 100 MHz, 298 K) δ (ppm): 169.0, 150.1, 144.4, 142.6, 136.5, 135.7, 132.7, 131.8, 129.6, 128.8, 128.0, 127.7, 126.6, 124.5, 122.9, 121.6, 54.0. **IR (ATR):** υ (cm⁻¹) = 2921, 2853, 1682, 1502, 1471, 1427, 1400, 1297, 1197, 1131, 912, 890, 829, 795, 760, 731, 682, 614, 560, 484, 462, 414. **HRMS** (ESI, m/z): Calculated for $C_{17}H_{12}N_2O$ [M+H]⁺ 261.1022, Found 261.1033. **R_f** : 0.37 (EtOAc/Hexane: 7/3). Column: EtOAc/Hexane (7:3) to EtOAc.

The product using arylboronic acid as a nucleophile was synthesized using the optimized reaction conditions from section 3.4.2.
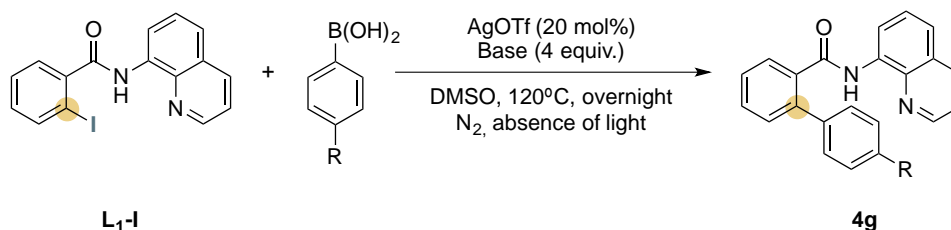

Scheme S4. Silver-catalyzed C–C bond formation reactions using arylboronic acid.

L₁-I, (0.1 mmol), AgOTf (5.2 mg, 20 mol%, 0.02 mmol), ᵗBuOK (45.0 mg, 4 equiv., 0.40 mmol), boronic acid (**g**) (10 equiv., 1 mmol) and 1 mL of dimethylsulfoxide were added to a glass vial under inert atmosphere and the vial was sealed. The resulting mixture was stirred at 120 ºC overnight. The resulting crude mixture was extracted with ethyl acetate (3 x 10 mL) and the organic layers were combined and dried over magnesium sulfate. The solvent was removed under reduced pressure and the product was purified using column chromatography.

### 4-methoxy-*N*-(quinolin-8-yl)-[1,1-biphenyl]-2-carboxamide (4g)

Prepared in accordance to the general synthesis described above: **L₁-I** (37.4 mg, 0.1 mmol) was converted to **4g**; 5.3 mg as a pale orange solid (15 %). **¹H-NMR** (CDCl₃, 400 MHz, 298 K) δ (ppm): 9.81 (s, 1H), 8.82 (dd, *J* = 7.6 Hz, 1.3 Hz, 1H), 8.53 (dd, *J* = 4.2 Hz, 1.7 Hz, 1H), 8.08 (dd, *J* = 8.3 Hz, 1.7 Hz, 1H), 7.90 (dd, *J* = 7.9 Hz, 1.4 Hz, 1H), 7.57-7.51 (m, 2H), 7.48-7.43 (m, 5H), 7.35 (dd, *J* = 8.2 Hz, 4.2 Hz, 1H), 6.82 (d, *J* = 8.8 Hz, 2H), 3.65 (s, 3H). **¹³C-NMR** (CDCl₃, 100 MHz, 298 K) δ (ppm): 168.2, 160.0, 147.9, 140.1, 138.6, 136.1, 136.0, 134.8, 132.6, 130.8, 130.6, 130.3, 129.4, 127.9, 127.5, 127.4, 121.6, 121.5, 116.5, 114.1, 55.3. **HRMS** (ESI, *m/z*): Calculated for $C_{23}H_{18}N_2O_2$ [M+Na]⁺ 377.1260, Found 377.1249. **Rf** : 0.77 (CH₂Cl₂). This compound is known and the data described are in agreement with the previous reports.[35]

5.4. Byproducts

### N-(quinolin-8-yl)benzamide (L₁-H)
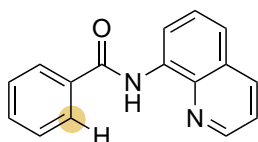
¹H-NMR (CDCl3, 400 MHz, 298 K) δ (ppm): 10.74 (s, 1H), 8.95 (dd, *J* = 7.6 Hz, 1.4 Hz, 1H), 8.83 (dd, *J* = 4.2 Hz, 1.7 Hz, 1H), 8.15 (dd, *J* = 8.4 Hz, 1.7 Hz, 1H), 8.10-8.08 (m, 2H), 7.60-7.51 (m, 5H), 7.45 (dd, *J* = 8.4 Hz, 4.2 Hz, 1H). **¹³C-NMR** (CDCl₃, 100 MHz, 298 K) δ (ppm): 165.5, 148.4, 138.8, 136.5, 135.2, 134.7, 131.9, 128.9, 128.1, 127.5, 127.4, 121.8, 116.6. **HRMS** (ESI, m/z): Calculated for $C_{16}H_{12}N_2O$ [M+Na]⁺ 271.0842, Found 271.0836. This compound is known and the data described are in agreement with the previous reports.[33]

2-((methylsulfinyl)methyl)-N-(quinolin-8-yl)benzamide (L₁-DMSO)
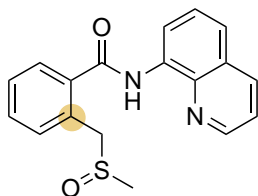
¹H-NMR (CDCl3, 400 MHz, 298 K) δ (ppm): 10.44 (s, 1H), 8.85 (dd, *J* = 6.2 Hz, 2.7 Hz, 1H), 8.81 (dd, *J* = 4.2 Hz, 1.6 Hz, 1H), 8.20 (dd, *J* = 8.3 Hz, 1.7 Hz, 1H), 7.87 (m, 1H), 7.62-7.50 (m, 5H), 7.48 (dd, *J* = 8.2 Hz, 4.2 Hz, 1H), 4.61 (d, *J* = 12.9 Hz, 1H), 4.25 (d, *J* = 12.9 Hz, 1H), 2.60 (s, 3H). **¹³C-NMR** (CDCl₃, 100 MHz, 298 K) δ (ppm): 167.1, 148.6, 138.8, 136.5, 136.2, 134.6, 133.0, 131.3, 130.7, 128.9, 128.2, 127.9, 127.5, 122.4, 122.0, 116.9, 58.2, 38.3. **HRMS** (ESI, m/z): Calculated for $C_{18}H_{16}N_2O_2S$ [M+Na]⁺ 347.0825, Found 347.0831. **IR (ATR):** υ (cm⁻¹) = 3374, 3284, 2962, 1671, 1651, 1595, 1523, 1477, 1328, 1259, 1090, 1020, 789, 751, 684, 594. **Rf** : 0.13 (EtOAc).

N²,N² -di(quinolin-8-yl)biphenyl-2,2'-dicarboxamide (L₁-L₁ homocoupling)
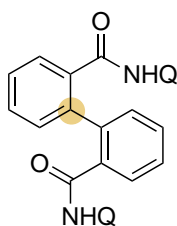
¹H-NMR (CDCl₃, 400 MHz, 298 K) δ (ppm): 10.36 (s, 2H), 8.69 (dd, J = 7.2 Hz, 1.9 Hz, 2H), 8.46 (dd, J = 4.2, 1.8 Hz, 2H), 7.95 (dd, J = 8.2 Hz, 1.8 Hz, 2H), 7.86 (dt, J = 7.2 Hz, 1.2 Hz, 2H), 7.46-7.43 (m, 4H), 7.42-7.37 (m, 2H), 7.31-7.23 (m, 6H). **¹³C-NMR** (CDCl₃, 100 MHz, 298 K) δ (ppm): 167.6, 147.8, 139.8, 138.5, 136.5, 135.9, 134.8, 131.0, 130.6, 128.1, 128.0, 127.6, 127.2, 121.5, 121.4, 116.7. **HRMS** (ESI, m/z): Calculated for $C_{32}H_{22}N_4O_2$ [M+Na]⁺ 517.1635, Found 517.1623. This compound is known and the data described are in agreement with the previous reports.[3]

10-methylbenzo[c][1,10]phenanthrolin-6(5H)-one (5a)
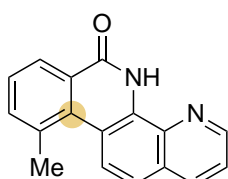
L$_2$-I, (0.077 g, 0.2 mmol), AgClO$_4$ (0.082 g, 0.4 mmol), NaCO$_3$ (0.042 g, 0.4 mmol), 2 mL of CH$_3$CN were added to a glass vial under inert atmosphere and the vial was sealed and covered with aluminum foil. The resulting mixture was stirred at 100 ºC for 24 h. The resulting crude mixture was extracted with dichloromethane (3 x 10 mL) and the organic layers were combined and dried over magnesium sulfate. The solvent was then removed under reduced pressure and the product was purified using column chromatography (CH$_2$Cl$_2$/EtOAc (7:3)). **^{1}H-NMR** (CDCl$_3$, 400 MHz, 298 K) δ (ppm): 10.40 (s, 1H), 8.96 (dd, J = 4.3 Hz, 1.7 Hz, 1 H), 8.48 (d, J = 8.8 Hz, 1H), 8.46 (m, 1H), 8.27 (dd, J = 8.3 Hz, 1.7 Hz, 1H), 7.65 (dd, J = 8.3 Hz, 4.3 Hz, 1H), 7.59 (m, 1H), 7.57 (d, J = 8.8 Hz, 1H), 7.29 (m, 1H), 2.76 (s, 3H).**^{13}C-NMR** (CDCl$_3$, 100 MHz, 298 K) δ (ppm): 178.3, 148.7, 139.1, 138.2, 137.7, 136.5, 134.0, 130.2, 125.4, 124.8, 124.2, 124.1, 123.2, 122.3, 119.8, 118.9, 17.0. **HRMS** (ESI, m/z): Calculated for C$_{17}$H$_{12}$N$_2$O [M+H]$^+$ 261.1022, Found 261.1028. **IR (ATR):** υ (cm^{-1}) = 3371.7, 2959.8, 2923.4, 2854.2, 1730.3, 1668.9, 1586.9, 1535.6, 1453.3, 1259.5, 1095.1, 1076.2, 1015.1, 791.7, 750.4, 616.6, 452.1. **R$_f$**: 0.72 (CH$_2$Cl$_2$/EtOAc (7:3)).

6. References

[1]   Whiteoak, C. J.; Planas, O.; Company, A.; Ribas, X. *Adv. Synth. Catal.* **2016,** *358*, 1679-1688.

[2]   Khan, B.; Kant, R.; Koley, D. *Adv. Synth. Catal.* **2016,** *358*, 2352-2358.

[3]   Grigorjeva, L.; Daugulis, O. *Org. Lett.* **2015,** *17*, 1204-1207.

[4]   Gou, F.-R.; Wang, X.-C.; Huo, P.-F.; Bi, H.-P.; Guan, Z.-H.; Liang, Y.-M. *Org. Lett.* **2009,** *11*, 5726-5729.

[5]   Aihara, Y.; Chatani, N. *J. Am. Chem. Soc.* **2013,** *135*, 5308-5311.

[6]   Frisch, M. J. T., G. W.; Schlegel, H. B.; Scuseria, G. E.; Robb, M. A.; Cheeseman, J. R.; Scalmani, G.; Barone, V.; Petersson, G. A.; Nakatsuji, H.; Li, X.; Caricato, M.; Marenich, A. V.; Bloino, J.; Janesko, B. G.; Gomperts, R.; Mennucci, B.; Hratchian, H. P.; Ortiz, J. V.; Izmaylov, A. F.; Sonnenberg, J. L.; Williams-Young, D.; Ding, F.; Lipparini, F.; Egidi, F.; Goings, J.; Peng, B.; Petrone, A.; Henderson, T.; Ranasinghe, D.; Zakrzewski, V. G.; Gao, J.; Rega, N.; Zheng, G.; Liang, W.; Hada, M.; Ehara, M.; Toyota, K.; Fukuda, R.; Hasegawa, J.; Ishida, M.; Nakajima, T.; Honda, Y.; Kitao, O.; Nakai, H.; Vreven, T.; Throssell, K.; Montgomery, J. A., Jr.; Peralta, J. E.; Ogliaro, F.; Bearpark, M. J.; Heyd, J. J.; Brothers, E. N.; Kudin, K. N.; Staroverov, V. N.; Keith, T. A.; Kobayashi, R.; Normand, J.; Raghavachari, K.; Rendell, A. P.; Burant, J. C.; Iyengar, S. S.; Tomasi, J.; Cossi, M.; Millam, J. M.; Klene, M.; Adamo, C.; Cammi, R.; Ochterski, J. W.; Martin, R. L.; Morokuma, K.; Farkas, O.; Foresman, J. B.; Fox, D. J. *Gaussian*, Gaussian Inc.: Wallingford CT, 2016.

[7]   Becke, A. D. *J. Chem. Phys.* **1993,** *98*, 1372-1377.

[8]   Lee, C.; Yang, W.; Parr, R. G. *Phys. Rev. B* **1988,** *37*, 785-789.

[9]   Vosko, S. H.; Wilk, L.; Nusair, M. *Can. J. Phys.* **1980,** *58*, 1200-1211.

[10]   Stephens, P. J.; Devlin, F. J.; Chabalowski, C. F.; Frisch, M. J. *J. Phys. Chem.* **1994,** *98*, 11623-11627.

[11]   McLean, A. D.; Chandler, G. S. *J. Chem. Phys.* **1980,** *72*, 5639-5648.

[12] Krishnan, R.; Binkley, J. S.; Seeger, R.; Pople, J. A. *J. Chem. Phys.* **1980,** *72*, 650-654.

[13] Binning, R. C.; Curtiss, L. A. *J. Comput. Chem.* **1990,** *11*, 1206-1216.

[14] McGrath, M. P.; Radom, L. *J. Chem. Phys.* **1991,** *94*, 511-516.

[15] Curtiss, L. A.; McGrath, M. P.; Blaudeau, J.-P.; Davis, N. E.; Binning, J., R. C.; Radom, L. *J. Chem. Phys.* **1995,** *103*, 6104-6113.

[16] Blaudeau, J.-P.; McGrath, M. P.; Curtiss, L. A.; Radom, L. *J. Chem. Phys.* **1997,** *107*, 5016-5021.

[17] Fuentealba, P.; Preuss, H.; Stoll, H.; Von Szentpály, L. *Chem. Phys. Lett.* **1982,** *89*, 418-422.

[18] Andrae, D.; Häußermann, U.; Dolg, M.; Stoll, H.; Preuß, H. *Theor. Chem. Acc.* **1990,** *77*, 123-141.

[19] Jr., T. H. D. *J. Chem. Phys.* **1989,** *90*, 1007-1023.

[20] Grimme, S.; Antony, J.; Ehrlich, S.; Krieg, H. *J. Chem. Phys.* **2010,** *132*, 154104.

[21] Marenich, A. V.; Cramer, C. J.; Truhlar, D. G. *J. Phys. Chem. B* **2009,** *113*, 6378-6396.

[22] Papajak, E.; Zheng, J.; Xu, X.; Leverentz, H. R.; Truhlar, D. G. *J. Chem. Theor. Comput.* **2011,** *7*, 3027-3034.

[23] Truhlar, D. G.; Cramer, C. J.; Lewis, A.; Bumpus, J. A. *J. Chem. Educ.* **2004,** *81*, 596.

[24] Jašík, J.; Žabka, J.; Roithová, J.; Gerlich, D. *Int. J. Mass Spectrom.* **2013,** *354–355*, 204-210.

[25] Jašík, J.; Navrátil, R.; Němec, I.; Roithová, J. *J. Phys. Chem. A* **2015,** *119*, 12648-12655.

[26] Becke, A. D. *J. Chem. Phys.* **1993,** *98*, 5648-5652.

[27] Miehlich, B.; Savin, A.; Stoll, H.; Preuss, H. *Chem. Phys. Lett.* **1989,** *157*, 200-206.

[28] Grimme, S.; Ehrlich, S.; Goerigk, L. *J. Comput. Chem.* **2011,** *32*, 1456-1465.

[29] Grimme, S.; Antony, J.; Ehrlich, S.; Krieg, H. *J. Chem. Phys.* **2010,** *132*, 154104.

[30] V., B. *J. Chem. Phys.* **2004,** *120*, 3059-3065.

[31] V., B. *J. Chem. Phys.* **2005,** *122*, 014108.

[32] Singh, B. K.; Polley, A.; Jana, R. *J. Org. Chem.* **2016,** *81*, 4295-4303.

[33] Grigorjeva, L.; Daugulis, O. *Org. Lett.* **2014,** *16*, 4684-4687.

[34] Zhu, W.; Zhang, D.; Yang, N.; Liu, H. *Chem. Commun.* **2014,** *50*, 10634-10636.

[35] Shang, R.; Ilies, L.; Asako, S.; Nakamura, E. *J. Am. Chem. Soc.* **2014,** *136*, 14349-14352.